Out-of-equilibrium many-body dynamics in Atomic, Molecular and Optical systems

A dissertation presented

by

Bingtian Ye

to

The Department of Physics

in partial fulfillment of the requirements

for the degree of

Doctor of Philosophy

in the subject of

Physics

Harvard University

Cambridge, Massachusetts

April 2024

Dissertation Advisor: Professor Norman Ying Yao Bingtian Ye

Out-of-equilibrium many-body dynamics
in Atomic, Molecular and Optical systems

Abstract

Recent advancements in atomic, molecular, and optical platforms have propelled the study of many-body physics into a new era. The ability to construct large ensembles of precisely manipulated elementary components is revolutionizing both the toolbox and the mindset for exploring the intricate relationship between microscopic details and macroscopic phenomena. This exploration lies at the heart of many-body physics, particularly in the context of out-of-equilibrium many-body dynamics. Indeed, the past decades have witnessed a resurgence of classic topics alongside the emergence of new inquiries in the field of many-body dynamics, covering a spectrum from fundamental dynamical properties to their practical applications in quantum technology. This thesis contributes to such a vibrant field by employing a combination of analytical and numerical methodologies to investigate various aspects of out-of-equilibrium dynamics, such as thermalization, hydrodynamics, and responses to drives. Furthermore, this study is intimately intertwined with experimental investigation, where empirical observations enrich theoretical frameworks, and theoretical predictions guide experimental pursuits and practical applications.

Contents

List of Tables

List of Figures

Citations to previously published work

Most of the contents of this thesis have appeared in print elsewhere. In order of appearance,

Chapter 2:

Bingtian Ye*, Francisco Machado*, Christopher D. White, Roger S. K. Mong, Norman Y. Yao, "Emergent hydrodynamics in nonequilibrium quantum systems", Phys. Rev. Lett., 125, 030601 (2020)

Chong Zu*, Francisco Machado*, Bingtian Ye*, Soonwon Choi, Bryce Kobrin, Thomas Mittiga, Satcher Hsieh, Prabudhya Bhattacharyya, Matthew Markham, Dan Twitchen, Andrey Jarmola, Dmitry Budker, Chris R. Laumann, Joel E. Moore, Norman Y. Yao , "Emergent hydrodynamics in a strongly interacting dipolar spin ensemble", Nature, 597, 45 (2021)

Pai Peng*, Bingtian Ye*, Norman Y. Yao, Paola Cappellaro, "Exploiting disorder to probe spin and energy hydrodynamics", Nat. Phys. 19, 1027 (2023)

Bingtian Ye*, Francisco Machado*, Jack Kemp*, Ross B. Hutson, Norman Y. Yao, "Universal Kardar-Parisi-Zhang dynamics in integrable quantum systems", Phys. Rev. Lett., 129, 230602 (2022)

David Wei, Antonio Rubio-Abadal, Bingtian Ye, Francisco Machado, Jack Kemp, Kritsana Srakaew, Simon Hollerith, Jun Rui, Sarang Gopalakrishnan, Norman Y. Yao, Immanuel Bloch, Johannes Zeiher, "Quantum gas microscopy of Kardar-Parisi-Zhang superdiffusion", Science, 376, 716 (2022)

Rahul Sahay*, Francisco Machado*, Bingtian Ye*, Chris R. Laumann, Norman Y. Yao, "Emergent ergodicity at the transition between many-body localized phases", Phys. Rev. Lett., 126, 100604 (2021)

Chapter 3:

Bingtian Ye, Francisco Machado, Norman Y. Yao, "Floquet phases of matter via classical prethermalization", Phys. Rev. Lett., 127, 140603 (2021)

Guanghui He*, Bingtian Ye*, Ruotian Gong, Zhongyuan Liu, Kater W. Murch, Norman Y. Yao, Chong Zu, "Quasi-floquet prethermalization in a disordered dipolar spin ensemble in diamond", Phys. Rev. Lett., 131, 130401 (2023)

Chapter 4:

Maxwell Block*, Bingtian Ye*, Brenden Roberts, Sabrina Chern, Weijie Wu, Zilin Wang, Lode

Pollet, Emily J. Davis, Bertrand I. Halperin, Norman Y. Yao, "Scalable spin squeezing as finite temperature easy-plane magnetism", Nat. Phys. (2024)

Guillaume Bornet*, Gabriel Emperauger*, Cheng Chen*, Bingtian Ye*, Maxwell Block*, Marcus Bintz, Jamie A. Boyd, Daniel Barredo, Tommaso Comparin, Fabio Mezzacapo, Tommaso Roscilde, Thierry Lahaye, Norman Y. Yao, Antoine Browaeys, "Scalable spin squeezing in a dipolar Rydberg atom array", Nature, 621, 728 (2023)

Chapter 5:

Emily J. Davis*, Bingtian Ye*, Francisco Machado*, Simon A. Meynell, Weijie Wu, Thomas Mittiga, William Schenken, Maxime Joos, Bryce Kobrin, Yuanqi Lyu, Zilin Wang, Dolev Bluvstein, Soonwon Choi, Chong Zu, Ania C. Bleszynski-Jayich, Norman Y. Yao, "Probing many-body dynamics in a two-dimensional dipolar spin ensemble", Nat. Phys. 19, 836 (2023)

Ruotian Gong, Xinyi Du, Eli Janzen, Vincent Liu, Zhongyuan Liu, Guanghui He, Bingtian Ye, Tongcang Li, Norman Y. Yao, James H. Edgar, Erik A. Henriksen, Chong Zu, "Isotope engineering for spin defects in van der Waals materials", Nat. Comm. 15, 104 (2024)

To my parents

Acknowledgments

First and foremost, I express my deepest gratitude to my research advisor, Prof. Norman Yao. Throughout our journey together, Norm has been more than just an patient advisor and mentor for my research; he has also been a trusted friend and confidant in my life. With his discerning eyes identifying both my strengths and weaknesses, he consistently provided me with challenging yet appropriate research projects. Additionally, his encouragement to cultivate and explore my own ideas has allowed me to form my research taste. Norm is among those I turn to first when making life decision, as he always offers sincere and comprehensive considerations and recommendations. In every aspect, I am immensely grateful for how Norm has illuminated both the path of my scientific inquiry and the corridors of my personal growth.

Heartfelt appreciation extends to my qualification exam and thesis committee members, Prof. Mikhail Lukin and Prof. Ashvin Vishwanath. Serving as additional pairs of eyes on my research topics, they have provided invaluable insights and feedback. Their diverse expertise and guidance have broadened my perspectives and greatly influenced my research trajectory, ensuring the relevance and innovation of my work.

Next, I would like to acknowledge all my collaborators within and outside of the Yao group (including but not limited to Francisco Machado, Prof. Chong Zu, Maxwell Block, Jack Kemp, Prof. Emily Davis, Rahul Sahay, Weijie Wu, Zilin Wang, Thomas Mittiga, Phil Crowley, Sabrina Chern, and Pai Peng, Guanghui He, Brenden Roberts, Chris White, Guillaume Bornet, Gabriel Emperauger, Cheng Chen, David Wei, Antonio Rubio, Johannes Zeiher, Ross Hudson, Simon Hollerith, Lilian Hughes, Ruotian Gong) for their dedication and collaboration throughout this journey. Special recognition goes to Francisco, whose consistent presence and collaboration in nearly all projects I have worked on have been instrumental in my growth as a researcher. Also, I am deeply appreciative of Chong, my closest experiment collaborator, for entrusting me as his primary theorist collaborator during both his postdoc and early career as a professor. With Maxwell, crafting my favorite project together was an immensely rewarding experience filled with great fun. Without their brilliance, insights and contribution, many of my projects would have hardly come to fruition.

In addition, I offer my deepest appreciation also to all the professors and senior physicists who

have treated me as, or more precisely, shaped me into an independent researcher and valued colleague. Special thanks are due to Prof. Ehud Altman, Prof. Soonwon Choi, Prof. Bertrand Halperin, Prof. Chris Laumann, Prof. Roger Mong, Prof. Joel Moore, Prof. Sarang Gopalakrishnan, Prof. Romain Vasseur, and Prof. Mike Zaletel for their invaluable teachings in many-body physics, guiding me from foundational knowledge to the frontiers of the field. I thank Prof. Laumann and Prof. Choi, who have essentially served as my additional research advisors, for taking me under their wings in my early years and providing invaluable guidance throughout my entire PhD journey. I thank Prof. Moore for generously dedicating his time to answering my questions and resolving my confusion in many late nights. I thank Prof. Halperin for his keen insights and wisdom, consistently leading me to the most precise and elegant physics picture. He led by example, showing me that one is never too old to work as a physicist. I am also indebted to Prof. Immanuel Bloch, Prof. Antoine Browaeys, Prof. Paola Cappellaro, Prof. Ania Jayich, and Prof. Jun Ye for introducing me to all the wonders, marvels and magics in AMO experiments.

Furthermore, my sincere gratitude goes to my office mates and everyone else in the Yao group (including but not limited to Tommy Schuster, Kam Akkaravarawong, Greg Meyer, Chris Olund, Prof. Quntao Zhuang, Prof. Marin Bukov, Satcher Hsieh, Pra Bhattacharyya, Marcus Bintz, Julia Wei, Andrea Pizzi, Yi Tan, Duy Vu, Che Liu, Haopu Yang, and Tasuku Ono) for their companionship, camaraderie, and the countless stimulating discussions we have shared about both physics and life. Special thanks to Tommy and Kam for creating a blend of weekday physics discussions and weekend basketball games, striking a perfect balance for me. I am also grateful to the Harvard physics community (including but not limited to Yicheng Bao, Nathan Leitao, Martin Leigh, Haoyang Gao, Alec Douglas, Lin Su and Yu Wang), as well as the Berkeley physics community (including but not limited to Canxun Zhang, Yimu Bao, Shubhayu Chatterjee, Zhehao Dai, Johannes Hauschild, Yantao Wu, Dan Park, and Sajant Anand) for their warmth and support. Their presence has made our workspace a vibrant hub of intellectual exchange. Special appreciation goes to Yicheng for organizing BBQ-plus-physics gatherings, and to Yimu for coordinating hotpot-plus-physics parties. I am particularly thankful to Canxun, for his enduring friendship throughout five years as my housemate, twelve years as my physics buddy and fifteen years as my schoolmate.

Lastly, but most importantly, I wish to express my deepest appreciation to my family for their understanding, support and companionship. I owe a tremendous debt of gratitude to my parents for their encouragement, especially during the challenging period of our separation across two continents for over three years of the pandemic. Being non-physics professionals, they possess a level of understanding and appreciation for my work that exceeds that of the average person. Being home-education professionals, they show remarkable familiarity with almost all the efforts I have undertaken. Their unwavering care for me has been a constant source of strength throughout my personal and academic journey. To my wife, I am eternally grateful. Much of my knowledge about cold atom experiments comes from her, from laser locking and beam shaping to double-pass AOM. Through her I have come to realize that beyond the oversimplified two-level systems, there are naughty real atoms that need to be babysat to stay cool. She even successfully taught me how to couple optical fibers with my clumsy hands. Beyond physics, and most significantly, I deeply appreciate her indispensable role [1] in every aspect of my personal life, where her love have been the cornerstone of my happiness and success.

[1] As the plan A.

Chapter 1

Introduction

1.1 Out-of-equilibrium many-body dynamics: A new frontier for atomic, molecular, and optical physics

In the vast landscape of physics research, three primary frontiers stand out prominently, two of which appear more natural to contemplate: astrophysics, exploring the cosmos at the *grandest scales*, and particle physics, probing the *tiniest scales* of matter. Yet, amidst these well-trodden paths lies a third, less apparent but equally profound direction, many-body physics, focusing on universal phenomena in large ensembles of physical objects and typically transcending the scale of each individual object. Within many-body systems, although interactions often distill to a few-body essence, the ensuing dynamics unfold with remarkable complexity compared to few-body systems. This duality underscores a fundamental principle: while collective many-body behaviors intimately rely on the microscopic details of few-body interactions, they often arise, seemingly independent of these microscopic intricacies. Indeed, new principles sometimes emerge solely from the sheer abundance of objects involved.

Historically, the study of emergent many-body phenomena has been tightly linked with condensed matter physics and material science. These systems, inherently many-body interacting, are often regarded as comprising an infinite number of degrees of freedom, thus residing in what is termed as the thermodynamic limit. In contrast, atomic, molecular and optical (AMO) physics, initially centered its investigation around few-body phenomena, such as atom and molecule spectroscopy. Only in recent decades has there been a *discernible but natural* shift in focus towards the exploration of many-body phenomena within AMO systems.

In theoretical study of many-body physics, the concept of toy models, or minimum models, plays a central role. A toy model possesses the minimum microscopic properties necessary for the macroscopic collective behaviors of interest, and in essence acts as a bridge between them in any physical system. However, real-world condensed matter systems often deviate significantly from idealized toy models. In practice, condensed matter physics typically commence the explorations from macroscopic behaviors, with considerable effort dedicated to making appropriate approximation of a complicated Hamiltonian, isolating the relevant degrees of freedom while discarding the irrelevant

Platform	Building Blocks	Interaction	Geometry
NMR [1–3]	Nuclear Spins	Magnetic Dipolar	$d = 1, 2, 3$ Regular lattice
Solid-state Spin Defects [4–9]	Electronic Spins	Magnetic Dipolar	$d = 2, 3$ Random position
Trapped Ion [10–16]	Atomic Ions (mostly alkali-earth)	Tunable Long-Range from Coulomb-collective Motion	$d = 1$ Disorder in coupling
Atoms in Cavity [17–21]	Neutral Atoms or Photons	Photon-Mediated Long-range or All-to-all coupling	Effectively $d = 0$
Photonics [22–28]	Photon	Arbitrary two-body	—
Superconducting Circuit [29–37]	Superconducting LC Oscillator	Nearest-neighbor or Long-range [1]	$d = 1, 2$
Optical Lattice [38–43]	Neutral Atoms (mostly alkali, alkali-earth)	Hubbard and Hopping	$d = 1, 2, 3$ Regular lattice
	Molecules (alkali-like, bi-alkali)	Electric Dipolar	
Tweezer Array [44–46]	Rydberg Atoms (alkali, alkali-earth)	Van der Waals or Magnetic Dipolar	$d = 1, 2$ Arbitrary geometry
	Molecules (alkali-like, bi-alkali)	Electric Dipolar	

Table 1.1: Overview of contemporary quantum platforms from the perspective of building controllable many-body quantum platforms from elementary quantum objects. In addition to the listed systems composed of any single type of elementary building blocks, there are also hybrid platforms combining various types [47–55].

weakly-coupled one, and ultimately leading to a connection with a toy model. This immediately raises the question: are there scenarios in which we can exclusively focus on pristine toy models? To put it in another way, how relevant are these toy models for experimental validations and practical applications?

Recent advancements in AMO physics–the ability to build relatively large many-body systems with the previously well-studied individual degrees of freedom–have provided partial answers to these inquiries. In contrast to condensed matter physics, a reversed perspective is often adopted for AMO systems. Here, microscopic details of interactions between individual degrees of freedom are usually well-understood and well-controlled. Consequently, these few-body systems serve as clean and simple

[1] Conventional approach to couple superconducting qubits by an intermediate electrical coupling circuit is inherently limited to nearest-neighbor coupling. Long-range interaction is enabled by recent developement of quantum bus, usually implemented as a microwave cavity [34–37].

building blocks for constructing many-body systems. However, the step of construction has long posed a significant challenge in AMO experiments. Nonetheless, the experimental techniques in various types of AMO systems have developed over the past decade, facilitating the creation of many-body systems with a diverse range of building blocks, spanning from natural objects such as photons, electrons, atoms, ions and molecules to "artificial atoms" like superconducting LC oscillators and quantum dots [56–63]. Each of these blocks possesses unique microscopic features, thereby paving the way for innovative explorations in a large variety of many-body phenomena (Table 1.1).

This systematic bottom-up construction of many-body systems in experiments yields a profound impact on theoretical investigations into many-body physics. Precise control of the microscopic details enables faithful realization of the toy models in experimental setups, allowing direct verification and exploration of the dictionary between microscopic details and emergent many-body behaviors predicted by theory. Furthermore, versatile manipulation of microscopic degrees of freedom has spurred the development of theoretical frameworks aimed at precisely designing many-body systems, which offers significant potential for practical applications. Indeed, the emergence of the entire field of quantum information, including quantum simulation and computation, quantum communication, and quantum metrology, owes much to the recent development in AMO physics [64–88].

Accompanied with the increasingly precise control of the microscopic details comes a parallel advancement of time-resolved and space-resolved measurements. In the context of many-body systems, this progress synchronizes with the shift in research focus from equilibrium to out-of-equilibrium dynamical properties. From an application standpoint, controlled dynamics, rather than mere equilibrium, of a system is almost a necessary starting point. A prime example is the long-term goal of building quantum computers, which essentially requires the generation of arbitrary quantum many-body dynamics. From a theory perspective, the exploration of dynamical properties holds significant importance but remains persistently challenging. While statistical mechanics has emerged as a simple yet powerful framework to capture the physics of many-particle systems in or close to thermal equilibrium over the past century, the dynamics of systems brought out of equilibrium, often referred to as quench dynamics, become notably more complicated and lack a unified theoretical description. Even for specific systems and simple product initial states, figuring out the subsequent

dynamics is typically a formidable task in both analytical and numerical studies.

The thesis will focus on out-of-equilibrium dynamical phenomena across a spectrum of many-body systems. These systems are in tight relation with the contemporary topics in AMO physics and quantum science, particularly quantum simulation and quantum metrology. For each topic, the thesis will offer theoretical investigations, usually involving a combination of analytical approaches and numerical simulations. Simultaneously, these theoretical investigations will be complemented by either a corresponding experimental study or a concrete experimental proposal, ensuring a comprehensive exploration of the subject matter.

1.2 Equilibration of quantum many-body systems

Equilibrium in the context of many-body systems refers to a status whose macroscopic properties remains time-invariant. The well-established theory of statistical mechanics provides a simple framework for describing equilibrium systems, defined through microcanonical ensemble

$$\hat{\rho}_{\text{micro},E} \propto \sum_{\epsilon \in [E, E+\delta E]} |\epsilon\rangle\langle\epsilon|, \tag{1.1}$$

or canonical ensemble

$$\hat{\rho}_{\text{canon},\beta} \propto e^{-\beta \hat{H}} = \sum_{\epsilon} e^{-\beta\epsilon} |\epsilon\rangle\langle\epsilon|. \tag{1.2}$$

In stark contrast, Understanding out-of-equilibrium systems proves significantly more challenging. Yet, empirical evidence suggests a universal property for such systems: they almost inevitably evolve towards equilibrium over time, a phenomenon known as thermalization. During the thermalization process, observables tend to approach values consistent with those calculated for a thermal ensemble [89–95]. To be more precise, for a physical observable $\hat{O}$, the infinite-time average

$$\mathcal{O}_\infty := \lim_{T\to\infty} \frac{1}{T} \int_0^T \langle \hat{O} \rangle dt, \tag{1.3}$$

agrees with that of a microcanonical (or canonical) ensemble

$$\mathcal{O}_\infty := \lim_{T\to\infty} \frac{1}{T} \int_0^T \langle \hat{O} \rangle dt = \mathcal{O}_{\text{micro},\langle \hat{H} \rangle} := \text{Tr}[\hat{\rho}_{\text{micro},\langle \hat{H} \rangle} \hat{O}], \tag{1.4}$$

where the energy $\langle \hat{H} \rangle$ of the microcanonical ensemble is determined to match the dynamical system. A stronger statement also requires the fluctuation of the observable

$$\delta\mathcal{O}_\infty^2 := \lim_{T\to\infty} \frac{1}{T} \int_0^T \langle (\hat{O} - \mathcal{O}_\infty)^2 \rangle dt \tag{1.5}$$

to agree with the ensemble value

$$\delta\mathcal{O}^2_{\text{micro},\langle \hat{H} \rangle} := \text{Tr}[\hat{\rho}_{\text{micro},\langle \hat{H} \rangle} \hat{O}^2] - \text{Tr}[\hat{\rho}_{\text{micro},\langle \hat{H} \rangle} \hat{O}]^2. \tag{1.6}$$

In open systems, thermalization toward a equilibrium state often manifests as a system becoming increasingly entangled with its environment, However, thermalization of closed systems is more

subtle. Intuitively, the remaining parts of the whole system acts as a thermal bath for sufficiently small subsystems [89, 91–96]. While this argument also works for both classical systems from deterministic initial states and quantum systems from pure initial states, the latter is more straighforward to illustrate. In particular, instead of considering an arbitrary operator, one can restrict the equilibration condition (Eq. 1.3) to few-body observables $\langle \hat{O} \rangle$. An equivalent statement can be made for the reduced density matrices of small enough subsystems: they approach a macrocanonical ensembles $\hat{\rho}_{\text{sub}} \propto e^{-\beta \hat{H}_{\text{sub}}}$ at late times.

Despite this simple intuition for equilibration in close systems, a plenty of questions remain unanswered, at least partially. Two very natural directions along this line arise. First, it is natural to ask whether a system can fail to thermalize and thus evade equilibrium even at infinitly long times. The prevailing conjectured many-body localization phase of disordered quantum systems is one of the promising candidate, but much about it still remains unknown [90, 95, 97–108]. Some other examples may not completely evade thermalization, but the equilibration process takes parametrically long times, known as prethermalization [109–115]. Second, what are the exact procedures for a quantum many-body system to thermalize? In general, during thermalization process, different parts of the system exchange information and conserved quantities, which should exhibit completely distinct behaviors. In particular, information scrambling is closely related to the loss of local quantum coherence, but the transport of conserved quantities is relatively independent of that and can be a purely classical process. This further leads to the question of how certain classical behaviors, such hydrodynamics, emerge in quantum systems.

Chapter Two will primarily explore several questions along these two lines. Moreover, the overarching concept of thermalization will also serve as the foundation for investigating a few other questions about quantum dynamics in subsequent chapters. For orientation, we introduce some fundamental background knowledge about thermalization in this section.

1.2.1 Eigenstate structure of quantum thermalization

In closed quantum systems, the properties of the eigenstates contain all information necessary for understanding their dynamics. Therefore, one approach to comprehending and analyzing thermlization

is to inspect the eigenstate structure of the system. Indeed, the current best understanding, relying on a few natural assumptions about eigenstate properties, can demonstrate the presence of thermalization in generic interacting quantum systems. The essence of these assumptions is the conjecture that a thermalizing Hamiltonian, when projected into a small energy window, resembles random matrices [89–93, 96, 116–118].

The most important result is the eigenstate thermalization hypothesis (ETH) [89–96, 106]. The motivation for ETH is simple. Decomposing the initial in the eigenstate basis, the infinite-time average (Eq. 1.3) becomes

$$\mathcal{O}_\infty = \lim_{T\to\infty} \frac{1}{T} \sum_{\epsilon,\epsilon'} \int_0^T dt e^{-i(\epsilon-\epsilon')t} c_\epsilon c_{\epsilon'}^* \langle \epsilon' | \hat{O} | \epsilon \rangle = \sum_\epsilon |c_\epsilon|^2 \langle \epsilon | \hat{O} | \epsilon \rangle, \tag{1.7}$$

where we assume no degeneracy. Similarly, the condition for the fluctuation (Eq. 1.5) becomes

$$\begin{aligned} \delta\mathcal{O}_\infty^2 &= \lim_{T\to\infty} \frac{1}{T} \sum_{\epsilon,\epsilon'} \int_0^T dt e^{-i(\epsilon-\epsilon')t} c_\epsilon c_{\epsilon'}^* \Big(\langle \epsilon' | \hat{O}^2 | \epsilon \rangle - 2\mathcal{O}_\infty \langle \epsilon' | \hat{O} | \epsilon \rangle + \mathcal{O}_\infty^2 \Big) \\ &= \sum_\epsilon |c_\epsilon|^2 \langle \epsilon | \hat{O}^2 | \epsilon \rangle - \mathcal{O}_\infty^2. \end{aligned} \tag{1.8}$$

Comparison between these two expressions and the microcanonical ensemble values motivates the ETH

$$\langle \epsilon' | \hat{O} | \epsilon \rangle = \delta_{\epsilon,\epsilon'} \mathcal{O}_{\text{micro},\bar{E}} + e^{-S_{\bar{E}}/2} R_{\epsilon,\epsilon'} f(\bar{E}, \Delta\epsilon), \tag{1.9}$$

where $S_{\bar{E}}$ is the thermodynamic entropy, $R_{\epsilon,\epsilon'}$ is a normal distributed random number, $\bar{E} = (\epsilon + \epsilon')/2$ and $\Delta\epsilon = (\epsilon - \epsilon')$ are the average energy and the energy difference of the two states, respectively. Crucially, ETH assumes that the expectation value of the local observable $\mathcal{O}_{\text{micro},\bar{E}}$ and the spectral function $f(\bar{E}, \Delta\epsilon)$ are smooth in $\bar{E}$ and $\Delta\epsilon$. Moreover, the spectral function is related with the fluctuation of the microcanonical ensemble:

$$\delta\mathcal{O}_{\text{micro},E}^2 = e^{-S_E} \int f(E, \Delta\epsilon)^2 \, d(\Delta\epsilon). \tag{1.10}$$

Seminal work has demonstrated that ETH is sufficient to ensure thermalization, given that energy fluctuation of δE determined by the initial state is sufficient small. Indeed, for any locally interacting system of size N, an initial state without macroscopic superposition has a sub-extensive energy fluctuation, i.e., $\delta E = \langle \hat{H}^2 \rangle - \langle \hat{H} \rangle^2 \propto \sqrt{N}$ (in comparison, energy is always extensive $\langle \hat{H} \rangle = \bar{E} \propto$

N), and thus naturally satisfies the above requirement. Hence, the diagonal (first) elements in Eq. 1.9 ensures that the infinite-time average agrees with a microcanonical ensemble at energy $\langle \hat{H} \rangle$:

$$\mathcal{O}_\infty = \sum_\epsilon |c_\epsilon|^2 \mathcal{O}_{\text{micro},\bar{E}} + e^{-S_{\bar{E}}/2} \overline{R_{\epsilon,\epsilon'}} f(\bar{E}, 0) = \mathcal{O}_{\text{micro},\langle \hat{H} \rangle}. \tag{1.11}$$

The off-diagonal (second) elements in Eq. 1.9 leads to the agreement between the time-averaged fluctuation with the microcanonical ensemble with energy $\bar{E}$ and energy fluctuation δE:

$$\delta\mathcal{O}_\infty^2 = \sum_{\epsilon,\epsilon'} |c_\epsilon|^2 \langle \epsilon | \hat{O} | \epsilon' \rangle \langle \epsilon' | \hat{O} | \epsilon \rangle - \mathcal{O}_\infty^2 = \int e^{-S_{\bar{E}}} \overline{R_{\epsilon,\epsilon'}^2} f(\bar{E}, \Delta\epsilon)^2 \, d(\Delta\epsilon) = \delta\mathcal{O}_{\text{micro},\langle \hat{H} \rangle}. \tag{1.12}$$

Note that although ETH is sufficient to guarantee thermalization, it remains an open question whether this is also a necessary condition [93–95].

Another related characteristic of thermalizing systems is the level statistics, more directly descent from random matrix theory [93, 116, 117, 119–122]. Here, the intuition is the level repulsion or avioded level crossing: a perturbation connects two approximately degenerate eigenstates will largely lift the degeneracy, given that the perturbation strength is larger than their original small gap. For generic thermalizing system, the matrix element of any local operator $\hat{O}$ between nearby eigenstates $e^{-S_{\bar{E}}/2} f(\bar{E}, \Delta\epsilon)$ decays at mort algebraically for $\Delta\epsilon \lesssim J_{\text{local}}$ [2], and thus is exponentially large than the many-body energy gaps. Therefore, adding any small perturbation $\lambda\hat{O}$ on a thermalizing Hamiltonian will lead to level repulsion between many-body engenstates. Considering a series of thermalizing Hamiltonians differing by a small perturbation $\lambda\hat{O}$, they can be thought of to relate to each other by adding $\lambda\hat{O}$, and should therefore all exhibit level repulsion. As the such repulsion happens between any pair of eigenstates, the energy gaps should follow a more homogeneous distribution [3]. Taking one step further, the random coupling with roughly uniform magnitude between any pair of eigenstates within $\Delta\epsilon \ll J_{\text{local}}$ suggests that the effective Hamiltonian in this energy window can be well approximated by a random matrix. Indeed, for static systems with time-reversal symmetry (i.e.,

[2] This decay saturates at the Thouless energy.

[3] Here we assume that the Hamiltonian does not have any symmetry, i.e., it does not have any conserved quantities. If the Hamiltonian has symmetries but still non-integrable, level repulsion applies to each symmetry sector independently. However, if the Hamiltonian is integrable, there are too many symmetries to resolve and level repulsion is practically hard to analyze.

all matrix elements in the Hamiltonian are real), such effective random Hamiltonian is captured by the so-called Gaussian orthogonal ensemble (GOE), predicting a Wigner–Dyson distribution for adjacent energy gaps $\delta_n = \epsilon_{n+1} - \epsilon_n$ [4] [93, 116, 117, 119–122]. In contrast, non-thermalizing systems do not exhibit level repulsion so that the many-body eigenenergies are random and uncorrelated, leading to a Poisson distribution for the adjacent energy gaps [100, 124–126].

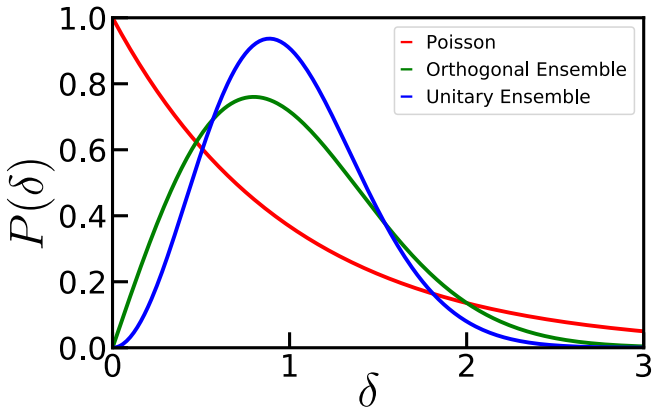

Figure 1.1: Statistics of energy gaps δ in non-thermalizing and thermalizing quantum systems are described by Poisson distribution and random matrix theory, respectively. For non-thermalizing systems, the energy gap has increasing probability as $\delta \to 0$. For thermalizing systems with [without] time reversal symmetries, captured by orthogonal[unitary] ensembles, the energy gap has a vanishing probability as $\delta \to 0$, which reflects the existence of level repulsion. Note that the energy gap distribution is agnostic of whether the system is static (Gasussian ensemble) or time-periodic (circular ensemble).

We conclude the above discussion with two complementary perspectives to view the relation between quantum thermalization and ETH as well as the random matrix theory. First, a pessimistic perspective is that ETH only converts one hypothesis that generic closed quantum systems always thermalize to another that they in general have certain eigenstate structures. Nevertheless, there is a more optimistic perspective: connecting thermalization to the eigenstate structure is a great achievement itself. Practically, this connection provides a way to numerically (and sometimes analytically) investigate whether a specific system thermalizes. Indeed, in the study of systems that escape thermalization, e.g., many-body localized systems, the energy gap distribution is the most effective diagnostic.

Although originated from the non-interacting counterpart Anderson localization [127, 128], many-

[4] Static systems without time-reversal symmetry are described by the Gaussian unitary ensemble (GUE), and the corresponding distribution of the adjacent energy gap is the same as the normalized spacing between the zeros of the Riemann's zeta function. Periodically driven (Floquet) systems with discreted time translation symmetry are described by the circular orthogonal ensemble (COE) and circular unitary ensemble (CUE) [123].

body localization exhibits fundamentally different features [90, 95, 97, 106–108]. In general, non-interacting systems never truly thermalizes, and therefore Anderson localization features disorder-induced localized wavefunctions but does not contrast clean systems in thermalization properties. In comparison, one defining feature of many-body localization is the emergent integrability, i.e., extensive number of quasilocal integrals of motion [129–132]. Therefore, similar to truly integrable systems, energy gaps of MBL systems follow Poisson distribution rather than Wigner-Dyson distribution. A convenient metric that distinguishes the two distributions is the so-called r-ratio between adjacent energy gaps, defined as

$$\langle r_n \rangle = \left\langle \frac{\min\{\delta_n, \delta_{n+1}\}}{\max\{\delta_n, \delta_{n+1}\}} \right\rangle \tag{1.13}$$

where $\langle \cdots \rangle$ denotes averaging over eigenstates (usually within a small energy window). Crucially, $\langle r_n \rangle_{\mathrm{POI}} = 2\log 2 - 1 \approx 0.3863$ Poisson distribution and $\langle r_n \rangle_{\mathrm{GOE}} \approx 0.5359$ for Wigner-Dyson distribution [5] [99, 100, 123, 134, 135]. The level statistics reflects the time dynamics, at any late times, the system will always have memory of the local details of the initial state and does not approach the thermal ensemble only determined by the initial energy [131, 136].

1.2.2 Two-step equilibration

For thermalizing many-body quantum systems, understanding how they reach thermal equilibrium is a natural inquiry. Here, we focus on systems with locality, meaning that each part of the systems solely interacts its neighbors only via its boundary. In such systems, achieving global equilibrium involves two steps, reflecting the equilibration of two distinct types of quantities: non-conserved and conserved quantities [137–140]. As a subsystem becomes significantly entangled with the rest of the system, the non-conserved local quantities supported only by that subsystem tend to forget their original values and approach their thermal equilibrium values. This process aligns with the maximal entropy principle. In contrast, local conserved quantities, such energy density, can only change via transport into other parts of the system, a process that occurs much more slowly. Combining these observations leads to the following self-consistent picture. In the first step of equilibration, small subsystems

[5] For GUE, COE and CUE, the corresponding r-ratios are $\langle r_n \rangle_{\mathrm{GOE}} \approx 0.6027$, $\langle r_n \rangle_{\mathrm{COE}} \approx 0.5269$ and $\langle r_n \rangle_{\mathrm{CUE}} \approx 0.5965$, respectively [123, 133].

approach local thermal equilibrium, described by a Gibbs ensemble whose properties are determined by the local density of a complete set of conserved quantities [137–140]. In general, such local densities exhibit inhomogeneity across the entire system, reflecting spatial variation of of temperature, pressure, chemical potential, etc. In the second step, the local conserved quantities get redistributed via transport process. Over an an extensively long time, the entire system eventually approaches global equilibrium. This second step is often referred to as the emergent hydrodynamics [141–148]. Specifically, by defining the density of the conserved quantities in a coarse-grained way, so that the underlying discrete structure, such as lattice structure, becomes irrelevant, one can then attempt to write down the continuous differential equations to capture transport dynamics (formally analogous to the study of fluid motion).

While diffusion represents the most common hydrodynamic behavior, characterized by the familiar diffusion equation $\partial_t^2 q = D\nabla^2 q$, the presence of disorder, symmetry types, and integrability can significantly impact the hydrodynamics in quantum systems, making it a vibrant area of research. For instance, disorder, even if not strong enough to prevent thermalization, may result in a parametric slow-down of transport, leading to investigations into subdiffusion [149–153]. Symmetry type can also qualitatively alter the transport dynamics: any continuous symmetry larger than $U(1)$ gives rise to more than one conserved quantity; the interplay between these conserved quantities sometimes requires a set of coupled hydrodynamical equations to capture the their transport behaviors.

Integrability plays a even more important role. The number of conserved quantities become extensive with system size in integrable systems, requiring an extensive number of hydrodynamical equations. From a complementary perspective, quasi-particles in integrable systems have a infinitely long lifetime so that the system never completely loses the memory about the initial state and thus never "truly" thermalizes. Consequently, a different framework is required to describe the dynamics of such systems. The key concepts behind this framework are the generalized Gibbs ensemble (GGE) and the generalized hydrodynamics (GHD) [154–157]. Under maximal-entropy principles, Gibbs states of a non-integrable are defined by $\rho_{\text{Gibbs}} = e^{-\beta H + \sum_i \mu_i Q_i}$, where $\{Q_i\}$ are a finite set of conserved quantities and $\{\mu_i\}$ are the corresponding chemical potentials [158–162]. In integrable systems, the GGE replaces Gibbs ensemble by taking into account an infinite set of conserved quantities.

Correspondingly, the two-step equilibration process of integrable systems is slightly modified: the system first approaches local equilibration characterized by a local GGE, and then all the conserved quantities transport across the system captured by the movement of quasi-particles rather than an infinite set of hydrodynamical equations for conserved quantities themselves [163–169]. Roughly speaking, quasi-particle basis and conserved quantity basis are related by a linear transform, but simplifying the analyze. One might wonder how a finite-size subsystem reflects the existence of an infinite number of conserved quantities. Generally, only the conserved quantities with a size smaller than the coarse-graining lengthscale have well-defined hydrodynamics. In most cases, these hydrodynamics are effectively decoupled from the sufficiently large quasi-particles, such as the spin hydrodynamics in the anisotropic one-dimensional nearest neighbor XXZ model, resulting in a closed set of equations [170–172]. However, in some exotic scenarios, such the KPZ-type hydrodynamics one-dimensional nearest-neighbor Heisenberg model, increasingly larger quasi-particles become relevant as the system equilibrates [171–173]. In these cases, the coarse graining lengthscale should be treated as a dynamic quantity, and there is likely not sharp separation between the local equilibration process and hydrodynamics.

1.3 Periodically driven systems

At a very high level, Floquet (periodically driven) systems can be viewed as sitting between systems with static Hamiltonians and those with very generic time-dependent Hamiltonians. On the one hand, Floquet systems are intrinsically non-equilibrium. Apparently, a quantum state (density matrix) cannot always be an eigenstate (Gibbs ensemble) of a time-dependent Hamiltonian as time changes. On the other hand, the Hamiltonian of Floquet systems still shares much similarity with a static one, as it remains simple and regularly repeats itself in the temporal direction. From the perspective of symmetry, continuous time-translation symmetry, which is the defining feature of static Hamiltonians, is not completely broken in Floquet systems; instead, it downgrades to discrete time-translation symmetry. The combination of these features makes it possible to transfer a few concepts, such as thermalization and phases of matter, from static to Floquet systems, albeit with significant modifications and the introduction of novel ingredients. In this section, I will introduce a few basic yet universal properties of Floquet systems, providing the background knowledge and motivation for the research results presented later.

1.3.1 Floquet Hamiltonian and quasi-energy

The most generic Hamiltonian for Floquet systems only requires periodicity in time, i.e., $H(t) = H(t+T)$ with T the Floquet period and $\omega = \frac{2\pi}{T}$ denoting the Floquet frequency. Thanks to the periodicity, solving the Floquet dynamics in the quantum case reduces to the study of two unitary operators:

$$U_F = \mathcal{T} e^{-i\int_0^T H(t)\,dt}, \tag{1.14}$$

$$U_0(t_0) = \mathcal{T} e^{-i\int_0^{t_0} H(t)\,dt}, \quad \text{for } t_0 < T. \tag{1.15}$$

In particular, U_F generates the evolution between integer multiples of the driving period, and $U(t_0)$ determines the evolution (usually referred to as micro-motion) within a driving period. The properties of the former are encoded in its eigenstates $|\psi_\alpha\rangle_F$ and the corresponding quasi-energy defined by ϵ_α via [174–178]

$$U_F|\psi_\alpha\rangle_F = e^{-i\epsilon_\alpha T}|\psi_\alpha\rangle. \tag{1.16}$$

Crucially, the quasi-energy is not unique and is determined only up to an additional integer multiples of $\frac{2\pi}{T}$, reflecting the freedom to add 2π phases when obtaining the Floquet Hamiltonian H_F as the logarithm of U_F [174–178]:

$$U_F = e^{-iH_F T}. \tag{1.17}$$

Similar to static models, these eigenstates provide a basis for the Floquet dynamics; they are stationary if one only measures the system at integer multiples of Floquet periods. Using the additional unitary operator U_0, one can construct the Floquet eigenstates $|\psi_\alpha(t)\rangle_F = e^{-i\epsilon_\alpha mT} U_0(t - mT)|\psi_\alpha\rangle$ with $m = \lfloor \frac{t}{T} \rfloor$, which satisfies $i\frac{d|\psi_\alpha(t)\rangle_F}{dt} = H(t)|\psi_\alpha(t)\rangle_F$ for all time. This explicit construction reproduces the Floquet-Bloch theorem, stating that any Floquet eigenstate must be a product of time periodic state and a non-periodic phase factor, i.e., $|\psi(t+T)\rangle_F = e^{-i\epsilon T}|\psi(t)\rangle_F$.

1.3.2 Floquet-Magnus expansion and Floquet heating

In most of the Floquet systems, the stroboscopic evolution at integer periods are enough to reflect the dynamical features, making the time-independent Floquet Hamiltonian, H_F, the focal point. While it is possible to calculate H_F from U_F, this process is generally more complex and less informative, since U_F is hard to compute at the first place and H_F does not contain more information than U_F. Alternatively, a more practical and meaningful pursuit is to construct H_F directly from $H(t)$. Indeed, the Floquet-Magnus expansion offers a partial solution, which aims to construct a perturbative series in T, or equivalently in $1/\omega$ [175–178]:

$$H_F = \sum_m \frac{1}{\omega^m} H_F^{(m)}. \tag{1.18}$$

The first few terms are

$$H_F^{(0)} = \frac{1}{T}\int_0^T dt H(t) = H_0, \tag{1.19}$$

$$H_F^{(1)} = \frac{2\pi}{2iT^2}\int_0^T dt \int_0^t dt' [H(t), H(t')] = \sum_{k\neq 0} \frac{[H_{-k}, H_k]}{2k}, \tag{1.20}$$

$$\begin{aligned} H_F^{(2)} &= -\frac{(2\pi)^2}{6T^3}\int_0^T dt \int_0^t dt' \int_0^{t'} dt'' \left([H(t),[H(t'),H(t'')]] + [H(t''),[H(t'),H(t)]]\right) \\ &= \sum_{k\neq 0} \frac{[[H_{-k}, H_0], H_k]}{2k^2} + \sum_{n\neq 0,k} \frac{[[H_{-k}, H_{k-k'}], H_{k'}]}{3kk'}, \end{aligned} \tag{1.21}$$

where $H_m = \frac{1}{T}\int_0^T H(t)e^{ik\omega t}dt$ denotes the k-th Fourier component of $H(t)$. Higher order terms $H_F^{(m)}$, containing multiple nested commutators involving $m+1$ copies of $H(t)$ in the time domain or H_k in the frequency domain, can be formally constructed in a similar way.

However, the Floquet-Magnus expansion is not guarenteed to converge, particularly for generic many-body Floquet systems in the thermodynamic limit, i.e., system size goes to infinity. In this scenario, the series diverges even as $\omega \to 0$. This divergence arises due to the proliferation of terms in the multiple commutators as m increases In particular, taking a locally interacting system of size N with at most l-body interaction, the multiple commutators in $H_F^{(m)}$ consists of $\sim N\,m!(2l)^m$ local terms. Then the magnitude of the m-th order term in the Floquet Magnus expansion goes as $\sim N\,m!(2J_{\text{local}}/\omega)^m/m^2$, where J_{local} is the local energy scale or more precisely the energy difference caused by changing a single local degree of freedom. Apparently, it decreases until $m_{\text{opt}} \propto \omega/J_{\text{local}}$, making Floquet-Magnus expansion an asymptotic series [176, 178, 179].

Upon initial inspection, the divergence of the expansion may appear to conflict with the existence of the Floquet Hamiltonian H_F. However, this apparent inconsistency can be reconciled by considering the role of locality [179]. The Floquet-Magnus series inherently preserves locality from $H(t)$ because of the specific way it is constructed. In contrast, H_F is in general highly non-local, even if $H(t)$ is a locally interacting Hamiltonian. This observation leads to a surprising physical consequence: while the stroboscopic dynamics of a Floquet system can be replicated exactly by a static Hamiltonian, its thermalization behavior is extremely distinct from that of a truly static, locally interacting Hamiltonian. Specifically, the long-time static state lacks non-trivial local features. To understand Floquet thermalization, there are two complementary pictures. For the eigenstates, ETH is modified to be Floquet ETH. The expectation value of any few-body observable is trivially the same for all Floquet eigenstates, i.e., $\langle\psi_\alpha|\hat{O}|\psi_\alpha\rangle = \text{Tr}[\hat{O}]/\dim(\hat{O})$. Consequently, regarding the long-time steady states, the reduced density matrix for any subsystem will approach the featureless identity operator. Since a featureless state typically signifies infinite temperature, the Floquet thermalization phenomenon is also known as Floquet heating. While the use of the word "heating" seems imprecise here, it will become much more evident and natural after the discussion in subsequent discussion.

1.3.3 Floquet prethermalization and effective Hamiltonian

Although the Floquet-Magnus expansion does not converge, in the high-frequency regime $\omega \gg J_{\text{local}}$ (so that the expansion does not immediately diverge at the lowest orders), the truncated expansion

$$H_F^{\text{trunc}} = \sum_m^{m_{\text{opt}}} \frac{1}{\omega^m} H_F^{(m)} \tag{1.22}$$

as a Hamiltonian still plays an important role in Floquet systems. Since the time-dependent Hamiltonian $H(t)$ is no longer a constant of motion, the conventional notion of energy does not apply to Floquet systems. It turns out that H_F^{trunc} provides the most natural definition of energy. Specifically, in a broad class of Floquet quench dynamics, it is demonstrated that $\langle\psi(t)|H_F^{\text{trunc}}|\psi(t)\rangle$ changes extremely slowly with time t before it eventually approaches $\text{Tr}[H_F^{\text{trunc}}]$ (infinite temperature), known as Floquet prethermalization [178–190]. The physical intuition is simple. Collective dynamics of clusters with a size much *smaller* than ω/J_{local} is off-resonant with the drive and thus the basis of the undriven Hamiltonian slightly mix to form a "dressed" basis, which is reflected by the fact that H_F^{trunc} not only includes the zero-th order time average of $H(t)$ but also a series of higher-order corrections. In contrast, correlated rearrangements of clusters with a size much *larger* than ω/J_{local} is resonant with the drive; however, they can only occur via $\sim \omega/J_{\text{local}}$ off-resonant intermediate steps, resulting in an effective amplitude on the order of $\exp(-\omega/J_{\text{local}})$. A rigorous proof further elaborates this intuition by decomposing $H_F = H_F^{\text{trunc}} + H_F^{\text{extra}}$, expanding $\left\| U_F^\dagger H_F^{\text{trunc}} U_F - H_F^{\text{trunc}} \right\|$ as multiple commutators between H_F^{trunc} and H_F^{extra}, and counting the number of disconnected few-body terms. More importantly, H_F^{trunc} may act as an effective Hamiltonian over timescales when Floquet heating is negligible [185, 191–197]. To be more precise, the dynamics of local observables under H_F^{trunc} and under $H(t)$ are nearly identical, i.e., $|\langle\psi(t)|\hat{O}|\psi(t)\rangle - \langle\psi(0)|e^{iH_F^{\text{trunc}}t}\hat{O}e^{-iH_F^{\text{trunc}}t}|\psi(0)\rangle| \ll \text{Tr}[\hat{O}]$ for evolution time $t < \exp(\omega/J_{\text{local}})$.

It is worth making a few important remarks. First, while the entire framework of divergent Floquet-Magnus expansions, Floquet heating and prethermalization applies to the most generic Floquet systems, there *exist* a few exceptions where the expansion converges in the first place. For example, strong disorder may make a Floquet many-body localized system, and the emergent local integral of motions largely reduces the amplitude of the commutators in the expansion (Eq. 1.3.2) [123, 133, 198–

201]. From a dynamics perspective, correlated rearrangements resonant with the drive are significantly suppressed by the disorder. Second, while Floquet prethermalization has been proven and demonstrated in a broad class of systems, it still remains an active and important direction to explore the minimum requirement for slow heating and the existence of a prethermal effective Hamiltonian. Finally, the effective Hamiltonian is more subtle and requires more stringent conditions than the slow heating. In the meantime, it play a more crucial role in Floquet dynamics. As presented in the following subsection, it serves as the workhorse for major applications of Floquet theory.

1.3.4 Application of Floquet theory

To date, most research on Floquet systems naturally falls into two categories. First, the stroboscopic dynamics of a Floquet system can be captured by a static Hamiltonian H_F. In the fast driving regime, the static Hamiltonian is well approximated by H_F^{trunc} with locality, suggesting that a Floquet Hamiltonian can be utilized to mimic a static one. Second, the Floquet system can exhibit intrinsically non-equilibrium phenomena that do not have any analogue in static systems.

Floquet engineering—Depending on the nature of microscopic structures, each individual AMO experimental system has a specific form of native Hamiltonian. However, much more forms of Hamiltonians are desired in the study of quantum dynamics as well as in the application of quantum technology. To resolve this tension, a widely used technique is to "decorate" the native Hamiltonians via the so-called Floquet engineering [2, 176, 177, 202–206]. The guiding principle is the (truncated) Floquet-Magnus expansion.

The most natural setup is as follows. The system primarily evolves freely under the native Hamiltonian H_0. At some specific intervals, one can turn on some simple terms with large amplitude but for a short time, so that the system undergoes controlled evolution through certain unitary operators $\tilde{U}$. Typical examples of $\tilde{U}$ include π-pulses and $\frac{\pi}{2}$-pulses. Through a sequence of alternating free evolution under H_0 and a series of intervention steps $\tilde{U}_i$, the dynamics of the system is generated by

$$\cdots \tilde{U}_3 e^{-iH_0 t_3} \tilde{U}_2 e^{-iH_0 t_2} \tilde{U}_1 e^{-iH_0 t_1}. \tag{1.23}$$

In the most general case, such evolution is complicated. Nevertheless, one can focus on a special

scenario where the Floquet theory can perfectly apply. Specifically, a finite series of $\{\tilde{U}_i, t_i\}$ are repeated in a pattern. Rewriting the repeated segment of Eq. 1.23 in a different form:

$$\left(\prod_{k=1}^{i}\tilde{U}_k\right)\left[\left(\prod_{k=1}^{i-1}\tilde{U}_k\right)^{\dagger}e^{-iH_0t_i}\left(\prod_{k=1}^{k-1}\tilde{U}_k\right)\right]\cdots\left[\left(\tilde{U}_2\tilde{U}_1\right)^{\dagger}e^{-iH_0t_3}\left(\tilde{U}_2\tilde{U}_1\right)\right]\left[\tilde{U}_1^{\dagger}e^{-iH_0t_2}\tilde{U}_1\right]e^{-iH_0t_1}. \tag{1.24}$$

In most situations, one further requires $\prod_{i=1}^{k}\tilde{U}_i = \mathbb{1}$, and the time-dependent Hamiltonian for a Floquet period becomes piece-wise, i.e., a Hamiltonian series $\left\{\left(\prod_{k=1}^{i-1}\tilde{U}_k\right)^{\dagger}H_0\left(\prod_{k=1}^{i-1}\tilde{U}_k\right)\right\}$ with a duration series $\{t_i\}$. The Floquet-Magnus expansion then naturally applies. At the leading order, the static Hamiltonian realized by Floquet engineering is

$$H_{\text{Engineer}} = \frac{\sum_i t_i\left(\prod_{k=1}^{i-1}\tilde{U}_k\right)^{\dagger}H_0\left(\prod_{k=1}^{i-1}\tilde{U}_k\right)}{\sum_i t_i}. \tag{1.25}$$

The magnitude of higher-order correction is in general controlled by $t_i\,\|H_i\|$, but there exist systematic ways to cancel out a few leading-order corrections: among different series of $\tilde{U}_i$ that realize the same desired effective Hamiltonian to the zero-th order, symmetry consideration can help to find the optimal choice [203, 207–211].

In spin-1/2 systems, two notable examples of Floquet engineering are the XY8 sequence and the WAHUHA (Waugh-Huber-Haeberlen) sequence:

- Carr-Purcell-Meiboom-Gill (CPMG) sequence and its derivatives consist of evenly spaced π-pulses [2, 203, 212–218]. The effective Hamiltonian differs from the original static Hamiltonian only by dropping all single-body term, or more generally all terms involving odd number of spin operators such as $\hat{s}_i^x\hat{s}_j^z\hat{s}_k^x$.
- WAHUHA sequence comprises a series of evenly spaced $\pi/2$-pulses (along different spin axes) [202, 219]. The effective Hamiltonian is a symmetrized version of the original static Hamiltonian along the three directions in terms of the spin operators $\hat{s}^x$, $\hat{s}^y$ and $\hat{s}^z$.

Floquet phases of matter—Due to the existence of a static Hamiltonian H_F that describes the Floquet dynamics, one might naively think the long-time steady states in Floquet system to be characterized by exactly the same framework for phases of matter in truly static systems [220].

However, this is not the case. Two key reasons underscore this distinction, each corresponding to an intriguing phenomenon which has recently attracted much attention.

First, phases of matter are not defined on a single point in the parameter space, but rather according to the robustness against a certain set of perturbations. In particular, perturbations allowed to exist in a static Hamiltonian are not the same as those emerging in H_F that are constrained by the original $H(t)$. For example, time-dependent perturbations, forbidden in intrinsically static systems, can be present in Floquet systems and make certain symmetry broken phases less stable. On the other hand, analogous to other discrete symmetries, the discrete nature of the time-translation in $H(t)$ makes it easier to spontaneously break than a continuous one. A notable example along this direction is the discrete time crystal [194–196, 221–231]. Here, the discrete time-translation symmetry can be the only symmetry in $H(t)$. However, another local symmetry (e.g., Z_2 symmetry of spin-up and spin-down) emerges in the effective Hamiltonian (H_F or H_F^{trunc}); when this symmetry is spontaneously broken, the dynamics also automatically breaks the time-translational symmetry and develops the time crystalline order. Crucially, the crystalline order is robust against perturbations that explicitly violates the emergent local symmetry in the original $H(t)$, but will immediately smooth out if $H(t)$ loses temporal periodicity.

Second, the discrete nature of H_F restricts its capture of dynamics to discrete points in time. Indeed, in the example of Floquet symmetry-protected-topological (SPT) matters [232–243], one must go beyond the stroboscopic picture. In static SPT systems, the energy bands that encodes the topological characteristics follow a natural order from the bottom to the top of energy spectrum. The number of edge modes can then be counted by summing up the topological number for the bands below an energy gap. In contrast, the quasi-energy spectrum of H_F is determined on a module, reflecting the fact that any integer multiples of ω can be freely added to a quasi-energy band. As a result, Floquet systems lack a notion of bands below energy gaps. The problem is more clear in the time domain. To determine the dynamics of an edge mode (e.g., to determine when it moves clockwise or anti-clockwise) requires *continuous* track the micromotions on the edge, instead of taking *discrete* snapshots in time.

Finally, one should always be aware that H_F tends to be highly non-local for many-body systems, leading to eventual thermalization to featureless thermal states. Escaping from such thermal states and realize non-equilibrium phases necessitates breaking ergodicity. Beyond the aforementioned Floquet

MBL and prethermalization, systems exhibiting quantum scar, stark localization, or Hilbert space fragmentation may also be possible candidates [244–247].

1.4 Quantum metrology

Measuring physical parameters with ever-increasing precision remains as an endless pursuit in nearly all scientific researches such as probing gravitational wave or measuring electron electric dipole moment, and technological applications such as sensing pressure or magnetic field strength. Modern metrology—scientific study of measurements—can be traced back to late 18th century when decimal-based metric system was created, well predating the discovery of quantum mechanics [248]. In classical systems, to achieve greater sensitivity in measurement is essentially equivalent to better isolate the sensor or the probe from the environment so that the classical fluctuations, such as thermal or magnetic noise, are reduced. However, quantum metrology, which utilizes quantum systems as sensors or probes, introduces fundamentally new principles. Even within a closed quantum system, the measurement outcome of an observable is generally not deterministic due to inherent quantum fluctuation [249, 250]. In this section, I introduce some fundamentals of quantum metrology, to better contextualizes and motivates the study in Chapter 4.

1.4.1 Phase estimation

In precision measurements, determining the strength of physical parameters often relies on mapping it to a relative phase shift between different components of a quantum state. Such phase shift cannot be directed measured but inferred from the measurement of certain physical observables. As a result, the precision of phase estimation is determined by the standard deviation of the observable, normalized by the sensitivity of its dependence on the phase, i.e., the derivative of the mean value with respect to the phase[6] [249–251].

The simplest prototypical example is the Ramsey interferometry [252]: let the the two eigenstates $|\uparrow\rangle$ and $|\downarrow\rangle$ (with an energy splitting caused by the external parameter to sense) of a two-level system acquire a relative phase θ during the sensing procedure and measure θ [253, 254]. Starting with the probe state $|\uparrow\rangle$, one can apply a $\pi/2$-pulse to transform it to $|x\rangle = (|\uparrow\rangle + |\downarrow\rangle)/\sqrt{2}$. Following the phase accumulation, the state becomes $(e^{-i\theta/2}|\uparrow\rangle + e^{i\theta/2}|\downarrow\rangle)/\sqrt{2}$. A final $\pi/2$-pulse is then

[6] For a given state, one should find out the most suitable observable that provides the best sensitivity.

applied to obtain the final state $\cos\frac{\theta}{2}|\uparrow\rangle + \sin\frac{\theta}{2}|\downarrow\rangle$, and the phase θ can be estimated by measuring the projection onto the initial state $\hat{P}_\uparrow = |\uparrow\rangle\langle\uparrow|$. In this protocol, the sensitivity of the phase estimation from a single two-level system is then determined by

$$[\delta\theta]_{\text{single}} = \left(\text{Var}[\hat{P}_\uparrow]\right)^{\frac{1}{2}} \Big/ \left|\frac{d\langle\hat{P}_\uparrow\rangle}{d\theta}\right| = \frac{|\sin\theta|}{2} \Big/ \left|\frac{d\,\cos^2\frac{\theta}{2}}{d\theta}\right| = 1. \tag{1.26}$$

However, to set a reference for the comparison with N entangled particles as discussed later, a more relevant scenario is to perform phase estimation with N uncorrelated two-level particles, which can be equivalently viewed as N identical copies of the same two-level system. According to the central limit theorem, the variance of the measurement outcome decreases by a factor of N while the mean remains the same, so the sensitivity of phase estimation becomes

$$\delta\theta = \frac{[\delta\theta]_{\text{single}}}{\sqrt{N}} = \frac{1}{\sqrt{N}}. \tag{1.27}$$

Despite illustrated in this specific example of Ramsey interferometry, such dependence on N turns out to be extremely general in quantum metrology, known as the standard quantum limit (SQL): the best sensitivity attainable without entanglement [7] [255, 256].

A complementary perspective of the Ramsey interferometry is a quantum spin-1/2 object sensing a magnetic field through its precession angle [257]. In this scenario, the spin-1/2 object is represented as a vector on the Bloch sphere. Initially oriented perpendicular to the magnetic field, the spin undergoes precession by an angle θ around the magnetic field. To determine θ requires mapping out the initial and the final directions of the spin. However, the projection of a spin-1/2 onto any direction yields $\pm 1/2$ for each individual spin. With N copies of spin-1/2, the measurement outcome follows a binomial distribution with a standard deviation of $\sim 1/\sqrt{N}$.

While these above two perspectives are equivalent, they naturally motivate two distinct approaches in entangled many-body systems, aimed at achieving more precise estimation of θ using an entangled N-body state [258]. To conduct the Ramsey interferometry with N entangled two-level systems, one straightforward method is to consider Greenberger-Horne-Zeilinger (GHZ) state $|\text{GHZ}\rangle = \frac{|\uparrow\uparrow\cdots\rangle + |\downarrow\downarrow\cdots\rangle}{\sqrt{2}}$ [259]. Simply substituting $\frac{|\uparrow\rangle+|\downarrow\rangle}{\sqrt{2}}$ with $|\text{GHZ}\rangle$, the total phase accumulation becomes

[7] Note that we focus on the physical quantity that acts independently on each quantum degree of freedom.

amplified by N, and the sensitivity improves to

$$\delta\theta = (\mathrm{Var}[\hat{P}_{\uparrow\uparrow\ldots}])^{\frac{1}{2}} / \left| \frac{d\langle \hat{P}_{\uparrow\uparrow\ldots} \rangle}{d\theta} \right| = |\sin N\theta| / \left| \frac{d\, \cos^2 \frac{N\theta}{2}}{d\theta} \right| = \frac{1}{N}. \tag{1.28}$$

In contrast to the standard quantum limit, this dependence is generally referred to as the *Heisenberg limit*, representing the best attainable sensitivity even in the presence of entanglement [8] [260, 261]. Relatedly, the sensitivity is referred to as exhibiting *Heisenberg scaling*, if it satisfies $\delta\theta \propto \frac{1}{N}$ with a larger prefactor.

To generalize the picture of a single precessing spin-1/2 vector to entangled N spins, one can consider the "Bloch sphere" of the total spin vector. Despite the spin precession angle around the magnetic field remaining θ, the variance of the total spin projection perpendicular to the mean spin direction can be reduced [262–264]. Such spin states with reduced variance are termed spin squeezed states, with the reduction characterized by the spin squeezing parameter [263, 264]

$$\xi^2 = N \frac{\min\limits_{\hat{n} \perp \langle \vec{S}_{\mathrm{total}} \rangle} \mathrm{Var}[\hat{n} \cdot \vec{S}_{\mathrm{total}}]}{|\langle \vec{S}_{\mathrm{total}} \rangle|^2}, \tag{1.29}$$

where the spin length as the denominator accounts for the fact that with a fixed precession angle θ, vectors with longer length induce a larger change in the mean value of their projection. Note that the squeezing parameters relates to the sensitivity by $\delta\theta = \frac{\xi}{\sqrt{N}}$. With N entangled spin-1/2 particles, it is proven that the squeezing parameter is at best $\frac{2}{N+2}$ and the corresponding sensitivity $\delta\theta = \frac{2}{\sqrt{N(N+2)}}$ [265, 266]. This bound is saturated by the state $\lim\limits_{\alpha \to 0} \sqrt{1-2\alpha^2} |\frac{N}{2}, 0\rangle + \alpha |\frac{N}{2}, 1\rangle + \alpha |\frac{N}{2}, -1\rangle$, where $|\frac{N}{2}, m_z\rangle$ is the Dicke state defined as the unique state with total angular momentum $\frac{N}{2}$ (the largest possible value for N spin-1/2) and the z-component m_z [267, 268].

While the GHZ state and the spin squeezed states are the most well-known and widely studied examples, they represent only a small subset of metrologically useful states [257, 269–274]. In fact, the general framework is as follows. To probe the strength α of a physical quantity $\hat{A}$, one can take a state $\hat{\rho}$ and evolve it as $e^{-i\theta\hat{A}} \hat{\rho} e^{i\theta\hat{A}}$, with $\theta = \alpha t$. Consequently, estimates of α can be directly translated into estimates of phase θ by measuring some observable $\langle \hat{O} \rangle(\theta) = \mathrm{Tr}[\hat{O}\hat{\rho}(\theta)]$. Then the precision to

[8] Here we still focus on the physical quantity that acts independently on each quantum degree of freedom. If the goal is to probe the phase shift caused by multi-body interaction, the best achievable sensitivity can exceed the Heisenberg limit.

estimate θ is given by:

$$\delta\theta_{\hat{O}} = \frac{(\mathrm{Var}[\hat{O}])^{\frac{1}{2}}}{\left|\partial_\theta \langle \hat{O} \rangle\right|} = \frac{(\mathrm{Var}[\hat{O}])^{\frac{1}{2}}}{\left|\mathrm{Tr}[i\hat{O}\hat{A}\hat{\rho} - i\hat{O}\hat{\rho}\hat{A}]\right|} = \frac{(\mathrm{Var}[\hat{O}])^{\frac{1}{2}}}{\left|\langle [\hat{O}, \hat{A}] \rangle\right|}. \tag{1.30}$$

In the aforementioned examples, $\hat{\rho} = \bigotimes_i^N \left(|x\rangle\langle x|\right)_i$ and $\hat{O} = \sum_i^N \left(|\uparrow\rangle\langle\uparrow| - |\downarrow\rangle\langle\downarrow|\right)_i = \sum_i^N \hat{S}_i^z$ for both cases; $\hat{A}_{\mathrm{GHZ}} = \frac{1}{2}\Big(|\uparrow\uparrow\cdots\rangle + |\downarrow\downarrow\cdots\rangle\Big)\Big(\langle\uparrow\uparrow\cdots| + \langle\downarrow\downarrow\cdots|\Big)$ and $\hat{A}_{\mathrm{squeezing}} = \sum_i^N \hat{S}_i^y$ for the GHZ state and the squeezed state respectively.

1.4.2 Quantum Fisher information and Cramér-Rao bound

Given numerous examples of metrologically useful quantum states, a natural question to ask arises as how to access their efficacy in probing physical quantities, or equivalently how to determine their sensitivity in phase estimation. This inquiry is partially addressed by the Cramér-Rao bound with the concept of quantum Fisher information (QFI) [84, 86, 275–277]. In particular, the goal is to calculate or bound Eq. 1.30. For pure states, the Heisenberg's uncertainty principle provides a straightforward answer:

$$\mathrm{Var}[\hat{O}]_{\mathrm{pure}}\mathrm{Var}[\hat{A}]_{\mathrm{pure}} \geq \frac{1}{4}\left|\langle [\hat{O}, \hat{A}] \rangle_{\mathrm{pure}}\right|^2 \qquad \Rightarrow \qquad \delta\theta_{\hat{O}} \geq \frac{1}{2\sqrt{\mathrm{Var}[\hat{A}]_{\mathrm{pure}}}}. \tag{1.31}$$

While analyzing mixed states is more complicated, the key principle remains the Heisenberg's uncertainty principle. Let us decompose the density matrix with a set of pure states $|\psi_k\rangle$:

$$\hat{\rho} = \sum_k p_k |\psi_k\rangle\langle\psi_k|, \tag{1.32}$$

where $|k\rangle$ do not need to form a orthogonal basis. The uncertainty principle for the operator $\hat{A}$ to sense and the operator $\hat{O}$ to measure in the sensing protocol applies for each pure state $|k\rangle$ as

$$\mathrm{Var}[\hat{O}]_k\mathrm{Var}[\hat{A}]_k \geq \frac{1}{4}\left|\langle [\hat{O}, \hat{A}] \rangle_k\right|^2. \tag{1.33}$$

Consequently, one can bound the measurement sensitivity with Cauchy-Schwarz inequality as

$$\delta\theta_{\hat{O}} \geq \frac{1}{2\sqrt{\sum_k p_k \mathrm{Var}(\hat{A})_k}}. \tag{1.34}$$

It has been shown that for any choice of $\{p_k, |\psi_k\rangle\}$, the denominator can be bounded [278–280]:

$$\mathrm{Var}(\hat{A}) \geq \sum_k p_k \mathrm{Var}(\hat{A})_k \geq \frac{1}{4} F_Q[\hat{\rho}, \hat{A}], \tag{1.35}$$

where $\mathrm{Var}(\hat{A}) = \mathrm{Tr}[\hat{A}^2\hat{\rho}] - \left(\mathrm{Tr}[\hat{A}\hat{\rho}]\right)^2$ is the variance computed for the state $\hat{\rho}$, and $F_Q[\hat{\rho}, \hat{A}]$ is the quantum Fisher information defined as [249, 251, 281, 282]

$$F_Q[\hat{\rho}, \hat{A}] := 2 \sum_{m,n} \frac{(\lambda_m - \lambda_n)^2}{\lambda_m + \lambda_n} \left|\langle m|\hat{A}|n\rangle\right|^2, \tag{1.36}$$

with λ_m and $|m\rangle$ the eigenvalues and the eigenvectors of $\hat{\rho}$, respectively. Crucially, both the upper and the lower bounds for $\sum_k p_k \mathrm{Var}(\hat{A})_k$ in Eq. 1.35 are tight, leading to the Cramér-Rao bound for the sensitivity [251, 256, 278, 282–284]

$$\delta\theta_{\hat{O}} \geq \frac{1}{\sqrt{F_Q[\hat{\rho}, \hat{A}]}} \geq \frac{1}{2\sqrt{\mathrm{Var}[\hat{A}]}}. \tag{1.37}$$

The second inequality is saturated when $\hat{\rho}$ is pure, and the result for pure states (Eq. 1.31) is recovered. Assuming $\hat{A}$ is a sum of single-body observable, it is straightforward to see the Heisenberg limit for sensitivity.

In general, one can formally construct the optimal observable $\hat{O}$ that saturates the Cramér-Rao bound. Specifically, decomposed in the orthogonal basis,

$$\hat{O} = \sum_m O_m |O_m\rangle\langle O_m| \tag{1.38}$$

where O_m and $|O_m\rangle$ are the corresponding eigenvalue and the eigenvector respectively. One optimal choice of $\hat{O}$ is determined as follows. First, $|O_m\rangle$ are chosen to be the eigenstates of the operator

$$\hat{L}_{\hat{A}} = 2i \sum_{m,n} \frac{\lambda_m - \lambda_n}{\lambda_m + \lambda_n} |m\rangle\langle m|\hat{A}|n\rangle\langle n|, \tag{1.39}$$

where $\hat{L}$ is named as the symmetric logarithmic derivative which satisfies $\frac{\partial\hat{\rho}(\theta)}{\partial\theta} = \frac{\hat{\rho}(\theta)\hat{L} + \hat{L}\hat{\rho}(\theta)}{2}$ [251]. Second, O_m is chosen to satisfy

$$O_m - \mathrm{Tr}[\hat{\rho}\hat{O}] \propto \frac{i\langle O_m|[\hat{\rho}, \hat{A}]|O_m\rangle}{\langle O_m|\hat{\rho}|O_m\rangle} \tag{1.40}$$

Note that this choice of $\hat{O}$ is sufficient but not necessary. Indeed, when measuring $\hat{O}$ in the experiment,

one actually obtains a histogram of O_m, or equivalently $|O_m\rangle\langle O_m|$. Namely, given the single-shot read-out, the information got from measurement outcomes of $\hat{O}$ is essentially independent of the choice of O_m. In particular, when measuring a different observable $\hat{O}' = \sum_m O'_m |O_m\rangle\langle O_m|$, each single-shot measurement outcome labeled by O'_m can be re-assigned with the correct O_m as per Eq. 1.40 so that $\langle\hat{O}\rangle$ can be constructed and used to estimate θ.

Moreover, the standard projection measurement (SPM) can be extended to positive-operator valued measure (POVM), a set of Hermitian operators $\hat{E}_\epsilon$ which are non-negative and satisfy $\sum_\epsilon \hat{E}_\epsilon = \mathbb{I}$, but are not necessarily orthogonal ($\mathrm{Tr}[\hat{E}_\epsilon \hat{E}'_\epsilon] = \delta_{\epsilon,\epsilon'}$ does not necessarily hold) [68]. Similar to SPM, the single-shot measurement outcomes of POVM are labelled by ϵ. In this generalized measurement framework, the special case of SPM (which is equivalent to measuring $\hat{O}$) is not necessary required to saturate the Cramér-Rao bound. Additionally, since one usually cares more about the large N limit for quantum sensing with entangled many-body systems, $\hat{O}$ can be chosen to asymptotically satisfy Eq. 1.40. Finally, for pure states $\rho = |\psi\rangle\langle\psi|$, the Cramér-Rao bound can be saturated by a much simpler measurement—projection onto the probe state itself, i.e., $\hat{O} = |\psi\rangle\langle\psi|$ [86, 277].

1.4.3 Metrological protocols

The specific example of interacting two-level systems and the the general Cramér-Rao bound provide a clear framework to perform quantum-enhanced metrology upon obtaining a quantum state with high QFI. A natural follow-up question is how to prepare such metrological useful states and to measure the desired observables. This is particularly relevant to the experiments, since almost all platforms only allow for a very limited set of manipulations, e.g., many experimental systems can only be initialized in a simple product state and the measurable observables are restricted to local (single-body) operators.

Probably the most straightforward protocol is to effectively perform the projection measurement that saturates the Cramér-Rao bound. A detailed protocol, known as Loschmidt echo [285], is as follows [286–288] [9]:

[9] In the $\mathrm{SU}(1,1)$ interferometry [289], the second optical parametric amplifiers can also be viewed as performing a time reversal evolution.

1. Evolve a product initial state $|\psi_0\rangle$ with a unitary evolution $\hat{U}$ to a state $|\psi\rangle = \hat{U}|\psi_0\rangle$ hopefully with a large $F_Q[|\psi\rangle, \hat{A}] = \mathrm{Var}_{|\psi\rangle}[\hat{A}]$;

2. Evolve under $\hat{A}$ to encode the information of the strength of $\hat{A}$ (the physical quantity to sense);

3. Evolve backward with $\hat{U}^\dagger$ and perform a projection measurement onto the initial state.

Formally, the measured signal is given by

$$\langle\psi_0|\left(\hat{U}^\dagger e^{-i\theta\hat{A}}\hat{U}|\psi_0\rangle\langle\psi_0|\hat{U}^\dagger e^{i\theta\hat{A}}\hat{U}\right)|\psi_0\rangle = \langle\psi|e^{-i\theta\hat{A}}|\psi\rangle\langle\psi|e^{i\theta\hat{A}}|\psi\rangle, \tag{1.41}$$

which is exactly equivalent to the standard protocol saturating the Cramér-Rao bound discussed in the previous subsection. While the entire procedure does not specify a $\hat{U}$ that prepares $|\psi\rangle$ or the corresponding operator $\hat{A}$ that provide large QFI, it avoids projection measurement on the complicated entangled state $|\psi\rangle$ by mapping the final measurement basis to the original simple product-state basis via backward evolution.

The projection measurement on the initial state requires single-site resolution, a capability not available in many experimental platforms, such as solid state defect systems and bulk gas of ultra-cold atoms. Nevertheless, a simplified protocol that only requires measurement of global averaged quantity can be applied. To be specific, one can initialize the system in a fully polarized initial state (in the spin representation), which has the maximum polarization, and correspondingly measure the total polarization of the final state [288, 290–296]. Crucially, the difference between the initial and the final polarization directly reflects the overlap between the two states, and thus provides the similar information as the projection measurement. It is essential to highlight that the global measurement is required to overcome the classical shot noise—the variance of the measurement outcome should faithfully reflect the quantum superposition states with different total polarization, rather than being dominated by classical noise, such as detection error and particle loss [10].

In the protocol outlined above for utilizing high QFI, a key step involves performing the backward evolution $\hat{U}^\dagger$. However, this poses a significant challenge in almost all experimental systems: even if achievable, it always demands dedicate control. Moreover, any backward evolution is exponentially

[10]The impact of classical noise is *not* catastrophic [288, 290]

susceptible to the inevitable noise present in real platforms. Thus, metrological protocols free of backward evolution are highly desired. Squeezing serves as a prime example of such protocols, which relies solely on forward evolution and the measurement of global sum of simple local quantities, such as total spin polarization [263, 264, 297–301]. However, achieving a squeezed state comes at an unavoidable cost–it necessitates not only high QFI but also a more refined entanglement structure.

Finally, it is important to emphasize that the starting point of all these protocols is a $\hat{U}$ generating metrologically useful states from a suitable initial state. While designing metrological protocols based on this assumption represents an active direction, an equally, if not more important pursuit, is to search for appropriate $\hat{U}$. Despite a few isolated example procedures, mostly via quench dynamics [256, 263, 264, 302–305], there still lack a more systematic framework and more general rules to generate metrologically useful states.

1.5 Simulating out-of-equilibrium many-body dynamics

To numerically investigate the dynamics of out-of-equilibrium quantum systems, a variety of numerical methods have been developed [306–319, 319–328]. Comprehensive explanations and detailed discussion of the intricacies of these methods are well covered in the literature [329–345]. Within this section, I will outline the fundamental concepts underlying a few of these numerical tools, along with their optimal applications to specific types of problems.

To compute the dynamics of quantum systems, two frameworks are generally employed: 1) Schrödinger's equations of motion, which describe the evolution of quantum states, and 2) Heisenberg's equations of motion, which govern the evolution of quantum operators. In the case of open systems, it becomes necessary to evolve the quantum density operators, instead of quantum states, and correspondingly to use master equations. Although these frameworks are physically equivalent, their numerical implementations vary significantly, particularly when incorporating approximations.

In Schrödinger's picture, one needs to keep track of a quantum state $|\psi(t)\rangle$, of which the evolution is generated by the Hamiltonian $H(t)$, through Schrödinger's equation:

$$i\frac{d}{dt}|\psi(t)\rangle = H(t)|\psi(t)\rangle, \tag{1.42}$$

with its formal solution given by

$$|\psi(t)\rangle = Te^{-i\int_0^t H(t')dt'}|\psi(0)\rangle. \tag{1.43}$$

In practical computations, discretization of the time step is often necessary, especially when $H(t)$ is time-dependent. This leads to iterative computation of the time trace:

$$|\psi(t+dt)\rangle \approx e^{-iH(t)dt}|\psi(t)\rangle. \tag{1.44}$$

Even in scenarios where H is time-independent, Eqn. 1.44 plays an fundamental role in simulating dynamics due to the following reasons: 1) approximations made to compute $e^{-H(t)dt}$ are typically valid only when $\|H\|dt \ll 1$, and 2) the operation $e^{-H(t)dt}$ needs to be computed only once and then applied iteratively to the state.

The evolution of mixed states $\rho = \sum_{\alpha,\beta}\rho_{\alpha,\beta}|\alpha\rangle\langle\beta|$, has a slightly different structure. For a generic

open quantum system, the Lindblad master equation takes the form:

$$\dot{\rho} = -i[H, \rho] + \sum_i \gamma_i (S_i \rho S_i^\dagger - \frac{1}{2} S_i^\dagger S_i \rho - \frac{1}{2} \rho S_i^\dagger S_i), \tag{1.45}$$

where H again generates the Hermitian Hamiltonian evolution, and $\{S_i, \gamma_i\}$ represent the Lindblad operators (with their corresponding rates) responsible for incoherent dynamics. Notably, the master equation is linear in ρ. Given this linearity, although we typically think of the density matrix, ρ, as a d-by-d matrix,

$$\rho = \begin{pmatrix} \rho_{11} & \rho_{12} & \cdots & \rho_{1d} \\ \rho_{21} & \rho_{22} & \cdots & \rho_{2d} \\ \cdots & \cdots & \cdots & \cdots \\ \rho_{d1} & \rho_{d2} & \cdots & \rho_{dd} \end{pmatrix}, \tag{1.46}$$

for numerical procedures, it is more convenient to represent ρ as a d^2-dimensional column vector:

$$\rho_{\text{vec}} = \begin{pmatrix} \rho_{11} & \rho_{12} & \cdots & \rho_{1d} & \rho_{21} & \cdots & \rho_{d1} & \cdots & \rho_{dd} \end{pmatrix}^T. \tag{1.47}$$

Based on this data structure, the Lindblad master equation can be reformulated as:

$$\dot{\rho}_{\text{vec}} = -iL\rho_{\text{vec}}, \tag{1.48}$$

where L is a d^2-by-d^2 dimensional matrix and can be expressed as

$$L = (H \otimes I - I \otimes H^T) + i \sum_i \gamma_i (S_i \otimes S_i^{\dagger T} - \frac{1}{2} S_i^\dagger S_i \otimes I - -\frac{1}{2} I \otimes S_i^\dagger S_i) \tag{1.49}$$

Consequently, the formal solution for ρ_{vec} mirrors the state evolution in Eq. 1.44:

$$\rho_{vec}(t + dt) = \mathrm{e}^{-iL(t)dt} \rho_{\text{vec}}(t). \tag{1.50}$$

This treatment of the density matrices simplifies the adaptation of most numerical methods designed for pure quantum states to accommodate mixed states.

The operator dynamics are similar to density matrices:

$$\dot{\hat{O}} = i[H, \hat{O}]. \tag{1.51}$$

However, in addition to their analogous treatment as the density matrices, operator evolution more closely resembles classical equations of motion, and thus is more amenable to semi-classical treatment.

The key steps to simulate evolution are: 1) representing the state $|\psi\rangle$ or the density operator $\hat{\rho}$, and 2) performing the linear operation $e^{-iH(t)dt}$ or $e^{-iL(t)dt}$ step-by-step. This immediately suggests an exponential difficulty. The dimension of Hilbert space, i.e., the size of the state vector and the Hamiltonian, grows exponentially with system sizes. Faithfully capturing the dynamics requires exponentially large memory to represent the quantum states and the Hamiltonian, as well as computing multiplication of exponentially large matrices. Conceptually, nearly all approximate methods essentially project the evolved state into a subspace, either by directly constructing such a subspace or by assuming an ansatz wavefunction parameterized by much fewer variables. This substantially reduce the complexity of matrix operation, and in some scenarios demands significantly less memory to track the quantum state. Consequently, all these constraints shape the current landscape of the numerical capability (Table 1.2).

Numerical method	**Ideal types of system to work in**	**System size**	**Evolution time**
ED [346]	Arbitrary geometry and interaction	$\lesssim 16$	Arbitrarily long
Krylov [347]		$\lesssim 30$	
TEBD [348]	1D short-range interaction; 2D or long-range interaction with smaller system size	$\lesssim 10^3$	$\sim 10/J$
TDVP [348]			
DMT [349]			$> 10^2/J$ [11]
TVMC	Homogeneous interaction	$\sim 10^2$	Depend on system type
TWA	When mean-field approximation applicable	$\sim 10^4$	

Table 1.2: Summary of numerical tools for simulating quantum many-body dynamics and the corresponding optimal regimes to work at. See the references for public packages implementing these numerical methods.

1.5.1 Exact diagonalization and Krylov

Implementing exact diagonalization is the most straightforward among all numerical methods [306, 331]. The Hamiltonian H is written in full matrix form spanning in the entire Hilbert space. Correspondingly, the unitary operation e^{-iHdt} is obtained by fully diagonalizing H: first decompose the Hamiltonian as $H = PDP^{-1}$, where D is diagonal and P is a unitary matrix, and then

[11] DMT may exhibit relatively large error in capturing early-time local equilibration dynamics from far-from-equilibrium pure initial states, but it quickly becomes more accurate afterwards.

compute $e^{-iHdt} = Pe^{-iDdt}P^{-1}$. With the presence of symmetries, H becomes block diagonal, and diagonalization is better performed in each individual symmetry sectors to mitigate numerical instability and reduce computational complexity. As of the current date, ED represent the most reliable method for studying quantum many-body dynamics, and can be applied to any generic system, irrespective of interaction type or geometry, albeit at the expense of being strictly limited by the exponentially increasing computation resources with system sizes.

In contrast to ED, Krylov subspace method accelerates the calculation of the matrix exponential by approximately projecting it onto a much smaller subspace [307, 332], spanned by

$$\{|\psi\rangle, H|\psi\rangle, H^2|\psi\rangle, \ldots, H^m|\psi\rangle\}, \tag{1.52}$$

where the subspace dimension m is much smaller than the Hilbert space dimension. Due to the small leakage out of the Krylov subspace, the error accumulates and is controlled by the size of the Krylov subspace m and the time step dt. However, computed evolution usually converges surprisingly fast as m increases and dt decreases, thereby also qualifying as an exact method for simulating quantum dynamics. While applicable to all types of Hamiltonians, Krylov method has a significant advantage when leveraging the fact that almost all the realistic Hamiltonians only consists of few-body interactions. In particular, when constructing the Krylov subspace, the multiplication is much faster if the Hamiltonian is sparse. Additionally, one can treat the Hamiltonian as rules to map between quantum states, instead of constructing the full matrix form the Hamiltonian, which helps to largely reduce the required memory.

1.5.2 Time evolving block decimation

At its core, TEBD consists of three essential ingredients: 1) representing a quantum state in a matrix-product form, 2) time-evolving the matrix-product state (MPS) leading to a new MPS with increased memory usage, 3) approximating the new MPS through a truncation procedure to lower the memory usage.

Matrix-product state—Taking spin systems as an example, the quantum state of spin-S system with size N (with local Hilbert space dimension $d = 2S + 1$) is fully determined by the d^N coefficients

in the local d^N-dimensional basis $|s_1, s_2, \ldots, s_N\rangle$:

$$|\psi\rangle = \sum_{\{s_1,s_2,\ldots,s_N\}}^{d} c_{s_1,s_2,\ldots,s_N} |s_1, s_2, \ldots, s_N\rangle. \tag{1.53}$$

The key idea behind MPS is to rewrite these coefficients as the contraction of a series of rank-3 tensors so that the quantum state is represented by a product of matrices [308–310, 333–336]:

$$c_{s_1,s_2,\ldots,s_N} = \sum_{\alpha_1,\alpha_2,\ldots,\alpha_{N-1}}^{\chi} \Gamma^{[1]s_1}_{\alpha_1} \Gamma^{[2]s_2}_{\alpha_1,\alpha_2} \Gamma^{[3]s_3}_{\alpha_2,\alpha_3} \cdots \Gamma^{[N-1]s_{N-1}}_{\alpha_{N-2},\alpha_{N-1}} \Gamma^{[N]s_N}_{\alpha_{N-1}}, \tag{1.54}$$

where s_i is the index for physical legs, α_i is the index for bond legs that are contracted between adjacent sites, and χ (called bond dimension) is the dimension of the bond legs. Crucially, $\log \chi$ constrains the quantum state an MPS can represent by setting the upper bound for the entanglement entropy (more strictly zeroth Rényi entanglement entropy) between the subsystems on the left and the right side of the bond. Obviously, with exponentially large $\chi = d^{N/2}$, an MPS can exactly represent any quantum states. However, this incurs excessive computational costs without providing commensurate benefits. Hence, much smaller χ is always utilized in practice at the cost of accuracy loss due to projecting the quantum states onto a low-entanglement subspace.

Unitary evolution— There are two primary ways to implement unitary evolution. If the system is one-dimensional and the Hamiltonian is finite-range interacting, i.e., $H = \sum_i h_i$, where h_i is the local Hamiltonian supported only on sites with finite separation, global unitary evolution can be approximated with a series of local unitaries by using the Suzuki–Trotter expansion:

$$e^{-iHdt} \approx e^{-ih_1 dt} e^{-ih_2 dt} \cdots e^{-ih_i dt} \cdots . \tag{1.55}$$

Therefore, in each step, only a few $\Gamma^{[i]}$ need to be updated locally. For example, a two-site local unitary operator $e^{-ih_i dt} = U^{[i],s_i,s_{i+1},s'_i,s'_{i+1}}$ (obtained by directly computing matrix exponential of a two-site Hamiltonian) can be viewed as a rank-4 tensor with a dimension of d along each axis. In a local update, $\sum_{\alpha_i} \Gamma^{[i]s_i}_{\alpha_{i-1},\alpha_i} \Gamma^{[i+1]s_{i+1}}_{\alpha_i,\alpha_{i+1}}$ becomes replaced by

$$\sum_{s'_i,s'_{i+1}}^{d} U^{[i],s_i,s_{i+1},s'_i,s'_{i+1}} \Gamma^{[i]s'_i}_{\alpha_{i-1},\alpha_i} \Gamma^{[i+1]s'_{i+1}}_{\alpha_i,\alpha_{i+1}}. \tag{1.56}$$

Following a Schmidt decomposition, this rank-4 tensor is split to two rank-3 tensors, restoring the

original form of $\Gamma^{[i]s_i}_{\alpha_{i-1},\alpha_i}$ with a larger bond dimension of at most χd

Alternatively, if the Hamiltonian is long-range (or effectively long-range when mapping higher-dimensional geometry to one dimension), the strategy of local operation will not be valid. In such cases, one can write the global unitary operator also in the matrix product form, i.e., matrix-product operator (MPO) [12]:

$$e^{-iHdt} = \sum_{\beta_1,\beta_2,\ldots,\beta_{N-1}}^{\lambda} U^{[1]s_1,s_1'}_{\beta_1} U^{[2]s_2,s_2'}_{\beta_1,\beta_2} U^{[3]s_3,s_3'}_{\beta_2,\beta_3} \cdots U^{[N-1]s_{N-1},s_{N-1}'}_{\beta_{N-2},\beta_{N-1}} U^{[N]s_N,s_N'}_{\beta_{N-1}}, \tag{1.57}$$

where s_i and s_i' are the indices for physical legs corresponding to bras and kets respectively, and λ is the bond dimension. After one step of time evolution, all $\Gamma^{[i]s_i}_{\alpha_{i-1},\alpha_i}$ are updated to

$$\sum_{s_i'}^{d} U^{[i]s_i,s_i'}_{\beta_{i-1},\beta_i} \Gamma^{[i]s_i'}_{\alpha_{i-1},\alpha_i}. \tag{1.58}$$

Combining the bond index α_i and β_i, the updated matrix restores to the original form as a rank-3 tensor, with a new bond dimension of $\chi\lambda$.

Truncation—Following each step of unitary evolution via either of the aforementioned methods, the bond dimension χ generally increases. In order to constrain memory usage, one must make approximations to $\Gamma^{[i]s_i}_{\alpha_{i-1},\alpha_i}$ to truncate the bond dimension to a preset maximum $\chi_{\max}$ [311–314, 336–338]. Truncation in TEBD involves performing a Schmidt decomposition of the rank-4 tensor $\sum_{\alpha_i} \Gamma^{[i]s_i}_{\alpha_{i-1},\alpha_i} \Gamma^{[i+1]s_{i+1}}_{\alpha_i,\alpha_{i+1}}$, and retaining only the vectors corresponding to largest Schmidt coefficients, i.e., the largest singular eigenvalues in the singular value decomposition (SVD). This procedure has a clear physical interpretation: it retains terms contributing the most and discards those contributing the least to the entanglement.

Error source and limitation—Two main sources of error affect the accuracy of TEBD. First, Trotter errors arise in the Suzuki-Trotter expansion (Eq. 1.55). Depending on details of the Hamiltonians and the specific expansion pattern (e.g., zig-zag or bricklayer), the approximation is correct up to different order of dt. Namely, the Trotter error in a single step $\sim (dt)^{\delta}$ with $\delta \geq 1$, leading to an error $\sim (dt)^{\delta-1}$ for the entire evolution. This means that reducing the time step dt can polynomially

[12] Note that to obtain the MPO for unitary operator, one usually starts from an MPO form of Hamiltonian, and directly perform MPO exponential using approximate algorithm [320].

improve the Trotter error.

The second type of error, truncation error, is more fundamental. It essentially reflects the fact that MPS with relatively small bond dimension cannot represent highly entangled states. A truncation procedure that enforces the dynamics to stay in the small-entanglement subspace is a drastic modification to the quantum states. Therefore, the limitation of TEBD is apparent: Since generic many-body quantum systems, especially those in higher dimensions or with long-range interactions, tend to become highly entangled at late times, TEBD is generally expected to better capture short-time dynamics from untangled initial states. Nevertheless, there are a few special scenarios where TEBD also works reasonably well even at relatively late times, such as many-body localized systems where entanglement grows slowly (typically logrithmically with time).

1.5.3 Density matrix truncation

DMT is spiritually very similar to TEBD, but incorporates several major modifications aimed to better capture late-time dynamics of strongly-interacting quantum systems as well as the Lindblad evolution of open quantum systems [317, 318]. The motivation for such modifications are based on the anticipated behaviors of relaxation process. At early times, the quantum states are simple in terms of low entanglement, and are thus easy to represent with a small number of parameters. In contrast, at late times, a thermalizing quantum system, despite being highly entangled, exhibit a different kind of simplicity: it becomes close to thermal equilibrium and few-body observables display short-range spatial correlations. A slightly deeper understanding suggests that the late-time dynamics are also easy to track. Near thermal equilibrium, the remainder part of the system can be thought of as an effective bath for a subsystem; capturing few-body observables is equivalent to correctly evolving the reduced density matrices of such small-size subsystems. All these insights suggest the desired features of DMT. First, it employs a density matrix instead of a pure quantum state to represent the status of the system. Second, time evolution and truncation procedure need to be modified to be compatible with density matrices. Finally, the truncation procedure should prioritize the treatment of few-body correlations over entanglement, as emphasized in TEBD.

Matrix product density operators—Vectorizing density matrices (Eq. 1.47) on local degrees of

freedom allows one to write the density operator of the entire system in mathematically the same form of a pure quantum state (Eq. 1.53). Therefore, analogous to MPS, a density operator can be encoded by a series of rank-3 tensor as a matrix-product density operator (MPDO), with the dimension for physical legs being d^2 [315, 316]. It is important to note that the local basis for vectorization is not necessarily the product basis of bras and kets. Choosing a Hermitian basis (e.g., Pauli basis for spin-1/2) ensures that all the coefficients are real numbers, and therefore saves roughly half of memory usage and improves numerical stability.

Time evolution—Working with MPDO, time evolution takes the same procedure as in the MPS case, consisting of either Trotterized local updates or a global MPO multiplication. The only adjustment is to replace the Hamiltonian in the MPS evolution with the superoperator L in Eq. 1.49.

Novel truncation procedure—A truncation to reduce the bond dimension χ is again required after each step of evolution. In contrast to TEBD where the preservation of components with large entanglement is prioritized, DMT explicitly prioritizes the preservation of short-range correlations. To this end, DMT divides χ into two components: $\chi = \chi^{\text{preserve}} + \chi^{\text{extra}}$. χ^{preserve} is allocated to store the information of all observables on ℓ (named the preservation diameter) contiguous sites around the truncated tensor, or more generally a set of selected operators in the MPO form [13]. χ^{extra} is then used to preserve the remaining correlations with largest magnitude. To be slightly more specific, consider the rank-4 tensor $\sum_{\alpha_i} \Gamma^{[i]s_i}_{\alpha_{i-1},\alpha_i} \Gamma^{[i+1]s_{i+1}}_{\alpha_i,\alpha_{i+1}}$ which can be viewed as a χd^2-by-χd^2 matrix, with the columns (rows) corresponding to the linear space spanned by operators living on the left (right) side of the truncation bond. After truncation, the projection of $\sum_{\alpha_i} \Gamma^{[i]s_i}_{\alpha_{i-1},\alpha_i} \Gamma^{[i+1]s_{i+1}}_{\alpha_i,\alpha_{i+1}}$ onto a χ-dimensional left (right) subspace can remain unchanged. Therefore, to preserve the local observables of choice and the observables with the largest correlations across the bond, one only need to identify the subspace spanned by the corresponding operators.

[13] Although truncation does not directly affect these operators, their dynamics are influenced by the truncation of larger sized operators via the evolution of the system.

1.5.4 Time-dependent variational methods

Any efficient numerical method for simulating dynamics of large quantum systems must feature a low-cost parametrization of the quantum wave function, usually with polynomially many parameters compared to the with exponentially many coefficients in the full quantum description. This parametrization serves as an ansatz wavefunction. From this perspective, its proximity to the actual quantum state determines the accuracy of the corresponding numerical methods [14]. Given such an ansatz wavefunction, there are two straightforward strategies to implement the time evolution step-by-step:

- *Allowing non-ansatz dynamics*. In this approach, the time dynamics in each step are first allowed to go outside othe ansatz form, then followed by an approximation to the closest ansatz wavefunction. Both TEBD and DMT methods discussed above follow this strategy.

- *Evolution within the anszatz manifold*. This strategy, formalized as the time-dependent variational principle (TDVP) [350], ensures that the system always evolves within the manifold spanned by the ansatz wavefunction.

To be specific, Schrodinger's equation (Eq. 1.42) for $|\psi(t)\rangle$ can also be interpreted as minimizing

$$\left\| \left(I - \frac{|\psi(t)\rangle\langle\psi(t)|}{\langle\psi(t)|\psi(t)\rangle} \right) \left(i\frac{d}{dt}|\psi(t)\rangle - \hat{H}(t)|\psi(t)\rangle \right) \right\|, \tag{1.59}$$

where the first multiplier accounts for removing the normalization condition for the wave function [15]. If $|\psi(t)\rangle$ is allowed to span the entire Hilbert space, then this equation can always be minimized to 0, recovering Schrodinger's equation. However, within the ansatz wave function manifold, this equation typically does not vanish, and the minimization problem results in an approximate solution for the dynamics.

MPS-based TDVP— One natural choice of the ansatz wavefunction is MPS, assumed to be parameterized by a set of time-dependent parameters $\{\lambda_1, \lambda_2, \ldots, \lambda_n\}$. At any time t, in order to stay in the MPS manifold, the change of the quantum state $\frac{d}{dt}|\psi(t)\rangle_{\text{approx}}$ must lie in the tangent space spanned by $\{\partial_{\lambda_1}|\psi(t)\rangle, \partial_{\lambda_2}|\psi(t)\rangle, \ldots, \partial_{\lambda_n}|\psi(t)\rangle\}$. Therefore, the optimal $\frac{d}{dt}|\psi(t)\rangle_{\text{approx}}$ that

[14] For example, MPS is a good ansatz wavefunction for states with low entanglement.

[15] We note that Eq. 1.59 can be rigorously derived with variation principle of least action

minimizes Eq. 1.59 is simply the projection of the exact $\frac{d}{dt}|\psi(t)\rangle_{\text{exact}}$ onto this tangent basis:

$$\begin{aligned}\frac{d}{dt}|\psi(t)\rangle_{\text{approx}} &= \sum_n \left(\partial_{\lambda_n}\langle\psi(t)|\right)\left(\frac{d}{dt}|\psi(t)_{\text{exact}}\rangle\right)\partial_{\lambda_n}|\psi(t)\rangle \\ &= -i\sum_n \left(\partial_{\lambda_n}\langle\psi(t)|\right)\left(\hat{H}(t)|\psi(t)\rangle\right)\partial_{\lambda_n}|\psi(t)\rangle.\end{aligned} \tag{1.60}$$

Crucially, the overlap between two quantum states, as the key ingredient in this above equation, can be efficiently evaluate with the MPS form [319, 319].

Time-dependent variational Monte Carlo— If the ansatz wave function takes the most general general form

$$|\psi\rangle = \sum_m c_m(\lambda_1,\dots,\lambda_n)|m\rangle, \tag{1.61}$$

where $|m\rangle$ forms a complete basis, the overlap between two states typically requires summation of exponentially many terms and thus is hard to compute. An alternative is to use Monte Carlo methods.

Plugging the ansatz wave function Eq. 1.61 into Eq. 1.59, it is straightforward to show that the optimal approximation of $\dot{\vec{\lambda}} := (\frac{d\lambda_1}{dt},\dots,\frac{d\lambda_1}{dt})$ is the best approximate solution of the over-determined linear equation systems

$$A\dot{\vec{\lambda}} - \vec{b} = 0 \tag{1.62}$$

where A is an m-by-n matrix with $A_{m,n} = i\frac{\partial c_m}{\partial\lambda_n} - i\frac{c_m}{\langle\psi(t)|\psi(t)\rangle}\sum_{m'} c^*_{m'}\frac{\partial c_{m'}}{\partial\lambda_n}$, and $\vec{v}$ is an length-m vector with $\vec{b}_m = \langle m|\hat{H}|\psi(t)\rangle - c_m\frac{\langle\psi(t)|\hat{H}|\psi(t)\rangle}{\langle\psi(t)|\psi(t)\rangle}$. Formally, the solution is given by

$$\dot{\vec{\lambda}} = (A^\dagger A)^{-1}A^\dagger\vec{b}, \tag{1.63}$$

where the calculation of $(A^\dagger A)_{n',n} = \sum_m A^*_{m,n'}A_{m,n}$ and $(A^\dagger\vec{b})_n = \sum_m A^*_{m,n}b_m$ should be evaluated via Monte Carlo methods.

To be more concrete, time-dependent variational Monte Carlo (tVMC) assumes a specific form of wave function:

$$c_m(\lambda_1,\dots,\lambda_n) = \exp\left(\sum_n O^{[n]}_m\lambda_n\right), \tag{1.64}$$

where $\hat{O}^{[n]} = \text{diag}(O^{[n]}_1, O^{[n]}_2,\dots)$ are observables diagonal in the $\{|m\rangle\}$ basis. In terms of $\hat{O}^{[n]}$, the

n-th column of A as a vector $\vec{A}^{[n]}$ can be written as

$$\vec{A}_m^{[n]} = i\langle m|\hat{O}^{[n]}|\psi(t)\rangle - ic_m \frac{\langle\psi(t)|\hat{O}^{[n]}|\psi(t)\rangle}{\langle\psi(t)|\psi(t)\rangle}. \tag{1.65}$$

The calculation of the two ingredients in Eq. 1.63 then becomes largely simplified to the evaluation of polynomially many observables:

$$(A^\dagger A)_{n',n} = \vec{A}^{[n']} \cdot \vec{A}^{[n]} = \langle \hat{O}^{\dagger[n']}\hat{O}^{[n]}\rangle - \langle \hat{O}^{\dagger[n']}\rangle\langle \hat{O}^{[n]}\rangle, \tag{1.66}$$

$$(A^\dagger \vec{b})_n = \vec{A}^{[n]} \cdot \vec{b} = \langle \hat{O}^{\dagger[n]}\hat{H}\rangle - \langle \hat{O}^{\dagger[n]}\rangle\langle \hat{H}\rangle, \tag{1.67}$$

where $\langle\cdots\rangle$ denotes $\langle\psi(t)|\cdots|\psi(t)\rangle$. For each of these observables, instead of matrix multiplication (which is still exponentially hard), Monte Carlo method should be employed [322, 339, 340, 342]. Specifically, one samples the coefficients $|c_m|^2$ using the Metropolis–Hastings algorithm [351]. Each update step has a time complexity proportional to the number of the parameters λ_m. If $\{|m\rangle\}$ forms local basis for the many-body system, and all the $\hat{O}^{[n]}$ in the ansatz are few-body operators, each update step will only cost constant time.

1.5.5 Semi-classical approach: truncated Wigner approximation

In the framework of Hamiltonian mechanics for classical systems, the equations of motion for classical variables O_{cl} are generated straightforwardly by the Poisson bracket,

$$\dot{O}_{cl} = \{H, O_{cl}\}. \tag{1.68}$$

The dynamics of a closed classical system can thus be conceptualized as an initial value problem of a non-linear first-order ordinary differential equation system. To obtain numerical solutions, temporal discretization and linear multistep (Runge-Kutta) methods are typically employed, with higher-order Runge-Kutta methods often being necessary in many-body dynamics to reduce discretization errors.

Switching back to quantum systems, the operator dynamics (Eq. 1.51) are formally identical to the dynamics of classical variables (Eq. 1.68), upon mapping quantum commutators to classical Poisson brackets. However, two fundamental distinctions arise due to quantum observables being operators rather than numbers. First, a simple replacement of quantum operators with their expectation

values in Eq. 1.51 loses the information about quantum fluctuations. Second, unlike in deterministic classical dynamics, the expectation values of quantum observables do not factorize, namely, $\langle \hat{O}_i \hat{O}_j \rangle \neq \langle \hat{O}_i \rangle \langle \hat{O}_j \rangle$. This non-factorizability complicates the equations of motion, as taking expectation values on both sides of Eq.1.51 for all single-body operators fails to yield a closed set of equations. Theoretically, a complete description involving exponentially many equations of motions can capture all the many multi-body observables. However, this becomes equivalent to Schrodinger's equation and the exponential difficulty reemerges.

Within the framework of operator evolution, the concept of Wigner quasiprobability distribution enables an approximate method, named truncated Wigner approximation, to numerically solve the quantum dynamics in a semi-classical way. In such approximation, quantum states with quantum fluctuations and probabilistic measurement outcomes are mimicked by classical ensembles with statistical fluctuations. In particular, this numerical protocol comprises three steps [325–328, 344, 345]: 1) Randomly select a classical state from an initial classical ensemble based on the Wigner quasiprobability distribution [16]; 2) Generate the subsequent dynamics as if the system is classical, i.e., treating the multi-body observables on the right-hand side of Eq. 1.51 as c-numbers, hence simply treating them as products of single-body observables; and 3) Iteratively repeat the previous two steps and average over enough classical trajectories to obtain the dynamics of the quantum system.

For continuous quantum degrees of freedom, the Wigner distribution typically forms a continuous function in the phase space. For instance, to simulate kinetic motions of quantum particles, the initial ensemble can be chosen as a normal distribution in the position-momentum phase space [328, 344, 345]. In contrast, internal degrees of freedom with discrete level structures requires a discrete version of Wigner function [352]. This leads to the discrete truncated Wigner approximation (dTWA) [325–327]. Consider spin-1/2 systems as an example: for a fully polarized initial state where all spins are aligned along x-axis, each classical spin vector $(S^x_{cl,i}, S^y_{cl,i}, S^z_{cl,i})$ in the associated initial discrete classical

[16]The Wigner distribution for the initial quantum state must be positive definite, which is generally satisfied for simple product states. This is consistent with the expectation that the dynamics from an highly entangled quantum states (which have negative Wigner distribution) in general cannot be simulated by classical methods.

ensemble follows an independent and identical distribution

$$P(\frac{1}{2},\frac{1}{2},\frac{1}{2}) = P(\frac{1}{2},-\frac{1}{2},\frac{1}{2}) = P(\frac{1}{2},\frac{1}{2},-\frac{1}{2}) = P(\frac{1}{2},-\frac{1}{2},-\frac{1}{2}) = \frac{1}{4}. \tag{1.69}$$

It is worth remarking that a less strict but more intuitive perspective is that this choice of initial ensemble ensures both the mean and the variance of the classical observables to agree with the corresponding quantum objects.

Chapter 2

Relaxation process to equilibrium

The prevailing consensus asserts that macroscopic classical phenomena naturally emerge from microscopic quantum laws [164, 353–358]. In the context of many-body system relaxing towards equilibrium, even in the absence of a precise microscopic description, classical hydrodynamics provides a powerful framework for characterizing the late-time macroscopic behavior of local, conserved quantities, such as energy. Typically, one expects a far-from-equilibrium system to initially undergo local thermalization and rapidly approaching local equilibrium. By then, the system becomes described by the density of a few spatially inhomogenous conserved quantities, such as energy density. These conserved charges then travel across and redistribute throughout the system, eventually leading to global equilibrium; in this latter step, a hydrodynamical description (i.e., a set of continuous classical differential equations for coarse-grained quantum observables) usually applies [164, 359–368].

Despite this seemingly intuitive process, the actual relaxation dynamics of quantum many-body systems are significantly more intricate. Firstly, for an open quantum system coupled to an environment, the shift towards classical behavior at late times is expected due to dephasing from the bath, erasing the intrinsic quantum coherence of the system. However, in an isolated strongly-interacting quantum system, understanding how classical description emerges and the requisite conditions for such emergence remain fundamental open questions [164, 166, 318, 367, 369–373]. In fact, exceptions exist, such as many-body localized systems, which do not evolve towards thermal equilibrium in the first place. Secondly, the quantitative prediction of emergent "classical" properties of a system (e.g., dif-

fusivity, viscosity, heating rate under a drive) from a generic microscopic quantum Hamiltonian poses a persistent challenge for analytics, numerics and experiments [164, 166, 318, 367, 369, 370, 373, 374]. Finally, while the general expectation of hydrodynamics usually holds, the late-time hydrodynamical behaviors may still be qualitatively distinct in different systems, systemically characterized by the concept "dynamical universality class". It has recently become another active direction to identify various universality classes and explore their relationship to the fundamental properties of quantum models, such as integrability, symmetries and the presence of disorder or external drive [367, 372, 373, 375–378]. This chapter will present several advancements along these research directions on both the theoretical and the experimental fronts.

2.1 Emergent hydrodynamics in nonequilibrium quantum systems

2.1.1 Introduction

Understanding the non-equilibrium dynamics of strongly correlated quantum systems represents a central challenge at the interface of condensed matter, atomic physics and quantum information science. This challenge stems in part from the fact that such systems can be taken out of equilibrium in a multitude of different ways, each with its own set of expectations and guiding intuition.

For example, under a quench, one typically expects a many-body system to quickly evolve toward local thermal equilibrium [89, 90, 92, 93, 96, 379]. At first sight, this suggests a simple description. However, capturing both the microscopic details of short-time thermalization as well as the cross-over to late-time hydrodynamics remains an open challenge [149, 150, 152, 153, 380–384]. Indeed, despite nearly a century of progress, no general framework exists for perhaps the simplest question: How does one derive a classical diffusion coefficient from a quantum many-body Hamiltonian?

Alternatively, a many-body system can also be taken out of equilibrium via periodic (Floquet) driving — a strategy which has received a tremendous amount of recent attention in the context of novel Floquet phases of matter [221–226, 232, 236, 385, 386]. In this case, the non-equilibrium system is generically expected to absorb energy from the driving field (so-called Floquet heating) until it approaches a featureless infinite temperature state [177, 387–391].

While these questions are naturally unified under the umbrella of non-equilibrium dynamics [1], understanding the interplay between Floquet heating, emergent hydrodynamics and microscopic thermalization represents a crucial step toward the characterization and control of non-equilibrium many-body systems [178, 180, 181, 191–194, 392]. That one expects such connections can already been seen in certain limits; for example, in the limit of a high-frequency Floquet drive, energy absorption is set by an extremely slow heating rate. Thus, one anticipates a relatively long timescale where the system's stroboscopic dynamics can be captured by an effective static *prethermal Hamiltonian*. These expectations immediately lead to the following question: How do the late-time dynamics of driven quantum systems account for both the prethermal Hamiltonian's hydrodynamics and the energy

[1] Many other phenomena also fall under this umbrella including dynamics in localized and open stochastic systems

absorption associated with Floquet heating?

Until now, such questions have remained largely unexplored owing to the fact that they sit in a region of phase space where neither theoretical techniques nor numerical methods easily apply. However, a number of recently proposed numerical methods [317, 321, 345, 371, 393] promise to bridge this gap and directly connect microscopic models to emergent macroscopic hydrodynamics. In this section, we will focus on one such method — density matrix truncation (DMT) [317] — which modifies time-evolving block decimation (TEBD) by representing states as matrix product density operators (MPDOs) and prioritizing short-range (over long-range) correlations.

Working with a generic, one-dimensional spin model, in this section, we use DMT to investigate a broad range of non-equilibrium phenomena ranging from Floquet heating to emergent hydrodynamics. Our main results are three fold. First, we find that DMT accurately captures two essential pieces of Floquet physics: prethermalization and heating to infinite temperature (Fig. 2.1). Crucially, the truncation step intrinsic to DMT enables us to efficiently explore the *late-time* dynamics of large-scale quantum systems (up to $L = 100$), at the cost of imperfectly simulating the system's *early-time* dynamics.

This trade-off hinges on DMT's efficient representation of local thermal states, making it a natural tool for studying emergent hydrodynamics. Our latter two results illustrate this in two distinct contexts: 1) directly measuring the energy diffusion coefficient for a static Hamiltonian, and 2) demonstrating the interplay between Floquet heating and diffusion in an inhomogeneously driven spin chain. We hasten to emphasize that such calculations are fundamentally impossible for either exact diagonalization based methods (owing to the size of the Hilbert space) or conventional TEBD methods (owing to the large amount of entanglement at late times).

2.1.2 Model and phenomenology

We study the dynamics of a one-dimensional spin-$1/2$ chain whose evolution is governed by a time periodic Hamiltonian $H(t) = H_{\text{static}} + H_{\text{drive}}(t)$, where

$$H_{\text{static}} = \sum_{i=1}^{L-1} [J\sigma_i^z\sigma_{i+1}^z + J_x\sigma_i^x\sigma_{i+1}^x] + h_x \sum_{i=1}^{L} \sigma_i^x \,, \tag{2.1}$$

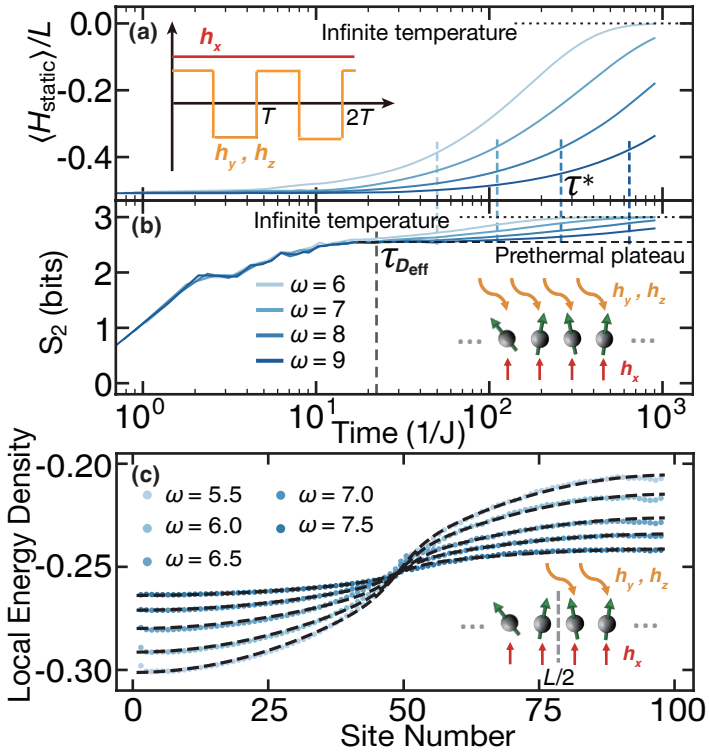

Figure 2.1: Floquet thermalization of an $L = 100$ spin chain. (a) Average energy density measured with respect to $H_{\text{static}} \approx D_{\text{eff}}$ under a global drive. The heating timescale τ^* is extracted from the energy's exponential approach to its infinite-temperature value, and depends exponentially on the driving frequency (for explicit scaling, see Fig. 2.7a.) (b) The second Rényi entropy of the leftmost three sites. The dashed lines are computed using the prethermal Gibbs ensemble. (c) Spatial profiles of energy density under a half-system drive with $\langle H_{\text{static}} \rangle / L = -0.25$. Insets: the drive's time dependence (a) and schematics of the global drive (b) and the half-system drive (c).

with σ_i^α being the Pauli operators acting on site i. The drive, $H_{\text{drive}}(t) = H_{\text{drive}}(t+T)$, exhibits a period $T = 2\pi/\omega$ and corresponds to an oscillating field in the $\hat{y}$ and $\hat{z}$ directions:

$$H_{\text{drive}}(t) = \sum_{i=1}^{L} v_i(t) \left(h_y \sigma_i^y + h_z \sigma_i^z\right). \tag{2.2}$$

In this work we will consider two different driving protocols (Fig. 2.1 insets) a **global drive**, with all spins driven [$v_i(t) = \text{sgn}\cos(\omega t)$], and a **half-system drive**, with only the right half driven [$v_{i\leq L/2}(t) = 0$ and $v_{i>L/2}(t) = \text{sgn}\cos(\omega t)$]. Throughout the letter, we work in the high-frequency regime with $\omega \geq 5J$, and choose the parameters to be $\{J, J_x, h_x, h_y, h_z\} = \{1, 0.75, 0.21, 0.17, 0.13\}$. We expect our choice of the model and parameters to be generic as we observe the same phenomenology upon varying both the parameters and the interaction Hamiltonian.

The quenched dynamics of a high-frequency driven system is characterized by two timescales. The heating timescale, τ^* (Fig. 2.1a), determines the rate of energy absorption from the drive and is proven to be at least exponential in the frequency of the drive, $\tau^* \geq \mathcal{O}(e^{\omega/J_{\text{local}}})$, where J_{local} is a local energy scale [178, 181, 191–194]. Up until τ^*, the stroboscopic dynamics of the system is well described by the *static* prethermal Hamiltonian $D_{\text{eff}} = H_{\text{static}} + \mathcal{O}(\omega^{-1})$, which can be obtained as the truncation of the Floquet-Magnus expansion of the evolution operator [178, 192, 193]. The prethermalization timescale, $\tau_{D_{\text{eff}}}$ (Fig. 2.1a,b), determines the time at which the system approaches an equilibrium state with respect to D_{eff}. When $\tau_{D_{\text{eff}}} \ll \tau^*$, the system exhibits a well defined, long-lived prethermal regime.

In Figs. 2.1a,b, we illustrate these two timescales by computing the dynamics of an $L = 100$ Floquet spin chain using DMT [2]. The average energy density $\langle H_{\text{static}}(t)\rangle / L$ exhibits the expected phenomenology (Fig. 2.1a): it remains constant (up to ω^{-1} corrections) until τ^*, after which it begins to approach its infinite temperature value $\langle H_{\text{static}}\rangle_{T=\infty} = 0$.

To probe the prethermalization timescale $\tau_{D_{\text{eff}}}$, a different diagnostic is needed. In particular, we compute the second Rényi entropy, $S_2 = -\log_2 \text{tr}\left[\rho_{\text{s}}^2\right]$, where ρ_{s} is the reduced density matrix of the three leftmost spins. While the system begins in a product state with $S_2 = 0$, its entropy quickly approaches a *prethermal plateau*, consistent with the Gibbs state of D_{eff} at a temperature that matches the initial energy density (Fig. 2.1b). The timescale at which this occurs corresponds to $\tau_{D_{\text{eff}}}$ and, indeed, we observe $\tau_{D_{\text{eff}}} \sim 1/J_{\text{local}}$ independent of the driving frequency ω. Similar to the energy density, at late times $t > \tau^*$, S_2 begins to approach its infinite temperature value, $S_2^{T=\infty} = 3$ bits.

2.1.3 Benchmarking DMT

To confirm the reliability of DMT in the simulation of Floquet dynamics, we compare it with Krylov subspace methods. This analysis not only gauges the applicability of DMT, but also leads to insights into the nature of the Floquet heating process. In particualr, we utilize three diagnostics to compare the time evolution between DMT and Krylov: the average energy density (Fig. 2.2a), local

[2] In our calculations, we consider a generic initial state, typically taken to be a Néel state with a domain wall every four spins. We have checked that our observations are independent of initial state.

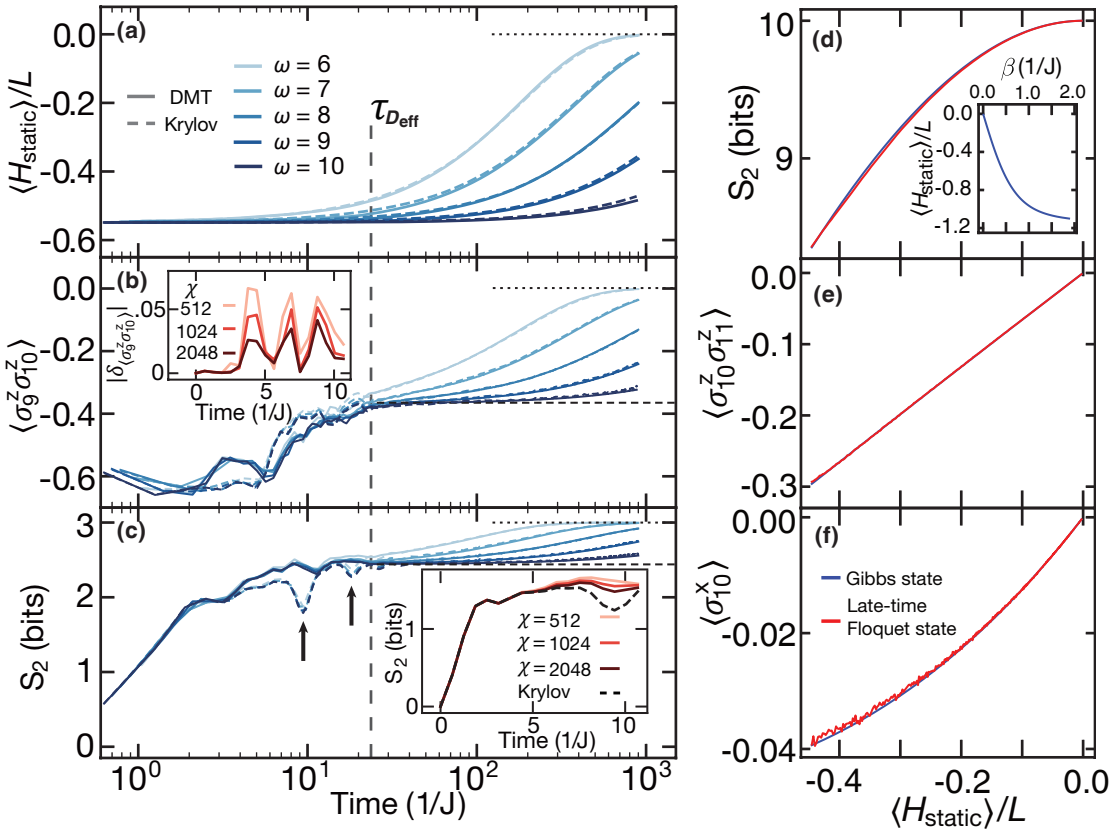

Figure 2.2: (a)(b)(c) Comparison between DMT and Krylov of the time evolution of an $L = 20$ spin chain under a global drive (at fixed bond dimension $\chi = 64$). (a) Average energy density $\langle H_{\text{static}} \rangle / L$. (b) A typical local observable $\sigma^z_9 \sigma^z_{10}$. (c) The second Rényi entropy S_2 of the leftmost three sites. The arrows mark resonance-like dips, which DMT fails to capture. The dashed lines are computed using the prethermal Gibbs ensemble. Insets (early-time behavior at frequency $\omega = 10$): (b) errors in the local observable $\delta_{\langle \sigma^z_9 \sigma^z_{10} \rangle} = \langle \sigma^z_9 \sigma^z_{10} \rangle_{\text{DMT}} - \langle \sigma^z_9 \sigma^z_{10} \rangle_{\text{Kry}}$, (c) errors in S_2. (d) Second Rényi entropy of the half chain, (e) a two-site local observable (f) a single-site local observable as functions of the average energy density for the imaginary-time evolved Gibbs state $e^{-\beta D_{\text{eff}}}$ and the late-time Floquet state ($L = 20$, $\omega = 6$). The agreement between the two states demonstrates that the late-time Floquet system is simply evolving between different Gibbs states of D_{eff}. Inset: The average energy density as a function of inverse temperature.

two-point correlation functions (Fig. 2.2b), and the second Rényi entropy (Fig. 2.2c).

At early times ($t < \tau_{D_{\text{eff}}}$), one observes substantial disagreements between DMT and Krylov (Fig. 2.2b,c). This is to be expected. Indeed, the accurate description of early-time thermalization dynamics depends sensitively on the details of long-range correlations which DMT does not capture. An exception to this is the energy density, whose changes are expected to be exponentially small in frequency [178, 181, 191, 193]. This is indeed born out by the numerics where one finds that $\langle H_{\text{static}} \rangle / L$ remains quasi-conserved and in excellent agreement with Krylov (Fig. 2.2a).

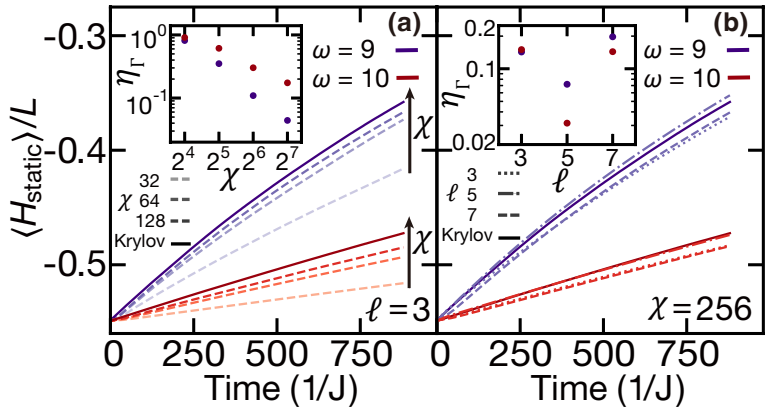

Figure 2.3: Energy density at (a) bond dimension $\chi = 32, 64, 128$ and (b) the preservation diameter $\ell = 3, 5, 7$. Insets: relative error in the heating rate $\eta_\Gamma = |\Gamma_{\text{DMT}} - \Gamma_{\text{Krylov}}|/\Gamma_{\text{Krylov}}$, where $\Gamma = 1/\tau_E^*$ is defined by $\frac{d}{dt}\langle H_{\text{static}} \rangle = -\Gamma \langle H_{\text{static}} \rangle$.

One might naively expect the early-time disagreements to lead to equally large intermediate-time ($\tau_{D_{\text{eff}}} < t < \tau^*$) deviations. This is not what we observe. Indeed, all *three* diagnostics show excellent agreement between DMT and Krylov (Fig. 2.2). This arises from a confluence of two factors. First, DMT accurately captures the system's energy density, which in turn, *fully* determines the prethermal Gibbs state; second, DMT can efficiently represent such a Gibbs state. Thus, although DMT fails to capture the *approach* to the prethermal Gibbs state, it nevertheless reaches the same equilibrium state at $t \sim \tau_{D_{\text{eff}}}$. Afterwards (for $t > \tau_{D_{\text{eff}}}$), the system is simply evolving between different Gibbs states of D_{eff} (Fig. 2.2def), wherein one expects agreement between DMT and Krylov even at relatively low bond dimension (Fig. 2.2abc).

Small disagreements between DMT and Krylov, however, re-emerge at very late times ($t > \tau^*$) and large frequencies, reflecting the physical nature of Floquet heating (Fig. 2.2a). In particular, as the frequency increases, absorbing an energy quantum from the drive requires the correlated rearrangement of a greater number of spins [181, 191, 193]. However, these longer-ranged correlations are *not* strictly preserved by DMT, leading to an artificial (truncation-induced) suppression of heating at large frequencies (Fig. 2.3).

This raises the question: How does the accuracy of DMT converge with both bond dimension and preservation diameter? As expected, increasing χ at fixed ℓ improves the accuracy of DMT since the amount of information preserved during each truncation step is greater, Fig. 2.3a. Curiously, tuning

ℓ at fixed χ can *also* affect the accuracy, despite not changing the amount of information preserved, Fig. 2.3b. This suggests the tantalizing possibility that one can achieve high accuracy at relatively low bond dimension by carefully choosing the operators which are preserved.

2.1.4 Floquet heating dynamics

As a first demonstration of DMT's potential for extracting quantitative information about the Floquet dynamics, we directly measure the heating rate. We find that both $\langle H_{\text{static}} \rangle / L$ and S_2 exhibit an exponential approach toward their infinite-temperature values: $|\langle H_{\text{static}} \rangle / L| \propto e^{-t/\tau_E^*}$ and $(S_2^{T=\infty} - S_2) \propto e^{-2t/\tau_S^*}$. To this end, we extract τ_E^* and τ_S^* as independent measures of the Floquet heating timescale [3]. For a Gibbs ensemble of H at temperature T, the probability p_i assigned to the i'th eigenstate (with ϵ_i being its eigenenergy) can be approximated to the first order as

$$p_i = \frac{e^{-\beta\epsilon_i}}{\text{tr}\left[e^{-\beta H}\right]} \approx \frac{1-\beta\epsilon_i}{\text{tr}[1-\beta H]} = 2^{-L}(1-\beta\epsilon_i), \tag{2.3}$$

where $\beta = 1/T$, 2^L is the dimension of the Hilbert space, and we can always set $\text{tr}\, H = 0$. The energy is then written as:

$$E = \sum_i p_i \epsilon_i \approx 2^{-L} \sum_i (1-\beta\epsilon_i)\epsilon_i = -2^{-L} \sum_i \beta\epsilon_i^2 \propto \beta. \tag{2.4}$$

A similar estimate can be made for the second Rényi entropy of the entire system:

$$\Delta S_2 = L - S_2 = L + \log_2 \sum_i p_i^2 \approx \log_2 \left[2^{-L} \sum_i (1-\beta\epsilon_i)^2 \right] = \beta^2 2^{-L} \sum_i \epsilon_i^2 \propto \beta^2 \propto E^2. \tag{2.5}$$

. Crucially, they agree with one another across all system sizes studied ($L = 20$–100), as shown in Fig. 2.7a. Varying the frequency of the drive further allows us to extract the effective local energy scale which controls the heating dynamics: $J^E_{\text{local}} = 1.21 \pm 0.04$ and $J^S_{\text{local}} = 1.16 \pm 0.04$. This is consistent with the microscopic onsite energy scale, $\|H_{\text{static}}\|/L \simeq 1.26$ [4].

---

[3] The factor of 2 difference in the definitions of τ_E^* and τ_S^* ensures the consistency between the extracted heating timescales from $\langle H_{\text{static}} \rangle$ and S_2 (in the high-temperature regime)

[4] We define the microscopic onsite energy scale as the norm of the local Hamiltonian on each bond $\|J\sigma_i^z\sigma_{i+1}^z + J_x\sigma_i^x\sigma_{i+1}^x + h_x(\sigma_i^x + \sigma_{i+1}^x)/2\|$; this differs by a (subextensive) boundary term from $\|H_{\text{static}}\|/L$.

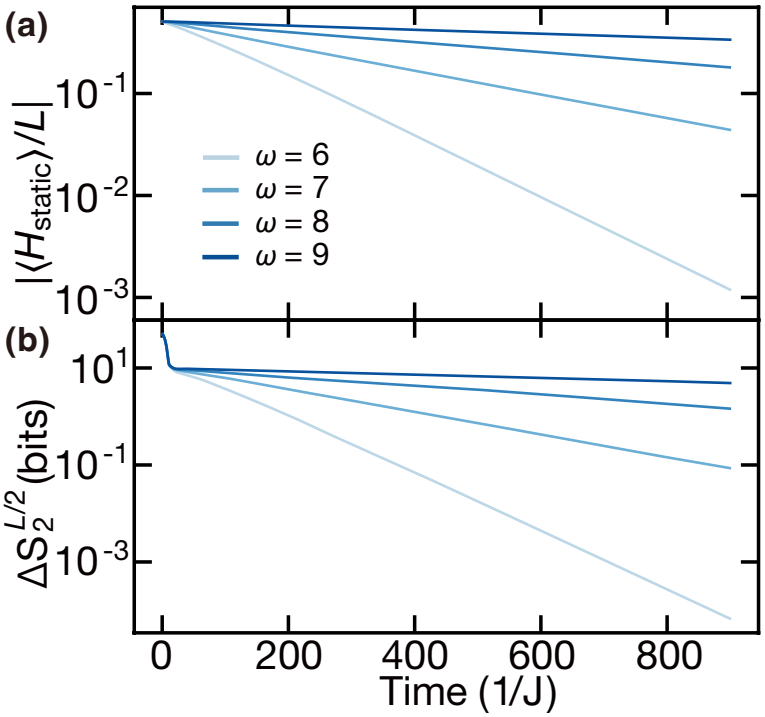

Figure 2.4: The average energy density $\langle H_{\text{static}}|H_{\text{static}}\rangle / L$ and the entropy $\Delta S_2 = S_2^{T=\infty} - S_2(t)$ decay exponentially zero. The Floquet heating rate corresponds to the slopes in the logarithmic scale.

2.1.5 Observing emergent hydrodynamics

Having established that DMT accurately captures the late-time thermalization of Floquet systems, we now apply it to the study of a much broader question: the emergent hydrodynamics of large (undriven) quantum spin chains ($L = 100$). In particular, our main goal here is to measure the diffusion coefficient as a function of temperature.

Our setup is the following. On top of an initial thermal state with respect to H_{static}, we add a small spatial inhomogeneity in the energy density (taken to be a Fourier mode). In particular, we consider an initial Gibb ensemble [5]

$$\rho_\beta = Z^{-1} \exp\left\{-\beta\left[H + \eta H^q_{\text{perturb}}\right]\right\} \tag{2.9}$$

[5] In DMT, the thermal state can be straightforwardly generated by performing imaginary time evolution on the infinite temperature state $\rho_{T=\infty} \propto \mathbb{1}$:

$$\rho_\beta = Z^{-1} \exp\left\{-\beta\left[H + \eta H_{\text{perturb}}\right]\right\} . \tag{2.6}$$

In contrast, because Krylov subspace methods can only treat pure states, it is impossible to directly compute expectations of the thermal state. Nevertheless, expectation values over the thermal density matrix ρ_β can be obtained by averaging over

where

$$H^{[k]}_{\text{perturb}} = \sum_{\text{site } i=0}^{L-1} h_i \cos \frac{ki\pi}{L-1} \tag{2.10}$$

represents a family of perturbation which generates the q-th mode of the excess local conserved quantity h_i. To probe the energy diffusion, we specifically choose h_i to be the local energy density operator $J\sigma^z_i\sigma^z_{i+1} + J_x\sigma^x_i\sigma^x_{i+1} + \frac{h_x}{2}(\sigma^x_i + \sigma^x_{i+1})$.

Once the initial state is generated, we evolve system with H_{static}, and observe that the initial spatial profile of the local energy quickly decays and the system becomes spatially uniform due to the diffusion of the energy density. Crucially, the amplitude of this spatial variation decays exponentially, with a rate that scales as k^2, where k is the wave-vector of the Fourier mode. This quadratic scaling is characteristic of diffusion and confirms the emergence of hydrodynamics from our microscopic quantum Hamiltonian.

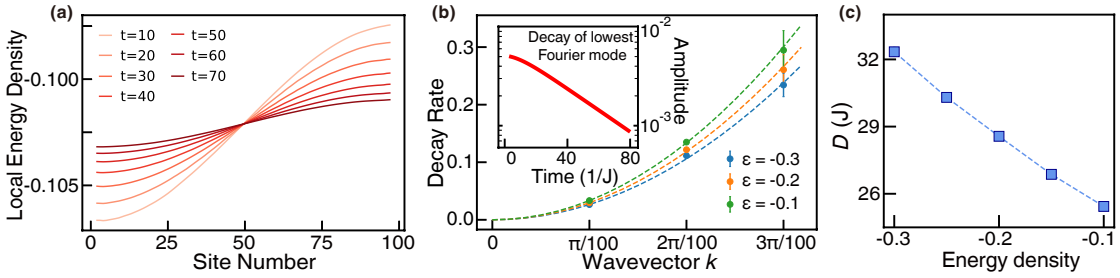

Figure 2.5: (a) The evolution of the first Fourier mode under H_{static}. (b) The decay rate of Fourier modes depends quadratically on the wavevector. The system size considered is $L = 100$. Inset: Decay of Fourier modes at large system size. β is chosen such that the average energy density is set to be $\bar{\epsilon} = -0.1$. (c) Extracted diffusion coefficient as a function of energy density in the undriven spin chain.

---

initial states, which are then imaginary time evolved:

$$\text{tr}\Big\{O\rho_\beta\Big\} = \frac{1}{D}\sum_{i=1}^{D}\Big\langle\psi_i\Big|\rho_\beta^{1/2}\,O\,\rho_\beta^{1/2}\Big|\psi_i\Big\rangle \approx \frac{1}{N_{ave}}\sum_{i=1}^{N_{ave}}\Big[\Big\langle\psi_i\Big|\rho_\beta^{1/2}\Big]\,O\,\Big[\rho_\beta^{1/2}\Big|\psi_i\Big\rangle\Big]\ . \tag{2.7}$$

Due to the large size D of the Hilbert space, we cannot perform the entire calculation. Instead we approximate it by averaging over N_{ave} number of *random* initial states $|\psi_i\rangle$:

$$|\psi_i\rangle \propto \sum_{i=1}^{D} c_i\,|i\rangle\,, \quad c_i \text{ normal distributed complex variables} \tag{2.8}$$

Due to quantum typicality, such random states behave as infinite temperature states (for local operators) [394], and so the number of N_{ave} need not be very large (we use $N_{ave} = 50$).

A few remarks are in order. First, by further varying the temperature of the initial Gibbs ensemble ($1/\beta$ in Eq. 2.9), one can also study the diffusion coefficient, $D(\epsilon)$, as a function of the energy density ϵ (Fig. 2.5c). Second, in this setup, we have also confirmed that DMT gives dynamics consistent with Krylov at small system sizes ($L = 20$). Third, our method, near infinite temperature ($\epsilon = 0$), matches independent calculations of the diffusion [395]. Finally, we emphasize that such a numerical observation of emergent hydrodynamics is well beyond the reach of conventional numerics and fundamentally leverages DMT's ability to prepare and evolve highly-entangled states near thermal equilibrium.

Setup	Probe	$J_z < 1$	$J_z = 1$	$J_z > 1$
Domain wall	$P(t) \propto t^{\alpha}$	$\alpha = 1$	$\alpha = 2/3$ [353]	$\alpha = 1/2$
Fourier mode	$A_k(t) = \tilde{A}(kt^{\beta})$	$\beta = 1$	$\beta = 3/2$	$\beta = 2$

Table 2.1: Depending on the value of anisotropy, spin transport in 1D XXZ model exhibit different types of hydrodynamics at high temperature.

Moreover, we note that our procedure can also be applied to the study of *integrable* systems, where different types of anomalous transport can occur, since integrable systems in general relax to generalized Gibbs ensembles (GGE) rather than simple Gibbs ensembles. [164, 166, 171, 353, 396–398]. We highlight this by computing spin transport in the XXZ model. Depending on the Ising anisotropy, one expect the spin transport to be ballistic, super-diffusive or diffusive (see Table 2.1). While these behaviors have been probed via other numerical methods in the setup of polarization transport across a domain wall, we corroborate the existing results by studying the decay of the Fourier modes in our setup described above ((Fig. 2.6)).

2.1.6 Interplay between driving and hydrodynamics

Taking things one step further, we now combine the two previous settings and explore a situation where the interplay between Floquet heating and diffusive transport is crucial for understanding the system's thermalization dynamics. In particular, let us consider the time evolution of a spin chain where only the right half of the system is periodically driven (inset, Fig. 2.1c). At time $t = 0$, the system is initialized in a Néel state with a domain wall every four spins.

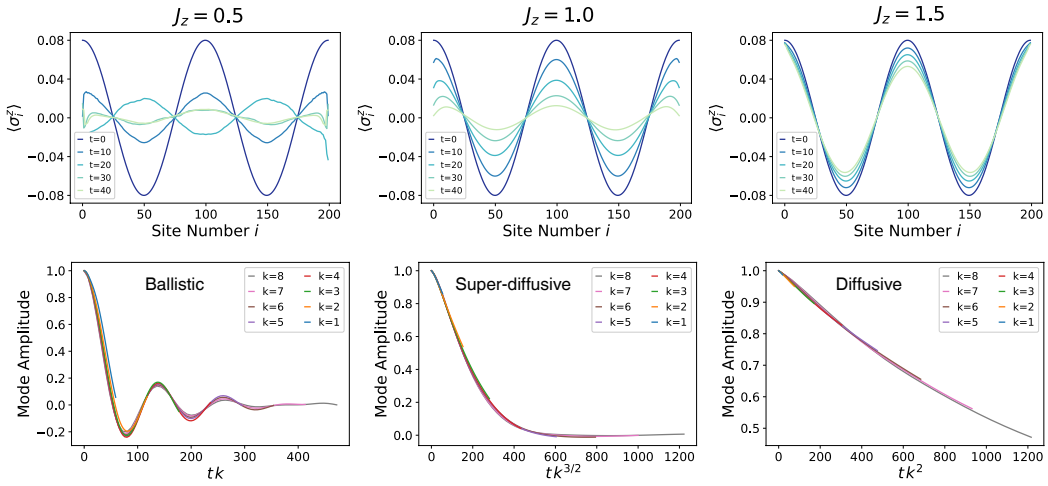

Figure 2.6: Spin relaxation dynamics in 1D XXZ model from initial Fourier modes. Upper panel: spatial profiles of local polarization. Lower panel: the amplitude of the Fourier modes as a function of time. In different parameter regimes, we utilize different scaling exponents to collapse the curves for different wavevectors k, again clearly demonstrating ballistic, super-diffusive and diffusive transport in agreement with Table 2.1.

After an initial period of local equilibration, the combination of inhomogenous driving and interactions leads to three distinct features in the dynamics of the local energy density, as illustrated in Fig. 2.7c. First, the local energy density on the right half of the spin chain is larger, reflecting the location where driving, and thus Floquet heating, is occurring. Second, the energy density across the entire chain gradually increases in time as energy from the right half is transported toward the left half. Third, as the system approaches its infinite temperature state, the overall energy-density inhomogeneity between the left and right halves of the system is reduced.

Leveraging our previous characterizations of both heating and transport, we combine them into such a single hydrodynamical description. The only missing element is a small correction to the transport due to the inhomogeneity of the drive, whose strength we characterize by a small, frequency dependent parameter η.

We now ask the following question: Can all three of these behaviors be *quantitatively* captured using a simple hydrodynamical equation? If so, one might naturally posit the following modified diffusion equation:

$$\partial_t \epsilon(x,t) = D(\epsilon)\partial_x^2\Big([1+\eta g(x)]\epsilon(x,t)\Big) - g(x)\frac{\epsilon(x,t)}{\tau_E^*}. \tag{2.11}$$

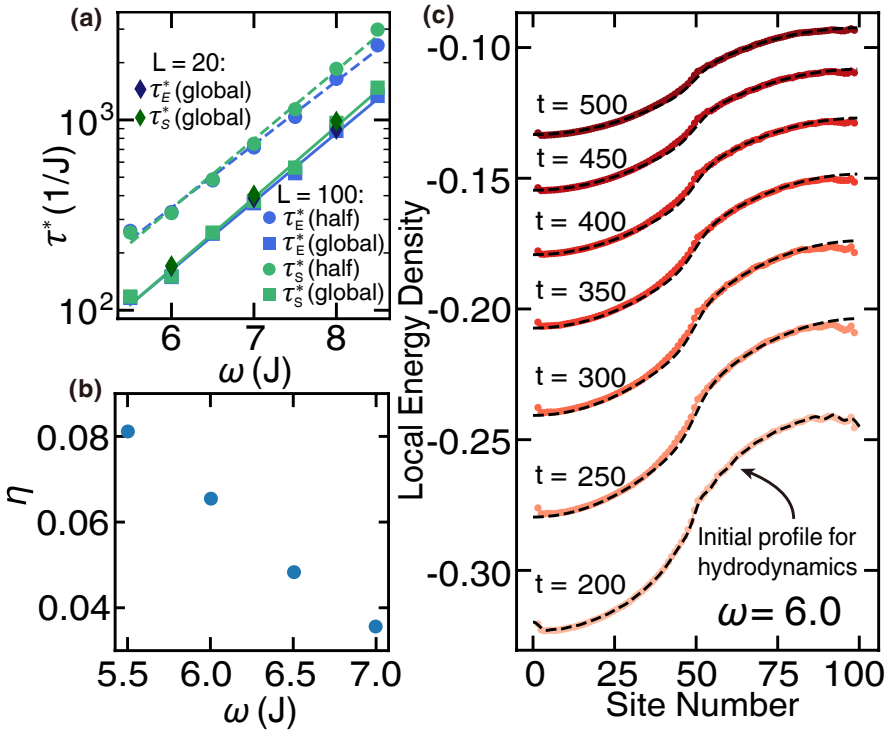

Figure 2.7: (a) Heating timescale, τ^*, extracted in energy density (E) and subsystem entropy (S_2) for $L = 20, 100$. In agreement with theoretical prediction, τ^* depends exponentially on ω. For both driving protocols, we extract the same local energy scale $J^E_{local} \approx 1.21$. However, the half-system drive exhibits a heating timescale twice as large as the global drive. (b) Extracted η decreases as the driving frequency increases. (c) Hydrodynamical description captures the interplay between Floquet heating and diffusive energy transport with half-system drive. Solid curves are computed using DMT. Dashed black curves are computed using a hydrodynamical equation, Eq. 2.11, where one feeds in the DMT-calculated energy-density profile at time $t = 200$. Subsequent time evolution under the differential equation quantitatively reproduces the exact results from DMT.

Here, $g(x)$ is a step-like spatial profile which accounts for the fact that only half the spin chain is being driven [6]. The term proportional to η corresponds to the aforementioned correction to the transport owing to the inhomogeneity of the drive, while the final term in the equation captures the Floquet heating. We emphasize that for the heating rate and the diffusion coefficient, we utilize the previously

[6]The equations governing the heat transport in classical systems are: $\partial_t \epsilon(x,t) = \partial_x j(x,t) + q(x,t)$ and $j(x,t) \propto \partial_x T(x,t)$. Since we drive only the right half of the chain, the mapping from energy density $\epsilon(x,t)$ to temperature $T(x,t)$, as well as the energy absorption $q(x,t)$, varies explicitly in position along the chain. The lowest order $\epsilon(x,t)$ correction to $T(x,t)$ yields a heat current $j(x,t) \propto \partial_x T(x,t) \propto \partial[(1+\eta g(x))\epsilon(x,t)]$, in which $g(x)$ captures this inhomogeneity in the mapping from ϵ to T, and the small parameter η characterizes its magnitude. Motivated by the heating term in the global drive case, we expect the local heating $q(x,t) = -g(x)\epsilon/\tau^*$. To be specific, $g(x) = \frac{1}{2} + \frac{1}{2}\tanh[(x - L/2)/\xi]$ with $\xi = 5$. Our results are not sensitive to the particular choice of $g(x)$, as long as it resembles a smoothed out step function.

(and independently) determined values $1/\tau_E^*$ and $D(\epsilon)$, respectively (Fig. 2.7a and Fig. 2.5c).

In order to test our hydrodynamical description, we feed in the energy density profile computed using DMT (at time $t = 200$) into Eq. 2.11 and check whether the differential equation can quantitatively reproduce the remaining time dynamics (Fig. 2.7c) [7]. Our only fitting parameter is η, and we take it to be constant across the entire evolution. We find that $\eta \ll 1$ and decreases as frequency increases, consistent with our expectation that for larger driving frequencies, D_{eff} is more homogenous across the chain [Fig. 2.7b]. Remarkably, we observe excellent agreement for the remaining time evolution across all frequencies tested (Fig. 2.1c and 2.7c)! To this end, our results confirm that only a few coarse-grained observables are relevant to the late-time evolution of an interacting quantum system, even under a periodic drive.

[7] We solve the hydrodynamical equation in the momentum space. In particular, by performing the Fourier transform: $\epsilon(x,t) = \sum_{n=0}^{\infty} f_n(t) \cos \frac{n\pi x}{L}$, the hydrodynamical equation becomes

$$\partial_t f_k(t) = -f_k(t) D \left[\frac{k\pi}{L}\right]^2 - \frac{2}{L(1+\delta_{k0})} \sum_{n=0}^{\infty} f_n(t) \left\{ D\eta \left[\frac{k\pi}{L}\right]^2 + \frac{1}{\tau^*} \right\} \int_0^L dx\, g(x) \cos \frac{k\pi x}{L} \cos \frac{n\pi x}{L},$$

which can be solved iteratively. In practice, we consider only the first 40 Fourier modes ($n \leq 40$), which does not inccur significant error.

2.2 Emergent hydrodynamics in a strongly interacting dipolar spin ensemble

2.2.1 Introduction

Unlike the analytical and numerical study, in which the major obstacle is to track the evolution of quantum states in an exponentially large Hilbert space, experimental exploration of late-time hydrodynamics is often challenging due to a few completely distinct reasons. First, while experimental systems by nature evolve quantum mechanically and encode all the information about the dynamics, preparing initial states and measuring final values of observables become two delicate operations. In addition, to investigate how the macroscopic quantities (e.g. diffusivity, viscosity, compressibility) are determined by microscopic degrees of freedom further demands flexible and versatile control of the quantum Hamiltonian. Despite these challenges, tremendous progress in time-resolved measurement techniques (also understood as "pump-and-probe" protocols) has enabled the direct experimental observation of emergent classical diffusion in several classes of quantum systems [354, 355, 399–403]. There are, however, a wide variety of classical dynamical "universality classes" other than diffusion[153, 171, 404, 405]; even within the most common universality of diffusion, certain substantial corrections may persist for extraordinarily long times [406–411]. In this section, we focus on time-resolved experiments in a closed quantum system, which exhibits an unconventional approach to late-time diffusion characterized by a long-lived, non-Gaussian polarization profile.

Our experimental platform consists of two strongly-interacting species of electronic spins in diamond: substitutional nitrogen defects (P1 centers) and nitrogen-vacancy (NV) color centers [6, 412]. By controlling the relative density of these two species, we demonstrate the ability to prepare inhomogeneous spatial profiles of a conserved spin density, as well as to locally probe the resulting nanoscale spin dynamics (Fig. 2.8). These dynamics can be tuned via three independent controls: 1) the initial spin polarization, 2) the average spacing between spins, and 3) the magnitude of the on-site random fields.

Exploring this phase space leads us to an understanding of how the details of the microscopic spin Hamiltonian modify conventional diffusion. By tracking the local autocorrelation function of the spin

polarization, $S_p(t)$, we observe the emergence of a long-time, diffusive power-law, $S_p(t) \sim t^{-3/2}$, for over an order of magnitude in time (Fig. 2.8b). However, the details of this autocorrelation function over a broad range of timescales indicate that, following local initialization, the spin polarization distribution remains non-Gaussian throughout the time-scales accessible in the experiment; this originates from the presence of strong disorder in our system, which leads to a *distribution* of local diffusion coefficients and a Yukawa-like spin polarization profile (Fig. 2.8d).

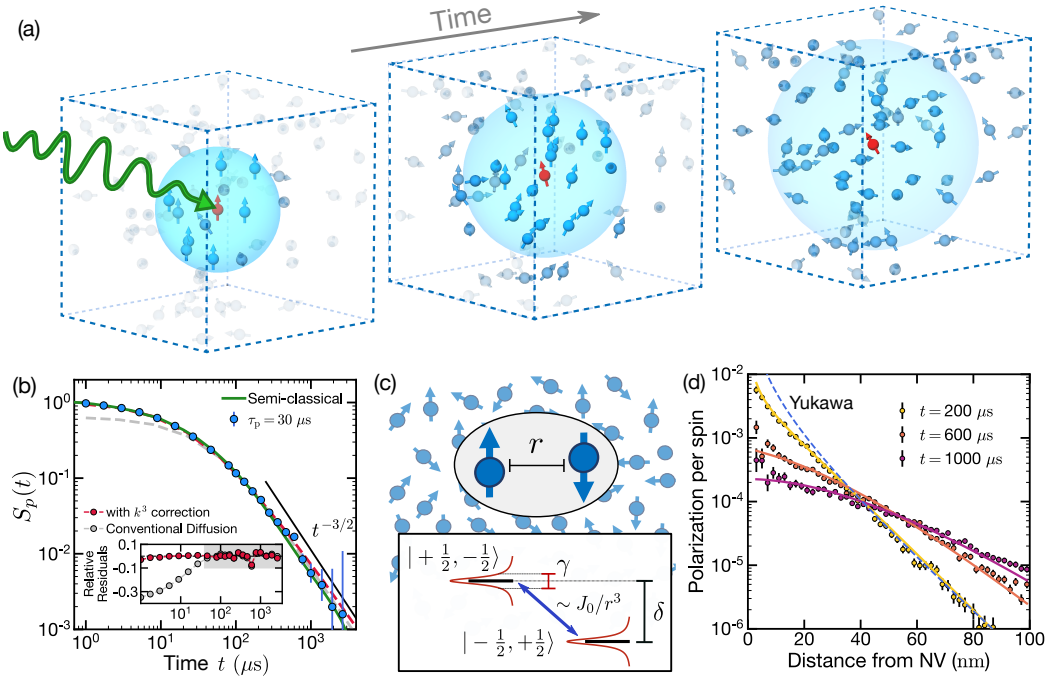

Figure 2.8: (a) Schematic depicting the emergence of hydrodynamics in a strongly interacting dipolar spin ensemble. Optical pumping (green arrow) of the NV center (red) enables it to behave as a polarization source for nearby P1 centers (blue), resulting in the preparation of a local, inhomogenous spin-polarization profile. Dynamics then lead to the spreading of this profile as a function of time. (b) Dynamics of the survival probability $S_p(t)$ of the $\nu = 1/3$ P1 subgroup in sample S2 at $T = 25$ K following a polarization period of $\tau_p = 30\ \mu$s. After an initial transient, $S_p(t)$ approaches a robust power-law decay $\sim t^{-3/2}$, indicating diffusion. The late-time dynamics are accurately described by the diffusion equation (gray dashed line). (inset) Relative residuals when fitting with (red) or without (grey) an additional long-range correction $C_{\rm lr}k^3$ (Fig. 2.12, Appendix A.3.2). In the hydrodynamical regime (grey shaded region) both models capture the data. (c) Illustration of our semi-classical description for the spin-polarization dynamics. Each pair of spins exchanges polarization via the dipolar interaction. The presence of other nearby P1 spins leads to an energy mismatch δ and a homogeneous broadening γ; these parameters are independently measured via pulsed optically detected magnetic resonance and spin-echo decoherence. (d) Initializing with unit polarization, a robust non-Gaussian polarization profile emerges from the semi-classical model for all experimentally accessible time-scales. The crossover from a Yukawa to Gaussian polarization profile is accurately captured by including the disorder-induced dynamical modification, $C_{\rm dyn}k^2\partial_t P_k$, in the diffusion equation with $C_{\rm dyn} = 204 \pm 45\ \text{nm}^3$.

2.2.2 Hybrid spin platform

We choose to work with samples containing a P1 density ~ 100 ppm and an NV density ~ 0.5 ppm, leading to a geometry where each spin-1 NV center is surrounded by a strongly-interacting ensemble of spin-1/2 P1 centers (Fig. 2.8a). In this geometry, the NV center naturally plays the role of both a polarization source and a local probe for nearby P1 centers. These roles rely upon two ingredients. First, the NV center can be optically initialized (to $|m_s^{\mathrm{NV}} = 0\rangle$) and read out using green laser illumination, which does not affect the P1 center. Second, the NV and P1 centers can coherently exchange spin polarization when brought into resonance via an external magnetic field (Fig. 2.9a) [412]; this polarization exchange is driven by the $\Delta m_s = \pm 2$ components of the magnetic dipole-dipole interaction:

$$H_{\text{NV-P1}} = -\sum_i \frac{J_0}{r_{\text{NV},i}^3} \left(A_i \left[S^+ P_i^+ + S^- P_i^- \right] + B_i S^z P_i^z \right), \tag{2.12}$$

where $J_0 = (2\pi) \times 52\ \text{MHz} \cdot \text{nm}^3$ characterizes the strength of the dipolar interaction, $r_{\text{NV},i}$ is the distance between the NV center and the i^{th} P1 center, A_i and B_i capture the angular dependence of the dipolar interaction (Appendix A.1), while $S^{\pm}$ and $P^{\pm}$ are raising and lowering operators for the NV and P1, respectively. We note that $H_{\text{NV-P1}}$ corresponds to the energy-conserving terms of the dipolar interaction, upon restricting our attention to the NV spin subspace $\{|0\rangle, |-1\rangle\}$ (Fig. 2.9a).

In addition, the P1 centers also exhibit dipolar interactions among themselves driven by the $\Delta m_s = 0$ component:

$$H_{\text{P1-P1}} = -\sum_{i<j} \frac{J_0}{r_{i,j}^3} \left(\tilde{A}_{i,j} \left[P_i^+ P_j^- + P_i^- P_j^+ \right] + \tilde{B}_{i,j} P_i^z P_j^z \right) \tag{2.13}$$

where $\tilde{A}_{i,j}$, $\tilde{B}_{i,j}$ are the analogous angular coefficients (Appendix A.1).

When the NV and P1 are off-resonant, we observe an NV depolarization timescale, $T_{\text{depol}} = 2.3 \pm 0.1$ ms, consistent with room-temperature, spin-phonon relaxation (Fig. 2.9b) [6]. By applying a magnetic field, $B = 511$ G, along the NV axis, the NV's $|0\rangle \leftrightarrow |-1\rangle$ transition becomes resonant with the P1's $\left|-\frac{1}{2}\right\rangle \leftrightarrow \left|+\frac{1}{2}\right\rangle$ transition (Fig. 2.9a), and we find that T_{depol} decreases by over two orders of magnitude to 8.9 ± 0.6 μs (Fig. 2.9b) [412]. We emphasize that the reduced T_{depol} should not be thought of as extrinsic decoherence, but rather as a consequence of coherent NV-P1 interactions

(Fig. 2.9e).

2.2.3 Local spin polarization

By continuously repolarizing the NV center via green laser excitation, one can use $H_{\text{NV-P1}}$ to transfer spin polarization to nearby P1 centers; this polarization is further spread-out among the P1s by $H_{\text{P1-P1}}$. The duration of the laser excitation, τ_{p}, then controls the amplitude, shape and width of the local spin polarization. A longer τ_{p} leads to a larger local P1 polarization, which acts as a "frozen core" around the NV center (inset, Fig. 2.9b), suppressing dipolar spin exchange from $H_{\text{NV-P1}}$ [413]. This suppression suggests that T_{depol}, measured *after* P1 polarization, should be significantly enhanced. This is indeed borne out by the data. As shown in Fig. 2.9b,d, T_{depol} is extended by an order of magnitude as a function of increasing τ_{p}. The increase saturates as τ_{p} approaches the spin-phonon relaxation time and the polarization process reaches a steady state (Fig. 2.9d) [414].

2.2.4 Probing nanoscale spin dynamics

To study the long-time dynamics associated with the dipolar-induced spreading of our initial polarization profiles, it is essential to distinguish between early-time local equilibration and late-time emergent dynamics. To this end, we introduce an experimental technique which allows us to explicitly observe local thermalization. In particular, after polarizing for τ_{p}, we utilize a microwave π-pulse to shelve the NV population from $|0\rangle$ into the highly off-resonant $|+1\rangle$ state (bottom inset, Fig. 2.9c). Next, we perform a global microwave π-pulse on the $\left|-\frac{1}{2}\right\rangle \leftrightarrow \left|+\frac{1}{2}\right\rangle$ P1-transition, flipping the ensemble's spin polarization. Finally, we unshelve the NV population, effectively preparing an initial condition where the NV is antipolarized relative to the P1 ensemble (top inset, Fig. 2.9c).

The dynamics starting from this antipolarized configuration are markedly distinct. First, the NV polarization quickly changes sign and reaches a negative value, indicating local thermalization with the oppositely oriented P1 ensemble. Second, the larger the antipolarization (controlled by τ_{p}), the faster the NV initially decays (Fig. 2.9c,d). Crucially, this allows us to extract a characteristic time-scale for local thermalization, $\tau_{\text{th}} \sim 12\ \mu$s.

Returning to the polarized case, we can now leverage the shelving technique to experimentally

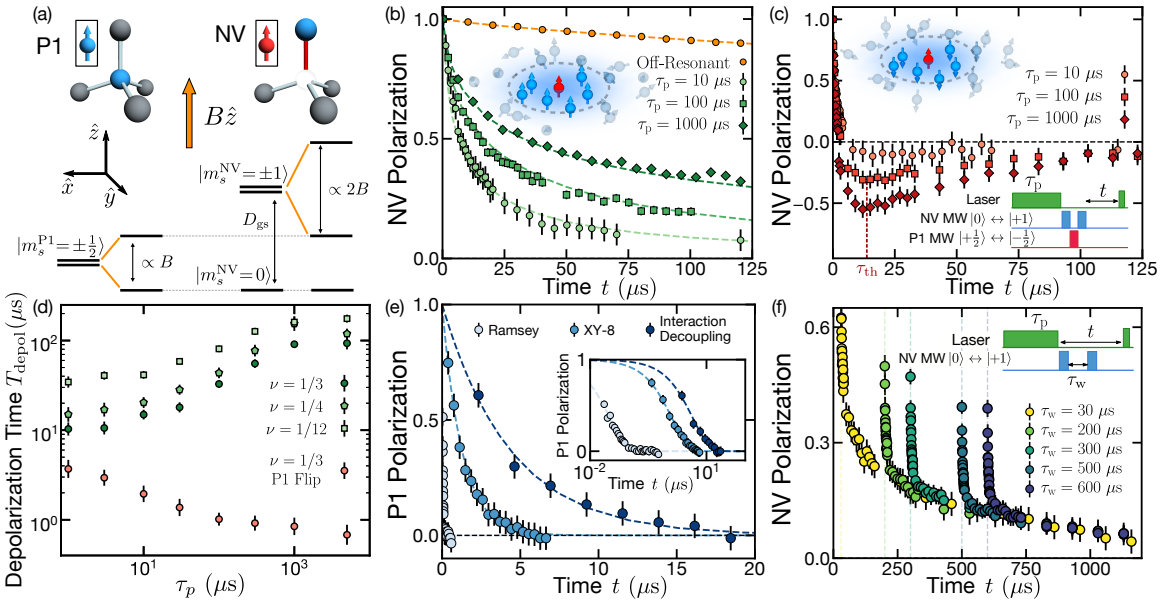

Figure 2.9: (a) In the absence of a magnetic field, the P1's spin-1/2 sub-levels are degenerate, while the NV's spin-1 sub-levels exhibit a zero field splitting, $D_{gs} = (2\pi) \times 2.87$ GHz. By applying an external magnetic field, the P1 and NV center can be brought into resonance. (b) When the NV and P1 are off-resonant (orange), $B = 360$ G, the NV exhibits a stretched exponential decay $\sim e^{-(t/T_1^{NV})^{0.8}}$ (dashed line) with $T_1^{NV} = 2.3 \pm 0.1$ ms, consistent with spin-phonon relaxation. When the NV is resonant with the $\nu = 1/3$ subgroup of P1s (green), $B = 511$ G, depolarization occurs significantly more rapidly and is strongly dependent upon the polarization time τ_p; a longer τ_p leads to a larger local polarization of P1 centers (inset) and a correspondingly longer NV relaxation time. Dashed green lines correspond to the NV dynamics as captured by our semi-classical model (Appendix A.2). (c) NV depolarization dynamics with an anti-polarized $\nu = 1/3$ P1 ensemble (top inset). Depolarization occurs in two distinct steps: an initial decay, $t \lesssim \tau_{th} \sim 12\ \mu$s, corresponding to local equilibration with the P1 ensemble, followed by late-time diffusion. (bottom inset) Pulse sequence describing the preparation of the anti-polarized P1 ensemble. (d) Depolarization time T_{depol} (extracted as the $1/e$ decay time of the initial polarization) as a function of τ_p for different effective P1 densities ν. The anti-polarized case for $\nu = 1/3$ is denoted as P1 Flip [panel (c) above]. As τ_p approaches P1's $T_1 \sim 1$ ms, T_{depol} saturates. (e) P1 spin coherence time, T_2, for different dynamical decoupling sequences, Ramsey [$0.032 \pm 0.005\ \mu$s], XY-8 [$1.27 \pm 0.02\ \mu$s] and an interaction decoupling sequence [$4.4 \pm 0.1\ \mu$s using DROID [210, 211]; coherence times are extracted from single exponential fits (dashed blue lines). (inset) Data plotted in semi-log. (f) Depolarization dynamics for $\tau_p = 1000\ \mu$s with variable NV-shelving time, τ_w (inset). The τ_w-independent collapse of the late-time data confirms the NV's role as a local probe of the P1's polarization dynamics. All data are taken using sample S1 at room temperature $T \sim 300$ K.

isolate the emergent late-time dynamics. In particular, we polarize for time τ_p, shelve the NV and then wait for a variable time τ_w to allow the P1 polarization to spread. Upon unshelving the NV, we observe a two-step relaxation process, as depicted in Fig. 2.9f. After an initial step of rapid local equilibration, the late-time dynamics exhibit a τ_w-independent collapse. Crucially, this demonstrates that for $t > \tau_{th}$, the NV polarization functions as a *local* probe of the amplitude of the P1 polarization profile, $P(t, \boldsymbol{r})$;

alternatively, one can also think of the NV's polarization as an autocorrelation function that captures the survival probability of the P1's polarization dynamics [415].

2.2.5 Observation of emergent diffusion

At late times, the conservation of total polarization and the dynamical exponent $z = 2$ determine the characteristic behavior of the survival probability in d dimensions, $S_p(t) \sim t^{-d/2}$; the simplest hydrodynamic model capturing this corresponds to Gaussian diffusion:

$$\partial_t P(t, \boldsymbol{r}) = D\nabla^2 P(t, \boldsymbol{r}) - \frac{P(t, \boldsymbol{r})}{T_1} + Q(t, \boldsymbol{r}), \tag{2.14}$$

where D is the diffusion coefficient. The latter two terms in Eqn. (2.14) are motivated by our experiment: $Q(t, \boldsymbol{r})$ is a source term that characterizes the P1 polarization process, while T_1 is an extrinsic relaxation time, after which the experimental signal becomes suppressed (Appendix A.3.1). In order to maximize the experimental window for observing emergent hydrodynamics, we work at low temperatures $T = 25$ K, where the NV's T_1^{NV} time extends by an order of magnitude, and the P1's T_1 time extends by a factor of three [416]. The source $Q(t, \boldsymbol{r})$ contains contributions from each of the randomly distributed NVs, whose finite density produces an overall uniform background polarization that decays exponentially in time. Isolating the nanoscale polarization dynamics from this background (Appendix A.3.1), we observe a robust power-law decay of the survival probability, $S_p(t) \sim t^{-3/2}$, for over a decade in time, demonstrating the emergence of spin diffusion [Fig. 2.8b] [415]. Extracting the corresponding diffusion coefficient from $S_p(t) = P_{\mathrm{total}}/(4\pi D t)^{3/2}$ requires one additional piece of information, namely, the total amount of spin polarization, P_{total}, transferred to the P1 ensemble. Fortunately, this is naturally determined by combining the height of the measured polarization background with the density of NVs, which we independently calibrate using a spin-locking experiment. This enables us to experimentally extract the spin-diffusion coefficient: $D = 0.35 \pm 0.05\ \mathrm{nm}^2/\mu\mathrm{s}$ [Table 2.2].

Effective density	$\nu = 1/3$		$\nu = 1/4$		$\nu = 1/12$
Sample	S1	S2	S1 undriven	S1 $\Omega_{\rm dr} = 11.7$ MHz	S1
D [nm^2/s]	0.28 ± 0.06	0.35 ± 0.05	0.25 ± 0.06	0.33 ± 0.09	0.11 ± 0.03
gD [nm^2/s]	0.82 ± 0.17	1.03 ± 0.13	0.74 ± 0.18	0.95 ± 0.26	0.33 ± 0.08
$D_{\langle r^2 \rangle}$ [nm^2/s]	0.98 ± 0.03	1.09 ± 0.02	0.66 ± 0.04	0.95 ± 0.02	0.21 ± 0.03

Table 2.2: Across all samples, temperatures, P1 densities and disorder strengths. Accounting for the appropriate non-Gaussian geometric factor, $g = 2\pi^{1/3}$, yields agreement between the diffusion coefficient extracted from the survival probability and that extracted from the growth of $\langle r^2 \rangle$ (computed via our semi-classical model). Samples S1 and S2 both contain a P1 density of ~ 110 ppm, while their NV densities are ~ 0.7 ppm and ~ 0.3 ppm, respectively. Measurements on S1 are performed at room temperature, while measurements on S2 are taken at $T = 25$ K. For sample S1, we also consider two additional tuning parameters: (i) different effective P1 densities, $\nu \in \{\frac{1}{3}, \frac{1}{4}, \frac{1}{12}\}$, tuned via the hyperfine structure (Fig. 2.11c), and (ii) different disorder strengths, W, tuned via continuous microwave driving (Fig. 2.11d). The reported uncertainties include propagated uncertainties from other experimentally extracted parameters (e.g. T_1 and $\rho_{\rm NV}$). Despite overlapping error bars, a detailed analysis 2.10 confirms that the driven diffusion coefficient is statistically larger than the undriven case. Error bars represent 1 s.d. accounting statistical uncertainties.

ℓ (nm)	$\nu = 1/3$	$\nu = 1/4$	$\nu = 1/12$
Sample S1	12.9 ± 1.4	13.6 ± 1.4	20.3 ± 1.9
Sample S2	14.3 ± 1.6	15.1 ± 1.5	19.3 ± 1.9

Table 2.3: Extracted ℓ from the spin polarization dynamics for the different sample considered (S1 and S2) and the different P1 subgroups. With decreasing density, we observe a corresponding increase in the lengthscale ℓ. Crucially, ℓ remains always larger than the P1-P1 distance highlighting that its value is not a simple consequence of the discrete nature of the spins in our system. Note that in order to extract $\ell = \sqrt{C_{\rm dyn}}$, we utilize our semi-classical model to obtain the full spatial profile of the polarization decay and fit the profile to the analytically solved dynamics under the diffusion correction (including the dynamical correction), starting from a Yukawa form for the polarization profile. To minimize finite size and time biases, we consider the dynamics between $t_{\rm min}$ and $t_{\rm max}$, the latter set to the time when the polarization per spin at the edge is larger than 3×10^{-6}.

2.2.6 An unconventional approach to diffusion

While the hydrodynamic model in Eqn. (2.14) captures the correct dynamical exponent, it assumes that the dynamics follow Gaussian diffusion at all times. However, disorder induces important modifications to this picture and leads to a novel dynamical correction. In particular, around each P1 center there is a distinct local environment, arising from both positional disorder and the presence of on-site random fields (generated by other paramagnetic spin defects). This leads to a spatially-varying local diffusion coefficient. As an initial polarization profile spreads, its dynamics naturally average over an increasing number of local P1 environments. This generates a *dynamical* modification to the

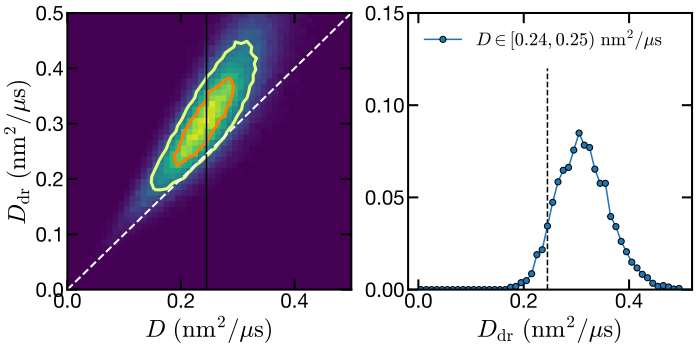

Figure 2.10: (Left Panel) Distribution of diffusion coefficients from our fitting procedure (lighter color corresponds to higher probability). Given a diffusion coefficient D, we observe that the extracted diffusion coefficient under a drive $D_{\rm dr}$ of the other $\nu = 1/4$ group is consistently larger, highlighting that the drive modifies the diffusive dynamics by changing the onsite disorder of the system. (Right panel) Distribution of $D_{\rm dr}$ for $D \in [0.24, 0.25)$. Dashed vertical line corresponds to the value of D.

diffusion equation, whose leading contribution is $C_{\rm dyn}k^2\partial_t$ (Appendix A.3.3):

$$\partial_t P_{\boldsymbol{k}}(t) = -\left[Dk^2 + C_{\rm dyn}k^2\partial_t + \cdots\right] P_{\boldsymbol{k}}(t), \tag{2.15}$$

where $P_{\boldsymbol{k}}(t)$ is the Fourier component of the polarization with wavevector $\boldsymbol{k}$. This term induces two striking modifications to the diffusive dynamics. First, the early time polarization profile follows a Yukawa-like form $\sim \frac{1}{r}e^{-r/\ell}$, and only crosses over to a Gaussian at late times (Appendix A.3.3). Second, the relationship between the height of the polarization profile $S_p(t)$, and its width $\sim \sqrt{Dt}$, is fundamentally altered; more precisely, in order to faithfully extract D from $S_p(t)$, one must account for the non-Gaussianity of the polarization profile.

To connect our nanoscale spin dynamics to these disorder-induced hydrodynamical features, we utilize a semi-classical description of the polarization evolution based upon Fermi's golden rule (Fig. 2.8c, Appendix A.2). Accounting for both positional disorder and on-site random fields, numerical simulations of the polarization dynamics exhibit excellent agreement with the experimentally measured $S_p(t)$ for over three decades in time (Fig. 2.8b). Our semi-classical model also provides direct access to the spatial polarization profile, which remains robustly non-Gaussian throughout the time-scale of the experiment, indicative of unconventional diffusion. Remarkably, the polarization profile precisely exhibits the predicted Yukawa to Gaussian crossover (Fig. 2.8d) and enables us to extract the coefficient of the dynamical modification [Eqn. (2.15)] as $C_{\rm dyn} = 204 \pm 45$ nm^2 [Table 2.3]. A few remarks are

in order. First, this coefficient defines a physical length scale, $\ell = \sqrt{C_{\text{dyn}}} = 14.3 \pm 1.6$ nm, which sets the decay of the Yukawa form $\sim \frac{1}{r} e^{-r/\ell}$ of the polarization profile. More intuitively, ℓ can be thought of as the length-scale over which the disorder-induced variations of the local P1 environments start to become averaged out. Thus, only when the polarization expands to a characteristic size much larger than ℓ, will the dynamics approach Gaussian diffusion.

Second, as evinced in Fig. 2.8d, for a wide range of intermediate time-scales, the polarization profile is well-described by a simple exponential, which modifies the relationship between the survival probability and the diffusion coefficient. This modification can be computed analytically and takes the form of a geometric factor $g = 2\pi^{1/3}$ [8], wherein $D \to gD$ (Table 2.2). Crucially, the mean square displacement of the polarization profile, $\langle r^2 \rangle(t) = 6D_{\langle r^2 \rangle} t$, provides an independent measure of the diffusion coefficient [417, 418]. As highlighted in Table 2.2, only by accounting for the disorder-induced geometric factor do we observe agreement between the diffusion coefficient extracted from $S_p(t)$ and $\langle r^2 \rangle(t)$; this agreement directly demonstrates the non-Gaussian nature of the observed dynamics.

2.2.7 Microscopic control of emergent spin diffusion

We now demonstrate the ability to directly translate changes in the underlying microscopic Hamiltonian to changes in the emergent macroscopic behavior. In order to engineer the Hamiltonian, we exploit the hyperfine structure of the P1 defect, enabling control over the effective density and the on-site random field disorder. In particular, sweeping the strength of the external magnetic field from 490 G to 540 G reveals five spectroscopically distinct subgroups of the P1 ensemble, each containing a different fraction of the total P1 spins, with density ratios $\nu = \{\frac{1}{12}, \frac{1}{4}, \frac{1}{3}, \frac{1}{4}, \frac{1}{12}\}$ (Fig. 2.11a and Supplementary Information) [6, 412]. Thus, tuning the external magnetic field provides discrete control over the average spacing between resonant P1 spins. As shown in Fig. 2.11c, the survival probability for both the $\nu = 1/4$ and $\nu = 1/12$ P1 subgroups exhibits significantly slower spin diffusion than the

[8] The difference in their shapes of the Gaussian and the exponential modifies the relationship between the height and the width of the distribution and thus how one can extract the diffusion coefficient. In the Gaussian case this relationship is given by $S_p^g(t) = P_{\text{tot}}/(2\pi\langle r^2 \rangle)^{3/2}$ while in the exponential case it is given by $S_p^e(t) = P_{\text{tot}}/[8\pi(\langle r^2 \rangle)^{3/2}]$, where P_{tot} is the total polarization in the system. Replacing with $\langle r^2 \rangle = 6Dt$ and equating the two survival probabilities leads to a constant factor correction $g = 2\pi^{1/3}$ between the two diffusion coefficients.

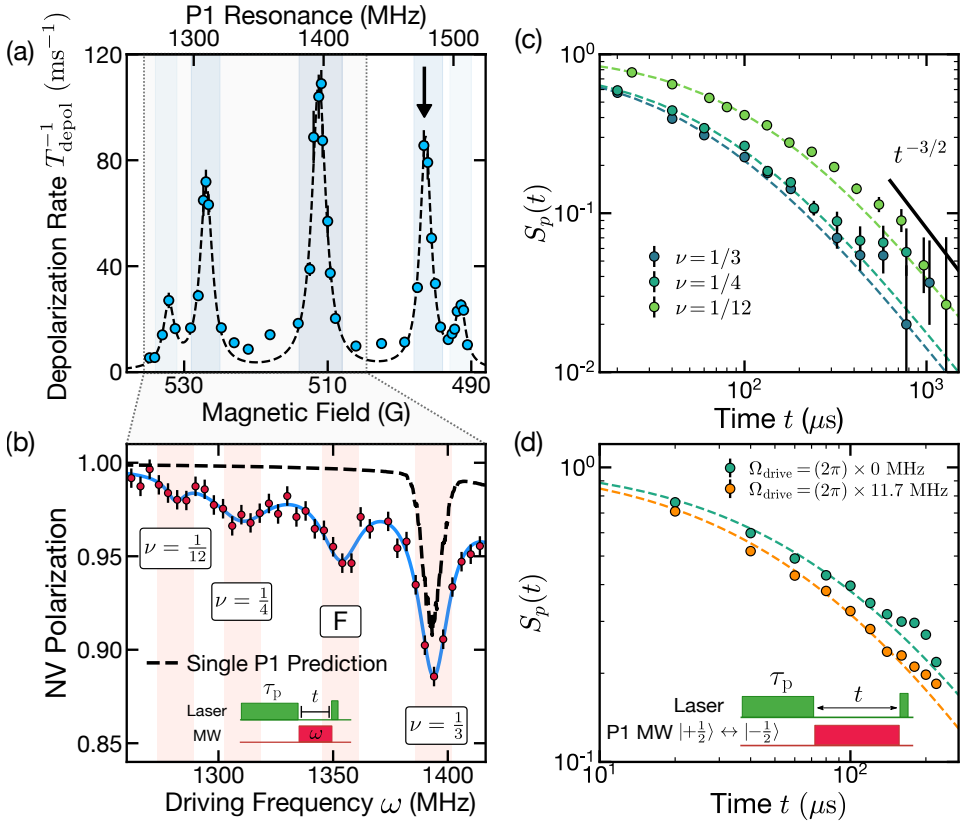

Figure 2.11: (a) Depolarization rate, $T_{\rm depol}^{-1}$, of the NV center as a function of magnetic field after $\tau_{\rm p} = 1$ μs. The NV exhibits five distinct resonances corresponding to five different subgroups of P1s with density ratios $\nu \in \{\frac{1}{12}, \frac{1}{4}, \frac{1}{3}, \frac{1}{4}, \frac{1}{12}\}$. For panels (b,d) below, we fix the magnetic field strength, $B = 496.5$ G, wherein the NV is resonant with a $\nu = 1/4$ P1 subgroup (indicated by the arrow); the top axis shows the frequency of the P1 subgroups at this field strength. (b) Fixing a polarization time, $\tau_{\rm p} = 300$ μs, and an interaction time $t = 3$ μs (inset), we probe the polarization transfer between the NV and the resonant $\nu = \frac{1}{4}$ P1 subgroup. By driving the *other* P1 subgroups, one can effectively reduce the magnitude of the on-site disorder by "echoing" out a portion of the Ising piece of the dipolar interactions. Sweeping the microwave driving frequency, ω, we observe an enhanced NV decay when it is resonant with the $\nu = \frac{1}{12}, \frac{1}{4}, \frac{1}{3}$ subgroups as well as an additional "forbidden" transition, F. By comparing against numerical simulations for a single P1 spin (dashed black line), we conclude that—aside from the $\nu = \frac{1}{3}$ resonance where an additional hyperfine depolarization channel plays a crucial role—echoing out disorder enhances the coherent many-body interactions and leads to faster dynamics. (c) Dynamics of $S_p(t)$ for different effective P1 densities with $\tau_{\rm p} = 100$ μs; control over the P1 density is achieved by tuning the external magnetic field to bring the NV into resonance with the $\nu = \frac{1}{3}, \frac{1}{4}$ and $\frac{1}{12}$ P1 subgroups. A smaller P1 density leads to correspondingly slower spin diffusion [Table 2.2]. (d) Dynamics of $S_p(t)$ for different on-site disorder strengths with $\tau_{\rm p} = 300$ μs. Under continuous microwave driving [$\Omega_{\rm drive} = (2\pi) \times 11.7$ MHz] of the *other* $\nu = \frac{1}{4}$ P1 subgroup (inset), the effective disorder is suppressed and spin diffusion is enhanced [Table 2.2]. Dashed lines in (c) and (d) correspond to $S_p(t)$ obtained via Eqn. (2.14). All experimental data are taken using sample S1 at room temperature $T \sim 300$ K.

$\nu = 1/3$ subgroup. This is consistent with the presence of weaker interactions arising from the larger spin spacing, and leads to smaller values for the measured diffusion coefficient (Table 2.2).

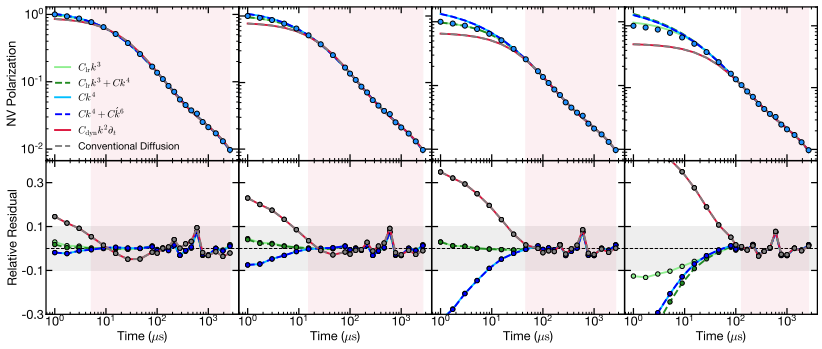

Figure 2.12: Fitting of the diffusive description with different terms and fixed $T_1 = 2.6$ ms in sample S2 with $\tau_p = 30$ μs. Different columns represent fitting to a different range of the data (highlighted by the red shaded region). The inclusion of more terms in the diffusive description allows for a better fit of the data, however the improvement in the fitting range is only significant when the fitting regimes includes early time data ($\lesssim 30$ μs), as highlighted in the second row of the relative residuals. All data are presented with logarithmically spaced y axis, except in the grey shaded region where a linear regime is used to highlight the fluctuations of the residuals around 0. Fits in Fig. 1b correspond to the third column.

Finally, one can also experimentally control the strength of the on-site random field disorder via continuous driving. Since these fields are dominated by the Ising portion of the interactions between the various P1 subgroups, rapid microwave driving of a single subgroup causes its contributions to the disorder to become averaged out (Fig. 2.11b). Indeed, by bringing the NV into resonance with one of the $\nu = 1/4$ subgroups (black arrow, Fig. 2.11a), while driving the other $\nu = 1/4$ subgroup, we observe faster spin diffusion, consistent with a reduction in disorder [Fig. 2.11d and Table 2.2].

2.2.8 Outlook

Looking forward, our work opens the door to a number of intriguing future directions. First, the presence of long-range, power-law interactions can lead to different dynamical universality classes [419]. Within our semi-classical model, the polarization dynamics are governed by an effective $\sim 1/r^6$ power-law (Eq. A.28 in Appendix A.3.1). Interestingly, much like disorder, this particular power-law also leads to an unconventional approach to diffusion, albeit governed by a distinct non-analytic correction $\sim C_{\mathrm{lr}}k^3$ (Appendix A.3.2); our data (Fig. 2.8b inset and Fig. 2.12) do not exhibit clear signatures of this power-law correction and we leave its observation to future work. Second, the ability to experimentally isolate local equilibration dynamics naturally points to the study of many-body localization and Floquet thermalization [95, 420]. In long-range interacting

systems, the precise criteria for delocalization remain unknown [421, 422], while in Floquet systems, the late-time dynamics involve a complex interplay between heating and hydrodynamic behaviour [189, 318]. Finally, the presence of a Yukawa-like polarization profile in our system is reminiscent of an open question in the biochemical sciences, namely, what is the underlying mechanism behind the wide-spread emergence of Fickian yet non-Gaussian diffusion in complex fluids [406–411]; in such systems, it is notoriously difficult to change the microscopic equations of motion, suggesting the possibility for our platform to be utilized as a controllable "simulator" of soft, heterogeneous materials. A direct route for exploring this question is to leverage sub-diffraction imaging techniques or magnetic field gradients in order to measure correlation functions between spatially separated NVs [423, 424].

2.3 Exploiting disorder to probe spin and energy hydrodynamics

2.3.1 Introduction

Owing to the development of large-scale quantum simulation platforms ranging from ultracold atoms and superconducting circuits, to solid-state spin systems [157, 364, 399, 425, 426], the pursuit to experimentally characterizing the nature of these hydrodynamical descriptions has seen tremendous advances [152, 153, 164, 166, 167, 170, 171, 173, 318, 354, 355, 357, 358, 369, 373, 378, 393, 427–429]. In order to control and probe many-body dynamics in such systems, one typically requires a combination of strong interactions, giving rise to the most interesting dynamical behaviors, and local addressing, that can probe them. In the majority of platforms, these two features are in tension: Strong interactions arise when the constituent degrees of freedom are closely spaced, which in turn challenges the ability to perform local measurements [430, 431]. The tension is particularly acute in solid-state platforms where electronic and nuclear spins can exhibit strong interactions only when spaced at nano-meter lengthscales. One of the solutions, as presented in the previous section, is to work with multiple species of defects in a hybrid system: The species with high density plays the role of a strongly interacting system, while a much more dilute species is used as the local probe.

In this section, we will demonstrate another protocol: Disorder, often times unavoidable in solids and long-considered detrimental for quantum coherence and transport, can be a powerful source of local control. First, by dephasing a homogenous state using the disorder, we demonstrate the preparation of states whose polarization on different sites is uncorrelated. Second, we show that single-site, spin-spin correlation functions can be directly measured using spin echo. The intuition behind our approach is the following – owing to the lack of spatial correlations, non-local components of the correlation function are averaged out, leaving only a sum of autocorrelations. Applying our technique in the context of nuclear magnetic resonance, we demonstrate the direct observation and characterization of nano-scale spin and energy transport, without the need for magnetic field gradients, sub-diffraction techniques, or multiple spin species [364, 400, 423, 424, 432–434]. Combining with Floquet driving technique to engineer the system's Hamiltonian, we investigate the cross-over between ballistic and diffusive hydrodynamics. Interestingly, in certain parameter regimes, we observe the coexistence of

diffusive spin transport with ballistic energy transport, a hallmark of interacting integrable systems.

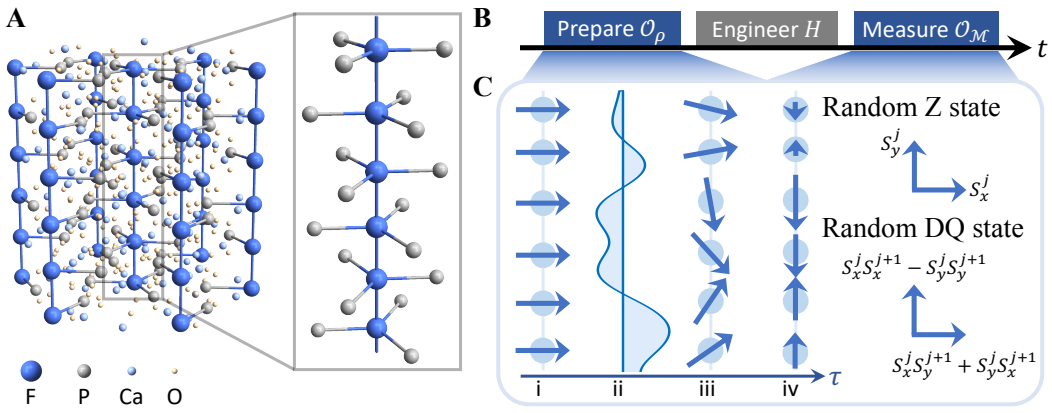

Figure 2.13: (a) Chemical structure of Fluorapatite. ^{19}F nuclear spins (blue balls) form a quasi-1D structure and can exhibit different classes of hydrodynamics under various effective Hamiltonians realized by Floquet engineering. ^{31}P atoms (gray) provide intrinsic on-site disordered fields on ^{19}F spins, which enables the preparation of random states and observables. (b), The experimental protocol to obtain local autocorrelations consists of three main stages. The central ingredient is to realize spatially uncorrelated random states and observables in the preparation and the measurement stages. Hamiltonian engineering enables varying the quantum dynamics. **c**, The sequence to prepare random states and observables contains four steps: (i) initialize the system to a spatially homogeneous state with polarization along x axis, (ii) apply disordered field along z axis to encode (iii) local information into the spin phases, (iv) perform phase cycling to eliminate the residual homogeneous part. The arrows represent spin operators whose bases are specified on the right for the random Zeeman state and the random DQ state, respectively. To effectively measure spatially random observables, we apply the same sequence in reverse order to the final state before measuring the homogeneous magnetization (Appendix A.4).

2.3.2 Experimental system

Our experiments are performed on $S = 1/2$ ^{19}F nuclear spins within a single crystal of fluorapatite. The sample in the experiment is a single crystal of fluorapatite (FAp) with formula $Ca_5(PO_4)_3F$. The most abundant isotopes of F and P have 1/2 nuclear spin, while the most abundant isotopes of Ca and O have zero nuclear spin. Fluorapatite is a hexagonal mineral with space group $P6_3/m$, where the ^{19}F spin-1/2 nuclei form linear chains along the c-axis. Each fluorine spin in the chain is surrounded by three equidistant ^{31}P spin-1/2 nuclei. The sample is placed at room temperature inside a superconducting magnet producing a uniform $B = 7$ T field aligning along the [001] axis. The

Hamiltonian of the system is given by

$$H_{\text{tot}} = \omega_F \sum_k S_z^k + \omega_P \sum_\kappa s_z^\kappa + H_{\text{dip}} \tag{2.16}$$

$$\begin{aligned} H_{\text{dip}} &= H_{\text{FF}} + H_{\text{FP}} + H_{\text{PP}} \\ &= \sum_{j<k} \frac{\hbar\gamma_j\gamma_k}{|\vec{r}_{jk}|^3} \left[\vec{S}_j \cdot \vec{S}_k - \frac{3(\vec{S}_j \cdot \vec{r}_{jk})\,(\vec{S}_k \cdot \vec{r}_{jk})}{|\vec{r}_{jk}|^2} \right], \end{aligned} \tag{2.17}$$

The first two terms represent the Zeeman interactions of the F(S) and P(I) spins, respectively, with frequencies $\omega_F = \gamma_F B \approx (2\pi)282.37$ MHz and $\omega_P = \gamma_P B = (2\pi)121.51$ MHz, where $\gamma_{F/P}$ are the gyromagnetic ratios, $\vec{r}_{jk}$ is the vector between the (j,k) spin pair.

A few approximations are made as follows. First, due to the strong external magnetic field, all the nuclear spins are quantized along the [001] axis with a Zeeman splitting much larger the dipolar interaction. Hence, we can truncate the dipolar Hamiltonian to its energy-conserving part (secular Hamiltonian), because . Second, since the coupling between ^{31}P spins (1.20 krad s^{-1} for nearest ^{31}P-^{31}P pairs) is much weaker than the coupling between ^{19}F spins (32.76 krad s^{-1} for nearest ^{19}F-^{19}F pairs), as well as the ^{19}F-^{31}P coupling (6.12 krad s^{-1}), dynamics of ^{31}P spins can be ignored for short time and I only provides a static random field. In addition, as the temperature is much higher than the Zeeman energy, each ^{31}P spin is randomly polarized with negligible correlation between different ^{31}P spins. As a result, H_{FP} can be viewed as an on-site disordered field for ^{19}F spins. Finally, the coupling between nearest ^{19}F spins within a 1D chain along [001] direction is much (~ 40 times) stronger than the coupling between nearest pairs along other directions. Therefore, we treat the ^{19}F as an ensemble of decoupled quasi-1D spin chains, and our 3D many-body system effectively reflects the dynamics of 1D spin chains with the Hamiltonian (Fig. 2.13):

$$H_{\text{dip}} = H_{\text{FF}} + H_{\text{dis}} = \frac{1}{2} \sum_{j<k} \frac{J}{2r_{jk}^3} (2S_z^j S_z^k - S_x^j S_x^k - S_y^j S_y^k) + \sum_j w_j S_z^j, \tag{2.18}$$

where H_{dis} is effectively an random on-site field with strength $w_j = \sum_\kappa J_{j,\kappa}^{FP} I_z^\kappa$ chosen from a Gaussian distribution with a width of 6 krad s^{-1}; H_{FF} describes a quasi-one-dimensional spin-1/2 system.

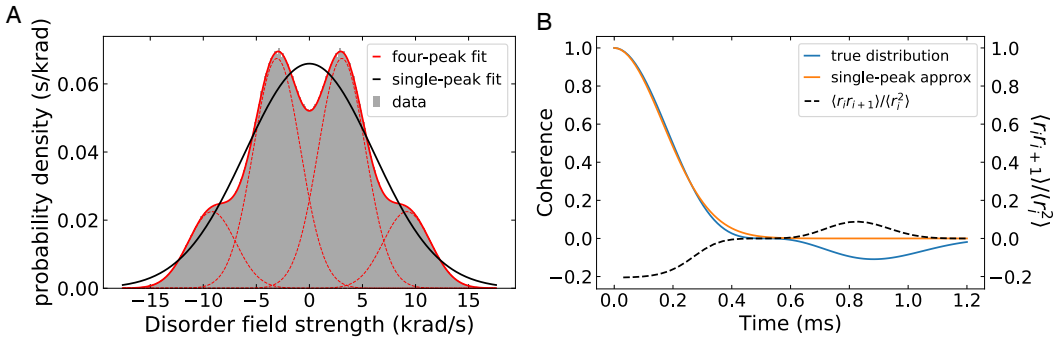

Figure 2.14: (a) Distribution of the on-site field strength on ^{19}F, computed under the assumption that each of its neighboring ^{31}P nuclear spins independently point along $+z$ or $-z$ direction with the same probability. The interaction strength between ^{19}F and ^{31}P are determined by their relative position (Fig. 2.13a) [435]. A total number of 45 closest ^{31}P are included in calculation. The distribution is perfectly fitted by a sum of four Gaussian distributions with the same width, the centers at $\pm\frac{1}{2}J^{FP}$ and $\pm\frac{3}{2}J^{FP}$ and the height ratio of $3:3:1:1$. A single Gaussian function can also capture the distribution reasonably well, and is used for simplicity in the numerical simulation for the transport dynamics. (b) Left axis: Decoherence profile generated by the calculated distribution of on-site field and the single-peak Gaussian approximation. Right axis: Statistical correlation between the random amplitudes of local observables on two closest ^{19}F. As the coherence approaches zero, the statistical correlation also vanishes. The decay profiles computed by assuming a single Gaussian distribtution and the true distribution are qualitatively consistent.

2.3.3 Protocol to measure autocorrelations

In order to probe the infinite temperature transport of spin and energy in our system, one must measure autocorrelation functions of the form $\sim \mathrm{Tr}[S_z^j(t)S_z^j(0)]$. To do so, we begin by evolving a weakly polarized thermal state $\rho_0 \propto (\mathbb{1} + \epsilon \sum_j S_z^j)$ into a target initial state $\rho \propto \mathbb{1} + \epsilon\mathcal{O}_\rho$. Next, we evolve this initial state under a desired Hamiltonian H for a time t, yielding $\rho(t) = e^{-iHt}\rho e^{iHt}$. Finally, we measure a tunable observable, $\mathcal{O}_\mathrm{m}$; in practice, via RF pulses, this observable is mapped onto the magnetization along the x-axis, $\mathcal{M} = \sum_j S_x^j$, which we directly read out via an inductive measurement. The resulting signal is equivalent to the infinite temperature correlation function, $\mathrm{Tr}[\mathcal{O}_\rho(t)\mathcal{O}_\mathrm{m}(0)]$. Clearly, if $\mathcal{O}_\rho$ and $\mathcal{O}_\mathrm{m}$ are translationally-invariant, the measured signal contains non-local correlations between all pairs of spins, e.g. $\sum_{jk}\mathrm{Tr}[S_z^j(t)S_z^k(0)]$.

To access local correlation functions, such as the spin survival probability [364, 415], we prepare initial states and measure observables such that the spin-polarization at different sites is uncorrelated and averages to zero. An exemplary goal is to prepare and measure the random Zeeman state given by $\mathcal{O}_\rho = \sum_j \alpha_j S_z^j(t)$, where α_j are independent and identically distributed random variables with

zero average. This would immediately enable the measurement of sum of single-site autocorrelations since $\sum_{j,k}\langle\alpha_j\alpha_k\rangle \mathrm{Tr}[S_z^j(t)S_z^k(0)] \propto \sum_{j,k}\delta_{jk}\mathrm{Tr}[S_z^j(t)S_z^k(0)] = \sum_j \mathrm{Tr}[S_z^j(t)S_z^j(0)]$, which is proportional to single-site autocorrelations $\mathrm{Tr}[S_z^j(t)S_z^j(0)]$ for translationally invariant Hamiltonian or disordered Hamiltonian with translationally invariant statistics.

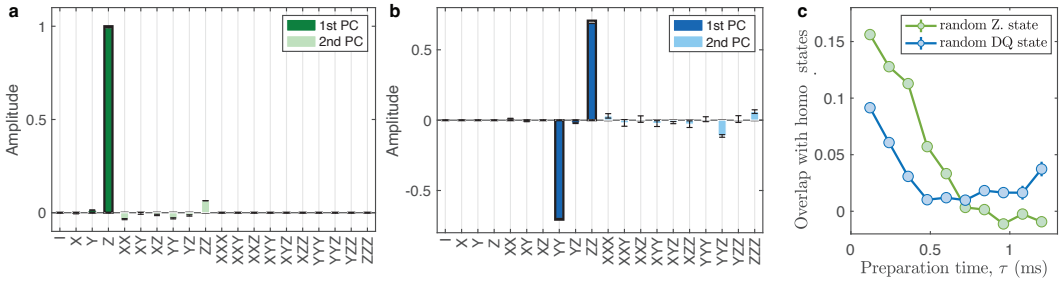

Figure 2.15: First two principal components (PC) of the experimentally prepared random Zeeman (a) and DQ states (b). The horizontal axis label stands for sum of all permutations of the corresponding spin operators, e.g. XY corresponds to $\sqrt{2}(S_x^j S_y^{j+1} + S_y^j S_x^{j+1})$ normalized such that the Frobenius norm is 2^L. The amplitude is weighted by the square root of the eigenvalue $\sqrt{\lambda_i}$. For random Zeeman state, $\lambda_1 = 0.985(1)$, $\lambda_2 = 0.0066(1)$; For random DQ state, $\lambda_1 = 0.963(9)$, $\lambda_2 = 0.0019(5)$. The eigenvalues are normalized such that $\sum_\mu \lambda_\mu = 1$. The preparation time is 1.08 ms for random Zeeman state and 0.96 ms for random DQ state. The green and blue bars show the experimental results, the black wireframes show the ideal states. (c), Overlap of experimentally prepared random Zeeman (green) and DQ (blue) state with the corresponding homogeneous state quickly decays to zero. The overlap of two observables $\mathcal{O}_1, \mathcal{O}_2$ are defined as $\mathrm{Tr}(\mathcal{O}_1\mathcal{O}_2)/\sqrt{\mathrm{Tr}(\mathcal{O}_1\mathcal{O}_1)\mathrm{Tr}(\mathcal{O}_2\mathcal{O}_2)}$.

Let us now describe our disorder-based experimental protocol for preparing $\mathcal{O}_\rho$ (Fig. 2.13c). First, we rotate the thermal polarization to the x-axis, initializing a state $\propto (\mathbb{1} + \epsilon \sum_j S_x^j)$. Then, we evolve under H_{dis} for a time τ, such that the excess magnetization of each spin is oriented along a random direction in the xy-plane. In order to ensure that the time evolution during τ is generated only by H_{dis}, we utilize concatenated WAHUHA sequences to dynamically decouple H_{FF} [219]. Next, we employ phase cycling to project the random polarization of each spin onto the y-axis. A final RF pulse returns the polarization along z, and we obtain $\mathcal{O}_\rho = \sum_j \alpha_j S_z^j$, with $\alpha_j = \sin(w_j\tau)$ [9]. A similar strategy can be used to enable a measurement of $\mathcal{O}_{\mathrm{m}} = \sum_j \alpha_j S_z^j$. In particular, just prior to the final inductive measurement of $\mathcal{M}$, we refocus the random state back to a uniform magnetization by applying the

[9]Since the disorder fields on different ^{19}F originates from the same ^{31}P bath, they inevitably have some statistical correlation. Indeed, we compute the correlation of the disordered fields on two neighboring ^{19}F, $\frac{\langle w_j w_{j+1}\rangle}{\langle w_j^2\rangle} \approx -0.2$. Nevertheless, $\langle\alpha_j\alpha_{j+1}\rangle = \langle\sin(w_j\tau)\sin(w_{j+1}\tau)\rangle \approx 0$ for $\tau > T_2$ (Fig. 2.14b), satisfying the condition required for our protocol to measure local autocorrelation.

disorder field again. The above single-site autocorrelation function can be used to detect spin transport. An analogous approach can be used to detect autocorrelations of two-site observables, such as the local energy density. We first use the Jeener-Broekaert pulse pair [436] to create a homogeneous two-body correlated initial state $\propto \mathbb{1} + \epsilon \sum_j (S_x^j S_y^{j+1} + S_y^j S_x^{j+1})$ [10]. Evolution under the disordered field and phase cycling yields the random double-quantum (DQ) state with $\mathcal{O}_\rho = \sum_j \alpha'_j (S_x^j S_x^{j+1} - S_y^j S_y^{j+1})$ where $\alpha'_j = \sin(w_j \tau + w_{j+1} \tau)$ and $\langle \alpha'_j \alpha'_k \rangle \propto \delta_{jk}$ for large τ. An additional $\pi/2$-pulse naturally realizes $\mathcal{O}_\rho = \sum_j \alpha'_j (S_y^j S_y^{j+1} - S_z^j S_z^{j+1})$. We note that linear combinations of these two initial states allow us to reconstruct all of the subsequent operators we will consider.

We can carefully characterize the initial state preparation, focusing on two properties: (i) demonstrating that $\mathcal{O}_\rho$ has support only on the desired operators and (ii) confirming that $\sum \alpha_j = 0$ and $\sum \alpha'_j = 0$. For the first property, we measure $I(\phi, \theta, \gamma) = \mathrm{Tr}[U_r(\phi, \theta, \gamma) \mathcal{O}_\rho U_r^\dagger(\phi, \theta, \gamma) \mathcal{O}_\rho]$ for various $\{\phi, \theta, \gamma\}$, where $U_r = \otimes_j e^{-i\gamma S_z^j} e^{-i\theta S_y^j} e^{-i\phi S_z^j}$. From $I(\phi, \theta, \gamma)$ we can obtain the principal components, $\mathcal{T}_\mu$, of the random observable up to a rotationally-invariant component, $\mathcal{O}_\rho = \sum_\mu d_\mu \mathcal{T}_\mu$, where d_μ are independent random variables satisfying $\mathbb{E}(d_\mu d_\nu) = \lambda_\mu \delta_{\mu\nu}$, with λ_μ being the eigenvalues of the correlation matrix in descending order (Appendix A.5); note that the principal components $\mathcal{T}_\mu$ are orthonormal, $\mathrm{Tr}(\mathcal{T}_\mu \mathcal{T}_\nu^\dagger) = 2^L \delta_{\mu\nu}$. The first two principal components confirm our preparation of the random Zeeman state $\mathcal{O}_\rho = \sum_j \alpha_j \sigma_z^j$ and the random DQ state $\mathcal{O}_\rho = \sum_j \alpha'_j (\sigma_x^j \sigma_x^{j+1} - \sigma_y^j \sigma_y^{j+1})$ with high fidelity (Fig. 2.15a,b). As $I(\phi, \theta, \gamma)$ is quadratic in $\mathcal{O}_\rho$, it does not contain information about the sign of the individual random coefficients α_j and α'_j. Therefore, for the second property, we measure the overlap of a random state $\mathcal{O}_\rho$ with its corresponding homogeneous state. Indeed, we observe that the overlap quickly decays to zero as a function of the preparation time (Fig. 2.15c), indicating that for sufficient time-evolution under the disordered field, one naturally realizes $\mathbb{E}\alpha_j = \mathbb{E}\alpha'_j = 0$.

2.3.4 Probing emergent spin and energy hydrodynamics

Having verified our initial state preparation, we now turn to exploring the infinite-temperature transport of both spin and energy for three distinct classes of Hamiltonians (Fig. 2.16b): (1) non-

[10] Here we assume nearest-neighbor coupling for representation simplicity, but the results also hold with $1/r^3$ long-range coupling.

interacting integrable, (2) interacting integrable, and (3) non-integrable. Utilizing Floquet engineering, we build each of these Hamiltonians from the native dipolar interaction [202, 437]. In particular, our experiments enable the realization of the following tunable model,

$$\begin{aligned} H =& u \sum_{j<k} \frac{J}{r_{jk}^3} \left(S_x^j S_x^k - S_y^j S_y^k \right) \\ &+ v \sum_{j<k} \frac{J}{r_{jk}^3} \left(S_z^j S_z^k - S_y^j S_y^k \right) \\ &+ h \sum_j w_j S_z^j, \end{aligned} \tag{2.19}$$

where the coefficients $\{u, v, h\}$ can be independently controlled. For $\{v, h\} = 0$ and restricting to nearest-neighbor couplings (i.e. truncating the long-range dipolar tail), the resulting XY model is integrable and free (case 1). Upon adding non-zero v, the model remains integrable, but becomes interacting (case 2). Finally, the addition of a weak on-site random field, h, causes the model to generically become non-integrable (case 3). We note that the long-range nature of the dipolar interaction renders H generically *non-integrable* for all of the above cases. However, our hope is that signatures of integrability will be present in the dynamics at short times; as we will see below, this is indeed borne out by the data.

These three different universality classes can be distinguished by the dynamical exponent, z, associated with their spin and energy transport. Crucially, z can be directly measured via the power-law decay of the autocorrelation function $\sim t^{-1/z}$, with $z = 1$ corresponding to ballistic motion, while $z = 2$ corresponds to diffusion.

Let us begin with case 1. We tune $\{u, v, h\} = \{0.5, 0, 0\}$ and measure the spin-spin autocorrelation function (Fig. 2.16c, green) and the energy autocorrelation function (Fig. 2.16c, blue). Both exhibit late-time power-laws consistent with $z = 1$, in agreement with the expectation that quasiparticles propagate ballistically in a non-interacting, integrable model. For case 2, we tune our system to $\{u, v, h\} = \{-0.15, 0.3, 0\}$. Intriguingly, we find that spin transports diffusively while energy transports ballistically (Fig. 2.16d). This phenomenon owes to the existence of stable spinless quasiparticles and is a central feature of infinite temperature transport in the so-called XXZ model [170, 171, 438–445]. Finally, for case 3, we set $\{u, v, h\} = \{-0.15, 0.3, 0.23\}$ and observe that both spin and energy

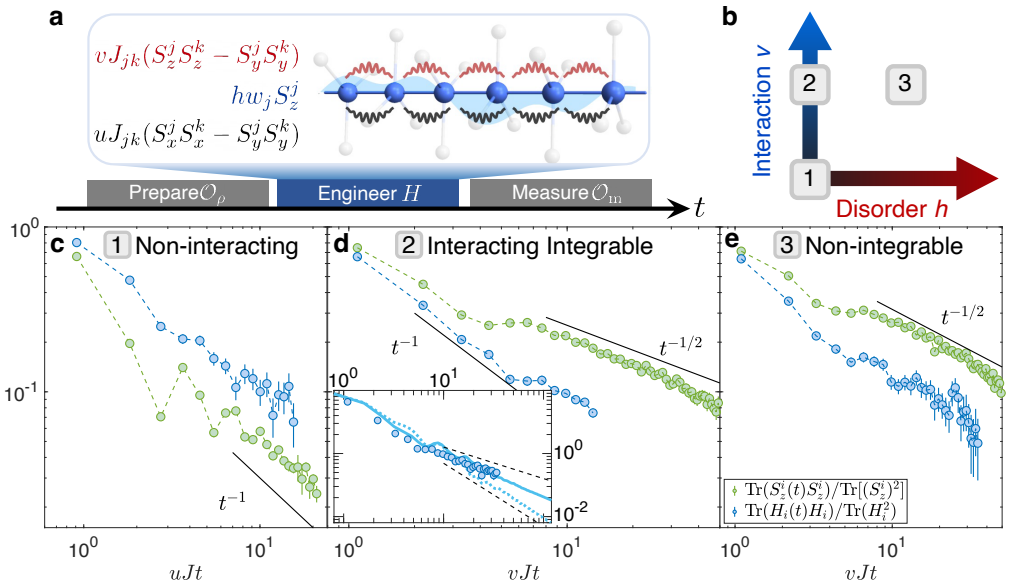

Figure 2.16: (a) Utilizing Floquet Hamiltonian engineering techniques, we can independently tune the strengths of two types of interactions (red and black wavy lines) and random on-site field (cyan shaded area). Different combinations of the three terms result in distinct classes of Hamiltonian: 1) Non-interacting, 2) interacting integrable, and 3) non-integrable. (b) Parameter space of the effective Hamiltonian in Eq. 2.19 with varying v, h and fixed u. (c)(d)(e) Local autocorrelations of spin and energy in non-interacting, interacting integrable, and non-integrable systems. All these autocorrelations follow power-law decay $t^{-1/z}$, in which the value of the dynamical exponent z distinguishes between different universality classes. Inset of (d): The measured energy autocorrelation (dark blue dots) agrees better with numerical simulation with next-nearest-neighbor coupling (solid curve) than without it (light blue dots), suggesting that the small deviation from ballistic transport at late times is due to the long-range interaction that weakly breaks the integrability of the system. Note that we normalize the local autocorrelations by the corresponding global autocorrelations, except the spin autocorrelation in the non-interacting case as we do not have access to the collective conserved quantity $\rho = \sum_j (-1)^j S^j_z$.

transport diffusively (Fig. 2.16e), consistent with a generic non-integrable model [359, 378]. The maximum time explored here is limited by the inter-chain coupling, which, albeit being 40 times smaller than intra-chain coupling, becomes non-negligible at $vJt \approx 50$ and breaks the quasi 1D approximation.

Two remarks are in order. First, the energy transport data in case 2 exhibit a weak deviation from ballistic transport at the longest times explored in the experiment (inset, Fig. 2.16d). In order to understand the origin of this deviation, we numerically compute the energy autocorrelation function in a 1D spin chain using density matrix truncation, with and without long-range couplings [318]. The agreement between our experiment and numerics in the former case suggests that the observed deviation results from the weak breaking of integrability associated with the long-range intra-chain

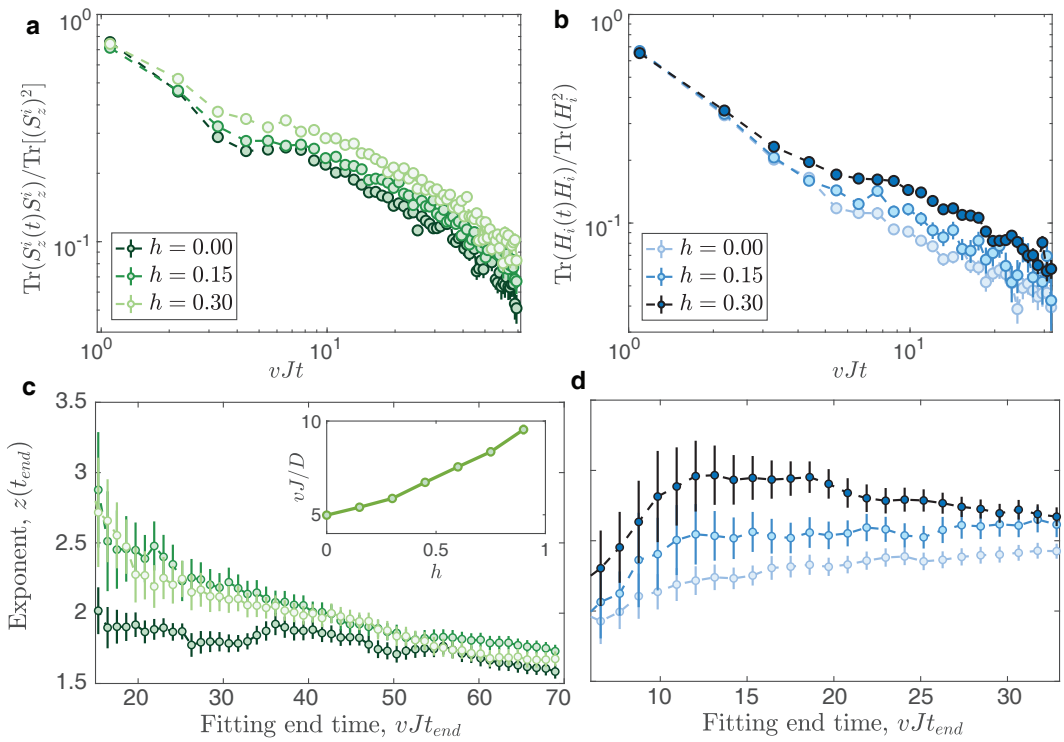

Figure 2.17: Spin (a) and energy (b) autocorrelation for various disorder field strength h. Extracted dynamical exponent of spin (c) and energy (d) transport in different fitting time windows. The fitting window starts after the transient dynamics [$Jt_{start} = 7.7$ for (c) and $Jt_{start} = 2.2$ for (d)]; note that the qualitative features we observed do not depend on this specific choice. Inset of (c): Inverse of the diffusion constant D extracted by fitting the data from $Jt_{start} = 7.7$ to $Jt_{end} = 60.0$, with $v = 0.3$ and $a = 3.442$Å the FAp lattice constant.

couplings, which is 8 times weaker than nearest-neighbor interaction. Second, by tuning the disorder strength during the evolution, we can controllably break integrability and access the nonintegrable regime on the experimental timescale. In particular, we measure the energy and spin transport as we tune h from 0 to 0.3 (Fig. 2.17a,b), and extract z using different time windows of the autocorrelation function, starting at $t_{start} = 7.7/J$ and ending at a variable t_{end} (Fig. 2.17c,d). For the spin transport (Fig. 2.17c), after an initial transient, all of the models exhibit a $z = 2$ at intermediate times. At the latest times, the inter-chain couplings begin to play a role, causing a decrease in z. Meanwhile, for the energy transport at $h = 0$, z remains close to its initial ballistic value for all times. However, for $h = 0.3$, the system reaches a diffusive exponent ($z = 2$) at intermediate times before exhibiting a weak decrease (possibly owing to inter-chain couplings).

In summary, our results introduce a novel method to probe local spin and energy transport in

solid-state spin ensembles. Our technique leverages the intrinsic disorder in such systems and requires only collective control. Our local probe enables exploration of quantum many-body phenomena unavailable in homogeneous systems, such as ballistic and diffusive hydrodynamics demonstrated here, or subdiffusion near the many-body localization transition and the emergence of superdiffusion with long-range interactions [149, 150, 152, 426, 446–448]. In addition to two-point correlation functions, which were the focus of the present work, our protocols can naturally be generalized to four-point, out-of-time-ordered correlations, and thus used to probe many-body quantum information scrambling [372, 383, 449–458]. Beyond quantum simulation, transport measurements provide rich information of the system, therefore can also boost quantum sensing applications in material and biological science. Finally, we point out that a general static inhomogeneous field can similarly induce the dephasing process and thus create random states, broadening the application of the present scheme to quantum platforms where disorder is not naturally present, including cold atoms, trapped ions and superconducting circuits.

2.4 Universal Kardar-Parisi-Zhang dynamics in integrable quantum systems

2.4.1 Introduction

Originally introduced in the context of surface growth [404], the Kardar-Parisi-Zhang (KPZ) equation has become central to our understanding of many stochastic processes [459–461]. While the central limit theorem ensures that the late-time physics of linear stochastic processes is typically Gaussian, the KPZ equation evades this fate. Instead, it represents a distinct universality class which emerges in myriad dynamical phenomena, ranging from directed polymers and traffic models to kinetic roughening [462–471].

The characterization of dynamical universality classes requires one to specify both the scaling exponents and functions of the theory. This is perhaps most familiar in the context of Brownian motion, where the diffusive late-time behavior follows a Gaussian scaling function; the width of the corresponding distribution grows as $\sim t^{1/z}$, where $z = 2$ is the dynamical scaling exponent. By contrast, the scaling functions for the KPZ universality class are significantly more complex and their exact functional form represents a relatively recent mathematical achievement [465, 472–476]. The associated dynamical scaling exponent is neither diffusive nor ballistic ($z = 1$), but rather superdiffusive with $z = 3/2$.

Typically, KPZ behavior is expected in non-linear, out-of-equilibrium *classical* systems subject to external noise; in this context, its observation is extremely robust and does not require any fine-tuning or the presence of a particular symmetry. To this end, the numerical and experimental observation of KPZ universality in a one-dimensional *quantum* spin-chain (i.e. the spin-$1/2$ Heisenberg model), fine-tuned for *both* integrability and SU(2) symmetry, has attracted widespread attention [171, 173, 353, 425, 427, 477–481]. Interestingly, this observation is at odds with conventional expectations for spin chain transport, which predict diffusion [144, 482–484]. This naturally motivates the following question: Is the Heisenberg chain an isolated exception, or the first example of a broader group of quantum models in the KPZ universality class?

Seminal recent work has made elegant progress on this question by proving that *all* integrable spin

chains with a non-Abelian symmetry exhibit superdiffusive transport with $z = 3/2$ (Fig. 2.18) [173, 480, 481]. However, a single scaling exponent does not uniquely specify the universality class and no analysis has been able to determine the nature of the corresponding scaling functions.

In this section, we present an extensive numerical investigation that supports the following stronger conjecture — the dynamics of all integrable spin chains with a non-Abelian symmetry belong to the KPZ universality class [480, 481]. Leveraging the density matrix truncation (DMT) numerical method [317, 318], we demonstrate that the spin dynamics of such models are precisely *captured by the KPZ scaling function* (Fig. 2.20). Intriguingly, our numerical observations suggest that the conjecture holds not only for static systems, but also for periodically driven (Floquet) systems [427, 485], as well as supersymmetric models.

By applying perturbations to break either the non-Abelian symmetry or the integrability, we characterize the approach to superdiffusive transport from regimes where there is analytical control on the dynamics. We reproduce these analytical results with unprecedented accuracy, both verifying and benchmarking our numerics, as well as providing independent evidence for the purported microscopic mechanism underlying superdiffusion [170, 171, 480, 481]. Finally, we propose an experimental implementation — based upon alkaline-earth atoms in optical lattices — capable of investigating KPZ transport in a variety of SU(N)-symmetric, integrable models.

2.4.2 Characterizing transport by dynamical university

To be more concrete, we study the universality classes describing the infinite-temperature dynamics for a variety of one-dimensional quantum spin-chains. We will focus on the dynamics of a locally conserved charge $\hat{Q} = \sum_r \hat{q}_r$, typically spin. If the system is characterized by a dynamical universality class, at late times the correlation function must collapse under an appropriate rescaling of space and time:

$$\langle \hat{q}_r(t)\hat{q}_0(0)\rangle_{T=\infty} \propto t^{-1/z} f\left(\frac{r}{t^{1/z}}\right). \tag{2.20}$$

This collapse defines the dynamical scaling exponent z and the scaling function $f(\xi)$, which together determine the universality class.

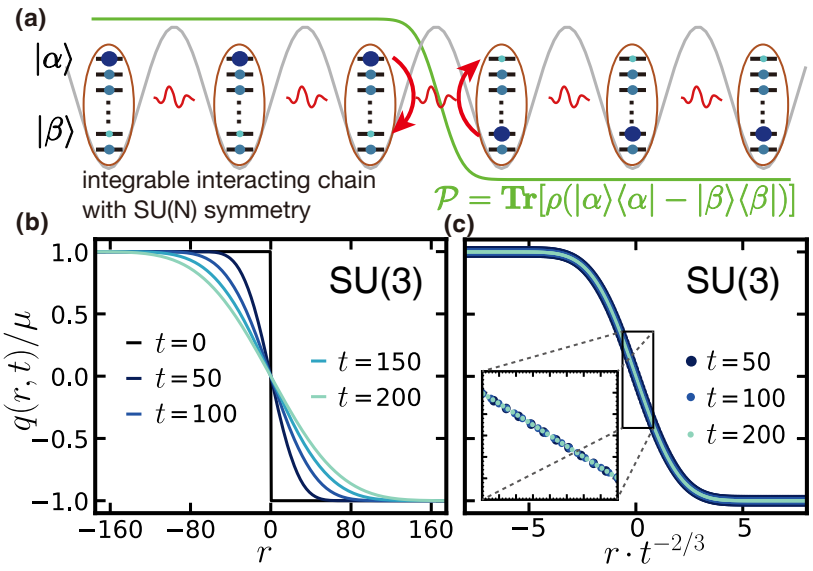

Figure 2.18: (a) Schematic depicting a one dimensional chain of alkaline-earth atoms (each with N-levels) trapped in an optical lattice and interacting via nearest-neighbor super-exchange. The equilibration of an initial domain-wall-like imbalance encodes the underlying KPZ dynamics. (b) Domain-wall dynamics as a function of time for an SU(3)-symmetric, integrable spin chain. (c) The polarization profiles at different times collapse upon rescaling with $t^{-1/z}$. The dynamical exponent, $z = 3/2$, indicates superdiffusion and is consistent with KPZ transport.

2.4.3 Probing transport dynamics

Let us begin by exploring the dynamical exponent. While z can in principle be extracted from the behavior of $\langle \hat{q}_r(t)\hat{q}_0(0)\rangle_{T=\infty}$, a simpler and more robust numerical setup is to consider the dynamics of a domain wall. More specifically, we perturb an infinite-temperature density matrix with a weak domain-wall-like imbalance in the charge density (Fig. 2.18a) [11]:

$$\rho(t=0) \propto (\mathbb{1} + \mu\hat{q})^{\otimes L/2} \otimes (\mathbb{1} - \mu\hat{q})^{\otimes L/2}, \tag{2.21}$$

where μ determines the strength of the perturbation and L is the length of the chain.

As the system equilibrates, charge crosses the domain wall—the precise details of how this occurs reveals properties of the dynamical universality class [Fig. 2.18(b)]. In particular, we focus on the spatial profile of the charge density $q(r,t) = \langle \hat{q}_r(t)\rangle$ (hereafter, denoted as polarization), as a function

[11] We choose to work with open boundary conditions. The boundary conditions do not affect the dynamics we observed within the timescale we considered. However, a strict analytical approach may require a careful treatment of the boundary conditions, which is important and subtle in integrable systems [486, 487].

of time t and displacement r from the domain wall. A natural measure of transport is the total polarization transferred across the domain-wall, $\mathcal{P}(t) = \sum_{r=1}^{L/2} (\mu - q(r,t))$, which provides a robust way to determine z: $\mathcal{P}(t) \propto t^{1/z}$.

Although we will explore a wide variety of integrable models (Fig. 2.20), let us begin by focusing our discussions on the SU(3)-symmetric, spin-1 chain [488–490]:

$$H_{\mathrm{SU(3)}} = \sum_i \vec{S}_i \cdot \vec{S}_{i+1} + (\vec{S}_i \cdot \vec{S}_{i+1})^2, \tag{2.22}$$

where $\vec{S}_i$ is the vector of spin-1 operators acting on site i. Figure 2.18(b) depicts the melting of the domain wall as a function of time, starting from the initial state, $\rho(t=0)$ with $\hat{q} = \hat{S}^z$ [Eqn. 2.21]. The corresponding polarization transfer, $\mathcal{P}(t)$, exhibits a power-law $\sim t^{2/3}$ (blue line, Fig. 2.19b), consistent with the expected $z = 3/2$ exponent [491]. This exponent can be independently confirmed via a scaling collapse of the polarization profile (Fig. 2.18c).

In order to tune the system away from superdiffusion, one can perturb the spin-chain by either breaking the non-Abelian symmetry of the underlying equilibrium initial state [480, 481] or the symmetry of the Hamiltonian. To study the former, we initialize the system in $\rho(t=0)$ and add a uniform magnetization, δ (along the $\hat{z}$-axis) on each site. The polarization transfer exhibits markedly distinct dynamics with a ballistic exponent, $z = 1$ (orange line, Fig. 2.19b). Analytically, for weak magnetizations, the velocity of this ballistic transport is expected to scale linearly with δ; this is indeed borne out by the data (Fig. 2.19c) [171, 492]. For the spin-$1/2$ Heisenberg model, an even stronger statement can be made—the velocity extracted from DMT quantitatively agrees with analytic calculations [via generalized hydrodynamics (GHD) (Appendix A.6)] even in the non-linear regime (inset, Fig. 2.19c) [170, 171].

Next, we break the symmetry of $H_{\mathrm{SU(3)}}$ down to U(1) by considering the so-called Izergin-Korepin family of integrable spin-1 models (Appendix A.7.3) [493–503]. We parametrize the symmetry-breaking strength by Δ, such that when $\Delta = 0$, we recover $H_{\mathrm{SU(3)}}$. For finite values of Δ, we observe diffusive transport with the polarization transfer scaling as $\mathcal{P}(t) \sim t^{1/2}$ (purple line, Fig. 2.19b). In addition, the extracted diffusion coefficient, D, diverges as $\Delta \to 0$, consistent with the approach to superdiffusion (Fig. 2.19d). The analogous numerical experiment in the Heisenberg model, where Δ

controls the anisotropy of the XXZ model in the easy-axis regime, again quantitatively agrees with analytic calculations.

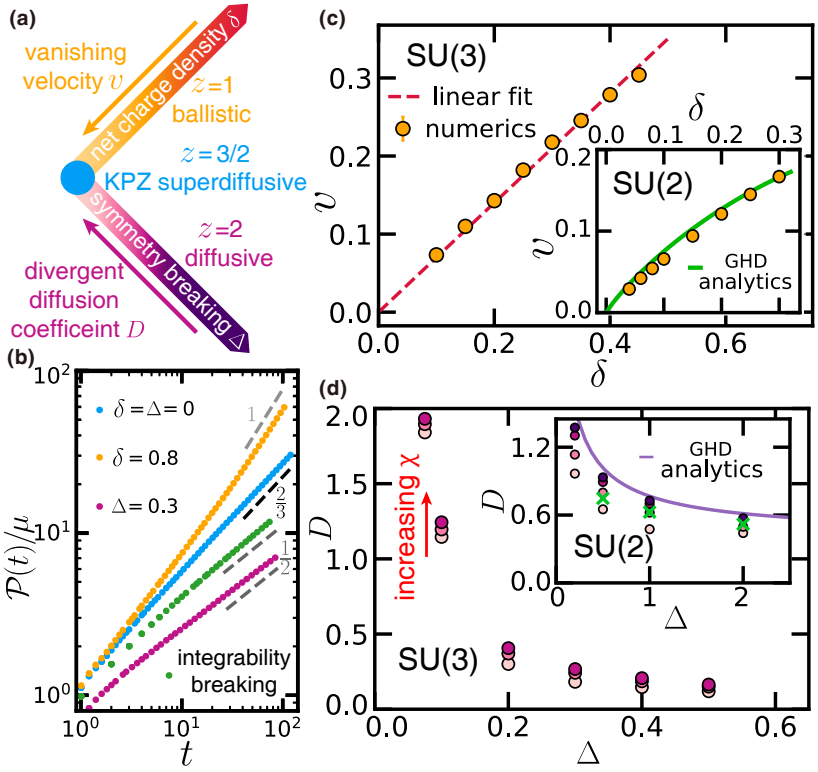

Figure 2.19: (a) Conjectured landscape of KPZ transport in integrable, non-Abelian-symmetric models (blue dot). The non-Abelian symmetry can be broken in two distinct ways, either by adding a finite charge density to the initial state (orange line) or by perturbing the underlying Hamiltonian (purple line). (b) The total polarization transferred across the domain wall, $\mathcal{P}(t)$, directly determines the dynamical exponent. For the integrable SU(3) model, $z = 3/2$; when either the integrability or the symmetry is broken in the Hamiltonian, $z = 2$ [12]; when the initial state has non-zero charge density, $z = 1$. Note that the curve for the integrability breaking case (green) is shifted down for clarity. (c) Depicts the charge transport velocity v as a function of charge density δ for both the SU(3) model and the SU(2) model (inset) [13]. (d) The diffusion coefficient, D, diverges as the Izergin-Korepin and XXZ (inset) integrable models approach the SU(3) and SU(2) (inset) symmetric points. The DMT bond dimension, χ, is chosen to be $\{64, 128, 256\}$ and $\{64, 128, 256, 512\}$ for the SU(3) and SU(2) cases, respectively. Green crosses in the inset mark previous numerical results obtained from tDMRG simulations with bond dimension $\chi \sim 2000$ [445].

[12]Here, we perturb $H_{\mathrm{SU(3)}}$ using SU(3)-symmetry-respecting, but *integrability-breaking* next-nearest-neighbor interactions. As expected for generic non-integrable models, $\mathcal{P}(t) \sim t^{1/2}$, consistent with diffusive transport [359, 378, 504].

[13]The agreement between DMT numerics and GHD analytics (which have different underlying assumptions) serves a dual benchmarking role; in particular, it highlights DMT's ability to faithfully characterize late-time transport dynamics and GHD's ability to quantitatively compute transport coefficients in integrable models [170, 445].

2.4.4 Probing KPZ dynamics

While our numerical observation of a $z = 3/2$ exponent in $H_{\mathrm{SU}(3)}$ clearly establishes the presence of superdiffusion, it does not determine the system's dynamical universality class. Indeed, such an exponent can also arise in long-range interacting systems exhibiting Lévy flights, as well as rescaled diffusion [353, 426, 427, 478, 505].

To this end, we now investigate the universal scaling function. In particular, using our domain-wall dynamics, we can compute the charge correlation function from the spatial gradient of the polarization profile [427]:

$$\langle \hat{q}_r(t)\hat{q}_0(0)\rangle_{T=\infty} = \lim_{\mu\to 0} \frac{\partial_r q(r,t)}{2\mu} = \frac{b}{t^{2/3}} f\left(\frac{br}{t^{2/3}}\right), \tag{2.23}$$

where b is a system-dependent parameter, and we use ∂_r as a short-hand for discrete difference in the our system: $\partial_r q(r,t) = \langle \hat{q}_{r+1}(t)\rangle - \langle \hat{q}_r(t)\rangle$.

As depicted in Figure 2.20a, $\partial_r q(r,t)$ indeed collapses under the rescaling, $f(\xi = brt^{-2/3})$. For Lévy flights, one expects power-law tails (gray dashed line), which are manifestly inconsistent with the data. However, the difference between rescaled diffusion and KPZ is more subtle: for the former, $f(\xi)$ is Gaussian, while for KPZ, $f(\xi)$ exhibits faster decaying tails $\sim \exp\left(-0.295|\xi|^3\right)$ [473–475]. The data quantitatively agree with the KPZ prediction: The longer the evolution time, the closer $\partial_r q(r,t)$ is to the KPZ scaling function (highlighted by the relative error, Fig. 2.20a inset). This agreement allows us to directly extract $b = 0.460 \pm 0.001$, which reflects the ratio between the diffusive smoothing, and the non-linear growth and noise in the KPZ equation. We emphasize that these observations apply to *any* conserved charges generated by the non-Abelian symmetry.

A complementary way to distinguish between rescaled diffusion and KPZ dynamics is to study the ratio between the spin current, $j(r,t) = -\int_{-\infty}^{r} \partial_t q(r',t)dr'$, and the polarization gradient. In rescaled diffusion, Fick's law ensures that the two are proportional, $j(r,t) \propto t^{1/3}\partial_r q(r,t)$, while the non-linearity of KPZ transport leads to the breakdown of this proportionality [427, 473]. Crucially, as illustrated in Fig. 2.20e, we find that the ratio is not constant (as would be predicted for rescaled diffusion) and rather, is in good agreement with the KPZ prediction.

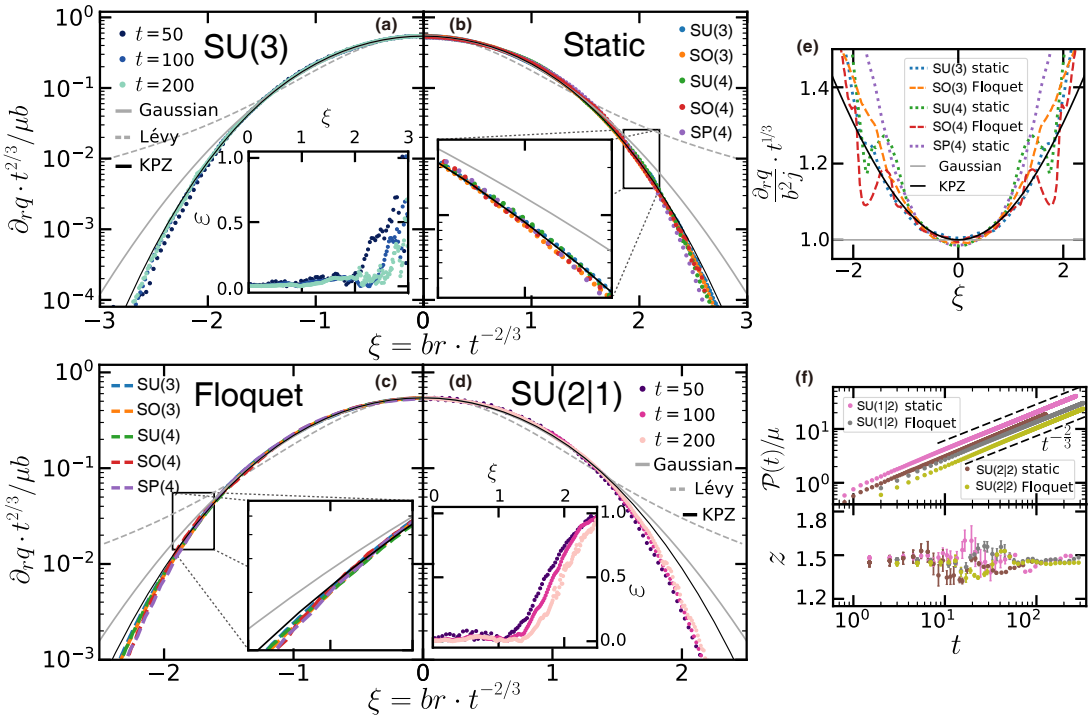

Figure 2.20: (a-d) The KPZ scaling function emerges from a wide variety of integrable dynamics: static, non-Abelian-symmetric models, their Floquet counterparts, and supersymmetric models. (a)[(d)] At late times, the rescaled polarization profiles of the SU(3)[SU(2|1)] model differ from both the Gaussian and Lévy-flight expectations, but exhibit excellent agreement with the KPZ scaling function. Insets of (a)[(d)]: relative difference with respect to the KPZ scaling function. We note that the agreement extends to longer length-scales as time is increased. (b)[(c)] Late-time, rescaled polarization profiles of static [Floquet] integrable models with different non-Abelian symmetries. For all symmetries explored, the dynamics exhibit excellent agreement with the KPZ scaling function. Insets of (b)[(c)]: zoom-in of the polarization profiles. The system sizes in the numerical simulation are chosen as: $L = 600$ for all static models, $L = 1200$ for Floquet SU(3) and SO(3) models, and $L = 800$ for other Floquet models. (e) For all models considered, the ratio between the polarization gradient and the current is inhomogeneous, in stark contrast with the expectation for any linear transport equation. The observed curvature is instead in agreement with KPZ transport. (f) In integrable supersymmetric models, the total charge transferred across the domain wall (upper panel) and the extracted dynamical exponent z (lower panel) are consistent with superdiffusion.

2.4.5 Universality of KPZ dynamics

We now turn our attention to the conjecture that KPZ dynamics emerge in several broad classes of integrable models. We will focus on three distinct settings: (i) static models with generic non-Abelian symmetries, (ii) periodically-driven (Floquet) models with non-Abelian symmetries, and (iii) supersymmetric models. In these latter two classes, even for the dynamical exponent, there are no generic results, although some particular instances are known to exhibit superdiffusion [427, 477, 491].

The construction of static, non-Abelian, integrable spin chains has a rich history, with different prescriptions for each of the four classes of simple Lie groups: SU(N), SO($2N$), SO($2N+1$) and SP($2N$) [14] [173, 497–503]. Following our previous strategy for $H_{\mathrm{SU}(3)}$, we analyze the transport dynamics of conserved charges for each of these models. In all cases, we observe excellent agreement with the KPZ universality class (Fig. 2.20b,e).

Extending this exploration to periodically driven systems requires systematically building the corresponding Floquet integrable models. Somewhat astonishingly, one can straightforwardly build such models from their static counterparts [485, 506]. The Hamiltonian is divided into terms acting on even and odd bonds (denoted as H_{even} and H_{odd}, respectively), which are then alternatingly applied, leading to a Floquet unitary: $U = e^{-iH_{\mathrm{odd}}T/2}e^{-iH_{\mathrm{even}}T/2}$. Using this procedure, we can extend our analysis to the Floquet regime for all of the previous non-Abelian models (Fig. 2.20c,e). Our conclusions are identical. The resulting transport falls within the KPZ universality class even though energy is no longer conserved.

Finally, let us consider integrable models where the non-Abelian symmetry is replaced with supersymmetry (Appendix A.7.2). Such models have been conjectured to exhibit superdiffusion, but observing this, either numerically or analytically, remains an open challenge [173, 477]. Here, we focus on a pair of spinful fermionic lattice models: the t-J model (with $t = 2J$), and the Essler-Korepin-Schoutens (EKS) model [503, 507–510]. These exhibit the two simplest supersymmetries, SU($1|2$) and SU($2|2$), respectively.

The defining feature of models with supersymmetry is that their conserved charges fall into two types: bosonic and fermionic, although only the bosonic charge can in principle exhibit superdiffusion [477]. For the t-J model, each lattice site can be occupied by either a spin-up fermion, a spin-down fermion, or a hole. The conserved bosonic charges are given by the total number of holes, and the total spin. Holes live in the Abelian U(1) sector and thus lack particle-hole symmetry leading to a finite Drude weight and ballistic transport [477]. Therefore, we study the spin polarization, given by the difference between the number of spin-up and spin-down particles. As before, we prepare a weak

[14] A systematic way to generate such integrable models with lower symmetries by breaking a non-Abelian symmetry is called q-deformation. The corresponding models are often called q-deformed vertex models. All the integrable models with non-Abelian symmetries studied in this work are with nearest-neighbor interaction (Appendix A.7.1).

domain-wall in the spin polarization while keeping the other charge densities—including the hole density—constant.

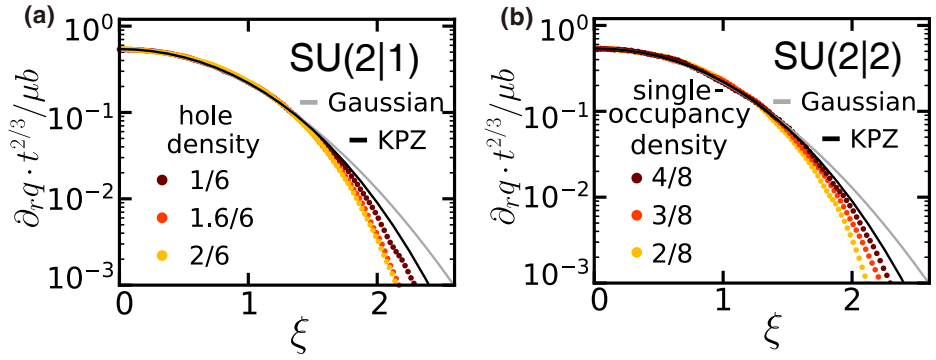

Figure 2.21: (a)[(b)] Polarization gradients in an integrable SU(2|1) [SU(2|2)] model with varying hole density. At the same evolution time, systems with a smaller hole density are closer to the KPZ expectation.

For both the static and Floquet t-J models, we observe superdiffusive spin transport (with $z = 3/2$) via both the polarization transfer (Fig. 2.20f) and the collapse of the polarization profile. The numerical evidence that spin transport falls within the KPZ universality class is more subtle. In particular, the polarization gradient, $\partial_r q(r,t)$, exhibits a discrepancy with both the KPZ and Gaussian expectations (Fig. 2.20d). However, the finite-time flow of $\partial_r q(r,t)$ approaches the KPZ scaling function in the same qualitative fashion as is observed in the SU(3) case (insets, Fig. 2.20a,d); we conjecture that finite-time effects are exacerbated in supersymmetric models owing to the presence of additional ballistic modes (Fig. 2.20g). Indeed, upon decreasing the hole density, we observe an improved convergence to KPZ universality. Note that when there are no holes, one recovers an SU(2)-symmetric model. Curiously, this suggests that KPZ dynamics might arise in supersymmetric systems for generic fermionic filling fractions. Moreover, a careful comparison of the relative error to the Gaussian model suggests that rescaled diffusion cannot be the correct limiting behavior.

2.4.6 Experimental proposal

Recent advances in the control and manipulation of alkaline-earth atoms in optical lattices have opened the door to studying SU(N)-symmetric spin models [511–520]. In particular, we consider a 1D chain of such Fermionic species of such atoms. The lack of hyperfine coupling in the $ns^2\ {}^1S_0$

electronic ground state then leads to an integrable SU(N) Fermi-Hubbard Hamiltonian:

$$H^{\mathrm{F-H}} = -t\sum_{i,\alpha}(c^{\dagger}_{i,\alpha}c_{i+1,\alpha} + c^{\dagger}_{i+1,\alpha}c_{i,\alpha}) + \frac{U}{2}\sum_{i} n_i(n_i - 1), \tag{2.24}$$

where t is the hopping strength of a fermion between two adjacent sites, U is the on-site repulsive interaction, n_i is the total fermion occupation operator on site i, $c^{\dagger}_{i,\alpha}$ and $c_{i,\alpha}$ are the creation and the annihilation operator of species α fermion on site i, respectively.

Assuming $U \gg t$ and the filling factor is $1/N$ (i.e., one fermion per site) the system is in the Mott-insulating phase. To the lowest order, the dynamics arise from virtual hopping processes and are generated by the following effective Hamiltonian:

$$\begin{aligned} H^{\mathrm{F-H}} &\approx \frac{2t^2}{U}\sum_{i,\alpha\neq\beta} c^{\dagger}_{i,\alpha}c_{i,\beta}c^{\dagger}_{i+1,\beta}c_{i+1,\alpha} - c^{\dagger}_{i,\alpha}c_{i,\alpha}c^{\dagger}_{i+1,\beta}c_{i+1,\beta} \\ &= \frac{2t^2}{U}\sum_{i,\alpha\neq\beta} S^{\alpha,\beta}_i \otimes S^{\beta,\alpha}_{i+1} - S^{\alpha,\alpha}_i \otimes S^{\beta,\beta}_{i+1} \\ &= \frac{2t^2}{U}\sum_{i,\alpha\neq\beta} S^{\alpha,\beta}_i \otimes S^{\beta,\alpha}_{i+1} + \frac{2t^2}{U}\sum_{i,\alpha} S^{\alpha,\alpha}_i \otimes S^{\alpha,\alpha}_{i+1} - \frac{2t^2}{U}\sum_{i}\left(\sum_{\alpha} S^{\alpha,\alpha}_i\right)\otimes\left(\sum_{\beta} S^{\beta,\beta}_{i+1}\right) \\ &= \frac{2t^2}{U}\sum_{i,\alpha,\beta} S^{\alpha,\beta}_i \otimes S^{\beta,\alpha}_{i+1} - \frac{2t^2}{U}\sum_{i}\mathbb{1}_i \otimes \mathbb{1}_{i+1}, \end{aligned} \tag{2.25}$$

where $s^{\alpha,\beta}_i = |\alpha\rangle\langle\beta|$ on site i; in one dimension, $H_{\mathrm{SU}(N)}$ is integrable and precisely corresponds to the models considered above (e.g. Eqn. 2.22), up to a constant energy shift. The observation and characterization of KPZ transport requires the ability to address two main experimental challenges: (i) preparing near infinite-temperature states with a well-defined domain-wall polarization and (ii) measuring the tails of the scaling function with sub-percent accuracy.

The former can be accomplished via a two step process: first, optical pumping via an intercombination transition (e.g. $ns^2\,{}^1S_0 \leftrightarrow nsnp\,{}^3P_1$) can be used to generate arbitrary magnetization distributions which are preserved upon cooling to the Mott insulator; second, with single-site addressing [425, 521–526], a coherent optical drive can be applied to half the system in order to prepare the domain wall. In current optical lattice experiments, the main challenge in preparing such states arises from the need to controllably add entropy to the system *after cooling the motional degrees of freedom*. In past experiments [425], this was accomplished by applying a combination of global rotations to control

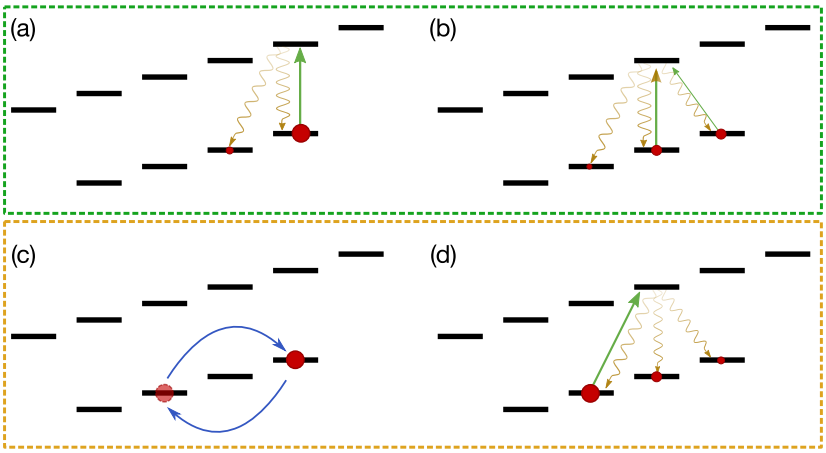

Figure 2.22: Two different approaches towards preparing arbitrary population distributions. (a) Starting from the $|F, m_F = F\rangle$ state in the ground state manifold, $\hat{z}$ polarized laser can be used to excite the system to $|F+1, F\rangle$. Spontaneous emission then leads to decay back to the ground state manifold, into $|F, F\rangle$ and $|F, F-1\rangle$, with a branching ratio dictated by Clebsch-Gordan coefficients. By timing the laser duration appropriately, this enables the arbitrary population transfer from the $|F, F\rangle$ to the $|F, F-1\rangle$ state. (b) To continue this process toward lower m_F states, e.g. from $|F, f\rangle$ to $|F, f-1\rangle$, one can again apply a $\hat{z}$ polarized laser. However, this would lead to additional leakage back to a $|F, f+1\rangle$ state. To counteract this effect, an additional σ^- polarized laser field to excite from $|F, f+1\rangle$ back into $|F+1, f\rangle$ should be applied. Doing this procedure repeatedly enables the preparation of an arbitrary spin population distribution. (c) Another approach to prepare a spin population distribution begins by moving the entire population from the $|F, F\rangle$ into the lowest $|F, f_{\text{min}}\rangle$ of interest. Starting again with unit population in the largest m_F state of the manifold $|F, F\rangle$, we begin by performing a coherent rotation between $|F, F\rangle$ and the lowest hyperfine state we wish to have finite population, say $|F, f_{\text{min}}\rangle$. (d) From $|F, f_{\text{min}}\rangle$, the population distribution can be built by iteratively applying a σ^+ polarized laser to move any extra polarization from $|F, f_{\text{min}}\rangle$ into $|F+1, f_{\text{min}}+1\rangle$, which then decays into higher hyperfine states, $|F, f_{\text{min}}+1\rangle$ and $|F, f_{\text{min}}+2\rangle$. As long as the upper manifold has equal or larger total angular momentum, this process can be carried out until reaching back to the $|F, F\rangle$ state, using an excitation from $|F, F-1\rangle$ to $|F+1, F\rangle$ to set its population

the spin population, and single-site rotations to dephase individual spins with respect to one another; however, when moving from spin-1/2 to larger spin systems, this protocol is not suitable to prepare arbitrary spin population distributions. To circumvent this, we propose a different scheme, which utilizes the flexibility provided by manipulating the atoms *before* loading them into the optical lattice. Crucially, this allows us to leverage optical pumping techniques using the excited hyperfine manifold to move population density across the different spin levels of interest (Fig. 2.22).

Achieving the latter is significantly more subtle. In order to distinguish between KPZ dynamics and rescaled diffusion, careful estimates suggest the need to experimentally resolve the scaling function with a relative error of $\delta\bar{m}/\mu \sim 10^{-3}$ (Fig. 2.23). In order to operate within the small domain-wall regime where the gradient of the polarization accurately captures the two-point correlation function,

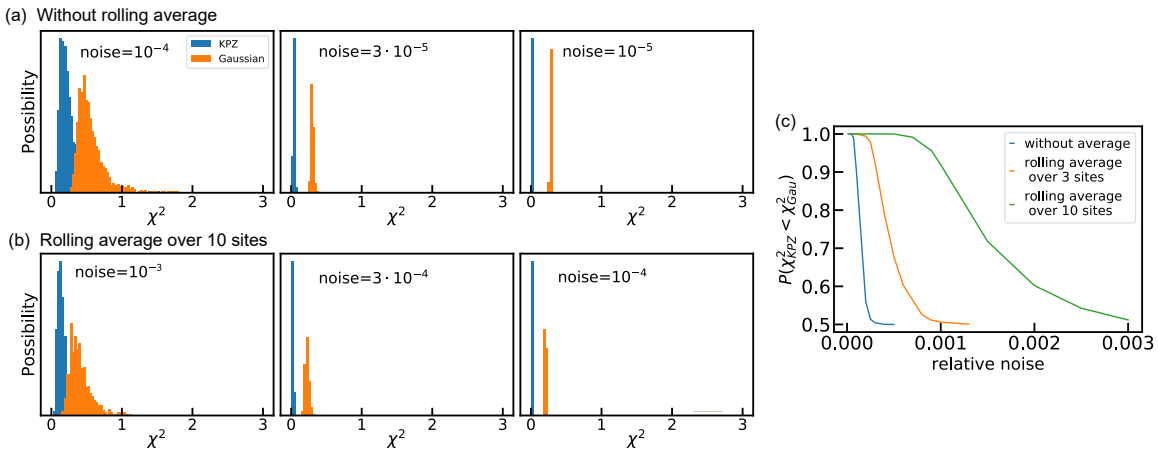

Figure 2.23: (a)(b) χ^2 analysis of the confidence to confirm the KPZ dynamics. By adding random noise on the data from DMT numerics, we can mimic experimental data. For each noise instance drawn from a normal distribution, we fit the noisy data with both the KPZ and the Gaussian expectations, and obtain the corresponding χ^2. By repeating this analysis for different noise instances, we obtain the distribution of χ^2. The histogram of χ^2 indicates the confidence of whether the data agrees better with KPZ or Gaussian expectation. As the size of noise decreases, χ^2 corresponding to KPZ approaches to zero and is separated from χ^2 corresponding to Gaussian fit. Performing rolling average of polarization profile over n consecutive sites can effectively reduce the effect of noise roughly by a factor of n. Using $\bar{n} = 10$, a relative error of $\sim 10^{-3}$ already distinguishes the two hypothesis. The numerics are performed on the integrable SU(3) model with $\mu = 0.1$ and $L = 150$. We choose to fit the polarization profile at $t = 52/J$. (c) χ^2 analysis to confirm KPZ dynamics and to exclude Gaussian expectation. To quantify the confidence with which we can conclude KPZ fits the data better, we compute the possibility of obtaining a smaller χ^2 in the KPZ fit than in the Gaussian fit. Without performing a rolling average, when the relative noise amplitude is below 10^{-4}, it becomes almost certain that the KPZ expectation fits the data better, suggesting that the experiment can conclusively confirm the KPZ expectation at such noise level. By further performing a rolling average over n sites, we can increase the minimum relative noise required by roughly n times.

we need the domain wall size to be at most $\mu \lesssim 0.2$, leading to an absolute uncertainty in the magnetization error of $\delta\bar{m} \sim 2 \times 10^{-4}$. Achieving this error floor requires the ability to spatially resolve spin-transport dynamics over long time-scales and large distances. For concreteness, let us consider ^{87}Sr atoms loaded into a two-dimensional optical lattice [519, 527, 528]. Recent experiments have demonstrated the elegant use of cavity-enhancement to realize homogeneous lattices capable of supporting Mott insulators with a diameter of ~ 300 sites [527]. By implementing strong confinement in one direction, one can subsequently divide the system into ~ 250 independent chains, each with length ~ 150 sites. Assuming an on-site interaction energy, $U \sim 3$ kHz, and a tunneling rate, $t \sim 300$ Hz, yields a spin-exchange interaction, $J = 2t^2/U \approx 60$ Hz [527]. Optimizing for an evolution time of $\sim 50/J$ and assuming an experimental cycle time of ~ 10 s [519], we estimate that

a magnetization error of $\delta\bar{m} \sim 2 \times 10^{-4}$ can be achieved within two days of averaging. Finally, the presence of a finite density ($\gtrsim 1\%$ [529]) of doublons and holes in the Mott insulator will perturb the polarization dynamics, but the exact nature of their effect remains an intriguing open question.

2.4.7 Outlook

Since it was first observed in the spin-1/2 Heisenberg model [353], the microscopic origin of KPZ dynamics in integrable quantum magnets has remained a mystery [530]. Our work suggests that any such understanding will need to encompass a broader physical setting, including both Floquet and supersymmetric systems. In the context of supersymmetry, an intriguing direction is to characterize the impact of ballistic fermionic modes on the KPZ dynamics. Finally, the ability to experimentally measure the full counting statistics of spin transport opens the door to studying KPZ dynamics from a new perspective, which is currently challenging to access both analytically and numerically [425, 531].

2.5 Quantum gas microscopy of Kardar-Parisi-Zhang superdiffusion

2.5.1 Introduction

First proposed to capture the spin transport of the spin-1/2 quantum Heisenberg chain at infinite temperature [171, 172, 353, 427, 444, 530, 532], KZP hydrodynamics have then been predicted to emerge in all one-dimentional integrable quantum systems exhibiting a non-abelian symmetry or a supersymmetry [164, 166, 167, 173, 396, 428, 533]. In contrast to those canonical examples of noisy classical systems, the appearance of KPZ scaling in quantum settings, which requires integrability and is thus fragile to noise, is very likely to rely on a fundamentally different mechanism [173, 480, 530, 533–535]; to date, a full theory of KPZ unversality in the quantum systems remains elusive [373, 536]. At the current stage, experimental input will not only confirm the theoretical expectation but may also provide deeper insights into understanding the emergent KPZ hydrodynamics. Indeed, experimentally characterizing the anomalous dynamical exponents of spin transport has been the subject of widespread effort [479, 537–539]. However, similar to theoretical approaches, it is also challenging in experiments to fully establish a system's hydrodynamical universality class, since it requires characterization beyond the dynamical exponent.

In this section, we explore the superdiffusive dynamics of the ferromagnetic Heisenberg model using a quantum-gas microscope with single-site resolution and single-spin-sensitive detection in spin chains of up to 50 spins. Our main results are three fold. First, we observe superdiffusive spin transport with the dynamical exponent $z = 3/2$, consistent with KPZ hydrodynamics. Second, we demonstrate that both integrability and a non-abelian symmetry are essential for observing superdiffusion: Breaking integrability by tuning dimensionality restores diffusion, and breaking the symmetry by preparing an initial state with net magnetization leads to ballistic transport (Fig. 2.24A). Finally, leveraging the ability of our experimental setup to detect spin-resolved snapshots of the entire sample, we map the shot-to-shot dynamical fluctuations (i.e., the "full counting statistics") of the magnetization. These fluctuations carry clear signatures of the intrinsic non-linearity associated with KPZ hydrodynamics [540], and distinguish it from other potential mechanisms for superdiffusion such as Lévy flights [536].

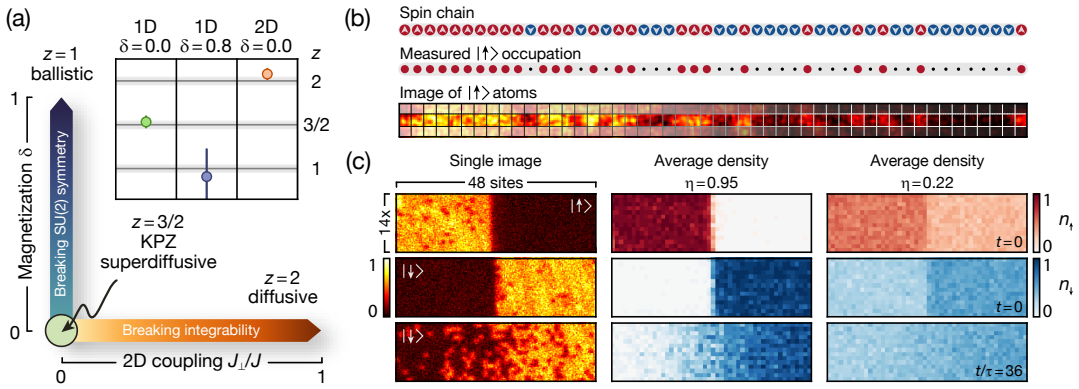

Figure 2.24: (a) Dynamical exponents for finite-temperature Heisenberg chains. Whereas integrable systems typically display ballistic transport (magnetized chains, $\delta > 0$), non-integrable systems are generically diffusive (2D Heisenberg model, $J_\perp > 0$). For unmagnetized Heisenberg chains, transport is expected to fall into the KPZ universality class with a superdiffusive exponent $z = 3/2$. Inset: By measuring polarization transfer $P(t)$ across a domain wall, we directly observe these transport regimes: superdiffusion in the unmagnetized case (green), ballistic transport at finite net magnetization (blue), and diffusion in 2D (orange). Exponents are extracted by fitting $P(t) \propto t^{1/z}$; for the ballistic case we additionally fit a vertical intercept to account for transient initial-time dynamics. Error bars denote the standard deviation (s.d.) of the fit. (b) In each experimental run, we measure the spin states of a Heisenberg chain (top) by removing one spin species (center) and imaging the atomic site occupation (bottom). (c) The Heisenberg chains are realized in a 2D atomic Mott insulator (analysis region depicted) with controllable inter-chain coupling. Our setup allows us to prepare domain walls with high purity η (left, center column) and low purity η (right). We measure the time evolution of both $|\uparrow\rangle$ (top) and $|\downarrow\rangle$ (center, bottom row) atoms to extract the polarization transfer.

2.5.2 Experimental system

In our experiment, we probed the transport dynamics of bosonic ^{87}Rb atoms trapped in an optical lattice; the atoms occupy the two hyperfine ground states $|\uparrow\rangle = |F = 1, m_F = -1\rangle$ and $|\downarrow\rangle = |F = 2, m_F = -2\rangle$ and their dynamics are captured by a two-species Bose-Hubbard model with on-site interaction U and tunnel coupling $\tilde{t}$. At unit filling and in the limit of strong interactions, the direct tunneling between lattice sites is suppressed and spin dynamics occur via second-order spin-exchange. The system can be mapped to the spin-1/2 XXZ model for $|\uparrow\rangle$ and $|\downarrow\rangle$ [541, 542], and, in one dimension (1D), is described by the Hamiltonian

$$\hat{H} = -J \sum_j \left(\hat{S}_j^x \hat{S}_{j+1}^x + \hat{S}_j^y \hat{S}_{j+1}^y + \Delta \hat{S}_j^z \hat{S}_{j+1}^z \right), \tag{2.26}$$

where Δ quantifies the interaction anisotropy and $J = 4\,\tilde{t}^2/U$ characterizes the spin-exchange coupling. In our system, the atomic scattering properties yield $\Delta \approx 1$ and the system maps to the isotropic

ferromagnetic Heisenberg model.

We began our experiment by loading a spin-polarized 2D degenerate gas of approximately 2000 atoms into a square optical lattice with a spacing of $a = 532\,\mathrm{nm}$. We realized a homogeneous box potential over 50×22 sites by additionally projecting light at a wavelength of 670 nm with a digital micromirror device (DMD), preparing a Mott insulator with a filling of $n_0 = 0.93(1)$ in this box. Local spin control was realized using light at a wavelength of 787 nm on the DMD [543] to apply a site-resolved differential light shift between $|\uparrow\rangle$ and $|\downarrow\rangle$; subsequent microwave driving allowed for local flips of the spatially addressed spins.

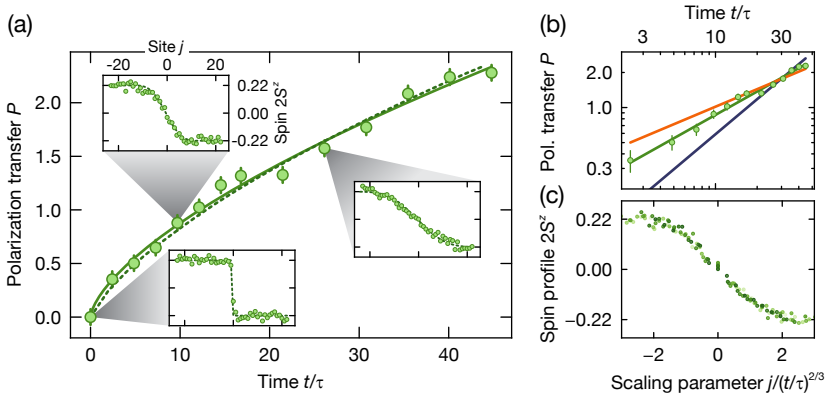

Figure 2.25: (a) The polarization transfer for a domain-wall initial state with a contrast of $\eta = 0.22(2)$ grows as a power law ($P(t) \propto t^{1/z}$) with a fitted exponent $z = 1.54(7)$ (solid line), indicating superdiffusive transport. The experimental data agrees well with numerical Heisenberg-model simulations (dashed line). The insets show the averaged spin profiles $2S^z_j(t)$ at times $t/\tau = 0, 10, 26$, which are compared to simulations (dashed lines). (b) Polarization transfer in a double-logarithmic plot. The solid lines are power-law fits with fixed exponents, where a distinction between $z = 3/2$ (green) and both $z = 2$ (brown) and $z = 1$ (blue) is visible. (c) When rescaling time by the inverse dynamical exponent, the spatial spin profiles at times $t/\tau = 5$ to 35 (light to dark green) collapse to a characteristic shape consistent with the integrated KPZ function. Error bars denote the standard error of the mean (s.e.m).

Such quantum control enabled us to prepare spin domain walls [353, 397, 427, 544] by spatially addressing half the system. Subsequently, we prepared high-entropy states by globally rotating the spins away from the S^z-axis using a resonant microwave pulse and then locally dephasing them by projecting a site-to-site random spin-dependent potential, which we modified from shot to shot (Fig. 2.24C). More precisely, our experiments focused on tracking spin dynamics starting from a class of initial states comprising a spin domain wall with magnetization difference 2η in the middle of the spin chain: i.e., one half of the system has magnetization η and the other half of the system has

magnetization $-\eta$. In the infinite-temperature limit, $\eta \to 0$, the relaxation of such states yields linear response transport coefficients, as the derivative of the spin profile is precisely the dynamical spin structure factor [353, 427].

In order to probe 1D spin dynamics in our system, we rapidly quenched the lattice depth along 1D tubes comprising 50 sites, which suddenly increased the spin-exchange coupling from zero to $J/\hbar = 64(1)\,\mathrm{s}^{-1}$. After tracking the spin dynamics for up to ~ 45 spin-exchange times $\tau = \hbar/J$, we removed one spin component and measured the remaining occupation via fluorescence imaging (Fig. 2.24B).

2.5.3 Superdiffusive spin transport

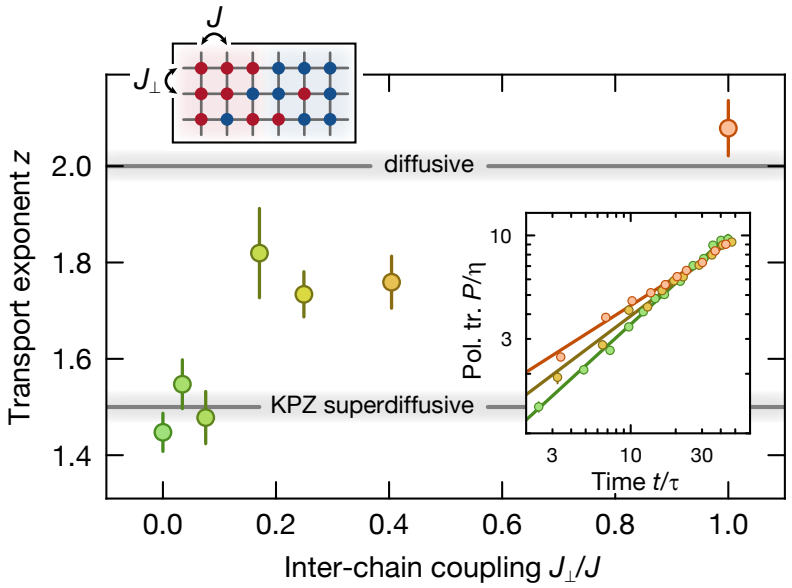

Figure 2.26: Fitted power-law exponent z for the spin polarization transfer at different coupling strengths between individual 1D chains with initial domain walls with $\eta \approx 0.9$. Starting from superdiffusive transport in the purely 1D case, $z = 1.45(5)$, increased inter-chain coupling breaks the integrability of the system and leads to a crossover towards diffusive transport, reaching $z = 2.08(4)$ in the 2D case, as generically expected for non-integrable systems. The inset depicts the normalized polarization transfer $P(t)/\eta$ for $J_\perp/J = 0, 0.40(1)$ and $1.00(5)$ (green to orange). Error bars denote s.d. of the fit.

To explore the nature of anomalous spin transport in the 1D Heisenberg model, we initialize the spins in a high-entropy domain-wall state with $\eta = 0.22(2)$. We characterize the subsequent spin transport by measuring the polarization transfer, $P(t)$, defined as the average total number of spins

that have crossed the domain wall by time t. The emergence of hydrodynamics is characterized by the power-law scaling of $P(t) \sim t^{1/z}$, and immediately enables us to extract the underlying dynamical exponent z. As depicted in Fig. 2.25A, the data exhibit a superdiffusive exponent, $z = 1.54(7)$, consistent with KPZ scaling. By comparison, neither a diffusive ($z = 2$) nor ballistic ($z = 1$) exponent accurately capture the observed dynamics (Fig. 2.25B). Somewhat surprisingly, we also observe a superdiffusive exponent of $z = 1.45(5)$ upon changing the initial state to a near-pure domain wall with $\eta = 0.95(2)$ (Fig. S8) [318, 397, 536, 545].

To further explore the superdiffusive dynamics, we investigate the spatially resolved spin profiles at $\eta = 0.22(2)$. Our experimental observations are in quantitative agreement with simulations based upon tensor-network numerical techniques [317, 318] and conform to KPZ dynamics (Fig. 2.25A). Crucially, when appropriately rescaled by the dynamical exponent, all of the observed spatio-temporal profiles collapse onto a scaling form consistent with the KPZ scaling function (Fig. 2.25C).

2.5.4 Microscopic origins of superdiffusion

To understand why the combination of integrability and a non-abelian symmetry leads to emergent superdiffusive transport, it is instructive to first consider the transport dynamics on top of a small net magnetization background [171, 172, 492, 532]. In our experiments, this corresponds to preparing domain walls with a finite overall magnetization δ, i.e. one half of the system has a magnetization $\eta + \delta$ and the other half $-\eta + \delta$. Stable quasiparticles then render spin transport ballistic (Fig. 2.24A), leading to a characteristic polarization-transfer rate that scales linearly with net magnetization δ [172]. Even when $\delta = 0$ on average, random local fluctuations of the magnetization will be present; thus, the net magnetization in a typical region of size ℓ will scale as $1/\sqrt{\ell}$. Therefore, the average spin transport rate across a region of size ℓ also scales as $1/\sqrt{\ell}$, implying that the transport time across the region scales as $\ell/(1/\sqrt{\ell}) \sim \ell^{3/2}$, precisely yielding the KPZ exponent $z = 3/2$ (Appendix A.6).

This intuitive analysis suggests two key requirements for superdiffusive transport: (i) integrability ensures the presence of stable quasiparticles that move ballistically, and (ii) the presence of a non-abelian SU(2) symmetry makes the characteristic velocity of the ballistic contribution to spin transport vanish. We can experimentally probe these requirements by individually breaking either the

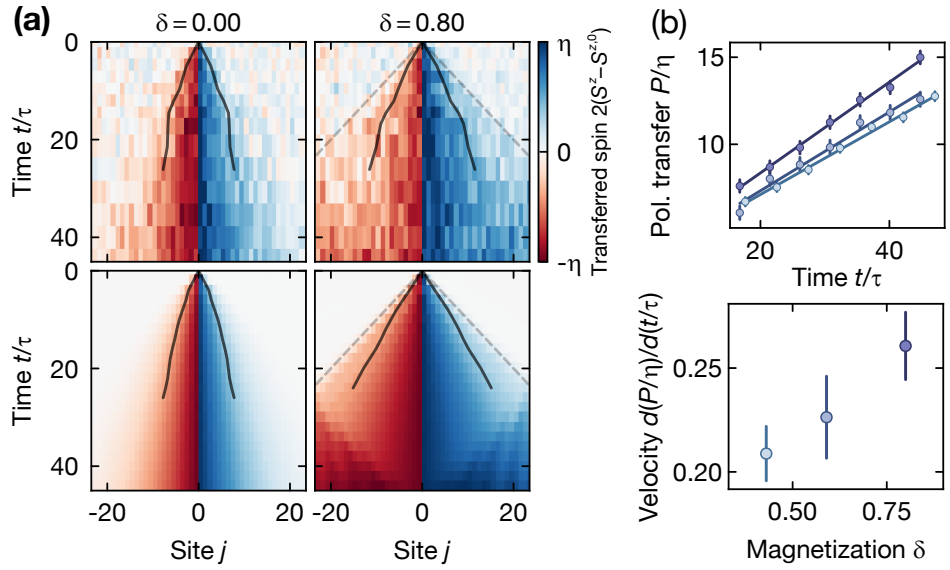

Figure 2.27: (a) Averaged experimental (top) and numerical (bottom) spin profiles $S_j^z(t)$, from which the initial profile $S_j^{z,0}$ is subtracted. (Left) Unmagnetized low-purity domain wall, $\delta = 0, \eta = 0.22(2)$ (from Fig. 2.25). Spin transport results from the increase of the spin profile width, which scales with the superdiffusive dynamical exponent. The black lines indicate the position j where the spin profile crosses $|2S_j^z(t) - \delta|/\eta = 0.4$; because the profiles themselves are scale-invariant, the position of any S^z value follows the $z = 3/2$ scaling. (Right) Magnetized domain wall, $\delta = 0.80(1), \eta = 0.12(1)$. At the outer edge the contribution of magnons is visible, transporting spin with the speed of the spin "light cone" (dashed line), which was measured with a quantum walk. The majority of the spin is carried by quasiparticles within the light cone, leading to the width of the profile (solid line) growing faster than in the unmagnetized case. The numerical simulation shows a qualitatively similar behavior. At $t/\tau \simeq 25$ the magnons reach the system edge and are reflected. (b) To extract the ballistic polarization-transfer velocity, we linearly fit the normalized polarization transfer after a crossover time, $t/\tau > 16$ (left). We observe a growth of the transfer velocity when increasing the initial domain-wall magnetization δ (right, light to dark blue). Error bars denote s.d. of the fit.

integrability or the SU(2) symmetry of the system.

To break integrability, we turn on a finite inter-chain coupling $J_\perp$ by lowering the lattice depth orthogonal to the 1D spin chains, which effectively causes the system to become 2D [546, 547]. We measure the dependence of the polarization transfer on the inter-chain coupling, starting from an unmagnetized domain wall ($\eta \approx 0.9$, $\delta = 0$). As shown in Fig. 2.26, the extracted dynamical exponents exhibit a clear flow from superdiffusive transport when $J_\perp = 0$ to diffusive transport, $z = 2.08(4)$, when $J_\perp = J$. Interestingly, for $J_\perp/J \lesssim 0.1$ integrability is strictly broken but the transport dynamics remain consistent with superdiffusion within experimentally accessible timescales. This observation bolsters recent theoretical expectations, which suggest that superdiffusion can be

particularly robust to perturbations that do not break the non-abelian symmetry [429].

Next, let us explore the effect of breaking the underlying SU(2) symmetry using initial states with finite net magnetization δ. Working with an imbalanced domain-wall initial state ($\eta = 0.12(1)$, $\delta = 0.80(1)$), we observe two main differences compared to the unmagnetized ($\delta = 0$) case (Fig. 2.27A). First, the polarization profile exhibits a fast ballistic component that follows the spin "light cone" of the dynamics (with a speed of $1/\tau$, dashed line in Fig. 2.27A). This contribution arises from the fastest quasiparticles, which transport spin above the magnetized background (Appendix A.6) [548]. Second, within this light cone, polarization spreads substantially faster compared to the unmagnetized case; this comprises the bulk of the spin transport and is mediated by slower-moving, net-magnetization-carrying quasiparticles.

At early times, the polarization-transfer dynamics exhibit a superdiffusive power law, before crossing over to linear ballistic transport at later times. In particular, by fitting a power law to the late-time data, $t/\tau > 16$, we extract a dynamical exponent $z = 0.9(3)$, consistent with ballistic spin transport (Fig. 2.27B). Although our results agree qualitatively with numerical simulations of the Heisenberg model, the magnitude of the measured polarization transfer is smaller; this can be understood as resulting from the presence of hole defects in the initial state [549]. In addition to verifying the ballistic nature of the spin dynamics, we can also directly extract the velocity of the underlying quasiparticles; by controlling the overall magnetization of the initial state, we observe the expected increase of the velocity with δ (Fig. 2.27B), an essential component for understanding the presence of KPZ superdiffusion in spin chains [172].

2.5.5 Observing KPZ hydrodynamics

Our previous observations have focused on characterizing superdiffusive spin transport; however, from the perspective of observing KPZ universality, this is insufficient, as multiple different classes of hydrodynamics can exhibit the same dynamical exponent of $z = 3/2$. To distinguish these classes, we go beyond measurements of the average polarization transfer and analyze the full distribution function of the polarization transfer $\Pr(P;t)$ across snapshots [540]. This distribution function can distinguish KPZ from potential alternatives such as Lévy flights: for all linear processes (such as Lévy flights or

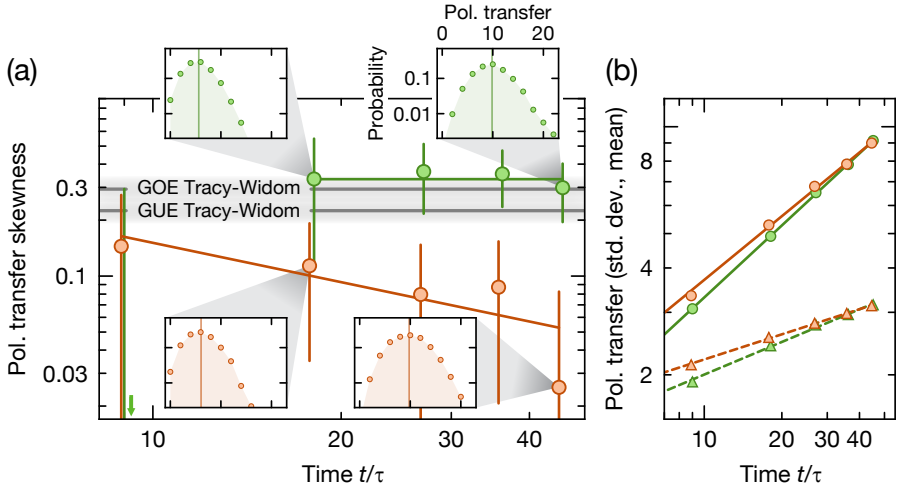

Figure 2.28: (a) The probability distribution asymmetry of the polarization transfer expected for KPZ transport is quantified by the skewness. We compare the pure domain-wall dynamics in the 1D case (green) with the non-integrable 2D case at $J_\perp/J = 0.25(1)$ (orange). Whereas the 2D case becomes symmetric at late times, the 1D distribution remains asymmetric with a skewness of $0.33(8)$. Gray lines indicate the skewness of the Gaussian-orthogonal-ensemble (GOE) and Gaussian-unitary-ensemble (GUE) Tracy-Widom (TW) distributions [550]. Colored lines serve as guides to the eye. (Insets) Probability distributions of the polarization transfer on a logarithmic scale. The vertical line marks the mean of the distribution. (b) The mean (circles) of the polarization transfer is consistent with the data shown in Fig. 2.26 and scales with the power-law (solid lines) exponent $1/z = 0.67(1)$ in 1D; $1/z = 0.60(2)$ in 2D. The standard deviation (triangles) features another characteristic transport exponent (the growth exponent [551]) which agrees with the extracted power-law (dashed lines) exponent, $\beta = 0.31(1)$ in 1D; $\beta = 0.24(1)$ in 2D. Error bars denote the s.d. obtained from a bootstrap analysis.

time-rescaled diffusion) the fluctuations of P at late times are necessarily symmetric about the mean; for KPZ, the limiting distribution $\Pr(P; t \to \infty)$ is the Tracy-Widom distribution (Appendix A.8), which is strongly asymmetric [550, 552].

Measuring the statistics of the polarization-transfer distribution therefore gives us a direct experimental observable to discern the underlying hydrodynamical transport equations; this analysis fundamentally relies on the single-shot nature and the single-spin sensitivity of our quantum-gas microscope. As we measure the occupation of a single spin species per snapshot, we approximate the polarization-transfer statistics by the statistics for the single-species atom-number transfer, $N_T^{\uparrow(\downarrow)} \approx P/2$, where $N_T^{\uparrow}$ is the number of $|\uparrow\rangle$ atoms on the side of the domain wall initialized with the opposite spin $|\downarrow\rangle$. We quantify the asymmetry of the distribution about its mean $\overline{P}$ by its skewness $(\mu_3(t) - \mu_3(0))/(\mu_2(t) - \mu_2(0))^{3/2}$, where $\mu_k(t) = \sum_P (P - \overline{P})^k \Pr(P; t)$ denotes the k-th central moment of the distribution (Appendix A.8).

To begin, we characterize the skewness of the polarization transfer starting from a high-purity domain wall ($\eta = 0.89(1)$, $\delta = 0$) for a 2D geometry with an inter-chain coupling strength $J_\perp / J = 0.25(1)$. The skewness of the polarization transfer distribution is overall small and is most consistent with a decay toward zero (Fig. 2.28) which corresponds to a fully symmetric distribution and which is expected for *linear* diffusive processes exhibited by the non-integrable 2D Heisenberg model.

If the 1D Heisenberg model is actually governed by non-linear KPZ hydrodynamics, one expects a markedly distinct behavior for the skewness as a function of time. In particular, the non-linearity of the KPZ equation would lead to a finite skewness, which is constant over time. We indeed observe that the skewness saturates to a finite value of $0.33(8)$ when starting from an initial state with $\eta = 0.91(2)$ and $\delta = 0$ (Fig. 2.28). In agreement with numerical simulations, this value is consistent with the skewness of the Gaussian-orthogonal-ensemble Tracy-Widom distribution, 0.294 [550]. Directly ruling out linear transport processes, our experiment thus provides a strong indication that transport in the 1D quantum Heisenberg chain is indeed governed by KPZ hydrodynamics.

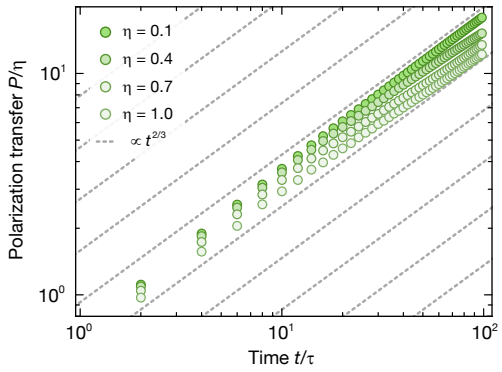

Figure 2.29: As the purity η increases, the dynamical exponent $z = 3/2$ as the diagnostic of superdiffusion persists, while the superdiffusion constant decreases. Gray dashes are guidelines for power-law growth with $z = 3/2$.

2.5.6 Discussion and Conclusion

Effect of purity η in the superdiffusive transport— The required SU(2) symmetry for the KPZ superdiffusion is only strictly present $\eta = 0$, where analytical results are best understood. However, we observe that even for quite large η of the initial state, the subsequent dynamics does not significantly

deviate from superdiffusion. A possible understanding may be that as the domain wall melts, the magnetization approaches zero and the SU(2) symmetry is restored in the middle of the chain. More importantly, the superdiffusive polarization transport is bottlenecked by such unmagnetized region, since finite net magnetization will lead to ballistic transport, which is faster than superdiffusion. Therefore, even for large (but non-unity) purity, it is natural to expect the superdiffusion behavior to still persist. In Fig. 2.29, we numerically study the effect of purity η in the measured polarization transfer. We see that, while the overall magnitude of polarization transferred varies with η, the associated dynamical exponent z remains consistent with KPZ superdiffusion ($z = 3/2$) up until the pure initial state, $\eta < 1$. This is consistent both with theoretical expectation and with the experimental observations of superdiffusion at finite and large η. Curiously, precisely at $\eta = 1$, the behavior is known to be diffusive with logarithmic corrections. However, distinguishing this behavior from superdiffusion, requires following the dynamical evolution to very late time in large system sizes [318, 353, 397].

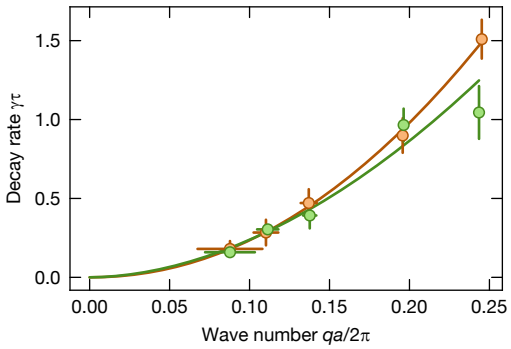

Figure 2.30: Decay rate γ of the $g^{(2)}_{n^\uparrow}$ correlator visibility of spin spirals with wave number q at a lattice depth of 10 E_r (green) and 8 E_r (orange). Both measurements give an exponent consistent with diffusive transport of $z = 1.9(2)$ and $2.0(1)$, respectively. Error bars denote s.d. of the fits.

Transport measurement with spin spiral—Our work builds and expands upon recent experimental explorations of Heisenberg-model spin dynamics. These experiments include neutron scattering studies of the quantum material $KCuF_3$ [479], as well as experiments probing the relaxation of spin-spiral initial states in ultracold gases [537–539]. In the 1D Heisenberg model, the relaxation of such spin-spiral states is non-generic because they are approximate eigenstates in the long-wavelength limit [536].

Empirically, spin spirals relax with a diffusive exponent $z \approx 2$. By considering a more generic family of domain-wall initial states, we are able to directly probe (and controllably move away from) the high-temperature linear-response limit where KPZ transport is conjectured to occur. For a direct comparison with the domain-wall initial state, we also studied the decay dynamics of longitudinal spin spirals. Analogous to the previous experiment in this setup [537], we prepared the spiral state via a Ramsey sequence, where a linear magnetic gradient imprinted a spiral pattern during the time between the pulses. We obtained the decay rates γ by fitting an exponential function to the visibility, $V(t) \propto e^{-\gamma t}$, of the second-order correlation function $\left\langle \hat{n}_i^{\uparrow}(t)\, \hat{n}_{i+d}^{\uparrow}(t) \right\rangle - \left\langle \hat{n}_i^{\uparrow}(t) \right\rangle \left\langle \hat{n}_{i+d}^{\uparrow}(t) \right\rangle$. Performing this measurement for varying spin spiral wave numbers q allows us to fit the transport power law $\gamma \propto q^z$. We can indeed reproduce the diffusive behavior observed in prior work [537] for both lattice depths of $10\, E_r$ and $8\, E_r$ (Fig. 2.30), which deviates significantly from the superdiffusive exponents extracted from the direct polarization transport measurements. This highlights that the dynamics of high-purity spin spiral states can be very distinct from the underlying (high-temperature) universal transport exhibited by the Heisenberg model. We would expect that, using this method, universal behavior can only be observed within a high-temperature background, where linear-response transport is valid.

To summarize, our results support the theoretical conjecture that spin transport in the 1D Heisenberg model belongs to the KPZ universality class, with a superdiffusive transport exponent $z = 3/2$. We have experimentally demonstrated that both integrability and a non-abelian symmetry are essential for stabilizing superdiffusive transport. Moreover, we exploit the single-spin sensitivity of our setup to extract the full distribution function of the polarization transfer. This distribution function exhibits a large skewness that does not decay in time, demonstrating that spin transport in this system belongs to a strongly coupled, non-linear dynamical universality class.

Our results open the door to a number of intriguing directions. First, the discrepancy between the relaxation of domain walls and spin spirals (away from linear response) indicates that relaxation in integrable systems is generally strongly state dependent; we lack a theory of this non-linear regime. Second, the robustness of our results along the crossover from the Heisenberg to the (non-integrable) Bose-Hubbard regime remains to be fully understood [429]. In this context, a comparison between the non-integrable Bose-Hubbard model and the integrable Fermi-Hubbard model [549] could be of

particular interest. Finally, the observable we introduced to capture fluctuation effects—namely, the statistics of single shots of the polarization transfer—promises to be a powerful diagnostic tool for new phases of interacting quantum systems. Fortuitously, a theory of this quantity already exists for the KPZ universality class; developing a more general theory of such transport fluctuations is an important task for future theoretical work.

2.6 Emergent ergodicity at the transition between many-body localized phases

2.6.1 Introduction

Traditionally, the classification of phases of matter has focused on systems at or near thermal equilibrium. Many-body localization (MBL) offers an alternative to this paradigm [95, 97, 106, 149, 553, 554]. In particular, owing to the presence of strong disorder, MBL phases are characterized by their failure to thermalize [89, 90, 140, 555]. This dynamical property imposes strong constraints on the structure of eigenstates; namely, that they exhibit area-law entanglement and can be described as the ground state of quasi-local Hamiltonians [129, 556]. Perhaps the most striking consequence is that such systems can exhibit order – previously restricted to the ground state – throughout their entire many-body spectrum. In particular, the interplay between strong disorder, symmetry, and topology has led to the characterization of a broad landscape of MBL phases ranging from spin glasses and time crystals to symmetry protected topological phases [131, 556–560]. This offers a particularly tantalizing prospect for near-term quantum simulators: The ability to observe phenomena, such as coherent topological edge modes, without the need to cool to the many-body ground state [221, 224, 238, 561, 562].

The presence of eigenstate order in the many-body localized phase also raises a more fundamental question: What is the nature of phase transitions between different types of MBL order? This question highlights a delicate balance between the properties of localization and phase transitions. On the one hand, the stability of MBL is contingent upon the existence of an extensive number of quasi-*local* conserved quantities ("ℓ-bits") [129, 130]. On the other hand, the correlation length at a second-order phase transition *diverges* [563]. Understanding and characterizing this interplay remains an outstanding challenge. Indeed, while certain studies suggest the presence of a direct transition between distinct MBL phases [131, 224, 560, 564–566], others have found signatures of delocalization at the transition [222, 567, 568].

In this section, we conjecture that any transition between distinct MBL phases is invariably forbidden and that an intervening ergodic phase always emerges (Fig. 2.31a). This conjecture is

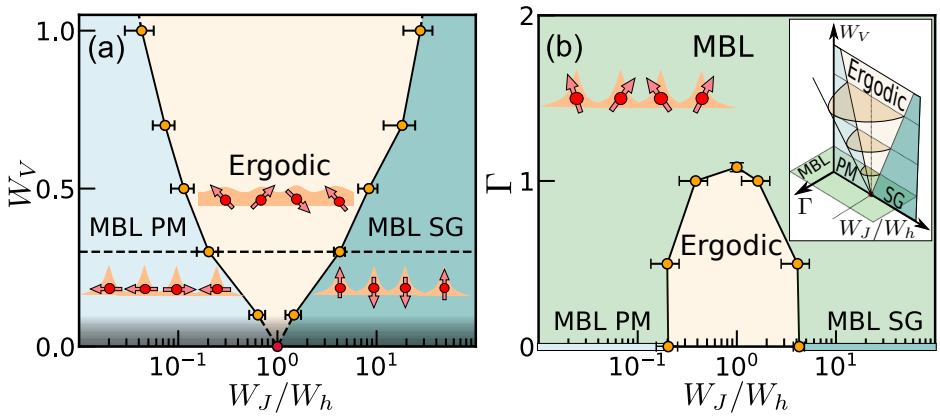

Figure 2.31: (a) Phase diagram of the symmetry breaking model, Eqn. 2.27, as a function of W_J/W_h and interaction strength W_V. For all numerically accessible W_V (outside the shaded region), we observe a finite width ergodic region between the two different MBL phases (PM and SG). At $W_V = 0$, the system is non-interacting and exhibits a critical point at $W_J/W_h = 1$ (red point). (b) Phase diagram as a function of a symmetry breaking field Γ and W_J/W_h for $W_V = 0.3$. With increasing Γ, the size of the ergodic region decreases until the system remain localized for all W_J/W_h. (inset) Schematic of the full phase diagram as a function of W_J/W_h, W_V and Γ.

motivated by an extensive numerical study of three classes of MBL transitions: (i) a symmetry-breaking transition, (ii) a symmetry-protected topological (SPT) transition, and (iii) a discrete time crystalline transition (in a Floquet system). By systematically constructing the various phase diagrams, we show that an intervening ergodic region emerges for all numerically-accessible interaction strengths. Moreover, we demonstrate that this emergent ergodicity is intimately tied to the presence of a phase transition; a *disorder-less*, symmetry-breaking field suppresses the intervening ergodic phase. In addition to numerics, we analyze two instabilities which could induce thermalization near the putative transition: (i) the proliferation of two-body resonances [553, 569, 570] and (ii) the run-away of avalanches [105, 571]. We find that the latter is marginal. Finally, we propose and analyze an experimental platform capable of directly exploring the emergence of ergodicity at the transition between MBL phases. Our proposal is motivated by recent advances in Rydberg-dressed, neutral-atom quantum simulators [572–579]; we demonstrate that the phase diagram depicted in Fig. 2.31 can be directly probed via quench dynamics of local observables within experimental decoherence time-scales.

2.6.2 Intervening ergodic phase between MBL paramagnet and MBL spin glass

Let us start by considering the paradigmatic example of a disordered one dimensional spin chain, which hosts two distinct MBL phases:

$$H = \sum_i J_i \sigma_i^z \sigma_{i+1}^z + \sum_i h_i \sigma_i^x + \sum_i V_i (\sigma_i^x \sigma_{i+1}^x + \sigma_i^z \sigma_{i+2}^z), \tag{2.27}$$

where $\vec{\sigma}$ are Pauli operators and all coupling strengths are disordered, with $J_i \in [-W_J, W_J]$, $h_i \in [-W_h, W_h]$, and $V_i \in [-W_V, W_V]$ [15]. We choose to work with the normalization $\sqrt{W_J W_h} = 1$ and perform extensive exact diagonalization studies up to system size $L = 16$. In the absence of V_i, the system reduces to the non-interacting, Anderson localized limit and for sufficiently strong disorder (in J_i and h_i), this localization persists in the presence of interactions.

The Hamiltonian (Eqn. 1) exhibits a $\mathbb{Z}_2$ symmetry corresponding to a global spin-flip, $G = \prod_i \sigma_i^x$. In the many-body localized regime, two distinct forms of eigenstate order emerge with respect to the breaking of this symmetry. For $W_h \gg W_J, W_V$, the transverse field dominates and the system is in the MBL paramagnetic (PM) phase. The conserved ℓ-bits simply correspond to dressed versions of the physical σ_i^x operators. For $W_J \gg W_h, W_V$, the Ising interaction dominates and the eigenstates correspond to "cat states" of spin configurations in the $\hat{z}$ direction. Physical states break the associated $\mathbb{Z}_2$ symmetry, the ℓ-bits are dressed versions of $\sigma_i^z \sigma_{i+1}^z$, and the system is in the so-called MBL spin-glass (SG) phase [557, 560].

These two types of eigenstate order can be distinguished via the Edwards-Anderson order parameter which probes the presence of long-range Ising correlations in eigenstates $|n\rangle$, $\chi = \left\langle\!\left\langle L^{-1} \sum_{i,j} \langle n| \sigma_i^z \sigma_j^z |n\rangle^2 \right\rangle\!\right\rangle$, where $\langle\!\langle \cdots \rangle\!\rangle$ denotes averaging over disorder realizations [560, 566]. In the SG phase, this order parameter scales extensively with system size, $\chi \propto L$, while in the PM phase, it approaches a constant $\mathcal{O}(1)$ value. Fixing $W_V = 0.7$, χ exhibits a clear transition from PM to SG as one tunes the ratio of W_J/W_h (Fig. 2a). The finite-size flow of χ is consistent with the presence of a *single* critical point at $W_J = 3.2, W_h = 0.32$ ($W_J/W_h \approx 10$).

However, thermalization diagnostics tell a different story. In particular, we compute the $\langle r \rangle$-ratio, a

[15] We remark that up to edge effects, the model is dual under the Kramers-Wannier map ensuring that any direct transition between the MBL SG and MBL PM phases must occur at $W_J/W_h = 1$.

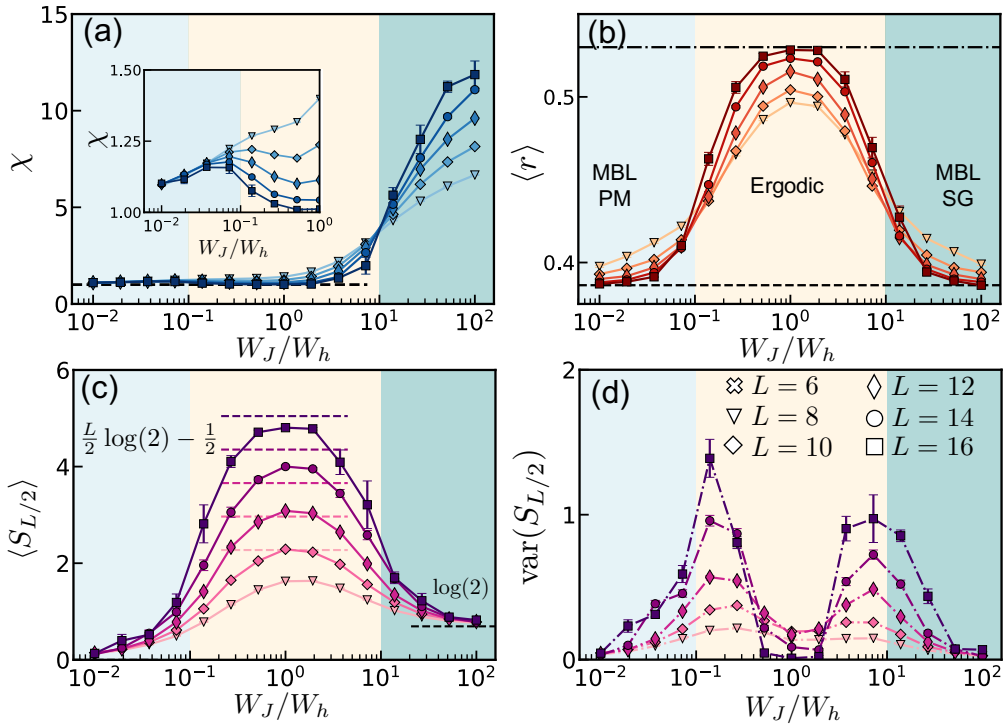

Figure 2.32: Characterization of the symmetry breaking model, Eqn. 2.27, for $W_V = 0.7$. (a) For $W_J/W_h \gtrsim 10$, χ increases with system size evincing the SG nature of the phase. In the PM phase, χ approaches a finite constant, albeit exhibiting two distinct behaviors (inset). (b) $\langle r \rangle$-ratio as a function of W_J/W_h reveals an intervening ergodic phase surrounded by two localized phases. The dash-dotted [dashed] line corresponds to the GOE [Poisson] expectation. (c) The half-chain entanglement entropy $S_{L/2}$ increases with system size for intermediate W_J/W_h, in agreement with the expected thermal volume-law. In the two localized phases, $S_{L/2}$ saturates to different values, highlighting the distinct nature of the underlying eigenstate order. (d) The variance of $S_{L/2}$ exhibits two distinct peaks in agreement with the presence of two distinct transitions. Each data point corresponds to averaging over at least 10^3 disorder realizations.

measure of the rigidity of the many-body spectrum: $\langle r \rangle = \langle\!\langle \min\{\delta_n, \delta_{n+1}\}/\max\{\delta_n, \delta_{n+1}\} \rangle\!\rangle$, where $\delta_n = E_{n+1} - E_n$, E_n is the n^{th} eigenenergy and averaging is also done across the entire many-body spectrum [99, 100]. In the MBL phase, energy levels exhibit Poisson statistics with $\langle r \rangle \approx 0.39$, while in the ergodic phase, level repulsion leads to the GOE expectation $\langle r \rangle \approx 0.53$ [90, 95, 106]. Unlike χ, which exhibits a single transition, the $\langle r \rangle$-ratio exhibits two distinct critical points, each characterized by its own finite-size flow (Fig. 2.32b). This demarcates three distinct phases: two many-body localized phases (for $W_J/W_h \lesssim 0.1$ and $W_J/W_h \gtrsim 10$) separated by an intervening ergodic phase. Interestingly, the location of the ergodic-MBL transition at $W_J/W_h \approx 10$ matches the location of the spin-glass transition observed via χ. The fact that an additional ergodic-MBL transition

is observed in the $\langle r \rangle$-ratio, but not in χ, suggests that the PM regime has slightly more structure.

In order to further probe this structure, we turn to the half-chain entanglement entropy, $S_{L/2} = -\mathrm{Tr}[\rho_\mathrm{s} \log(\rho_\mathrm{s})]$, where $\rho_\mathrm{s} = \mathrm{Tr}_{i \leq L/2}[|n\rangle \langle n|]$ [95, 129, 560, 580–587]. The behavior of $S_{L/2}$, illustrated in Fig. 2.32c, allows us to clearly distinguish three phases: the MBL paramagnet, the ergodic paramagnet, and the MBL spin-glass. For $W_J/W_h \ll 0.1$, the eigenstates are close to product states and the entanglement entropy $S_{L/2}$ is independent of L, consistent with a localized paramagnet. Near $W_J/W_h \approx 1$, $S_{L/2}$ increases with system size, approaching $(L \log 2 - 1)/2$, consistent with an ergodic paramagnet [588]. Finally, for $W_J/W_h \gg 10$, the half-chain entanglement again becomes independent of L and, for very large W_J/W_h, approaches $\log 2$, consistent with the cat-state-nature of eigenstates in the MBL SG phase.

A few remarks are in order. First, the variance of $S_{L/2}$ across the ensemble of disorder realizations provides a complementary diagnostic to confirm the presence of two distinct ergodic-MBL transitions (Fig. 2.32d) [560, 581–584, 584–587]. Indeed, one observes two well-separated peaks in $\mathrm{var}(S_{L/2})$, whose locations are consistent with the transitions found in the $\langle r \rangle$-ratio. Second, although χ only scales with system size in the SG phase, one expects its behavior to be qualitatively different in the MBL versus ergodic paramagnet. In particular, in the MBL paramagnet, the ℓ-bits have a small overlap with $\sigma_i^z \sigma_j^z$ and one expects $\chi > 1$; meanwhile, in the ergodic paramagnet, for a state chosen at the center of the many-body spectrum, one expects that $\chi \to 1$ rapidly with increasing system size (owing to the eigenstate thermalization hypothesis) [89–91, 96]. This is indeed borne out by the numerics, as shown in the inset of Fig. 2.32a.

Diagnostics in hand, we now construct the full phase diagram as a function of W_V and W_J/W_h (Fig. 2.31a). Even for the smallest interaction strengths accessible $W_V \sim 0.07$ (i.e. where the minimum interaction coupling remains larger than the mean level spacing) one observes a finite width region where the $\langle r \rangle$-ratio increases with system size [580, 589–592].

To verify that the presence of a phase transition is indeed responsible for the intervening ergodic region, one can explicitly break the $\mathbb{Z}_2$ symmetry in Eqn. 2.27. We do so by adding a *disorder-less*, on-site longitudinal field, $\Gamma \sum_i \sigma_i^z$. Despite the fact that the field is uniform, it causes the $\langle r \rangle$-ratio to systematically decrease (Figs. 2.33a,b), and for a sufficiently large symmetry breaking field, all

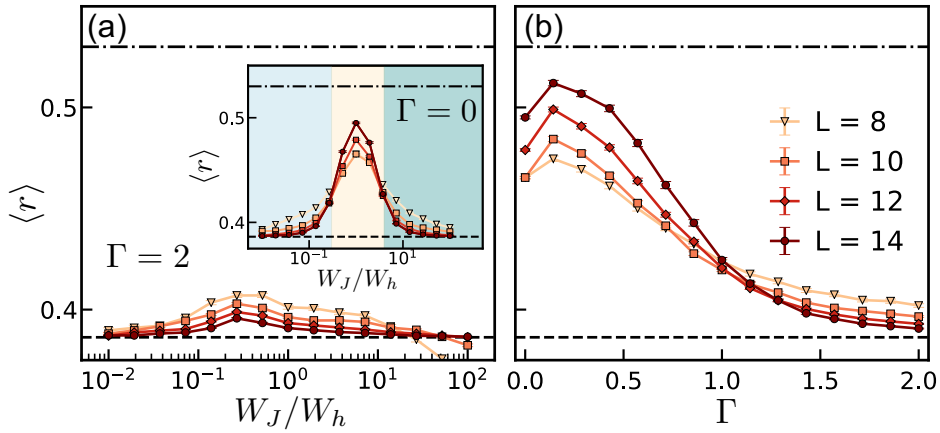

Figure 2.33: (a) $\langle r \rangle$-ratio as a function of W_J/W_h at $W_V = 0.3$ in the presence of an explicit symmetry breaking field $\Gamma = 2$. The dash-dotted [dashed] line corresponds to the GOE [Poisson] expectation. Unlike the symmetry respecting case ($\Gamma = 0$, inset), the system remains localized for all values of W_J/W_h. (b) Within the ergodic region (here with $W_J/W_h = 1$), an increasing symmetry-breaking field drives the system towards localization. Each data point corresponds to averaging over at least $3 \cdot 10^2$ disorder realizations.

finite-size flow tends toward localization. This allows us to construct the phase diagram in the presence of finite Γ, as depicted in Fig. 2.31b.

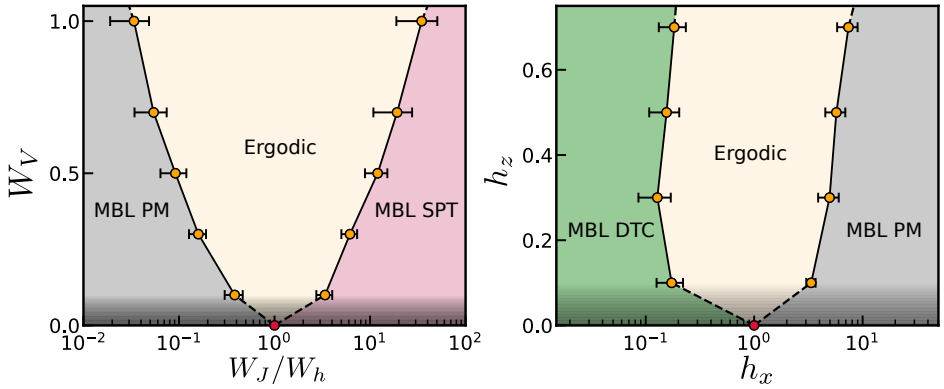

Figure 2.34: Phase diagrams of the SPT (left panel) and DTC (right panel) models. For all interaction strengths, we find an intervening ergodic phase separating the two MBL phases. The red point on the x-axis of either diagram indicates the location of the non-interacting critical point.

2.6.3 Generality of intervening ergodic phase

To understand the generality of an emergent ergodic region between many-body localized phases, we now consider two additional types of MBL transitions: a symmetry-protected topological (SPT)

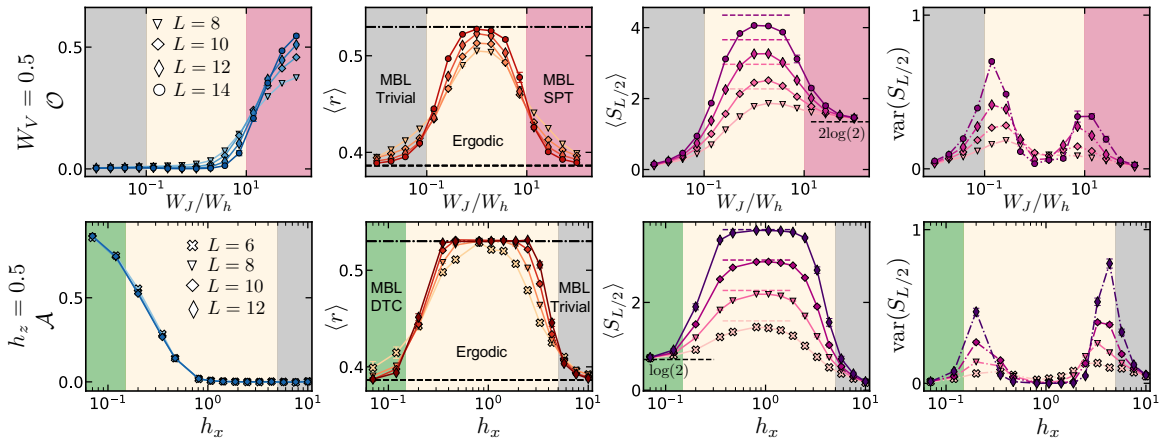

Figure 2.35: The SPT [DTC] model of Eqn. 2.28 [Eqn. 2.29] also exhibits an intervening ergodic phase. Upper row: The order parameter $\mathcal{O}$, the $\langle r \rangle$-value, the half-chain entanglement $S_{L/2}$, and the variance of the entanglement var$(S_{L/2})$ for interaction strengths $W_V = 0.5$ for the SPT model. For panels depicting the $\langle r \rangle$-value, the dash-dotted [dashed] line corresponds to the GOE [Poisson] value. At least $9 \cdot 10^2$ disorder averages were performed for each system size. Lower row: The order parameter $\mathcal{A}$, the $\langle r \rangle$-value, the half-chain entanglement $S_{L/2}$, and the variance of the entanglement var$(S_{L/2})$ for interaction strengths $h_z = 0.5$ for the DTC model. For panels depicting the $\langle r \rangle$-value, the dash-dotted [dashed] line corresponds to the GOE [Poisson] value. Each data point corresponds to averaging over at least $3 \cdot 10^2$ disorder realizations.

transition and a discrete time-crystalline (DTC) transition. The Hamiltonian of the SPT model is given by [16]:

$$\begin{aligned} H_{\text{SPT}} &= \sum_i J_i \sigma^z_{i-1} \sigma^x_i \sigma^z_{i+1} + \sum_i h_i \sigma^x_i \\ &+ \sum_i V_i (\sigma^x_i \sigma^x_{i+1} + \sigma^z_{i-1} \sigma^y_i \sigma^y_{i+1} \sigma^z_{i+2}) \,, \end{aligned} \tag{2.28}$$

with $J_i \in [-W_J, W_J]$, $h_i \in [-W_h, W_h]$, and $V_i \in [-W_V, W_V]$. H_{SPT} exhibits a $\mathbb{Z}_2 \times \mathbb{Z}_2$ symmetry, which gives rise to an MBL SPT (Haldane) phase for $W_J \gg W_h, W_V$ and a topologically-trivial MBL phase for $W_J \ll W_h, W_V$ [559, 561, 593]. For the DTC model, we consider the Floquet unitary evolution $U_F = \mathcal{T} \exp\left(-i \int_0^T H_F(t) dt\right)$ generated by the stroboscopic Hamiltonian:

$$H_F(t) = \begin{cases} \sum_i J_i \sigma^z_i \sigma^z_{i+1} + h_i \sigma^x_i + V_i \sigma^z_i & t \in [0, T/2) \\ -\frac{\pi}{T} \sum_i \sigma^x_i & t \in [T/2, T) \end{cases} \tag{2.29}$$

[16] We chose the form of our interaction such that, in the thermodynamic limit, the MBL SPT and MBL PM are dual to one another under the duality transformation $\sigma^z_i \to \sigma^z_i \sigma^x_{i+1}$ and $\sigma^x_i \to \sigma^z_{i-1} \sigma^x_i \sigma^z_{i+1}$.

where $J_i \in [0.5, 1.5]$, $T = 2$, $h_i \in [0, h]$ and $V_i \in [0, 2V]$. When $h \ll 1$, the Floquet system spontaneously breaks time-translation symmetry and is in the so-called DTC phase, while for $h \gg 1$, the system is in a Floquet paramagnetic phase [200, 221, 222, 224, 594, 595]. We analyze each of these models using the four diagnostics previously described: (i) the order parameter, (ii) the $\langle r \rangle$-ratio, (iii) the half-chain entanglement, and (iv) the variance, var$(S_{L/2})$. We observe the same qualitative behavior for both transitions across all diagnostics: An intervening ergodic phase emerges which terminates at the non-interacting critical point (Fig. 2.34). This is illustrated by the same diagnostics (the order parameter, half-system entanglement entropy $S_{L/2}$, the $\langle r \rangle$-value, and the variance of the entanglement var$(S_{L/2})$) for both the SPT model (for an eigenstate of H_{SPT} at zero energy density) and the DTC model (for an eigenstate of U_F at π quasi-energy) (Fig. 2.35). We further analyze the finite-size effects arising from small couplings, which we believe underlie previous numerical observations of apparent direct transitions [224, 564–566].

2.6.4 Experimental Realization

Motivated by recent advances in the characterization and control of Rydberg states, we propose an experimental protocol to directly explore the emergence of ergodicity between MBL phases. Our protocol is most naturally implemented in one dimensional chains of either alkali or alkaline-earth atoms [572–579]. To be specific, we consider ^{87}Rb with an effective spin-1/2 encoded in hyperfine states: $|\downarrow\rangle = |F = 1, m_F = -1\rangle$ and $|\uparrow\rangle = |F = 2, m_F = -2\rangle$. Recent experiments have demonstrated the ability to generate strong interactions via either Rydberg-dressing in an optical lattice (where atoms are typically spaced by $\sim 0.5\ \mu$m) or via Rydberg-blockade in a tweezer array (where atoms are typically spaced by $\sim 3\ \mu$m) [572–579]. Focusing on the optical lattice setup, dressing enables the generation of tunable, long-range soft-core Ising interactions, $H_{ZZ} = \sum_{i,j} J_{ij} \sigma_i^z \sigma_j^z$, with a spatial profile that interpolates between a constant at short distances (determined by the blockade radius) and a $1/r^6$ van der Waals tail.

A particularly simple implementation of a PM-SG Hamiltonian (closely related to Eqn. 2.27) is to alternate time evolution under H_{ZZ} and $H_X = \sum_i h_i \sigma_i^x$, with the latter being implemented via a two-photon Raman transition (Fig. 2.36a). In the high frequency limit, the dynamics are governed by

an effective Hamiltonian:

$$H_{\text{eff}} = \frac{\tau_1}{\tau_1+\tau_2}\sum_i h_i \sigma_i^x + \frac{\tau_2}{\tau_1+\tau_2}\sum_{ij} J_{ij}\sigma_i^z\sigma_j^z \ , \tag{2.30}$$

where H_X is applied for time τ_1, H_{ZZ} is applied for time τ_2, and the Floquet frequency $\omega = 2\pi/(\tau_1+\tau_2) \gg h_i, J_{ij}$. This latter inequality ensures that both Floquet heating and higher-order corrections to H_{eff} can be safely neglected on experimentally relevant time-scales [181, 391]. Note that unlike the DTC model (Eqn. 2.29), here Floquet engineering is being used to emulate a static MBL PM-SG Hamiltonian [210, 238].

Although our prior analysis has focused on eigenstate properties, we will now demonstrate, that the phase diagram can also be characterized via the dynamics of local observables. To investigate this behavior, we use Krylov subspace methods to numerically simulate the dynamics of H_{eff} with $\tau_1 = \tau_2 = 1$, $J_{i,i+1} \in [-1,-3]$, $J_{i,i+2} = 0.6J_{i,i+1}$ and $h_i \in [h, 3h]$. We note that the ratio of the nearest- to next-nearest-neighbor coupling strength is chosen based upon the experimentally measured Rydberg-dressing-interaction profile and a 1D zig-zag chain geometry (Fig. 2.36a) [17][41, 574].

For system sizes up to $L = 20$, we compute the dynamics of initial states $|\psi_x\rangle$ and $|\psi_{zz}\rangle$ [18]; both states are easily preparable in experiment, close to zero energy density, and chosen such that $\langle\psi_x|\,\sigma^x_{L/2}\,|\psi_x\rangle = 1$ and $\langle\psi_{zz}|\,\sigma^z_{L/2-1}\sigma^z_{L/2}\,|\psi_{zz}\rangle = 1$. Starting with $|\psi_x\rangle$ as our initial state and large h, we observe that $\langle\sigma^x_{L/2}(t)\rangle$ plateaus to a finite value at late-times, indicating the system is in the MBL PM phase (Fig. 2.36c). Analogously, for $|\psi_{zz}\rangle$ and small h, we observe that $\langle\sigma^z_{L/2-1}(t)\sigma^z_{L/2}(t)\rangle$ plateaus to a finite value at late-times, indicating the system is in the MBL SG phase (Fig. 2.36e). For $h \sim 1$, *both* observables decay to zero, indicating the system is the ergodic phase (Fig. 2.36d). The plateau value of the two observables as a function of h clearly identifies the intervening ergodic region (Fig. 2.36f).

To ensure that one can observe the intervening ergodic phase within experimental coherence times,

[17] An analogous behavior can be found in a linear geometry where the ration between nearest and next-nearest neighbor interactions is $J_{i,i+2} = 0.2J_{i,i+1}$.

[18] $|\psi_x\rangle$ is polarized along $+\hat{y}$ except at sites $L/2, L/2+1$ where it is polarized in the $+\hat{x}$ and $-\hat{x}$ direction respectively. Analogously $|\psi_{zz}\rangle$ is polarized along $+\hat{y}$ except at sites $L/2-1$ through $L/2+2$ where the spins are polarized in the $\hat{z}$ direction with the pattern $\uparrow\uparrow\downarrow\downarrow$.

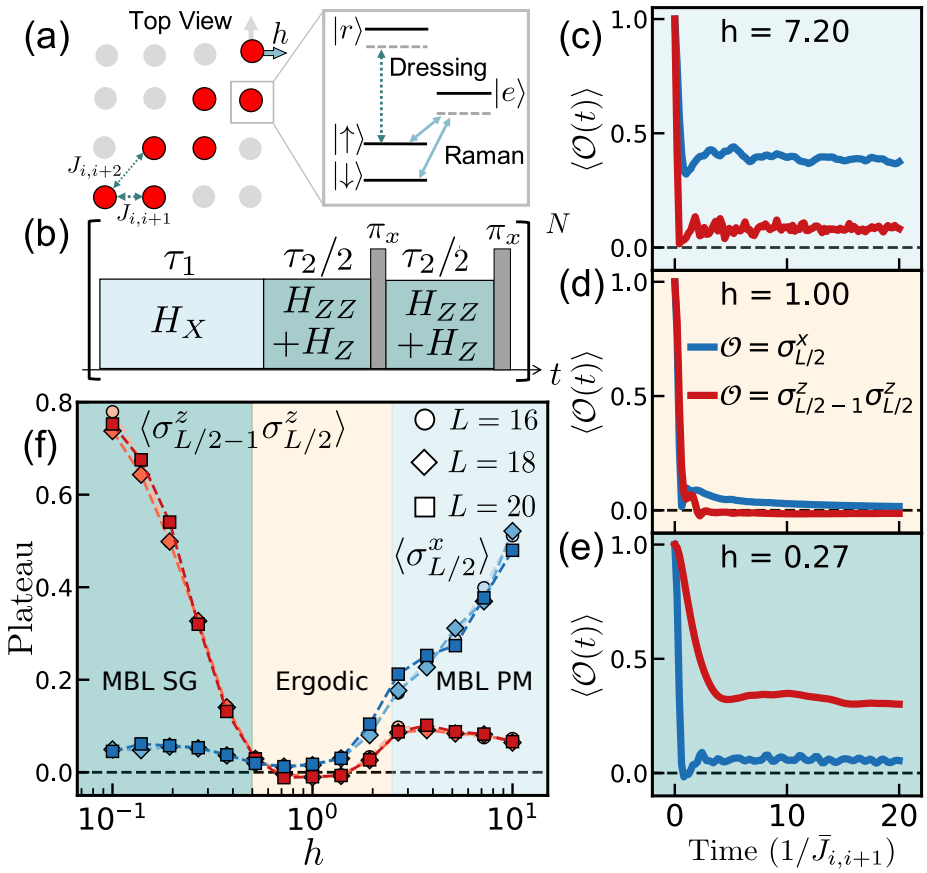

Figure 2.36: (a) Schematic of the proposed experimental protocol. Within an optical lattice, neutral atoms are prepared along two adjacent diagonals (i.e. with a gas microscope), defining a zig-zag spin chain configuration. Dressing with a Rydberg state $|r\rangle$ leads to H_{ZZ} with an additional onsite field $H_Z \propto \sum_i \sigma_i^z$, while a two-photon Raman transition mediated by an excited state $|e\rangle$ leads to H_X. (b) By combining rapid spin echo pulses with Floquet evolution under H_X and $H_{ZZ} + H_Z$, one can engineer H_{eff} (Eqn. 2.30). (c-e) Dynamics of $\sigma^x_{L/2}$ (blue) and $\sigma^z_{L/2-1}\sigma^z_{L/2}$ (red) under H_{eff} starting with initial states $|\psi_x\rangle$ and $|\psi_{zz}\rangle$, respectively. Different panels correspond to representative behaviors for the three distinct phases (tuned via h). (f) The height of the late-time plateau distinguishes between the three phases. Each data point corresponds to averaging over at least 10^2 disorder realizations.

we now estimate the time-scales necessary to carry out our protocol. Previous experiments using Rydberg dressing have demonstrated coherence times $T_2 \sim 1$ ms, with nearest neighbor couplings $J_{i,i+1} \sim (2\pi) \times 13$ kHz and a microwave-induced π-pulse duration ~ 25 μs [574]. Taken together, this leads to an estimate of ~ 55 μs for the Floquet period (Fig. 2.36). Crucially, within T_2 (i.e.~ 20 Floquet cycles), all observables approach their late-time plateaus.

2.6.5 Analytic Discussion

We conclude by discussing previous analytical results and how they may shed light on the origins of the intervening ergodic phase. In the absence of interactions, the Hamiltonian transitions we consider all fall into infinite-randomness universality classes characterized by both a divergent single-particle density of states (DOS, $D(\varepsilon) \sim |\varepsilon \log^3 \varepsilon|^{-1}$ near zero single-particle energy ε) and single-particle orbitals with diverging mean and typical localization lengths ($\xi_{\text{mean}} \sim |\log^2 \varepsilon|$ and $\xi_{\text{typ}} \sim |\log \varepsilon|$ respectively) [596–601]. These divergences suggest that two-body resonances might directly destabilize MBL upon the introduction of interactions; however, a simple counting of resonances in typical blocks does not produce such an instability: In a block of length l, there are $lN(\varepsilon)$ "active" single particle orbitals with $\xi_{\text{typ}}(\varepsilon) \geq l$, where $N(\varepsilon) = \int^{\varepsilon} d\varepsilon'\, D(\varepsilon')$ is the integrated DOS [421, 570]. These orbitals overlap in real space and are thus susceptible to participating in perturbative two-body resonances. A perturbative instability of the localized state arises if lN diverges as $\varepsilon \to 0$; even for arbitrarily small interactions, a large network of resonant pairs can be found at low enough energy. Using the DOS and localization lengths of the infinite-randomness transition, we find $lN \sim 1/|\log \varepsilon|$ which vanishes slowly as $\varepsilon \to 0$ (Appendix A.9.1).

Alternatively, one might consider the susceptibility to 'avalanches' due to rare thermal bubbles induced by the interactions [105, 602, 603]. For a system with a distribution of localization lengths, it has recently been shown that the *average* localization length controls this instability [571]: for $\overline{\xi} > 2/\log 2$, thermal bubbles avalanche. However, this is within a model where the orbitals have a single localization center. Near the infinite-randomness transition, the orbitals have two centers whose separation is controlled by ξ_{mean} but whose overlap onto a putative thermal bubble is controlled by ξ_{typ}. Thus, while $\overline{\xi_{\text{mean}}}$ diverges logarithmically, the more appropriate $\overline{\xi_{\text{typ}}}$ remains finite and this criterion does not produce an absolute instability ((Appendix A.9.2)).

Finally, let us note that the direct numerical observation of avalanche instabilities remains extremely challenging [105, 604]; the presence of a robust intervening ergodic region in our study suggests that an alternate mechanism might be at the heart of our observations.

Chapter 3

Prethermalization and prethermal phases in periodically driven systems

Floquet (periodic) driving has recently emerged as a powerful technique for manipulating quantum systems and realizing intrinsically non-equilibrium phases of matter [140, 177, 195, 196, 201, 204–206, 210, 220–222, 224–229, 233, 238, 238, 240, 242]. In particular, the interplay of symmetry, topology and the driving field has been utilized to realize discrete time crystals as well as Floquet symmetry-protected topological matters [221, 222, 224, 232, 235, 238, 605, 606]. Despite its promise, a critical challenge in harnessing Floquet driving lies in mitigating Floquet heating. In essence, when a generic isolated many-body interacting system is periodically driven, it consistently absorbs energy from the driving field and eventually approaches a featureless state [177, 387–390]. So far, various strategies have been developed to address this challenge. One approach involves introducing strong disorder and interactions, inducing a many-body localized phase that prevents Floquet heating; the system can then persist in an out-of-equilibrium state for arbitrarily extended times [95, 199, 389, 390]. Alternatively, one can leverage prethermalization, where the high frequency of the drive delays heating to exceptionally late times [178, 181–184, 191–193, 195, 227, 318, 607–609]. The underlying intuition is simple: directly absorption of energy from the drive is highly off-resonant, and heating occurs only via higher-order processes that involve multiple, correlated local rearrangements. In the prethermal regime, it is generally expected that the dynamics can be approximately generated

by an effective Hamiltonian [178, 191, 192, 391]; integrating different symmetries or non-trivial topology into such prethermal Hamiltonian enables diverse prethermal phases of Floquet systems. While such expectation has been demonstrated in systems meeting specific conditions, the universality of prethermal phenomena remains an open question, dependent on nuanced system details such as the interaction range [182, 185, 186, 195]. This chapter explores the broader landscape of Floquet dynamics, extending present some generalization to much broader classes of Floquet dynamics, along a few different directions: classical Floquet systems, systems with long-range interaction, and systems under quasi-periodic (quasi-Floquet) drive.

3.1 Floquet phases of matter via classical prethermalization

3.1.1 Introduction

The most striking examples of many-body Floquet phases are known within quantum settings; by contrast, progress has not been so swift in classical Floquet systems. To overcome the central challenge—Floquet heating—in stabilizing such phases [177, 387–390], strong disorder can be utilized to induce many-body localization (MBL) in quantum systems, which further enables the system to remain in a non-equilibrium steady state until arbitrarily late times [95, 199, 389, 390]. Since localization relies upon the discreteness of energy levels, this specific approach is intrinsically quantum mechanical and naturally begs the following question: To what extent do Floquet non-equilibrium phases require either quantum mechanics or disorder [230, 610–617]?

An elegant, but partial, answer to this question is provided within the framework of Floquet prethermalization in disorder-free systems [178, 181–184, 191–193, 195, 227, 318, 607–609]. While the simple underlying intuition—directly absorbing energy from a fast drive being highly off-resonant process—holds for both quantum and classical systems, Floquet prethermalization has an additional feature in the quantum setting: There exists an effective Hamiltonian that accurately captures the dynamics of the system in the prethermal regime. Whenever the periodic drive induces an emergent symmetry in this effective Hamiltonian, novel non-equilibrium prethermal phases of matter, such as discrete time crystals or Floquet symmetry-protected topological phases, can emerge [194, 195, 205, 221–224, 227, 232, 235–238, 241, 605, 606, 618, 619]. Whether analogous phases are also possible in classical many-body systems is significantly more subtle; in particular, although classical prethermalization features slow Floquet heating, there is no effective Hamiltonian that accurately captures the prethermal dynamics [183].

In this section, we show that the lack of an effective Hamiltonian does not preclude the existence of novel, non-equilibrium phases in classical Floquet systems; we highlight this by explicitly constructing a classical prethermal discrete time crystal (CPDTC). Our main results are three fold. First, we demonstrate that the inability of an effective Hamiltonian to generate the Floquet dynamics is a direct consequence of classical chaos—small errors at early times lead to exponentially diverging single

trajectories. This connection to chaos suggests that one should forgo the focus on individual trajectories and rather ask whether there is an effective Hamiltonian that captures the prethermal dynamics of an *ensemble* of trajectories (Fig. 3.1). We show that this is indeed the case. Second, we prove that, much like the quantum case, the effective Hamiltonian can host an emergent symmetry which is protected by the discrete time translation symmetry of the periodic drive. Finally, the spontaneous breaking of such an emergent symmetry leads to a sub-harmonic response, characteristic of time crystalline order, that survives to exponentially late times in the frequency of the drive. To this end, we propose, analyze and numerically simulate a variety of different classical prethermal time crystals with different dimensions and ranges of interaction, including higher order and fractional time crystals.

3.1.2 Prethermalization in classical dynamics

Consider a classical Floquet Hamiltonian, $H_F(t) = H_F(t+T)$, with period $T = 2\pi/\omega$. For $\omega \gg J_{\text{local}}$, one can construct a perturbative expansion of the Floquet dynamics in powers of J_{local}/ω [1]. In general, this Floquet-Magnus expansion diverges, reflecting the many-body system's late-time approach to infinite temperature (via energy absorption from the drive). However, when truncated at an appropriate order, $n^* \sim \omega/J_{\text{local}}$, the expansion defines a static Hamiltonian, D, which remains quasi-conserved for exponentially long times (under the full Floquet dynamics) [181–183]:

$$\frac{1}{N}|D(t=mT) - D(t=0)| < mJ_{\text{local}} \cdot \mathcal{O}(e^{-\omega/J_{\text{local}}}), \tag{3.1}$$

where N is the system size and $m \in \mathbb{N}$ is the number of Floquet cycles. To this end, Eqn. 3.1 precisely formalizes the existence of an intermediate, prethermal regime. In particular, for times $t < \tau_{\text{heat}} \sim \mathcal{O}(e^{\omega/J_{\text{local}}})$, the energy density of the system (measured with respect to D), remains constant up to $\sim \mathcal{O}(J_{\text{local}})$.

Nevertheless, the question remains: Is D also the effective prethermal Hamiltonian, which gener-

[1] More precisely, we note that the classical Floquet dynamics are generated by the superoperator $L(t)[\cdot] = \{\cdot, H_F(t)\}$. The time evolution operator over a single period is then given by $U_F = \mathcal{T}e^{\int_0^T L(t)dt} \equiv e^{L_F T}$, where L_F is a time-independent superoperator. The static Hamiltonian, $\mathcal{H}_F$, corresponding to L_F is then given by $L_F = \{\cdot, \mathcal{H}_F\}$. The Floquet-Magnus expansion constructs $\mathcal{H}_F$ order-by-order in $\frac{J_{\text{local}}}{\omega}$, i.e. $\mathcal{H}_F = \sum_{n=0}^{\infty} \left(\frac{J_{\text{local}}}{\omega}\right)^n D^{(n)}$, where $D^{(n)}$ is the n^{th} order term of the expansion. Note that the effective static Hamiltonian, D, is then defined as $D = \sum_{n=0}^{n^*} \left(\frac{J_{\text{local}}}{\omega}\right)^n D^{(n)}$.

ates the dynamics before τ_{heat}? In the quantum setting, the answer is yes, assuming that the system is extensive and power-law light-cones exist as defined via Lieb-Robinson bounds [191, 192, 195]. However, in classical systems, D is only proven to faithfully reproduce the Floquet evolution over a *single* driving period [183]:

$$|O(T) - O'(T)| \leq \mathcal{O}(e^{-\omega/J_{local}}). \tag{3.2}$$

Here, O is a generic local observable and $O(T)$ represents its evolution under the full Floquet Hamiltonian [i.e. $H_F(t)$], while $O'(T)$ represents its evolution under D. Note that hereon out, observables with a prime, will always correspond to evolution under D.

Naively, one might expect the single period errors in Eqn. 3.2 to accumulate additively as one evolves to later times. However, this does not account for compounding effects, where early-time errors propagate through the many-body system and induce additional deviations. In the quantum case, the existence of Lieb-Robinson bounds constrains the propagation of errors and enables one to prove that deviations grow algebraically in the number of Floquet cycles: $|O(mT) - O'(mT)| \leq m^p \mathcal{O}(e^{-\omega/J_{\text{local}}})$; this immediately indicates that D is indeed the effective prethermal Hamiltonian [178, 191–193, 195]. In contrast, classical systems exhibit no such bounds—chaos causes the exponential divergence of nearby trajectories, suggesting that errors can in principle accumulate exponentially quickly.

To sharpen this intuition, we numerically explore the Floquet dynamics of a generic classical spin model [2]:

$$H_F(t) = \begin{cases} \sum_{i,j} J_z^{i,j} S_i^z S_j^z + \sum_i h_z S_i^z & 0 \leq t < \frac{T}{3} \\ \sum_i h_y S_i^y & \frac{T}{3} \leq t < \frac{2T}{3} \\ \sum_{i,j} J_x^{i,j} S_i^x S_j^x + \sum_i h_x S_i^x & \frac{2T}{3} \leq t < T \end{cases} \tag{3.3}$$

where $\vec{S}_i$ is a three-dimensional unit vector. Spin dynamics are generated by Hamilton's equations of motion $\dot{S}_i^\mu = \{S_i^\mu, H(t)\}$, using the Poisson bracket relation $\{S_i^\mu, S_j^\nu\} = \delta_{ij}\epsilon^{\mu\nu\rho}S_i^\rho$. The classical dynamics of an observable O, are then given by $O(t) = \mathcal{T} e^{\int_0^t L(t')\, dt'}[O]$, where the superoperator

[2] We choose the following generic set of parameters $\{J_z, J_x, h_x, h_y, h_z\} = \{-1.0, 0.79, 0.17, 0.23, 0.13\}$.

$L[\cdot]$ is defined by $L[\cdot] = \{\cdot, H_F\}$ [3]. At lowest order in the Floquet-Magnus expansion, the static Hamiltonian is given by:

$$D = \frac{1}{3}\left(\sum_{i,j} J_z^{i,j} S_i^z S_j^z + J_x^{i,j} S_i^x S_j^x + \vec{h}\cdot\vec{S}_i\right) + \mathcal{O}\left(\frac{1}{\omega}\right). \tag{3.4}$$

To investigate the accumulation of errors, we compare the dynamics of local observables evolving under $H_F(t)$ and D in a one dimensional spin chain $(N = 10^4)$ with nearest neighbor interactions [4]. Deviations from the exact Floquet dynamics are measured by computing the magnetization difference between the two trajectories: $\delta M(t) = 1 - \frac{1}{N}\sum_i \vec{S}_i(t)\cdot\vec{S}_i'(t)$. As depicted in Fig. 3.1(b) [top panel], $\delta M(t)$ quickly increases to a plateau value consistent with the spins in the two trajectories being completely uncorrelated; thus, D cannot be thought of as the effective prethermal Hamiltonian for $H_F(t)$. By contrast, the energy density remains conserved throughout the time evolution [bottom panel, Fig. 3.1(b)], demonstrating slow Floquet heating.

In order to pinpoint the role of chaos in the dynamics of $\delta M(t)$, we consider a slightly modified trajectory; in particular, starting with the same initial state, we first evolve under D for a few Floquet cycles and then under $H_F(t)$ for all subsequent times. Comparing to the exact Floquet dynamics (i.e. evolution under $H_F(t)$ for all times), this protocol only differs at very early times. Indeed, beyond an initial, exponentially-small difference in the trajectories [arising from Eqn. 3.2], any additional deviation solely arises from the chaotic compounding of errors. As depicted in Fig. 3.1(b) [dashed curves], the magnetization difference between the modified trajectory and that of the exact Floquet dynamics, tracks $\delta M(t)$ for all times. Crucially, this agreement demonstrates that chaos dominates the growth of $\delta M(t)$ and prevents D from being the effective prethermal Hamiltonian.

---

[3] We note that the multiplication of the superoperators (functions of observables) should be understood as function composition. In particular, $(L_1 \circ L_2)[\cdot] = L_1[L_2[\cdot]]$. The n^{th} power of L is then defined inductively by $L^n = L \circ L^{n-1}$. Therefore, evolving under the Floquet Hamiltonian for m periods, an observable becomes $O(mT) = \left(\mathcal{T} e^{\int_0^T L(t)dt}\right)^m [O]$. In a similar fashion, let us define X^{-1} as the inverse of the map X.

[4] In general, the chaotic nature of D means that numerically integrating the equations of motion to later times requires exponentially better precision, making the numerical treatment very difficult. By contrast, each term of $H_F(t)$ corresponds to a precession of the spins along one of three axis, which can be straightforwardly analytically calculated without resorting to numerical integration methods.

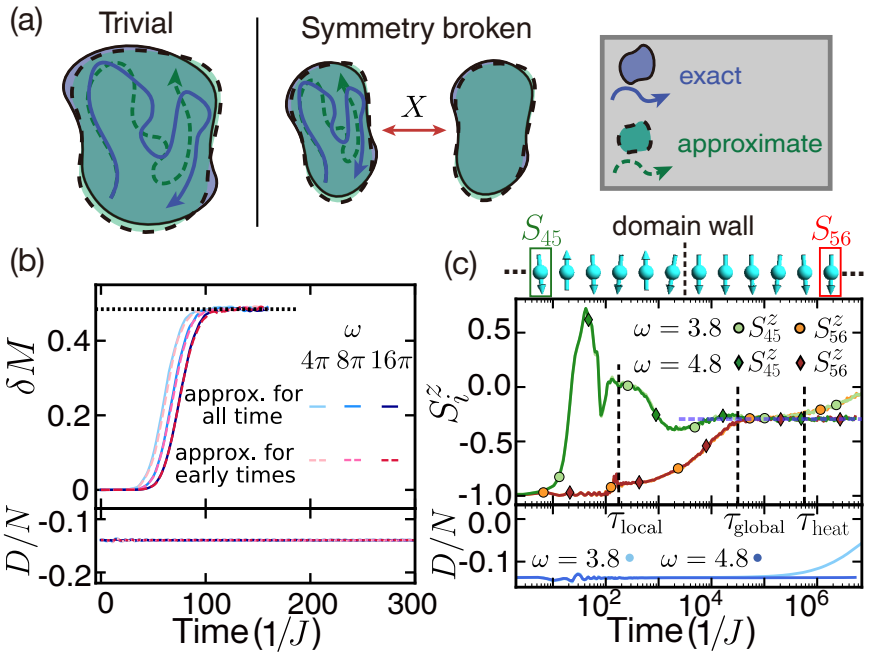

Figure 3.1: (a) Schematic depicting trajectories in a classical phase space. The exact Floquet trajectory (blue) diverges from the approximate trajectory under the effective Hamiltonian (green). However, the exact evolution of a *finite region* in phase space is well-captured by the effective Hamiltonian. (b) The dynamics of the magnetization difference, $\delta M(t)$, and the energy density, D/N, for a single initial state with $N = 10^4$. Solid lines depict approximate evolution under D for all times. Dashed lines indicate approximate evolution under D for short times ($t \leq 1/J$), followed by exact Floquet evolution. Agreement between solid and dashed curves highlights the role of classical chaos in the growth of errors. While errors in local observables [i.e. $\delta M(t)$] accumulate rapidly, the energy density remains conserved throughout the dynamics. (c) The prethermal dynamics of an ensemble of initial states quickly converge with increasing frequency. Before Floquet heating brings the system to infinite temperature, the magnetization approaches the value associated with the corresponding prethermal ensemble of D [(]blue dashed line, computed via Monte Carlo (Fig. 3.2)].

3.1.3 Prethermal dynamics of trajectory ensembles

While the evolution of a single trajectory cannot be captured by an effective Hamiltonian, we conjecture that D captures the dynamics of *ensembles* of trajectories [Fig. 3.1(a)]; by considering an initial state composed of a region of phase space (as opposed to a single point), the details of individual chaotic trajectories become "averaged out". This conjecture is made up of two separate components: (i) during the prethermal plateau, the system approaches the canonical ensemble of D, and (ii) D accurately captures the dynamics of observables as the system evolves from local to global equilibrium. This last component highlights the two stage approach to the prethermal canonical ensemble. First, observables on nearby sites approach the same value and the system *locally*

equilibrates (this occurs at time τ_{local}). Afterwards, the system becomes globally homogeneous as it approaches global equilibrium at time τ_{global}.

To investigate these components, we implement the following numerical experiment: Starting from an $N = 100$ spin chain, we construct an ensemble of initial states with a domain wall in the energy density at the center of the chain and study the Floquet dynamics of the local magnetization S_i^z and energy density D/N [Fig. 3.1(c)] [5]. The presence of a domain wall in the energy density enables us to distinguish between local and global equilibration.

Focusing on the late time regime (but before Floquet heating), we find that the magnetization on opposite sides of the domain wall approaches the *same prethermal plateau* [Fig. 3.1(c)]; this precisely corresponds to the global equilibration of our spin chain. Crucially, the value of this plateau *quantitatively* agrees with the mean magnetization of the corresponding canonical ensemble of D calculated at the same energy density via Monte Carlo [Fig. 3.1(c) and Fig. 3.2(a)]. Notably, we find agreement not only with the average value, but also with the entire distribution [Fig. 3.2(b)(c)], thus verifying the first component of the conjecture.

To compare the Floquet prethermal plateau with the thermal ensemble of D, we compute the average magnetization S^z_{avg} at a function of the energy density D/N (Fig. 3.2(a)). Crucially, we also plot the observed prethermal plateau value in Fig. 3.2(a), and observe great agreement with the thermal ensemble value.

Beyond the mean value, the complete description of an ensemble also includes its fluctuations. Therefore, to fully verify that the system approaches the thermal ensemble of D in the prethermal regime, we further study the full distribution of the local observables. In Fig. 3.2(b), for the distributions of both the single-site and the two-site observables (i.e. local magnetization and its correlation), we observe excellent agreement between the Floquet prethermal state and the thermal (canonical) ensemble of D. In Fig. 3.2(c), the local energy also exhibit the same great agreement. Such agreement highlights that the Floquet prethermal state is indeed well approximated by the thermal canonical state of D.

---

[5] We initialize each spin along either $+\hat{z}$ or $-\hat{z}$ direction. By tuning the number of domain walls, we can control the local energy density of the system. While the spins on the right half of the chain are initialized in a completely ferromagnetic state, the spins on the left half repeat the following pattern: $\downarrow\uparrow\downarrow$. Therefore, the energy density across the chain exhibits a domain wall at the center of the chain. To bring out the ensemble effect, we add small random noise to the azimuthal angle and perform an average of the subsequent dynamics over these slightly different initial states.

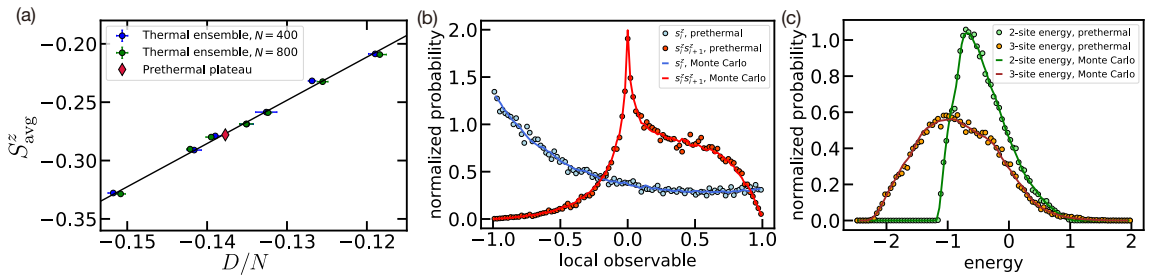

Figure 3.2: (a) The average magnetization S^z_{avg} as a function of the energy density D/N. To calculate S^z and D/N of a thermal ensemble with respect to D, we perform classical Monte Carlo simulations at different temperatures. The prethermal plateau value is obtained by directly compute the observables of the fast-driving Floquet system in the prethermal regime. Crucially, the prethermal plateau precisely agrees with the thermal ensemble of D. Probability distribution of (b) local observables and (c) energies corresponding to a Floquet prethermal state and a canonical ensemble. The 2-site and the 3-site energy refers to the energy measured on 2 and 3 consecutive sites, respectively. The canonical ensemble is obtained via Monte Carlo simulation. For both the local observables and the energy, the distributions of the Floquet prethermal state correponding to $H_F(t)$ perfectly agree with that of the true thermal state corresponding to D.

To investigate the second component, we time evolve the same ensemble of initial states for different frequencies of the drive [6]. So long as $\tau_{\text{heat}} \gg \tau_{\text{global}}$, we find that the dynamics of local observables rapidly converge as a function of increasing frequency [Fig. 3.1(c)]. Since the $\omega \to \infty$ limit of $H_F(t)$ precisely corresponds to Trotterized evolution under D, the convergence observed in Fig. 3.1(c) indicates that D is indeed the prethermal Hamiltonian for trajectory ensembles. This is in stark contrast to the dynamics of a *single* trajectory, where local observables fail to converge with increasing frequency.

Interestingly, however, even for a single trajectory, the Floquet dynamics of either *spatially* or *temporally* averaged quantities are well captured by D. The intuition is simple: by averaging over different times or different spatial regions, a single trajectory effectively samples over an ensemble of different configurations [Fig. 3.1(a)]. This insight yields a particularly useful consequence, namely, that the dynamics of a *single trajectory* already encode the prethermal properties of the many-body system.

[6] The local equilibration time τ_{local} corresponds to the time when nearby spins approach the same value. To identify τ_{local}, we measure the time when S^z_{43} and S^z_{45}, initially pointing in opposite directions, exhibit the same magnetization.

3.1.4 Prethermal dynamics with symmetry breaking

Throughout our previous discussions, energy conservation is the only constraint that restricts the many-body dynamics within phase space. However, symmetry-breaking can lead to additional constraints; for example, if D exhibits a discrete symmetry and this symmetry is broken at low energy densities, then phase space is naturally split into multiple disjoint regions corresponding to different values of the order parameter. As a result, the many-body dynamics under D are restricted to one such region.

Floquet evolution complicates this story. In particular, one might worry that the micro-motion of the Floquet dynamics could move the system between different symmetry-broken regions of phase space. If this were the case, prethermal symmetry-breaking phases would not be stable. Fortunately, the ability of D to approximate the dynamics over a single period (i.e. Eqn. 3.2), is sufficient to constrain the Floquet evolution to a specific symmetry-broken region.

To see this, consider, for example, a system where D exhibits a discrete $\mathbb{Z}_2$ symmetry and hosts a ferromagnetic phase whose order parameter is given by the average magnetization. When the energy density is below the critical value, the magnetization of the system can either be S^z_{avg} or $-S^z_{avg}$. Given energy conservation, under a single period of evolution, the magnetization must remain the same or change sign. However, Eqn. 3.2 guarantees that the time evolved magnetization density can change, at most, by an exponentially small value in frequency. This ensures that for sufficiently large driving frequencies, the magnetization cannot change sign (i.e. move to the other symmetry-broken region) and the prethermal ferromagnet remains stable.

Crucially, symmetries of D can have two different origins: they can be directly inherited from $H_F(t)$, or they can emerge as a consequence of the time translation symmetry of the drive [194, 195]. In the latter case, this can give rise to intrinsically non-equilibrium phases of matter. To date, the study of such non-equilibrium prethermal phases has been restricted to quantum systems [188, 189, 227, 240, 241, 620–623], where one can explicitly prove their stability [194, 195]. Here, we generalize and extend this analysis to classical many-body spin systems, by taking the large-S limit of the quantum dynamics (Appendix B.1) [183].

Consider a Floquet Hamiltonian which is the sum of two terms, $H_F(t) = H_X(t) + H_0(t)$. During

a single driving period, $H_X(t)$ generates a global rotation $X[\cdot] = \mathcal{T}e^{\int_0^T \{\cdot, H_X(t)\}dt}$, such that the system returns to itself after M periods (i.e. $X^M[\cdot] = \mathbb{I}[\cdot]$, where $\mathbb{I}$ is the identity map). $H_0(t)$ captures the remaining interactions in the system [7]. For sufficiently large frequencies, the single period dynamics (in a slightly rotated frame) are accurately captured by $X \circ e^{T\{\cdot, D\}}$, where D is obtained via a Magnus expansion in the toggling frame; this expansion guarantees that the dynamics generated by D commute with X and thus, X generates a discrete $\mathbb{Z}_M$ symmetry of the effective Hamiltonian [194, 195]. Indeed, at lowest order, D is simply given by the time-independent terms of $H_0(t)$ that are invariant under the global rotation.

The resulting prethermal Floquet dynamics are most transparent when analyzed at stroboscopic times $t = mT$ in the toggling frame of the X rotations, wherein an observable O becomes $\widetilde{O}(mT) = X^{-m}[O(mT)]$. In this context, the dynamics of $\widetilde{O}$ are simply generated by D, i.e. $\widetilde{O}(mT) = e^{mT\{\cdot, D\}}[\widetilde{O}(t = 0)]$. Thus, if the emergent $\mathbb{Z}_M$ symmetry of D becomes spontaneously broken, the system will equilibrate to a thermal ensemble of D with a non-zero order parameter.

In the lab frame, the dynamics of O are richer: The global rotation changes the order parameter every period, only returning to its original value after M periods. As a result, the system exhibits a sub-harmonic response at frequencies $1/(MT)$ [194, 195]. This is precisely the definition of a classical prethermal discrete time crystal.

3.1.5 Building a CPDTC

Let us now turn to a numerical investigation of the classical prethermal discrete time crystal. Consider the Floquet Hamiltonian in Eqn. 3.3 with an additional global π rotation around the $\hat{x}$-axis at the end of each driving period [8]. At leading order, X corresponds to the global π rotation, while

[7] We note that the multiplication of the superoperators (functions of observables) should be understood as function composition. In particular, $(L_1 \circ L_2)[\cdot] = L_1[L_2[\cdot]]$. The n^{th} power of L is then defined inductively by $L^n = L \circ L^{n-1}$. Therefore, evolving under the Floquet Hamiltonian for m periods, an observable becomes $O(mT) = \left(\mathcal{T}e^{\int_0^T L(t)dt}\right)^m [O]$. In a similar fashion, let us define X^{-1} as the inverse of the map X

[8] The π rotation can be generated by a magnetic field along the $\hat{x}$ direction for time τ_π with strength $\pi/2\tau_\pi$. Since the dynamics are independent of τ_π chosen, we consider it to be an instantaneous rotation, $\tau_\pi \to 0$.
In order to better highlight the role of D throughout the prethermal regime, we consider instead a symmetrized version of $H_F(t)$ such that its first-order contribution in inverse frequency is zero and thus the dynamics are better captured by the zero-th order terms. We note that this does not change the results qualitatively.

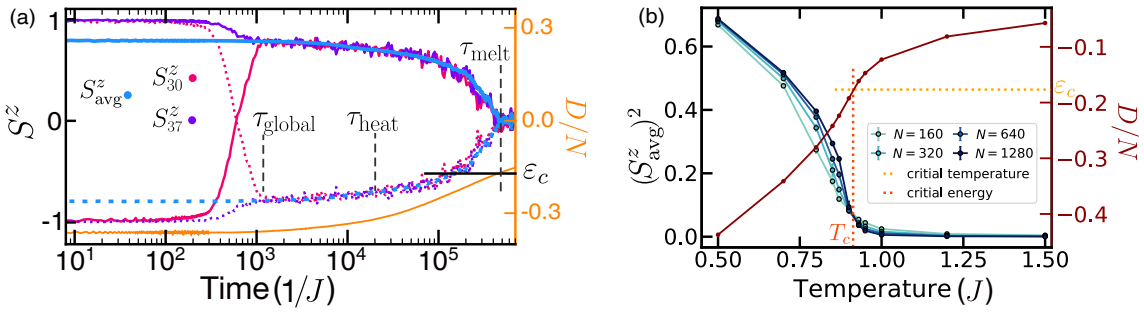

Figure 3.3: (a) Dynamics of a classical prethermal time crystal in a one-dimensional long-range interacting spin chain. At τ_{global}, different sites exhibit the same magnetization, indicating equilibration. For an exponentially long intermediate time window, $\tau_{\text{global}} < t < \tau_{\text{melt}}$, the system oscillates between positive and negative magnetization values for even (solid line) and odd periods (dotted line). This subharmonic response remains stable until the energy density crosses $\varepsilon_c \approx -0.53$ and the CPDTC melts. (b) The ferromagnetic order parameter $(S^z_{\text{avg}})^2$ and the energy density D/N as a function of the temperature, calculated by Monte Carlo simulation. As the system size N increases, the transition of the order parameter from zero to non-zero becomes sharper. We identify the critical temperature as the crossing point of the curves with different system sizes. The energy density as a function of temperature then allows us to obtain the critical energy density $\varepsilon_c \approx -0.53$, which we use to compare against the melting point of the CPDTC.

D is given by the time averaged terms of $H_F(t)$ that remain invariant under X (i.e. Eqn. 3.4 with $h_y = h_z = 0$). To this end, we will utilize the energy density, D/N, and the average magnetization, S^z_{avg}, to diagnose the prethermal dynamics and the CPDTC phase.

Let us begin by considering a one-dimensional system with long-range interactions $J_z^{i,j} = J_z|i-j|^{-\alpha}$; when $\alpha \leq 2$, D exhibits ferromagnetic order below a critical temperature (or, equivalently, a critical energy density ε_c which can be determined via Monte Carlo calculations) [624]. Taking $\alpha = 1.8$ and $N = 320$, we compute the Floquet dynamics starting from an ensemble with energy below ε_c [Fig. 3.3(a)] [9]. After the initial equilibration to the prethermal state ($t \gtrsim \tau_{\text{global}}$), the magnetization becomes homogeneous across the entire chain, signaling equilibration with respect to D [10]. Crucially, as depicted in Fig. 3.3(a), throughout this prethermal regime, the magnetization exhibits robust period doubling, taking on positive values at even periods and negative values at odd periods. This behavior remains stable until the CPDTC eventually "melts" at an exponentially late time τ_{melt} when the energy density crosses the critical value ε_c of the ferromagnetic transition of D [Fig. 3.3(a)(b)].

[9] To prepare the initial state ensemble, we first start with the fully polarized system, flip every tenth spin, and then add a small amount of noise to the azimuthal angle. The energy density of the resulting ensemble is $\varepsilon = -1.10$.

[10] We note that the fluctuations of S^z_i are local thermal fluctuations, and they decrease as we average over more realizations.

Three remarks are in order. First, because τ_{heat} is significantly longer than the interaction timescale, the system evolves between different thermal states of D as it absorbs energy from the drive. Second, the lifetime of the CPDTC is controlled by the Floquet heating rate and thus the frequency of the drive. Indeed, by increasing ω, the lifetime of the CPDTC is exponentially enhanced, while the global equilibration time remains constant [Fig. 3.4(a)]. Third, we emphasize that the observed CPDTC is fundamentally distinct from period-doubling bifurcations in classical dynamical maps (e.g. the logistic map) or the subharmonic response of a parametrically-driven non-linear oscillator [230, 625–641]. In particular, it occurs in an *isolated many-body classical system with conservative dynamics*.

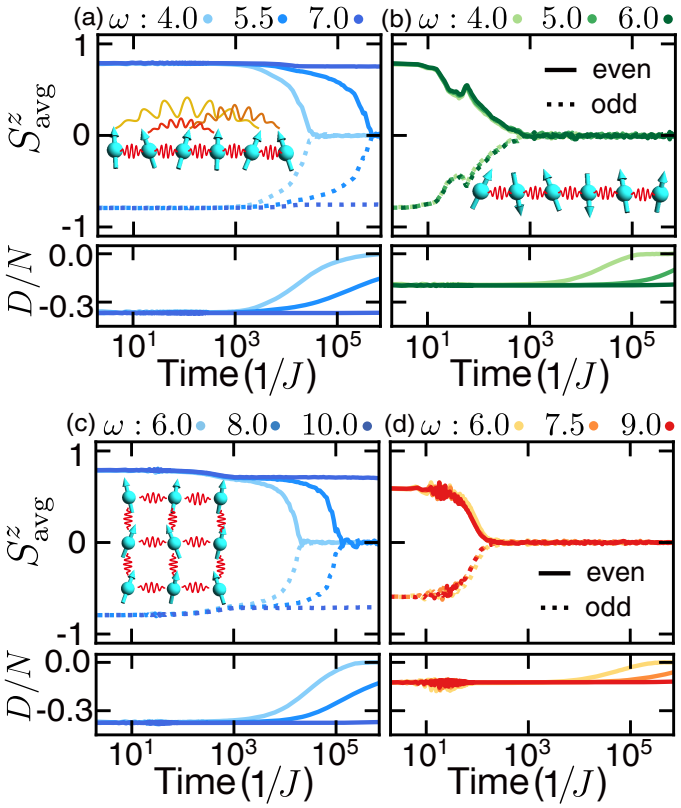

Figure 3.4: (a),(b) Prethermal dynamics of the spin chain for different frequencies ω with either long-range [a] or short-range [b] interactions. For long-range interactions, the lifetime of the CPDTC is exponentially enhanced by increasing the frequency of the drive. For short-range interactions, transient period doubling decays at a frequency independent timescale, which is significantly shorter than the Floquet heating time (bottom panel). (c),(d) Prethermal dynamics of a nearest-neighbor interacting classical spin model on the square lattice, from a low-energy-density [c] or [d] high-energy-density initial state. For a low-energy-density initial state, the system exhibits robust period doubling until exponentially late times. For a high-energy-density initial state, the magnetization decays to zero rapidly, well before the Floquet heating time. This highlights the presence of a critical energy density and the importance of symmetry-breaking for the existence of a CPDTC.

Let us conclude by highlighting the central role of spontaneous symmetry breaking in observing the CPDTC. We do so by controlling the range of interactions, the dimensionality, and the energy density of the initial ensemble. To start, we consider the short-ranged version (i.e. nearest neighbor interactions) of the 1D classical spin chain discussed above. Without long-range interactions, ferromagnetic order is unstable at any finite temperature [642], and this immediately precludes the existence of a CPDTC. This is indeed borne out by the numerics [Fig. 3.4(b)]: We observe a fast, frequency-independent decay of the magnetization to its infinite-temperature value.

While nearest-neighbor interactions cannot stabilize ferromagnetism in 1D, they do so in higher dimension. To this end, we explore the same Floquet model (i.e. Eqn. 3.3) on a two dimensional square lattice. For sufficiently low energy densities, the system equilibrates to a CPDTC phase [Fig. 3.4(c)], while above the critical temperature, the system equilibrates to a trivial phase [Fig. 3.4(d)].

3.1.6 Different Classes of Prethermal Time Crystals

Our framework is not restricted to the period-doubled ($M = 2$) CPDTC and it immediately ports over to more general notions of time crystalline order, including both higher-order ($M > 2$) and *fractional* CPDTCs [616]. By tuning the symmetry operation X, one can obtain D with different emergent symmetries, and further realize CPDTC with different periods. Here, we provide two such examples: 1) a 3-DTC with a period of $3T$ and 2) a fractional DTC with a period of $\frac{5}{2}T$.

In particular, we focus on the 1D long-range interacting spin chains, which allows a spontaneously broken symmetry phase at low temperatures. However, if the effective Hamiltonian only includes two-body interactions, then the existence of any $\mathbb{Z}_M$ symmetry with $M > 2$ will actually imply that the system has a $U(1)$ symmetry. Therefore, in order to introduce a $\mathbb{Z}_M$ symmetry while avoiding the continuous $U(1)$ symmetry, we add a nearest-neighbor three-body term ($J_{zz} S^z_{i-1} S^z_i S^z_{i+1}$) in the Hamiltonian, and keep other two-body terms the same as Eqn. 4 in the main text. Another important modification to the Floquet Hamiltonian is that instead of having a π-rotation around the $\hat{x}$-axis, we evolve the system with a $\frac{2\pi}{M}$-rotation at the end of each driving period. More specifically, the Floquet

Hamiltonian is written as:

$$H_F(t) = \begin{cases} \sum_{i,j} \frac{J_z}{|i-j|^\alpha} S_i^z S_j^z + \sum_i J_{zz} S_{i-1}^z S_i^z S_{i+1}^z + \sum_i h_z S_i^z & 0 \le t < \frac{T}{6}, \frac{5T}{6} \le t < T \\ \sum_i J_y S_i^y S_{i+1}^y + \sum_i h_y S_i^y & \frac{T}{6} \le t < \frac{T}{3}, \frac{2T}{3} \le t < \frac{5T}{6} \\ \sum_i J_x S_i^x S_{i+1}^x + \sum_i h_x S_i^x & \frac{T}{3} \le t < \frac{2T}{3} \\ g \sum_i S_i^x & T \le t < T + T' \end{cases} \tag{3.5}$$

where $gT' = \frac{2\pi}{M}$.

Following exactly the same recipe for the 2-DTC, we now choose $M = 3$ and thus the effective Hamiltonian will have an emergent $\mathbb{Z}_3$ symmetry. Initializing the system with a low-energy state (with respect to the effective Hamiltonian), we observe a local equilibration process followed by a subharmonic response with a period of $3T$, which can be diagnosed by the magnetization, Fig. 3.5(a).

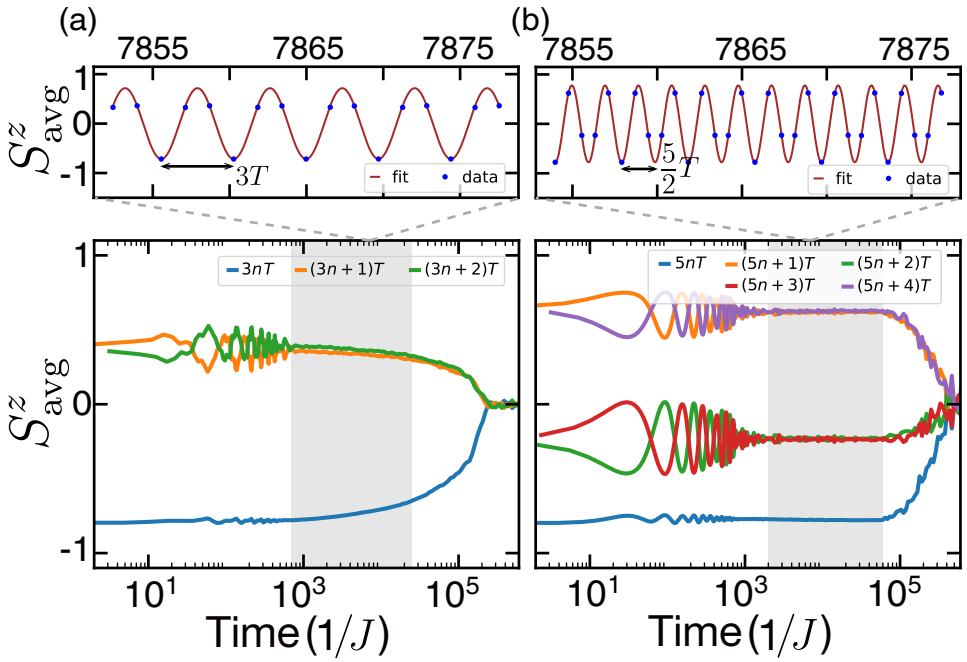

Figure 3.5: Dynamics of higher-order CPDTC in a long-range interacting spin chain. Lower panels: the magnetization exhibits an oscillation with a period of $3T$ [(a)] or $\frac{5}{2}T$ [(b)] in the prethermal regime (shaded regions) until the exponentially late the Floquet heating times. Upper panels: zoom-in of magnetization over a few driving cycles in the prethermal regime. The parameters chosen in the simulations are $\{\alpha, J_z, J_{zz}, J_x, J_y, h_x, h_y, h_z, gT, \omega\} = \{1.5, -0.383, 0.53, 0.28, 0.225, 0.13, 0.09, 0.06, 2\pi/3, 4.0\}$ and $\{\alpha, J_z, J_{zz}, J_x, J_y, h_x, h_y, h_z, gT, \omega\} = \{1.5, -0.383, 0.58, 0.13, 0.225, 0.03, 0.03, 0.06, 4\pi/5, 8.0\}$ for the 3-DTC and the $\frac{5}{2}$-DTC, respectively.

When M is chosen to be a fraction, the dynamics are slightly different from the integer case. Previous work studied a similar situation in a nearly all-to-all interacting system, and observed signatures of robust subharmonic response at fractional frequencies [616]. These results can be framed within the CPDTC construction presented: namely, by choosing $M = 5/2$, the effective Hamiltonian satisfies a $\mathbb{Z}_5$ symmetry, however, the rotation under $H_X(t)$ performs a 4π-rotation every 5 driving cycles instead of a single 2π-rotation as considered in the previous examples. Crucially, this results is a fractional time translational symmetry breaking with a new period of $5T/2$ (Fig. 3.5b). This is in stark contrast to the case when $M = 5$: while in both cases, the energy shell of the effective Hamiltonian breaks into 5 disjoint regions, the symmetry operation brings the system between these regions in different orders. As a result, the observation of a different Fourier spectrum for each of two phases relied on the fact that the magnetization is treated as a continuous variable which imbues the visited symmetry sectors with a particular order.

3.1.7 Outlook

Our work opens the door to a number of intriguing directions. First, it would be interesting to explore the generalization of classical prethermal time crystals to quasi-periodic driving [185]. Second, although we have presented extensive numerical and analytic evidence for the presence of an effective Hamiltonian (for trajectory ensembles), sharpening our analysis into a proof would provide additional insights in the nature of many-body classical Floquet systems.

3.2 Quasi-floquet prethermalization in a disordered dipolar spin ensemble in diamond

3.2.1 Introduction

Floquet theory describes the dynamics of a system whose Hamiltonian exhibits a *single* time-translation symmetry. Often used as a tool to control quantum systems, Floquet engineering has enabled the study of novel quantum dynamical phenomena [210–212, 216, 219, 643, 644]. Even richer non-equilibrium behaviors can arise in "quasi-Floquet" systems, where a *single* time-translation symmetry is replaced by *multiple* time-translation symmetries [185, 201, 645–648]. For instance, the spontaneous breaking of the latter can result in time quasi-crystalline order, which features a subharmonic response that is fundamentally distinct from conventional time crystals [185, 201].

A critical obstacle to stabilizing and observing such phenomena is to prevent the Floquet heating effect. In the fast driving regime where the driving frequency ω is much larger than the local energy scale J, to absorb a single photon from the drive requires $\sim \omega/J$ off-resonant rearrangements of local degrees of freedom, leading to the Floquet prethermalization effect with an exponentially slow heating rate $\sim \mathcal{O}(e^{-\omega/J})$. Given this underlying intuition, it is natural to notice two scenarios where prethermalization can break down: (i) systems with long-range, power-law interactions where a single local rearrangement may significantly change the energy of the system [182, 195] and (ii) quasi-Floquet systems where multi-photon processes can enable resonant energy absorption [185].

In this section, we present the experimental observation of Floquet prethermalization in a long-range interacting quantum system under quasi-periodic driving. The experimental platform consists of a dense ensemble of dipolar interacting nitrogen-vacancy (NV) centers in diamond (Fig. 3.6a) [6, 210, 211, 226, 364, 649]. Our main results are three fold. With single-frequency modulation, we observe a heating time, τ^*, that scales exponentially with the driving frequency (Fig. 3.7c). In contrast, by driving quasi-periodically with two different frequencies, we find that Floquet heating exhibits a stretched exponential profile consistent with $\tau^* \sim \mathcal{O}(e^{\omega^{\frac{1}{2}}})$ [185]. Interestingly, in the quasi-periodic case, the heating is extremely sensitive to the *smoothness* of the drive; indeed, when the system is driven via rectangular pulses (as opposed to sinusoidal pulses), we observe a significant enhancement

in the heating rate (Fig. 3.7c) [185]. Our results open the door to stabilizing and characterizing non-equilibrium phenomena in quasi-periodically driven systems.

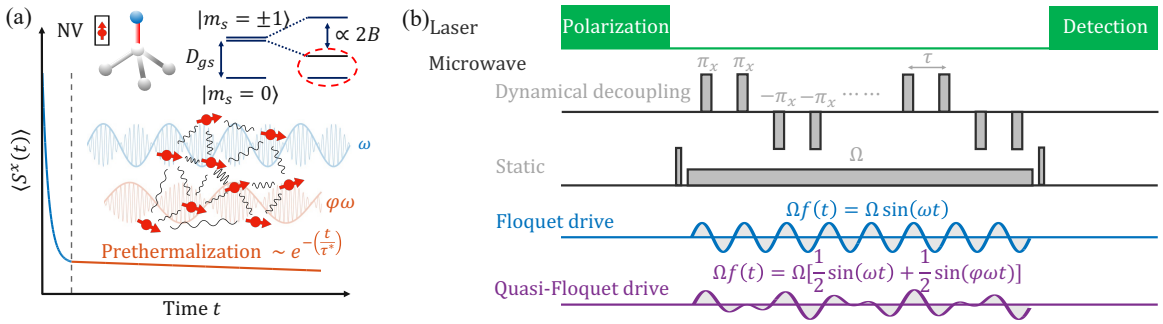

Figure 3.6: (a) Quasi-periodic driving of a strongly interacting ensemble of NV centers in diamond with two incommensurate frequencies ω and $\varphi\omega$, where φ is the golden ratio. Typical thermalization dynamics of the average spin polarization $\langle S^x(t)\rangle$ exhibit an initial fast decay followed by a late-time slow relaxation. Top: Spin level structure of NV center. In the absence of an external field, the $|m_s = \pm 1\rangle$ sublevels are degenerate and sit $D_{gs} = (2\pi) \times 2.87$ GHz above $|m_s = 0\rangle$ state. A magnetic field $B \sim 350$ G along the NV axis splits $|m_s = \pm 1\rangle$ via Zeeman effect, enabling the isolation of a two-level system $|m_s = 0, -1\rangle$ for each spin. (b) Pulse sequence for the experiment. After laser pumping, a $\frac{\pi}{2}$-pulse along $\hat{y}$ axis rotates the spin ensemble to $\hat{x}$. The dynamical decoupling sequence eliminates the on-site random fields induced by NV environmental bath spins. The sequence includes a series of fast π-pulses with alternating phases along $\hat{x}$ and $-\hat{x}$ axes to compensate the pulse errors. The inter-pulse spacing is fixed at $\tau = 0.1$ μs, much smaller than the interaction timescale between NV centers. A static microwave $\Omega \sum_i S_i^x$ together with dipolar interaction serves as the static Hamiltonian $\mathcal{H}_0$, and a time-dependent microwave $\Omega f(t) \sum_i S_i^x$ serves as the Floquet and quasi-Floquet drives. A final $\frac{\pi}{2}$-pulse along $\mp\hat{y}$ axis rotates the spin polarization back to $\hat{z}$ axis for optical detection.

3.2.2 Experimental system

We choose to work with a diamond sample containing a dense ensemble of spin-1 NV centers with concentration, $\rho \sim 4.5$ ppm [6]. The NV centers can be optically initialized (to $|m_s = 0\rangle$, where m_s is the spin quantum number) and read out using green laser excitation. In the presence of an external magnetic field ~ 350 G, the $|m_s = \pm 1\rangle$ sublevels are Zeeman split, allowing us to isolate and manipulate an effective two-level system, $\{|m_s = 0\rangle, |m_s = -1\rangle\}$ (Fig. 3.6a). By applying a resonant microwave field with Rabi frequency Ω, the effective Hamiltonian governing the NV centers (in the rotating frame) is given by [210, 226, 364]:

$$\mathcal{H}_0 = -\sum_{i<j} \frac{J_0 \mathcal{A}_{i,j}}{r_{i,j}^3} (S_i^z S_j^z - S_i^x S_j^x - S_i^y S_j^y) + \Omega \sum_i S_i^x, \tag{3.6}$$

where $J_0 = (2\pi) \times 52$ MHz·nm^3, $\mathcal{A}_{i,j}$ characterizes the angular dependence of the long-range dipolar interaction, $r_{i,j}$ is the distance between the i^{th} and j^{th} NV centers, and $\hat{S}$ is the NV spin operator.

We note that $\mathcal{H}_0$ contains only the energy-conserving terms of the dipolar interaction under the rotating-wave approximation. The approximation holds because the microwave drive is resonant with the NV transition $|m_s = 0\rangle \leftrightarrow |m_s = -1\rangle$ at $\Delta = (2\pi) \times 1.892$ GHz, which is more than three orders of magnitude larger than any other terms in the interacting Hamiltonian. The presence of other paramagnetic spin defects in the diamond lattice (e.g. ^{13}C nuclear spins and substitutional nitrogen impurities) leads to additional on-site random fields, $h_i S_i^z$, at each NV center; in our experiments, we eliminate these static fields via dynamical decoupling (Fig. 3.6b).

Let us begin by characterizing the dynamics of the NV ensemble under the static Hamiltonian $\mathcal{H}_0$. We set $\Omega = (2\pi) \times 0.05$ MHz, comparable to the average dipolar interaction strength. After optically initializing the NV spins to $|m_s = 0\rangle$, we then prepare a product state, $\otimes_i \frac{|0\rangle_i + |-1\rangle_i}{\sqrt{2}}$, by applying a global $\pi/2$-pulse around the $\hat{y}$ axis. We let the system evolve under $\mathcal{H}_0$ for a time t, before measuring the final NV polarization, $\langle S^x(t)\rangle$, along the $\hat{x}$ direction.

The polarization dynamics proceed in two steps. At early times, $t \lesssim 100$ μs, the polarization exhibits rapid decay toward a plateau value, reflecting local equilibration under $\mathcal{H}_0$ (Fig. 3.7a). Following these initial dynamics, the system exhibits a slow exponential decay $\sim A_0 e^{-\frac{t}{T_0}}$ with $A_0 = (0.43 \pm 0.01)$ and a time-scale $T_0 = (0.82 \pm 0.03)$ ms that is consistent with spin-phonon relaxation [416]. To ensure that the observed spin dynamics does not come from the incorporated dynamical decoupling pulses, we also investigate the corresponding spin dynamics at $\Omega = 0$. The measured NV polarization quickly decays to zero, in agreement with the expectation of thermalization behavior (Fig. 3.7a inset). Moreover, such behavior is independent of the inter-pulse spacing τ we choose in the experiment.

3.2.3 Floquet prethermalization

To probe the nature and existence of Floquet prethermalization in our system, we modulate the Rabi frequency as $\Omega(t) = \Omega[1 + f(t)]$, where $f(t) = \sin(\omega t)$ (Fig. 3.6b). We note that $\Omega(t)$ contains two fundamentally different components: the constant field, $\Omega \sum_i S_i^x$, is a part of the previous

undriven Hamiltonian $\mathcal{H}_0$, while the time-dependent component $\Omega f(t) \sum_i S_i^x$ acts as the Floquet drive.

Starting with a driving frequency $\omega = (2\pi) \times 0.07$ MHz, which is comparable to energy scales within $\mathcal{H}_0$, we perform the same spin polarization measurement (light blue curve in Fig. 3.7a). The measured spin dynamics at stroboscopic times, $t = 2\pi N/\omega$ (where N is an integer), exhibit an initial relaxation, which is qualitatively similar to the undriven case (red curve). However, the late-time dynamics exhibit a significantly faster polarization decay, arising from Floquet heating. To obtain the heating timescale τ^*, we fit the experimental data to $\sim Ae^{-(\frac{t}{\tau^*}+\frac{t}{T_0})}$, where T_0 is the previously extracted spin-phonon lifetime. As shown in Fig. 3.7a, by increasing the driving frequency, one can extract the frequency dependence of the amplitude, $A(\omega)$, and the heating time-scale, $\tau^*(\omega)$; both are crucial for understanding the nature of Floquet prethermalization.

Focusing first on the heating time-scale, we find that τ^* increases exponentially with ω for more than an order of magnitude, demonstrating the existence of a parametrically long-lived prethermal regime (Fig. 3.7c). In fact, at the largest frequencies, $\omega \approx (2\pi) \times 0.185$ MHz (dark blue curve in Fig. 3.7a), the polarization dynamics approach that of the undriven case. The observed exponential scaling also allows us to extract a phenomenological local energy scale of the NV many-body system, $J_{\text{exp}} = (2\pi) \times (0.032 \pm 0.006)$ MHz.

Intuitively, this J_{exp} extracted from Floquet heating process is expected to agree with the local energy scale of the system. However, for systems with power-law interaction as ours ($\sim 1/r^3$ in 3D), a naive estimation of the local energy scale $J \approx \int \frac{J_0}{r^3} \rho d^3\mathbf{r}$ is divergent, and thus, one should expect the prethermalization to not exist. Nevertheless, an important missing piece to this puzzle is the angular dependence of the dipolar interaction, $\mathcal{A}_{i,j}$ [182]. Crucially, the combination of this angular dependence and the NV's random positioning in the diamond lattice ensures that the average, $\overline{\mathcal{A}}_{i,j} = 0$, which helps to mitigate the divergence of the above integral [11].

A more careful analysis reveals that the relevant local energy scale is the variance of the interaction, $\widetilde{J} \approx [\int (\frac{J_0 \mathcal{A}_{i,j}}{r^3})^2 \rho d^3\mathbf{r}]^{\frac{1}{2}} = \sqrt{\frac{16\pi}{15}} J_0 \rho$, which is convergent (Appendix B.2). As long as the driving frequency $\omega > \widetilde{J}$, one should expect the presence of prethermalization in our long-range interacting

[11] Even if the NV centers are located on a three-dimensional regular lattice, we expect the angular dependence should also average to zero over a large lenthscale, so the positional disorder is not necessary here.

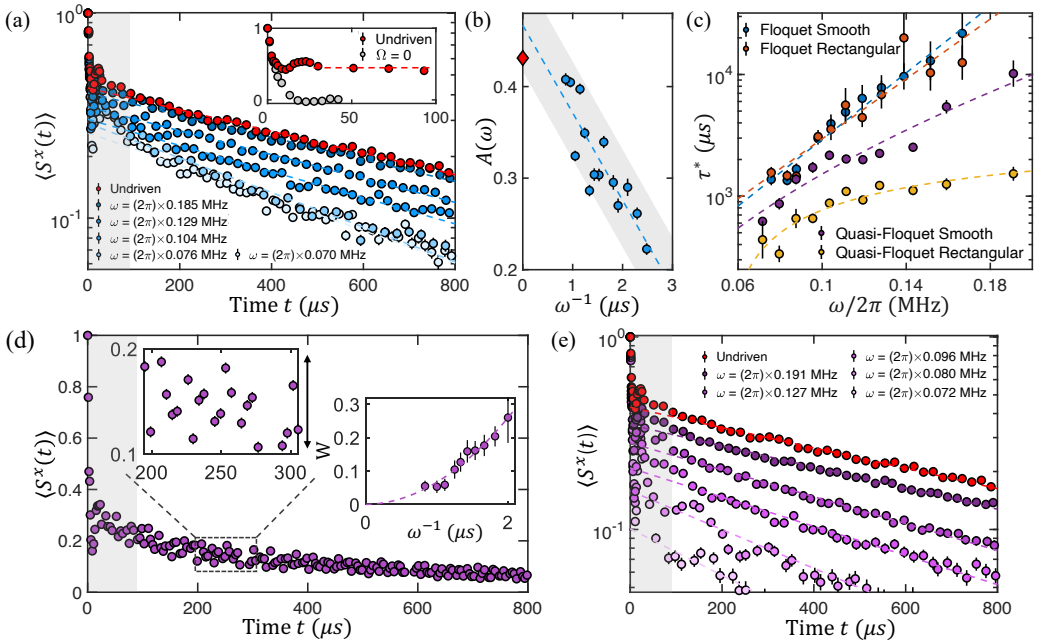

Figure 3.7: (a) The measured spin polarization dynamics $\langle S^x(t)\rangle$ under Floquet drive. After an initial fast decay (gray shaded area), a long-lived prethermal regime persists for a timescale τ^* depending on the driving frequency ω. Dashed lines are fits of the late-time dynamics using single exponential decay. Inset: A zoom-in of the measured initial spin polarization dynamics for the undriven case (red) and $\Omega = 0$ (gray). After the initial fast relaxation, the undriven polarization decays to an equilibration plateau, due to the finite static field, $\Omega \sum_i S_i^x$; while the measured polarization with only the dynamical decoupling pulses ($\Omega = 0$) quickly decays to zero, in agreement with the expectation of thermalization behavior. The dash line indicates the equilibrium plateau value. (b) Measured prethermal equilibrium value, $A(\omega)$, as a function of ω^{-1}. Dashed line is a linear fit with the gray shaded area representing the 95% confidence interval. The red diamond marks the measured amplitude, A_0, for the undriven case. (c) Heating timescale τ^* as a function of the driving frequency ω. For both smooth and rectangular single-frequency drives (blue and red), $\tau^* \sim \mathcal{O}(e^{\omega/J})$. For smooth quasi-periodic drive (purple), $\tau^* \sim \mathcal{O}(e^{\omega^{\frac{1}{2}}})$; while for rectangular quasi-periodic drive (yellow), $\tau^* \sim \mathcal{O}(\omega^{\frac{1}{2}})$, indicating the breakdown of prethermalization. Error bars represent 1 s.d. from the fitting. (d) Measured spin dynamics with two incommensurate driving frequencies [$\omega = (2\pi) \times 0.103$ MHz]. After the initial fast decay, we observe that on top of a slow spin relaxation, there exists an additional small time-quasiperiodic micromotion. Left inset: a zoom-in of the micromotion. Right inset: relative amplitude of the micromotion, W, scales quadratically with the inverse of driving frequency, ω^{-2}. (e) Using rolling-average to remove the micromotion, we observe a quasi-Floquet prethermal regime, whose lifetime τ^* increases with ω. Dashed lines are fits of the late-time dynamics using single exponential decay. Error bars represent 1 s.d. accounting statistical uncertainties.

spin ensemble, in agreement with previous theoretical studies [182]. Using the independently calibrated NV density, ρ, in the sample, we estimate the local energy scale $\widetilde{J} \approx (2\pi) \times 0.02$ MHz, which is indeed comparable with J_{exp} extracted from Floquet heating.

Next, let us turn to analyzing the frequency dependence of the amplitude, $A(\omega)$. Having established a long-lived prethermal regime, one can think of $A(\omega)$ as the value of the prethermal plateau.

condition		exponentially slow heating	effective prethermal Hamiltonian
$\alpha \leq D/2$		✗	✗
$D/2 < \alpha \leq D$	$\bar{J}(r) \neq 0$	✗	✗
	$\bar{J}(r) = 0$	analytical proof [182] experimental evidence [*this work*]	lack analytical proof experimental evidence [*this work*]
$D < \alpha \leq 2D$		analytical proof [178, 191, 192] lack experimental evidence	lack of analytical proof numerical evidence [391] lack of experimental evidence
$\alpha > 2D$ short-range		analytical proof [178, 191, 192] experimental evidence [188, 189]	analytical proof [178, 191, 192] experimental evidence [188, 189]

Table 3.1: Summary of the results on prethermalization in the literature.

In general, for short-range interactions, it is expected that $A(\omega)$ is determined by a time-independent effective Hamiltonian, $\mathcal{H}_{\text{eff}}(\omega) = \mathcal{H}_0 + \mathcal{O}(\frac{\tilde{J}}{\omega})$, which can be calculated order-by-order via a Magnus expansion [178]. In this case, $A(\omega) = \text{Tr}[\sum_i S_i^x e^{-\beta H_{\text{eff}}(\omega)}] = A_0 + \mathcal{O}(\frac{\tilde{J}}{\omega})$, where the inverse temperature β, is set by the energy density of the initial state.

For sufficiently long-range interactions (such as dipolar interactions in 3D), the existence of $\mathcal{H}_{\text{eff}}$ is unproven [178, 191, 192, 194, 195]. However, by probing the functional form of $A(\omega)$ and its extrapolated value as $\omega \to \infty$, one can provide experimental evidence for the existence of an effective Hamiltonian. As depicted in Fig. 3.7b, we find that the frequency dependence of $A(\omega)$ is linear in ω^{-1}, allowing us to extrapolate $A(\omega \to \infty) = (0.47 \pm 0.06)$. This is consistent with the measured value in the undriven case, $A_0 = (0.43 \pm 0.01)$, suggesting that despite the presence of strong long-range interactions, the effective Hamiltonian exists and can be well-approximated by $\mathcal{H}_0$ at leading order.

3.2.4 Quasi-Floquet prethermalization

Having established the existence of Floquet prethermalization in three-dimensional dipolar spin ensembles for single-frequency driving, we now turn to the quasi-Floquet setting. Specifically, we choose $f(t) = \frac{1}{2}[\sin(\omega t) + \sin(\varphi\omega t)]$, where $\varphi = (\sqrt{5}-1)/2 \approx 0.618$ is the golden ratio, so that the system is driven by two incommensurate frequencies (Fig. 3.6a). From the perspective of Floquet heating, the situation is significantly more complex. In particular, recall that within

Fermi's golden rule, the heating rate can be estimated from the overlap between the Fourier spectrum of the drive, $F(\nu) = \int f(t)e^{i\nu t}dt$, and the local spectral function of the spin ensemble, $S(\nu) = \sum_{i,j}\delta(E_i - E_j - \nu)|\langle i|S^x|j\rangle|^2$ [12].

This picture immediately provides a more formal intuition for the exponentially slow heating observed in the context of single-frequency driving (Fig. 3.8c). In particular, for $f(t) = \sin(\omega t)$, $F(\nu)$ exhibits a cut-off at frequency ω. Meanwhile, as aforementioned, $S(\nu)$ exhibits an exponentially small tail for frequencies $\nu > \widetilde{J}$ [13]. In combination, this implies that for a single driving frequency, $\omega > \widetilde{J}$, energy absorption is strongly suppressed leading to $\tau^* \sim e^{\omega/\widetilde{J}}$.

For driving with two incommensurate frequencies, even when $\omega > \widetilde{J}$, there are multi-photon processes that are effectively resonant within the local energy scale; these processes correspond, for example, to the absorption of n_1 photons of energy ω and the emission of n_2 photons of energy $\varphi\omega$. This intuition is better illustrated in the two-dimensional Fourier spectrum of the quasi-periodic drive: we can express $f(t)$ using a two-dimensional Fourier space,

$$f(t) = \sum_{n_1,n_2=0,\pm1,\ldots} F_{n_1,n_2}e^{i(n_1\omega+n_2\varphi\omega)t}, \tag{3.7}$$

where F_{n_1,n_2} characterizes the Fourier component of the driving field at frequency $\nu = (n_1\omega + n_2\varphi\omega)$; projecting the two-dimensional F_{n_1,n_2} onto a one-dimensional line with slope φ leads to the Fourier spectrum $F(\nu)$ of the quasi-periodic drive (Fig. 3.8c). Clearly, there is no strict cut-off for $F(\nu)$, and the drive spectrum exhibits a non-zero amplitude for all frequencies $\nu = |n_1\omega - n_2\varphi\omega| < \widetilde{J}$. Interestingly, despite this, for sufficiently large driving frequencies, seminal results have proven that the quasi-Floquet heating timescale remains extremely slow, exhibiting a stretched exponential lower-bound, $\mathcal{O}(e^{C(\omega/\widetilde{J})^{\frac{1}{m}}})$; here, m is the number of incommensurate driving frequencies and C is a dimensionless factor [185].

In our experiments, in contrast to the Floquet case, we measure the dynamics at evenly spaced time points, since there does not exist a stroboscopic time which is an integer multiple of *both* drives.

---

[12] where E_i and $|i\rangle$ are the eigenenergy and eigenstate of the spin system.

[13] this is specifically for our case where we need the dipolar interaction to average to zero, in general this is true for the local energy scale J.

Much like the single-frequency drive, after an early-time transient, the spin polarization exhibits a slow decay. However, we observe small oscillations scaling as $\sim \omega^{-2}$ on top of the decay (Fig. 3.7d), corresponding to the micromotion of the quasi-Floquet system [176, 650, 651]). We note that for a single-frequency drive, similar micromotion will also emerge if one does not measure the spin dynamics at stroboscopic times. Intuitively, such micromotion arises from the time-dependent portion of the Hamiltonian which only averages to zero for each complete Floquet cycle. To reliably extract a heating timescale τ^* from our quasi-Floquet measurements, we perform a rolling average to obtain the overall decay profile (Fig. 3.7e). By varying the driving frequency, we extract a heating time-scale, $\tau^* \sim e^{\omega^{\frac{1}{2}}}$ (Fig. 3.7c), which is consistent with the theoretically predicted stretched exponential form.

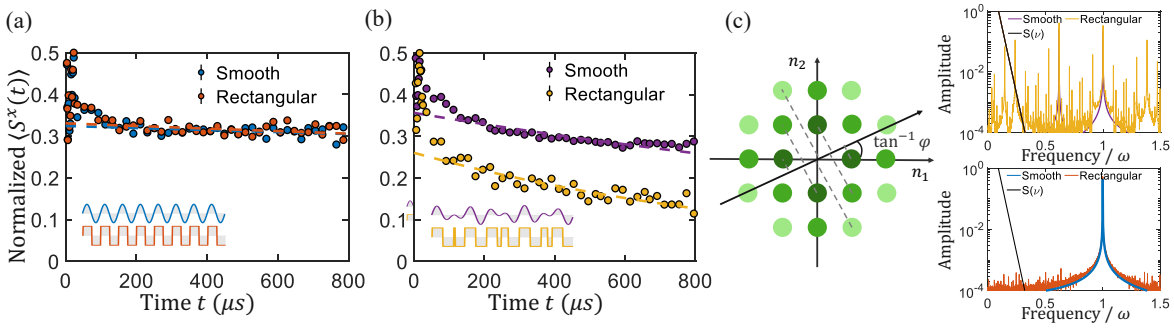

Figure 3.8: (a) A representative late-time dynamics of the spin ensemble under single-frequency (Floquet) drive with $\omega = (2\pi) \times 0.151$ MHz. Here the plotted spin dynamics is normalized by the intrinsic decay timescale, T_0, measured without the driving field, i.e. normalized $\langle S^x(t)\rangle \sim e^{-t/\tau^*}$. We observe that the relaxation profile does not depend on the smoothness of the driving field. (b) Under quasi-periodic drive [$\omega = (2\pi) \times 0.143$ MHz], the corresponding spin dynamics is extremely sensitive to the smoothness of the drive. The spin polarization displays a significantly faster decay under a rectangular drive. Error bars represent 1 s.d. accounting statistical uncertainties. (c) Two-dimensional Fourier spectrum F_{n_1,n_2} of the quasi-periodic driving field $f(t)$ [14]. In particular, the horizontal (vertical) axis corresponds to the absorption of n_1 (n_2) photons with energy ω ($\varphi\omega$) from the drive, where $n_1, n_2 = 0, \pm 1, \pm 2, ...$ The color of each green dot characterizes the amplitude of F_{n_1,n_2} at frequency $\nu = n_1\omega + n_2\varphi\omega$ (darker color represents larger amplitude). The Fourier spectrum $F(\nu)$ can be thought of as a projection of green dots onto a one-dimensional line with slope φ, the ratio between the two driving frequencies. Top inset: Fourier spectrum $F(\nu)$ of quasi-periodic drive $f(t)$ with smooth sinusoidal (purple) and non-smooth rectangular (yellow) amplitude in time. Crucially, the spectrum with rectangular drive exhibits many resonances at the small frequency range, which overlaps with the system's local spectral function $S(\nu)$ (black) and leads to energy absorption from the drive. Bottom inset: Fourier spectrum of a single-frequency drive (effectively project the green dots onto n_1 axis). A rectangular drive does not lead to resonances at the low frequency range.

[14] The quasi-Floquet drive $f(t)$ can be decomposed in a two-dimensional Fourier space,

$$f(t) = \sum_{n_1,n_2=0,\pm1,...} F_{n_1,n_2} e^{i(n_1\omega + n_2\varphi\omega)t}, \tag{3.8}$$

3.2.5 Robustness of quasi-Floquet prethermalization

Interestingly, the stability of slow prethermal heating is quite different depending on whether one considers the Floquet or quasi-Floquet setting. For the Floquet setting, the exponential behavior of τ^* is robust to the functional form of the drive amplitude $f(t)$. However, in the quasi-Floquet setting, the stretched exponential behavior of τ^* is *only* predicted to hold when $f(t)$ is smooth. In particular, when $f(t)$ is smooth, even though $F(\nu)$ does not exhibit a cut-off for small ν, its amplitude is exponentially small in this regime (Fig. 3.6c) [185, 186]. This behavior can be understood within the picture of the two-dimensional Frourier spectrum: for any given driving frequency ω, only when $n_1, n_2 \gtrsim \omega/\widetilde{J}$, one can find $\nu = n_1\omega + n_2\varphi\omega < \widetilde{J}$. Therefore, as long as F_{n_1,n_2} is sufficiently small with increasing n_1 and n_2 [equivalently, $f(t)$ is sufficiently smooth in time], the energy absorption from the multi-photon processes is suppressed.

These expectations are indeed borne out by the data (Fig. 3.7c, Fig. 3.8). Using a rectangular wave $f(t) = \mathrm{Sgn}[\frac{1}{2}\sin(\omega t) + \frac{1}{2}\sin(\varphi\omega t)]$, we observe (in the quasi-Floquet case) that the heating timescale is significantly shortened and scales as a power-law with increasing driving frequency $\sim \omega^{\frac{1}{2}}$, as opposed to a stretched exponential. In contrast, for a single-frequency drive, the smoothness of the driving field is not critical: the Floquet heating time-scale exhibits an exponential scaling for both sinusoidal and rectangular forms of $f(t)$. The above distinction highlights that realizing long-lived prethermal dynamics under a quasi-periodic drive requires more stringent conditions than in conventional Floquet systems.

3.2.6 Outlook

Looking forward, our work opens the door to a number of intriguing future directions. First, it is interesting to ask whether the restriction on $\overline{\mathcal{A}}_{i,j} = 0$ (which arises from averaging the angular dependence of the dipolar interaction) is essential for realizing prethermalization in long-range interacting systems [182, 195, 391]. As an example, for high temperature systems, the local interactions can still average to almost zero owing to randomness of the spin configurations; this could be explored

where F_{n_1,n_2} characterizes the Fourier component of the driving field at frequency $\nu = (n_1\omega + n_2\varphi\omega)$. By projecting the two-dimensional F_{n_1,n_2} onto a one-dimensional line with slope φ, we obtain the Fourier spectrum $F(\nu)$ of the quasi-periodic drive.

in systems exhibiting tunable long-range interactions such as trapped ions [16, 227]. Second, the observed long-lived quasi-Floquet prethermal regime can enable the experimental realization of novel non-equilibrium phases of matter, including discrete time quasicrystals and quasi-Floquet topological states [232, 233, 238, 242, 243, 652–656]. Finally, our experiments suggest the presence of power-law-slow-heating in the case of a quasi-Floquet, rectangular-wave drive; however, the precise frequency dependence of the heating rate remains unknown and a more systematic investigation of the relationship between the functional form of the driving and the scaling of τ^* would be extremely valuable.

Chapter 4

Generating metrologically useful states via quench dynamics

The standard quantum limit bounds the precision of measurements that can be achieved by ensembles of uncorrelated or only classically correlated particles. Fundamentally, this limit arises from the non-commuting nature of quantum mechanics, leading to the presence of fluctuations often referred to as quantum projection noise. Quantum metrology relies on the use of non-classical (entangled) states of quantum many-body systems in order to enhance the precision of measurements beyond the standard quantum limit [84–86, 657–659]. Identifying states suitable for quantum metrology is a delicate challenge: nearly all states in Hilbert space are highly entangled, but only a few of them exhibit the structured entanglement required for enhanced sensing, e.g., GHZ states and Dicke states [86, 660–668]. An even more relevant and demanding task is to design implementable protocols to prepare such states. One natural and prominent idea is to reshape the quantum projection noise (usually via quench dynamics)—a strategy known as *squeezing* [262, 264, 297, 669–672]. Compared to other metrological protocols, squeezing has a few unique advantages: It only requires measurement of global quantities and does not consist of any backward evolution.

In the context of many-body spin systems, recent studies have shifted interest from the very originally proposed one-axis twisting (all-to-all interacting) spin model [264], to more generic systems with local interactions. On the experimental front, squeezing within locally interacting systems are

more relevant since it can be directly implemented in a number of AMO platforms for quantum simulation and quantum sensing, including for example atom tweezer arrays, solid-state spin defects, and ultra-cold polar molecules. From theoretical perspective, it is intriguing to identify the minimum requirements for a system to develop squeezing. Specifically, one may wonder whether squeezing is intrinsically related to other more fundamental dynamical or equilibrium properties of a many-body quantum system. This chapter will present theoretical results answering the above question, as well as experimental results demonstrating spin squeezing in locally interacting systems.

4.1 Scalable spin squeezing as finite temperature easy-plane magnetism

4.1.1 Introduction

At the core of quantum enhanced metrology, identifying universal principles for finding and preparing metrologically useful states, especially from un-entangled product states, has long been an important challenge. One such principle, which is particularly powerful, stems from the observation that the quantum Fisher information (QFI) for pure states is fundamentally connected to spontaneous symmetry breaking [Fig. 4.1]. On the one hand, the QFI characterizes the maximum sensitivity of a given quantum state, $|\psi\rangle$, to a specific perturbation, $\hat{\mathcal{O}} = \sum_i \hat{\mathcal{O}}_i$ and simply reduces to the variance of $\hat{\mathcal{O}}$ [251]. On the other hand, spontaneous symmetry breaking (SSB) leads to the existence of long-range connected correlations of the order parameter $\mathcal{O}$ (provided that $\mathcal{O}$ does not commute with the Hamiltonian) and thus a variance which scales quadratically in system size (Appendix C.1). Thus, any pure quantum state exhibiting long-range connected correlations can be utilized to perform Heisenberg-limited sensing. Combining these considerations with the eigenstate thermalization hypothesis—which asserts that generic quantum dynamics cause few-body observables to reach thermal equilibrium [89, 90, 96]—suggests a broad and simple guiding principle for preparing metrologically useful states from product states: Identify a Hamiltonian, H, exhibiting finite temperature order. Then, find an unentangled state $|\psi_0\rangle$ whose effective temperature is below T_c and time evolve. The effective temperature, T, of the initial state $|\psi_0\rangle$ is defined by its energy density, such that $\mathrm{Tr}[\rho\ H] = \langle\psi_0|\, H\, |\psi_0\rangle$, where $\rho = \frac{e^{-H/T}}{\mathcal{Z}}$ is a thermal density matrix.

Asymptotic Correlation Function		QFI Scaling	Sensitivity Scaling
$\sim e^{-\lvert x-y\rvert/\xi}$		N	$\frac{1}{\sqrt{N}}$
$\sim \frac{1}{\lvert x-y\rvert^p}$	$p \geq d$	N	$\frac{1}{\sqrt{N}}$
	$0 < p < d$	$N^{2-p/d}$	$\frac{1}{N^{1-p/2d}}$
$\sim$ const.		N^2	$\frac{1}{N}$

Table 4.1: Relation between order, QFI and sensitivity in the case of short range, quasi long-range order, and true long-range order. See also [673].

The above strategy for generating metrologically useful states may seem surprising. Indeed, seminal work exploring the relationship between the QFI and equilibrium phases of matter has come

to the opposite conclusion: Thermal density matrices cannot be used to perform metrology beyond the standard quantum limit [674, 675]. This limitation applies even for thermal states below the critical temperature, T_c, for spontaneous symmetry breaking. The key ingredient which allows one to escape this thermal bind is that the non-equilibrium quench can generate coherences which are not present in the thermal state. Thus, despite having the same energy density, the quenched state and the thermal density matrix can exhibit extremely different metrological properties.

The efficiency of our proposed strategy depends crucially on the nature of the symmetry being broken. For discrete symmetries, it takes an exponentially long time (in system size) to develop a large QFI. For continuous symmetries however, a large QFI can develop significantly faster (i.e. in polynomial time) [676, 677]. To this end, we apply the above principle to the case of $U(1)$ symmetry breaking and provide extensive numerical and analytic evidence for the following remarkable conjecture: Finite-temperature easy-plane ferromagnetism (i.e. XY magnets) enables the preparation of states with large QFI, specifically in the form of scalable spin squeezing.

The main results presented in this section are three fold. First, we establish a phase diagram for spin squeezing (Fig. 4.1), with a sharp transition distinguishing scalable squeezing from non-squeezing. Second, we argue that this transition occurs precisely when the effective temperature of the initial state $|\psi_0\rangle$ equals the critical temperature for continuous symmetry breaking (CSB). Finally, we show that the squeezing manifests a novel scaling with system size—whose origin is extremely subtle—that leads to a phase sensitivity $\sim N^{-\frac{7}{10}}$, between the standard quantum limit ($\sim N^{-\frac{1}{2}}$) and the Heisenberg limit ($\sim N^{-1}$). Intriguingly, for parametrically long time-scales in the inverse temperature of the initial state, we observe a sensitivity scaling as $\sim N^{-\frac{5}{6}}$, matching that achieved in all-to-all coupled easy-plane spin models, i.e., so-called one-axis twisting (OAT) models [264]. A corollary of our conjecture is that short-ranged (i.e. not all-to-all connected) generalizations of the two-axis twisting model cannot yield scalable metrological gain, a fact which we numerically verify.

Our results are based on the principle that after a short initial period of time, the long-wavelength, low-frequency properties of the system can be described by hydrodynamic equations involving the conserved z-component of the spin-density and the orientation of the magnetization in the x-y plane [678]. While the form of these hydrodynamical equations is fixed, their parameters depend on the

microscopic Hamiltonian; to this end, we utilize a variety of approximate numerical methods to investigate both the squeezing dynamics as well as the equilibrium phase diagram of a broad class of easy-plane spin models.

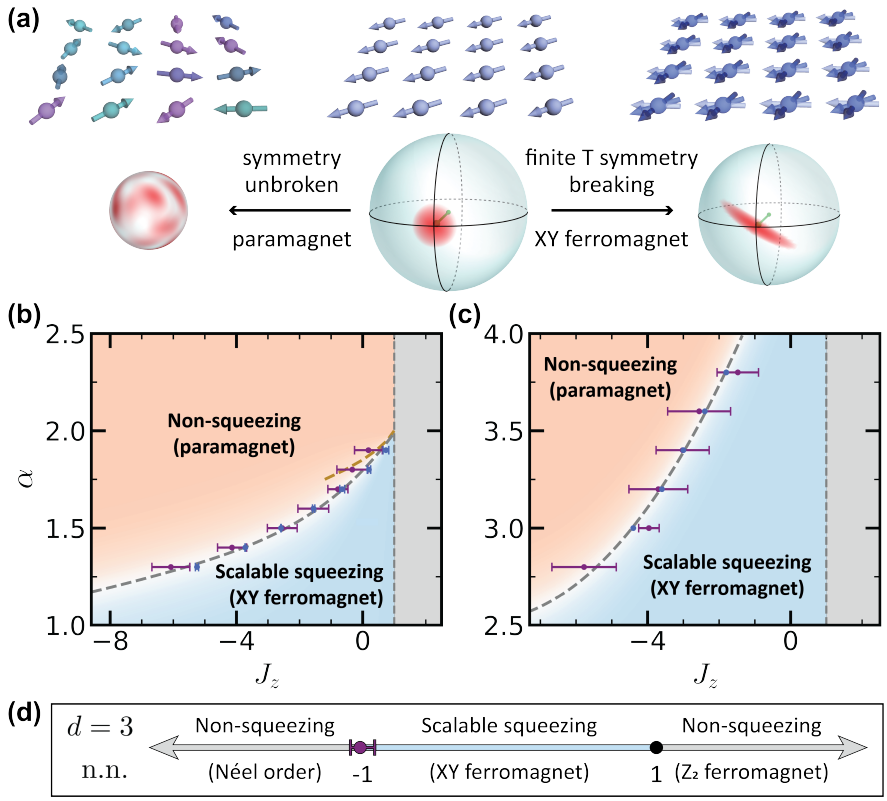

Figure 4.1: (a) Illustration of the connection between spin squeezing and XY ferromagnetic order. The central panel shows an initial product state polarized in the equatorial plane, with a schematic of its quantum projection noise (i.e. spin Husimi-Q distribution) indicated in red. When the effective temperature of the initial state is below the critical temperature for $U(1)$ symmetry breaking (right panel), the system equilibrates to an XY ferromagnet and exhibits scalable squeezing. When the initial state is above the critical temperature, the system equilibrates to a paramagnet, where the total spin length vanishes, precluding spin squeezing (left panel). (b,c) Phase diagrams for scalable spin squeezing as a function of the XXZ anisotropy, J_z, and the interaction power-law, α, in dimensions $d = 1, 2$. The location of the squeezing phase transition is computed via DTWA (purple markers). In 1D, the location of the XY ordering transition is computed via imaginary time evolution on matrix product operators (blue markers, dashed line guide to the eye), while in 2D, the transition is computed via finite temperature quantum Monte Carlo (blue markers, dashed line guide to the eye). In both cases, the phase boundaries are in close agreement. The gold dashed line in (b) corresponds to the phase boundary computed analytically from spin-wave theory (Appendix C.4). (d) Phase diagram for scalable squeezing as a function J_z for a nearest-neighbor interacting system in dimension $d = 3$. For $|J_z| > 1$, there is Néel or Ising order (rather than CSB), so squeezing does not occur.

4.1.2 Connecting squeezing to XY magnetism

To investigate our conjecture, let us consider the paradigmatic family of $U(1)$-symmetric spin Hamiltonians: the long-range $S = 1/2$ XXZ model

$$H_{\mathrm{XXZ}} = -\sum_{i<j} \frac{J_\perp(\sigma_i^x\sigma_j^x + \sigma_i^y\sigma_j^y) + J_z\sigma_i^z\sigma_j^z}{r_{ij}^\alpha}, \tag{4.1}$$

where $J_\perp/J_z$ characterizes the easy-plane anisotropy and α is the long-range power law. This class of Hamiltonians is the most natural and widely studied generalization of one-axis twisting [679–685] and is also realized in a number of quantum simulation platforms ranging from solid-state spins and optical-lattice Hubbard models to ultracold polar molecules and Rydberg atom arrays [41, 649, 676, 686–689]. While our conjecture applies in all dimensions,we note that in $d = 1, 2$ [Fig. 4.1(b,c)] finite-temperature continuous symmetry breaking is only possible for sufficiently long-range power laws whereas in $d = 3$ [Fig. 4.1(d)] it is possible even with nearest-neighbor interaction [1][690, 691]. To establish the connection between squeezing and order we utilize a variety of numerical tools: the discrete truncated Wigner approximation (DTWA) for spin-squeezing dynamics, imaginary time evolution of matrix product operators for diagnosing finite-temperature $U(1)$ symmetry breaking order in $d = 1$, and finite-temperature path integral quantum Monte Carlo for diagnosing order in $d = 2, 3$ [326]. In addition, whenever possible, our numerical results are carefully benchmarked with a combination of time-dependent variational Monte Carlo, Krylov subspace methods, and exact diagonalization.

Let us begin in $d = 1$ with ferromagnetic XY interactions (hereafter, we set $J_\perp = 1$). For $J_z > 1$, the Hamiltonian lies in the easy-axis regime and can only exhibit discrete (Ising) symmetry breaking; this immediately rules out the possibility of quantum-enhanced sensing at accessible time scales [Fig. 4.1(b)]. For $J_z < 1$, the system can exhibit continuous symmetry breaking at finite temperatures provided that $\alpha < 2$. Consider the parameter space with weak power laws and strong antiferromagnetic Ising interactions [pink, Fig. 4.1(b)]. Taking our initial state as the fully polarized coherent spin state in the x direction, $|x\rangle = |\rightarrow\cdots\rightarrow\rangle$, we evolve under H_{XXZ} and measure

[1]For $\alpha > d$, we can choose $J_\perp = 1$ and let the N go to infinity and maintain finite energy density. For $\alpha < d$, to have a finite energy density we need to let $J_\perp$ go to 0 as N goes to infinity. The all-to-all model is realized when we take $\alpha \to 0$ and $J_\perp = 1/N$. Our analysis is restricted to $\alpha > d$.

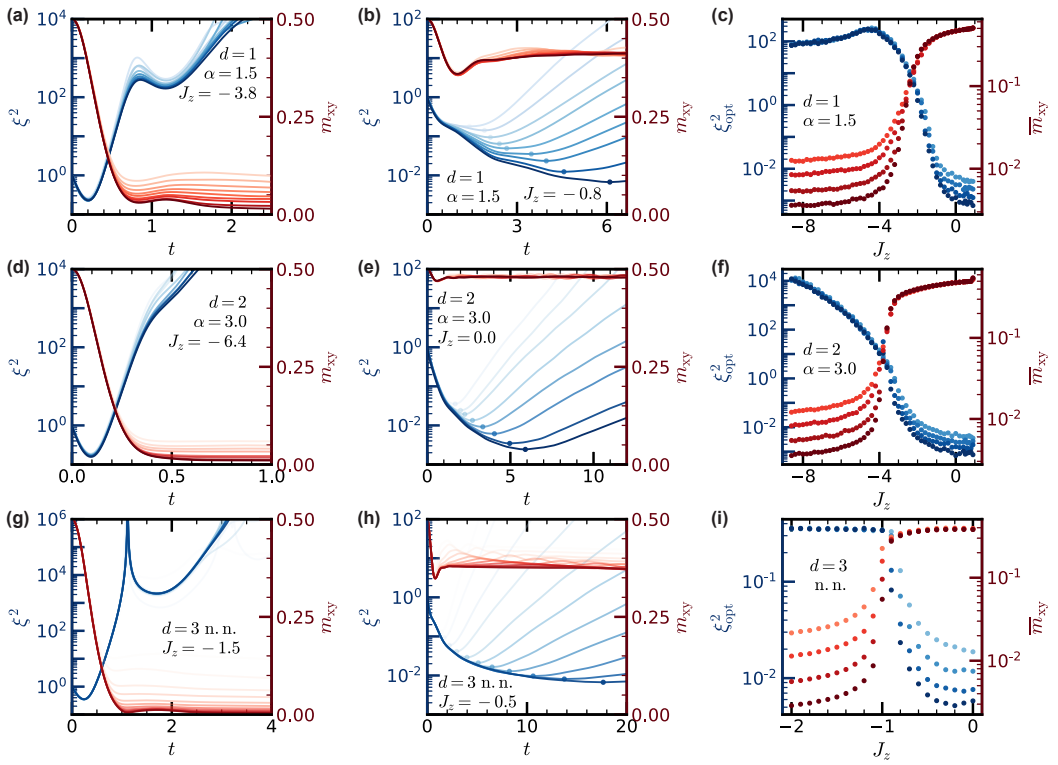

Figure 4.2: (a,b) Depicts the dynamics ($d = 1$) of the squeezing parameter ξ^2 (blue) and the XY order, $m_{\rm xy}$ (red), as a function of time, upon quenching from an initial product state polarized in the $\hat{x}$ direction. Opacity increases with system size (from $N = 10^2 - 10^4$). In the paramagnetic phase (a), $m_{\rm xy}$ decays to zero, while the squeezing parameter does not improve with system size. In the ferromagnetic phase (b), $m_{\rm xy}$ plateaus to a finite value, and the squeezing parameter scales with system size. (d,e) and (g,h) Depict the analogous dynamics for $d = 2$ and $d = 3$, with system sizes $N = 10^2 - 10^4$ and $N = 10^2 - 10^5$. (c) Fixing $\alpha = 1.5$ in $d = 1$, the optimal squeezing parameter (blue) and the plateau value of the XY order (red) are shown as a function of J_z. Darker color shades correspond to larger system sizes (with $N = 5 \cdot 10^3 - 5 \cdot 10^4$). In the paramagnetic phase (large J_z magnitude), the XY order decays with increasing system size, while in the ferromagnetic phase the XY order is independent of system size, indicating a phase transition at $J_c \approx -2.4$. The behavior of the optimal squeezing exhibits a separatrix at the same value of J_c, where it transitions from being system-size independent to scaling with N. (f) and (i) Depict analogous J_z-cuts in the phase diagrams for $d = 2$ fixing $\alpha = 3.0$ (with $N = 5 \cdot 10^3 - 5 \cdot 10^4$) and $d = 3$ (with $N = 2 \cdot 10^3 - 10^5$). Calculations were performed using the DTWA approximation.

both the average XY magnetization, $m_{\mathrm{xy}} = [\langle X^2 + Y^2 \rangle / N^2]^{1/2}$ and the squeezing parameter $\xi^2 \equiv N \min_{\hat{n} \perp \hat{x}} \mathrm{Var}[\hat{n} \cdot \vec{S}] / \langle X \rangle^2$ (which entails a phase sensitivity of $\Delta\phi = \sqrt{\frac{\xi^2}{N}}$); here, $X = \frac{1}{2} \sum_i \sigma_i^x$ (with Y and Z defined analogously) and $\vec{S} = (X, Y, Z)$. As a function of increasing system size, the magnetization decays to zero, indicating thermalization to a disordered state [Fig. 4.2(a)]. Meanwhile, the squeezing parameter, which quantifies the enhancement in sensitivity over the initial coherent state, exhibits marginal improvement at short times. However, this improvement *does not* scale with system size and at late times, ξ^2 steadily worsens [Fig. 4.2(a)].

The dynamics in the opposite parameter space [blue, Fig. 4.1(b)], with strong power laws and weak antiferromagnetic Ising interactions is markedly distinct. Here, the XY magnetization rapidly equilibrates to a system-size-independent value, providing a signature of robust continuous symmetry breaking [Fig. 4.2(b)]. Accompanying the presence of order is the existence of scalable spin squeezing, where the optimal squeezing value improves with system size (i.e. $\xi^2_{\mathrm{opt}} \sim N^{-\nu}$ with $\nu > 0$) and occurs at later and later times [Fig. 4.2(b)]. This is precisely reminiscent of the behavior in the one-axis-twisting model, where $\xi^2_{\mathrm{opt}} \sim N^{-\frac{2}{3}}$.

The essence of our conjecture is already captured by the above dichotomy: thermalizing to a disordered state correlates with non-squeezing, while thermalizing to an ordered state correlates with scalable squeezing. But our conjecture is stronger than claiming an association between squeezing and finite-temperature order; rather, we argue that they are two facets of the same phase. To more quantitatively investigate this, for each point in parameter space, $\{\alpha, J_z\}$, we extract the optimal squeezing and the late-time XY magnetization as a function of system size. Depicted in Figure 4.2(c), is a cut across parameter space, fixing $\alpha = 1.5$ and varying J_z. For large, negative J_z, the XY magnetization plateau vanishes with increasing system size. As J_z becomes weaker and enters the ferromagnetic regime, there is a clear separatrix — indicative of a symmetry-breaking phase transition — where the value of the magnetization plateau becomes system-size independent. Remarkably, the scaling behavior of the optimal squeezing is in perfect correspondence with the magnetization. In the region where the magnetization vanishes, the squeezing does not scale. In the opposite regime, the optimal squeezing exhibits its own separatrix and shows a pronounced scaling with system size.

This change in scaling provides a simple method to determine the location of the squeezing

transition: for each value of J_z, we fit $\xi^2_{\rm opt} \sim N^{-\nu}$ and associate the critical point, J_c, with the onset of $\nu \gtrsim 0$. Repeating this procedure as a function of α leads to the squeezing phase boundary demarcated by the purple data points in Figure 4.1(b). Similarly, one can also define a $U(1)$ symmetry-breaking phase boundary, which occurs when the effective temperature of the initial state, $|x\rangle$, crosses the critical temperature for XY order. To identify this phase boundary, we cool an infinite temperature matrix product operator (representing the density matrix) to the energy density of the $|x\rangle$-state using imaginary time evolution under $H_{\rm XXZ}$. A finite-size scaling analysis then yields the XY-ordering phase boundary demarcated by the blue data points in Figure 4.1(b). That the squeezing and ordering phase boundaries coincide within error bars not only provides evidence for our conjecture but also shows that the DTWA is remarkably accurate in the region of the transition [2].

A few additional remarks are in order. First, we notice that the system always undergoes some *non-scalable* squeezing at early times [692]. In a regime of modest easy-axis coupling and small system sizes, this early time minimum can actually be quantitatively better than the late time minimum that *scales* with system size. To mitigate the influence of such early-time squeezing in the analysis and properly evaluate the squeezing transition, we isolate the late-time, scalable squeezing, by identifying $\xi^2_{\rm opt}$ as the smallest value of $\xi^2(t)$ at a local minima in the derivative $\frac{d}{dt}\xi^2(t)$ after the local thermalization time. In the squeezing phase, this definition coincides with the true minimum of $\xi^2(t)$. Second, one can analytically estimate the CSB phase boundary within spin-wave theory [dashed gold line, Fig. 4.1(b)]. A particularly nice feature of this analysis is that it predicts the observed behavior, where J_c approaches the Heisenberg point as $\alpha \to 2$ (beyond which there is no finite temperature order). Third, we demonstrate precisely the same correspondence between squeezing and order in $d = 2$ [Fig. 4.2(d-f)] and in $d = 3$ [Fig. 4.2(g-i)], by determining the squeezing critical point from DTWA simulation and obtaining the thermal critical point via quantum Monte Carlo with worm-type updates [693]. Interestingly, the topology of the squeezing phase diagram in $d = 2$ is slightly distinct — in particular, even as $\alpha \to 4$ (beyond which there is no finite temperature order), J_c does

[2] We note that DTWA dynamics cannot accurately capture the short-range spin fluctuations (after local equilibration) deep in the quantum regime, i.e. where the effective temperature of the initial state $T \ll J_\perp$. However, this is of little consequence: for $T \ll J_\perp$, finite temperature effects are important only for very long time-scales at systems sizes beyond our power to investigate. Close to the phase transition, where T is of order $J_\perp$, our results suggest that the semiclassical description is more accurate.

not approach the Heisenberg point, so there remains a finite interval $-1 \lesssim J_z < 1$ where scalable squeezing occurs. Moreover, in $d = 1, 2$, scalable squeezing disappears as J_z decreases because the temperature of the initial $|x\rangle$-state becomes higher than the critical temperature; however, in $d = 3$, at least for the nearest-neighbor model we consider, the squeezing disappears for $J_z < -1$, because the continuous-symmetry-breaking XY ferromagnet is replaced by discrete-symmetry-breaking Néel order.

Finally, a semiclassical view of the dynamics provides the essential intuition for the connection between squeezing and order. In this framework, the initial state $|x\rangle$ is viewed as a quasi-probability distribution on the total-spin phase space, represented by a sphere of radius $|S| = N/2$ [middle, Fig. 4.1(a)]. In the all-to-all coupled case ($\alpha \to 0$), one-axis twisting dynamics yield squeezing by causing slices from this distribution to rotate about the $\hat{z}$-axis with an angular velocity proportional to total $Z = \frac{1}{2}\sum_i \sigma_i^z$. Our key insight is that even in the power-law coupled case with $\alpha > d$, or the short-ranged case with $d \geq 3$, a similar picture should hold as long as the state remains ordered. Specifically, if the effective temperature of $|x\rangle$ is below the equilibrium CSB critical temperature, then $m_{\mathrm{xy}}^2 > 0$ [Fig 4.2(b,e,h)] and the initial quasi-probability distribution will simply relax, on a microscopic timescale independent of N, to a slightly distorted distribution on a smaller phase space of radius $m_{\mathrm{xy}}N$ [Fig 4.1(a), right]. This "dressed" distribution will then evolve qualitatively similarly to the all-to-all coupled case.

4.1.3 Scalable squeezing in the XY magnet

Based upon the semi-classical intuition from above, one might naively expect that squeezing in the finite-temperature XY magnet should exhibit the same scaling as in one-axis twisting. However, this is oversimplified. Perhaps the easiest way to see this is to consider the conditional variance of Y given Z, denoted as $\mathrm{Var}[Y|Z]$, within the semi-classical approximation. As illustrated in Fig. 4.3(a), for one-axis twisting, $\mathrm{Var}[Y|Z]$ is a constant of motion: each Z-slice of the probability distribution rotates rigidly about the sphere. But in a system that does not conserve total spin, e.g. H_{XXZ}, the conditional variance will increase as a function of time [Fig. 4.3(a)]; indeed, the hydrodynamic model suggests that $Y|Z$ evolves diffusively, so $\mathrm{Var}[Y|Z]$ grows linearly in time with a slope that depends strongly on

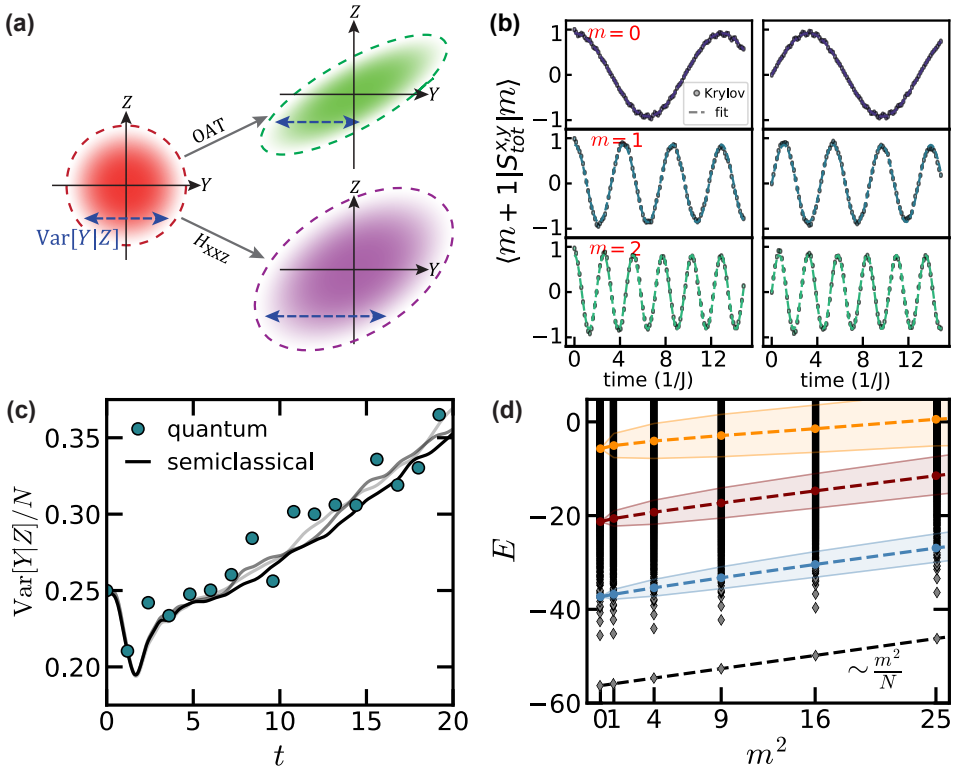

Figure 4.3: (a) Schematic illustrating the dynamics of the conditional variance in the OAT model (green) and the XXZ model (purple) at finite temperature. In the OAT model, $\mathrm{Var}[Y|Z]$ remains constant, while in the XXZ model, the conditional variance exhibits an additional linear growth in time. (b) Time-dependent matrix elements of S^x_{tot}, S^y_{tot}, computed via Krylov subspace method. Semiclassically, χ determines the angular velocity at which m-sectors rotate. Quantum mechanically, this corresponds to rate of relative phase accumulation between two adjacent m-sectors: $\langle m+1|\hat{X}|m\rangle \sim \cos(\Delta E \cdot t)$ and $\langle m+1|\hat{Y}|m\rangle \sim \sin(\Delta E \cdot t)$, where $\Delta E = (2m+1)\chi$. Fit to sinusoid oscillations is used to determine ΔE, from which χ is further extracted. Note that these oscillations are damped in principle (reflecting the linear growth of $\mathrm{Var}_{\mathrm{q}}[Y|Z]$), but this is neglible in our fits. (c) In the squeezing phase, both semi-classical DTWA simulations (for $N = 1000, 2000, 4000$ with $Z = 0$) and exact quantum dynamics ($N = 18$) show the conditional variance growing linearly in time. Their quantitative agreement lends support to the quantum-mechanical origin of the variance growth. (d) Diamonds depict the spectrum of a $d = 1$ H_{XXZ} model for $N = 24$. The eigenstates in different m-sectors are connected by total-spin raising and lowering operators. The ground state manifold exhibits a so-called "Anderson tower" structure where the energies scale as $E \sim m^2/N$ [694]. At finite temperatures, this manifold becomes a distribution with an approximate "Anderson tower" structure: The set of states that are connected to a given initial finite-energy state upon successive applications of the total-spin raising or lowering operator will have a distribution of energies, which is illustrated here for three initial states with $m = 0$ but differing energies E_0. The dashed lines, which indicate the mean values of the distributions, exhibit the same scaling, $E - E_0 \sim m^2/N$, but the variance (shaded region) increases with E_0 . In all (b-f), $\alpha = 1.5$ for $d = 1$, $\alpha = 3.0$ for $d = 2$ and $J_z = 0$.

temperature (Appendix C.3). To understand the impact of this variance growth, we note that (within a semi-classical picture) :

$$\xi^2(t) \approx \frac{\mathrm{Var}[Y|Z]/N}{4m_{\mathrm{xy}}^4(\chi t)^2} + \frac{(\chi t)^4}{24 m_{\mathrm{xy}}^2 N^2}, \tag{4.2}$$

where χ is the effective one-axis twisting strength, related to the z-axis spin susceptibility (Appendix C.3) [264, 677]. When the conditional variance remains constant (i.e. one-axis twisting), optimizing over t yields $\xi^2 \sim N^{-\frac{2}{3}}$ (leading to a phase sensitivity $\sim N^{-\frac{5}{6}}$). However, linear growth of the conditional variance predicts instead that $\xi^2 \sim N^{-\frac{2}{5}}$ (leading to a phase sensitivity $\sim N^{-\frac{7}{10}}$).

At low temperatures, the slope of the variance growth is small, suggesting that the asymptotic scaling behavior will only be observed at extremely large system sizes. To control the temperature (without changing the local energy scale of H), we introduce an additional tuning parameter: the polarization of the initial state. For polarization p, we initialize a product state, where each spin points along $+x$ with probability $(1+p)/2$ and along $-x$ with probability $(1-p)/2$. This polarization tunes the effective temperature of the initial state. At low temperatures ($p \approx 1$), the squeezing appears to scale as $\sim N^{-\frac{2}{3}}$ (Fig. 4.4a,b). At intermediate temperatures near the transition, the squeezing scales as $\sim N^{-\frac{2}{5}}$ over multiple decades in system size (Fig. 4.4a,b). As soon as the polarization tunes the temperature above T_c, a "gap" emerges in the scaling behavior and ξ^2 becomes independent of system size (Fig. 4.4a,b). We note that the low-temperature scaling of $N^{-\frac{2}{3}}$ is not expected to hold as $N \to \infty$; rather, the scaling will eventually cross over to the asymptotic behavior of $N^{-\frac{2}{5}}$ (Fig. 4.4c).

One might naturally wonder whether the above analysis for partially polarized product states could also apply to partially polarized *mixed* initial states? To be specific, let us consider a density matrix of the form, $\rho = [(1+p)/2\,|{\rightarrow}\rangle\langle{\rightarrow}| + (1-p)/2\,|{\leftarrow}\rangle\langle{\leftarrow}|]^{\otimes N}$, which is particularly relevant to experiments [676]. From a computational perspective, calculating the squeezing parameter for pure states and mixed states is nearly identical, with the only difference being an order of averages (Appendix C.2). In principle, since squeezing is a nonlinear function of expectation values, this averaging can matter. However, we find that the results for pure and mixed states converge together extremely rapidly with system size, and are essentially identical for $N \gtrsim 10^2$. This leads us to the intriguing conclusion that XY magnetism enables scalable squeezing *even* of certain mixed initial states. Most optimistically, one might hope that this applies to *any* mixed initial state with finite polarization—exploring this tantalizing possibility remains a direction for future research.

Let us return now to the task of understanding the distinction between squeezing in all-to-all and finite-range interacting systems. Although our semi-classical analysis provides a coarse-grained

explanation for the difference between the scaling of the squeezing in these systems, the microscopic dynamics are fundamentally quantum mechanical. This raises the question: is the asymptotic squeezing scaling also modified in the true quantum dynamics?

To answer this, we begin by developing a quantum interpretation of $\mathrm{Var}[Y|Z]$. Intuitively, $\mathrm{Var}[Y|Z]$ can also be computed as the remaining variance of Y *after* one has counter-rotated each Z-slice of the probability distribution back to its original mean. Crucially, both semi-classically and quantum mechanically, this counter-rotation can be realized by evolving the system under one-axis twisting (Fig. 4.3b). From this perspective, the quantum analog of $\mathrm{Var}[Y|Z]$ is closely connected to a Loschmidt echo of the form:

$$\mathrm{Var}_{\mathrm{q}}[Y|Z] = \langle x|\, e^{it[H_{\mathrm{XXZ}} - \chi \frac{\hat{Z}^2}{N}]}\, \hat{Y}^2\, e^{-it[H_{\mathrm{XXZ}} - \chi \frac{\hat{Z}^2}{N}]}\, |x\rangle\,. \tag{4.3}$$

Since the thermalization induced by the XXZ-dynamics cannot be perfectly undone by one-axis twisting, $\mathrm{Var}_{\mathrm{q}}[Y|Z]$ will grow in time until saturating at its equilibrium value of $m_{\mathrm{xy}}^2 N^2/2$. Indeed, we compute the variance growth for a 1D system at $\alpha = 1.5$, $J_z = 0$ and find that (at least in this parameter regime), $\mathrm{Var}_{\mathrm{q}}[Y|Z]$ for $N = 18$ indeed agrees extremely well with the semi-classical conditional variance in the thermodynamic limit (Fig. 4.3c).

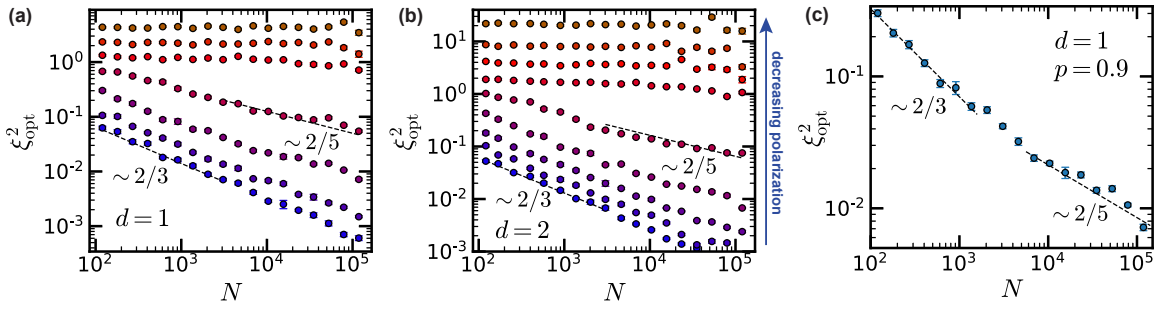

Figure 4.4: (a) DTWA simulations depicting the optimal squeezing as a function of system size. The polarization of the initial state decreases from $p = 1.0$ (blue) to $p = 0.7$ (red); this tunes the effective temperature of the initial state across the critical temperature for XY order. As the polarization decreases, the scaling changes sharply from $N^{-2/5}$ to N^0. At lower effective temperatures ($p \approx 1$), the asymptotic $N^{-2/5}$ scaling emerges only for larger system sizes. (b) Depicts the analogous results for $d = 2$, where the polarization ranges from $p = 1.0$ (blue) to $p = 0.6$ (red). (c) Shows a crossover in the scaling behavior for $d = 1$ with polarization $p = 0.9$. At small system sizes, the squeezing scales as $N^{-2/3}$ consistent with OAT. However, at larger system sizes, the scaling crosses over to the asymptotic prediction of $N^{-2/5}$.

Interestingly, a complementary picture for the behavior of $\mathrm{Var}_{\mathrm{q}}[Y|Z]$ emerges from the spectral structure of H_{XXZ}. The ground states of adjacent magnetization sectors of H_{XXZ} are connected by

the total spin raising and lower operator. Taken together, they form a so-called "Anderson tower" with energies scaling as $E \sim m^2/N$ (Fig. 4.3d). In the one-axis-twisting model, squeezing arises from the fact that the *entire* spectrum exhibits this "Anderson tower" structure. By contrast, at finite energy densities, the spectrum of H_{XXZ} features only approximate "Anderson towers": the raising and lowering operator connect a given eigenstate in an m-sector to several others in adjacent sectors, leading to a distribution of energies (Fig. 4.3d). It is precisely the variance of this distribution which drives thermalization in the XXZ model, and thus the growth of $\mathrm{Var}_{\mathrm{q}}[Y|Z]$.

4.1.4 Outlook

Our work provides fundamental insight into the landscape of Hamiltonians that can be used to generate metrologically useful quantum states and in the meanwhile opens the door to a number of intriguing directions. First, while we have established the presence of a phase transition between scalable squeezing and non-squeezing, the nature of this transition remains an open question. In particular, it would be interesting to derive whether the critical properties of the optimal squeezing solely from the universal properties of the CSB transition. Second, our framework connecting the quantum Fisher information of pure states to spontaneous symmetry breaking suggests a new strategy for preparing metrologically useful states. However, the ability to prepare a state with large QFI does not immediately imply that one can straightforwardly utilize it for sensing; indeed, in the most general case, it is necessary to time-reverse the dynamics, in order to extract the metrological signal [287, 290, 295]. In the case of $U(1)$ symmetry breaking, the emergence of squeezing *does* guarantee a simple way to harness the metrological gain [669]. Thus, generalizing our results to finite-temperature *non-abelian* continuous symmetry breaking raises the question: is there any higher-symmetry analogue of spin-squeezing, which might enable sensitivity to perturbations beyond scalar fields? Finally, our work implies that scalable squeezing can be realized in a variety of quantum simulation platforms with resonant dipolar interactions [649, 676, 687, 688, 695, 696]. For example, ultracold polar molecules in an optical lattice as well as Rydberg atoms in a tweezer array can both implement the two-dimensional XY model with $1/r^3$ interactions, which is deep in the scalable squeezing phase. The discovery of optically-active spin defects in 2D quantum materials [689, 697, 698] as well as advances in delta-

doped crystal growth [699, 700] also suggest a route toward spin squeezing in the solid state; in this setting, the robustness of easy-plane ferromagnetism to the positional disorder of the underlying spin defects is crucial.

4.2 Scalable spin squeezing in a dipolar Rydberg atom array

4.2.1 Introduction

The past decade has witnessed the use of squeezed states of light and spin ensembles to improve upon a multitude of applications, ranging from gravitational wave detectors [701] and atom interferometers [297] to optical atomic clocks [702, 703]. The realization of spin squeezing via global interactions has been demonstrated using a variety of platforms, including atomic vapors coupled to light, trapped ions, ultracold gases and cavity QED [86]. Whether short-range interaction (decaying as a power of the distance larger than the dimensionality) can yield *scalable* spin squeezing has remained an essential open question [679, 704, 705]. The previous section, as well as other recent theoretical advances, points to an affirmative answer [677, 679, 680, 706–708], proposing a deep connection between spin squeezing and continuous symmetry breaking (CSB) [677, 680, 708, 709]. This connection to CSB order broadens the landscape of systems expected to exhibit scalable spin squeezing, and suggests that both power-law interactions, and even nearest-neighbour couplings, can lead to sensitivity beyond the standard quantum limit [677, 708]. Of particular relevance is the ferromagnetic, dipolar XY model; indeed, this model is naturally realized in a number of quantum simulation platforms ranging from ultracold molecules [695, 710–712] and solid-state spin defects [9] to Rydberg atom arrays [676, 696].

In this section, we demonstrate the generation of spin-squeezed states using a square lattice of up to $N = 100$ Rydberg atoms. Our main results are three-fold. First, we explore the quench dynamics of an initially polarized spin-state evolving under the dipolar XY model, using a procedure analogous to the one introduced for the case of all-to-all interactions [264]. We show that the resulting state exhibits spin squeezing and characterize the generation of multipartite entanglement as a function of time. Moreover, the squeezing improves with increasing system size, providing evidence for the existence of scalable spin squeezing. Second, we introduce a multi-step approach to squeezing, where the quench dynamics are interspersed with microwave rotations. We demonstrate that this technique leads to an improvement in the amount of spin squeezing and also enables the squeezing to persist to longer time-scales. Finally, motivated by metrological applications, we show that it is possible to freeze the squeezing dynamics (e.g. when accumulating a signal) by performing Floquet engineering.

In particular, we transform the dipolar XY model into a dipolar Heisenberg model [206, 713], so that the squeezing remains constant in time.

4.2.2 Experimental setup

Our experimental setup [714] consists of a two-dimensional square array of ^{87}Rb atoms trapped in optical tweezers (see Fig. 4.5a). To implement the dipolar XY model [715], we rely on resonant dipole-dipole interactions between two Rydberg states of opposite parities. In particular, we encode an effective spin-$1/2$ degree of freedom as $|\uparrow\rangle = |60S_{1/2}, m_j = +1/2\rangle$ and $|\downarrow\rangle = |60P_{3/2}, m_j = -1/2\rangle$, leading to an interaction Hamiltonian:

$$H_{\mathrm{XY}} = -\frac{J}{2}\sum_{i<j}\frac{a^3}{r_{ij}^3}(\sigma_i^x\sigma_j^x + \sigma_i^y\sigma_j^y), \tag{4.4}$$

where $\sigma_i^{x,y,z}$ are Pauli matrices, r_{ij} is the distance between spins i and j, $J/h = 0.25$ MHz is the dipolar interaction strength, and $a = 15$ μm is the lattice spacing. A magnetic field perpendicular to the lattice plane defines the quantization axis and ensures that the dipolar interactions are isotropic.

We begin by investigating the squeezing dynamics generated by H_{XY}. The atoms are initially excited from the ground state to the Rydberg state $|\uparrow\rangle$, using stimulated Raman adiabatic passage (Fig 4.5). Using a microwave $\pi/2$-pulse tuned to the transition between the spin states, we prepare an initial coherent spin state along the y-axis, $|\psi(0)\rangle = |\rightarrow\cdots\rightarrow\rangle$ (see Fig. 4.5b). Next, we allow the system to evolve under H_{XY} and measure the squeezing as a function of time.

4.2.3 Observing scalable squeezing

Since squeezing manifests as a change in the shape of the noise distribution, one must measure the variance of the collective spin operator in the plane perpendicular to the mean spin direction; to this end, we define $J_\theta = \cos(\theta)J_z + \sin(\theta)J_x$, where $J_{x,y,z} = \frac{1}{2}\sum_i \sigma_i^{x,y,z}$ are collective spin operators. We characterize the amount of spin squeezing via the parameter [262, 669],

$$\xi_R^2(t) = \frac{N\min_\theta\left(\mathrm{Var}\left(J_\theta\right)\right)}{\langle J_y\rangle^2}, \tag{4.5}$$

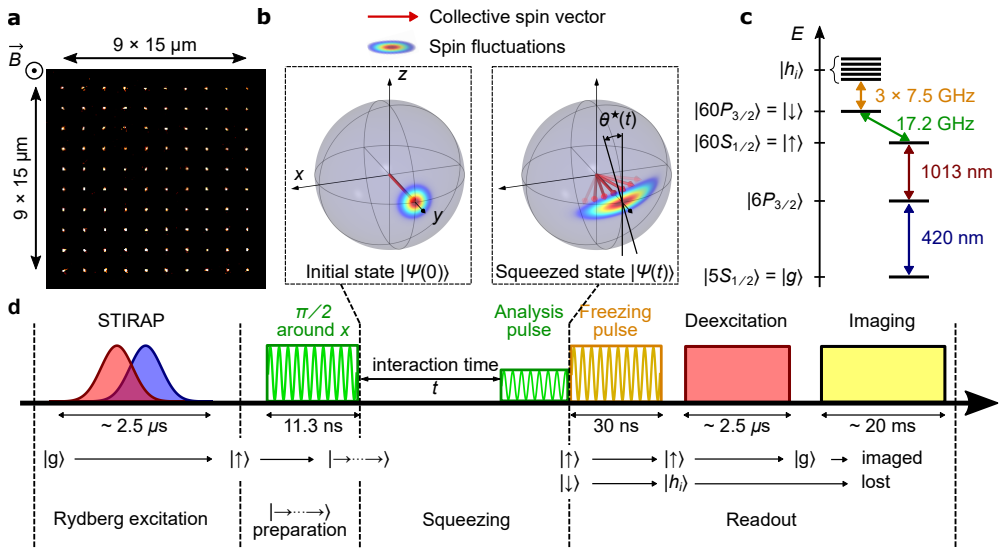

Figure 4.5: (a), Fluorescence image of a fully assembled 10×10 ^{87}Rb array. (b), Spin fluctuations represented via the Husimi Q-distributions (colored area) [86] of the initial coherent spin state $|{\rightarrow}\cdots{\rightarrow}\rangle$ (left panel) and of a squeezed state obtained during the dynamics (right panel), depicted on a generalized Bloch sphere. The angle $\theta^{\star}(t)$ corresponds to the direction of the narrowest noise distribution. The squeezed state is schematically depicted by a superposition of coherent states (red arrows). (c), Schematics of the atomic levels relevant for the experiment. (d), Sequence of optical and microwave pulses (not to scale) used for the spin squeezing protocol. After randomly loading atoms into 1-mK deep optical tweezers (with a typical filling fraction of 60%), the array is assembled one atom at a time [716]. The atoms are then cooled to a temperature of $10\,\mu$K using Raman sideband cooling and optically pumped to $|g\rangle = |5S_{1/2}, F = 2, m_F = 2\rangle$. Following this, the power of the trapping light is adiabatically ramped down reducing the tweezer depth by a factor ~ 50 and is then switched off. By applying a two-photon stimulated Raman adiabatic passage (STIRAP) with 421-nm and 1013-nm lasers, the atoms are excited to the Rydberg state $|{\uparrow}\rangle$. To generate the initial coherent spin state along $\hat{y}$, a global resonant microwave $\pi/2$ pulse around $\hat{x}$ is applied, with a Rabi frequency $\Omega = 2\pi \times 22.2$ MHz. After an interaction time t, an analysis microwave pulse is applied to change the measurement basis: a θ pulse around $\hat{y}$ is applied to measure the variance $\mathrm{Var}(J_\theta)$ along any direction θ; a $\pi/2$ pulse around $\hat{x}$ is applied to measure the spin length $|\langle J_y\rangle|$. When measuring $\mathrm{Var}(J_\theta)$, the Rabi frequency of the analysis pulse is reduced down to $2\pi \times 4.1$ MHz in order to perform rotations with a higher angular resolution. The detection procedure comprises three steps. In the first step, a 7.5 GHz microwave "freezing pulse" pulse is used to transfer the spin population from $|{\downarrow}\rangle$ to the $n = 58$ hydrogenic states (labelled by $|h_i\rangle$) via a three-photon transition, in order to avoid detrimental effects of interactions with those remaining in $|{\uparrow}\rangle$ during the remainder of the read-out sequence. In the second step, a de-excitation pulse is performed by applying a 2.5 μs laser pulse on resonance with the transition between $|{\uparrow}\rangle$ and the short-lived intermediate state $6P_{3/2}$ from which the atoms decay back to $5S_{1/2}$. The final step consists of switching the tweezers back on to recapture and image (via fluorescence) *only* the atoms in $5S_{1/2}$ (while the others are lost).

which quantifies the metrological gain in a Ramsey interferometry experiment. To measure $|\langle J_y\rangle|$, we simply rotate the state $|\psi(t)\rangle$ back to the z-axis using a second $\pi/2$-pulse around x. To measure $\mathrm{Var}\,(J_\theta)$, we instead perform a microwave rotation around the y-axis, where the angle θ is tuned via the duration of the pulse. Finally, we read out the state of each atom with a detection efficiency of

97.5% for $|\uparrow\rangle$ and 99% for $|\downarrow\rangle$. Operationally, each experimental sequence is repeated ~ 200 times, and from this series of snapshots, we calculate the average and variance of all collective spin operators. For a given interaction time, t, the noise distribution has a specific direction of smallest uncertainty, corresponding to the angle $\theta^\star(t)$ that minimizes the variance of J_θ (see Fig. 4.5b). Beginning with a 6×6 array, we measure $\mathrm{Var}\,(J_\theta)$ as a function of θ for $t = 0.3$ μs. As shown in Fig. 4.6a, the variance exhibits a sinusoidal shape that reveals the underlying elliptical distribution of the spin fluctuations and allows us to determine $\theta^\star$. We then investigate the time evolution of both $|\langle J_y\rangle|$ and $\mathrm{Var}\,(J_{\theta^\star})$. As the system evolves, the initial coherent spin state expands into a superposition of states (fan of red arrows, Fig. 4.5b), which causes the mean spin length, $|\langle J_y\rangle|$ (red circles, Fig. 4.6b), to decay toward zero [206, 713]. At the same time, the variance of J_θ (blue circles, Fig. 4.6b) initially decreases below its $t = 0$ value, reaches a minimum, and then increases, exceeding its $t = 0$ value at late times [677].

Taken together, $|\langle J_y\rangle|$ and $\mathrm{Var}\,(J_{\theta^\star})$ allow us to reconstruct the squeezing parameter ξ_R^2 (or $10\log_{10}(\xi_R^2)$ when expressed in dB) as a function of time. As illustrated in Fig. 4.6b, the dynamics of the squeezing parameter are qualitatively similar to those of the variance: ξ_R^2 initially decreases below the standard quantum limit (SQL), reaches an optimum $\xi_R^{2\star}$ at time $t^\star$, and then increases, exceeding the SQL at late times. The system remains in a squeezed state (i.e. $\xi_R^2 < 1$) for approximately 0.5 μs and exhibits an optimal squeezing parameter of -2.7 ± 0.3 dB. The optimal squeezing is highly sensitive to detections errors, and analytically correcting for these errors (diamond markers, Fig. 4.6, Appendix C.5) leads to a minimum squeezing parameter of -3.9 ± 0.3 dB. However, even this corrected value does not reach the optimum (approximately -6.7 dB) predicted for the dipolar XY model. We attribute this to two other types of experimental imperfections, which also degrade the squeezing parameter: errors in the initial state preparation and imperfections in our microwave pulses. In contrast to detection errors, these imperfections directly affect the many-body squeezing dynamics; accounting for these additional errors leads to significantly better agreement between theory and experiment (Fig. 4.6c).

At a fundamental level, a squeezing parameter $\xi_R^2 < 1$ necessarily implies the presence of entanglement in our system [268, 717]. We quantify the entanglement depth as a function of time; an entanglement depth of k means that the many-body state cannot be written as a statistical mixture

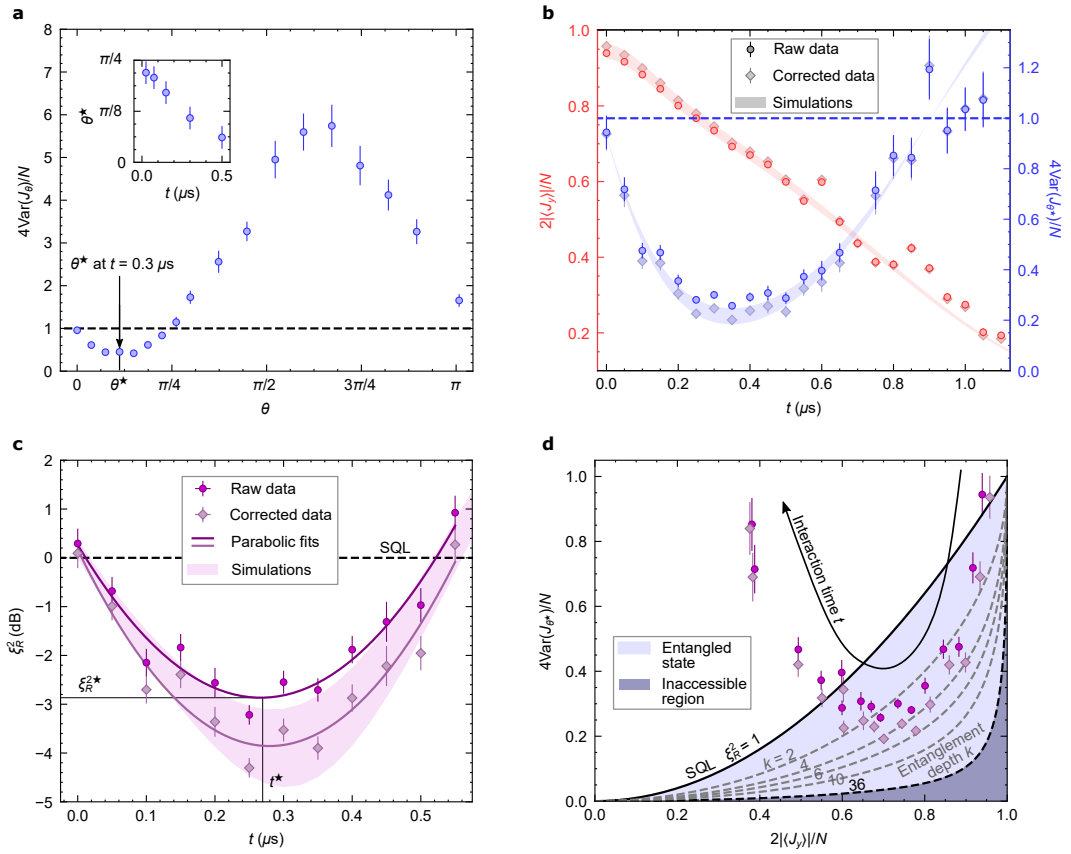

Figure 4.6: (a), Determination of the angle $\theta^\star$ that minimizes the spin fluctuations for a fixed interaction time, $t = 0.3$ μs. The inset shows $\theta^\star(t)$ determined for different times, t. The dashed line in **a** and **b** corresponds to the uncorrelated case $4\mathrm{Var}(J_\theta)/N = 1$. (b), Measurements of the spin length $|\langle J_y\rangle|$ (red circles) and of the minimum variance $\mathrm{Var}(J_{\theta^\star})$ (blue circles). The diamond markers are the data corrected for the detection errors (Appendix C.5). The shaded regions represent the results of the unitary spin dynamics, without any free parameter, including $97.5 \pm 1\%$ ($99 \pm 1\%$) detection efficiency for $|\uparrow\rangle$ ($|\downarrow\rangle$). (c), Squeezing parameter $\xi_R^2(t)$ as a function of time. The solid curves are parabolic fits used to determine the optimal squeezing parameter $\xi_R^{2\star}$ and the optimal squeezing time $t^\star$. As in (c), the shaded area shows simulations including $\pm 1\%$ uncertainty in the detection efficiencies. (d), Parametric plot of the variance as a function of the spin length. The colored area, delimited by the black solid curve $\xi_R^2 = 1$, depicts the region where entanglement exists in the system. The grey dashed curves correspond to entanglement depths of k and the dashed black curve to a maximal entanglement depth of $k = 36$. The black arrow shows the direction of increasing interaction time.

of states factorized into clusters containing up to $(k-1)$ particles – that is, at least one k-particle subsystem is entangled [268, 301, 670]. For a particular spin length, $|\langle J_y\rangle|$, the minimum attainable variance of the quantum state gives a lower bound on the entanglement depth [268]. Fixed contours of this bound for different values of k are shown in Fig. 4.6d: if a data point falls below the line labelled by k, the entanglement depth is thus at least $k+1$. The many-body dynamics of our system leads to a

state whose entanglement depth increases rapidly at early times. Near the optimal squeezing time, $t^\star$, the entanglement depth reaches a maximum of $k = 3$ (for the measurement-corrected data, we find $k = 5$) for our 36-atom system.

One of the distinguishing features of spin squeezing in all-to-all interacting models is that it is *scalable*—the optimal squeezing parameter, $\xi_R^{2\star}$, scales non-trivially with system size as $N^{-\nu}$ with $\nu = 2/3$ [264]. Whether this is the case for power-law interacting, or more general systems is significantly more subtle. In particular, scalable spin squeezing has been recently conjectured to be closely related to continuous symmetry breaking (ferromagnetic XY) order [677, 679, 680, 708]. The mean-spin direction is the order parameter of such a system, and thus, in the ordered phase, it should equilibrate to some nonzero value; this is clearly a pre-requisite for scalable squeezing, since the denominator of the squeezing parameter, ξ_R^2, is precisely the square of the mean-spin length, $\langle J_y \rangle^2$ (Eq. 4.5). More subtly, the low-energy spectrum associated with ferromagnetic XY order is expected to consist of so-called "Anderson towers", wherein the energy is proportional to J_z^2 [718, 719]. Crucially, this leads to the emergence and persistence of OAT-like dynamics *even* until late times, $t \sim \mathcal{O}(Nh/J)$; these dynamics "twist" the initial quantum fluctuations, shrinking the minimum variance in the y-z plane (Eq. 4.5), thus leading to scalable spin squeezing. Finally, let us emphasize that even this picture is only approximate: The eventual thermalization of the dipolar XY model implies that its dynamics (even at low energies) cannot be perfectly captured by one-axis twisting [708].

For the dipolar XY interactions that we investigate here, continuous symmetry breaking, and thus scalable squeezing, is expected in $d = 2$ [677, 679, 680, 708], but not in $d = 1$ [680, 708]. To this end, we measure the squeezing dynamics in systems ranging from $N = 2 \times 2$ to 10×10 atoms. In principle, determining the minimum squeezing parameter requires optimizing over both time and θ for each system size; as N increases, the optimal time, $t^\star$, is expected to increase while the optimal $\theta^\star$ is expected to decrease. Analogous to our previous procedure, we begin by extracting $\theta^\star$ at a fixed time t, and measuring the time evolution of $|\langle J_y \rangle|$ and $\mathrm{Var}(J_{\theta^\star})$; the time at which the variance is minimized provides a self-consistent way to experimentally verify that we are working near the two-parameter optimum.

At short times ($t < 0.25$ μs), the dynamics of $|\langle J_y \rangle|$ collapse (i.e. exhibit a size-independent

decay) for all N owing to rapid local relaxation of the magnetization (Fig. 4.7a), At later times, $|\langle J_y \rangle|$ decreases more slowly for increasing system size, indicative of continuous symmetry breaking order. The dynamics of the variance also depend on N (see Fig. 4.7b): the minimum variance improves and occurs at later times as the system size increases. From these measurements, for each system size, we compute the squeezing dynamics, and extract both the optimal squeezing parameter, $\xi_R^{2\star}$, and the corresponding optimal interaction time, $t^\star$.

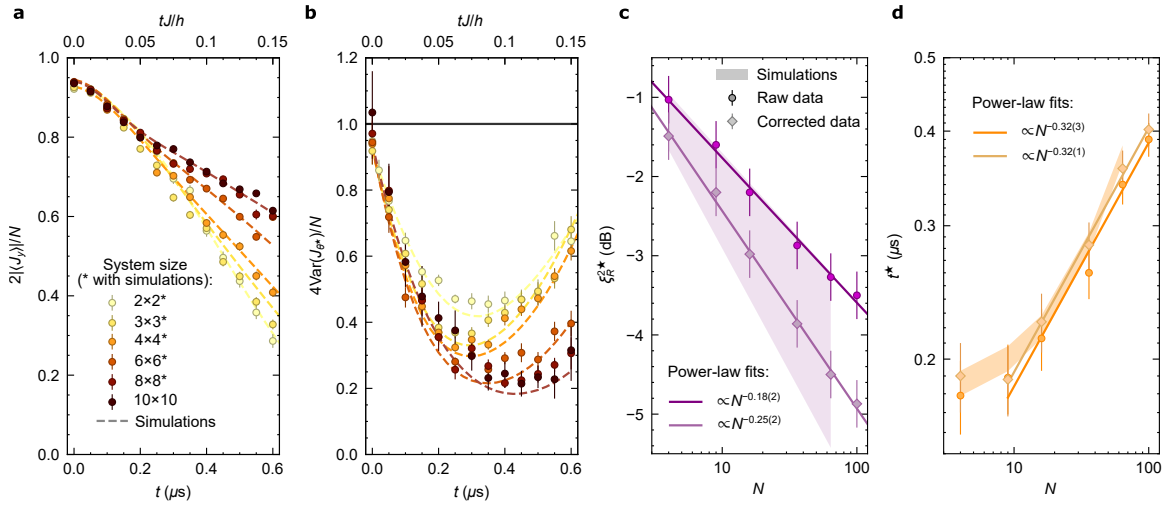

Figure 4.7: (a), (b), Measurement of the spin length $|\langle J_y \rangle|$ and of $\mathrm{Var}(J_{\theta^\star})$ as a function of time for various system sizes. The dashed lines correspond to the results from Krylov methods (for system sizes 2×2, 3×3 and 4×4) using Dynamite[720] or exponential of matrix product operators (for system sizes 6×6 and 8×8) as implemented in TenPy [336]. Both methods faithfully capture the dynamics over the time scales relevant to the experiment, so the numerical error associated with this method is negligible. (c), (d), Minimum squeezing parameter $\xi_R^{2\star}$ and associated optimal interaction time $t^\star$, as a function of N. The circles and diamonds correspond to the raw and detection-error corrected data, respectively. The solid lines are power-law fits. The shaded regions are the results of the simulations for values of the detection efficiency of $|\uparrow\rangle$ ($|\downarrow\rangle$), $97.5 \pm 1\%$ ($99 \pm 1\%$), between their lower and upper limit.

As previously mentioned, in the all-to-all interacting case, both optima are expected to scale with system size [256, 264]. Recent theoretical work predicts that scalable squeezing can also arise in our 2D dipolar XY model [677, 708, 709]. This expectation is indeed borne out by our data. As shown in Fig. 4.7(c,d), we find that $\xi_R^{2\star} \sim N^{-\nu}$ and $t^\star \sim N^{\mu}$ with $\nu = 0.18(2)$ and $\mu = 0.32(3)$; when correcting for detection errors, we find that $\nu = 0.25(5)$, while μ does not change. Interestingly, the exponent that we observe for the optimal squeezing time is in agreement with that observed in the all-to-all coupled case, where $t^\star \sim N^{1/3}$ [264]. However, the scaling of the optimal squeezing

parameter is significantly weaker than that predicted for both all-to-all interactions, as well as the dipolar XY model [677, 708]. Again, we attribute this to a combination of experimental imperfections, which, when accounted for, leads to a relatively good agreement between theory and experiment (Fig. 4.7b,c) [3]. We note that this difference in agreement for $t^\star$ and $\xi_R^{2\star}$ is perhaps not unexpected; for example, measurement errors decrease the amount of achievable spin squeezing but do not change the optimal squeezing time.

4.2.4 Multi-step spin squeezing

The fact that squeezing exhibits an optimum in time arises from a competition between the generation of entanglement and the curvature of the Bloch sphere (Fig. 4.5b). Microscopically, the squeezing dynamics causes the coherent superposition of states to wrap around the Bloch sphere, but squeezing (Eq. 4.5) is measured via the variance projected in the plane perpendicular to the mean spin direction. Thus, the curvature of the Bloch sphere leads to a noise distribution which deviates from an elliptical shape [86] and manifests as additional variance. This suggests that one can improve the optimum squeezing by utilizing a time-dependent protocol. In particular, by continuously rotating the elliptical noise distribution toward the equator, one can minimize the impact of the projection on the measured variance [721, 722].

To this end, working with a 6×6 array, we implement a discretized, single-step version of this protocol. We initialize the system in the same initial state, $|\psi(0)\rangle = |\rightarrow \cdots \rightarrow\rangle$, and let the squeezing dynamics proceed for $t = 0.13$ μs. Then, we perform a 25° rotation around the y-axis in order to nearly align the noise distribution's major axis parallel to the equator. The subsequent dynamics of the squeezing parameter are shown in Fig. 4.8 (green data). Three effects are observed. First, the optimal squeezing occurs at a later time, $t^\star \sim 0.45$ μs. Second, consistent with the intuition above, the system remains near its optimal squeezing value for approximately twice as long. Third, the value of the

[3] The simulation takes into account all the known experimental imperfections as follows [676]. 1) Missing atoms: On average, a fraction $\eta = 2\%$ of the atoms remains in the state $|g\rangle$ after excitation and hence do not participate in the dynamics and are finally imaged as a spin $|\uparrow\rangle$. 2) Finite-duration pulses, reducing the initial polarization by 1%. 3) Measurement errors: An atom in $|\uparrow\rangle$ ($|\downarrow\rangle$) has a probability $\sim 2.5\%$ ($\sim 1.0\%$) to be detected in the opposite state due to the efficiency of the de-excitation pulse and collisions with the background gas. 4) Positional disorder, which is negligible. 5) Van der Waals interaction, which is also negligible. Simulating missing atoms and positional disorder requires significant sampling, which we find converges after ~ 100 samples.

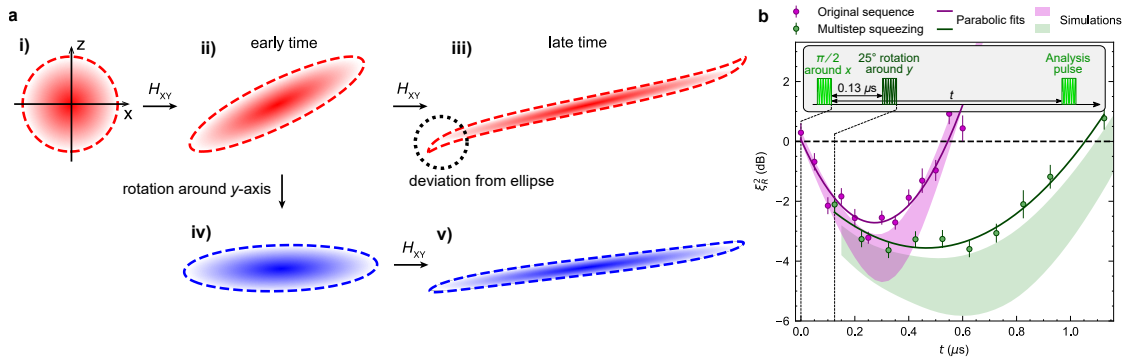

Figure 4.8: Multi-step spin squeezing protocol. (a), Schematic depicting the multi-step squeezing protocol. i) In a semi-classical description, the y-polarized initial state $|\psi(0)\rangle$ can be treated as a Gaussian distribution with the same variance $\sim \sqrt{N}$ along the z and x axes (i.e. a disc in the $x-z$ plane). ii), In normal spin squeezing dynamics, each point rotates around the z-axis with an angular velocity proportional to its z polarization. Consequently, the disc approximately deforms into an ellipse. iii) Due to the curvature of the Bloch sphere, the distribution deviates from a perfect ellipse (which happens at earlier times for larger z). Optimal squeezing is achieved when such deviation becomes larger than the minor-axis of the ellipse. iv), In multi-step squeezing protocol, before the deviation becomes the bottleneck, the major axis of the ellipse is rotated towards x-axis. v) As the typical z value of the distribution becomes smaller, the impact of non-elliptical deviation gets delayed to later times. (b), Measurements of the squeezing parameter obtained with two different spin squeezing protocols for a 6×6 array. The first one (purple dots) is the original sequence (Fig. 4.5c). The second one (dark green dots) is a multi-step sequence depicted in the inset, where an additional 25° rotation pulse is used to rotate the elliptical noise distribution toward the equator. The solid curves are parabolic fits to guide the eye. The shaded regions show the simulations including $97.5 \pm 1\%$ (resp. $99 \pm 1\%$) detection efficiency of $|\uparrow\rangle$ (resp. $|\downarrow\rangle$).

optimal squeezing parameter is improved by approximately 1 dB, reaching a value of -3.6 ± 0.3 dB.

4.2.5 Freezing spin squeezed states

In order to perform sensing, it is desirable to freeze the squeezing dynamics while acquiring the signal of interest. The simplest way to do so is to turn off the Hamiltonian. However, it is challenging to directly turn off the dipolar exchange interaction between the Rydberg atoms.

To this end, we utilize an alternate approach, where Floquet driving [206, 713] engineers an effective dipolar Heisenberg interaction, $H_{\text{Heis}} = -\frac{2J}{3}\sum_{i<j}\frac{a^3}{r_{ij}^3}\vec{\sigma}_i \cdot \vec{\sigma}_j$, from our original XY model. Crucially, the Heisenberg interaction commutes with all collective spin operators, ensuring that: (i) it does not change the spin squeezing and (ii) it does not affect the sensing signal associated, for example, to the presence of a uniform external field [4].

[4]The Floquet sequence that generates the Heisenberg interaction leads to a rescaling of the strength an external field by a factor of $1/3$.

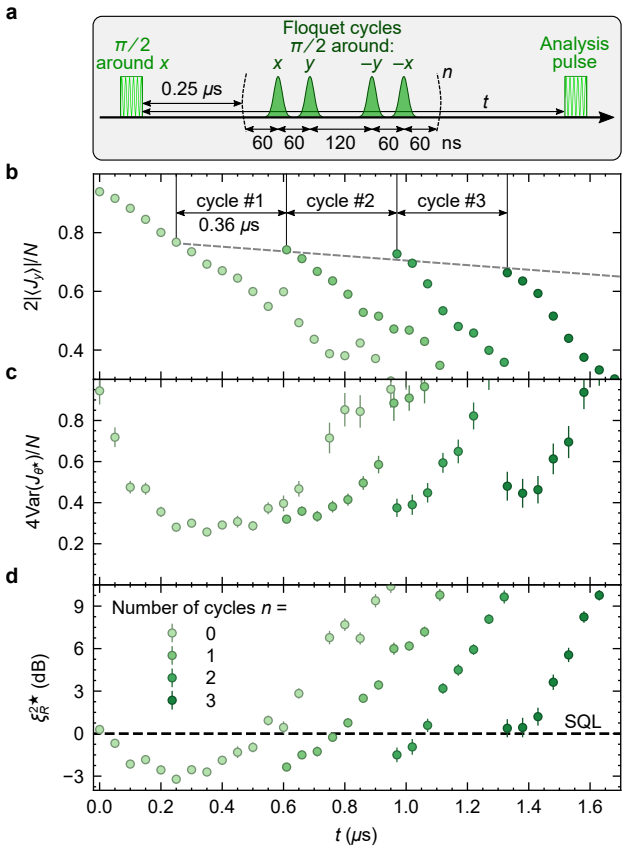

Figure 4.9: Floquet engineering to freeze spin squeezing. (a), Experimental WAHUHA sequence using Floquet engineering to realize an effective dipolar Heisenberg interaction in a $N = 6 \times 6$ array. The system is periodically driven using n Floquet cycles, each composed of four $\pi/2$ Gaussian microwave pulses (of half-width 6.5 ns at $1/\sqrt{e}$), whose phases are chosen to realize rotations around the $(x, y, -y, -x)$ axes. (b), (c), and (d), Spin length $|\langle J_y \rangle|$, minimal variance $\mathrm{Var}(J_{\theta^\star})$, and squeezing parameter ξ_R^2 as a function of the total interaction time t for different numbers, n, of applied Floquet cycles. The grey dashed line in **b** is a guide to the eye to highlight the spin length measured immediately after each Floquet cycle.

To explore this behavior, we let our system evolve to the optimal squeezing time and then attempt to freeze the dynamics via the Floquet WAHUHA sequence (Fig. 4.9a) [219]. A full Floquet cycle lasts $t_\mathrm{F} = 0.36$ μs and for rapid driving, $Jt_\mathrm{F} \ll 2\pi$, the time-averaged Hamiltonian is approximately H_Heis [713]. We repeat this experiment for different numbers of Floquet cycles ranging from $n = 0$-3. The Floquet dynamics of $|\langle J_y \rangle|$ and $\mathrm{Var}(J_{\theta^\star})$ are illustrated in Fig. 4.9b,c. For perfectly frozen dynamics, each set of curves (with different n) would simply be off-set in time from one another. This expectation is in good agreement with the data. Indeed, we observe that the dynamics of $|\langle J_y \rangle|$ are translated in time, except for a small downward drift (indicated by the grey dashed line in Fig. 4.9b). We

note that this downward drift is significantly weaker than the intrinsic dynamics of $|\langle J_y \rangle|$. Comparable behaviour is observed for $\mathrm{Var}(J_{\theta^\star})$ [Fig. 4.9c]. Finally, as illustrated by the squeezing parameter in Fig. 4.9d, the Floquet sequence prolongs the time-scale over which squeezing remains below the SQL by nearly a factor three.

4.2.6 Conclusion and outlook

To conclude, our work represents the first observation of scalable spin squeezing in a many-body system with short-range, power-law interactions. It is complementary to the recent results obtained with Rydberg-dressed atoms [723, 724] and long-range interactions in an ion string [725]. Our findings and methods are applicable to any quantum systems implementing the dipolar XY Hamiltonian, such as molecules [695, 710–712] or solid-state spin defects [9]. Within the context of tweezer arrays, our work lays the foundation for several research directions. First, by generalizing our approach to alkaline-earth Rydberg tweezer arrays [576, 726, 727], it may be possible to map the spin squeezing from the Rydberg manifold to the so-called clock transition, in order to improve tweezer-based atomic clocks [728, 729]. Second, by investigating squeezing as a function of the initial polarization, e.g. by introducing disorder in the initial state preparation, it may be possible to test theoretical predictions that spin squeezing in short-range interacting systems is fundamentally distinct from that achieved in all-to-all coupled systems [708]. Finally, by implementing a continuous version of the multi-step squeezing protocol, it may be possible to improve the scaling of the observed spin squeezing toward the Heisenberg limit.

Chapter 5

Characterizing interacting spin defects in solids by dynamical properties

Strongly interacting spin defects in solids, as a platform to study many-body quantum dynamics, sits at the interface between condensed matter, material and AMO physics [6–9, 51]. On the one hand, like other AMO systems, more detailed properties of the microscopic quantum degrees of freedom are known in the spin defect ensembles than in those typical systems studied in traditional condensed matter physics, such as high-temperature superconductors. On the other hand, the synthesis and fabrication procedure of the solid-state spin defects is under much less control than other AMO systems, such as optical lattice and optical tweezer arrays. Therefore, it is sometimes still challenging to fully characterize such systems before utilizing them in quantum sensing or simulation. While the most direct approach for characterizing a strongly-interacting system is to measure the time-evolution of its full many-body state, it is generally impractical as one usually only have limited control and access to a certain subset of the system's observables. Nevertheless, it turns out that some simple dynamical properties, even decoherence process (often referred to as T_2 decay) can reveal considerable amount of knowledge of the system, such as dimensionality, interaction range, and relative importance of different defects. This chapter, combining theory with experiment, will present how decoherence dynamics can be used to characterize spin defect systems.

5.1 Probing many-body dynamics in a two-dimensional dipolar spin ensemble

5.1.1 Introduction

Understanding and controlling the interactions between a single quantum degree of freedom and its environment represents a fundamental challenge within the quantum sciences [216, 730–737]. Typically, one views this challenge through the lens of mitigating decoherence—enabling one to engineer a highly coherent qubit by decoupling it from the environment [216, 731–733, 738–740]. However, the environment itself may consist of a strongly-interacting many-body system, which naturally leads to an alternate perspective; namely, using the decoherence dynamics of the qubit to probe the fundamental properties of the many-body system [734, 735, 741–746].

The complementary goals of probing and eliminating many-body noise have motivated progress in magnetic resonance spectroscopy for decades [734, 735, 741–744, 747], and more recently have re-emerged in the study of solid-state spin ensembles containing optically-polarizable color centers. The ability to prepare spin-polarized pure states enables fundamentally new prospects in quantum science, from the exploration of novel phases of matter [226] to the development of new sensing protocols [748]. Prospects for optically-polarizable spin ensembles in quantum sensing and simulation could be further enhanced by moving to two-dimensional systems, which represents a long-standing engineering challenge for the color-center community [699, 749, 750]. Despite continued advances in fabrication, the stochastic nature of defect generation strongly constrains the systems one can create. The potential rewards are substantial enough to merit repeated engineering efforts: Two-dimensional, long-range interacting spin systems are known to host interesting ground state phases such as spin liquids [688, 751, 752]. Moreover, two-dimensional spin ensembles enable improved sensing capabilities owing to increased coherence times and uniform distance from the target.

In this section, we investigate many-body noise generated by a thin layer of paramagnetic defects in diamond. Specifically, we combine nitrogen delta-doping during growth with local electron irradiation to fabricate a diamond sample (S1) where paramagnetic defects are confined to a layer whose width is, in principle, much smaller than the average spin-defect spacing [Fig. 5.1(a, b)] [699, 749, 750].

This layer contains a hybrid spin system consisting of two types of defects: spin-1 nitrogen-vacancy (NV) centers and spin-1/2 substitutional nitrogen (P1) centers. The dilute NV centers can be optically initialized and read-out, making them a natural probe of the many-body noise generated by the strongly-interacting P1 centers. In addition, we demonstrate a complementary role for the NV centers, as a source of spin polarization for the optically-dark P1 centers; in particular, by using a Hartmann-Hahn protocol, we directly transfer polarization between the two spin ensembles.

We characterize the P1's many-body noise via the decoherence dynamics of NV probe spins. To elucidate our results, we first present a theoretical framework that unifies and generalizes existing work, predicting a non-trivial temporal profile that exhibits a crossover between two distinct stretched exponential decays (for the average coherence of the probe spins) [Fig. 5.1] [734, 741–744, 747, 753]. Beyond solid-state spin systems, the framework naturally extends to a broader class of quantum simulation platforms, including trapped ions, Rydberg atoms, and ultracold polar molecules [72]. Crucially, we demonstrate that the associated stretch powers contain a wealth of information about both the static and dynamical properties of the many-body spin system.

We focus on three such properties. First, the stretch power contains a direct signature revealing the dimensionality of the disordered many-body system. Unlike previous work on lower-dimensional ordered systems in magnetic resonance spectroscopy [754–756], we cannot leverage conventional methods such as X-ray diffraction to characterize our disordered spin ensemble. To the best of our knowledge, studying the decoherence dynamics provides the only robust method to determine the effective dimensionality seen by the spins.

Second, the stretch power of the NV centers' decoherence can also distinguish between different forms of spectral diffusion, shedding light on the nature of local spin fluctuations. In particular, we demonstrate that the P1 spin-flip dynamics are inconsistent with the conventional expectation of telegraph noise, but rather follow that of a Gauss-Markov process (Table 5.1). Understanding the statistical properties of the many-body noise and the precise physical settings where such noise emerges remains the subject of active debate [732, 734, 744, 757–763].

Finally, the crossover in time between different stretch powers allows one to extract the many-body system's correlation time. We demonstrate this behavior by actively controlling the correlation time of

the P1 system via polychromatic driving, building upon techniques previously utilized in broadband decoupling schemes [764].

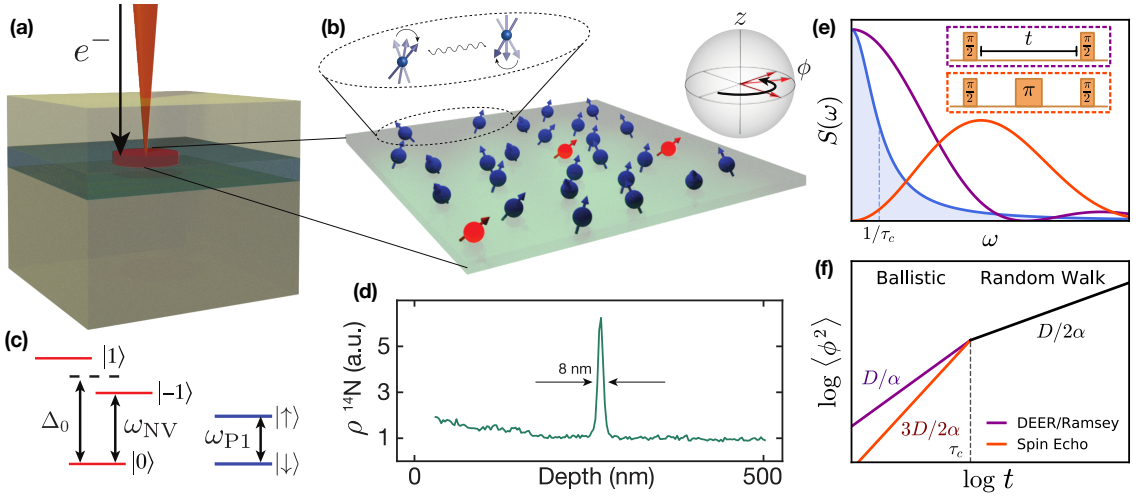

Figure 5.1: Experimental platform and theoretical framework (a) A delta-doped layer of ^{14}N (green) is grown on a diamond substrate. NV centers are created via local electron irradiation (orange beam) and subsequent high-temperature annealing. (b) Schematic depiction of a two-dimensional layer of NV (red) and P1 (blue) centers. Dilute NV centers function as probe spins of the dense, disordered P1 system. The P1s exhibit spin-flip dynamics driven by magnetic dipole-dipole interactions (zoom). Ising interactions with the P1 system cause the NV to accumulate phase, ϕ, during noise spectroscopy (Bloch sphere). (c) NV and P1 level structure in the presence of a magnetic field, B, applied along the NV axis. We work within an effective spin-1/2 subspace of the NV center, $\{|0\rangle, |-1\rangle\}$, with level splitting, ω_{NV}. The corresponding P1 splitting, ω_{P1}, is strongly off-resonant from the NV transition. (d) Secondary ion mass spectrometry (SIMS) measurement of the density of ^{14}N as a function of depth for sample S1. The presence of a 2D layer is indicated by a sharp Nitrogen peak with a SIMS-resolution-limited 8 nm width. (e) The overlap between the many-body spectral function (blue) and the power spectrum of the filter function $|f(\omega;t)|^2$ determines the variance of the phase $\sim \chi(t)$ [Eqn. 5.2]. $|f(\omega;t)|^2$ for both a Ramsey/DEER pulse sequence (purple) and a spin echo pulse sequence (orange) are shown. (f) Schematic depiction of the variance of the phase, $\langle \phi^2 \rangle = -2 \log C(t)$, as a function of the measurement duration t, for both Ramsey/DEER (purple) and spin echo (orange). The labeled slopes indicate the predicted stretch powers in both the early-time ballistic regime and the late-time random-walk regime [Table 5.1]; the crossover occurs at the correlation time, τ_c.

5.1.2 Theoretical framework for decoherence dynamics induced by many-body noise

We first outline a framework, building upon classic results in NMR spectroscopy, for understanding the decoherence dynamics of probe spins coupled to an interacting many-body system; this will enable us to present a unified theoretical background for understanding the experimental results in subsequent sections [734, 742, 743, 747, 753, 765–767]. The dynamics of a single probe spin generically depend on three properties: (i) the nature of the system-probe coupling, (ii) the system's

many-body Hamiltonian H_{int}, and (iii) the measurement sequence itself. Crucially, by averaging across the dynamics of many such probe spins, one can extract global features of the many-body system (Fig. 5.1b). We distinguish between two types of ensemble averaging which give rise to distinct signatures in the decoherence: (i) an average over *many-body trajectories* (i.e. both spin configurations and dynamics) yields information about the microscopic spin fluctuations (for simplicity, we focus our discussion on the infinite-temperature limit, and the analysis can be extended to finite temperature), (ii) an average over *positional randomness* (i.e random locations of the system spins) yields information about both dimensionality and disorder.

To be specific, let us consider a single spin-1/2 probe coupled to a many-body ensemble via long-range, $1/r^{\alpha}$ Ising interactions:

$$H_z = \sum_i \frac{J_z}{r_i^{\alpha}} \hat{s}_p^z \hat{s}_i^z, \tag{5.1}$$

where r_i is the distance between the probe spin $\hat{s}_p$ and the i-th system spin $\hat{s}_i$, and Ising coupling strength J_z implicitly includes any angular dependence. Such power-law interactions are ubiquitous in solid-state, atomic and molecular quantum platforms (e.g. RKKY interactions, electric/magnetic dipolar interactions, van der Waals interactions, etc.).

Physically, the system spins generate an effective magnetic field at the location of the probe (via Ising interactions), which can be measured with Ramsey spectroscopy [inset, Fig. 5.1(e)] [735]. In particular, we envision initially preparing the probe in an eigenstate of $\hat{s}_p^z$ and subsequently rotating it with a $\pi/2$-pulse such that the initial normalized coherence is unity, $C \equiv 2\langle \hat{s}_p^{\rangle} = 1$. The magnetic field, which fluctuates due to many-body interactions, causes the probe to Larmor precess (inset, Fig. 5.1(b)). The phase associated with this Larmor precession can be read out via a population imbalance, after a second $\pi/2$ pulse.

Average over many-body trajectories—For a many-body system at infinite temperature, $C(t) = 2\text{Tr}[\rho(t)\hat{s}_p^x]$, where $\rho(t)$ is the full density matrix that includes both the system and the probe. The spin fluctuations are determined by the microscopic details of the many-body dynamics whose full analysis is intractable. To make progress, we approximate each spin as a stochastic classical variable $\hat{s}_i^z(t) \rightarrow s_i^z(t)$. The statistical properties of such variables, and their resulting ability to capture the experimental observations, provide important insights into the nature of fluctuations in strongly-

interacting spin systems.

The phase of the Larmor precession is given by $\phi(t) = \int_0^t dt'\, J_z \sum_i s_i^z(t')/r_i^\alpha$. Assuming that $\phi(t)$ is Gaussian-distributed, one finds that the average probe coherence decays exponentially as $C(t) = \langle \mathrm{Re}[e^{-i\phi(t)}]\rangle = e^{-\langle\phi^2/2\rangle}$, where $\langle\phi^2\rangle \sim \sum_i J_z^2 \chi(t)/r_i^{2\alpha}$ (Appendix D.1.1) [732, 741, 763, 768]. Here, $\chi(t)$ encodes the response of the probe spins to the noise spectral density, $S(\omega)$, of the many-body system:

$$\chi(t) \equiv \int d\omega\, |f(\omega;t)|^2 S(\omega), \tag{5.2}$$

where $f(\omega;t)$ is the filter function associated with a particular pulse sequence (e.g. Ramsey spectroscopy or spin echo) of total duration t (Fig. 5.1e).

Intuitively, $S(\omega)$ quantifies the noise power density of spin flips in the many-body system; it is the Fourier transform of the autocorrelation function, $\xi(t) \equiv 4\langle s_i^z(t) s_i^z(0)\rangle$, and captures the spin dynamics at the level of two-point correlations [769]. For Markovian dynamics, $\xi(t) = e^{-|t|/\tau_c}$, where τ_c defines the correlation time after which a spin, on average, retains no memory of its initial orientation. In this case, $S(\omega)$ is Lorentzian and one can derive an analytic expression for χ (Appendix D.1.1) [743, 747, 761, 765].

A few remarks are in order. First, the premise that many-body Hamiltonian dynamics produce Gaussian-distributed phases $\phi(t)$—while oft-assumed—is challenging to analytically justify [734, 743, 744, 757, 770]. Indeed, a well-known counterexample of non-Gaussian spectral diffusion occurs when the spin dynamics can be modeled as telegraph noise – i.e. stochastic jumps between discrete values $s_i^z = \pm s_i$ [744, 758]; the precise physical settings where such noise emerges remains the subject of active debate [732, 734, 744, 757–763]. Second, we note that our Markovian assumption is not necessarily valid for a many-body system at early times or for certain forms of interactions, which can also affect the decoherence dynamics.

Average over positional randomness—The probe's decoherence depends crucially on the spatial distribution of the spins in the many-body system. For disordered spin ensembles, explicitly averaging over their random positions yields a decoherence profile (Appendix D.1.1):

$$C(t) = \int \prod_{i=1}^{N} \frac{d^D r_i}{V} \exp\left[\frac{-J_z^2 \chi(t)}{2 r_i^{2\alpha}}\right] = e^{-an[J_z^2\chi(t)]^{D/2\alpha}}, \tag{5.3}$$

where a is a dimensionless constant, N is the number of system spins in a D-dimensional volume V at a density $n \equiv N/V$ [747]. By contrast, for spins on a lattice or for a single probe spin, the exponent of the coherence scales as $\sim J_z^2 \chi(t)$.

A resonance-counting argument underlies the appearance of both the dimensionality and the interaction power-law in Eqn. (5.3). Roughly, a probe spin is only coupled to system spins that induce a phase variance larger than some cutoff ϵ. This constraint on the minimum variance defines a volume of radius $r_{\max} \sim (J_z^2 \chi(t)/\epsilon)^{1/2\alpha}$ containing $N_s \sim n r_{\max}^D$ spins, implying that the total variance accrued at any given time is $\epsilon N_s \sim [J_z^2 \chi(t)]^{D/2\alpha}$. Thus, the positional average simply serves to count the number of spins to which the probe is coupled.

Decoherence profile—The functional form of the probe's decoherence, $C(t)$, encodes a number of features of the many-body system. We begin by elucidating them in the context of Ramsey spectroscopy. First, one expects a somewhat sharp cross-over in the behavior of $C(t)$ at the correlation time τ_c. For early times, $t \ll \tau_c$, the phase variance accumulates as in a ballistic trajectory with $\chi \sim t^2$, while for late times, $t \gg \tau_c$, the variance accumulates as in a random walk with $\chi \sim t$ [743, 753, 765]. This leads to a simple prediction: namely, that the stretch-power, β, of the probe's exponential decay [i.e. $-\log C(t) \sim t^\beta$] changes from D/α to $D/2\alpha$ at the correlation time [Fig. 5.1(f)].

Many-body noise properties	Measurement sequence	Early-time (ballistic regime) stretch power	Late-time (random walk regime) stretch power
Gauss – Markov Noise 	DEER/Ramsey	D/α	$D/2\alpha$
	Spin Echo	$3D/2\alpha$	$D/2\alpha$
Telegraph Noise 	DEER/Ramsey	D/α	$D/2\alpha$
	Spin Echo	$1 + D/\alpha$	$D/2\alpha$

Table 5.1: Predicted early and late-time stretch powers of the probe spin decoherence profile when coupled to a $D-$dimensional system via power-law Ising interactions $\sim 1/r^\alpha$. We distinguish between Gaussian and telegraph spin-flip noise in the many-body system, which gives rise to different predictions for the early-time spin echo stretch power.

Second, moving beyond Ramsey measurements by changing the filter function, one can probe more subtle properties of the many-body noise. In particular, a spin-echo sequence filters out the leading order DC contribution from the many-body noise spectrum, allowing one to investigate higher-frequency correlations of the spin-flip dynamics. Different types of spin-flip dynamics naturally lead

to different phase distributions. For the case of Gaussian noise, one finds that (at early times) $\chi \sim t^3$; however, in the case of telegraph noise the analysis is more subtle, since higher-order moments of $\phi(t)$ must be taken into account. This leads to markedly different early-time predictions for β—dependent on both the measurement sequence as well as the many-body noise [Table 5.1].

At late times, however, one expects the probe's coherence to agree across different pulse sequences and spin-flip dynamics. For example, in the case of spin-echo, the decoupling π-pulse [inset, Fig. 5.1(e)] is ineffective on timescales larger than the correlation time, since the spin configurations during the two halves of the free evolution are completely uncorrelated. Moreover, this same loss of correlation implies that the phase accumulation is characterized by incoherent Gaussian diffusion regardless of the specific nature of the spin dynamics (e.g. Markovian versus non-Markovian, or continuous versus telegraph).

5.1.3 Experimentally probing many-body noise in strongly-interacting spin ensembles

Our experimental samples contain a high density of spin-1/2 P1 centers (blue spins, Fig. 5.1b), which form a strongly-interacting many-body system coupled via magnetic dipole-dipole interactions [1]:

$$H_{\text{int}} = \sum_{i<j} \frac{J_0}{r_{ij}^3} \left[c_{ij}(\hat{s}_i^+ \hat{s}_j^- + \hat{s}_i^- \hat{s}_j^+) + \tilde{c}_{ij} \hat{s}_i^z \hat{s}_j^z \right], \tag{5.4}$$

where $J_0 = 2\pi \times 52$ MHz·nm^3, r_{ij} is the distance between P1 spins i and j, and $c, \tilde{c}$ capture the angular dependence of the dipolar interaction.

The probes in our system are spin-1 NV centers, which can be optically initialized to $|m_s = 0\rangle$ using 532 nm laser light. An applied magnetic field B along the NV axis splits the $|m_s = \pm 1\rangle$ states, allowing us to work within the effective spin-1/2 manifold $\{|0\rangle, |-1\rangle\}$.Microwave pulses at frequency ω_{NV} are used to perform coherent spin rotations (i.e. for Ramsey spectroscopy or spin echo) within this manifold (Fig. 5.1c).

Physically, the NV and P1 centers are also coupled via dipolar interactions. However, for a generic magnetic field strength, they are highly detuned, i.e. $|\omega_{\text{NV}} - \omega_{\text{P1}}| \sim$ GHz, owing to the zero-field splitting of the NV center ($\Delta_0 = 2\pi \times 2.87$ GHz) [Fig. 5.1(c)]. Since typical interaction strengths

[1] We note that H_{int} contains only the energy-conserving terms of the dipolar interaction

in our system are on the order of $\sim$ MHz, direct polarization exchange between an NV and P1 is strongly off-resonant. The strong suppression of spin-exchange interactions between NV and P1 centers simplifies the full magnetic dipole-dipole Hamiltonian to a system-probe Ising coupling of precisely the form given by Eqn. 5.1 with $\alpha = 3$.

Delta-doped sample fabrication—Sample S1 was grown via homoepitaxial plasma-enhanced chemical vapor deposition (PECVD) using isotopically purified methane (99.999% ^{12}C) [749]. The delta-doped layer was formed by introducing natural-abundance nitrogen gas during growth (5 sccm, 10 minutes) in between nitrogen-free buffer and capping layers. To create the vacancies necessary for generating NV centers, the sample was electron-irradiated with a transmission electron microscope set to 145 keV [750] and subsequently annealed at 850° C for 6 hours.

Two-dimensional spin dynamics—We begin by performing double electron-electron resonance (DEER) measurements on sample S1. While largely analogous to Ramsey spectroscopy (Table 5.1), DEER has the technical advantage that it filters out undesired quasi-static fields (e.g. from hyperfine interactions between the NV and host nitrogen nucleus) [699, 735]. As shown in Fig. 5.2(a) [blue data, inset], the NV's coherence decays on a time scale ~ 5 μs.

To explore the functional form of the probe NV's decoherence, we plot the negative logarithm of the coherence, $-\log C(t)$, on a log-log scale, such that the stretch power, β, is simply given by the slope of the data. At early times, the data exhibit $\beta = 2/3$ for over a decade in time [blue data, Fig. 5.2(a)]. At a timescale ~ 3 μs (vertical dashed line), the data crosses over to a stretch power of $\beta = 1/3$ for another decade in time. This behavior is in excellent agreement with that expected for two-dimensional spin dynamics driven by dipolar interactions [Fig. 5.1(f), Table 5.1].

For comparison, we perform DEER spectroscopy on a conventional three-dimensional NV-P1 system (sample S2 [2]). As shown in Fig. 5.2(a) (orange), the data exhibit $\beta = 1$ for a decade in time, consistent with the prediction for three-dimensional dipolar interactions [Table 5.1]. However, the

[2]The three-dimensional sample S2 was grown by depositing a 32 nm diamond buffer layer, followed by a 500 nm nitrogen-doped layer (99% ^{15}N), and finished with a 50 nm undoped diamond capping layer [699] (sample C041). Vacancies were created by irradiating with 145 keV electrons at a dosage of 10^{21} cm^{-2}, and vacancy diffusion was activated by annealing at 850°C for 48 hours in an Ar/Cl atmosphere. The resulting NV density is $\sim$ 0.4 ppm, obtained through instantaneous diffusion measurements. The P1 density is measured to be $\sim$ 20 ppm through a modified DEER sequence. The average spacing between P1 centers ($\sim$ 4 nm) is much smaller than the thickness of the nitrogen doped layer, ensuring three-dimensional behavior of the spin ensemble (Table 5.2).

crossover to the late-time "random walk" regime is difficult to experimentally access because the larger early-time stretch power causes a faster decay to the noise floor.

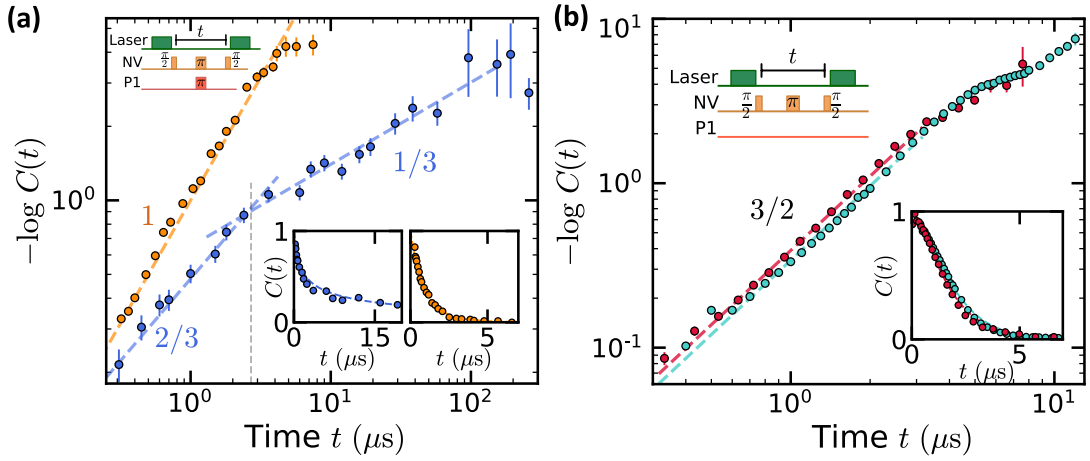

Figure 5.2: Spin decoherence dynamics from many-body noise in different dimensions (a) Depicts the normalized coherence for a DEER measurement on sample S1 (blue) and sample S2 (yellow) as a function of the free evolution time t. Dashed blue lines indicate the predicted early- and late-time stretch powers of 2/3 and 1/3, respectively, for a dipolar spin system in two dimensions. Dashed yellow line depicts the predicted early-time stretch power of 1 for a dipolar spin system in three dimensions [Table 5.1]. Together, these data demonstrate the two- and three-dimensional nature of samples S1 and S2, respectively. Lower right insets show the same data on a linear scale. Top left inset shows the DEER pulse sequence. (b) Spin echo measurements on three-dimensional dipolar spin ensembles in samples S3 (teal) and S4 (pink) clearly exhibit a stretch power of 3/2 (dotted lines) over nearly two decades in time. This is consistent with the presence of Gaussian noise and allows one to explicitly rule out telegraph noise. Lower right inset shows the same data on a linear scale. Top left inset shows the spin echo pulse sequence. All data are presented as mean values $\pm$ SEM.

Parameter	S1	S2	S3	S4
P1 Density	85(10) ppm · nm	20(1) ppm	∼100 ppm	∼100 ppm
NV Density	24(2) ppm · nm	0.43(1) ppm	∼0.5 ppm	∼0.5 ppm
Diamond cut	[100]	[100]	[111]	[100]
Nitrogen isotope	14	15	14	14
Isotopically purified	Yes	Yes	No	No
Additional Comments	CVD grown	CVD grown	Type Ib	Type Ib

Table 5.2: Summary of sample parameters for the spin decoherence experiment.

Characterizing microscopic spin-flip dynamics—To probe the nature of the microscopic spin-flip dynamics in our system, we perform spin-echo measurements on three dimensional samples [S3, S4

(Type IB)], which exhibit a significantly higher P1-to-NV density ratio[3]. For lower relative densities (i.e. samples S1 and S2), the spin echo measurement contains a confounding signal from interactions between the NVs themselves.

In both samples (S3, S4), we find that the coherence exhibits a stretched exponential decay with $\beta = 3/2$ for well over a decade in time [Fig. 5.2(b)]. Curiously, this is consistent with Gaussian spectral diffusion where $\beta = 3D/2\alpha = 3/2$ and patently inconsistent with the telegraph noise prediction of $\beta = 1 + D/\alpha = 2$. While in agreement with prior measurements on similar samples [762], this observation is actually rather puzzling and related to a question in the context of dipolar spin noise [732, 734, 735, 741–744, 747, 753, 757–763, 771–773]. In particular, one naively expects that spins in a strongly interacting system should be treated as stochastic binary variables, thereby generating telegraph noise; for the specific case of dipolar spin ensembles, this expectation dates back to seminal work from Klauder and Anderson [734]. The intuition behind this noise model is most easily seen in the language of the master equation—each individual spin "sees" the remaining system as a Markovian bath. The resulting local spin dynamics are then characterized by a series of stochastic quantum jumps that flip the spin orientation and give rise to telegraph noise. Alternatively, in the Heisenberg picture, the same intuition can be understood from the spreading of the operator $\hat{s}_i^z$; this spreading hides local coherences in many-body correlations, leading to an ensemble of telegraph-like, classical trajectories (Appendix D.1.1).

We conjecture that the observation of Gaussian spectral diffusion in our system is related to the presence of disorder, which strongly suppresses operator spreading [774]. To illustrate this point, consider the limiting case where the operator dynamics are constrained to a single spin. In this situation, the dynamics of $\hat{s}_i^z(t)$ follow a particular coherent trajectory around the Bloch sphere, and the rate at which the probe accumulates phase is continuous. Averaging over different trajectories of the coherent dynamics naturally leads to Gaussian noise (Appendix D.1.1).

Controlling the P1 spectral function—Next, we demonstrate the ability to directly control the P1

[3]Samples S3 and S4 used are synthetic type-Ib single crystal diamonds (Element Six) with intrinsic substitutional ^{14}N concentration ~ 100 ppm (calibrated with an NV linewidth measurement [364]). To create NV centers, the samples were first irradiated with electrons (2 MeV energy and 1×10^{18} cm^{-2} dosage) to generate vacancies, and then annealed in vacuum ($\sim 10^{-6}$ Torr) with temperature > 800°C. The NV densities for both samples were measured to be ~ 0.5 ppm using a spin-locking measurement (Table 5.2).

noise spectrum for both two- and three-dimensional dipolar spin ensembles (i.e. samples S1, S2). In particular, we engineer the shape and linewidth of $S(\omega)$ by driving the P1 system with a polychromatic microwave tone [764]. This drive is generated by adding phase noise to the resonant microwave signal at ω_{P1} in order to produce a Lorentzian drive spectrum with linewidth $\delta\omega$ [Fig. 5.3(c)]. While such techniques originated in the context of broadband noise decoupling [764], here, we directly tune the correlation time of the P1 system and measure a corresponding change in the crossover timescale between coherent and incoherent spin dynamics [743, 773].

Microscopically, the polychromatic drive leads to a number of physical effects. First, tuning the Rabi frequency, Ω, of the drive provides a direct knob for controlling the correlation time, τ_c, of the P1 system. Second, since the many-body system inherits the noise spectrum of the drive, one has provably Gaussian statistics for the spin variables s_i^z. Third, our earlier Markovian assumption is explicitly enforced by the presence of a Lorentzian noise spectrum. Taking these last two points together allows one to analytically predict the precise form of the NV probe's decoherence profile, $-\log C(t) \sim \chi(t)^{D/2\alpha}$, for either DEER or spin-echo spectroscopy:

$$\begin{aligned}\chi^{\mathrm{DEER}}(t) &= 2\tau_c t - 2\tau_c^2\left(1-\mathrm{e}^{-\frac{t}{\tau_c}}\right),\\ \chi^{\mathrm{SE}}(t) &= 2\tau_c t - 2\tau_c^2\left(3+\mathrm{e}^{-\frac{t}{\tau_c}}-4\mathrm{e}^{-\frac{t}{2\tau_c}}\right).\end{aligned} \tag{5.5}$$

We perform both DEER and spin-echo measurements as a function of the power ($\sim \Omega^2$) of the polychromatic drive for our two-dimensional sample (S1) [Fig. 5.3(a)]. As expected, for weak driving [top, Fig. 5.3(a)], the DEER signal (blue) is analogous to the undriven case, exhibiting a cross-over from a stretch power of $\beta = 2/3$ at early times to a stretch power of $\beta = 1/3$ at late times. For the same drive strength, the spin echo data (red) also exhibit a cross over between two distinct stretch powers, with the key difference being that $\beta = 3D/2\alpha = 1$ at early times. This represents an independent (spin-echo-based) confirmation of the two-dimensional nature of our delta-doped sample.

Recall that at late times (i.e. $t \gtrsim \tau_c$), one expects the NV's coherence $C(t)$ to agree across different pulses sequences [Fig. 5.1(f)]. This is indeed borne out by the data [Fig. 5.3]. In fact, the location of this late-time overlap provides a proxy for estimating the correlation time and is shown as the dashed grey lines in Fig. 5.3(a). As one increases the power of the drive [Fig. 5.3(a)], the noise spectrum,

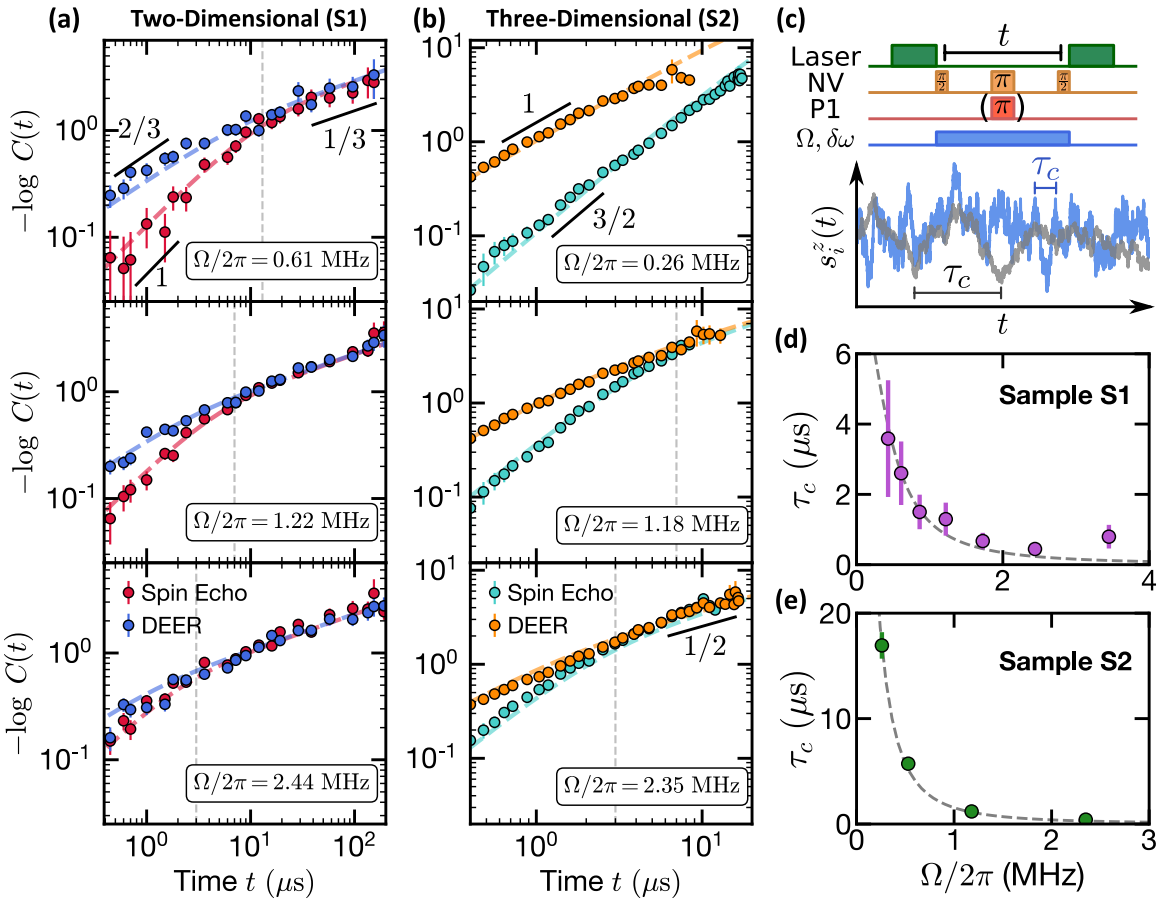

Figure 5.3: Tuning the correlation time of the bath (a,b) Measurements of DEER (blue, orange) and spin echo (red, teal) on two- and three-dimensional samples (S1, S2) for different powers of the polychromatic (i.e. incoherent) drive at fixed linewidth $\delta\omega = 2\pi \times (18, 20)$ MHz, respectively. The time at which the two signals overlap (vertical dashed lines) functions as a proxy for the correlation time and decreases as the power of the incoherent driving increases (top to bottom panels). The data is well-fit by analytic expressions for $[\chi(t)]^{D/2\alpha}$ [Eqn. 5.5] (dashed curves). Data are presented as mean values $\pm$ SEM. (c) An incoherent drive field (light blue) with power $\sim \Omega^2$ and linewidth $\delta\omega$ is applied to the P1 spins during the free evolution time t of both DEER and spin echo sequences in order to tune the correlation time of the many-body system. In this case, $s_i^z(t)$ evolves as a Gaussian random process schematic for short and long correlation time τ_c). (d,e) The correlation times, τ_c, extracted from fitting the data to Eqn. 5.5 for samples S1 (purple) and S2 (green) are plotted as a function of Ω, and agree well with a simple theoretical model (dashed grey curves). Data are presented as best fit values $\pm$ fitting error.

$S(\omega)$, naturally broadens. In the data, this manifests as a shortened correlation time, with the location of the DEER/echo overlap shifting to earlier time-scales [Fig. 5.3(a)].

Analogous measurements on a three-dimensional spin ensemble (sample S2), reveal much the same physics [Fig. 5.3(b)], with stretch powers again consistent with a Gauss-Markov prediction [Table 5.1]. For weak driving, $C(t)$ is consistent with the early-time ballistic regime for over a

decade in time [Fig. 5.3b, top panel]; however, it is difficult to access late enough time-scales to observe an overlap between DEER and spin echo. Crucially, by using the drive to push to shorter correlation times, we can directly observe the late-time random-walk regime in three dimensions, where $\beta = 1/2$ [Fig. 5.3b, middle and bottom panels].

Remarkably, as evidenced by the dashed curves in Fig. 5.3(a,b), our data exhibit excellent agreement—across different dimensionalities, drive strengths, and pulse sequences—with the analytic predictions presented in Eqn. 5.5. Moreover, by fitting $\chi^{D/2\alpha}$ simultaneously across spin echo and DEER datasets for each Ω, we quantitatively extract the correlation time, τ_c. Up to an $\mathcal{O}(1)$ scaling factor, we find that the extracted τ_c agrees well with the DEER/echo overlap time. In addition, the behavior of τ_c as a function of Ω also exhibits quantitative agreement with an analytic model that predicts $\tau_c \sim \delta\omega/\Omega^2$ in the limit of strong driving (Fig. 5.3d,e).

We emphasize that although one observes $\beta = 3D/2\alpha$ in both the driven [Fig. 5.3(a,b)] and undriven [Fig. 5.2(b)] spin echo measurements, the underlying physics is extremely different. In the latter case, Gaussian spectral diffusion emerges from isolated, disordered, many-body dynamics, while in the former case, it is imposed by the external drive.

5.1.4 A two-dimensional solid-state platform for quantum simulation and sensing

Our platform offers two distinct paths toward quantum simulation and sensing using strongly-interacting, two-dimensional, spin-polarized ensembles. First, treating the NV centers themselves as the many-body system directly leverages their optical polarizability. However, given their relative diluteness, it is natural to ask whether one can access regimes where the NV-NV interactions dominate over other energy scales. Conversely, treating the P1 centers as the many-body system takes advantage of their higher densities and interaction strengths, with the key challenge being that these dark spins cannot be optically pumped. Here, we demonstrate that both of these paths are viable for sample S1: (i) we show that the dipolar interactions among NV centers can dominate their decoherence dynamics, using advanced dynamical decoupling sequences; (ii) we demonstrate direct polarization exchange between NV and P1 centers, providing a mechanism to spin-polarize the P1 system.

Interacting NV ensemble—To demonstrate NV-NV-interaction-dominated dynamics, we com-

pare the decoherence timescales between spin echo, XY-8, and DROID dynamical decoupling sequences [211]. The spin echo effectively decouples static disorder, while the XY-8 sequence further decouples NV-P1 interactions. As depicted in Fig. 5.4(a), XY-8 pulses extend the spin-echo decay time (defined as the $1/e$-time) by approximately a factor of two. With NV-P1 interactions decoupled, our hypothesis is that the dynamics are now driven by dipolar interactions *between* the NV centers. To test this, we perform a DROID decoupling sequence, which eliminates the dipolar dynamics between NV centers [211] (Fig. 5.4b). Remarkably, this extends the coherence time by nearly an order of magnitude, demonstrating that NV-NV interactions are, by far, the dominant source of many-body dynamics in this regime. Moreover, the XY-8 decoherence thus provides an estimate of an average NV spin-spin spacing of 15 nm.

Interacting P1 ensemble—The polarization of the optically-dark P1 ensemble can be realized by either (i) working at low temperatures and large magnetic fields [414], or (ii) using NV centers to transfer polarization to the P1 centers. Here, we focus on the latter. While NV-P1 polarization transfer has previously been demonstrated [775, 776], it has not been measured in a two-dimensional system; indeed, conjectures about localization in such systems indicate that polarization transfer could be highly suppressed [421, 777].

To investigate, we employ a Hartmann-Hahn sequence designed to transfer polarization between NV and P1 spins in the rotating frame [775, 776]. In particular, we drive the NV and P1 spins independently, with Rabi frequencies Ω_{NV} and Ω_{P1}. When only the NV centers are driven, we are effectively performing a so-called spin-locking measurement [778]; for $\Omega_{\mathrm{NV}} = 2\pi \times 5$ MHz, we find that the NV centers depolarize on a timescale $T_{1\rho} = 1.05(3)$ ms [Fig. 5.4c, orange]. The data are cleanly fit by a simple exponential and consistent with phonon-limited decay [Fig. 5.4c, inset]. By contrast, when the driving satisfies the Hartmann-Hahn condition, $\Omega_{\mathrm{NV}} = \Omega_{\mathrm{P1}}$, the NV and P1 spins can resonantly exchange polarization. To characterize this, we fix $\Omega_{\mathrm{NV}} = 2\pi \times 5$ MHz and choose a spin-locking duration $t_s = 200$ μs. By sweeping the P1 Rabi frequency, we indeed observe a resonant polarization-exchange feature centered at $\Omega_{\mathrm{P1}} = 2\pi \times 5$ MHz with a linewidth $\sim 2\pi \times 1.2$ MHz [Fig. 5.4(d)], consistent with the intrinsic P1 linewidth. As illustrated in Figure 5.4(c), on resonance, the NV depolarization is significantly enhanced via polarization transfer to the P1 centers

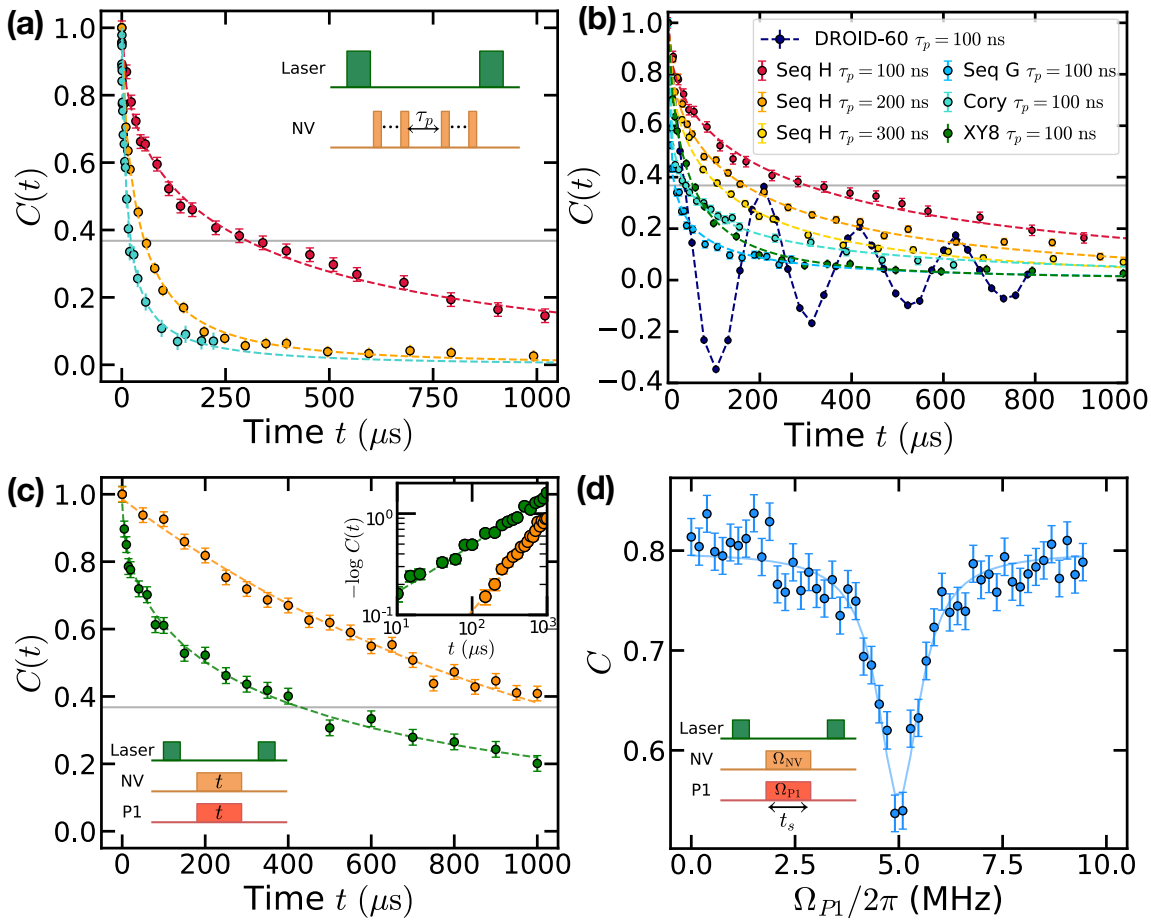

Figure 5.4: Hybrid two-dimensional spin system for simulation and sensing (a) We measure T_2 with spin echo (blue), XY-8 (orange) and DROID (red) pulse sequences with interpulse spacing $\tau_p = 100$ ns. The spin echo and XY-8 decoherence profiles are fitted by Eqn. 5.5 while DROID is fitted by a stretched exponential $\sim e^{-(t/T_2)^{0.5}}$. The $1/e$ lifetimes (gray line) for spin echo, XY-8 and DROID are 22 μs, 47 μs and 302 μs, respectively. Inset: schematic of dynamical decoupling sequence with interpulse spacing τ_p. (b) The measured decoherence profiles of variations on DROID-60 [210]. Due to imperfections in our composite microwave pulses, pulse error accumulates coherently in the DROID-60 sequence and a pronounced oscillation is observed (purple points). To avoid such oscillations, we implement sequences that do not require composite pulses, see e.g. Seqs. A, H, G in Fig. 9 of Ref. [210] The data exhibiting the longest coherence time (Seq. H, $\tau_p = 100$ ns, red points) are also shown in Figure 4(a) of the main text. (c) Spin-locked NV depolarization profile. Only NV centers (orange) or both NV and P1 centers (green) are driven at a Rabi frequency of $2\pi \times 5$ MHz. The resonant spin-exchange interactions reduce the spin-locking relaxation time $T_{1\rho}$ by a factor of ~ 3. Top inset shows the same data plotted on a log-log scale to elucidate stretch powers. Bottom inset: spin-locking pulse sequence. (d) Hartmann-Hahn polarization exchange resonance. The NV Rabi frequency Ω_{NV} is fixed at $2\pi \times 5$ MHz. When the P1 Rabi frequency Ω_{P1} matches Ω_{NV}, a reduction in contrast is induced by the resonant polarization exchange between NV and P1 centers. The data is fitted by a Lorentzian (dashed curve) with a linewidth of $2\pi \times 1.2$ MHz. Inset: Hartmann-Hahn pulse sequence, with fixed spin-locking duration $t_s = 200$ μs. All data are presented as mean values $\pm$ SEM.

and the data exhibit a three-fold decrease in the decay time. Moreover, the data are well-fit with a stretch power $\beta = 1/3$ [Fig. 5.4c, inset], which is also indicative of interaction-dominated decay [771].

5.1.5 Conclusion and Outlook

Our results demonstrate the diversity of information that can be accessed via the decoherence dynamics of a probe spin ensemble. For example, we shed light on a long-standing debate about the nature of spin-flip noise in a strongly-interacting dipolar system [732, 734, 744, 757–763, 772, 773]. Moreover, we directly measure the correlation time of the many-body system and introduce a technique to probe its dimensionality. This technique is particularly useful for disordered spin ensembles embedded in solids [779, 780], where a direct, non-destructive measurement of nanoscale spatial properties is challenging with conventional toolsets.

One can imagine generalizing our work in a number of promising directions. First, the ability to fabricate and characterize strongly-interacting, two-dimensional dipolar spin ensembles opens the door to a number of intriguing questions within the landscape of quantum simulation. Indeed, dipolar interactions in 2D are quite special from the perspective of localization, allowing one to experimentally probe the role of many-body resonances [421, 777]. In the context of ground state physics, the long-range, anisotropic nature of the dipolar interaction has also been predicted to stabilize a number of exotic phases, ranging from supersolids to spin liquids [688, 751]. Connecting this latter point back to noise spectroscopy, one could imagine tailoring the probe's filter function to distinguish between different types of ground-state order.

Second, dense ensembles of two dimensional spins also promise a number of unique advantages with respect to quantum sensing [699, 748, 749]. For example, a 2D layer of NVs fabricated near the diamond surface would exhibit a significant enhancement in spatial resolution (set by the depth of the layer) compared to a three-dimensional ensemble at the same density, ρ [749, 781]. In addition, for samples where the coherence time is limited by spin-spin interactions, a lower dimensionality reduces the coordination number and leads to an enhanced T_2 scaling as $n^{-\alpha/D}$.

Third, one can probe the relationship between operator spreading and Gauss-Markov noise by exploring samples with different relaxation rates, interaction power-laws, disorder strengths and spin

densities [757, 773]. One could also utilize alternate pulse sequences, such as stimulated echo, to provide a more fine-grained characterization of the many-body noise (e.g. the entire spectral diffusion kernel) [753, 757].

Finally, our framework can also be applied to long-range-interacting systems of Rydberg atoms, trapped ions, and polar molecules. In such systems, the ability to perform imaging and quantum control at the single-particle level allows for greater freedom in designing methods to probe many-body noise. As a particularly intriguing example, one could imagine a non-destructive, time-resolved generalization of many-body noise spectroscopy, where one repeatedly interrogates the probe without projecting the many-body system.

5.2 Coherent dynamics of strongly interacting electronic spin defects in hexagonal boron nitride

5.2.1 Introduction

Solid-state point defects with optically addressable electronic spin states have become a fertile playground for new quantum technologies [6, 7, 9, 51, 85, 228, 364, 782–792]. Significant progress has recently been made in creation, control and application of such spin-active quantum emitters in atomic-thin van der Waals materials [793–796]. From a wide range of contestant spin defects in these materials, the negatively charged boron vacancy center, V_B^- , in hexagonal boron nitride (hBN) has particularly attracted substantial research interest in the past few years [697, 797–804]. Importantly, it has been demonstrated that the spin degree of freedom of V_B^- can be optically initialized and readout, as well as coherently manipulated at room temperature. Compared to conventional spin qubits in three-dimensional materials, such as nitrogen-vacancy (NV) center in diamond, V_B^- features several unique advantages in quantum sensing and simulation. From the perspective of quantum sensing, the atomically-thin structure of hBN and the wide use of hBN as the encapusulation material allow the V_B^- sensor to be easily positioned in close proximity with the target materials to achieve unprecedented spatial resolution and sensitivity [798, 805–812]. On the quantum simulation front, the ability to prepare and control strongly interacting, 2D spin ensembles opens the door to exploring a number of intriguing many-body quantum phenomena [95, 182, 421, 573, 649, 813–816].

V_B^- in hBN, like solid-state spin defects in general, suffers from decoherence. To this end, research effort has been devoted to characterizing the coherence process of V_B^-. However, the measured spin echo timescale, T_2^{Echo}, in several studies varies from tens of nanoseconds to a few microseconds [797, 817–819]. This immediately begs the question that where does such discrepancy originate from, and what are the different decoherence mechanisms in dense ensemble of V_B^- ?

In this section, we present three main results. First, we introduce a robust differential measurement scheme to reliably characterize the spin coherent dynamics of V_B^- ensemble (Fig. 5.5 and Fig. 5.6). We observe spin-echo $T_2^{\text{Echo}} \approx 70$ ns across three hBN samples with distinct V_B^- densities (created via ion implantation with dosages spanning two orders of magnitude), consistent with the expectation

that the spin-echo coherence time is dominated by the Ising coupling to the nearby nuclear spin and dark electronic spin bath [817, 820]. Second, by applying a more advanced dynamical decoupling sequence, XY-8, to better isolate V_B^- from the bath spin environment [732, 821, 822], we observe substantial extensions in the measured coherent timescales, T_2^{XY8}. Interestingly, the extracted T_2^{XY8} decreases with increasing V_B^- density, indicating that the dipolar interaction within the V_B^- ensemble is critical for understanding the coherent dynamics and can be further utilized to directly estimate the concentration of V_B^- . To further corroborate this, we apply the DROID pulse sequence to decouple the $V_B^- - V_B^-$ dipolar interaction [210, 823], and achieve an additional $\sim$ 2-fold improvement in the measured coherence time, T_2^D. Finally, by comparing the experimentally measured T_2^{XY8} and T_2^D to Krylov numerical simulations, we directly estimate the spin density of V_B^- across three hBN samples. We find that the ratio of negatively charged V_B^- to total created boron vacancy defects (V_B) decreases significantly with increasing ion implantation dosage (Fig. 5.7).

5.2.2 Experimental system

To investigate the coherent spin dynamics of V_B^- ensemble at various defect densities, we prepare three hBN samples with different implantation dosages. Specifically, we irradiate hBN flakes (thickness $\sim$ 100 nm) using 3 keV He^+ ion beams with dose densities, 0.30 ± 0.03 nm^{-2} (sample S1), 1.1 ± 0.1 nm^{-2} (sample S2), and 10 ± 1 nm^{-2} (sample S3), respectively, to create V_B^- defects [800, 818]. Here error bars on the implantation dosages account for the current fluctuations during the implantation process. We remark that, given an ion implantation dosage, the total created V_B concentration can be estimated via SRIM simulation [824], yet the actual density of the negatively-charged V_B^- has remained unknown.

The V_B^- center has a spin triplet ground state ($|m_s = 0, \pm 1\rangle$), which can be initialized and read out via optical excitation and coherently manipulated using microwave fields [697, 803]. In the absence of any external perturbations, the $|m_s = \pm 1\rangle$ states are degenerate and separated from $|m_s = 0\rangle$ by $D_{gs} \approx 3.48$ GHz (Fig. 5.5b). In the experiment, we apply an external magnetic field $B \approx 250$ G along the c-axis of the hBN lattice to separate the $|m_s = \pm 1\rangle$ states via the Zeeman effect and isolate an effective two-level system $|m_s = 0, -1\rangle$. A microwave field is used to coherently manipulate the spin

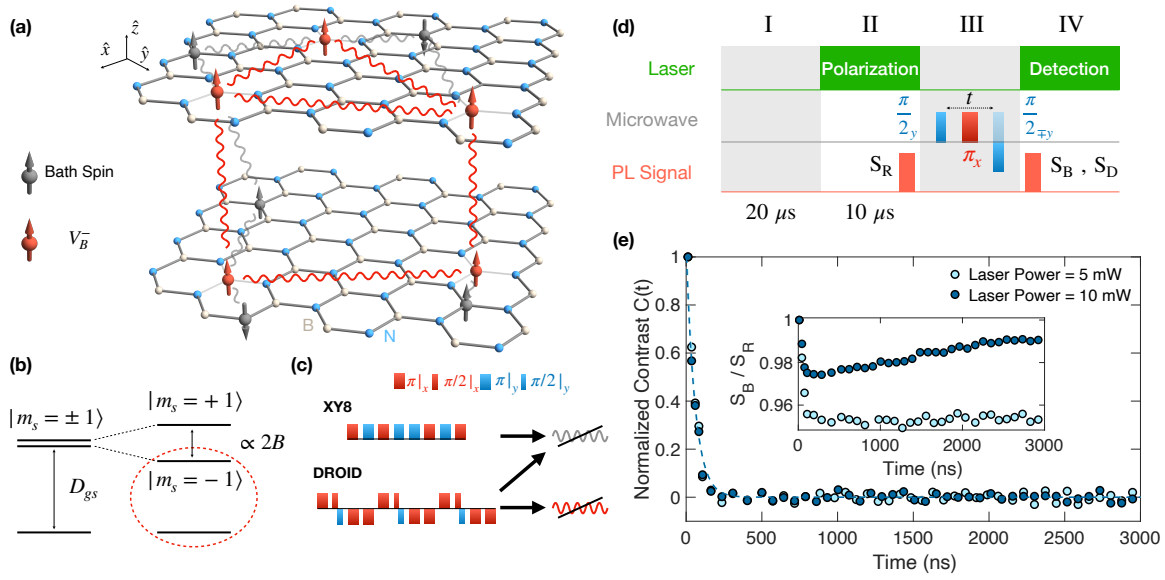

Figure 5.5: Spin dynamics of V_B^- ensemble (a) Schematic of V_B^- spin ensemble (red spins) inside hBN crystal lattice (Nitrogen–blue; Boron–white); $\hat{z}$ is defined along the c-axis (perpendicular to the lattice plane). $\hat{x}$ and $\hat{y}$ lie in the lattice plane, with $\hat{x}$ oriented along one of the three V_B^- Nitrogen bonds. Here we only include two layers for the purpose of demonstration, but all our samples have a thickness $\sim$ 100 nm. Two types of decoherence sources are presented here for V_B^- spin ensemble: the Ising coupling (grey wavy lines) to the bath spins (grey), and the dipolar interaction within V_B^- themselves (red wavy lines). (b) Energy level diagram of the defect spin ground-state. In the absence of any external perturbation, the $|m_s = \pm 1\rangle$ states are degenerate and separated by $D_{gs} \approx 3.48$ GHz from the $|m_s = 0\rangle$ state. Under an external magnetic field B along the c-axis of hBN, the degeneracy between $|m_s = \pm 1\rangle$ states are lifted via the Zeeman effect, with a splitting $\propto$ 2B. We choose $|m_s = 0\rangle$ and $|m_s = -1\rangle$ states as our two-level system. (c) Experimental pulse sequences for XY-8 (top) and DROID (bottom). The rotations along the positive $\hat{x}$ and $\hat{y}$ axes are plotted above the line, while the rotations along the negative axes are plotted below the line. (d) Differential measurement sequence for spin echo. I: 20 μs wait time to reach charge state equilibration. II: 10 μs laser pulse to initialize the V_B^- spin to $|m_s = 0\rangle$, with the reference signal, $S_R(t)$, collected at the end of the laser pulse. III: microwave wave pulses for spin echo measurement; for the bright signal, a final $\frac{\pi}{2}$ pulse along the $-\hat{y}$ axis is applied; while for the dark signal, a final $\frac{\pi}{2}$ pulse along the $+\hat{y}$ axis is applied to rotate the spin to an orthogonal state. IV: laser pulse to detect the spin state. (e) Spin echo measurement on sample S3 at two different laser powers. Without differential measurement, the measured signal, S_B/S_R exhibits a laser power dependence which comes from charge relaxation dynamics (inset). Using differential measurement, the measured contrast, $C(t)$, is independent of the laser power. Error bars represent 1 s.d. accounting statistical uncertainties.

ensemble with a Rabi frequency $\Omega \approx 83$ MHz (π-pulse length $\tau_\pi = 6$ ns). We note that such a strong Rabi drive is crucial for the high fidelity control of V_B^- , as the spin transition is largely broadened by the hyperfine interaction to the nearby nuclear spin bath.

5.2.3 Robust measurement scheme

To reliably probe the spin dynamics of a dense ensemble of V_B^- , we introduce a robust differential measurement scheme illustrated in Figure 5.5d [771, 825]. Specifically, after letting the spin system reach charge state equilibration for 20 μs without any laser illumination (I), we apply a 10 μs laser pulse (532 nm) to initialize the spin state of V_B^- (II), followed by the measurement pulse sequences (III). Taking spin echo coherent measurement as an example, we first apply a $\frac{\pi}{2}$-pulse along the $\hat{y}$ axis to prepare the system in a superposition state $\otimes_i \frac{|0\rangle_i+|-1\rangle_i}{\sqrt{2}}$, and then let it evolve for time t. A refocusing π-pulse along the $\hat{x}$ axis at time $t/2$ is used to decouple the spin ensemble from static magnetic noise. A final $\frac{\pi}{2}$-pulse along the $-\hat{y}$ direction rotates the spin back to the $\hat{z}$ axis for fluorescence detection (IV), and the measured photon count is designated as the bright signal, $S_B(t)$. By repeating the same sequence but with a final $\frac{\pi}{2}$-pulse along the positive $+\hat{y}$ axis before readout, we measure the fluorescence of an orthogonal spin state to be the dark signal, $S_D(t)$. The difference between the two measurements, $C(t) = [S_B(t) - S_D(t)]/S_R(t)$, can faithfully represent the measured spin coherent dynamics of V_B^- , where $S_R(t)$ is a reference signal we measure at the end of the initialization laser pulse (II).

Figure 5.5e shows the measured spin echo dynamics of the highest dosage hBN sample S3. We find that the measured fluorescence contrast, $S_B(t)/S_R(t)$ [$S_D(t)/S_R(t)$], changes dramatically with different laser powers (inset), originating from the charge state relaxation dynamics after the laser pumping. This is particularly prominent at high laser power, where the optical ionization of the defect charge state is enhanced. This effect can lead to an artifact in the extracted spin echo timescales, which may explain the previous discrepancy in the measured T_2^{Echo}. However, the obtained fluorescence contrast from differential measurement, $C(t)$, is consistent across different laser powers, enabling an accurate extraction of the spin coherent timescales.

A few remarks are in order. First, this differential measurement scheme has been widely employed in the studies of the dense ensemble of NV centers in diamond to counter the ionization process [364, 412, 649, 771, 826]. Secondly, previous theoretical studies predict that the ionization of V_B^- requires significantly higher energy ($\sim$ 4.46 eV) than the ionization of NV centers ($\sim$ 2.7 eV) [826–828]. This may explain why our experimental observation that the two-photon ionization process for V_B^-

only becomes evident under strong laser power ($\sim$ 10 mW); while the ionization of NV centers happens at $\sim 10-20$ μW laser [771, 826]. Third, we note that unlike neutral NV^0 centers which emit fluorescence starting at 575 nm, neutral boron-vacancy V_B^0 has not been directly observed from photoluminescence signals. Therefore the proposed ionization process only offers a potential explanation of the experiment.

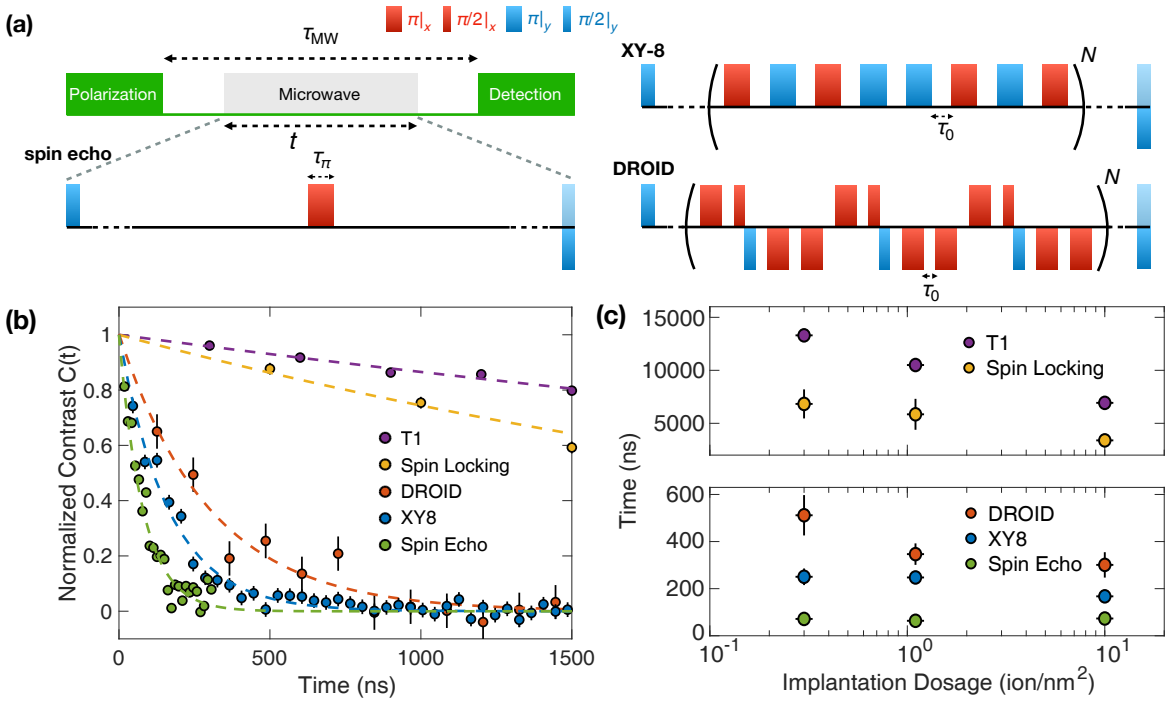

Figure 5.6: Spin coherent and relaxation dynamics. a) Sequence schematic for laser and microwave. The duration between polarization and detection, τ_{MW}, is fixed around 3500 ns to account for the effect of T_1 relaxation on the T_2 measurement. In spin echo sequence, π-pulse duration, τ_π, is fixed at 6 ns with adjusted microwave power referencing to the Rabi oscillation recorded. In both XY-8 and DROID sequences, the pulse interval τ_0 is fixed at 4 ns, and the coherent timescales are measured by varying N. To increase the total number of data points, Mmeasurement is taken every 4 pulses in XY-8, and the DROID sequence is a truncated version of the original DROID sequence to increase the total number of data points [210]. (b) The spin coherent and relaxation timescales measured on sample S3 with the highest ion implantation dosage. Dashed lines are data fitting with single exponential decays. (c) The extracted coherence timescales T_2 and relaxation timescales T_1 for the three hBN samples.

5.2.4 Coherent dynamics

Equipped with the robust differential measurement scheme, we now turn to the investigation of coherent dynamics of V_B^- ensemble at various defect densities. The decoherence mechanism of V_B^-

consists of two major contributions: (1) the Ising coupling to the bath spins in the environment; (2) the dipolar interaction between V_B^- ensemble themselves (Figure 5.5a) [210]. To isolate the effect of each component, we measure the coherent dynamics of V_B^- using three different dynamical decoupling pulse sequences (Fig. 5.6a).

We start with the spin echo pulse sequence, which is commonly used to characterize the coherent properties of a quantum system. Spin echo can decouple the static components of the Ising coupling between V_B^- and the spin bath. By fitting the measured dynamics to a single exponential decay, $\sim e^{-(t/T_2^{\text{Echo}})}$, we extract $T_2^{\text{Echo}} \approx 70$ ns across all three hBN samples (Figure 5.6b). This observation indicates that the spin echo decoherence of V_B^- is predominantly limited by the spin fluctuation within the environmental spin bath, which does not depend on the V_B^- concentration. Indeed, a previous study has shown that the Ising coupling to the local nuclear spin bath (nitrogen-14, boron-10, and boron-11), as well as the dark electronic spins, can accurately account for the measured spin echo timescales [817].

Next, we apply a more advanced dynamical decoupling pulse sequence, XY-8, to better decouple the V_B^- ensemble from the environment. Instead of a single refocusing π-pulse, XY-8 employs a series of π-pulses with alternating phases (Fig. 5.5c). We fix the time intervals between pulses, $\tau_0 = 4$ ns, sufficiently smaller than the correlation timescale of the local spin bath (estimated from the spin echo timescale) [573, 649]. As a result, XY-8 is expected to further suppress the fluctuations within the local spin noise and improve the measured spin coherent timescales. This is indeed borne out by our data. As shown in Figure 5.6, the extracted coherence times, T_2^{XY8}, are significantly extended in all three samples. In contrast to the previous spin echo measurement where T_2^{Echo} does not depend on V_B^- density, here we observe that $T_2^{\text{XY8}} = [250 \pm 35]$ ns of sample S1 is longer than sample S3, $T_2^{\text{XY8}} = [167 \pm 10]$ ns. This suggests that $V_B^- - V_B^-$ interaction plays a key role in the measured XY-8 coherent timescales. Indeed, in XY-8 measurement, since the refocusing π-pulses flip all V_B^- spins together, there is no suppression of the dipolar interaction between V_B^- .

To this end, we introduce DROID pulse sequence to further decouple the dipolar interaction within V_B^- themselves (Fig. 5.5c) [210]. By applying a series of $\pi/2$ rotations along different spin axes to change the frames of interaction (also known as toggling frames), DROID modifies the dipolar

Hamiltonian to an isotropic Heisenberg interaction, where the initial state, $\otimes_i \frac{|0\rangle_i + |-1\rangle_i}{\sqrt{2}}$, constitutes an eigenstate of the Heisenberg interaction, and consequently does not dephase. As shown in Figure 5.6, the measured coherent timescales, T_2^{D}, indeed exhibit an approximate two-fold increase compared to T_2^{XY8} across all three samples, agreeing with the cancellation of dipolar-induced decoherence. Interestingly, we also observe that the spin relaxation time, T_1, and spin-locking time, T_1^{ρ}, both decrease with increasing ion implantation dosages (Figure 5.6b). In principle, the dipolar interaction between $\mathrm{V_B^-}$ will not lead to a decrease of T_1 due to the conservation of total spin polarization during the flip-flop process. This T_1 related trend may be attributed to the presence of lattice damage during the implantation process or local charge state fluctuations [771]. We note that the spin relaxation process will introduce an additional decay to the coherent dynamics. However, the measured T_1 and T_1^{ρ} are much longer than T_2 across all three samples at room temperature (Figure 5.6). Nevertheless, we fix the duration between the polarization (II) and the read-out (IV) laser pulses to account for the effect of T_1 relaxation on the T_2 measurement.

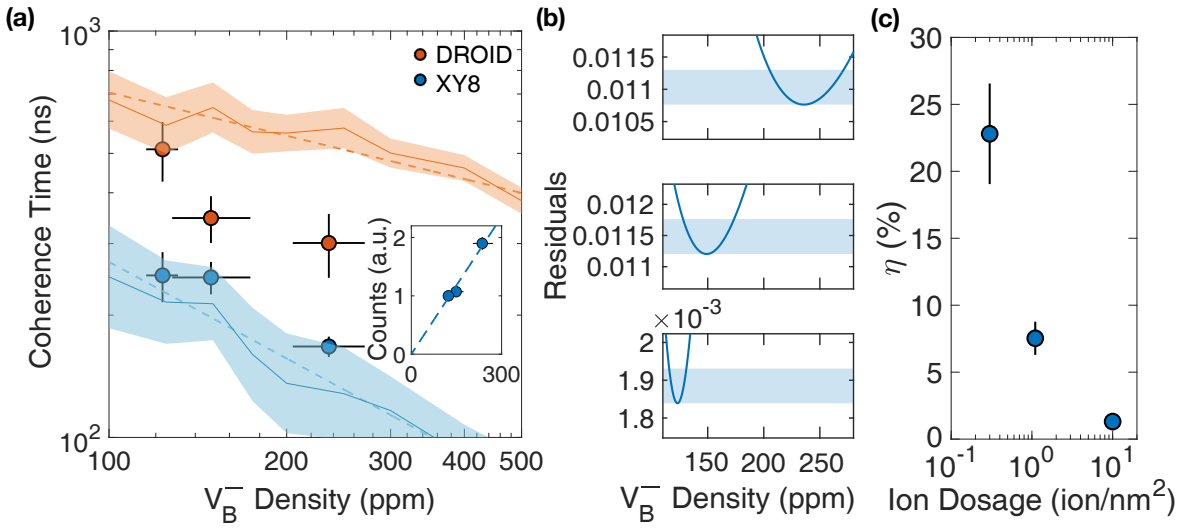

Figure 5.7: Characterizing $\mathrm{V_B^-}$ density (a) Comparison between the experimentally measured and numerically simulated coherent timescales, T_2, for DROID and XY-8 pulse sequences. The solid lines show the timescales extracted from simulations with error bars plotted as semi-transparent colored areas. To determine $\mathrm{V_B^-}$ densities for the three hBN samples, we minimize the relative squared residuals of T_2^{XY8} and T_2^{D} between simulations and experiments. Inset: fluorescence counts versus extracted densities after contrast adjustment. (b) The sum of squared relative residuals of XY-8 and DROID between the experimental values and the fitted T_2 plotted against $\mathrm{V_B^-}$ densities used in simulations. From bottom to top are residuals for sample S_1, S_2, and S_3 respectively, and the blue shaded regions are the 5% error ranges from the minimum residuals. (c) The measured $\mathrm{V_B^-}$ charge state ratio $\eta = \rho_{\mathrm{V_B^-}} / \rho_{\mathrm{V_B}}$ for three hBN samples with different ion implantation dosages.

5.2.5 Extracting V_B^- density

The difference between T_2^{XY8} and T_2^D originates from the $V_B^- - V_B^-$ dipolar interaction, which can be used to estimate the density of V_B^- directly. In particular, by randomly positioning 12 electronic spins at different sampling concentrations, we construct the dipolar interacting Hamiltonian of the system,

$$\mathcal{H}_{\text{dip}} = \sum_{i<j} -\frac{J_0 \mathcal{A}_{i,j}}{r_{i,j}^3}(S_i^z S_j^z - S_i^x S_j^x - S_i^y S_j^y), \tag{5.6}$$

where $J_0 = 52$ MHz·nm^3, $\mathcal{A}_{i,j}$ and $r_{i,j}$ represent the angular dependence and the distance between the i^{th} and j^{th} V_B^- spins, and $\{S_i^x, S_i^y, S_i^z\}$ are the spin-1/2 operators for i^{th} V_B^- center. By evolving the many-body system under different pulse sequences and averaging the spin coherent signals across random spin positional configurations, we obtain the simulated results of the corresponding XY-8 and DROID coherent timescales (Fig. 5.7a) [364, 771, 829]. We observe from our simulation that both T_2^{XY8} and T_2^D indeed decrease with increasing V_B^- density, while T_2^D exhibits a longer timescale than T_2^{XY8} across the density range surveyed. By minimizing the relative squared residuals of T_2^{XY8} and T_2^D between simulation and experiment, we estimate the V_B^- concentration to be $\rho_{V_B^-}^{S1} \approx 123^{+8}_{-8}$ ppm, $\rho_{V_B^-}^{S2} \approx 149^{+25}_{-21}$ ppm, and $\rho_{V_B^-}^{S3} \approx 236^{+35}_{-31}$ ppm (Fig. 5.7a,b). The discrepancy between the measured and simulated timescales may stem from imperfect spin rotations in the experiment, as well as finite-size effects from the simulations. To further validate our V_B^- density estimation, we measure the fluorescence count rates for the three hBN samples and find them to be proportional to the estimated V_B^- densities $\rho_{V_B^-}$ (Fig. 5.7a inset Table 5.3).

Sample	S1	S2	S3
$\rho_{V_B^-}$ Extracted from Experiment (ppm)	123^{+8}_{-8}	149^{+25}_{-21}	236^{+35}_{-31}
Counts N ($\times 10^6$ photons/s)	0.64 ± 0.03	0.84 ± 0.03	1.44 ± 0.04
Contrast C (%)	4.74 ± 0.27	3.89 ± 0.19	4.00 ± 0.17
Adjusted Counts N_A (a.u.)	1.00 ± 0.06	1.07 ± 0.06	1.90 ± 0.11

Table 5.3: Summary of the estimated V_B^- concentration from coherent measurement, fluorescence counts, and contrasts for the three hBN samples

We highlight that although the ion implantation dosage spans nearly two orders of magnitude across three hBN samples, the estimated V_B^- density only differs approximately by a factor of 2. This

indicates that with larger implantation dosage, one may create more V_B defects, but most of them remain charge neutral [826, 830–832]. Using SRIM (Stopping and Range of Ions in Matter) program, we estimate the created V_B defect density in the experiment to be $\rho_{V_B}^{S1} \approx (5.4 \pm 0.5) \times 10^2$ ppm, $\rho_{V_B}^{S2} \approx (2.0 \pm 0.2) \times 10^3$ ppm and $\rho_{V_B}^{S3} \approx (1.8 \pm 0.2) \times 10^4$ ppm, increasing linearly with the implantation dosage. Figure 5.7b shows the negatively charged V_B^- ratio, $\eta \equiv \rho_{V_B^-}/\rho_{V_B}$, which exhibits a substantial drop with increasing implantation dosages. This suggests that one may need to seek alternative solutions other than simply cranking up the irradiation dosage to achieve higher V_B^- concentration for future applications in quantum information. We note that if one directly uses ρ_{V_B} from SRIM to represent the negatively charged V_B^- density, the simulated coherent timescales T_2^{XY8} and T_2^D will be significantly shorter than the experimental results.

5.2.6 Outlook

Looking forward, our work opens the door to a number of intriguing directions. First, the characterization and control of coherent dipolar interaction in dense ensembles of spin defects in 2D materials represent the first step to using such platforms for exploring exotic many-body quantum dynamics. One particularly interesting example is to investigate the stability of phenomena such as many-body localization and Floquet thermalization in two and three dimensions. In fact, in long-range interacting systems, the precise criteria for delocalization remain an open question; whereas in Floquet systems, the thermalization dynamics involve a complex interplay between interaction and dimensionality [95, 182, 190, 421]. Secondly, the measured low negatively charged V_B^- ratio at high ion implantation dosage suggests that one may be able to use external electric gating to substantially tune and enhance the portion of V_B^- concentration. Indeed, electric gating has been recently demonstrated as a powerful tool to engineer the charge state of optical spin defects in solid-state materials [833–836]. Finally, the estimated transverse electric field susceptibility highlights the potential use of V_B^- as an embedded electric field sensor for *in-situ* characterization of heterogeneous materials [831, 837–839].

Appendix A

Appendix to Chapter 2

A.1 Hamiltonian in interaction frame

In this section, we derive the secular Hamiltonian in an NV-P1 spin-defect system. The Hamiltonian of the entire system is separated into two parts, the on-site energy of each defect (NV and P1) and the interaction between the different defects, given by the dipole-dipole interaction. We first consider the NV-P1 interaction in the laboratory frame,

$$H_{dip} = -\frac{J_0}{r^3}[3(\hat{S}\cdot\hat{n})(\hat{P}\cdot\hat{n}) - \hat{S}\cdot\hat{P}] \tag{A.1}$$

where $J_0 = (2\pi)\ 52\ \text{MHz}\cdot\text{nm}^3$, $\hat{S}$ and $\hat{P}$ are the spin operators of the two defects. In our case we will label the NV center by spin 1 operators $\hat{S}$ and the P1 centers by spin 1/2 operators $\hat{P}$. Moreover our dynamics only focuses on $m_s = 0, -1$ of the NV, so we restrict the Hilbert space to those two levels. In extent:

$$\begin{aligned} S_z &= \begin{bmatrix} 0 & 0 \\ 0 & -1 \end{bmatrix} \quad , \quad S_x = \frac{1}{\sqrt{2}}\begin{bmatrix} 0 & 1 \\ 1 & 0 \end{bmatrix} \quad , \quad S_y = \frac{1}{\sqrt{2}}\begin{bmatrix} 0 & -i \\ i & 0 \end{bmatrix} \\ P_z &= \frac{1}{2}\begin{bmatrix} 1 & 0 \\ 0 & -1 \end{bmatrix} \quad , \quad P_x = \frac{1}{2}\begin{bmatrix} 0 & 1 \\ 1 & 0 \end{bmatrix} \quad , \quad P_y = \frac{1}{2}\begin{bmatrix} 0 & -i \\ i & 0 \end{bmatrix} \end{aligned} \tag{A.2}$$

We can also define the raising and lowering operators for both spin systems:

$$\begin{aligned} P_+ &= \begin{bmatrix} 0 & 1 \\ 0 & 0 \end{bmatrix} = P_x + iP_y \quad , \quad P_- = \begin{bmatrix} 0 & 0 \\ 1 & 0 \end{bmatrix} = P_x - iP_y \\ S_+ &= \begin{bmatrix} 0 & 1 \\ 0 & 0 \end{bmatrix} = \frac{1}{\sqrt{2}}(S_x + iS_y) \quad , \quad S_- = \begin{bmatrix} 0 & 0 \\ 1 & 0 \end{bmatrix} = \frac{1}{\sqrt{2}}(S_x - iS_y) \end{aligned} \tag{A.3}$$

Now we write the interaction in terms of the raising and lowering operators as:

$$\begin{aligned} S_x = \frac{1}{\sqrt{2}}(S_+ + S_-) \quad , \quad S_y = \frac{1}{i\sqrt{2}}(S_+ - S_-) \\ P_x = \frac{1}{2}(P_+ + P_-) \quad , \quad P_y = \frac{1}{i2}(P_+ - P_-) \end{aligned} \tag{A.4}$$

and expand the dipole interaction as:

$$
\begin{aligned}
&H_{dip} = \\
&-\frac{J_0}{r^3} \times \Big\{ 3 \left[S_z n_z + n_x \frac{(S_+ + S_-)}{\sqrt{2}} + n_y \frac{(S_+ - S_-)}{i\sqrt{2}} \right] \left[P_z n_z + n_x \frac{(P_+ + P_-)}{2} + n_y \frac{(P_+ - P_-)}{2i} \right] \\
&- S_z P_z - \frac{(S_+ + S_-)}{\sqrt{2}} \frac{(P_+ + P_-)}{2} - \frac{(S_+ - S_-)}{i\sqrt{2}} \frac{(P_+ - P_-)}{2i} \Big\}
\end{aligned}
\tag{A.5}
$$

Having written down the Hamiltonian in the laboratory frame we now go into the rotating frame of the NV and resonant P1 centers, and only keep the energy conserving terms of the dipolar interaction (rotating-wave approximation).

In the laboratory frame, each defect has a splitting Δ separating the two levels of interest. Since the splitting is in the z direction (NV-axis), we are interested in the evolution of $|\psi\rangle = e^{-i\delta s_z t}|\phi\rangle$, where s_z can either represent the NV or the P1 spin operator:

$$
\begin{aligned}
i\partial_t e^{-i\delta s_z t}|\phi\rangle &= (\delta s_z + H_{dip}) e^{-i\delta s_z t}|\phi\rangle \\
\delta s_z e^{-i\delta s_z t}|\phi\rangle + i e^{-i\delta s_z t}\partial_t|\phi\rangle &= (\delta s_z + H_{dip}) e^{-i\delta s_z t}|\phi\rangle \\
i\partial_t|\phi\rangle &= e^{i\delta s_z t} H_{dip} e^{-i\delta s_z t}|\phi\rangle = \tilde{H}_{dip}|\phi\rangle
\end{aligned}
\tag{A.6}
$$

Now we need to write the spin operators in the rotation frame:

$$
\begin{aligned}
\tilde{s}_z &= e^{i\Delta s_z t} s_z e^{-i\Delta s_z t} = \hat{s}_z \\
\tilde{s}_+ &= e^{i\Delta s_z t} s_+ e^{-i\Delta s_z t}|0\rangle = e^{-i(\Delta)t}\hat{s}_+ \\
\tilde{s}_- &= e^{i\Delta s_z t} s_- e^{-i\Delta s_z t}|1\rangle = e^{+i(\Delta)t}\hat{s}_-
\end{aligned}
\tag{A.7}
$$

In the case of the NV and P1 center we have:

$$
\begin{aligned}
\tilde{S}_z = S_z \quad \tilde{S}_+ = e^{-i\Delta_{NV} t} S_+ \quad \tilde{S}_- = e^{i\Delta_{NV} t} S_- \\
\tilde{P}_z = P_z \quad \tilde{P}_+ = e^{i\Delta_{P1} t} P_+ \quad \tilde{P}_- = e^{-i\Delta_{P1} t} P_-
\end{aligned}
\tag{A.8}
$$

Now we can compute the dipolar interaction in the rotational frame:

$$\begin{aligned}\tilde{H}_{dip} = -\frac{J_0}{r^3} \times \Big\{ & 3\left[S_z n_z + n_x \frac{(S_+ e^{-i\Delta_{NV}t} + S_- e^{i\Delta_{NV}t})}{\sqrt{2}} + n_y \frac{(S_+ e^{-i\Delta_{NV}t} - S_- e^{i\Delta_{NV}t})}{i\sqrt{2}}\right] \\ & \times \left[P_z n_z + n_x \frac{(P_+ e^{i\Delta_{P1}t} + P_- e^{-i\Delta_{P1}t})}{2} + n_y \frac{(P_+ e^{i\Delta_{P1}t} - P_- e^{-i\Delta_{P1}t})}{2i}\right] \\ & - S_z P_z - \frac{(S_+ e^{-i\Delta_{NV}t} + S_- e^{i\Delta_{NV}t})}{\sqrt{2}} \frac{(P_+ e^{i\Delta_{P1}t} + P_- e^{-i\Delta_{P1}t})}{2} \\ & + \frac{(S_+ e^{-i\Delta_{NV}t} - S_- e^{i\Delta_{NV}t})}{\sqrt{2}} \frac{(P_+ e^{i\Delta_{P1}t} - P_- e^{i\Delta_{P1}t})}{2} \Big\}\end{aligned} \tag{A.9}$$

which simplifies to:

$$\begin{aligned}\tilde{H}_{dip} = -\frac{J_0}{r^3} \times \Big\{ & (3n_z^2 - 1) S_z P_z + \frac{3S_+ P_+}{2\sqrt{2}} e^{-i(\Delta_{NV} - \Delta_{P1})t} \left[n_x^2 - n_y^2 - 2in_x n_y\right] \\ & + \frac{3S_- P_-}{2\sqrt{2}} e^{i(\Delta_{NV} - \Delta_{P1})} \left[n_x^2 - n_y^2 + 2in_x n_y\right] \\ & + \left(e^{-i(\Delta_{NV} + \Delta_{P1})} \frac{P_- S_+}{2\sqrt{2}} + e^{i(\Delta_{NV} + \Delta_{P1})} \frac{P_+ S_-}{2\sqrt{2}}\right) (3n_x^2 + 3n_y^2 - 2) \\ & + 3n_z S_z \left[n_x \frac{(P_+ e^{i\Delta_{P1}t} + P_- e^{-i\Delta_{P1}t})}{2} + n_y \frac{(P_+ e^{i\Delta_{P1}t} - P_- e^{-i\Delta_{P1}t})}{2i}\right] \\ & + 3n_z P_z \left[n_x \frac{(S_+ e^{-i\Delta_{NV}t} + S_- e^{i\Delta_{NV}t})}{\sqrt{2}} + n_y \frac{(S_+ e^{-i\Delta_{NV}t} - S_- e^{i\Delta_{NV}t})}{i\sqrt{2}}\right] \Big\}\end{aligned} \tag{A.10}$$

In the rotation frame we can drop the last three lines because they always have a time dependence that is much faster than the average interaction strength between spins (rotating-wave approximation). There are two other possibilities, either for resonant P1 group $\Delta_{NV} = \Delta_{P1}$ on which flip-flip interactions are meaningful because they conserve energy so all of the first line matters, or $\Delta_{NV} \neq \Delta_{P1}$, on which only the Ising term matters.

Summarizing for the interaction between NV and resonant P1 groups:

$$\tilde{H}_{NV-P1} = -\frac{J_0}{r^3} \left\{ (3n_z^2 - 1) S_z P_z + \frac{3S_+ P_+}{2\sqrt{2}} (n_x - in_y)^2 + \frac{3S_- P_-}{2\sqrt{2}} (n_x + in_y)^2 \right\} \tag{A.11}$$

For off-resonant P1 groups:

$$\tilde{H}_{NV-P1} = -\frac{J_0}{r^3} \times (3n_z^2 - 1) S_z P_z \tag{A.12}$$

The previous result corresponds to the interaction between NV and P1. In the case of the P1-P1 interaction, the interaction should be spin conserving. This corresponds to taking $\Delta NV = -\Delta P1$ in

the previous computation, which leaves us with the Ising term as well as the spin conserving terms. Moreover we need to exchange the $\sqrt{2} \rightarrow 2$ from the different definitions of the raising and lowering operator between the spin 1/2 and spin 1 systems. The result is then:

$$\tilde{H}_{P1-P1} = -\frac{J_0}{r^3} \times \left\{ (3n_z^2 - 1) P_z^{(1)} P_z^{(2)} + \left(\frac{P_-^{(1)} P_+^{(2)}}{4} + \frac{P_+^{(1)} P_-^{(2)}}{4} \right) (1 - 3n_z^2) \right\} \tag{A.13}$$

while the off-resonant interaction is the same as NV-P1 interaction.

A.2 Rate equation model

In this section we derive our semi-classical diffusion model for the NV-P1 system using two different formalisms: the master equation and Fermi's golden rule [375, 840–842].

A.2.1 Master equation approach

In developing a master equation approach to the polarization transfer rate in our spin system, we begin by isolating a single pair of spins whose polarization dynamics we wish to study. Let us denote them by S and P (here we restrict our analysis of the NV center to the two lowest levels of interest in the polarization transfer dynamics dynamics) The two-spin Hamiltonian can be written as:

$$H = (\Delta + \delta_S)\frac{S_z}{2} + (\Delta + \delta_P)\frac{P_z}{2} + J_{zz}S_zP_z + J_\perp(S_+P_- + S_-P_+) \tag{A.14}$$

where we already focus on the approximate energy conserving terms $J_{zz}, J_\perp, \delta^S, \delta^P \ll \Delta$. The only two states that can exhibit dynamics due to the interactions live in the zero magnetization subspace $\{|\uparrow_S\downarrow_P\rangle = |A\rangle, |\downarrow_S\uparrow_P\rangle = |B\rangle\}$ with Hamiltonian:

$$H_{sub} = \delta\,|A\rangle\langle A| + J_\perp\left[|A\rangle\langle B| + |B\rangle\langle A|\right], \tag{A.15}$$

where δ accounts for the energy mismatch between the two levels. In isolation, the population of the two states would coherently oscillate with a well-defined frequency; the presence of a bath of P1s and optical pumping leads to additional decoherence dynamics that modify the dynamics strikingly. These can be self-consistently included within the density matrix formalism, by adding a off-diagonal decoherence decay rate and optical pumping to an additional level.

Optical pumping to another state—In simulating the dynamics of the experiment, one important feature is the polarization of the NV via its internal structure. Briefly, the full structure of the NV includes two excited spin-1 manifolds, as well as a singlet level, Fig. A.1. The various decay rates between the different states (independently studied in Refs. [843, 844]) leads to a preferential polarization of the $|m_s = 0\rangle$ state in the ground state manifold, under spin-conserving optical polarization from the ground state to the excited states—let the rate of this process be Γ_{p} and the natural decay rate to be Γ_{dec}.

	Rate $[\mu s^{-1}]$
$\Gamma_{dec} = k_{41} = k_{52} = k_{63}$	66 ± 5
k_{47}	7.9 ± 4.1
$k_{57} = k_{67}$	53 ± 7
k_{71}	1.0 ± 0.8
$k_{72} = k_{73}$	0.7 ± 0.5

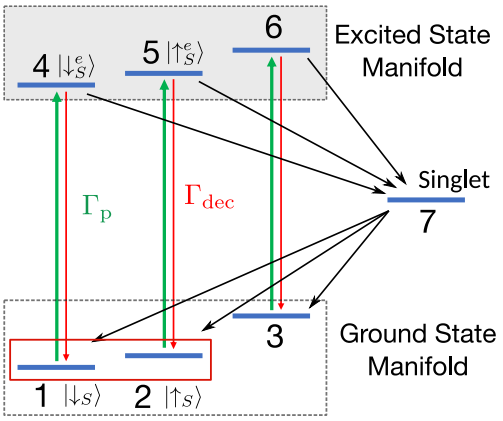

Figure A.1: Diagram of the NV internal structure with $|m_s = 0\rangle = |\downarrow_S\rangle$ and $\left|m_s = -\frac{1}{2}\right\rangle = |\uparrow_S\rangle$ levels highlighted. The NV level structure is composed of a spin-1 ground state and excited manifold as well as a single level. Rates between the different NV levels (table) as measured in Refs. [843, 844].

To study this effect, let us consider optical pumping of the ground state levels $|\uparrow_S\rangle$ and $|\downarrow_S\rangle$ to the corresponding excited states $\left|\uparrow_S^e\right\rangle$ and $\left|\downarrow_S^e\right\rangle$. In the full Hilbert space, these induce transition $|A\rangle = |\uparrow_S\downarrow_P\rangle \leftrightarrow \left|\uparrow_S^e\downarrow_P\right\rangle = |C\rangle$ and $|B\rangle = |\downarrow_S\uparrow_P\rangle \leftrightarrow \left|\downarrow_S^e\uparrow_P\right\rangle = |D\rangle$. The corresponding Linbladian quantum jump term for both pumping and decay are given by:

$$\begin{aligned}
&\dot{\rho}_{\text{opt+dec}} = \\
&-\frac{\Gamma_p}{2}\left[|A\rangle\langle A|\rho + \rho|A\rangle\langle A| - |C\rangle\langle C|\rho_{AA} + |B\rangle\langle B|\rho + \rho\,|B\rangle\langle B| - 2|D\rangle\langle D|\rho_{BB}\right] \\
&-\frac{\Gamma_{dec}}{2}\left[|C\rangle\langle C|\rho + \rho|C\rangle\langle C| - 2|A\rangle\langle A|\rho_{CC} + |D\rangle\langle D|\rho + \rho|D\rangle\langle D| - 2|B\rangle\langle B|\rho_{DD}\right],
\end{aligned} \tag{A.16}$$

which becomes a bit more insightful in matrix form:

$$\dot{\rho}_{\text{opt+dec}} = \left[\begin{array}{cc|cc}
-\Gamma_p\rho_{AA} + \Gamma_{dec}\rho_{CC} & -\Gamma_p\rho_{AB} & -\bar{\gamma}\rho_{AC} & -\bar{\gamma}\rho_{AD} \\
-\Gamma_p\rho_{BA} & -\Gamma_p\rho_{BB} + \Gamma_{dec}\rho_{DD} & -\bar{\gamma}\rho_{BC} & -\bar{\gamma}\rho_{BD} \\
\hline
-\bar{\gamma}\rho_{CA} & -\bar{\gamma}\rho_{CB} & \Gamma_p\rho_{AA} - \Gamma_{dec}\rho_{CC} & -\Gamma_{dec}\rho_{CD} \\
-\bar{\gamma}\rho_{DA} & -\bar{\gamma}\rho_{DB} & -\Gamma_{dec}\rho_{DC} & \Gamma_p\rho_{BB} - \Gamma_{dec}\rho_{DD}
\end{array}\right] \tag{A.17}$$

where $\bar{\gamma} = (\Gamma_p + \Gamma_{dec})/2$.

Immediately, we observe that the off-diagonal corrections with the $|C\rangle$ and $|D\rangle$ states are simply decaying. Since they start at zero, they remain zero and do not affect the dynamics of the system. The

pumping only affects the dynamics between $|A\rangle$ and $|B\rangle$ by inducing an additional decoherence of off-diagonal ρ_{AB} term. The remaining dynamics affect only the diagonal component, which correspond to the populations in each of the levels.

This highlights that the presence of the complex structure of the NV center can be accounted by the diagonal components of the density matrix, up to an additional decoherence rate causes by the pumping to the excited manifold.

Extrinsic decoherence—By contrast, adding the extrinsic decoherence rate arising from other spins in the system is much simpler and corresponds to an additional decay of the off-diagonal terms with rate γ.

Putting everything together, the equations of motion are given by:

$$\begin{cases} \dot{\rho}_{AA} &= -iJ_{\perp}(\rho_{BA}-\rho_{AB}) - \Gamma_{\mathrm{p}}\rho_{AA} + \Gamma_{\mathrm{dec}}\rho_{CC} \\ \dot{\rho}_{BB} &= -iJ_{\perp}(\rho_{AB}-\rho_{BA}) - \Gamma_{\mathrm{p}}\rho_{BB} + \Gamma_{\mathrm{dec}}\rho_{DD} \\ \dot{\rho}_{CC} &= \Gamma_{\mathrm{p}}\rho_{AA} - \Gamma_{\mathrm{dec}}\rho_{CC} \\ \dot{\rho}_{DD} &= \Gamma_{\mathrm{p}}\rho_{BB} - \Gamma_{\mathrm{dec}}\rho_{DD} \\ \dot{\rho}_{AB} &= (i\delta - \gamma - \Gamma_{\mathrm{exc}})\rho_{AB} - iJ_{\perp}(\rho_{BB}-\rho_{AA}) = [\dot{\rho}_{BA}]^{*} \end{cases}, \tag{A.18}$$

while the remaining terms are zero. Adiabatically eliminating the coherence between $|A\rangle$ and $|B\rangle$, we get a modified set of equations for ρ_{AA} and ρ_{BB}:

$$\begin{cases} \dot{\rho}_{AA} &= -2|J_{\perp}|^2(\rho_{AA}-\rho_{BB})\frac{\gamma+\Gamma_{\mathrm{p}}}{(\gamma+\Gamma_{\mathrm{p}})^2+\delta^2} - \Gamma_{\mathrm{p}}\rho_{AA} + \Gamma_{\mathrm{dec}}\rho_{CC} \\ \dot{\rho}_{BB} &= -2|J_{\perp}|^2(\rho_{BB}-\rho_{AA})\frac{\gamma+\Gamma_{\mathrm{p}}}{(\gamma+\Gamma_{\mathrm{p}})^2+\delta^2} - \Gamma_{\mathrm{p}}\rho_{BB} + \Gamma_{\mathrm{dec}}\rho_{DD} \end{cases}. \tag{A.19}$$

Finally, we assume that the density matrix remains diagonal, $\rho_{AA} \approx \rho^{S}_{\uparrow\uparrow}\rho^{P}_{\downarrow\downarrow}$ and $\rho_{BB} \approx \rho^{S}_{\downarrow\downarrow}\rho^{P}_{\uparrow\uparrow}$. In a similar way we assume $\dot{\rho}_{AA}$ captures the polarization transfer rate so $\dot{\rho}_{AA} \approx \dot{\rho}^{S}_{\uparrow\uparrow} = -\dot{\rho}^{P}_{\downarrow\downarrow}$.

A.2.2 Fermi's golden rule

A different way to derive our semi-classical model is through Fermi's golden rule; polarization exchange corresponds to decay of a single spin to a bath composed of all other spin in the system. Owing to the presence of strong disorder (both on on-site fields and position), the spectrum of the bath

modes should exbhibit important structure—peaked around the energy difference of each spin and with some broadening γ induced by interactions.

A more precise analysis of the decay closely follows the analysis of decay of an atom in electromagnetic field. Focusing on a two level spin $|s\rangle = \in \{|\uparrow\rangle, |\downarrow\rangle\}$ and a set of bath modes $|k\rangle$, the Hilbert space of the system undergoing decay can be written as $\{|\uparrow, 0\rangle = |e\rangle, |\downarrow, k\rangle = |g_k\rangle\}$, interacting via the Hamiltonian:

$$H = (\Delta + \delta) |e\rangle \langle e| + \sum_k \epsilon_k |g_k\rangle \langle g_k| + \sum_k J[\, |e\rangle \langle g_k| + |g_k\rangle \langle a|\,] \tag{A.20}$$

where $\Delta + \delta$ corresponds to the splitting of the spin of interest and ϵ_k the energy of the mode k of the bath. Moving into the the interaction picture of $|e\rangle$ and $|g_k\rangle$:

$$H_{int} = \sum_k J_k \left[e^{-i((\Delta+\delta)-\epsilon_k)t} |e\rangle \langle g_k| + e^{i((\Delta+\delta)-\epsilon_k)t} |g_k\rangle \langle e| \right] . \tag{A.21}$$

In the case when either of the spins is being pumped (like the NV must be during polarization), there will be an additional decoherence channel proportional to the strength of the pumping Γ_{p}. Including this contribution is most straightforwardly done via the density matrix ρ, where it emerges as a decay of the off-diagonal component.

$$\begin{cases} \dot{\rho}_{ee} & = -i \sum_k J \left[e^{-i((\Delta+\delta)-\epsilon_k)t} \rho_{g_k e} - e^{i((\Delta+\delta)-\epsilon_k)t} \rho_{e g_k} \right] \\ \dot{\rho}_{e g_k} & = -iJ e^{-i((\Delta+\delta)-\epsilon_k)t} (\rho_{g_k g_k} - \rho_{ee}) - \Gamma_{\mathrm{p}} \rho_{e g_k} \end{cases} . \tag{A.22}$$

Formally integrating the second equation assuming zero coherence at $t = 0$, $\rho_{e g_k}(t = 0) = 0$ yields:

$$\rho_{e g_k} = -iJ \int_0^t dt' \, (\rho_{g_k g_k}(t') - \rho_{ee}(t')) e^{-i((\Delta+\delta)-\epsilon_k)t'} e^{-\Gamma_{\mathrm{p}}(t-t')} \tag{A.23}$$

Inserting into the Eqn. A.22 and focusing on the first term, we have:

$$\begin{aligned} e^{-i((\Delta+\delta)-\epsilon_k)t} \int_0^t dt' \, [\rho_{g_k g_k}(t') - \rho_{ee}(t')] e^{i((\Delta+\delta)-\epsilon_k)t'} e^{-\Gamma_p(t-t')} \\ &\approx \sum_k [\rho_{g_k g_k}(t) - \rho_{ee}(t)] \int_0^t dt' \, e^{[-i((\Delta+\delta)-\epsilon_k)-\Gamma_p](t-t')} \\ &\approx \lim_{t\to\infty} \sum_k (\rho_{g_k g_k}(t) - \rho_{ee}(t)) \frac{1 - e^{[-i((\Delta+\delta)-\epsilon_k)-\Gamma_p]t}}{i((\Delta+\delta)-\epsilon_k)+\Gamma_p} \\ &\approx \sum_k (\rho_{g_k g_k}(t) - \rho_{ee}(t)) \frac{1}{i((\Delta+\delta)-\epsilon_k)+\Gamma_p} \\ &\approx (\rho_{BB} - \rho_{AA}) \int_{-\infty}^{\infty} d\epsilon \frac{\rho(\epsilon)}{i((\Delta+\delta)-\epsilon_k)+\Gamma_p} \, , \end{aligned} \tag{A.24}$$

where, we have have taken $\rho_{g_k g_k}$ to be slowly varying across different modes g_k around the center frequency of the bath modes and thus the average $\overline{\rho_{g_k g_k}}$. Physically, this corresponds to coupling to a single other spin, where the bath modes correspond to a broadening of the spin energy levels and their occupation is determined by the state of the spin (either in $|\uparrow\rangle$ or $|\downarrow\rangle$). Considering the interaction of multiple such modes corresponds to summing over many independent channels as described above.

$\rho(\epsilon)$ is the density of states of the bath modes, allowing us to transform the sum into an integral, which is a necessary input in our theory. Motivated by the usual broadening in atomic physics, we take $\rho(\epsilon)$ to a Lorentzian, that in the rotating frame, is centered around Δ, with FWHM 2γ:

$$\rho(\epsilon) = \frac{1}{\pi} \frac{\gamma}{\gamma^2 + (\epsilon - \Delta)^2} \, . \tag{A.25}$$

As such δ alone captures the energy mismatch between the spin and the center of the bath. Solving for the integral in Eqn. A.24 and including the second term (which is the complex conjugate of the first), we arrive at the formula for polarization transfer:

$$\dot{\rho}_{ee} = |J|^2 (\overline{\rho_{g_k g_k}} - \rho_{ee}) 2 \, \mathrm{Re} \left[\frac{1}{(\gamma + \Gamma_p) + i\delta} \right] = -2|J|^2 \frac{\gamma + \Gamma_p}{(\gamma + \Gamma_p)^2 + \delta^2} (\rho_{ee} - \overline{\rho_{g_k g_k}}) \, . \tag{A.26}$$

Analogous to the master equation case, we assume that the density matrix is separable between the two spins involved analyzed and thus $\rho_{ee} = \rho^{(1)}_{\uparrow\uparrow} \rho^{(2)}_{\downarrow\downarrow}$ while $\overline{\rho_{g_k g_k}} = \rho^{(1)}_{\downarrow\downarrow} \rho^{(2)}_{\uparrow\uparrow}$ and $\dot{\rho}_{ee} \approx \dot{\rho}^{(1)}_{\uparrow\uparrow} = -\dot{\rho}^{(2)}_{\downarrow\downarrow}$.

Generalizing to many different spins corresponds to summing over the different bath spins that the first spin can decay to—each spin gives rise to a decay channel with slightly broadened levels and interacting with different couplings J. Labelling the bath spins with j, we arrive at the total

depolarization of the initial spin as:

$$\dot{\rho}^{(1)}_{\uparrow\uparrow} = \sum_j -2|J_j|^2 \frac{\gamma + \Gamma_\mathrm{p}}{(\gamma + \Gamma_\mathrm{p})^2 + \delta^2} (\rho^{(1)}_{\uparrow\uparrow}\rho^{(j)}_{\downarrow\downarrow} - \rho^{(1)}_{\downarrow\downarrow}\rho^{(j)}_{\uparrow\uparrow}) \tag{A.27}$$

under pumping of spin (1) of strength Γ_p.

The polarization-transfer rate, Γ_{ij}, between any pair of P1 spins via Fermi's golden rule (Fig. 2.8c):

$$\Gamma_{ij} = \left(\frac{J_0 \tilde{A}_{i,j}}{r^3_{ij}}\right)^2 \frac{2\gamma}{\gamma^2 + (\delta_i - \delta_j)^2} \,. \tag{A.28}$$

Each of the relevant parameters can be independently measured: γ represents the interaction-induced linewidth and is characterized by the spin-echo decoherence time of the NV center; δ_i represents the strength of the on-site random fields and is drawn from a distribution with width W, characterized by the NV linewidth. The analogous polarization transfer rate between NV and P1 spins is obtained by replacing $\tilde{A}_{i,j}$ with A_i.

A.2.3 Computing the diffusion coefficient from the semi-classical model

Armed with the rate of polarization transfer, we numerically study the polarization dynamics of the system by reducing the exponentially large quantum state of the system (2^N coefficients for N spins), into $2N$ coefficients that capture the individual populations $\rho_{i,\sigma}$ of each of the levels σ of each spin i of the system. For the P1 $\sigma \in \{-\frac{1}{2}, +\frac{1}{2}\}$, while for NV $\sigma \in \{0, -1\}$. One then obtains a differential equation for the populations:

$$\partial_t \rho_{i,\sigma} = \sum_j \Gamma_{i,j} (\rho_{i,\bar{\sigma}}\rho_{j,\sigma'} - \rho_{i,\sigma}\rho_{j,\bar{\sigma}'}), \tag{A.29}$$

where $\bar{\sigma}$ corresponds to the other level of the spin i and σ' corresponds to the level of spin j such that interactions lead to a transition $\sigma\bar{\sigma}' \leftrightarrow \bar{\sigma}\sigma'$.

To simulate the spin polarization process, we further extend the differential equations to include the remaining ground and excited states of the NV center. Focusing our analysis on the dynamics of the P1 centers, we can disregard the details of the NV and transform our semi-classical model into a

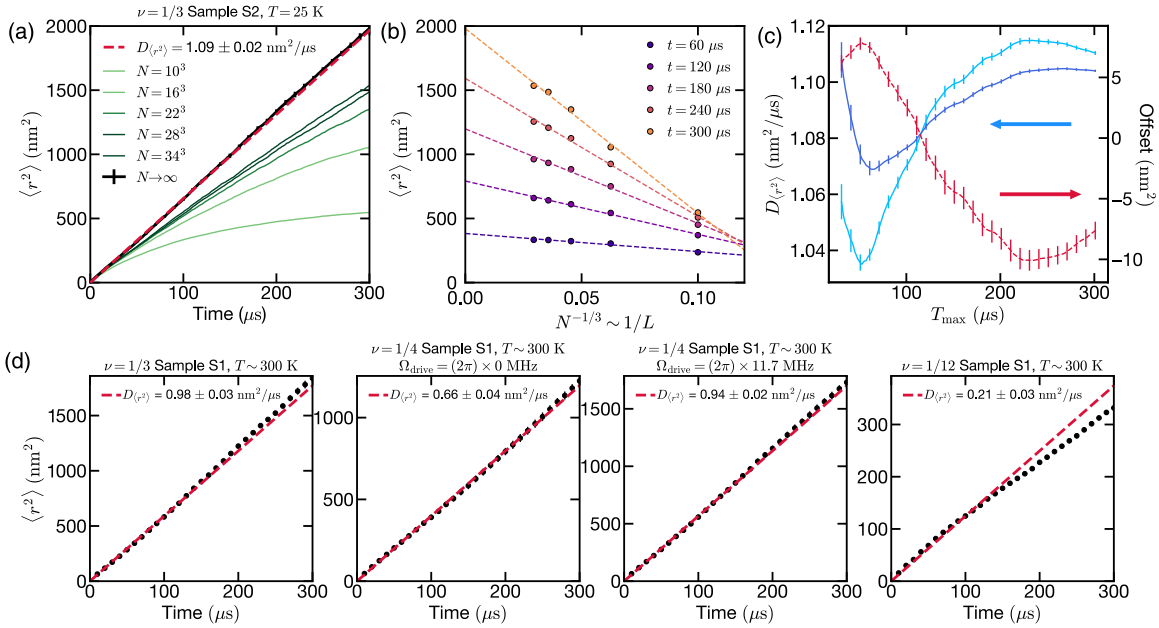

Figure A.2: Summary of extraction of diffusion coefficient. (a-c) Extraction of diffusion coefficient of Sample S2 at low temperature. (a) Growth of $\langle r^2 \rangle$ for different system sizes N and the infinite system scaling (black line). (b) Finite size scaling of $\langle r^2 \rangle$ to $N \to \infty$ assuming a linear in $L^{-1} \sim N^{-1/3}$ correction for representative values of t. (c) Fitting the early-time growth of $\langle r^2 \rangle$ up to different times $T_{\max} \in [30, 300]$ leads to slightly different values of the diffusion coefficient, whether including a constant offset (light blue) or not (dark blue). Considering the fit without an offset, the final diffusion coefficient is taken to be the average with an uncertainty given by half the range of diffusion coefficients. (d) For the different experimental conditions, we extract the diffusion coefficient from the growth of $\langle r^2 \rangle$, which is in great agreement with the experimentally extracted values after correcting for the non-Gaussian polarization profile (Table 2.2).

set of linear differential equations on the polarization of the P1 centers $P_i = \rho_{i,\uparrow} - \rho_{j,\downarrow}$:

$$\dot{P}_i = \sum_j \Gamma_{ij}(P_j - P_i) \tag{A.30}$$

Crucially, this linearity condition enables us to map this set of differential equations into a continuous time random walk of the polarization through the positions of the defects. Such approach enables us to consider the polarization dynamics of much larger system sizes (up to $N \sim 4 \times 10^4$ P1s) because we no longer need to build the dense transition rate matrix Γ_{ij} and solve for the associated eigenvalue problem.

One feature of our semi-classical model is the ability to access the *spatial* profile of the polarization, enabling an *independent* characterization of the diffusive dynamics via the direct study of the spread of the entire polarization profile. In particular, we leverage our semi-classical model to compute the

mean-squared displacement of the polarization and observe the characteristic linear growth with time (Fig. A.2). From this linear growth, we can directly extract the diffusion coefficient of the dynamics via

$$\langle r^2 \rangle = 6D_{\langle r^2 \rangle} t \,, \tag{A.31}$$

where the coefficient $6 = 2d$ includes the information about the dimensionality d of our system.

Our simulation protocol is then as follows. We first generate an ensemble of P1 spins with random positions $\boldsymbol{r}_i$ and onsite energies δ_i surrounding a P1 spin at position $\boldsymbol{r}_0 = (0,0,0)$. Starting with the polarization at $\boldsymbol{r}_0$ at $t = 0$, we compute its dynamics through the system as follows: When the polarization is on spin i (at position $\boldsymbol{r}_i$), the hopping rate away from spin i is given by $\Gamma_{\text{tot}} = \sum_j \Gamma_{ij}$; thus the polarization remains in spin i for time δt which is a Poisson random variable with mean Γ_{tot}^{-1}. The probability of hopping to spin j is given by the branching ratio $\beta_j = \Gamma_{ij}/\Gamma_{\text{tot}}$. We repeat this process until a time $t_{\text{max}} \sim 1000\ \mu$s has elapsed.

Computing the mean-square displacement— For each random walk, we record the displacement squared of the polarization from its original position $\boldsymbol{r}_0$ as a function of time t. Averaging over many random walks immediately yields the mean squared displacement of the polarization profile.

A.3 Continuous diffusive model

A.3.1 Simple diffusion model

In this subsection, we present a detailed derivation of the solution of the diffusion equation for the NV-P1 system, which we use as the fitting functional form to analyze the experimental data and extract the diffusion coefficient.

In the simplest case, the diffusion equation is written as

$$\partial_t P(t,\boldsymbol{r}) = D\nabla^2 P(t,\boldsymbol{r}) - \frac{P(t,\boldsymbol{r})}{T_1} + Q(t,\boldsymbol{r}), \tag{A.32}$$

where $P(t,\boldsymbol{r})$ is the polarization depending on both position r and time t, D is the diffusion coefficient, T_1 is the intrinsic depolarization time scale of our system, and $Q(t,\boldsymbol{r})$ corresponds to the polarization source (the NV). Considering our experimental geometry and polarization protocol, we assume:

$$Q(t,\boldsymbol{r}) = \begin{cases} \frac{\Gamma}{(2\pi b^2)^{3/2}} e^{-r^2/(2b^2)} & -\tau_p < t < 0 \\ 0 & t > 0 \end{cases}, \tag{A.33}$$

where Γ is the polarization rate, and b reflects the range of the polarization transfer process from the NV and also guarantees that the polarization does not diverge at short times.

To solve this partial differential equation (PDE), we follow the Green's function approach. In particular the corresponding impulse response problem is

$$\begin{cases} \partial_t P(t,\boldsymbol{r}) = D\nabla^2 P(t,\boldsymbol{r}) - \frac{P(t,\boldsymbol{r})}{T_1}, \\ P(t=t_0,\boldsymbol{r}) = \delta(\boldsymbol{r}-\boldsymbol{r}_0), \end{cases} \tag{A.34}$$

in real space, or

$$\begin{cases} \partial_t P_{\boldsymbol{k}}(t) = -Dk^2 P_{\boldsymbol{k}}(t) - \frac{P_{\boldsymbol{k}}(t)}{T_1}, \\ P_{\boldsymbol{k}}(t=t_0) = 1, \end{cases} \tag{A.35}$$

in Fourier space. With the solution of the above equation (Green's function) denoted as $G(t,t_0,\boldsymbol{r},\boldsymbol{r}_0)$,

we can obtain the survival probability given our polarization scheme:

$$P(t, \boldsymbol{r} = 0) = \int_{-\tau_p}^{0} dt_0 \int d\boldsymbol{r}_0 G(t, t_0, \boldsymbol{r}, \boldsymbol{r}_0) Q(t_0, \boldsymbol{r}_0). \tag{A.36}$$

In the undriven case, we can simply get

$$G(t, t_0; \boldsymbol{r}, \boldsymbol{r}_0) = \frac{1}{[4\pi D(t-t_0)]^{3/2}} \exp\left[-\frac{(\boldsymbol{r}-\boldsymbol{r}_0)^2}{2D(t-t_0)}\right] \exp\left[-\frac{t-t_0}{T_1}\right]. \tag{A.37}$$

Correspondingly, the survival probability is

$$P(t, \boldsymbol{r} = 0) = \frac{\Gamma e^{\frac{b^2}{DT_1}}}{4\pi D^{3/2}\sqrt{T_1}} \left\{ F\left[\left(t + \frac{b^2}{D}\right)\frac{1}{T_1}\right] - F\left[\left(t + \tau_p + \frac{b^2}{D}\right)\frac{1}{T_1}\right]\right\}, \tag{A.38}$$

where

$$F(x) = \frac{1}{\sqrt{\pi}}\frac{e^{-x}}{\sqrt{x}} - \mathrm{erfc}(\sqrt{x}). \tag{A.39}$$

In the driven case, we have a different diffusion coefficient (denoted as D^{dr}) and a different decay time (denoted as T_1^{dr}) in Eqs. A.34, A.35 for $t > 0$. With these modifications, the Green's function then reads

$$G(t, t_0; \boldsymbol{r}, \boldsymbol{r}_0) = \frac{1}{[4\pi(D^{\mathrm{dr}}t - Dt_0)]^{3/2}} \exp\left[-\frac{(\boldsymbol{r}-\boldsymbol{r}_0)^2}{2(D^{\mathrm{dr}}t - Dt_0)}\right] \exp\left[-\left(\frac{t}{T_1^{\mathrm{dr}}} - \frac{t}{T_1}\right)\right]. \tag{A.40}$$

Similarly, using Eqn. A.36, we obtain the survival probability as

$$\begin{aligned} P(t, \boldsymbol{r} = 0) = \frac{\Gamma e^{\frac{b^2}{DT_1} + (\frac{D^{\mathrm{dr}}}{D} - \frac{T_1}{T_1^{\mathrm{dr}}})\frac{t}{T_1}}}{4\pi D^{3/2}\sqrt{T_1}} \Bigg\{ & F\left[\left(\frac{D^{\mathrm{dr}}}{D}t + \frac{b^2}{D}\right)\frac{1}{T_1}\right] \\ & - e^{(\frac{T_1^{\mathrm{dr}}}{T_1} - \frac{D}{D^{\mathrm{dr}}})\frac{\tau_p}{T_1^{\mathrm{dr}}}} F\left[\left(\frac{D^{\mathrm{dr}}}{D}t + \tau_p + \frac{b^2}{D}\right)\frac{1}{T_1}\right]\Bigg\}. \end{aligned} \tag{A.41}$$

Up until now, we have been considering the dynamics of a single NV center surrounded by an ensemble of P1 spins. However, the finite NV defect density in our sample leads to the polarization overlap between different NV-P1 systems. Owing to the randomness in the NV center positions, this effect can be captured by a simple constant background. In particular, since each NV is randomly placed in the system and we measure all NVs, the above overlap effect is spatially averaged and can be treated as a homogeneous background whose dynamics is governed only by depolarization. Given the

volume of each NV-P1 system, $V = 1/\rho_{NV}$, the background polarization is simply written as:

$$P_{bg}(t) = \frac{1}{V}\int_{-\tau_p}^{0} \Gamma e^{-(t-t_0)/T_1} dt_0 = \rho_{NV}\Gamma T_1 \left(e^{-t/T_1} - e^{-(t+\tau_p)/T_1}\right). \tag{A.42}$$

Combining the background P_{bg} with the survival probability $P(t, \vec{r} = 0)$ (i.e., Eqn. A.38,A.41) yields the experimental signal, from where we extract the diffusion coefficient D and the range of polarization b. To be more specific, the data measured under the same conditions and parameters (sample, temperature, peak ν) except τ_{p} should be fitted with the same global value of D and b, while Γ changes across different τ_{p}. In addition, T_1 and T_1^{dr} are independently extracted from the polarization decay at a substantially late time. We also remark that ρ_{NV} (which is independently measured) provides the necessary length scale that connects the measured decay timescales to the diffusion coefficient.

A.3.2 Long-range modifications to diffusion

In building a description that goes beyond the leading order term, we consider the problem in Fourier space

$$\begin{cases} \partial_t P_{\boldsymbol{k}}(t) = -f(\boldsymbol{k}) P_{\boldsymbol{k}}(t) - \frac{P_{\boldsymbol{k}}(t)}{T_1}, \\ P_{\boldsymbol{k}}(t = t_0) = 1. \end{cases} \tag{A.43}$$

where $f(\boldsymbol{k})$ can be thought of as the decay rate of the Fourier mode with a wavevector $\boldsymbol{k}$. To the leading order, the diffusive nature of the dynamics arises as a term Dk^2 in $f(\boldsymbol{k})$, and we recover the simple diffusion equation (Eqn. A.35).

Denoting the polarization transfer rate as $h(\boldsymbol{r})$, we can obtain the decay rate of Fourier modes in a d-dimensional system as

$$f(\boldsymbol{k}) = \int [1 - \cos(\boldsymbol{k}\cdot\boldsymbol{r})] h(\boldsymbol{r})\, d^d\boldsymbol{r}. \tag{A.44}$$

To be more concrete, we consider a transfer rate where beyond some short-range cutoff r_0 the transfer decays simply decays as a power-law $\sim 1/r^{\alpha}$. Focusing only on the long-range part (since any

non-singular short-range contribution just leads to even-order terms in $f_{\rm lr}(\boldsymbol{k})$), we have:

$$\begin{aligned}
f_{\rm lr}(\boldsymbol{k}) &= \int \frac{1-\cos(\boldsymbol{k}\cdot\boldsymbol{r})}{r^{\alpha}} d^d\boldsymbol{r} \\
&= \frac{\pi^{\frac{d}{2}}}{\Gamma(\frac{d}{2})} \int \frac{1-\cos(kr\cos\theta)}{r^{\alpha}} r^{d-1}\, d\cos\theta\, dr = \frac{2\pi^{\frac{d}{2}}}{\Gamma(\frac{d}{2})} \int_{r_0}^{\infty} \left[1-\frac{\sin(kr)}{kr}\right] r^{d-\alpha-1} dr \\
&= \frac{2\pi^{\frac{d}{2}}}{\Gamma(\frac{d}{2})} \Bigg\{ \Gamma(d-\alpha-1)\sin\left(\frac{\alpha+1-d}{2}\pi\right) k^{\alpha-d} \\
&\qquad + \frac{r_0^{d-\alpha}}{d-\alpha}\left[-1+{}_1F_2\left(\frac{d-\alpha}{2};\frac{3}{2},1+\frac{d-\alpha}{2};-\frac{k^2r_0^2}{4}\right)\right]\Bigg\} \\
&= \frac{2\pi^{\frac{d}{2}}}{\Gamma(\frac{d}{2})} \Bigg\{ \Gamma(d-\alpha-1)\sin\left(\frac{\alpha+1-d}{2}\pi\right) k^{\alpha-d} \\
&\qquad + \left[\frac{r_0^{d-\alpha+2}}{6(\alpha-d-2)}k^2 + \frac{r_0^{d-\alpha+4}}{120(d-\alpha+4)}k^4 + \mathcal{O}(k^6)\right]\Bigg\},
\end{aligned} \tag{A.45}$$

where $\frac{2\pi^{\frac{d}{2}}}{\Gamma(\frac{d}{2})}$ is the surface area of a d-dimensional ball with unit radius, and ${}_1F_2(a_1;b_1,b_2;x)$ is the generalized hypergeometric function, which can be expanded as a power series of the variable x. The interpretation is simple: while the last term only contains terms with even power of k (similar to diffusion in short-range systems), the first term ($\sim k^{\alpha-d}$) captures the long-range nature, making the dynamics qualitatively different from short-range interacting systems. Therefore, with the presence of long-range interaction, $f(\boldsymbol{k})$ in general can be written as:

$$f(\boldsymbol{k}) = Dk^2 + C_{\rm lr}k^{\alpha-d} + Ck^4 + \cdots \tag{A.46}$$

where D, $C_{\rm lr}$ and C are model-dependent coefficients. This result immediately highlights three import regimes.

- Ford long-range interacting systems with $d+4<\alpha$ (and also short-range interacting systems), neither the leading nor the sub-leading term arises from the long-range transfer rate and the dynamics do not deviate significantly from the short-range case:

$$f(\boldsymbol{k}) = Dk^2 + Ck^4 + \cdots; \tag{A.47}$$

- For long-range interacting systems $d+2<\alpha<d+4$, the leading order term remains the

diffusive term but the sub-leading correction that control the approach to diffusion is set by a $k^{\alpha-d}$ term:

$$f(\boldsymbol{k}) = Dk^2 + \mathrm{C_{lr}} k^{\alpha-d} + \cdots ; \tag{A.48}$$

- For long-range interacting systems $d < \alpha < d+2$, the leading power is no longer the k^2 term and instead a $k^{\alpha-d}$ term becomes the leading contribution—the system is no longer diffusive and enters the Lévy-flight regime [419, 505]:

$$f(\boldsymbol{k}) = \mathrm{C_{lr}} k^{\alpha-d} + \cdots . \tag{A.49}$$

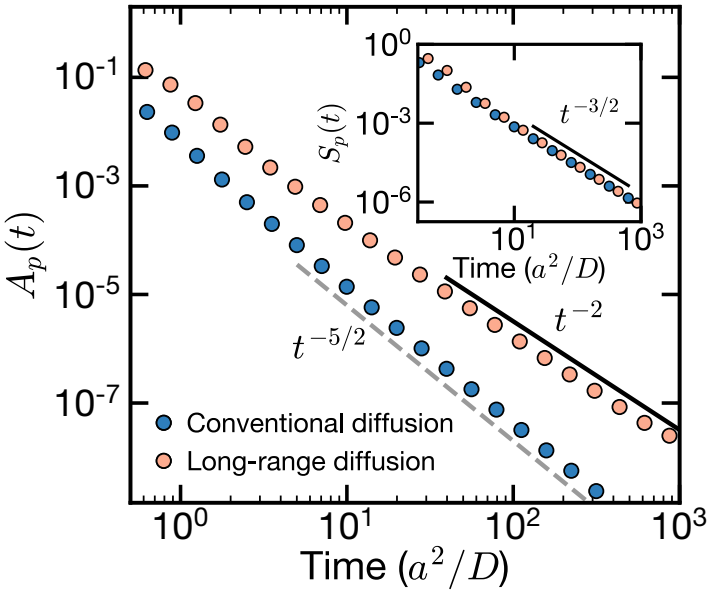

Figure A.3: Long-range modification to conventional diffusion. The presence of a long-range k^3-term parametrically modifies the approach, $A_p(t) = S_p(t) - (4\pi Dt)^{-3/2}$, to the late-time Gaussian fixed point, as high-lighted in a three-dimensional, disorder-less numerical simulation, with lattice constant a and diffusion coefficient D).

With the functional form of $f(\boldsymbol{k})$, we can obtain the survival probability as

$$G(t_0, t; \boldsymbol{r} = \boldsymbol{r}_0) = \frac{\mathrm{e}^{-\frac{t-t_0}{T_1}}}{(2\pi)^d} \int d^d \boldsymbol{k} e^{-f(k)(t-t_0)}. \tag{A.50}$$

At late times, k^2 term in Eqns. A.47-A.48 dominates the dynamics, while the subleading correction

can be evaluated by expanding the exponential in Eqn. A.50 as follows [1].

- When $d = 3$ and $\alpha \geq 7$,

$$\begin{aligned} G(t_0, t; \boldsymbol{r} = \boldsymbol{r}_0) &\approx \frac{\mathrm{e}^{-\frac{t-t_0}{T_1}}}{(2\pi)^3} \int d^3\boldsymbol{k} e^{-Dk^2(t-t_0)} \{1 + D'k^4(t-t_0)\} \\ &= \mathrm{e}^{-\frac{t-t_0}{T_1}} \left\{ \frac{1}{[4\pi D(t-t_0)]^{3/2}} + \frac{15C}{32\pi^{3/2}D^{7/2}(t-t_0)^{5/2}} \right\}. \end{aligned} \tag{A.51}$$

- When $d = 3$ and $\alpha = 6$ (our experimental setup),

$$\begin{aligned} G(t_0, t; \boldsymbol{r} = \boldsymbol{r}_0) &\approx \frac{\mathrm{e}^{-\frac{t-t_0}{T_1}}}{(2\pi)^3} \int d^3\boldsymbol{k} e^{-Dk^2(t-t_0)} \{1 + C_{\mathrm{lr}}k^3(t-t_0)\} \\ &= \mathrm{e}^{-\frac{t-t_0}{T_1}} \left\{ \frac{1}{[4\pi D(t-t_0)]^{3/2}} + \frac{C_{\mathrm{lr}}}{2\pi^2 D^3(t-t_0)^2} \right\}. \end{aligned} \tag{A.52}$$

We emphasize that the subleading correction $\sim (t-t_0)^{-2}$ distinguishes our long-range interacting system from the normal diffusion whose subleading correction $\sim (t-t_0)^{-5/2}$. We also remark that, similar to the calculation assuming only the simple diffusion, we can also convolve the above survival probability with the polarization process to obtain the correct form for our experimental signal.

A.3.3 Dynamical correction to diffusion

The experiments average over both NV centers within the sample and shot-to-shot fluctuations in the environment. Thus, the quantity of interest is the disorder-averaged diffusion kernel, or Green's function. In frequency and momentum space, this is given by:

$$G(\boldsymbol{k}, \omega) = \frac{1}{-i\omega + Dk^2 + \Sigma(\boldsymbol{k}, \omega)} \tag{A.53}$$

where $-i\omega + Dk^2$ describes the eventual diffusive dynamics at asymptotically late times and long wavelengths while the self-energy $\Sigma(\boldsymbol{k}, \omega)$ captures the corrections due to disorder averaging. Focusing on the leading corrections in this limit, the small ω and $\boldsymbol{k}$ expansion of $\Sigma(\boldsymbol{k}, \omega)$ can be constrained by noting that it is (1) analytic, (2) isotropic, and (3) probability conserving:

$$\Sigma(\boldsymbol{k}, \omega) = D'k^2 + Ck^4 + \ldots + (-i\omega)(\ell^2 k^2 + \ell'^4 k^4 + \ldots) + \ldots\ , \tag{A.54}$$

[1] Here, we only show the case with $d = 3$, and results for other dimensions can be derived in a similar way.

where $\ell^2 = C_{\rm dyn}$ in the main text.

A few remarks are in order. First, the $D'k^2$ term simply corrects the bare diffusion coefficient, $D \to D + D'$, and can be absorbed into a new definition of D. Second, the Ck^4 and $\ell^2(-i\omega)k^2$ terms have the same scaling dimension near the diffusive fixed point (where $z = 2$); they are accordingly the leading irrelevant corrections in the renormalization group sense. Third, the dynamical corrections (involving powers of ω) do not appear in translationally invariant classical hopping systems, where the only corrections in Σ arise due to the spatial Fourier transform of the hopping kernel. This picture is modified in disordered systems, where a diagrammatic analysis of the disorder average generically yields the dynamical corrections.

While Eqn. A.54 follows on very general symmetry grounds, for completeness we include a short derivation of the one-loop self-energy in a continuum model with a spatially random local diffusion coefficient in order to indicate how it is generated. The actual coefficient ℓ^2 produced in this calculation depends on the UV-cutoff (as expected) and thus its detailed numerical form is of limited utility. We assume that the diffusivity is $D(x) = D + \delta D(x)$ is Gaussian with

$$\overline{\delta D(x)\delta D(x')} = \Delta_D \delta(x - x') \tag{A.55}$$

The Martin-Siggia-Rose (MSR) [845] action generating the Green's function of the polarization $P(x,t)$ in a *fixed* diffusion environment $D(x)$ is given by

$$S_D = i\int dt d^d x\, \hat{P}(x,t)(\partial_t - D\vec{\nabla}^2)P(x,t) + i\int dt d^d x\, (\vec{\nabla}\hat{P}(x,t))\cdot(\vec{\nabla}P(x,t))\delta D(x) \tag{A.56}$$

where $\hat{P}(x,t)$ is the MSR conjugate response field to $P(x,t)$. Here,

$$\langle \hat{P}(x,t)P(x',t')\rangle_D = -iG_D(x',t';x,t) \tag{A.57}$$

provides the fixed environment Green's function of the polarization. The action generating the disorder averaged Green's function can be obtained by integrating over the fluctuations in $\delta D(x)$. Technically, this is straightforward because in the MSR approach, the normalization $Z_D = \int DPD\hat{P}e^{S_D} = 1$ is independent of the realization of $D(x)$; see Ref. [846] for more discussion. We obtain the effective

action

$$S = S_0 + S_1 \tag{A.58}$$

$$S_0 = i \int dt d^d x \, \hat{P}(x,t)(\partial_t - D\vec{\nabla}^2)P(x,t) \tag{A.59}$$

$$S_1 = -\frac{\Delta_D}{2} \int dt dt' d^d x \, \left[(\vec{\nabla}\hat{P}(x,t)) \cdot (\vec{\nabla}P(x,t))\right] \left[(\vec{\nabla}\hat{P}(x,t')) \cdot (\vec{\nabla}P(x,t'))\right] \tag{A.60}$$

We now compute $-iG(x,t) = \langle \hat{P}(0,0)P(x,t)\rangle$ using perturbation theory to leading loop order. The bare propagator, $-iG_0(\boldsymbol{k},\omega)$, can be taken as an arrow pointing from $\hat{P}$ to P:

$$\underset{\boldsymbol{k},\omega}{\longrightarrow} = \frac{-i}{-i\omega + Dk^2} \tag{A.61}$$

The interaction vertex (S_1) is

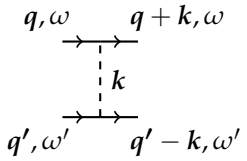

$$= -\frac{\Delta_D}{2}(\boldsymbol{q} \cdot (\boldsymbol{q}+\boldsymbol{k}))(\boldsymbol{q}' \cdot (\boldsymbol{q}'-\boldsymbol{k})) \tag{A.62}$$

We note that causality implies that any diagrams with closed P-loops are identically zero, since G_0 is retarded. As usual, we can organize the perturbative expansion for the full propagator $-iG$ in terms of a self-energy $G^{-1} = G_0^{-1} + \Sigma$,

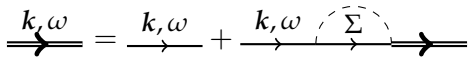

(A.63)

To one loop, the only diagram contributing to Σ is

$$\Sigma^{(1)}(\boldsymbol{k},\omega) = \underset{\boldsymbol{q},\omega}{\overset{\boldsymbol{k}-\boldsymbol{q}}{\circlearrowright}} = -\frac{\Delta_D}{2} \int \frac{d^d q}{(2\pi)^d} \frac{(\vec{q}\cdot\vec{k})^2}{-i\omega + Dq^2} \tag{A.64}$$

This is clearly isotropic and quadratic in $\vec{k}$. It is straightforward to evaluate $\Sigma^{(1)}$ as an expansion in $-i\omega$ (in 3d):

$$\Sigma^{(1)} = -\frac{\Delta_D \Lambda^3}{36\pi^2 D} k^2 + \frac{\Delta_D \Lambda}{12\pi^2 D^2}(-i\omega)k^2 + \cdots \tag{A.65}$$

where Λ is a UV momentum cutoff. As expected we find a correction to the long-wavelength diffusion constant $D'k^2$ and a dynamical correction $\ell^2(-i\omega)k^2$.

We now tease out the phenomenological role of the dynamical correction term for the observed diffusion. Focusing on the short-range case (without $k^{\alpha-d}$ correction):

$$G(\boldsymbol{k},\omega) = \frac{1}{-i\omega(1+\ell^2k^2)+Dk^2} \Rightarrow G(\boldsymbol{k},t) = \frac{e^{-Dk^2t/(1+\ell^2k^2)}}{1+\ell^2k^2}\,. \tag{A.66}$$

In the $t \to 0$ limit, the polarization profile approaches the Yukawa potential form $G(\boldsymbol{k}, t=0) = \frac{1}{1+\ell^2k^2}$ [847]. Returning to real space in three dimensions,

$$G(\boldsymbol{r}, t=0) = \frac{e^{-r/\ell}}{4\pi\ell^2 r}\,. \tag{A.67}$$

We note that this form should be interpreted as the shape to be expected of G at early times in the crossover to Gaussian behavior. It does not reduce to a delta function because we have neglected the higher order k and ω corrections which govern the short-distance, early-time dynamics.

However, the presence of this dynamical correction has important late time effects as well. From Eqn. (A.66), one observes that the large k modes now decay with a *constant* rate. This implies that the short-distance singularity of the Yukawa-potential decays only after the timescale ℓ^2/D.

We end this section with a few remarks. First, at even later times, the weight of the singularity decays exponentially while the diffusive behavior of the survival probability decays as a power-law in time, $S_p(t) \sim t^{-d/2}$, dominating the late-time physics. This is in agreement with the presence of the late-time diffusive fixed point. Second, such a singularity cannot be experimentally observable owing to the short-range cutoff of our system: we measure the polarization of the NV centers which must remain finite. One can understand this singularity as being regularized by the short-range details arising from the discrete nature of our randomly positioned spin system. Finally, while the $D'k^4$ term has the same scaling dimension as $(-i\omega)\ell^2k^2$, its inclusion in the analysis above does not change the qualitative statements, nor does it alter the nature of the early time behavior (it only appears in the exponent of Eqn. (A.66) and does not change the $t \to 0$ behavior).

Following the analytical derivation of the disorder-induced dynamical correction, we now present numerical evidence that highlights the role of disorder in the resulting long-lived exponential polarization profile, whether it arises from positional disorder or random onsite fields. To this end, we consider two different models where we include the two effects separately: first, we consider positional disorder

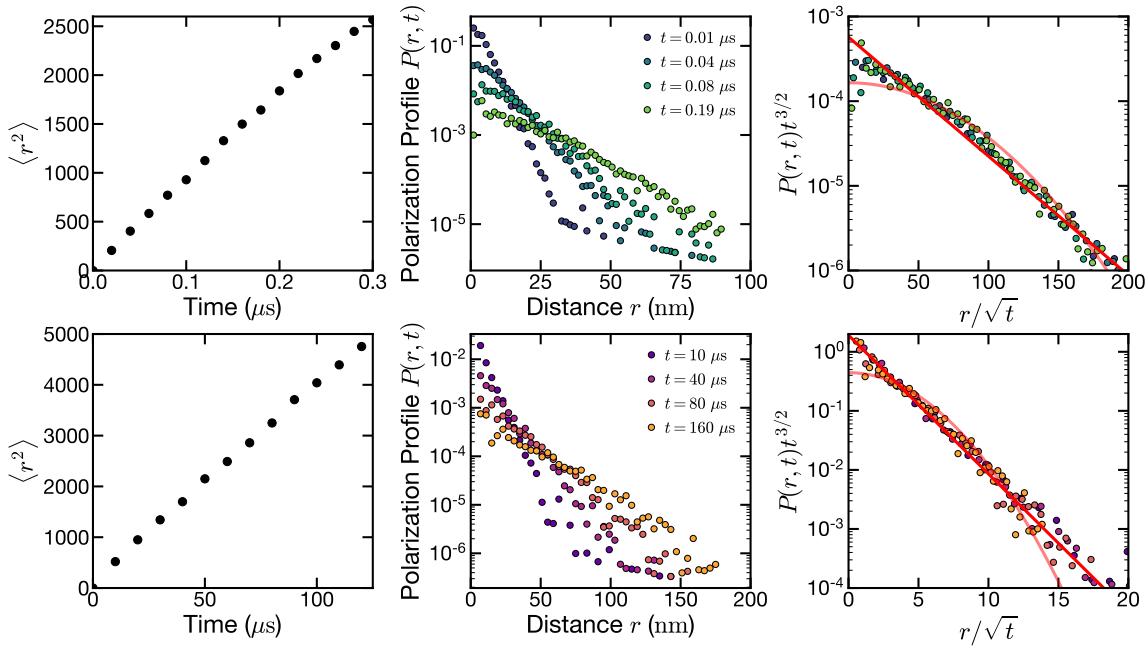

Figure A.4: Diffusive dynamics of a long-range system $\alpha = 6$ for two types of disorder. In the top row we consider positional disorder without onsite fields, in the bottom row we consider random onsite fields with spins placed within a cubic lattice. In either case of disorder we observe, an early time linear growth of the mean square displacement (left column) that highlights the diffusive nature of the dynamics, but the polarization profile remains non-Gaussian (middle column) throughout the evolution considered. This latter point is highlighted by rescaling the polarization profile $P(r,t)$ according to the diffusive dynamical exponent (right column), and observing that the collapse of different time traces agree with a simple exponential profile (Gaussian profile plotted for comparison).

of P1 centers with same density as sample S2 in the manuscript, but without onsite random fields; second, we consider no positional disorder by placing the P1 defects in a cubic lattice (with matching density as that considered in sample S2) and include the same strength of onsite random fields.

Our results are summarized in Fig. A.4, where for both models (albeit with different timescales owing to the different average hopping rates) we observe that the polarization profile remains non-Gaussian throughout the time considered (fact made clearer when considering the rescaled polarization profile in the right column). These results agree with the field theoretical calculation of the source of the dynamical correction, as this term arises from the presence of a spatially varying diffusion coefficient which arises from either positional disorder or a onsite random fields in the sample.

A.4 Details about random state creation and detection

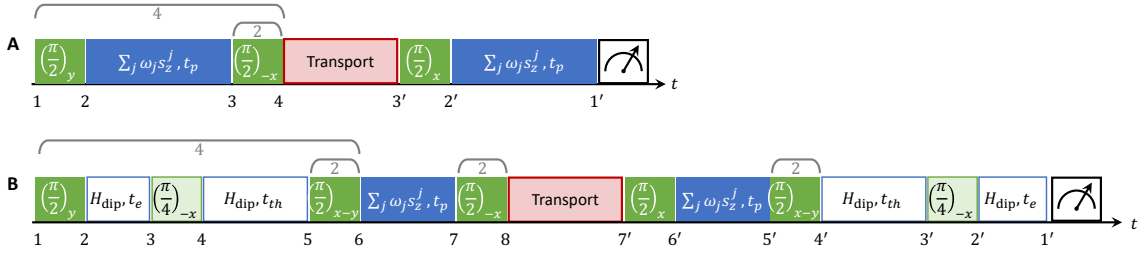

Figure A.5: Detailed sequence of the creation and detection of random Zeeman state (a) and double quantum state (b). Phase cycling is mark by brackets above the sequence, with the number under the bracket labels number of experiments with that phase cycling. For easier reference, we label different part of the sequence by numbers listed in the bottom.

The sequences we use to study transport contains 3 parts – state engineering, transport Hamiltonian engineering and observable engineering. The total unitary propagator U_{tot} is thus a product of 3 unitaries, $U_{tot} = U_\rho U_H U_\mathcal{O}$ and the NMR signal is then $\mathrm{Tr}(U_{tot}\rho_0 U_{tot}^\dagger \mathcal{O}_0)$. Figure A.5 shows the sequences we use to create, evolve, and detect random states. In the following we explain the sequence step by step.

Engineering random Zeeman states

1: The state is initially the high-temperature equilibrium state, $\rho \propto \mathbb{1} + \epsilon\rho_1$, with -$\rho_1 = Z = \sum_j S_z^j$. Since the identity does not evolve nor give rise to signal, in the following we only report the dynamics of the deviation ρ_1.

2: $\rho_2 = X$ thanks to a $\pi/2$ pulse along the y axis.

3: The disorder Hamiltonian is engineered with two concatenated WAHUHA sequences (eight $\pi/2$ pulses along x, y, -y, -x, -x, -y, y, x, named WAHUHA8) [219]. The WAHUHA8 sequence cancels the ^{19}F couplings, yielding the average Hamiltonian $\sum_j \omega_j S_z^j$, with $\omega_j = (1/3)w_j$. The total sequence length is 60μs. All the disorder Hamiltonians in Fig. A.5 are engineered by this sequence. The state becomes $\rho_3 = \sum_j \cos(\omega_j\tau) S_x^j + \sin(\omega_j\tau) S_y^j$.

4: To cancel the S_x component, we apply a 2-fold phase cycle over the $\pi/2$ pulse between 3 and 4. That is, we implement the sequence shown in Fig. A.5A twice, one with $(\pi/2)_x$

yielding $\rho_4^{(1)} = \sum_j [\cos(\omega_j\tau) S_x^j + \sin(\omega_j\tau) S_z^j]$, the other with $(\pi/2)_{-x}$ yielding $\rho_4^{(2)} = \sum_j [\cos(\omega_j\tau) S_x^j - \sin(\omega_j\tau) S_z^j]$. Then we take the difference of the signals from the two experiments as the final signal $S = \frac{1}{2}[\mathrm{Tr}(\rho_4^{(1)}(t)\mathcal{O}) - \mathrm{Tr}(\rho_4^{(2)}(t)\mathcal{O})] = \mathrm{Tr}(\rho_4(t)\mathcal{O})$, with $\rho_4 = \frac{1}{2}(\rho_4^{(1)} - \rho_4^{(2)}) = \sum_j \sin(\omega_j\tau) S_z^j$. We further implement a 4-fold phase cycle over all pulses before step 4, by a 4-fold rotation along z. This amounts to implementing each of the two repetitions discussed above 4 times, with 90° phase increments of all pulses before step 4 each time, and average over the results. Ideally the rotation along z axis should not affect ρ_4, but due to experimental imperfections ρ_4 also contains some unwanted terms that can be averaged out under this 4-fold phase cycling. There are 8 repetitions in total.

Engineering random Zeeman observables

$1'$: Creating the random observable can be best analyzed by describing the steps from later to earlier times. The final observable is $\mathcal{O}_{1'} = X$.

$2'$: Evolution under the disorder Hamiltonian (obtained with a WAHUHA8 sequence) yields $\mathcal{O}_{2'} = \sum_j [\cos(\omega_j\tau) S_x^j - \sin(\omega_j\tau) S_y^j]$.

$3'$: $\mathcal{O}_{3'} = \sum_j [\cos(\omega_j\tau) S_x^j + \sin(\omega_j\tau) S_z^j]$. If the transport Hamiltonian does not contain a disordered field, then the first term has zero overlap with the density matrix ρ_4 and can be neglected, leading to $\mathcal{O} = \sum_j \sin(\omega_j\tau) S_z^j$. If the transport Hamiltonian contains the disordered field, then another 2-fold phase cycling over the $\pi/2$ pulse between step $3'$ and $2'$ is needed to engineer the same observable, similar to step 4 above.

- Signal: The final signal after all phase cycling is $S = \mathrm{Tr}(\rho(t)\mathcal{O})$, with $\rho(0) = \mathcal{O} = \sum_j \sin(\omega_j\tau) S_z^j$. This already looks like the autocorrelation of random Zeeman state with random coefficient $\alpha_j = \sin(\omega_j\tau)$. It is easy to show $\sin(\omega_j\tau)$ has zero mean. We will show $\mathbb{E}[\sin(\omega_j\tau)\sin(\omega_k\tau)] \propto \delta_{jk}$ later (Appendix A.5).

- Variations: If we want to measure autocorrelation of random Zeeman state along y axis, we can simply move the transport step after the $\pi/2$ pulse between $3'$ and $2'$. That $\pi/2$ pulse is then considered part of initial state engineering, and the final effective initial state density

matrix is $\rho = \sum_j \sin(\omega_j \tau) S_y^j$ and observable is $\mathcal{O} = \sum_j \sin(\omega_j \tau) S_y^j$. Random Zeeman state along x axis can be engineered with 90° rotation of all pulses (except the transport Hamiltonian engineering pulses) along z axis. Random Zeeman state along any other axis can be decomposed in to correlations of random Zeeman states along x, y, z axes.

Engineering random double-quantum states

1: $\rho_1 = Z$.

2: $\rho_2 = X$.

3: $\rho_3 = X - i[H_{\text{dip}}, X]t_e + O(t_e^2) = X - \frac{3}{4}\sum_{j<k} J_{jk}(S_z^j S_y^k + S_y^j S_z^k)t_e + \sum_j w_j t_e S_y^j + O(t_e^2)$.

4: $\rho_4 = \sum_j S_x^j + \frac{3}{4}\sum_{j<k} J_{jk}(S_z^j S_z^k - S_y^j S_y^k)t_e + \sum_j w_j t_e (S_y^j - S_z^j)/\sqrt{2} + O(t_e^2)$.

5: The evolution time between step 4 and 5 is very long $|H_{\text{dip}} t_{th}| \gg 1$ such that state ρ_4 thermalizes to $e^{-\beta H_{\text{dip}}}/\text{Tr}(e^{-\beta H_{\text{dip}}})$ [89, 96]. The inverse temperature β is determined by the energy conservation $\text{Tr}[H_{\text{dip}}(1 - \epsilon\rho_4)] = \text{Tr}(H_{\text{dip}} e^{-\beta H_{\text{dip}}})/\text{Tr}(e^{-\beta H_{\text{dip}}})$. The state after thermalization is still a high temperature state with $\beta = O(\epsilon)$, therefore we have $e^{-\beta H_{\text{dip}}}/\text{Tr}(e^{-\beta H_{\text{dip}}}) \approx (\mathbb{I} - \beta H_{\text{dip}})/\text{Tr}(\mathbb{1})$ and the non-identity part is $\rho_5 \propto H_{\text{dip}}$. The sequence to create dipolar state was first demonstrated in Ref. [436].

6: $\rho_6^{(0)} = -\frac{1}{2}D_z + \frac{3}{4|k-j|^3}\sum_{j<k}(S_x^j S_y^k + S_y^j S_x^k) + \sum \frac{w_j}{\sqrt{2}}(S_x^j + S_y^j)$, the superscript (0) indicates this is the density matrix before phase cycling. The last term can be cancelled by 2-fold phase cycling of the $\pi/2$ pulse between step 5 and 6, i.e. averaging two experiments one with $(\pi/2)_{x-y}$ the other with $(\pi/2)_{y-x}$. The first term can be cancelled by 4-fold phase cycling of all previous pulses, i.e.

$$\begin{aligned}\rho_6 &= \frac{1}{4}[\rho_6^{(0)} - e^{-i(\pi/2)Z}\rho_6^{(0)} e^{i(\pi/2)Z} + e^{-i\pi Z}\rho_6^{(0)} e^{i\pi Z} - e^{-i(3\pi/2)Z}\rho_6^{(0)} e^{i(3\pi/2)Z}] \\ &= \frac{3}{4|k-j|^3}\sum_{j<k}(S_x^j S_y^k + S_y^j S_x^k),\end{aligned} \tag{A.68}$$

notice the minus sign in first and third line.

7: $\rho_7 = \frac{3}{4|k-j|^3}\sum_{j<k}(S_x^j S_y^k + S_y^j S_x^k)\cos(\omega_j\tau + \omega_k\tau) + (S_y^j S_y^k - S_x^j S_x^k)\sin(\omega_j\tau + \omega_k\tau)$.

8: A 2-fold phase cycling over $\pi/2$ pulse between step 7 and 8 cancels the first term in ρ_7. $\rho_8 = \frac{3}{4|k-j|^3}\sum_{j<k}(S_z^jS_z^k - S_x^jS_x^k)\sin\big(\omega_j\tau+\omega_k\tau\big)$.

Engineering random double-quantum observables

$1'$: $\mathcal{O}_{1'} = -X$.

$2'$: $\mathcal{O}_{2'} = -X + i[H_{\text{dip}}, -X]t_e + O(t_e^2) = -X - \frac{3}{4}\sum_{j<k}J_{jk}(S_z^jS_y^k + S_y^jS_z^k)t_e + \sum_j w_j t_e S_y^j + O(t_e^2)$. Notice for observable engineering we consider backward evolution so that the effective Hamiltonian is $-H_{dip}$.

$3'$: $\mathcal{O}_{3'} = -X - \frac{3}{4}\sum_{j<k}J_{jk}(S_z^jS_z^k - S_y^jS_y^k)t_e + \sum_j w_j t_e(S_y^j + S_z^j)/\sqrt{2} + O(t_e^2)$.

$4'$: Thermalization, $\mathcal{O}_{4'} \propto -H_{\text{dip}}$

$5'$: $\mathcal{O}_{5'}^{(0)} = \frac{1}{2}D_z - \frac{3}{4}\sum_{j<k}(S_x^jS_y^k + S_y^jS_x^k)/|k-j|^3 - \sum\frac{w_j}{\sqrt{2}}(S_x^j + S_y^j)$. The last term can be cancelled by 2-fold phase cycling of the $\pi/2$ pulse between step $5'$ and $4'$. $\mathcal{O}_{5'} = \frac{1}{2}D_z - \frac{3}{4}\sum_{j<k}(S_x^jS_y^k + S_y^jS_x^k)/|k-j|^3$.

$6'$: $\mathcal{O}_{6'} =$

$$\frac{1}{2|k-j|^3}\sum_{jk}S_z^jS_z^k - \frac{1}{2}(S_x^jS_x^k + S_y^jS_y^k)\cos\big(\omega_j\tau-\omega_k\tau\big) - \frac{1}{2}(S_x^jS_y^k - S_y^jS_x^k)\sin\big(\omega_j\tau-\omega_k\tau\big)$$
$$+\frac{3}{4|k-j|^3}\sum_{j<k} -(S_x^jS_y^k + S_y^jS_x^k)\cos\big(\omega_j\tau+\omega_k\tau\big) + (S_y^jS_y^k - S_x^jS_x^k)\sin\big(\omega_j\tau+\omega_k\tau\big).$$

$7'$: $\mathcal{O}_{7'} =$

$$\frac{1}{2|k-j|^3}\sum_{jk}S_y^jS_y^k - \frac{1}{2}(S_x^jS_x^k + S_z^jS_z^k)\cos\big(\omega_j\tau-\omega_k\tau\big) - \frac{1}{2}(S_x^jS_z^k - S_z^jS_x^k)\sin\big(\omega_j\tau-\omega_k\tau\big)$$
$$+\frac{3}{4|k-j|^3}\sum_{j<k} -(S_x^jS_z^k + S_z^jS_x^k)\cos\big(\omega_j\tau+\omega_k\tau\big) + (S_z^jS_z^k - S_x^jS_x^k)\sin\big(\omega_j\tau+\omega_k\tau\big).$$

When the transport Hamiltonian does not contain a disorder field, only the term

$$\frac{3}{4|k-j|^3}\sum_{j<k}(S_z^jS_z^k - S_x^jS_x^k)\sin\big(\omega_j\tau+\omega_k\tau\big)$$

in $\mathcal{O}_{7'}$ has nonzero overlap with the initial state, therefore

$$\begin{aligned}\mathcal{O} &= \frac{3}{4|k-j|^3}\sum_{j<k}(S_z^j S_z^k - S_x^j S_x^k)\sin\big(\omega_j\tau + \omega_k\tau\big) \\ &\approx \frac{3}{4}\sum_{j}(S_z^j S_z^{j+1} - S_x^j S_x^{j+1})\sin\big(\omega_j\tau + \omega_k\tau\big)\end{aligned}$$

.

- Signal: The final signal after phase cycling is $S = \mathrm{Tr}(\rho(t)\mathcal{O})$, with both ρ and $\mathcal{O}$ of the form rDQ_y. The random coefficient $\alpha_j' = \sin\big(\omega_j\tau + \omega_k\tau\big)$.

- Variations: Random double quantum state in xy place can be engineered with rotation of all pulses (except the transport Hamiltonian engineering pulses) along z axis. Autocorrelation of random double quantum state along z axis can be measure by moving the transport step after the $\pi/2$ pulse between step $7'$ and $6'$.

A.5 Multiple quantum coherence

A general Hermitian observable can be expanded in Pauli string basis

$$\mathcal{O}_\rho = \sum_s a_s \sigma_s, \tag{A.69}$$

where s is a tuple $s = (\alpha_1, \alpha_2, \cdots, \alpha_L)$ and $\alpha_j = 0, x, y, z$; a_s is a scalar coefficient (may be random); $\sigma_s = \otimes_{j=1}^L \sigma_{\alpha_j}$ is Pauli string with $\sigma_0 = \mathbb{1}$. Here we use Pauli operators $\sigma_\alpha^j = 2S_\alpha^j$ so that the normalization factors is a constant for all s, $\mathrm{Tr}(\sigma_s^2) = 2^L$. As we are interested in autocorrelation functions, it is sufficient to evaluate the correlation $C_{ss'} = \mathbb{E}(a_s a_{s'})$. In particular, by diagonalizing the correlation matrix $C_{ss'}$, we can get the principal components of the random state

$$\mathcal{O}_\rho = \sum_\mu d_\mu \mathcal{T}_\mu, \tag{A.70}$$

where d_μ are independent random variables $\mathbb{E}(d_\mu d_\nu) = \Lambda_\mu \delta_{\mu\nu}$, with Λ_μ being the eigenvalues of $C_{ss'}$ in decreasing order; $\mathcal{T}_\mu$ are orthonormal operators that we name as principal components, $\mathrm{Tr}(\mathcal{T}_\mu \mathcal{T}_\nu^\dagger) = 2^L \delta_{\mu\nu}$. As we do not have universal control, we cannot run a state tomography to determine $C_{ss'}$. Instead, we diagnose the state by global rotations, as different Pauli strings respond differently to global rotations. With some reasonable assumptions, we can then derive $C_{ss'}$.

Global rotations are commonly used in solid-state NMR to analyze spin states, a technique known as multiple quantum coherence (MQC) [848, 849]. MQC characterizes the state by its response to global rotations, therefore it is useful to write the state in the basis of irreducible spherical tensor operators (ISTOs) instead of Pauli strings

$$\mathcal{O}_\rho = \sum_{lm\lambda} a_{lm}^{(\lambda)} T_{lm}^{(\lambda)}, \tag{A.71}$$

where $l = 1, 2, \cdots$, $m = -l, -l+1, \cdots, l$, $a_{lm}^{(\lambda)}$ are scalar coefficients. λ is an additional index that labels different ISTOs in the spin chain with the same values l and m. The ISTOs form an orthonormal basis, $\mathrm{Tr}[T_{lm}^{(\lambda)} (T_{l'm'}^{(\lambda')})^\dagger] = 2^L \delta_{\lambda\lambda'} \delta_{ll'} \delta_{mm'}$. The ISTOs are defined by the following rotational property

$$U(\phi, \theta, \gamma) T_{lm}^{(\lambda)} U^\dagger(\phi, \theta, \gamma) = \sum_{m'} D_{lmm'}(\phi, \theta, \gamma) T_{lm}^{(\lambda)}, \tag{A.72}$$

where $U(\phi,\theta,\gamma) = e^{-i\phi\sum_j S^j_z} e^{-i\theta\sum_j S^j_y} e^{-i\gamma\sum_j S^j_z}$, $D_{lmm'}(\phi,\theta,\gamma) = e^{-im'\phi} d_{lmm'}(\theta) e^{-im\gamma}$ is the Wigner D-matrix [850]. We list ISTOs for the j^{th} nearest-neighbor spin pair, with $\lambda = j = 1, 2, \cdots, L$

$$\begin{aligned}
T^{(j)}_{00} &= \mathbb{1} \\
T^{(j)}_{10} &= \sigma^j_z \\
T^{(j)}_{11} &= \sigma^j_+ \\
T^{(j)}_{20} &= \frac{1}{\sqrt{6}}(2\sigma^j_z\sigma^{j+1}_z - \sigma^j_x\sigma^{j+1}_x - \sigma^j_y\sigma^{j+1}_y) \\
T^{(j)}_{21} &= \frac{1}{\sqrt{2}}(\sigma^j_z\sigma^{j+1}_+ + \sigma^j_+\sigma^{j+1}_z) \\
T^{(j)}_{22} &= \sigma^j_+\sigma^{j+1}_+.
\end{aligned} \tag{A.73}$$

ISTOs with $m < 0$ can be obtained via $Y_{l,-m} = (-1)^m Y^\dagger_{lm}$. We consider periodic boundary condition here. These ISTOs have the shortest correlation length (distance between furthest non-trivial Pauli operators). ISTOs with longer correlation length and same l, m can be formed by (i) multiplying by $(\sigma^k_x\sigma^l_x + \sigma^k_y\sigma^l_y + \sigma^k_z\sigma^l_z)$ (ii) inserting identities between nontrivial Pauli operators. Similarly, ISTO with larger l, m but shortest correlation lengths can be written in terms of triplets, and multiplets of contiguous spins.

In experiments, we rotate the state $\mathcal{O}_\rho$ along the z axis by an angle γ, then along y axis by an angle θ, then along y axis by ϕ and finally we measure the overlap of the rotated density matrix with the original one. The signal is

$$I(\phi,\theta,\gamma) = \mathrm{Tr}\left[U(\phi,\theta,\gamma)\mathcal{O}_\rho U^\dagger(\phi,\theta,\gamma)\mathcal{O}_\rho\right]. \tag{A.74}$$

From experiments involving global rotation only, such as MQC experiment, one can distinguish between ISTOs with different l and/or m [851], but it is fundamentally impossible to distinguish those with same l and m but different λ. Therefore we make the following assumptions. First, for given l and m, we consider only ISTOs with the smallest correlation length. Indeed, during the random-state preparation only rotations and disorder field are applied, which do not create many-body correlation. Operators with longer correlation length can be created only due to higher order effects of the Floquet engineering sequence or experimental imperfections. Therefore, if we detect a spherical component

with a given l, m, it is most likely to be from the ISTOs with shortest correlation length. With the above assumption, we can consider only $\lambda = 1, 2, \cdots, L$,

$$\mathcal{O}_\rho \approx \sum_{j=1}^{L} \sum_{l=0}^{\infty} \sum_{m=-l}^{l} a_{lm}^{(j)} T_{lm}^{(j)}. \tag{A.75}$$

For given l and m, the terms $T_{lm}^{(j)}$ are related by spatial translation. The second assumption is that the state is statistically translational invariant, meaning although the coefficient $a_{lm}^{(j)}$ depends on j, its statistics is independent of j. This is reasonable because we use a macroscopic crystal, and the chains are only interrupted by rare defects. For our purpose, we only use the translation invariance of correlation, $\mathbb{E}(a_{lm}^{(j)} a_{lm'}^{(j)}) = c_{lmm'}$. Using Eq. A.73 we can then get $C_{ss'}$ from $c_{lmm'}$.

Next we discuss how to extract $c_{lmm'}$ from experimental signal $I(\phi, \theta, \gamma)$. Plugging the simplified density matrix in Eq. A.75 into the signal in Eq. A.74, we obtain

$$I(\phi, \theta, \gamma) = L \sum_{l=0}^{\infty} \sum_{m=-l}^{l} \sum_{m'=-l}^{l} c_{lmm'} D_{lmm'}(\phi, \theta, \gamma), \tag{A.76}$$

where we used the fact that $\mathcal{O}_\rho$ is hermitian. To extract $c_{lmm'}$, we Fourier transform over ϕ and γ,

$$I_{mm'}(\theta) = L \sum_{l=0}^{\infty} c_{lmm'} d_{lmm'}(\theta), \tag{A.77}$$

where $I_{mm'}(\theta) = \int_0^{2\pi} d\phi \int_0^{2\pi} d\gamma e^{im'\phi} I(\phi, \theta, \gamma) e^{im\gamma} / (2\pi)^2$. $c_{lmm'}$ can be obtained by fitting to the experimentally measure $I_{mm'}^{\exp}(\theta)$,

$$c_{lmm'} = \arg\min_{c_{lmm'}} \sum_{\theta} \left(S_{mm'}^{\exp}(\theta) - L \sum_{l=0}^{\infty} c_{lmm'} d_{lmm'}(\theta) \right)^2. \tag{A.78}$$

$c_{lmm'} = \mathbb{E}(a_{lm}^{(j)} a_{lm'}^{(j)})$ form a correlation matrix, which should be positive semi-definite. However, due to experimental errors, the fitted $c_{lmm'}$ may not be positive semi-definite so we replace the negative eigenvalues by zeros.

In experiments, we vary ϕ, θ, γ independently from 0 to 345 degree with a step of 45 degree, so we can evaluate m, m' from -3 to 4. To evaluate Eq. A.78, we assume the maximum correlation length in the prepared states is l_{max}, i.e. $a_{lm} = 0$ for $l > l_{max}$. For the random Zeeman state (random DQ state), the residual of the fitting to $I(\phi, \theta, \gamma)$ stays stable for $l_{max} \geq 1$ ($l_{max} \geq 2$) (Fig. A.6A). Therefore in

the experiment we use $l_{max} = 3$ for both states (Fig. 2.15). Here, we show the largest eigenvalue of correlation matrix $C_{SS'}$ as a function of l_{max} and confirm that the largest principal component remains dominant regardless of l_{max} (Fig. A.6B).

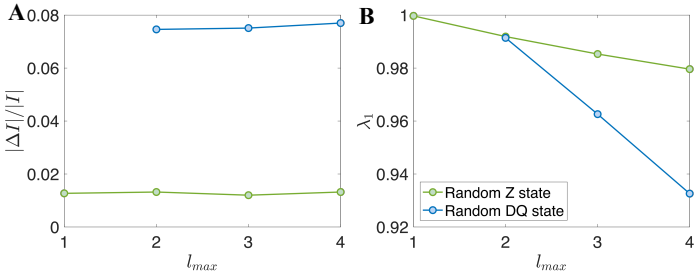

Figure A.6: (a) Relative difference the measured $I(\phi,\theta,\gamma)$ and fitted $\hat{I}(\phi,\theta,\gamma)$ as a function of l_{max}. $\Delta I = I - \hat{I}$ and $|\cdot|$ denotes Frobenius norm. (b) Largest eigenvalue of the correlation matrix as a function of l_{max}. The correlation matrix are normalized such that the positive eigenvalues sum to 1.

Finally, we note that for conventional states without randomness, fixing $\gamma = 0$ and varying ϕ and θ is sufficient to determine the coefficients $a_{lm}^{(j)}$ [848, 849]. The reason is that $a_{lm}^{(j)}$ are deterministic thus $c_{lmm'}$ are dependent, $c_{lmm'} = \sqrt{c_{lmm}c_{lmm'}}$. However, the above equation does not hold for random states and $c_{lmm'}$ contains more degrees of freedom, so independently varying ϕ, θ and γ is required here.

A.6 Polarization transfer in the GHD framework

In what follows we briefly explain how to compute polarization transfer $P(t)$ within the Generalized Hydrodynamics (GHD) framework, in the limit of weak quenches, $\eta \ll 1$. In this limit, one can express $P(t)$ in terms of linear-response correlation functions. As we will see, this quantity is related to (but subtly different from) the transport coefficients that have previously been calculated in the literature.

In the $\eta \ll 1$ limit, it is known [353] that the magnetization profile $\rho(x,t) = \langle \hat{S}^z_x(t) \rangle$ is related to the linear-response dynamical correlation function $C(x,t) \equiv \langle \hat{S}^z_x(t) \hat{S}^z_0(0) \rangle$ via the expression

$$C(x,t) = \partial_x \rho(x,t) \tag{A.79}$$

where we used the continuum notation for derivatives, for simplicity, although in a lattice model they should strictly be expressed in terms of discrete differences. We can invert this relation to read:

$$\rho(x,t) = \rho(-\infty) + \int_{-\infty}^{x} dx' C(x',t). \tag{A.80}$$

The polarization transfer is (up to time-independent constants) given by

$$P(t) = \int_{-\infty}^{0} \int_{-\infty}^{x} dx dx' C(x',t). \tag{A.81}$$

In the hydrodynamic limit, $C(x,t)$ will take the scaling form $t^{-1/z} C(x^z/t)$, where z is the dynamical exponent. By dimensional analysis of the expression for $P(t)$ one can see that this in general implies $P(t) \sim t^{1/z}$.

We now discuss the scaling of this quantity within GHD in the Heisenberg model, working at $\delta \neq 0$. In the Heisenberg model, there are infinitely many quasiparticle species, labeled by the "string index" s. Each quasiparticle species propagates ballistically ($z = 1$); the velocity of a quasiparticle (and the density of such quasiparticles $\rho_s(\theta)$) depends on both s and the quasimomentum θ. In terms of these, $C(x,t)$ can be written as [852]

$$C(x,t) = \sum_s \int d\theta \rho_s(\theta) [m^{\mathrm{dr}}_s(\theta)]^2 \delta(x - v^{\mathrm{eff}}_s(\theta) t). \tag{A.82}$$

This expression can be interpreted as follows: each quasiparticle propagates ballistically with some

velocity $v_s^{\text{eff}}(\theta)$ that depends on the nature of the background state, and carries some effective spin (which, again, depends on the background state via dynamical screening). Correlations between the spacetime points $(0,0)$ and (x,t) come from all quasiparticles whose trajectories pass through both spacetime points. The thermodynamic Bethe ansatz provides a framework within which all the quantities appearing in Eq. (A.82) can straightforwardly be computed. In the high temperature limit, closed-form expressions exist [477] for all the quasiparticle data in Eq. (A.82). After some coarse-graining the correlator can be written as [172]

$$C(x,t) = \sum_s \frac{1}{\tilde{v}_s t} \rho_s (m_s^{\text{dr}})^2 \Theta(x - \tilde{v}_s t) \tag{A.83}$$

where $\tilde{v}_s$ is some characteristic velocity for quasiparticles of species s, and Θ is the Heaviside step function. Plugging this form into Eq. (A.81) we find that

$$P(t) = t \sum_s \rho_s (m_s^{\text{dr}})^2 \tilde{v}_s. \tag{A.84}$$

In the Heisenberg model at nonzero δ, one has the following scaling forms. For $s\delta \lesssim 1$, we have $\rho_s \sim 1/s^3$ and $m_s^{dr} \sim \delta s^2$, while for $s\delta \gtrsim 1$, we have $\rho_s \sim \exp(-\delta s)$ and $m_s^{dr} = s$. For all s we have the scaling $v_s \sim 1/s$. Thus the sum over species gets cut off at $s \sim 1/\delta$, yielding the expression

$$P(t) \sim \delta^2 \sum_{s<1/\delta} O(1) \sim \delta t. \tag{A.85}$$

Superdiffusion can be recovered within this framework by noting that even when $\delta = 0$, fluctuations of δ cause quasiparticles to move in a time-dependent apparent magnetic field.

It is interesting to contrast the expression (A.84) with that for the Drude weight $\mathcal{D}$ (i.e., singular part of the zero-frequency conductivity) of the Heisenberg model:

$$\mathcal{D} = \sum_s \rho_s (m_s^{\text{dr}})^2 |\tilde{v}_s|^2. \tag{A.86}$$

Because of the extra factor of velocity in Eq. (A.86) relative to Eq. (A.84), the contribution of slow quasiparticles to the polarization transfer is much larger than their contribution to the Drude weight.

A.7 Integrable models with non-Abelian symmetries and supersymmetries

In this section, we explicitly list the matrix form of all the Hamiltonians we have studied to explore the KPZ superdiffusion, including those with each of the four classes of simple non-Abelian symmetries, those with super-symmetries, the symmetry-breaking model, and the integrability-breaking model. To simplify the notation, we use $S^{\alpha,\beta}$ to denote the matrix with all elements being 0 except the α^{th} row and the β^{th} column which takes value 1: $S^{\alpha,\beta} = |\alpha\rangle\langle\beta|$. It is easy to notice

$$[S^{\alpha,\beta}, S^{\mu,\nu}] = \delta_{\beta,\mu} S^{\alpha,\nu} - \delta_{\nu,\alpha} S^{\mu,\beta}. \tag{A.87}$$

We note that one can use any sets of operators satisfying this commutation relation to replace $S^{\alpha,\beta}$ in the following Hamiltonians, and obtain integrable models with the same symmetries.

A.7.1 Non-Abelian symmetry

We focus on models with the non-Abelian symmetries that can be described by simple Lie algebras. The simple Lie algebras fall into four classical series A_N [SU(N)], B_N [SO($2N+1$)], C_N [SP($2N$)] and D_N [SO($2N$)], and five exceptional cases G_2, F_4, E_6, E_7, and E_8. Here, we only focus on the classical series.

Let us define two operators acting on site i and j as

$$\begin{aligned} \Pi_{ij} &= \sum_{\alpha,\beta} S_i^{\alpha,\beta} \otimes S_j^{\beta,\alpha} \\ \Xi_{ij}^{\mathrm{SO}} &= \sum_{\alpha,\beta} S_i^{\alpha,\beta} \otimes S_j^{N-\alpha,N-\beta} \\ \Xi_{ij}^{\mathrm{SP}} &= \sum_{\alpha,\beta} \theta_\alpha \theta_\beta S_i^{\alpha,\beta} \otimes S_j^{N-\alpha,N-\beta} \end{aligned} \tag{A.88}$$

where N is the dimension of the local Hilbert space, and $\theta_\alpha = \delta_{1\le\alpha\le\frac{N}{2}} - \delta_{\frac{N}{2}+1\le\alpha\le N}$. We can then

write down the two-site Hamiltonian for different symmetries as

$$\begin{aligned} H_{ij}^{\mathrm{SU}} &= \Pi_{ij} \\ H_{ij}^{\mathrm{SO}} &= \Pi_{ij} - \frac{2}{N-2}\Xi_{ij}^{\mathrm{SO}} \\ H_{ij}^{\mathrm{SP}} &= \Pi_{ij} + \frac{2}{N+2}\Xi_{ij}^{\mathrm{SP}} \end{aligned} \tag{A.89}$$

with appropriate N [173, 499, 500, 502].

The integrable static model then has the Hamiltonian $H = \sum_i H_{i,i+1}^{\mathrm{sym}}$, where "sym" can be SU, SO or SP. For the integrable Floquet model, we further define: $H_{\mathrm{even}} = \sum_i H_{2i,2i+1}^{\mathrm{sym}}$ and $H_{\mathrm{odd}} = \sum_i H_{2i-1,2i}^{\mathrm{sym}}$. The Floquet evolution is generated by alternately evolving the system with H_{even} and H_{odd} for time $T/2$, where T is the Floquet period.

A.7.2 Supersymmetry

Similar to the fact that the non-Abelian symmetries are characterized by Lie algebras, supersymmetries are characterized by Lie super-algebra, which is a generalization of Lie algebra with a $\mathbb{Z}_2$-grading. Moreover, the simple Lie super-algebras also fall into two classical series (i.e. superunitary and orthosymplectic) plus several exceptional cases. Here, we focus on the superunitary series denoted as SU($M|N$), as a generalization of the unitary series of Lie algebra with a $\mathbb{Z}_2$-grading. A $\mathbb{Z}_2$-grading can be understood as follows: Lie algebras describe the commutation relation between the generators of symmetry groups; with $\mathbb{Z}_2$-grading, the generators are divided into two sets; while the generators from the same set are still defined according to commutation relation, those from different groups are defined by an anti-commutation relation.

In particular with the SU($M|N$) supersymmetry, the $(M+N)$-dimensional local Hilbert space is spanned by two sets of states, each of which includes M and N states respectively. The transition operators $S^{\alpha,\beta}$ between any two states are then classified according to whether the two states are from the same set or not. Based on this intuition, it is natural to expect that an SU($M|N$) Hamiltonian has a similar form of an SU($M+N$) Hamiltonian with some additional minus sign for certain terms in Eq. A.88. Indeed, the two-site Hamiltonian of an integrable system with supersymmetry SU(m|n) can

be written as:

$$H_{ij}^{\mathrm{Sup}} = \Pi_{ij}^{\mathrm{Sup}} = \sum_{\alpha,\beta} (-1)^{P(\alpha)\cdot P(\beta)} S_i^{\alpha,\beta} \otimes S_j^{\beta,\alpha}, \tag{A.90}$$

where $P(\alpha) = 0$ if $\alpha \leq M$, otherwise $P(\alpha) = 1$. Similar to the symmetric case, the static Hamiltonian is the sum of all two-site operators, while the Floquet dynamics is generarted by alternately applying two-site Hamiltonians on even and odd bonds.

A.7.3 Symmetry breaking

To break the SU(3) symmetry while still keeping the model integrable, we considered the Izergin-Korepin model, whose Hamiltonian only consists of nearest-neighbor interaction, i.e., $H^{\mathrm{I-K}} = \sum_i H_{i,i+1}^{\mathrm{I-K}}$, where the two-body interaction is written as [494–496]:

$$\begin{aligned}
H_{i,j}^{\mathrm{I-K}} = & \frac{1}{\cosh 3\Delta \cosh 2\Delta} \times \\
& \Big\{ \cosh 5\Delta \ (S_i^{1,1} S_j^{1,1} + S_i^{3,3} S_j^{3,3}) + \cosh \Delta \ (S_i^{1,3} S_j^{3,1} + S_i^{3,1} S_j^{1,3}) \\
& + 2 \sinh \Delta \sinh 2\Delta \ (e^{-2\Delta} S_i^{1,1} S_j^{3,3} + e^{2\Delta} S_i^{3,3} S_j^{1,1}) \\
& + \sinh 2\Delta \ (\sinh 3\Delta - \cosh 3\Delta)(S_i^{1,1} S_j^{2,2} + S_i^{2,2} S_j^{3,3}) \\
& + \sinh 2\Delta \ (\sinh 3\Delta + \cosh 3\Delta)(S_i^{2,2} S_j^{1,1} + S_i^{3,3} S_j^{2,2}) \\
& + \cosh 3\Delta \ (S_i^{1,2} S_j^{2,1} + S_i^{2,1} S_j^{1,2} + S_i^{2,2} S_j^{2,2} + S_i^{2,3} S_j^{3,2} + S_i^{3,2} S_j^{2,3}) \\
& - e^{-2\Delta} \sinh 2\Delta \ (S_i^{1,2} S_j^{3,2} + S_i^{2,1} S_j^{2,3}) + e^{2\Delta} \sinh 2\Delta \ (S_i^{2,3} S_j^{2,1} + S_i^{3,2} S_j^{1,2}) \Big\}.
\end{aligned} \tag{A.91}$$

It is easy to notice that the Izergin-Korepin Hamiltonian always has a U(1) conserved charge $\sum_i (S_i^{1,1} - S_i^{3,3})$, and the SU(3) symmetry recovers when $\Delta = 0$.

A.7.4 Integrability breaking

To break the integrability of the SU(3) model while keeping the symmetry, we add next-nearest-neighbor interaction to the system. This modification is in general also valid for models with other symmetries. To be specific, the non-integrable symmetric Hamiltonian can be written as:

$$H = \sum_i H_{i,i+1} + J_{nnn} H_{i,i+2}, \tag{A.92}$$

where J_{nnn} is the strength of the next-nearest-neighbor interaction.

The intuition for why the integrability is broken is simple. The integrability of the nearest-neighbor-interacting models results from a special property that any multi-body scattering process in the system is reducible to a series of two-body scattering. This is further guaranteed by a combination of Yang-Baxter equation and the fact that all scattering processes follow a certain order. To be specific, imagine three particles placed on different sites undergo a scattering process. With only nearest-neighbor interaction, the leftmost particle and the rightmost one can interact only after either of them scatters with the middle one, which sets the order of the scattering process. However, the next-nearest-interacting term can break such order, and thus break the reducibility of the multi-body scattering.

A.8 Fluctuations in KPZ dynamics

One of the key features that distinguishes KPZ dynamics from other $z = 3/2$ dynamical processes (such as rescaled diffusion and Lévy flights) is the non-linearity of the underlying dynamical process. This non-linearity has an important consequence: fluctuations of the polarization transfer are not symmetric around the mean.

In the case of KPZ dynamics in the 1D Heisenberg model, the magnetization profile $S^z(x,t)$ is mapped to the spatial derivative of the height field $h(x,t)$ of the KPZ equation, $S^z(x,t) \sim \partial_x h(x,t)$ [427]. The initial state studied in our work, i.e. the domain wall in magnetization $S^z(x,0) \sim 2\Theta(x) - 1$ (with Heaviside function Θ), then maps to a wedge initial state of the height field $h(x,0) \sim -|x|$. The polarization transfer $P(t)$, being the spatially integrated magnetization profile $P(t) \sim \int_{-\infty}^{0} S^z(x,t)\,dx$, thus maps to the height field at the peak of the wedge $h(0,t)$. The dynamical fluctuations of precisely this quantity, $h(0,t)$, were numerically studied in Ref. [540] for a classical lattice model known to be in the KPZ universality class. At late times, these fluctuations showed an approach to the GUE Tracy-Widom (TW) distribution, which (owing to universality) also describes the distribution of largest eigenvalue of random matrices from the Gaussian unitary ensemble (GUE).

This feature provides a path to directly observing the underlying KPZ dynamics. Leveraging the access to single experimental snapshots in quantum-gas microscopes, as well as the single-site resolution, we can immediately build the distribution of the polarization transfer and measure the aforementioned asymmetry via the skewness of the distribution.

A.8.1 Polarization transfer fluctuations near pure state

In order to better highlight the fluctuations of magnetization, we begin by considering the pure domain wall dynamics. While at the Heisenberg point, the late-time dynamics approaches a logarithmically corrected diffusion [545], the approach to this universal behavior is very slow and the system exhibits superdiffusion with KPZ characteristics for intermediate timescales.

We then study the dynamics of the pure domain wall under three different Hamiltonians: the Heisenberg Hamiltonian (Eq. 2.26), the easy-plane XXZ model, and a next-nearest neighbor interacting

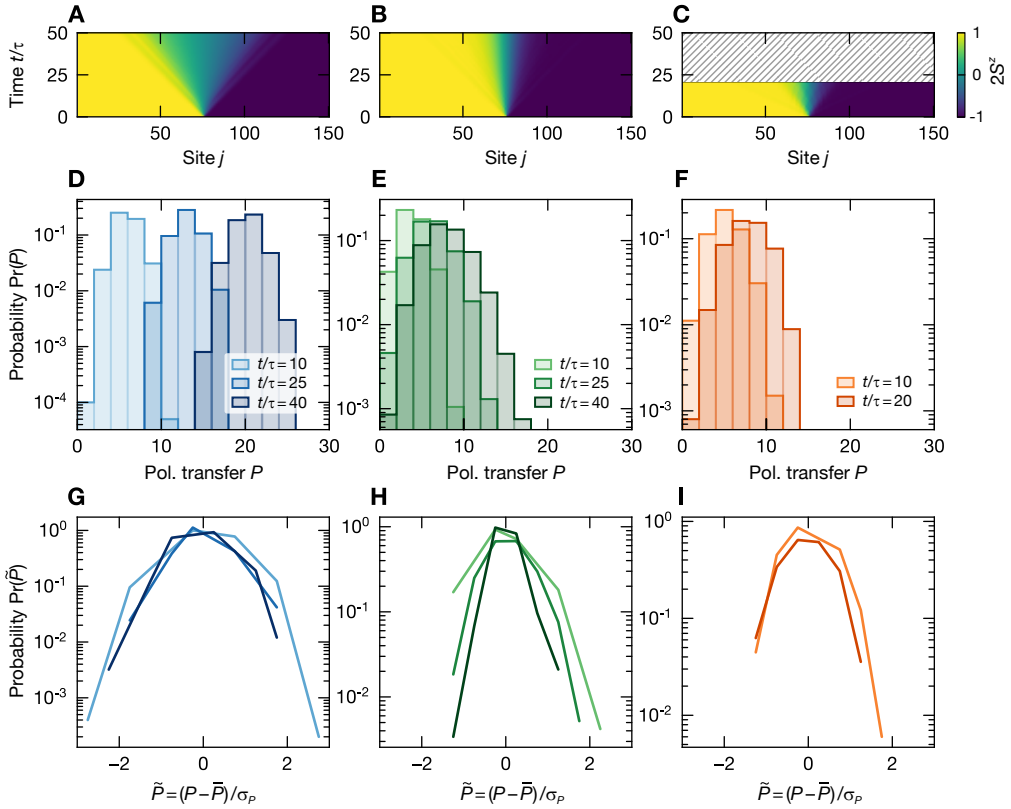

Figure A.7: Magnetization dynamics in different transport regimes. Ballistic (**A**,**D**,**G**), KPZ superdiffusive (**B**,**E**,**H**), diffusive (**C**,**F**,**I**, simulated up to $t/\tau = 20$) transport for different models initialized in a pure domain wall ($\eta = 1$). (**A**-**C**) Polarization-profile dynamics for the entire chain as a function of time. (**D**-**F**) Distribution of the polarization transfer P with respect to the initial state measured by projecting the quantum state into the measurement basis according to the Born rule (akin to the single-shot measurement procedure performed in the experiments). (**G**-**I**) Rescaled probability distribution $\tilde{P}$ according to the average $\overline{P}$ and standard deviation σ_P of the transferred polarization.

Heisenberg model with Hamiltonian:

$$\begin{aligned}\hat{H}_{\mathrm{NNN}}/J = &\sum_i \hat{S}_i^x \hat{S}_{i+1}^x + \hat{S}_i^y \hat{S}_{i+1}^y + 1.05\hat{S}_i^z \hat{S}_{i+1}^z \\ &-0.764 \sum_i \hat{S}_i^x \hat{S}_{i+2}^x + \hat{S}_i^y \hat{S}_{i+2}^y + 1.05\hat{S}_i^z \hat{S}_{i+2}^z\end{aligned} \tag{A.93}$$

These models allow us to display the three universality classes of the dynamics: KPZ, ballistic and diffusive dynamics, respectively. Using an MPS representation of the quantum state, we perform time evolution of a chain of 150 spins; using a TEBD algorithm with step size $\delta t = 0.1$ and large enough bond dimension to observe convergence. Leveraging the MPS representation, average quantities can

be directly computed via the expectation value of the corresponding observables (Figs. A.7A-C). At the same time, the single-shot experimental measurement can be simulated by sampling the quantum state over the measurement basis (according to the Born rule). By computing the number of spins that crossed the initially pure domain wall, we can directly obtain, not only the average polarization profile, but its entire distribution (Figs. A.7D-F).

Crucially, the resulting distributions in these three cases look very different. In both ballistic and diffusive cases (Figs. A.7D,F), the distributions remain symmetric, while in the superdiffusive case (Figs. A.7E), the distribution develops a tail towards large polarization transfer. Such behavior is easier to observe upon subtracting the average P and rescaling with the standard deviation (Figs. A.7G-I).

These differences can be quantified by looking at the evolution of the different moments of the distribution: average, standard deviation and (normalized) skewness Fig. A.8. We note that the average and standard deviation scale differently with time, highlighting the different dynamical exponents. More importantly, we observe that the skewness for both ballistic and diffusive regimes decays to zero (signifying that the distribution is symmetric), while, in the superdiffusive case, the skewness remains non-zero and approaches a finite value. While this value approaches the skewness of a Tracy-Widom distribution (green line, Fig. A.8C), it corresponds to the Gaussian-orthogonal-ensemble (GOE) TW distribution (with skewness ~ 0.294), which is expected for a different set of initial conditions. Namely, for the wedge initial configuration we expect the fluctuation distribution to approach the GUE Tracy-Widom distribution whose skewness is ~ 0.225 (red dashed line, Fig. A.8C) [550]. At present, the origin of this deviation remains unclear. These numerics highlight two important facts: first, that the skewness can identify the underlying nature of the transport dynamics, and second, that this distinction occurs within the experimentally accessible time.

A.8.2 Polarization transfer fluctuations for imperfect initial states

We can also obtain the statistics of the polarization transport for $\eta < 1$ using DMT, which is beyond the scope of the TEBD simulation and allows us to simulate the evolution of the skewness for mixed states. However, due to the nature of the DMT method, the distribution of the total polarization transfer converges more slowly; for a bond dimension of $\chi = 512$ we find convergence up to time

$t/\tau = 30$.

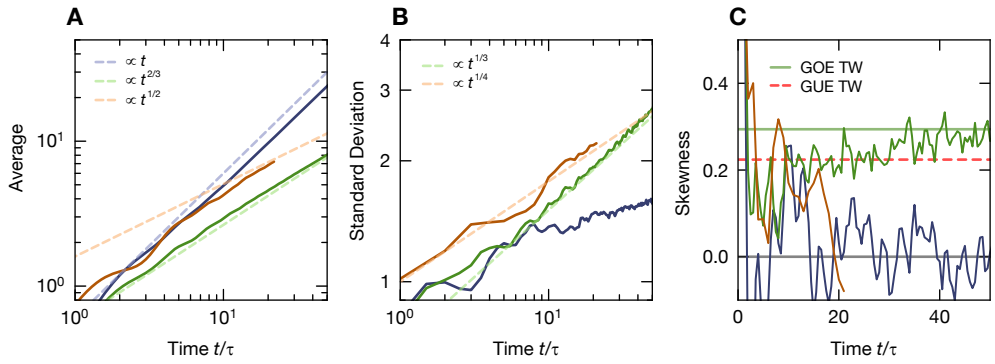

Figure A.8: Statistical moments of polarization-transfer distribution in different transport regimes. Average (**A**), standard deviation (**B**) and skewness (**C**) of the distribution of transferred polarization P for the different models exhibiting ballistic (blue), KPZ superdiffusive (green), diffusive (orange) transport. Dashed lines indicate expected scaling behavior. In **C**, the constant lines mark the late-time expectation for KPZ (red dashed for our initial state, green for different one), and for both diffusive and ballistic (black).

From the experimental data, we obtain the skewness by subtracting the initial variance and the third moment due to the finite-η initial-state fluctuations. Here, we justify this data processing procedure using DMT simulation results (Fig. A.9).

In particular, we observe that after the subtraction procedure the skewness is consistent with that of the pure domain wall with $\eta = 1$ (Fig. A.9A). In contrast, the unsubtracted data exhibit much larger deviations and approaches the late-time skewness from above. This behavior matches our experimental data (Figs. 2.28), where both the unsubtracted data approaches the asymptotic skewness from above while the subtracted data approaches it from below.

Moreover, we study how the experimental imperfections of domain-wall preparation can affect the resulting skewness (Fig. A.9B). In the experiment, with 20% probability, the prepared domain wall is one site off the targeted position. Numerically reproducing this behavior shows that the subtraction procedure is also robust to this uncertainty.

A.8.3 Decay of skewness in linear transport

In this section we describe why, in linear transport, the skewness of the polarization transfer distribution always decays. Leveraging the linearity of the transport equations, we can compute the magnetization distribution $F(x_0, t)$ via a convolution of the initial domain, with the Green's

function of equation $f(x,t)$ (i.e. the magnetization profile dynamics starting from a delta-function of magnetization at time $t = 0$):

$$F(x_0,t) \propto \int_{-\infty}^{0} dx\, f(x-x_0,t) = \int_{-\infty}^{x_0} dx\, f(x,t). \tag{A.94}$$

If the linear transport has dynamical exponent z, $f(x,t)$ (for large enough x and t) is given by a scaling function:

$$f(x,t) = t^{-1/z} g\left(\frac{x}{t^{1/z}}\right), \tag{A.95}$$

which implies that $F(x_0,t) = G(x_0/t^{1/z})$. This exactly corresponds to the rescaling one should perform to collapse the magnetization profile at different times.

This means that all moments of the distribution, which are integrals of powers of $F(x_0,t)$, at fixed time, will scale with $t^{1/z}$. Since the skewness is given by the ratio of the third moment and the second moment to the $3/2$ power, we have that the skewness will decay as $t^{-1/2z}$ and thus become zero at late enough times. This holds for all higher moments, ensuring that the rescaled distribution of the polarization transfers approaches the normal distribution.

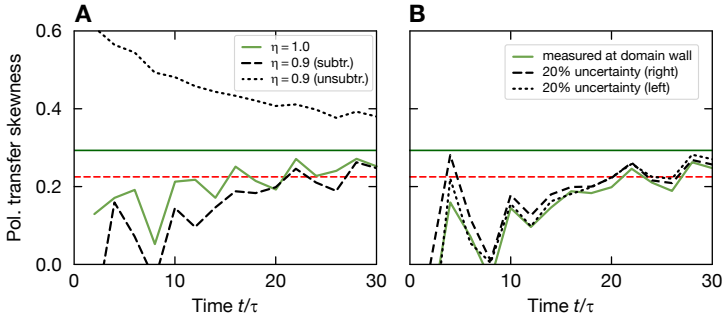

Figure A.9: DMT-simulated skewness of polarization-transfer distribution using subtracted statistics. (**A**) The skewness of the $\eta = 1$ domain wall (green) grows towards the asymptotic value and agrees with the TEBD simulation shown in Fig. A.8. For $\eta < 1$ domain walls, the skewness decreases towards the asymptotic value due to thermal fluctuations of the initial state (black dotted). When using subtracted statistics for the calculation of the skewness (black dashed), the initial-state artefacts are reduced and the skewness evolves similarly to the $\eta = 1$ case. (**B**) The skewness using subtracted statistics is also robust to imperfections in the domain-wall position: Assuming that the domain wall was prepared on the wrong site (one site left/right of the targeted site, black dotted/dashed) with 20% probability (corresponding to the experimental uncertainty), the skewness agrees with the ideal case (green). Green and red horizontal lines indicate the skewness of the GOE and GUE TW distributions, respectively.

A.9 Two-Body Resonance Counting and Avalanche Instabilities at Infinite-Randomness

In the absence of interactions, the transitions we consider fall into an infinite-randomness universality class characterized by a divergent single-particle density of states and divergent mean and typical orbital localization lengths (diverging as $D(\varepsilon) \sim |\varepsilon \log^3 \varepsilon|^{-1}$, $\xi_{\text{mean}} \sim |\log^2 \varepsilon|$, and $\xi_{\text{typ}} \sim |\log \varepsilon|$ respectively in single particle energy ε). In this section, we investigate how such divergences may potentially trigger delocalization via the accumulation of two-body resonances or via avalanche instabilities.

A.9.1 Two-body Resonance Counting

To begin, we expand on the resonance counting criterion for the stability of localization of a non-interacting chain at infinite randomness against perturbative interactions. We consider a non-interacting Anderson-localized chain characterized by its density of single-particle states (DOS) $D(\varepsilon)$ and the localization length $\xi(\varepsilon)$ of single-particle orbitals (with energy ε). At the infinite randomness fixed point, the localization length and DOS both diverge as $|\epsilon| \to 0$ and it is the interplay of such overlapping orbitals that could lead to two-body resonance proliferation. We assume each orbital has a "center" at position α and an exponentially scaling envelope $\psi^*_\alpha \sim \frac{1}{\sqrt{\xi(\varepsilon_\alpha)}} e^{-|x-\alpha|/\xi(\varepsilon_\alpha)}$ determined by its energy ε_α. The presence of multiple centers (e.g. two in a typical state produced by the strong disorder renormalization group treatment of the Ising model) does not parametrically modify the estimates below. Similarly, the presence of 'pairing' terms in the fermionization of the Ising model is not parameterically important.

We consider a generic local interaction, which we schematically model by a density-density operator $\sim V \int dx\, \hat{n}(x)\hat{n}(x)$. Writing it in terms of the non-interacting orbitals, we have

$$\begin{aligned} V_{\alpha\beta\gamma\delta} &= V \int dx\; \psi_\alpha(x)\psi_\beta(x)\psi^*_\gamma(x)\psi^*_\delta(x) \\ &\sim \frac{V}{\sqrt{\xi_\alpha \xi_\beta \xi_\gamma \xi_\delta}} \int dx\; e^{-(|x-\alpha|/\xi_\alpha + |x-\beta|/\xi_\beta + |x-\gamma|/\xi_\gamma + |x-\delta|/\xi_\delta)} \,. \end{aligned} \tag{A.96}$$

Two-body resonances occur when $V_{\alpha\beta\gamma\delta} > |(\varepsilon_\alpha - \varepsilon_\delta) - (\varepsilon_\gamma - \varepsilon_\beta)|$. In general, any small finite

strength of interactions produces some density of resonances, but this need not modify the ergodic properties of the system; instead it can "dress" the local conserved quantities to be many-particle operators—this is at the heart of MBL. However, if the number of resonances in a localization volume becomes sufficiently large, then the local character of the conserved quantity is lost and we expect delocalization. Counting the number of perturbative resonances, induced by interactions, can then identify instabilities to thermalization.

Owing to the localized nature of the single-particle orbitals, the matrix element will only be large whenever all four orbitals overlap. Without loss of generality, we can take α to be the orbital with *smallest* localization length $\xi_\alpha < \xi_\beta, \xi_\gamma, \xi_\delta$. For ease of notation let $\varepsilon = \varepsilon_\alpha$. This suggests the following organization of our counting: given such an orbital, first we compute how many other orbitals (labeled orbital δ) exist within a block of size $\ell = \xi_\alpha$ around α and with energy $\delta\varepsilon$ around ε; second, given the energy difference between orbital α and δ, what is the number of pairs of orbitals β and γ that have an energy difference within $V_{\alpha\beta\gamma\delta}$ of the initial pair. Under this organization, one must have that both estimates diverge: the first ensures that there is always an initial pair that can transition, while the second ensures that, given a particular pair of orbitals, additional pairs can resonantly transition. While the former can be simply estimated as $\delta\varepsilon D(\varepsilon)\ell$, the latter requires a more careful analysis. Fixing the pair of resonances α and δ, we must find the number of pairs of orbitals β and γ that satisfy three conditions: (1) the within ℓ distance from orbital α, (2) their localization length is larger than ℓ, and (3) their energy difference close to the energy difference between α and γ (where close is given by the strength of the matrix element). The number R of such pairs can be estimated as follows: given an orbital γ within the block ℓ, we need to find another orbital β whose energy is in a window of size $V_{\alpha\beta\gamma\delta}$ around $\varepsilon_\gamma - \delta\varepsilon$. At some energy $\varepsilon_\gamma < \varepsilon$, the number of such orbitals γ is $\sim \ell D(\varepsilon_\gamma) d\varepsilon_\gamma$ and the number of corresponding orbitals β is $\sim \ell D(\varepsilon_\beta) V_{\alpha\beta\gamma\delta}$, where $\varepsilon_\beta = \varepsilon_\gamma - (\delta\varepsilon)$. Integrating yields the total number of resonances:

$$R = \int_0^\varepsilon d\varepsilon_\gamma \ell D(\varepsilon_\gamma) \ell D(\varepsilon_\beta) V_{\alpha\beta\gamma\delta} \sim \int_0^\varepsilon d\varepsilon_\gamma \ell D(\varepsilon_\gamma) \ell D(\varepsilon_\beta) \frac{V\ell}{\sqrt{\xi_\alpha \xi_\beta \xi_\gamma \xi_\delta}} \,. \tag{A.97}$$

We make progress under the following approximation: take $\delta\varepsilon = C\varepsilon$ with a small C. Physically, this means that the initial orbitals have similar energies, and thus similar localization lengths, $\xi_\delta \approx \xi_\alpha = \ell$.

We can check that this counting argument reproduces previous work on interaction instabilities of localized systems [570]. There, $D(\varepsilon)$ remains a constant, while the localization length diverges as a power-law, $\xi(\varepsilon) \sim \varepsilon^{-\nu}$. The two conditions are then:

$$\begin{aligned} &C\varepsilon D(\varepsilon)\xi(\varepsilon) \sim \varepsilon^{1-\nu} \\ &R \sim V\ell^2 \int_0^{\varepsilon} d\varepsilon' \; |\varepsilon' + C\varepsilon|^{\nu/2}|\varepsilon'|^{\nu/2} \sim \ell^2 |\varepsilon|^{\nu/2}|\varepsilon|^{1+\nu/2} \sim \varepsilon^{1-\nu} \end{aligned} \tag{A.98}$$

Both quantities diverge when $1-\nu < 0$, which agrees with previous estimates, $\nu > 1/d$ where $d = 1$, using a diagramatic approach.

We can turn to the infinite randomness fixed point, which is characterized by a Dyson singularity with $D(\varepsilon) \sim [\varepsilon \log^3 \varepsilon]^{-1}$ and $\xi(\varepsilon) \sim \log \varepsilon$. We note that the $\xi(\varepsilon)$ corresponds to the *typical* localization length. Owing to the bi-locality of the free fermion wave functions [596, 597], the average localization length captures the distance between the two localization centers while the typical localization length captures the spread around each center—the latter is responsible for the mixing between orbitals and thus controls the matrix element.

In such systems we have:

$$C\varepsilon \frac{1}{\varepsilon \log^3 \varepsilon} \log \varepsilon \sim \frac{1}{\log^2 \varepsilon} \to 0 \tag{A.99}$$

$$\begin{aligned} R \; &\sim V\ell^2 \int_0^{\varepsilon} d\varepsilon' \; \frac{|\log(\varepsilon' + C\varepsilon)|^{-3-1/2} |\log(\varepsilon')|^{-3-1/2}}{|\varepsilon' + C\varepsilon||\varepsilon'|} \\ &\gtrsim 2V\ell^2 \frac{|\log(\varepsilon)|^{-3-1/2}}{|\varepsilon|} \int_0^{\varepsilon} d\varepsilon' \; \frac{|\log(\varepsilon')|^{-3-1/2}}{|\varepsilon'|} \\ &\sim V\ell^2 \frac{|\log(\varepsilon)|^{-3-1/2}}{|\varepsilon|} |\log(\varepsilon)|^{-2-1/2} \sim \frac{1}{\varepsilon} |\log(\varepsilon)|^{-4} \end{aligned}$$

While the latter condition diverges as $\varepsilon \to 0$, the former does not. This means that, within a block of size ℓ we are not guaranteed to find an appropriate orbital to start the resonance process.

A.9.2 Avalanche instability

We now turn our attention to the susceptibility of infinite-randomness transitions to thermalization "avalanches" triggered by rare thermal bubbles induced by the presence of interactions. For a system with a distribution of localization lengths, it has shown that the *average* localization length $\overline{\xi}$ controls

this instability: for $\overline{\xi} > 2/\log 2$, thermal bubbles lead to a global thermalization of the system [571]. When relating this prediction to the physics of the infinite-randomness fixed point, it is important to understand the different lengthscales. In particular, at the infinite-randomness fixed point, each orbital is located around two distinct positions whose separation is given by ξ_{mean}; around each position the orbital decays with a length scale given by ξ_{typ}. Crucially, it is the latter lengthscale that leads to the avalanche instability as it control the number of ℓ-bits that can interact with a rare thermal region. Thus, while $\overline{\xi_{\text{mean}}} \sim \int_0^\varepsilon d\varepsilon \frac{1}{\varepsilon \log^3 \varepsilon} |\log^2(\varepsilon)|$ diverges logarithmically, the more appropriate $\overline{\xi_{\text{typ}}} \sim \int_0^\varepsilon d\varepsilon \frac{1}{\varepsilon \log^3 \varepsilon} |\log(\varepsilon)|$ remains finite and this criterion does not conclusively produce an ergodic instability. We highlight that the difference between a converging or divergent average localization length depends on a single logarithmic term; unaccounted channels or higher order corrections might provide an additional corrections that lead to an absolute avalanche instability. We leave this analysis to future work.

Finally, let us note that the direct numerical observation of avalanche instabilities remains extremely challenging; the presence of a robust intervening ergodic region in our study suggests that an alternate mechanism might be at the heart of our observations.

Appendix B

Appendix to Chapter 3

B.1 Proof for prethermalization with the presence of symmetries

In this section we prove that the prethermal effective Hamiltonian can exhibit an emergent symmetry (protected by the time translation symmetry), while preserving the remaining properties of the prethermal regime, namely, exponentially slow heating (Eqn. 3.2) and an approximate description of the dynamics at the single trajectory level for a single period of the drive (Eqn. 3.1). This generalization follows closely the quantum results presented in Refs. [194, 195] using the machinery first introduced in Ref. [183] to extend it to classical systems. More specifically, we treat the classical spin as the large-S limit of the quantum spin model; for arbirtrarily large S, each spin-S degree of freedom can be separated into multiple spin-1/2 degrees of freedom. This approach allows one to immediately translate the quantum results to the corresponding classical system.

Let us begin by reviewing the quantum case. Without loss of generality, we consider a quantum spin-S system with one-body and two-body terms:

$$\hat{H}_F(t) = \underbrace{g(t)\sum_i^N \hat{S}_i^x}_{\hat{H}_X(t)} + \underbrace{\frac{1}{2S}\sum_{ij}^N \sum_{\mu\nu=x,y,z} J_{\mu\nu}^{ij}(t)\hat{S}_i^\mu \hat{S}_j^\nu + \sum_i^N \vec{h}^i(t)\cdot\hat{\vec{S}}_i}_{\hat{H}_0(t)}, \tag{B.1}$$

where $g(t)$, $J^{ij}(t)$ and $\vec{h}^i(t)$ are periodic functions of time with a period of T, and the dynamics are generated by the Heisenberg equations of motion for $\hat{S}_i^\mu$, or equivalently the Schrödinger equation for the quantum state. Here, we assume that the interactions are not extensive, i.e. $\sum_j \sum_{\mu\nu} \max_t |J_{\mu\nu}^{ij}(t)|$ is finite for all i. Crucially, we assume that $g(t)$ satisfies $M\int_0^T g(t)dt = 2k\pi$, where M and k are two coprime integers. This means that, under the dynamics generated by $\hat{H}_X(t)$, the system will return to the same state every M driving cycles, i.e. $\hat{X}^M = \left[\mathcal{T}e^{-i\int_0^T \hat{H}_X(t)dt}\right]^M = \mathbb{1}$. The corresponding maximal local energy scale is then defined as

$$J_{\text{local}} := \max_{\text{site } i} \sum_{A:i\in A} \left\|\hat{c}^A\right\|, \tag{B.2}$$

where $\hat{c}^A$ correspond to local terms in $\hat{H}_0 = \sum_A \hat{c}^A$ with support on the set of spins A, and $\|\cdot\|$ is the operator norm.

In this particular model of Eqn. B.1, the local terms are:

$$\begin{cases} \hat{c}^A = \frac{1}{S}\sum_{\mu\nu=x,y,z} J^{ij}_{\mu\nu}(t)\hat{S}^\mu_i \hat{S}^\nu_j, & \text{for } A = \{i,j\}; \\ \hat{c}^A = \vec{h}^i(t)\cdot\hat{\vec{S}}_i, & \text{for } A = \{i\}. \end{cases} \tag{B.3}$$

Crucially, it is proven that, when the frequency of the drive is much larger than the local energy scale, i.e:

$$J_{\text{local}} \ll \frac{1}{MT}, \tag{B.4}$$

there exist a prethermal Hamiltonian D and a (slightly rotated) symmetry operation $\hat{X}_{\text{rot}} \approx \hat{X}$ such that [194, 195]:

$$\hat{X}^M_{\text{rot}} = \mathbb{1}, \tag{B.5}$$

$$[\hat{D}, \hat{X}_{\text{rot}}] = 0, \tag{B.6}$$

$$\frac{1}{N}\|\hat{D}(mT) - \hat{D}(0)\| < c_1 \cdot mJ_{\text{local}} \cdot \mathcal{O}(e^{-\omega/J_{\text{local}}}), \tag{B.7}$$

$$\|\hat{O}(T) - \hat{X}^{-1}_{\text{rot}}\hat{O}'(T)\hat{X}_{\text{rot}}\| < c_2 \cdot \|\hat{O}\| \cdot \mathcal{O}(e^{-\omega/J_{\text{local}}}), \tag{B.8}$$

where $\hat{O}$ is any local observable and c_1, c_2 are constants independent of frequency and J_{local}. We note that $\hat{O}'(T)$ corresponds to operator $\hat{O}$ evolved under $\hat{D}$ for time T, i.e. $\hat{O}'(T) = e^{i\hat{D}T}\hat{O}(0)e^{-i\hat{D}T}$. When the system has a polynomial Lieb-Robinson bound, the error of the operator (Eqn. B.8) grows algebraically with time and the dynamics remain well approximated by $\hat{D}$ for an exponentially long time in the frequency of the drive.

Moving on to the classical case, the corresponding classical spin system can be treated using Eqn. B.1 by taking $S \to \infty$. Correspondingly, the classical spin variable (i.e. a unit vector) can be viewed as $\vec{S} = \langle\hat{\vec{S}}\rangle/S$ [183]. However, the results for finite S in Eqn. B.5 cannot be immediately applied to the classical case, since the local energy scale diverges, $J_{\text{local}} = ||\hat{H}_0|| \propto S$, which invalidates the high-frequency condition (Eqn. B.4). Fortunately, previous work introduced a mathematical treatment of the Hamiltonian that solved this precise problem [183]. The main idea is as follows: We start by decomposing each spin $\hat{\vec{S}}_i$ into $2S$ spin-1/2 operators $\{\hat{\vec{s}}_{i,a}\}$:

$$\hat{S}^\mu_i = \sum_{a=1}^{2S} \hat{s}^\mu_{i,a}. \tag{B.9}$$

With this substitution, the two parts of the Floquet Hamiltonian become:

$$\begin{aligned}\hat{H}_X(t) &= g(t)\sum_{i,a}\hat{s}^x_{i,a}\\ \hat{H}_0(t) &= \frac{1}{2S}\sum_{i,a,j,b}^{N}\sum_{\mu\nu=x,y,z}J^{ij}_{\mu\nu}\hat{s}^\mu_{i,a}\hat{s}^\nu_{j,b}+\sum_i\vec{h}_i(t)\cdot\hat{\vec{s}}_{i,a}.\end{aligned} \tag{B.10}$$

From the perspective of the spin-1/2, $\hat{H}_X$ still respects its distinguishing property: after M cycles of evolution under $\hat{H}_X$ alone, each individual spin-1/2 returns to the initial state. Meanwhile, the local energy scale of $\hat{H}_0$ remains finite:

$$\frac{1}{S}\sum_j\sum_{b=1}^{2S}\sum_{\mu\nu}|J^{ij}_{\mu\nu}|\cdot\|\hat{s}^\mu_{i,a}\|\cdot\|\hat{s}^\nu_{j,b}\|+\sum_\mu|h^\mu_i(t)|\cdot\|\hat{s}^\mu_{i,a}\|\leq\frac{1}{2}\sum_j\sum_{\mu\nu}|J^{ij}_{\mu\nu}|+\frac{1}{2}\sum_\mu|h^\mu_i(t)|. \tag{B.11}$$

Therefore, as this construction holds for any S, one can then safely take the $S\to\infty$ limit and extend the conclusions of quantum derivation (Eqns. B.5-B.8) to classical systems, immediately proving Eqn. 1 and Eqn. 2 in the main text for the prethermal dynamics of *classical systems* with an *emergent symmetry*.

Here, we remark that by splitting the large-S spins into $2S$ spin-1/2 degrees of freedom, one reduces the local energy scale of each spin degrees at the expense of generating an additional dimension (where position is labeled by the index of the spin-1/2) and all-to-all coupling along this virtual dimension. Although these very long-range interactions do not lead to the divergence of the local energy scale, it precludes the notion of locality and thus meaningful Lieb-Robinson—as a result, $\hat{D}$ cannot reproduce the dynamics over multiple Floquet cycles.

Let us end this section by formalizing these results in the language of classical dynamics. In classical spin systems, the dynamics are generated by Hamilton's equations of motion $\dot{S}^\mu_i=\{S^\mu_i,H(t)\}$, using the Poisson bracket relation $\{S^\mu_i,S^\nu_j\}=\delta_{ij}\epsilon^{\mu\nu\rho}S^\rho_i$. Equivalently, at any time t, any observable $O(t)$ can thought of a function of the initial values of all observables. This can be expressed by formally integrating the equations of motion: $O(t)=\mathcal{T}e^{\int_0^t L(t')dt'}[O]$, where the superoperator $L[\cdot]$ is defined by $L[\cdot]=\{\cdot,H_F\}$. We note that the multiplication of the superoperators (functions) should be understood as function composition, i.e. $(L_1\circ L_2)[\cdot]=L_1[L_2[\cdot]]$. Correspondingly, the n^{th} power of L is then defined inductively by $L^n=L\circ L^{n-1}$, and the exponential function of the superoperators is

naturally defined by its Taylor expansion.

With such notations for classical dynamics, the properties of the classical prethermalization can be stated as the follows. Consider a classical spin system with a Hamiltonian consisting of two parts:

$$H_F(t) = H_X(t) + H_0(t), \tag{B.12}$$

where $H_X(t)$ generates a global rotation $X = \mathcal{T} e^{\int_0^T \{\cdot, H_X(t)\} dt}$ over a single period such that the system returns to itself every M periods, i.e. $X^M[\cdot] = \mathbb{I}[\cdot]$. If the local energy scale of $H_0(t)$ is sufficiently small:

$$J_{\text{local}} := \max_{\text{site } i} \sum_{A: i \in A} \left\| c^A \right\| \ll \frac{1}{MT}, \tag{B.13}$$

where c_A corresponds to classical analogue of $\hat{c}_A$ in Eqn.B.3 (i.e. local terms with support in A), then there exists a prethermal Hamiltonian D and a (slightly) tilted symmetry operation $X_{\text{rot}}[\cdot] \approx X[\cdot]$ such that

$$X_{\text{rot}}^M[\cdot] = \mathbb{I}[\cdot], \tag{B.14}$$

$$X_{\text{rot}}[D] = D, \tag{B.15}$$

$$\frac{1}{N} |D(mT) - D(0)| < c_1. \cdot m J_{\text{local}} \cdot \mathcal{O}(e^{-\omega / J_{\text{local}}}), \tag{B.16}$$

$$\left\| O(T) - X_{\text{rot}}[O'(T)] \right\| < c_2. \cdot |O| \cdot \mathcal{O}(e^{-\omega / J_{\text{local}}}), \tag{B.17}$$

where c_1, c_2 are constants independent of frequency and J_{local}, O is any classical local observable evolving under $H_F(t)$, and $O'(T)$ corresponds to the observable O evolved under D for time T, i.e. $O'(T) = e^{T\{\cdot, D\}}[O(0)]$.

B.2 Estimate local energy scale in long-range interacting Floquet systems

Let us start with the physical intuition of the local energy scale in our long-range dipolar interacting system with angular dependence. The interactions can be both positive and negative which accords a cancellation of many terms in the response function of the system. Crucially, the angular dependence of the dipolar interaction leads to an exact cancellation of the positive and the negative interaction strength to the leading order. Therefore, to estimate the local energy scale in the response function, one needs to go to at least the second order, i.e., the variance of the interaction.

To be more concrete, we also sketch the essence in the mathematical proof of the estimation of local energy scale to ensure that the major claims of this Letter is self-contained, as a strict analytical study of the prethermalization with the presence of disorder can be found in the previous literature [182], which further clarify how the lowest order of the interaction strength gets averaged out.

Let us consider a generic model with both long-range two-body interaction and single-body terms, of which the Hamiltonian is written as:

$$H = \sum_{ij} J_{ij}\hat{O}_{ij} + \sum_{i} J_i\hat{O}_i, \tag{B.18}$$

where $\hat{O}_{ij}$ ($\hat{O}_i$) are two-body (single-body) operators, and J_{ij} (J_i) are the corresponding coupling strengths which varies in time with a frequency of ω. In the high-frequency regimes, considering the high-order processes, the heating effect is induced by the transition rate between different energy levels and is thus bounded by the high-order commutators [178, 182, 191, 192]

$$\frac{1}{\omega^p}\langle J_{\mu_1}J_{\mu_2}J_{\mu_3}J_{\mu_4}\cdots\rangle \mathrm{Tr}(\hat{O}_{\mu_1}[[[\hat{O}_{\mu_2},\hat{O}_{\mu_3}],\hat{O}_{\mu_4}],\cdots]^{(p)}), \tag{B.19}$$

where the superscript (p) denotes that there are p layers of commutator in the expression, the subscript μ denotes either the two indices associated with a two-body term or the index associated with a single-body term, and the bracket $\langle\cdots\rangle$ denotes the average over positional configurations of the spins. In generic short-range systems, all the $\langle J_{\mu_i}\rangle$ remains finite and non-zero, so Eqn. B.19 $\sim p!(\frac{J}{\omega})^p$, where $J = \langle J_{\mu_i}\rangle$ is considered as the local energy scale. One can eventually prove an exponentially

small heating rate by finding the optimal $p \sim \omega$ [178, 182, 191, 192]. In contrast, for each two-body interaction J_{μ_i}, if $\langle J_{\mu_i} \rangle = 0$, then it has to appear at least twice for non-zero $\langle J_{\mu_1} J_{\mu_2} J_{\mu_3} J_{\mu_4} \cdots \rangle$. Therefore, the size of Eq. S5 should be estimated as

$$\sim p! \frac{\langle J_\mu^2 \rangle^{\frac{p}{2}}}{\omega^p}. \tag{B.20}$$

Let us note that such estimation of the local energy scale only accounts the terms in Eq. S5, in which only two-body terms are involved. However, one should also, in principle, consider single-body terms, with the requirement that each two-body J_{μ_i} term has to appear twice still being satisfied. Nevertheless, as long as the local energy scale of the two-body terms $\langle J_\mu^2 \rangle^{\frac{1}{2}}$ is of the same order of the single-body field, we can use their values as a typical local energy scale to estimate the heating rate. Going back to our dipolar interaction in experiment

$$\langle J_\mu^2 \rangle^{\frac{1}{2}} = \{ \int [\frac{J_0}{r^3}(3\cos^2\theta - 1)]^2 \, \rho r^2 \sin\theta \, dr \, d\theta \, d\phi) \}^{\frac{1}{2}} = \sqrt{\frac{16\pi}{15}} J_0 \rho. \tag{B.21}$$

Appendix C

Appendix to Chapter 4

C.1 General argument for the relation between order and metrology

For pure states, there is a simple connection between SSB order and QFI (Table 4.1), since the variance of the order parameter is nothing but a sum over the connected two-site correlation function. In this section, we discuss how this relation enables the preparation of metrologically useful states via a Hamiltonian quench.

In particular, we still consider the scheme, where we quench an initial product state with an effective temperature below T_c and assume SSB with order parameter $\mathcal{O} = \sum_i \mathcal{O}_i$. We further assume $\mathcal{O}$ is purely off-diagonal in the symmetry sectors of the Hamiltonian. Given this assumption, $\langle \mathcal{O} \rangle$ must approach 0 at late times, since all phase coherence between symmetry sectors will be lost. On the other hand, $\mathcal{O}^2$ has some diagonal elements that act only within symmetry sectors. Since we are assuming that the initial state has effective temperature below T_c, the expectation value of these diagonal elements should be $O(N^2)$ [93, 94]. This leads to the conclusion $\langle \mathcal{O}^2 \rangle - \langle \mathcal{O} \rangle^2 \sim O(N^2)$, i.e., the late time state exhibits a large QFI with respect to $\mathcal{O}$. Note that if $\mathcal{O}$ is *diagonal* in the symmetry sectors, then $\langle \mathcal{O} \rangle$ can be large at all times and this expression can be small (i.e. $O(N)$).

For the above argument to be physically relevant, it must further be shown that that the "late time" at which $\langle \mathcal{O} \rangle$ approaches 0 does not diverge too rapidly in system size. In the most general case, it is difficult to analyze this time scale based on the symmetry of H alone. However, assuming the finite-temperature SSB derives from zero-temperature SSB of the same kind, e.g. long-range interactions stabilizing CSB in $1D$ or $2D$, one can plausibly estimate this time scale from the ground-state manifold itself. Specifically, models with discrete symmetry have exponentially small finite-size gaps between ground-states, leading to an exponentially long dephasing time between symmetry sectors. On the other hand, models with continuous symmetry breaking, such $U(1)$, should exhibit $\sim O(1/N)$ gaps between symmetry sectors, so the dephasing time scale between sectors is only linear in system size and QFI develops relatively quickly.

We note that the above arguments require few body operators to thermalize quickly and thus do not apply to integrable models, to models that have anomalously slow thermalization for certain initial states (e.g., quantum many-body scars), or to models with super-extensive energy ($\alpha \leq d$) [67]. Assuming conventional local thermalization, the key conditions for generating large QFI from a quench

are therefore 1) a Hamiltonian with continuous symmetry breaking *and* an order parameter off-diagonal in the symmetry sectors and 2) the existence of a low-temperature symmetry breaking initial state that is easy to prepare, e.g., a product state.

C.2 Scalable Squeezing with Mixed Initial States

Here we elaborate on the order-of-averaging distinction between calculating squeezing for partially-polarized random pure states vs. a partially polarized mixed state. In the first case, we fix a product state $|\psi(p)\rangle$, where each spin is independently chosen to point in $\pm\hat{x}$ with probability $(1 \pm p)/2$. To determine the typical value of the squeezing given p, we average over the squeezing parameter for each $|\psi(p)\rangle$,

$$\xi_p^2 = \mathbb{E}_{\psi(p)}\left[\frac{\min_{\hat{n}\perp\hat{x}} \mathrm{Var}_{|\psi(p)\rangle}[\hat{n}\cdot\vec{S}]}{\langle\psi(p)|\, X\, |\psi(p)\rangle^2}\right] \tag{C.1}$$

For a mixed initial state of the form $\rho = [(1+p)/2\,|{\rightarrow}\rangle\langle{\rightarrow}| + (1-p)/2\,|{\leftarrow}\rangle\langle{\leftarrow}|]^{\otimes N}$, the trace over ρ to compute expectation values again becomes an average over $|\psi(p)\rangle$. This leads to a squeezing parameter of

$$\xi_{\mathrm{mix}}^2 = \frac{\min_{\hat{n}\perp\hat{x}} \mathrm{Var}_{\rho}[\hat{n}\cdot\vec{S}]}{[\mathrm{Tr}(\rho X)]^2} = \frac{\mathbb{E}_{\psi(p)}[\min_{\hat{n}\perp\hat{x}} \mathrm{Var}_{|\psi(p)\rangle}[\hat{n}\cdot\vec{S}]]}{\mathbb{E}_{\psi(p)}[\langle\psi(p)|\, X\, |\psi(p)\rangle]^2} \tag{C.2}$$

Note that squeezing is now calculated *after* the averaging. Due to the non linearity of the squeezing parameter, ξ_p^2 and ξ_{mix}^2 could, in principle, be very different (and even have different scaling properties). However, these quantities agree extremely well for even modestly sized systems $N \gtrsim 10^2$. This is because, for large systems, mean spin direction becomes essentially a constant – it is $\sim pN + \mathcal{O}(\sqrt{N})$, and decays a negligible amount before the optimal squeezing time.

C.3 Hydrodynamic model for squeezing dynamics

Spin-squeezing dynamics are well described by a semi-classical picture that approximates the quasi-probability distribution as a true probability distribution evolving on the global Bloch sphere. In this section, based on a hydrodynamic description of spontaneous symmetry breaking, we analytically derive the equations of motion for the probability distribution, which we further use to calculate the optimal squeezing. Our main assumption is that after a relatively short time (of order $1/J$), the system achieves local thermal equilibrium and the subsequent dynamics of coarse-grained variables can be described by hydrodynamic equations.

C.3.1 Equations of motion for squeezing in thermal systems

The hydrodynamic description focuses on two coarse-grained variables that evolve only slowly in time at long wavelengths, the z-component of the magnetization density, denoted $m(\mathbf{r})$ (the $U(1)$ charge), and an angle $\phi(\mathbf{r})$ describing the orientation of the magnetization in the x-y plane. The magnitude of the in-plane component, m_{xy}, is assumed to have relaxed rapidly to a value determined by the temperature T, which we take to be uniform in space. The phase ϕ will vary slowly at long wavelengths because the restoring force vanishes for long wavelength fluctuations, and m varies slowly because it is a conserved quantity. A hydrodynamic description should apply for sufficiently long wavelengths at any non-zero temperature, regardless of whether the underlying microscopic system obeys classical or quantum dynamics.

Integrating the partition function over short range fluctuations in m and ϕ, and over all other variables in the problem, we may define a free energy functional, which we assume to take the form

$$F[m,\phi] = \int d^d r \left(\chi m(\mathbf{r})^2 + u_4 m(\mathbf{r})^4 + ...\right) + \int d^d r_1 d^d r_2 \tilde{J}(\mathbf{r}_1 - \mathbf{r}_2) \cos z\phi(\mathbf{r}_1) - \phi(\mathbf{r}_2)], \quad \text{(C.3)}$$

where $\tilde{J}(\mathbf{r}) \sim (J_\perp/2) m_{\mathrm{xy}}^2 r^{-\alpha}$ for large separations r. The hydrodynamic equations of motion take the

form

$$\begin{aligned}
\frac{\partial \phi}{\partial t} &= g\frac{\delta F}{\delta m} - \Gamma\frac{\delta F}{\delta \phi} + \eta_\phi(t,\vec{r}), \\
\frac{\partial m}{\partial t} &= -g\frac{\delta F}{\delta \phi} + \nabla^2\left[\Lambda\frac{\partial F}{\partial m} + \eta_m(t,\mathbf{r})\right], \\
\langle \eta_\phi(t,\vec{r})\rangle &= \langle \eta_\phi(t,\vec{r})\rangle = 0, \\
\langle \eta_\phi(t,\vec{r})\eta_\phi(t',\vec{r}')\rangle &= 2\Gamma T\delta(t-t')\delta(\vec{r}-\vec{r}'), \\
\langle \eta_m(t,\vec{r})\eta_m(t',\vec{r}')\rangle &= 2\Lambda T\delta(t-t')\delta(\vec{r}-\vec{r}'),
\end{aligned} \tag{C.4}$$

where η_ϕ and η_m originate from the thermal fluctuations. Here we define the global quantity $\Phi|Z$, where

$$\Phi = \frac{\int d^d\vec{r}\phi(\vec{r})}{V} \tag{C.5}$$

is the phase averaged over the entire system, given fixed total magnetization along z-axis,

$$\int m(\vec{r})\, d^d r = Z. \tag{C.6}$$

The coefficient g in the hydrodynamic equations is determined by the commutator of m and ϕ. In the present problem, $g = 1$. Our hydrodynamic equations are a generalization to the case of long-range spin interactions of the hydrodynamic equations that are commonly used for an XY magnet with short-range interactions in two or more dimensions [678, 853]. It is expected that these equations should be valid at any temperature in the broken symmetry phase at sufficiently long wave lengths. The hydrodynamic equations are also believed to be valid in the low-temperature phase of the two-dimensional system with short range forces, where there is no true broken symmetry but only quasi-long-range order of the x-y magnetization. We do not have a rigorous derivation of these equations starting from the microscopic Hamiltonian, but one can at least perform some consistency checks. For example, one can confirm that non-linear coupling to thermally excited long-wavelength spin fluctuations does not lead to a divergence of the coefficient Γ. We note that the equations of motion conserve the value of M, and they are consistent with a time-independent thermal distribution of the form $P[m,\phi] = \mathcal{Z}^{-1}e^{-F[m,\phi]/T}$.

For small fluctuations about the equilibrium state, where $m = 0$ and ϕ is independent of space,

one can solve the dynamics of Eq. (C.4) by performing a Fourier transform. This leads to the following equations of motion in momentum space

$$\frac{d\phi_{\mathbf{k}}}{dt} = 2g\chi m_{\mathbf{k}} - \Gamma K_{\mathbf{k}}\phi_{\mathbf{k}} + \eta_{\phi,\mathbf{k}}(t) \tag{C.7}$$

$$\frac{dm_{\mathbf{k}}}{dt} = -gK_{\mathbf{k}}\phi_{\mathbf{k}} - k^2[2\Lambda\chi m_{\mathbf{k}} + \eta_{m,\mathbf{k}}(t)], \tag{C.8}$$

where $K_{\mathbf{k}}$ is related to $J_{\mathbf{k}}$, the Fourier transform of $\hat{J}$, by

$$K_{\mathbf{k}} = 2(J_0 - J_{\mathbf{k}}). \tag{C.9}$$

The noise terms satisfy

$$\left\langle \tilde{\eta}_{\phi,\mathbf{k}}(t)\tilde{\eta}^*_{\phi,\mathbf{k}}(t')\right\rangle = \frac{2\Gamma T}{N}\delta(t-t'), \quad \left\langle \tilde{\eta}_{m,\mathbf{k}}(t)\tilde{\eta}^*_{m,\mathbf{k}}(t')\right\rangle = \frac{2\Lambda T}{N}\delta(t-t'). \tag{C.10}$$

For small wave vectors, one finds $K_{\mathbf{k}} \sim \tilde{K}k^{\alpha-d}$, where the coefficient $\tilde{K}$ is proportional to $J_\perp m_{\mathrm{xy}}^2$. Then, for $k \neq 0$, the equations of motion lead to propagating spin waves, with frequency $\omega_{\mathbf{k}} \sim (2g^2\chi K_{\mathbf{k}})^{1/2}$ and a damping rate proportional to $\Gamma K_{\mathbf{k}} + 2\Lambda\chi k^2$.

Crucially, the $k = 0$ mode is different from the other modes. The first term in Eq. (C.7) just gives a constant precession rate, $2Z\chi/N$ due to fixed total magnetization, and the second term also vanishes for $\alpha > d$. The equation of motion for Φ then reads

$$\frac{d\Phi}{dt} = \frac{2Z\chi}{N} + \tilde{\eta}_\phi(t). \tag{C.11}$$

Thus the mean value of the precession angle grows linearly,

$$\Phi(t)|Z = \frac{2Z\chi t}{N}. \tag{C.12}$$

Whereas the second term, which drives a random walk, leads to linear growth of the variance in a fixed Z sector:

$$\mathrm{Var}[\Phi(t)|Z] = \mathrm{Var}[\Phi(0)] + \frac{2\Gamma T}{N}t. \tag{C.13}$$

We note that the spin operators X, Y, Z and Φ are related by:

$$\begin{aligned} X|Z &= Nm_{\mathrm{xy}}\cos(\Phi|Z), \\ Y|Z &= Nm_{\mathrm{xy}}\sin(\Phi|Z). \end{aligned} \tag{C.14}$$

And therefore

$$\mathrm{Var}[Y|Z] \approx m_{\mathrm{xy}}^2 N^2 \mathrm{Var}[\Phi|Z], \tag{C.15}$$

for small mean precession angle, which holds for $t \ll \Gamma T N$.

Two remarks are in order. First, the linear growth rate vanishes when temperature $T \to 0$, suggesting that such effect is very weak for the quench dynamics from a low-temperature initial state. This explains why our proposed scaling behavior of squeezing is hard to observe at low temperature. We note that the linear growth rate will probably vanish *faster* then T at low temperature, since the noise strength Γ can also depend on temperature and vanish itself when $T \to 0$. Second, the behavior of the non-zero momentum modes ($k \neq 0$) is qualitatively different from the zero-momentum mode: due to the non-zero restoring force, $\mathrm{Var}[\phi_k(t)]$ cannot increase to infinity and will instead saturate to a temperature-dependent equilibrium value. This effect manifests as the evolution towards local equilibration in the quench dynamics.

We remark that the analysis described above is restricted to the case where the z-component of the total magnetization is confined to a small interval about $Z = 0$. At finite value of Z/N, the hydrodynamic description must take into account fluctuations in energy density, which gives rise to an additional slow mode due to energy conservation. Energy fluctuations couple linearly to the spin modes for $Z/N \neq 0$, and this coupling can have significant effects. Because the initial state is a superposition of states with different energies, and these energies persist to infinite times, we expect that in the large N limit, the quantity $\mathrm{Var}[\Phi(t)]$ should grow as t^2/N for large t. This reflects the fact that systems with slightly different total energies will have slightly different values of the parameter χ. For a state where Z/N is of order $N^{-1/2}$, however, the quantity $\mathrm{Var}[\Phi(t)]$ should grow as t^2/N^2 for large t, which is too small to affect the squeezing behavior.

C.3.2 Derivation of the optimal squeezing parameter

With the equations of motion for the probability distribution in hand, we now present an analytical calculation of the optimal squeezing (Eq. 4.2). The expression of the spin squeezing parameter ξ^2 consists of the mean spin length $\langle X \rangle$ and the minimum variance $\min_{\hat{n}\perp\hat{x}} \mathrm{Var}[\hat{n}\cdot\vec{S}]$ in the y-z plane. The latter is of course the smallest eigenvalue of Y, Z covariance matrix,

$$\begin{pmatrix} \langle Z^2 \rangle & \langle ZY \rangle \\ \langle YZ \rangle & \langle Y^2 \rangle \end{pmatrix}. \tag{C.16}$$

Therefore, to calculate the squeezing we only need to evaluate the observables $\langle X \rangle$, $\langle Z^2 \rangle$, $\langle Y^2 \rangle$ and $\langle ZY \rangle = \langle YZ \rangle$.

Since Z is a conserved quantity, we can consider the evolution of each Z-slice of the probability distribution separately. The population within each slice is conserved and determined by the initial binomial distribution of Z, which can be well approximated by a Gaussian distribution in the thermodynamic limit. That is,

$$P(Z) = \sqrt{\frac{2}{\pi N}} \mathrm{e}^{-\frac{2Z^2}{N}}. \tag{C.17}$$

As per Eq. C.12 and Eq. C.14, the dynamics in each Z-slice are described by a rotation with a angular velocity of $\frac{2Z\chi}{N}$ given as the follows:

$$\begin{aligned} X|Z &= N m_{\mathrm{xy}} \cos\left(\frac{2Z\chi t}{N}\right), \\ Y|Z &= N m_{\mathrm{xy}} \sin\left(\frac{2Z\chi t}{N}\right). \end{aligned} \tag{C.18}$$

Therefore, all the terms in ξ^2 can be evaluated as

$$\begin{aligned} \langle X \rangle &= \int N m_{\mathrm{xy}} \cos\left(\frac{2Z\chi t}{N}\right) P(Z) dZ = N m_{\mathrm{xy}} \mathrm{e}^{-\frac{(\chi t)^2}{2N}} \\ \langle Z^2 \rangle &= \int Z^2 P(Z) dZ = \frac{N}{4} \\ \langle ZY \rangle = \langle YZ \rangle &= \int Z N m_{\mathrm{xy}} \sin\left(\frac{2Z\chi t}{N}\right) P(Z) dZ = \frac{1}{2} N m_{\mathrm{xy}} \chi t \, \mathrm{e}^{-\frac{(\chi t)^2}{2N}}, \\ \langle Y^2 \rangle &= \mathrm{Var}[Y|Z] + \int N^2 m_{\mathrm{xy}}^2 \sin^2\left(\frac{2Z\chi t}{N}\right) P(Z) dZ \\ &= \mathrm{Var}[Y|Z] + \frac{1}{2} N^2 m_{\mathrm{xy}}^2 [1 - \mathrm{e}^{-\frac{2(\chi t)^2}{N}}]. \end{aligned} \tag{C.19}$$

Plugging the above last three lines into Eq. C.16, we obtain the minimum variance in the y-z plane as

$$\min_{\hat{n}\perp\hat{x}} \mathrm{Var}[\hat{n}\cdot\vec{S}] = \frac{1}{2}\left\{\mathrm{Var}[Y|Z] + \frac{N}{4} + \frac{1}{2}N^2 m_{\mathrm{xy}}^2[1-\mathrm{e}^{-\frac{2(\chi t)^2}{N}}]\right\} - \frac{1}{2}\left[\left\{\mathrm{Var}[Y|Z] - \frac{N}{4} + \frac{1}{2}N^2 m_{\mathrm{xy}}^2[1-\mathrm{e}^{-\frac{2(\chi t)^2}{N}}]\right\}^2 + N^2 m_{\mathrm{xy}}^2\chi^2 t^2 \mathrm{e}^{-\frac{(\chi t)^2}{N}}\right]^{1/2}. \tag{C.20}$$

Scalable squeezing occurs at later and later times as N increases, but occurs *before* the quantum fisher information reaches maximum at $\sim\sqrt{N}$ [677]. Hence we consider the following limit

$$\chi t \to \infty, \qquad \frac{\chi t}{\sqrt{N}} \to 0, \tag{C.21}$$

and expand the minimum variance in series

$$\min_{\hat{n}\perp\hat{x}} \mathrm{Var}[\hat{n}\cdot\vec{S}] = \frac{N}{4}\left\{\frac{\mathrm{Var}[Y|Z]/N}{m_{\mathrm{xy}}^2(\chi t)^2} + \frac{(\chi t)^4}{6N^2} + \mathcal{O}\left[\frac{1}{(\chi t)^2}\right] + \mathcal{O}\left[(\frac{\chi t}{\sqrt{N}})^4\right]\right\}. \tag{C.22}$$

We note the mean spin length is simply constant in this limit:

$$\langle X\rangle^2 = N^2 m_{\mathrm{xy}}^2\left\{1 + \mathcal{O}\left[(\frac{\chi t}{\sqrt{N}})^2\right]\right\} \tag{C.23}$$

Combining the above, we obtain Eq. (2) in the main text.

Let us finally remark that the time dependence of the conditional variance $\mathrm{Var}[Y|Z]$ fully determines the scaling behavior of ξ_{opt} and t_{opt} as a function of N. Assuming $\mathrm{Var}[Y|Z] \propto N(\chi t)^\gamma$ (with $0 \le \gamma < 2$), by minimizing Eq. (2) we expect

$$\xi_{\mathrm{opt}} \propto N^{-2+\frac{8}{6-\gamma}}, \qquad t_{\mathrm{opt}} \propto N^{\frac{2}{6-\gamma}}. \tag{C.24}$$

In particular, for OAT model, $\mathrm{Var}[Y|Z]$ is constant in time, i.e. $\gamma = 0$, leading to the scaling behavior $\xi_{\mathrm{opt}} \propto N^{-\frac{2}{3}}$ and $t_{\mathrm{opt}} \propto N^{\frac{1}{3}}$. In contrast, for the ordered phase in a thermalizing model, as shown in Eq. C.13 and Eq. C.14, we expect $\mathrm{Var}[Y|Z] = 2Nm_{\mathrm{xy}}^2\Gamma T\cdot t \propto t$, i.e. $\gamma = 1$. Correspondingly, we predict a different scaling behavior $\xi_{\mathrm{opt}} \propto N^{-\frac{2}{5}}$ and $t_{\mathrm{opt}} \propto N^{\frac{2}{5}}$.

C.4 Analytic calculation of finite-temperature phase diagram for long-range XXZ model

In this section, we develop an analytic approximation for the finite-temperature symmetry breaking transition. The key issue we wish to resolve analytically is whether order, at the effective temperature of the coherent-spin state (CSS) $|x\rangle$, requires $\alpha < 2$ for $J_z < 1$ (as opposed to persisting at $\alpha = 2$). To this end, we focus on the vicinity of $\alpha \lesssim 2d$, $J_z \lesssim 1$ where the system can be modeled as Bose gas, based on previous work in Refs. [854, 855], which were in turn motivated by the exact solution of the Haldane–Shastry spin chain [856, 857]. The key physical intution is that the ground state manifold of the model with SU(2) symmetry contains $|x\rangle$, and with weak anisotropy, $0 \leq \delta \equiv 1 - J_z << 1$, this state remains at a low effective temperature so the relevant equilibrium states are still well described as Gaussian states with few excitations.

C.4.1 Holstein–Primakoff bosonization: using z-vacuum

We perform a Holstein–Primakoff bosonization of the model, assuming the fully polarized state along z-axis as the vacuum and making a large-S approximation:

$$\begin{aligned} S_i^+ &= (2S - b_i^\dagger b_i)^{1/2}\, b_i\,, \\ S_i^- &= b_i^\dagger (2S - b_i^\dagger b_i)^{1/2}\,, \\ S_i^z &= S - b_i^\dagger b_i\,, \end{aligned} \tag{C.25}$$

where $\sqrt{2S - b_i^\dagger b_i} = \sqrt{2S}\left(1 - \frac{1}{4S} b_i^\dagger b_i + O(1/S)\right)$. This approach may seem surprising, however we observe that it is necessary to choose a vacuum that respects U(1) symmetry in order to capture the ordering transition. Consequently, the vacuum has finite energy density except at the spin-isotropic point, where it is a member of the degenerate ground state manifold. The applicability of this theory away from this point is nontrivial: however, as we shall see, the primary effect of anisotropy is to introduce an energy offset between symmetry sectors, and it does not affect the single-particle dynamics at leading order.

Fourier transforming via $b_i^\dagger = \frac{1}{\sqrt{N}} \sum_{\boldsymbol{q}} e^{-i\boldsymbol{q}\cdot\boldsymbol{r}_i} b_{\boldsymbol{q}}^\dagger$ and defining $\eta(\boldsymbol{q}) = \sum_{\boldsymbol{r}\neq 0} |\boldsymbol{r}|^{-\alpha} e^{i\boldsymbol{q}\cdot\boldsymbol{r}}$, the power-

law XXZ Hamiltonian is represented in momentum space as

$$\begin{aligned} H &= S^2 H^{(0)} + S H^{(2)} + H^{(4)} + O(1/S)\,, \\ H^{(0)} &= \text{constant}\,, \\ H^{(2)} &= \sum_{\boldsymbol{q}} b^\dagger_{\boldsymbol{q}} b_{\boldsymbol{q}} (\omega(\boldsymbol{q}) - \delta\eta(0))\,, \quad \omega(\boldsymbol{q}) \equiv \eta(0) - \eta(\boldsymbol{q})\,, \\ H^{(4)} &= \frac{1}{8N} \sum_{\substack{\boldsymbol{q}+\boldsymbol{q}'= \\ \boldsymbol{q}''+\boldsymbol{q}'''}} b^\dagger_{\boldsymbol{q}} b^\dagger_{\boldsymbol{q}'} b_{\boldsymbol{q}''} b_{\boldsymbol{q}'''} \left(\eta(\boldsymbol{q}) + \eta(\boldsymbol{q}') + \eta(\boldsymbol{q}'') + \eta(\boldsymbol{q}''') - 4J_z \eta(\boldsymbol{q} - \boldsymbol{q}'')\right)\,. \end{aligned} \tag{C.26}$$

As $\boldsymbol{q}$ is a momentum eigenvalue, $\eta(\boldsymbol{q}) = \eta(-\boldsymbol{q}) = \eta(\boldsymbol{q})^*$; so $\eta(\boldsymbol{q})$ is real. We proceed following a standard treatment by minimizing the free energy in the variational manifold of Gaussian states of the form $\left|\{n_{\boldsymbol{q}}\}\right\rangle = \prod_{\boldsymbol{q}} (n_{\boldsymbol{q}}!)^{-1/2} (b^\dagger_{\boldsymbol{q}})^{n_{\boldsymbol{q}}} \left|\Psi_{\text{vac}}\right\rangle$, keeping only terms up to $O(1/S)$. The minimization depends only on the effective single particle dispersion $\epsilon(\boldsymbol{q}) = \frac{\partial \langle H\rangle}{\partial n_{\boldsymbol{q}}}\big|_{n_{\boldsymbol{q}'\neq\boldsymbol{q}}}$, and quite generally obtains the Bose-Einstein distribution [858]. In the disordered phase this results in the self-consistency condition

$$M = \sum_{\boldsymbol{q}} n(\boldsymbol{q}) = \sum_{\boldsymbol{q}} \frac{1}{e^{(\epsilon(\boldsymbol{q})-\mu)/T} - 1}. \tag{C.27}$$

We emphasize that Eq. (C.27) only counts particles in *excited* modes due to the vanishing density of states at $q = 0$. Therefore, while the variational states have fixed particle number M we are able to treat the problem in the *grand canonical* ensemble by allowing the Bose-Einstein condensate to act as a source of particles, whose average is set by μ. Above T_c one can self-consistently determine $\mu < 0$, and we identify T_c as the temperature satisfying Eq. (C.27) with $\mu = 0$, where exactly M particles are extracted from the condensate into excited modes.

To determine $\epsilon(\boldsymbol{q})$ explicitly, we apply Wick's theorem and Eq. C.27 to find

$$\begin{aligned} \langle H\rangle = \eta(0) \left(-\frac{1}{2} N S^2 J_z - \delta\left(SM - \frac{M(M-1)}{2N}\right)\right) + \sum_{\boldsymbol{q}} n(\boldsymbol{q}) \left(S - \frac{M-1}{2N}\right) \omega(\boldsymbol{q}) \\ - \frac{1}{2N} \sum_{\boldsymbol{q}} n(\boldsymbol{q}) \sum_{\boldsymbol{q}'\neq\boldsymbol{q}} n(\boldsymbol{q}') (J_z \eta(\boldsymbol{q} - \boldsymbol{q}') - \eta(\boldsymbol{q}'))\,. \end{aligned} \tag{C.28}$$

From Eq. (C.28), we can gain further insight into the validity of our approximation away from the Heisenberg point. Specifically, while the anisotropy δ contributes an M-dependent offset leading to a unique ground state sector with $M = SN$, it does not directly modify the quadratic terms.

While $|x\rangle$ superposes particle number sectors, the fluctuations are small and we work in the sector $M = \langle M \rangle = SN$. This renders the leading order effect of the anisotropy irrelevant. Moreover, for small anisotropy, which perturbs $|x\rangle$ away from the ground-state manifold, interactions are suppressed, as for low temperature only very low momentum modes have significant occupation. The quartic term is then suppressed by the width of the momentum distribution $n(\boldsymbol{q})$.

C.4.2 Condensation and effective initial temperatures

Based on the above, as an approximation, we discard the interaction term, making H diagonal in $\boldsymbol{q}$. Now there is no remaining $\boldsymbol{q}$-dependent term involving anisotropy, so this result is the for the SU(2) model [854, 855].

To leading order, the estimate of the critical temperature is

$$T_c = \begin{cases} -\dfrac{\pi S}{2\Gamma(\alpha)\cos\left(\frac{\pi\alpha}{2}\right)} \left(\dfrac{\pi S(\alpha-1)}{\Gamma(\frac{1}{\alpha-1})\zeta(\frac{1}{\alpha-1})} \right)^{\alpha-1}, & d = 1\,, \\ -\dfrac{2^{1-\alpha}\pi^2 S}{\Gamma(\frac{\alpha}{2})^2 \sin\left(\frac{\pi\alpha}{2}\right)} \left(\dfrac{2\pi S(\alpha-2)}{\Gamma(\frac{2}{\alpha-2})\zeta(\frac{2}{\alpha-2})} \right)^{\frac{\alpha-2}{2}}, & d = 2\,. \end{cases} \tag{C.29}$$

In $d = 1$ the leading behavior as $\alpha \to 2$ from below is $T_c \sim \frac{\pi^2}{2} S^2 (2-\alpha)$. In $d = 2$ the critical temperature jumps discontinuously at $\alpha = 4$, from $\lim_{\alpha\to 4} T_c = \frac{\pi^2}{8}$ to 0, as required by rigorous bounds [690].

Using the same picture of the low-energy thermodynamics allows to compute the effective temperature T_0 of the CSS initial state. Its energy is exactly $E_{\mathrm{CSS}} = -\frac{N}{8}\eta(0)$, which turns out to be (as $N \to \infty$) the lowest variational energy for $M = SN = \frac{N}{2}$. Given the ground state energy density, we can compute the excitation energy per site of the CSS and relate this to its temperature in the Bose gas. To leading order

$$T_0 = \begin{cases} \left(-\dfrac{\pi S}{2\Gamma(\alpha)\cos\left(\frac{\pi\alpha}{2}\right)} \right)^{\frac{1}{\alpha}} \left(\dfrac{\pi(\alpha-1)\mathcal{E}(\alpha, J_z)}{\Gamma(\frac{\alpha}{\alpha-1})\zeta(\frac{\alpha}{\alpha-1})} \right)^{\frac{\alpha-1}{\alpha}}, & d = 1\,, \\ \left(-\dfrac{2^{1-\alpha}\pi^2 S}{\Gamma(\frac{\alpha}{2})^2 \sin\left(\frac{\pi\alpha}{2}\right)} \right)^{\frac{2}{\alpha}} \left(\dfrac{2\pi(\alpha-2)\mathcal{E}(\alpha, J_z)}{\Gamma(\frac{\alpha}{\alpha-2})\zeta(\frac{\alpha}{\alpha-2})} \right)^{\frac{\alpha-2}{\alpha}}, & d = 2\,, \end{cases} \tag{C.30}$$

where $\mathcal{E}(\alpha, J_z)$ is the energy density of the CSS in the thermodynamic limit.

To determine $\mathcal{E}(\alpha, J_z)$, we extrapolate results from DMRG on periodic systems of length $N = 64, 96, 128$ using ITensor [859]. This provides an unbiased estimate accounting for all quantum fluctuations, at the cost of only being able to compute T_0 for specific points in the parameter space. To estimate the critical $J_c(\alpha)$ such that $T_0 = T_c$ more precisely, we we use a simple polynomial fit of $\mathcal{E}(\alpha, J_z)$. The resulting phase boundary is shown in gold in Fig. 1(b) of the main text, and shows good agreement with the boundary obtained from MPS numerics, especially as $J_z \to 1$ where this approximation should be most accurate.

C.5 Impact of detection error on squeezing

The finite detection errors impose a lower bound on the observed minimum variance. More specifically, the experimental magnetizations $\langle J_{y,\theta}\rangle$ and variance $\mathrm{Var}(J_\theta)$ are related to the same quantities $\langle \tilde{J}_{y,\theta}\rangle$ and $\mathrm{Var}(\tilde{J}_\theta)$ *without* detection errors by the following equations (valid to first order in $\epsilon_{\uparrow,\downarrow}$):

$$\begin{aligned}\langle J_{y,\theta}\rangle &= \frac{N}{2}(\epsilon_\downarrow - \epsilon_\uparrow) + (1-\epsilon_\downarrow-\epsilon_\uparrow)\langle \tilde{J}_{y,\theta}\rangle \\ \mathrm{Var}\,(J_\theta) &= (1-2\epsilon_\downarrow-2\epsilon_\uparrow)\mathrm{Var}(\tilde{J}_\theta) \\ &\quad + \epsilon_\downarrow(N/2-\langle \tilde{J}_\theta\rangle) + \epsilon_\uparrow(N/2+\langle \tilde{J}_\theta\rangle).\end{aligned} \tag{C.31}$$

By inverting the above equations, we calculate the mean-spin length and minimal variance free from detection errors (experimentally, the magnetization along the θ-axis, not shown, verifies $|\langle J_\theta\rangle| \ll N/2$, leading to a negligible contribution to the correction). The data corrected in this way are shown as diamond symbols in the figures of the main text.

Appendix D

Appendix to Chapter 5

D.1 Analytical derivation of the decoherence profile

In this section, we provide a detailed derivation for the decoherence dynamics. We will present a strict calculation within a semi-classical description that assumes Gaussian fluctuations. This presentation collects many ideas found in previous works [734, 742, 743, 743, 747, 747, 753, 761, 765, 765–768, 773, 860–862]. We aim to provide a clear, self-contained discussion and to derive a highly general expression for the decoherence dynamics which can be applied to a range of spin systems. Moreover, we will also provide a complementary quantum mechanical description of the same decoherence dynamics, which enables us to frame the distinction between Gauss-Markov and telegraph noise in terms of the delocalization of quantum information.

Throughout this section, we consider the following setup: a probe spin-1/2 $\hat{s}_p$ interacting via long-range, $1/r^\alpha$, Ising interactions with system spins $\hat{s}_i$:

$$H_z = \sum_i \frac{J_z g_i}{r_i^\alpha} \hat{s}_p^z \hat{s}_i^z, \tag{D.1}$$

where we have explicitly separated the overall interaction strength J_z from any angular dependence $g_i \sim \mathcal{O}(1)$.

We are interested in the decoherence dynamics where the probe spin is initially prepared along the $\hat{x}$-axis of the Bloch sphere and the Ising interactions (Eqn. D.1) cause its precession in the equatorial plane. The coherence of the spin is defined as the (normalized) projection of the spin into the $\hat{x}$-axis at a later time, $C(t) = 2\langle \hat{s}_p^x(t) \rangle$.

During the evolution, a decoupling sequence can be applied which flips the probe spin. In the rotating frame, the decoupling sequence can be thought of as changing the sign of the Ising interaction. This can be straightforwardly accounted for by introducing a function, $\eta(t';t)$, which captures the sign of H_z at time t' for a pulse sequence of duration t. For example, for a Ramsey measurement $\eta_{\mathrm{R}}(t';t) = 1$, while for spin echo

$$\eta_{\mathrm{SE}}(t';t) = \begin{cases} 1 & 0 < t' < t/2 \\ -1 & t/2 < t' < t. \end{cases} \tag{D.2}$$

We note that this analysis focuses only on Ising interactions and thus ignores the effects of

depolarization on the decoherence dynamics [1].

D.1.1 Semi-classical approach

Average over trajectories— In the semi-classical picture, we analyze the decoherence problem by treating the system spins as fluctuating classical variables $\hat{s}_i^z(t) \to s_i^z(t)$. As such, instead of analysing the details of the dynamics of $\hat{s}_i^z$, we can relate the decoherence of the probe spin to the statistical properties of the fluctuating classical variables $s_i^z(t)$.

Within this framework, every trajectory of $s_i^z(t')$ induces a precession angle $\phi(t)$. The observed coherence is then given by the ensemble average of the coherence over all trajectories:

$$C = 2\langle \hat{s}_p^x(t)\rangle = \left\langle \mathrm{Re}\left[e^{-i\phi(t)}\right]\right\rangle, \quad \text{with} \quad \phi(t) = \sum_j \frac{J_z g_j}{r_j^\alpha}\int_0^t \eta(t';t)s_i^z(t')dt', \tag{D.3}$$

where $\langle\cdots\rangle$ denotes the average over the ensemble of trajectories.

In order to proceed from Eqn. D.3 into a closed form solution for the decoherence dynamics, we must relate the system dynamics to the statistical properties of $s_i^z(t)$ and $\phi(t)$; for simplicity, and following previous literature [732, 741, 763, 768, 860, 861], we assume that both $\phi(t)$ and $s_i^z(t)$ are accurately captured by Gauss-Markov processes. We postpone a detailed discussion about the validity of this assumption to a later section. This simplification allows us to obtain the decoherence dynamics in terms of the variance of $\phi(t)$:

$$\begin{aligned} C(t) &= \langle \mathrm{Re}[e^{-i\phi(t)}]\rangle = e^{-\langle\phi^2\rangle/2} \\ &= \exp\left\{-\frac{1}{2}\left\langle\left|\sum_i \frac{J_z g_i \int_0^t \eta(t';t)s_i^z(t')dt'}{r_i^\alpha}\right|^2\right\rangle\right\} \\ &= \prod_i \exp\left\{-\frac{1}{2}\left[\frac{J_z|g_i|\chi(t)^{\frac{1}{2}}}{2r_i^\alpha}\right]^2\right\}. \end{aligned} \tag{D.4}$$

Here, we assume that each spin is independent and define $\chi(t)$ as follows:

$$\chi(t) \equiv 4\left\langle\left[\int_0^t \eta(t';t)s_i^z(t')dt'\right]^2\right\rangle = \int_0^t dt'\int_0^t dt''\eta(t';t)\eta(t'';t)\left\langle 4s_i^z(t')s_i^z(t'')\right\rangle. \tag{D.5}$$

[1] This is a natural assumption for NV-P1 systems where the two spin defects are far detuned ($\sim$ GHz) and inter-species spin-exchange interactions ($\sim$ MHz) are highly off-resonant and suppressed [364].

The assumption of Gauss-Markov noise enables us to write down the two-point correlation function in terms of a decaying exponential with time scale τ_c:

$$\xi(\tau) \equiv \langle 4 s_i^z(t) s_i^z(t+\tau) \rangle = \mathrm{e}^{-|\tau|/\tau_c}. \tag{D.6}$$

The factor of 4 ensures that the correlation function $\xi(\tau)$ is normalized for spin-1/2 particles when $\tau = 0$. Depending on the specific pulse sequence applied to the system spins, captured by $\eta(t';t)$, we can analytically obtain the expression for $\chi(t)$ in Table D.1.

A few remarks are in order. First, $\chi(t)$ has an intuitive and straightforward interpretation in Fourier space. Defining $f(\omega;t)$ as the Fourier transform of $\eta(t';t)$ and $S(\omega)$ as the Fourier transform of $\xi(\tau)$, $\chi(t)$ can be rewritten as

$$\chi(t) = \int d\omega \, |f(\omega;t)|^2 S(\omega), \tag{D.7}$$

which recovers Eqn. 5.2. In this language, the role of the pulse sequence becomes clear: given the noise spectrum $S(\omega)$ of the spin dynamics $s_i^z(t)$, the pulse sequence acts as a filter function $f(\omega;t)$. Changing the pulse sequence modifies the sensitivity of the probe spin to different frequency components of the noise.

Second, for a single realization, the time-dependence of the decoherence dynamics is entirely determined by $\chi(t)$. If $\chi(t)$ only depends on τ_c and the pulse sequence, the decoherence dynamics is not sensitive to the dimensionality of the spin system. The ability to probe the dimensionality of the spin system arises from the interplay between the positional disorder and the power-law interactions, as discussed in detail in the next section.

Average over positional randomness— Until now, we have considered only the role of dynamical fluctuations in our analysis of the decoherence. In the next step, we compute the positional disorder average by first considering N system spins occupying a volume V in D dimensions, and explicitly

Sequence	$\eta(t';t)$	$\chi(t)$	short-time $t \ll \tau_c$	long-time $t \gg \tau_c$
Ramsey (DEER)	1	$2\tau_c t - 2\tau_c^2\left(1-\mathrm{e}^{-\frac{t}{\tau_c}}\right)$	$t^2 - \frac{t^3}{3\tau_c}$	$2\tau_c t - 2\tau_c^2$
Spin Echo	$\begin{cases} 1 & 0 \le t' < t/2 \\ -1 & t/2 \le t' < t \end{cases}$	$2\tau_c t - 2\tau_c^2\left(3+\mathrm{e}^{-\frac{t}{\tau_c}} - 4\mathrm{e}^{-\frac{t}{2\tau_c}}\right)$	$\frac{t^3}{6\tau_c}$	$2\tau_c t - 6\tau_c^2$
XY-8	$\begin{cases} 1 & \frac{t'}{\tau_p} \in [m-\frac{1}{4}, m+\frac{1}{4}) \\ -1 & \frac{t'}{\tau_p} \in [m+\frac{1}{4}, m+\frac{3}{4}) \end{cases}$	$\frac{\tau_p^2}{12\tau_c}t$	$\frac{\tau_p^2}{12\tau_c}t$	$\frac{\tau_p^2}{12\tau_c}t$

Table D.1: Expressions of $\eta(t';t)$ and $\chi(t)$ for Ramsey/DEER, spin echo, and XY-8. In XY-8, we assume the inter-pulse spacing $\tau_p \ll \tau_c$.

performing the volume integration of each spin as follows [747]:

$$\begin{aligned}
\text{Signal} &= \frac{1}{2}\int\cdots\int \frac{d^D\vec{r}_1}{V}\frac{d^D\vec{r}_2}{V}\cdots\frac{d^D\vec{r}_N}{V}\prod_{i=1}^{N}\exp\left\{-\frac{1}{2}\left[\frac{J_z|g_i|\chi(t)^{\frac{1}{2}}}{2r_i^\alpha}\right]^2\right\} \\
&= \frac{1}{2}\left[\int\frac{d^D\vec{r}}{V}\exp\left\{-\frac{1}{2}\left[\frac{J_z|g_i|\chi(t)^{\frac{1}{2}}}{2r^\alpha}\right]^2\right\}\right]^N \\
&= \frac{1}{2}\left[1-\frac{1}{V}\int\left(1-\exp\left\{-\frac{1}{2}\left[\frac{J_z|g|\chi(t)^{\frac{1}{2}}}{2r^\alpha}\right]^2\right\}\right)d^D\vec{r}\right]^N .
\end{aligned} \tag{D.8}$$

This last equality gives us the limit definition of the exponential ($\lim_{N\to\infty}(1+x/N)^N = e^x$) and, in the thermodynamic limit ($N, V \to \infty$ with fixed density $n \equiv \frac{N}{V}$), is given by:

$$\begin{aligned}
\text{Signal} &= \frac{1}{2}\exp\left\{-n\int\left(1-\mathrm{e}^{-\frac{1}{2}\left[\frac{J_z|g|\chi(t)^{\frac{1}{2}}}{2r^\alpha}\right]^2}\right)d^D\vec{r}\right\} \\
&= \frac{1}{2}\exp\left\{-n\int\left(1-\mathrm{e}^{-\frac{1}{2}z^2}\right)r^{D-1}drd\Omega\right\} \\
&= \frac{1}{2}\exp\left\{-\frac{n}{\alpha}\left(\frac{J_z\chi^{\frac{1}{2}}}{2}\right)^{\frac{D}{\alpha}}\int\left(1-\mathrm{e}^{-\frac{1}{2}z^2}\right)z^{-\frac{D}{\alpha}-1}dz\int|g|^{\frac{D}{\alpha}}d\Omega\right\} \\
&= \frac{1}{2}\exp\left\{-\frac{nDA_D}{\alpha}\left[-\frac{\Gamma(-\frac{D}{2\alpha})}{2^{\frac{D}{2\alpha}+1}}\right]\left[\frac{|\bar{g}|J_z\chi(t)^{\frac{1}{2}}}{2}\right]^{\frac{D}{\alpha}}\right\},
\end{aligned} \tag{D.9}$$

where we make the substitution $z = \frac{J_z|g|\chi(t)^{\frac{1}{2}}}{2r^\alpha}$, $A_D = \frac{\pi^{\frac{D}{2}}}{\Gamma(\frac{D}{2}+1)}$ is the volume of a D-dimensional unit

ball, and $\overline{g} = \left(\frac{\int |g|^{\frac{D}{\alpha}} d\Omega}{\int d\Omega} \right)^{\frac{\alpha}{D}}$ is the averaged angular dependence over a D-dimensional solid angle.

We note that the integral converges only when $2\alpha > D$. This condition captures the physical intuition that, for very long-range interactions (small α), the probe spin interacts strongly with an extensive number of spins. More precisely, the number of spins at distance r from the probe increases as $r^{D-1}dr$, while their contribution scales as $r^{-2\alpha}$. The variance of the phase ϕ, at any fixed time, is then given by $\int_0^R dr\ r^{D-2\alpha-1}$, which precisely diverges with increasing R when $2\alpha > D$. In this regime, which does not apply for our measurements, the standard deviation of $\phi(t)$ becomes unbounded in the thermodynamic limit, the Gaussian approximation $C = e^{-\langle \phi^2 \rangle / 2}$ no longer applies, and a more careful analysis is required.

Combining the results in Table D.1 and Eqn. D.9, we obtain the analytical form of the decoherence signal as measured in our system. In both the short-time and the long-time limits, $\chi(t)$ has a simple power-law dependence on time t. In each limit, the form of the decay profile is a simple stretched exponential, from which we can also obtain the decay timescale as a function of the defect density. For example, for the early-time Ramsey decay, we have:

$$\begin{aligned} C^{\text{Ramsey}}(t \ll \tau_c) &= \exp\left\{ -\frac{nDA_D}{\alpha} \left[-\frac{\Gamma(-\frac{D}{2\alpha})}{2^{\frac{D}{2\alpha}+1}} \right] \left[\frac{\overline{g} J_z t}{2} \right]^{\frac{D}{\alpha}} \right\} \\ &= \exp\left\{ -\left[\left(-\frac{\Gamma(-\frac{D}{2\alpha})}{2^{\frac{3D}{2\alpha}+1}} \frac{DA_D}{\alpha} \right)^{\frac{\alpha}{D}} n^{\frac{\alpha}{D}} \overline{g} J_z t \right]^{\frac{D}{\alpha}} \right\} \\ &= \exp\left\{ -\left(\frac{t}{T_2^{\text{Ramsey}}} \right)^{\frac{D}{\alpha}} \right\}, \end{aligned} \tag{D.10}$$

where

$$T_2^{\text{Ramsey}} = \left[\left(-\frac{\Gamma(-\frac{D}{2\alpha})}{2^{\frac{3D}{2\alpha}+1}} \frac{DA_D}{\alpha} \right)^{\frac{\alpha}{D}} n^{\frac{\alpha}{D}} \overline{g} J_z \right]^{-1} \propto n^{-\frac{\alpha}{D}}. \tag{D.11}$$

Similarly, we can obtain the analytical forms for other pulse sequences and in different time regimes, with all results summarized in Table D.2.

Here, let us emphasize the role of positional disorder in determining the shape of the decoherence decay profile, as highlighted by the differences between Eqns. D.4 and D.9. To explain this difference, it is important to emphasize that the main contribution to the average coherence is dominated by different

	Early-time $t \ll \tau_c$		Late-time $t \gg \tau_c$	
	Stretch power	Decay timescale	Stretch power	Decay timescale
Ramsey (DEER)	$\frac{D}{\alpha}$	$\left(K\overline{g}n^{\frac{\alpha}{D}}J_z\right)^{-1}$	$\frac{D}{2\alpha}$	$\left(\frac{1}{2\tau_c}\right)\left(K\overline{g}n^{\frac{\alpha}{D}}J_z\right)^{-2}$
Spin Echo	$\frac{3D}{2\alpha}$	$(6\tau_c)^{\frac{1}{3}}\left(K\overline{g}n^{\frac{\alpha}{D}}J_z\right)^{-\frac{2}{3}}$	$\frac{D}{2\alpha}$	$\left(\frac{1}{2\tau_c}\right)\left(K\overline{g}n^{\frac{\alpha}{D}}J_z\right)^{-2}$
XY8	$\frac{D}{2\alpha}$	$\left(\frac{12\tau_c}{\tau_p^2}\right)\left(K\overline{g}n^{\frac{\alpha}{D}}J_z\right)^{-2}$	$\frac{D}{2\alpha}$	$\left(\frac{12\tau_c}{\tau_p^2}\right)\left(K\overline{g}n^{\frac{\alpha}{D}}J_z\right)^{-2}$

Table D.2: Ensemble averaged decay profiles for Ramsey/DEER, spin echo, and XY-8 pulse sequences; $\overline{g}$ is the averaged angular dependence, and $K = \frac{1}{2}\left[-\frac{DA_D}{\alpha}\frac{\Gamma(-\frac{D}{2\alpha})}{2^{\frac{D}{2\alpha}+1}}\right]^{\frac{\alpha}{D}}$ is a dimensionless constant only depending on D and α.

positional configurations at different times. For example, at early times, only the configurations with very nearby spins are able to decohere, while configurations with distant spins have yet to contribute to the signal. Similarly, at late times, the configurations with fast decay rates have fully decohered, so the signal is dominated by configurations where the spins are far away from the probe and decoherence is slow. This explains why the stretch power is determined by both dimensionality (which determines how many system spins can be close to the probe) and the exponent of the power-law interactions (which determines how fast those configurations decohere).

By contrast, if the system spins are positioned on a regular lattice, the decay profile no longer exhibits a distribution of time scales and thus follows the shape of the single positional realization case (Eqn. D.4). In particular, for a regular lattice, the spin echo always decays as a stretched exponential with a stretch exponent of 3 (Table D.1), independent of both D and α.

D.1.2 Quantum description

In the semi-classical approach, we assumed that the spin dynamics can be captured by classical Gaussian random variables. In general this need not be true, and one should treat the spin dynamics quantum-mechanically. The main goal of such an analysis is to highlight how the distinction between Gauss-Markov and telegraph noise can be cast as a property of the scrambling dynamics of the system

spin operators $\hat{s}_i^z(t)$.

The full Hamiltonian H governing the dynamics in our experiments is composed of the Ising interaction H_z between the probe spin and the systems spins, as well as H_s which determines the interactions between the system spins. Including the effect of the pulse sequence yields

$$H_{\text{tot}}(t') = \eta(t';t)H_z + H_{\text{s}}. \tag{D.12}$$

The initial density matrix of the system immediately encodes the ensemble of possible initial states. In particular, we consider initial state of the system to be a fully mixed state for the system's spins, while the probe spin is initialized in the $\hat{x}$ direction. This corresponds to the following density matrix:

$$\rho(t=0) = \frac{\mathbb{1}}{\mathcal{N}_s} \otimes \left(\frac{|\uparrow\rangle + |\downarrow\rangle}{\sqrt{2}}\right)\left(\frac{\langle\uparrow| + \langle\downarrow|}{\sqrt{2}}\right), \tag{D.13}$$

where $\mathcal{N}_s$ is the size of the Hilbert space of the spin system.

The probe coherence then becomes:

$$C(t) = 2\text{Tr}\left[\hat{s}_p^x U(t)\rho U^\dagger(t)\right], \quad \text{where} \quad U(t) = \mathcal{T}\exp\left[-i\int_0^t dt' H_{\text{tot}}(t')\right]. \tag{D.14}$$

Because the dynamics conserve $\hat{s}_p^z$, the unitary operator U can be divided into two operators $U_{\uparrow/\downarrow}$, which act only on the system spins and compute their evolution conditioned on the state of the probe:

$$U(t) = U_\uparrow(t) \otimes |\uparrow\rangle\langle\uparrow| + U_\downarrow(t) \otimes |\downarrow\rangle\langle\downarrow|, \tag{D.15}$$

where

$$U_\uparrow(t) = \mathcal{T}\text{e}^{-i\int_0^t [H_{\text{s}} + \eta(t';t)\sum_i \frac{l_z g_i}{2r_i^\alpha}\hat{s}_i^z]dt'}, \qquad U_\downarrow(t) = \mathcal{T}\text{e}^{-i\int_0^t [H_{\text{s}} - \eta(t';t)\sum_i \frac{l_z g_i}{2r_i^\alpha}\hat{s}_i^z]dt'}. \tag{D.16}$$

The coherence can then be written in terms of $U_{\uparrow/\downarrow}(t)$ acting on the spin system:

$$C(t) = \frac{1}{\mathcal{N}_s}\text{Tr}\left[U_\uparrow(t)U_\downarrow^\dagger(t) + U_\downarrow(t)U_\uparrow^\dagger\right] = \frac{2}{\mathcal{N}_s}\text{Re}\left(\text{Tr}\left[U_\uparrow(t)U_\downarrow^\dagger(t)\right]\right) \tag{D.17}$$

The dynamics $U_{\downarrow/\uparrow}(t)$ remain very complex because they include a contribution from both the system's dynamics and the probe-system coupling. To understand how the probe spin is sensitive to the spin dynamics generated by the many-body interactions H_s, we move to the interaction frame of

H_s by making the following substitution:

$$U_{\uparrow/\downarrow}(t) = U_0(t)\tilde{U}_{\uparrow,\downarrow}(t), \quad \text{with} \quad U_0(t) = \mathrm{e}^{-itH_\mathrm{s}}, \tag{D.18}$$

where

$$\tilde{U}_{\uparrow/\downarrow} = \mathcal{T}\mathrm{e}^{\mp i\int_0^t \eta(t';t)\sum_i \frac{J_{z\xi_i}}{2r_i^\kappa}\hat{s}_i^z(t')dt'}, \quad \text{and} \quad \hat{\tilde{s}}_i^z(t) = U_0^\dagger(t)\hat{s}_i^z(t)U_0(t). \tag{D.19}$$

In this frame, the two evolution operators lose an explicit reference to H_s at the expense of the spin operators $\hat{s}_i^z$ becoming time-dependent. The resulting coherence remains in the same form, but with the unitaries now referring to the interaction frame:

$$C(t) = \frac{2}{\mathcal{N}_s}\mathrm{Re}\left(\mathrm{Tr}\left[\tilde{U}_\uparrow(t)\tilde{U}_\downarrow^\dagger(t)\right]\right) \tag{D.20}$$

Note that Eqn. D.20 is formally similar to Eqn. D.3. Especially, replacing the quantum operator $\hat{\tilde{s}}_i^z(t)$ with a classical variable immediately reduce this equation to Eqn. D.3.

While Eqn. D.20 already averages over the possible initial states of $\hat{s}_i^z$, one must independently average the signal over the different spin ensembles (which arise, for example, from different positions of the spins, coupling to a polychromatic driving field or to other classical fluctuating degrees of freedom, etc.) While these two kinds of averages (one from different configurations of the many-body system and the other from the randomness of H_s) can lead to the same auto-correlator $\xi(t) \propto \left\langle \hat{\tilde{s}}_i^z(t)\hat{\tilde{s}}_i^z(0)\middle|\hat{\tilde{s}}_i^z(t)\hat{\tilde{s}}_i^z(0)\right\rangle$, they are essential for determining higher order moments of the distribution and, thus, whether a telegraph or a continuous (Gaussian) random variable is a good description of the many-body noise of $\hat{s}_i^z$ and thus the decoherence signal of the probe spin.

While Eqn. D.20 provides the generic expression for the decoherence dynamics of a spin coupled to a dynamical system, it is intractable to directly compute the decoherence profile from this equation except in specific cases. Nevertheless, such solvable points can provide important intuition for the conditions under which Eqn. D.20 reduces to a semi-classical description with either Gauss-Markov or telegraph noise. As follows, we provide two instructive examples where an explicit computation can be performed, and the relationship between the nature of the system and its noise properties is made clear.

Probe coupled to a single spin evolving under an external drive— First, we consider the scenario

where the noise that leads to the decoherence of the probe is generated by a single system spin, whose dynamics are controlled by an *external random* drive. In this case, the interaction Hamiltonian is given by:

$$H_{\mathrm{s}} = \Omega[\hat{s}_i^x \cos\theta(t) + \hat{s}_i^y \sin\theta(t)] \tag{D.21}$$

where Ω characterizes the strength of the drive and $\theta(t)$ is a time-dependent phase. The presence of such a time-dependent phase mirrors to the polychromatic drive—$\theta(t)$ is chosen to follow a Gaussian stochastic process [863], and is randomized across different runs of the experiment. Crucially, for each run of the experiment, the dynamics induced by H_{s} generate a particular trajectory around the Bloch sphere without any loss of single-particle coherence. As a result, the continuous spin rotation leads to a continuous change in the strength of the noise generated—this leads to the natural description of $s_i^z(t)$ as a continuous classical variable.

We emphasize that, within this framework, there is a single phase accumulated due to the noise for the particular driving $\theta(t)$. As a result, to obtain Gaussian-distributed noise, one must additionally average over different instances of $\theta(t)$. In the experiment this corresponds exactly to the polychromatic drive, where the phase accumulation rate in each experimental run is random and changes continuously in time.

Probe coupled to a system strongly interacting with a large bath— We now turn to the opposite limit, where the noise is generated by spins coupled to a Markovian bath. The dynamics of $\hat{s}_i^z(t)$ can be thought to undergo spontaneous emission and absorption of photons/phonons—starting in either the state $|\uparrow\rangle$ or $|\downarrow\rangle$, the system undergoes quantum jumps into the opposite state at a rate given by $1/\tau_c$ [864]. In this intuitive picture, the decoherence of the probe spin should be evaluated by averaging over all the possible quantum jump trajectories of the system spins—this precisely corresponds to a telegraph-like classical noise.

We can make this picture more precise, using Eqn. D.19 as well as intuition from the perspective of operator dynamics. In particular, if the operator $\hat{\hat{s}}_i^z(t)$ spreads across a large number of degrees of freedom much faster than the interaction time scale with the probe spin, then the probe spin is interacting with independent, commuting operators at different times, $[\hat{\hat{s}}_z^i(t), \hat{\hat{s}}_z^i(t')] = 0$. This immediately leads to two consequences: (i) the time-ordering operator in Eqn. D.19 acts trivially on

the exponential, and the eigenvalues of the exponential are simply given by the exponential of the eigenvalues of $\int_0^t \eta(t')\hat{\tilde{s}}_i^z(t')dt'$; (ii) $\hat{\tilde{s}}_i^z(t)$ can be simultaneously diagonalized for different times.

The latter fact enables a very simple analysis of the dynamics. To see this more easily, let us simplify our problem by dividing the time evolution into M independent blocks of duration $\delta t = t/M$:

$$\tilde{U}_{\uparrow/\downarrow} = \prod_j \exp\left[\mp i\eta(j\delta t;t)\sum_i \frac{J_z g_i}{2r_i^\alpha}\hat{\tilde{s}}_i^z(j\delta t)\right], \tag{D.22}$$

where $\hat{\tilde{s}}_i^z(j\delta t)$ commute with one another for different i and time $j\delta t$. Because there is a single eigenbasis $|\mu\rangle$ that diagonalizes all these operators, when computing $\langle\mu|\,\tilde{U}_{\uparrow/\downarrow}\,|\mu\rangle$, the operators can be substituted by the corresponding eigenvalues $\lambda_\mu^i(j\delta t)$, and the exponent simply becomes the sum of individual contributions. Crucially, since $\hat{s}_z^2(t) = 1/4$, $\lambda_\mu^i(t)$ can only be $\pm 1/2$ [2]. The last necessary ingredient is the understanding of how $\lambda_\mu^i(j\delta t)$ at different times relate with one another. In general, this depends on the details of the dynamics. But, owing to the size of the Hilbert space, $2\mathcal{N}_s$, one can take a statistical approach to this question. Namely, over the ensemble of eigenstates and operators, changing the sign of the eigenstate is expected to follow a Poisson process with time scale τ_c, $\langle\lambda_\mu^i(t)\lambda_\mu^i(t')\rangle \propto \mathrm{e}^{-|t-t'|/\tau_c}$. We note that this correlation decay can be exactly recast as an exponential decay correlation function for the spin operators. The dynamics of each $\lambda_\mu^i(t)$ can then be understood as either a single quantum jump trajectory (in the quantum language), or a single classical telegraph noise realization (in the classical description). Summing over all the eigenstates $|\mu\rangle$ completes the trace operation in Eqn. D.20 and yields the final coherence of the probe spin.

Here, we hasten to emphasize that unlike the single driven spin case, one does not have to compute an average over different trajectories of the spin dynamics, that is already incorporated within the trace operation and the sum over the different eigenstates. This contrasts with the single spin example, where an explicit averaging over the driving fields was necessary to obtain the distribution of accumulated phases.

Spin coupled to a generic many-body interacting system— Taking the above two examples into consideration, whether a generic many-body system is described by the Gauss-Markov or the Telegraph

[2] As long as the eigenspectrum of the original local operator is discrete, so will $\lambda_\mu(t)$; as a result, we expect the same telegraph noise description in the context of higher spin systems.

random variable is determined by the speed of the operator spreading. If the spreading of the operator is slow, the dynamics of $\hat{\tilde{s}}_z^i(t)$ remain constrained to a few sites throughout the measurement duration and the system appears coherent (leading to continuous Gaussian noise). If the spreading of the operator is fast, $\hat{\tilde{s}}_z^i(t)$ quickly spreads across many spins and the rest of the system acts as an effective Markovian bath, leading to telegraph noise.

In our disordered, strongly-interacting system, we conjecture that disorder leads to the slow spread of $\hat{\tilde{s}}_i^z$, and the decay of the auto-correlator $\langle \hat{\tilde{s}}_i^z(0)\hat{\tilde{s}}_i^z(t)\rangle$ mostly results from the different trajectories of local dynamics (originating from different H_{s} owing to different initial configurations of the bath spins). This is consistent with our experimental observation of the spin-echo decay stretch power $\beta = 3D/2\alpha$ for a three-dimensional dipolar ensemble, and is characteristic of the Gaussian noise model.

References

[1] Cory, D. G. *et al.* NMR based quantum information processing: Achievements and prospects. *Fortschritte der Physik: Progress of Physics* **48**, 875–907 (2000).

[2] Vandersypen, L. M. & Chuang, I. L. Nmr techniques for quantum control and computation. *Reviews of Modern Physics* **76**, 1037 (2005).

[3] Jones, J. A. Quantum computing with NMR. *Progress in Nuclear Magnetic Resonance Spectroscopy* **59**, 91–120 (2011).

[4] Weber, J. *et al.* Quantum computing with defects. *Proceedings of the National Academy of Sciences* **107**, 8513–8518 (2010).

[5] Childress, L. & Hanson, R. Diamond NV centers for quantum computing and quantum networks. *MRS bulletin* **38**, 134–138 (2013).

[6] Doherty, M. W. *et al.* The nitrogen-vacancy colour centre in diamond. *Physics Reports* **528**, 1–45 (2013).

[7] Awschalom, D. D., Hanson, R., Wrachtrup, J. & Zhou, B. B. Quantum technologies with optically interfaced solid-state spins. *Nature Photonics* **12**, 516–527 (2018).

[8] Pezzagna, S. & Meijer, J. Quantum computer based on color centers in diamond. *Applied Physics Reviews* **8** (2021).

[9] Wolfowicz, G. *et al.* Quantum guidelines for solid-state spin defects. *Nature Reviews Materials* **6**, 906–925 (2021).

[10] Leibfried, D., Blatt, R., Monroe, C. & Wineland, D. Quantum dynamics of single trapped ions. *Reviews of Modern Physics* **75**, 281 (2003).

[11] Blatt, R. & Wineland, D. Entangled states of trapped atomic ions. *Nature* **453**, 1008–1015 (2008).

[12] Häffner, H., Roos, C. F. & Blatt, R. Quantum computing with trapped ions. *Physics Reports* **469**, 155–203 (2008).

[13] Duan, L.-M. & Monroe, C. Colloquium: Quantum networks with trapped ions. *Reviews of Modern Physics* **82**, 1209 (2010).

[14] Monroe, C. & Kim, J. Scaling the ion trap quantum processor. *Science* **339**, 1164–1169 (2013).

[15] Bruzewicz, C. D., Chiaverini, J., McConnell, R. & Sage, J. M. Trapped-ion quantum computing: Progress and challenges. *Applied Physics Reviews* **6** (2019).

[16] Monroe, C. *et al.* Programmable quantum simulations of spin systems with trapped ions. *Reviews of Modern Physics* **93**, 025001 (2021).

[17] Raimond, J.-M., Brune, M. & Haroche, S. Manipulating quantum entanglement with atoms and photons in a cavity. *Reviews of Modern Physics* **73**, 565 (2001).

[18] Lukin, M. Colloquium: Trapping and manipulating photon states in atomic ensembles. *Reviews of Modern Physics* **75**, 457 (2003).

[19] Ritsch, H., Domokos, P., Brennecke, F. & Esslinger, T. Cold atoms in cavity-generated dynamical optical potentials. *Reviews of Modern Physics* **85**, 553 (2013).

[20] Forn-Díaz, P., Lamata, L., Rico, E., Kono, J. & Solano, E. Ultrastrong coupling regimes of light-matter interaction. *Reviews of Modern Physics* **91**, 025005 (2019).

[21] Mivehvar, F., Piazza, F., Donner, T. & Ritsch, H. Cavity qed with quantum gases: new paradigms in many-body physics. *Advances in Physics* **70**, 1–153 (2021).

[22] O'brien, J. L. Optical quantum computing. *Science* **318**, 1567–1570 (2007).

[23] Kok, P. *et al.* Linear optical quantum computing with photonic qubits. *Reviews of Modern Physics* **79**, 135 (2007).

[24] Aspuru-Guzik, A. & Walther, P. Photonic quantum simulators. *Nature physics* **8**, 285–291 (2012).

[25] Chang, D. E., Vuletić, V. & Lukin, M. D. Quantum nonlinear optics—photon by photon. *Nature Photonics* **8**, 685–694 (2014).

[26] Flamini, F., Spagnolo, N. & Sciarrino, F. Photonic quantum information processing: a review. *Reports on Progress in Physics* **82**, 016001 (2018).

[27] Slussarenko, S. & Pryde, G. J. Photonic quantum information processing: A concise review. *Applied Physics Reviews* **6** (2019).

[28] Wang, J., Sciarrino, F., Laing, A. & Thompson, M. G. Integrated photonic quantum technologies. *Nature Photonics* **14**, 273–284 (2020).

[29] Clarke, J. & Wilhelm, F. K. Superconducting quantum bits. *Nature* **453**, 1031–1042 (2008).

[30] You, J.-Q. & Nori, F. Atomic physics and quantum optics using superconducting circuits. *Nature* **474**, 589–597 (2011).

[31] Houck, A. A., Türeci, H. E. & Koch, J. On-chip quantum simulation with superconducting circuits. *Nature Physics* **8**, 292–299 (2012).

[32] Devoret, M. H. & Schoelkopf, R. J. Superconducting circuits for quantum information: an outlook. *Science* **339**, 1169–1174 (2013).

[33] Wendin, G. Quantum information processing with superconducting circuits: a review. *Reports on Progress in Physics* **80**, 106001 (2017).

[34] Krantz, P. *et al.* A quantum engineer's guide to superconducting qubits. *Applied Physics Reviews* **6** (2019).

[35] Kjaergaard, M. *et al.* Superconducting qubits: Current state of play. *Annual Review of Condensed Matter Physics* **11**, 369–395 (2020).

[36] Blais, A., Girvin, S. M. & Oliver, W. D. Quantum information processing and quantum optics with circuit quantum electrodynamics. *Nature Physics* **16**, 247–256 (2020).

[37] Blais, A., Grimsmo, A. L., Girvin, S. M. & Wallraff, A. Circuit quantum electrodynamics. *Reviews of Modern Physics* **93**, 025005 (2021).

[38] Lewenstein, M. *et al.* Ultracold atomic gases in optical lattices: mimicking condensed matter physics and beyond. *Advances in Physics* **56**, 243–379 (2007).

[39] Bloch, I., Dalibard, J. & Zwerger, W. Many-body physics with ultracold gases. *Reviews of Modern Physics* **80**, 885 (2008).

[40] Bloch, I., Dalibard, J. & Nascimbene, S. Quantum simulations with ultracold quantum gases. *Nature Physics* **8**, 267–276 (2012).

[41] Gross, C. & Bloch, I. Quantum simulations with ultracold atoms in optical lattices. *Science* **357**, 995–1001 (2017).

[42] Schäfer, F., Fukuhara, T., Sugawa, S., Takasu, Y. & Takahashi, Y. Tools for quantum simulation with ultracold atoms in optical lattices. *Nature Reviews Physics* **2**, 411–425 (2020).

[43] Gross, C. & Bakr, W. S. Quantum gas microscopy for single atom and spin detection. *Nature Physics* **17**, 1316–1323 (2021).

[44] Browaeys, A. & Lahaye, T. Many-body physics with individually controlled rydberg atoms. *Nature Physics* **16**, 132–142 (2020).

[45] Morgado, M. & Whitlock, S. Quantum simulation and computing with rydberg-interacting qubits. *AVS Quantum Science* **3** (2021).

[46] Kaufman, A. M. & Ni, K.-K. Quantum science with optical tweezer arrays of ultracold atoms and molecules. *Nature Physics* **17**, 1324–1333 (2021).

[47] Xiang, Z.-L., Ashhab, S., You, J. & Nori, F. Hybrid quantum circuits: Superconducting circuits interacting with other quantum systems. *Reviews of Modern Physics* **85**, 623 (2013).

[48] Kurizki, G. *et al.* Quantum technologies with hybrid systems. *Proceedings of the National Academy of Sciences* **112**, 3866–3873 (2015).

[49] Reiserer, A. & Rempe, G. Cavity-based quantum networks with single atoms and optical photons. *Reviews of Modern Physics* **87**, 1379 (2015).

[50] Gu, X., Kockum, A. F., Miranowicz, A., Liu, Y.-x. & Nori, F. Microwave photonics with superconducting quantum circuits. *Physics Reports* **718**, 1–102 (2017).

[51] Atatüre, M., Englund, D., Vamivakas, N., Lee, S.-Y. & Wrachtrup, J. Material platforms for spin-based photonic quantum technologies. *Nature Reviews Materials* **3**, 38–51 (2018).

[52] Tomza, M. *et al.* Cold hybrid ion-atom systems. *Reviews of Modern Physics* **91**, 035001 (2019).

[53] Lachance-Quirion, D., Tabuchi, Y., Gloppe, A., Usami, K. & Nakamura, Y. Hybrid quantum systems based on magnonics. *Applied Physics Express* **12**, 070101 (2019).

[54] Elshaari, A. W., Pernice, W., Srinivasan, K., Benson, O. & Zwiller, V. Hybrid integrated quantum photonic circuits. *Nature Photonics* **14**, 285–298 (2020).

[55] Clerk, A., Lehnert, K., Bertet, P., Petta, J. & Nakamura, Y. Hybrid quantum systems with circuit quantum electrodynamics. *Nature Physics* **16**, 257–267 (2020).

[56] Monroe, C. Quantum information processing with atoms and photons. *Nature* **416**, 238–246 (2002).

[57] Saffman, M., Walker, T. G. & Mølmer, K. Quantum information with rydberg atoms. *Reviews of Modern Physics* **82**, 2313–2363 (2010).

[58] Buluta, I., Ashhab, S. & Nori, F. Natural and artificial atoms for quantum computation. *Reports on Progress in Physics* **74**, 104401 (2011).

[59] Saffman, M. Quantum computing with atomic qubits and rydberg interactions: progress and challenges. *Journal of Physics B: Atomic, Molecular and Optical Physics* **49**, 202001 (2016).

[60] Hartmann, M. J. Quantum simulation with interacting photons. *Journal of Optics* **18**, 104005 (2016).

[61] Noh, C. & Angelakis, D. G. Quantum simulations and many-body physics with light. *Reports on Progress in Physics* **80**, 016401 (2016).

[62] Gaita-Ariño, A., Luis, F., Hill, S. & Coronado, E. Molecular spins for quantum computation. *Nature Chemistry* **11**, 301–309 (2019).

[63] Adams, C. S., Pritchard, J. D. & Shaffer, J. P. Rydberg atom quantum technologies. *Journal of Physics B: Atomic, Molecular and Optical Physics* **53**, 012002 (2019).

[64] Bennett, C. H. & DiVincenzo, D. P. Quantum information and computation. *Nature* **404**, 247–255 (2000).

[65] Braunstein, S. L. & Van Loock, P. Quantum information with continuous variables. *Reviews of Modern Physics* **77**, 513 (2005).

[66] O'brien, J. L., Furusawa, A. & Vučković, J. Photonic quantum technologies. *Nature Photonics* **3**, 687–695 (2009).

[67] Defenu, N. *et al.* Long-range interacting quantum systems. *Reviews of Modern Physics* **95**, 035002 (2023).

[68] Nielsen, M. A. & Chuang, I. L. *Quantum computation and quantum information* (Cambridge University Press, Cambridge, UK, 2010).

[69] Lloyd, S. Universal quantum simulators. *Science* **273**, 1073–1078 (1996).

[70] Buluta, I. & Nori, F. Quantum simulators. *Science* **326**, 108–111 (2009).

[71] Cirac, J. I. & Zoller, P. Goals and opportunities in quantum simulation. *Nature Physics* **8**, 264–266 (2012).

[72] Georgescu, I. M., Ashhab, S. & Nori, F. Quantum simulation. *Reviews of Modern Physics* **86**, 153 (2014).

[73] Chang, D., Douglas, J., González-Tudela, A., Hung, C.-L. & Kimble, H. Colloquium: Quantum matter built from nanoscopic lattices of atoms and photons. *Reviews of Modern Physics* **90**, 031002 (2018).

[74] Altman, E. *et al.* Quantum simulators: Architectures and opportunities. *PRX Quantum* **2**, 017003 (2021).

[75] Daley, A. J. *et al.* Practical quantum advantage in quantum simulation. *Nature* **607**, 667–676 (2022).

[76] Briegel, H. J., Browne, D. E., Dür, W., Raussendorf, R. & Van den Nest, M. Measurement-based quantum computation. *Nature Physics* **5**, 19–26 (2009).

[77] Ladd, T. D. *et al.* Quantum computers. *nature* **464**, 45–53 (2010).

[78] Campbell, E. T., Terhal, B. M. & Vuillot, C. Roads towards fault-tolerant universal quantum computation. *Nature* **549**, 172–179 (2017).

[79] Hauke, P., Katzgraber, H. G., Lechner, W., Nishimori, H. & Oliver, W. D. Perspectives of quantum annealing: Methods and implementations. *Reports on Progress in Physics* **83**, 054401 (2020).

[80] Gisin, N. & Thew, R. Quantum communication. *Nature Photonics* **1**, 165–171 (2007).

[81] Pirandola, S. *et al.* Advances in quantum cryptography. *Advances in Optics and Photonics* **12**, 1012–1236 (2020).

[82] Wehner, S., Elkouss, D. & Hanson, R. Quantum internet: A vision for the road ahead. *Science* **362**, eaam9288 (2018).

[83] Wei, S.-H. *et al.* Towards real-world quantum networks: a review. *Laser & Photonics Reviews* **16**, 2100219 (2022).

[84] Giovannetti, V., Lloyd, S. & Maccone, L. Advances in quantum metrology. *Nature Photonics* **5**, 222–229 (2011).

[85] Degen, C. L., Reinhard, F. & Cappellaro, P. Quantum sensing. *Reviews of Modern Physics* **89**, 035002 (2017).

[86] Pezze, L., Smerzi, A., Oberthaler, M. K., Schmied, R. & Treutlein, P. Quantum metrology with nonclassical states of atomic ensembles. *Reviews of Modern Physics* **90**, 035005 (2018).

[87] Pirandola, S., Bardhan, B. R., Gehring, T., Weedbrook, C. & Lloyd, S. Advances in photonic quantum sensing. *Nature Photonics* **12**, 724–733 (2018).

[88] Ludlow, A. D., Boyd, M. M., Ye, J., Peik, E. & Schmidt, P. O. Optical atomic clocks. *Reviews of Modern Physics* **87**, 637 (2015).

[89] Deutsch, J. M. Quantum statistical mechanics in a closed system. *Physical Review A* **43**, 2046–2049 (1991).

[90] Srednicki, M. Chaos and quantum thermalization. *Physical Review E* **50**, 888–901 (1994).

[91] Srednicki, M. The approach to thermal equilibrium in quantized chaotic systems. *Journal of Physics A: Mathematical and General* **32**, 1163 (1999).

[92] Gogolin, C. & Eisert, J. Equilibration, thermalisation, and the emergence of statistical mechanics in closed quantum systems. *Reports on Progress in Physics* **79**, 056001 (2016).

[93] D'Alessio, L., Kafri, Y., Polkovnikov, A. & Rigol, M. From Quantum Chaos and Eigenstate Thermalization to Statistical Mechanics and Thermodynamics. *Advances in Physics* **65**, 239–362 (2016).

[94] Deutsch, J. M. Eigenstate thermalization hypothesis. *Reports on Progress in Physics* **81**, 082001 (2018).

[95] Abanin, D. A., Altman, E., Bloch, I. & Serbyn, M. Colloquium: Many-body localization, thermalization, and entanglement. *Reviews of Modern Physics* **91**, 021001 (2019).

[96] Rigol, M., Dunjko, V. & Olshanii, M. Thermalization and its mechanism for generic isolated quantum systems. *Nature* **452**, 854–858 (2008).

[97] Gornyi, I. V., Mirlin, A. D. & Polyakov, D. G. Interacting electrons in disordered wires: Anderson localization and low-t transport. *Physical Review Letters* **95**, 206603 (2005).

[98] Basko, D. M., Aleiner, I. L. & Altshuler, B. L. Metal–insulator transition in a weakly interacting many-electron system with localized single-particle states. *Annals of physics* **321**, 1126–1205 (2006).

[99] Oganesyan, V. & Huse, D. A. Localization of interacting fermions at high temperature. *Physical Review B* **75**, 155111 (2007).

[100] Pal, A. & Huse, D. A. Many-body localization phase transition. *Physical Review B* **82**, 174411 (2010).

[101] Imbrie, J. Z. On many-body localization for quantum spin chains. *tical Physics* **163**, 998–1048 (2016).

[102] Schreiber, M. *et al.* Observation of many-body localization of interacting fermions in a quasirandom optical lattice. *Science* **349**, 842–845 (2015).

[103] Smith, J. *et al.* Many-body localization in a quantum simulator with programmable random disorder. *Nature Physics* **12**, 907–911 (2016).

[104] De Roeck, W., Huveneers, F., Müller, M. & Schiulaz, M. Absence of many-body mobility edges. *Physical Review B* **93**, 014203 (2016).

[105] De Roeck, W. & Huveneers, F. m. c. Stability and instability towards delocalization in many-body localization systems. *Physical Review B* **95**, 155129 (2017).

[106] Nandkishore, R. & Huse, D. A. Many-body localization and thermalization in quantum statistical mechanics. *Annual Review of Condensed Matter Physics* **6**, 15–38 (2015).

[107] Altman, E. & Vosk, R. Universal dynamics and renormalization in many-body-localized systems. *Annu. Rev. Condens. Matter Phys.* **6**, 383–409 (2015).

[108] Altman, E. Many-body localization and quantum thermalization. *Nature Physics* **14**, 979–983 (2018).

[109] Berges, J., Borsányi, S. & Wetterich, C. Prethermalization. *Physical Review Letters* **93**, 142002 (2004).

[110] Gring, M. *et al.* Relaxation and prethermalization in an isolated quantum system. *Science* **337**, 1318–1322 (2012).

[111] Bertini, B., Essler, F. H. L., Groha, S. & Robinson, N. J. Prethermalization and thermalization in models with weak integrability breaking. *Physical Review Letters* **115**, 180601 (2015).

[112] Langen, T., Gasenzer, T. & Schmiedmayer, J. Prethermalization and universal dynamics in near-integrable quantum systems. *Journal of Statistical Mechanics: Theory and Experiment* **2016**, 064009 (2016).

[113] Tang, Y. *et al.* Thermalization near integrability in a dipolar quantum newton's cradle. *Physical Review X* **8**, 021030 (2018).

[114] Mallayya, K., Rigol, M. & De Roeck, W. Prethermalization and thermalization in isolated quantum systems. *Physical Review X* **9**, 021027 (2019).

[115] Luitz, D. J., Moessner, R., Sondhi, S. & Khemani, V. Prethermalization without temperature. *Physical Review X* **10**, 021046 (2020).

[116] Guhr, T., Müller-Groeling, A. & Weidenmüller, H. A. Random-matrix theories in quantum physics: common concepts. *Physics Reports* **299**, 189–425 (1998).

[117] Alhassid, Y. The statistical theory of quantum dots. *Reviews of Modern Physics* **72**, 895 (2000).

[118] Kota, V. K. B. *Embedded random matrix ensembles in quantum physics*, vol. 3 (Springer, New York, 2014).

[119] Brody, T. A. *et al.* Random-matrix physics: spectrum and strength fluctuations. *Reviews of Modern Physics* **53**, 385 (1981).

[120] Bohigas, O., Giannoni, M. J. & Schmit, C. Characterization of chaotic quantum spectra and universality of level fluctuation laws. *Physical Review Letters* **52**, 1–4 (1984).

[121] Mehta, M. L. *Random matrices* (Elsevier, New York, 2004).

[122] Santos, L. F. & Rigol, M. Onset of quantum chaos in one-dimensional bosonic and fermionic systems and its relation to thermalization. *Physical Review E* **81**, 036206 (2010).

[123] D'Alessio, L. & Rigol, M. Long-time behavior of isolated periodically driven interacting lattice systems. *Physical Review X* **4**, 041048 (2014).

[124] Berry, M. V. & Tabor, M. Level clustering in the regular spectrum. *Proceedings of the Royal Society of London. A. Mathematical and Physical Sciences* **356**, 375–394 (1977).

[125] Santos, L. F. & Rigol, M. Localization and the effects of symmetries in the thermalization properties of one-dimensional quantum systems. *Physical Review E* **82**, 031130 (2010).

[126] Nandkishore, R., Gopalakrishnan, S. & Huse, D. A. Spectral features of a many-body-localized system weakly coupled to a bath. *Physical Review B* **90**, 064203 (2014).

[127] Anderson, P. W. Absence of diffusion in certain random lattices. *Physical Review* **109**, 1492–1505 (1958).

[128] Abrahams, E., Anderson, P. W., Licciardello, D. C. & Ramakrishnan, T. V. Scaling theory of localization: Absence of quantum diffusion in two dimensions. *Physical Review Letters* **42**, 673–676 (1979).

[129] Serbyn, M., Papić, Z. & Abanin, D. A. Local conservation laws and the structure of the many-body localized states. *Physical Review Letters* **111**, 127201 (2013).

[130] Huse, D. A., Nandkishore, R. & Oganesyan, V. Phenomenology of fully many-body-localized systems. *Physical Review B* **90**, 174202 (2014).

[131] Pekker, D., Refael, G., Altman, E., Demler, E. & Oganesyan, V. Hilbert-glass transition: New universality of temperature-tuned many-body dynamical quantum criticality. *Physical Review X* **4**, 011052 (2014).

[132] Pekker, D., Clark, B. K., Oganesyan, V. & Refael, G. Fixed points of wegner-wilson flows and many-body localization. *Physical Review Letters* **119**, 075701 (2017).

[133] Ponte, P., Papić, Z., Huveneers, F. & Abanin, D. A. Many-body localization in periodically driven systems. *Physical Review Letters* **114**, 140401 (2015).

[134] Atas, Y. Y., Bogomolny, E., Giraud, O. & Roux, G. Distribution of the ratio of consecutive level spacings in random matrix ensembles. *Physical Review Letters* **110**, 084101 (2013).

[135] Johri, S., Nandkishore, R. & Bhatt, R. N. Many-body localization in imperfectly isolated quantum systems. *Physical Review Letters* **114**, 117401 (2015).

[136] Vosk, R. & Altman, E. Many-body localization in one dimension as a dynamical renormalization group fixed point. *Physical Review Letters* **110**, 067204 (2013).

[137] Landau, L. D. & Lifshitz, E. M. *Course of theoretical physics* (Elsevier, Amsterdam, 2013).

[138] Liboff, R. L. *Kinetic theory: classical, quantum, and relativistic descriptions* (Springer, New York, 2003).

[139] Lebon, G., Jou, D. & Casas-Vázquez, J. *Understanding non-equilibrium thermodynamics*, vol. 295 (Springer, New York, 2008).

[140] Eisert, J., Friesdorf, M. & Gogolin, C. Quantum many-body systems out of equilibrium. *Nature Physics* **11**, 124–130 (2015).

[141] Nozieres, P. *Theory of quantum liquids* (CRC Press, Boca Raton, FL, 2018).

[142] Sieniutycz, S. *Conservation laws in variational thermo-hydrodynamics*, vol. 279 (Springer, New York, 2012).

[143] Wyatt, R. E. *Quantum dynamics with trajectories: introduction to quantum hydrodynamics*, vol. 28 (Springer, New York, 2005).

[144] Jeon, S. & Yaffe, L. G. From quantum field theory to hydrodynamics: Transport coefficients and effective kinetic theory. *Physical Review D* **53**, 5799–5809 (1996).

[145] Tsubota, M., Kobayashi, M. & Takeuchi, H. Quantum hydrodynamics. *Physics Reports* **522**, 191–238 (2013).

[146] Bhaseen, M., Doyon, B., Lucas, A. & Schalm, K. Energy flow in quantum critical systems far from equilibrium. *Nature Physics* **11**, 509–514 (2015).

[147] Bernard, D. & Doyon, B. A hydrodynamic approach to non-equilibrium conformal field theories. *Journal of Statistical Mechanics: Theory and Experiment* **2016**, 033104 (2016).

[148] Bernard, D. & Doyon, B. Conformal field theory out of equilibrium: a review. *Journal of Statistical Mechanics: Theory and Experiment* **2016**, 064005 (2016).

[149] Vosk, R., Huse, D. A. & Altman, E. Theory of the Many-Body Localization Transition in One-Dimensional Systems. *Physical Review X* **5**, 031032 (2015).

[150] Potter, A. C., Vasseur, R. & Parameswaran, S. Universal properties of many-body delocalization transitions. *Physical Review X* **5**, 031033 (2015).

[151] Bar Lev, Y., Cohen, G. & Reichman, D. R. Absence of diffusion in an interacting system of spinless fermions on a one-dimensional disordered lattice. *Physical Review Letters* **114**, 100601 (2015).

[152] Agarwal, K., Gopalakrishnan, S., Knap, M., Müller, M. & Demler, E. Anomalous diffusion and griffiths effects near the many-body localization transition. *Physical Review Letters* **114**, 160401 (2015).

[153] Žnidarič, M., Marko, Scardicchio, A. & Varma, V. K. Diffusive and subdiffusive spin transport in the ergodic phase of a many-body localizable system. *Physical Review Letters* **117**, 040601 (2016).

[154] Essler, F. H. & Fagotti, M. Quench dynamics and relaxation in isolated integrable quantum spin chains. *Journal of Statistical Mechanics: Theory and Experiment* **2016**, 064002 (2016).

[155] Bastianello, A., Bertini, B., Doyon, B. & Vasseur, R. Introduction to the special issue on emergent hydrodynamics in integrable many-body systems. *Journal of Statistical Mechanics: Theory and Experiment* **2022**, 014001 (2022).

[156] Doyon, B., Gopalakrishnan, S., Møller, F., Schmiedmayer, J. & Vasseur, R. Generalized hydrodynamics: a perspective. *arXiv preprint arXiv:2311.03438* (2023).

[157] Malvania, N. *et al.* Generalized hydrodynamics in strongly interacting 1d bose gases. *Science* **373**, 1129–1133 (2021).

[158] Kinoshita, T., Wenger, T. & Weiss, D. S. A quantum newton's cradle. *Nature* **440**, 900–903 (2006).

[159] Rigol, M., Dunjko, V., Yurovsky, V. & Olshanii, M. Relaxation in a completely integrable many-body quantum system: An ab initio study of the dynamics of the highly excited states of 1d lattice hard-core bosons. *Physical Review Letters* **98**, 050405 (2007).

[160] Rigol, M. & Srednicki, M. Alternatives to eigenstate thermalization. *Physical Review Letters* **108**, 110601 (2012).

[161] Langen, T. *et al.* Experimental observation of a generalized gibbs ensemble. *Science* **348**, 207–211 (2015).

[162] Vidmar, L. & Rigol, M. Generalized gibbs ensemble in integrable lattice models. *Journal of Statistical Mechanics: Theory and Experiment* **2016**, 064007 (2016).

[163] Caux, J.-S. & Essler, F. H. L. Time evolution of local observables after quenching to an integrable model. *Physical Review Letters* **110**, 257203 (2013).

[164] Castro-Alvaredo, O. A., Doyon, B. & Yoshimura, T. Emergent hydrodynamics in integrable quantum systems out of equilibrium. *Physical Review X* **6**, 041065 (2016).

[165] Doyon, B. & Yoshimura, T. A note on generalized hydrodynamics: Inhomogeneous fields and other concepts. *SciPost Physics* **2**, 014 (2017).

[166] Bertini, B., Collura, M., De Nardis, J. & Fagotti, M. Transport in out-of-equilibrium XXZ chains: Exact profiles of charges and currents. *Physical Review Letters* **117**, 207201 (2016).

[167] Ilievski, E. & De Nardis, J. Microscopic origin of ideal conductivity in integrable quantum models. *Physical Review Letters* **119**, 020602 (2017).

[168] Bastianello, A., Alba, V. & Caux, J.-S. Generalized hydrodynamics with space-time inhomogeneous interactions. *Physical Review Letters* **123**, 130602 (2019).

[169] Ruggiero, P., Calabrese, P., Doyon, B. & Dubail, J. Quantum generalized hydrodynamics. *Physical Review Letters* **124**, 140603 (2020).

[170] De Nardis, J., Bernard, D. & Doyon, B. Diffusion in generalized hydrodynamics and quasiparticle scattering. *SciPost Physics* **6**, 049 (2019).

[171] Gopalakrishnan, S. & Vasseur, R. Kinetic theory of spin diffusion and superdiffusion in XXZ spin chains. *Physical Review Letters* **122**, 127202 (2019).

[172] Gopalakrishnan, S., Vasseur, R. & Ware, B. Anomalous relaxation and the high-temperature structure factor of XXZ spin chains. *PNAS* **116**, 16250–16255 (2019).

[173] Ilievski, E., De Nardis, J., Gopalakrishnan, S., Vasseur, R. & Ware, B. Superuniversality of superdiffusion. *Physical Review X* **11**, 031023 (2021).

[174] Chu, S.-I. & Telnov, D. A. Beyond the Floquet theorem: generalized Floquet formalisms and quasienergy methods for atomic and molecular multiphoton processes in intense laser fields. *Physics Reports* **390**, 1–131 (2004).

[175] Blanes, S., Casas, F., Oteo, J.-A. & Ros, J. The magnus expansion and some of its applications. *Physics Reports* **470**, 151–238 (2009).

[176] Eckardt, A. & Anisimovas, E. High-frequency approximation for periodically driven quantum systems from a floquet-space perspective. *New Journal of Physics* **17**, 093039 (2015).

[177] Bukov, M., D'Alessio, L. & Polkovnikov, A. Universal high-frequency behavior of periodically driven systems: from dynamical stabilization to Floquet engineering. *Adv. Phys.* **64**, 139–226 (2015).

[178] Kuwahara, T., Mori, T. & Saito, K. Floquet-magnus theory and generic transient dynamics in periodically driven many-body quantum systems. *Annals of Physics* **367**, 96–124 (2016).

[179] D'Alessio, L. & Rigol, M. Long-time behavior of isolated periodically driven interacting lattice systems. *Physical Review X* **4**, 041048 (2014).

[180] Bukov, M., Gopalakrishnan, S., Knap, M. & Demler, E. Prethermal Floquet steady states and instabilities in the periodically driven, weakly interacting bose-hubbard model. *Physical Review Letters* **115**, 205301 (2015).

[181] Abanin, D. A., De Roeck, W. & Huveneers, F. Exponentially slow heating in periodically driven many-body systems. *Physical Review Letters* **115**, 256803 (2015).

[182] Ho, W. W., Protopopov, I. & Abanin, D. A. Bounds on energy absorption and prethermalization in quantum systems with long-range interactions. *Physical Review Letters* **120**, 200601 (2018).

[183] Mori, T. Floquet prethermalization in periodically driven classical spin systems. *Physical Review B* **98**, 104303 (2018).

[184] Howell, O., Weinberg, P., Sels, D., Polkovnikov, A. & Bukov, M. Asymptotic prethermalization in periodically driven classical spin chains. *Physical Review Letters* **122**, 010602 (2019).

[185] Else, D. V., Ho, W. W. & Dumitrescu, P. T. Long-lived interacting phases of matter protected by multiple time-translation symmetries in quasiperiodically driven systems. *Physical Review X* **10**, 021032 (2020).

[186] Mori, T., Zhao, H., Mintert, F., Knolle, J. & Moessner, R. Rigorous bounds on the heating rate in thue-morse quasiperiodically and randomly driven quantum many-body systems. *Physical Review Letters* **127**, 050602 (2021).

[187] Singh, K. *et al.* Quantifying and controlling prethermal nonergodicity in interacting Floquet matter. *Physical Review X* **9**, 041021 (2019).

[188] Rubio-Abadal, A. *et al.* Floquet prethermalization in a bose-hubbard system. *Physical Review X* **10**, 021044 (2020).

[189] Peng, P., Yin, C., Huang, X., Ramanathan, C. & Cappellaro, P. Floquet prethermalization in dipolar spin chains. *Nature Physics* **17**, 444–447 (2021).

[190] He, G. *et al.* Quasi-Floquet prethermalization in a disordered dipolar spin ensemble in diamond. *Physical Review Letters* **131**, 130401 (2023).

[191] Mori, T., Kuwahara, T. & Saito, K. Rigorous bound on energy absorption and generic relaxation in periodically driven quantum systems. *Physical Review Letters* **116**, 120401 (2016).

[192] Abanin, D. A., De Roeck, W., Ho, W. W. & Huveneers, F. A rigorous theory of many-body prethermalization for periodically driven and closed quantum systems. *Communications in Mathematical Physics* **354**, 809–827 (2017).

[193] Abanin, D. A., De Roeck, W., Ho, W. W. & Huveneers, F. Effective Hamiltonians, prethermalization, and slow energy absorption in periodically driven many-body systems. *Physical Review B* **95**, 014112 (2017).

[194] Else, D. V., Bauer, B. & Nayak, C. Prethermal phases of matter protected by time-translation symmetry. *Physical Review X* **7**, 011026 (2017).

[195] Machado, F., Else, D. V., Kahanamoku-Meyer, G. D., Nayak, C. & Yao, N. Y. Long-range prethermal phases of nonequilibrium matter. *Physical Review X* **10**, 011043 (2020).

[196] Ye, B., Machado, F. & Yao, N. Y. Floquet phases of matter via classical prethermalization. *Physical Review Letters* **127**, 140603 (2021).

[197] Ho, W. W., Mori, T., Abanin, D. A. & Dalla Torre, E. G. Quantum and classical floquet prethermalization. *Annals of Physics* 169297 (2023).

[198] D'Alessio, L. & Polkovnikov, A. Many-body energy localization transition in periodically driven systems. *Annals of Physics* **333**, 19–33 (2013).

[199] Ponte, P., Chandran, A., Papić, Z. & Abanin, D. A. Periodically driven ergodic and many-body localized quantum systems. *Annals of Physics* **353**, 196–204 (2015).

[200] Abanin, D. A., De Roeck, W. & Huveneers, F. Theory of many-body localization in periodically driven systems. *Annals of Physics* **372**, 1–11 (2016).

[201] Dumitrescu, P. T., Vasseur, R. & Potter, A. C. Logarithmically slow relaxation in quasiperiodically driven random spin chains. *Physical Review Letters* **120**, 070602 (2018).

[202] Haeberlen, U. & Waugh, J. S. Coherent averaging effects in magnetic resonance. *Physical Review* **175**, 453 (1968).

[203] Suter, D. & Álvarez, G. A. Colloquium: Protecting quantum information against environmental noise. *Reviews of Modern Physics* **88**, 041001 (2016).

[204] Eckardt, A. Colloquium: Atomic quantum gases in periodically driven optical lattices. *Reviews of Modern Physics* **89**, 011004 (2017).

[205] Oka, T. & Kitamura, S. Floquet engineering of quantum materials. *Annual Review of Condensed Matter Physics* **10**, 387–408 (2019).

[206] Geier, S. *et al.* Floquet Hamiltonian engineering of an isolated many-body spin system. *Science* **374**, 1149–1152 (2021).

[207] Rhim, W.-K., Elleman, D., Schreiber, L. & Vaughan, R. Analysis of multiple pulse nmr in solids. ii. *The Journal of Chemical Physics* **60**, 4595–4604 (1974).

[208] Burum, D. & Rhim, W. Analysis of multiple pulse nmr in solids. III. *The Journal of Chemical Physics* **71**, 944–956 (1979).

[209] Viola, L. & Knill, E. Random decoupling schemes for quantum dynamical control and error suppression. *Physical Review Letters* **94**, 060502 (2005).

[210] Choi, J. *et al.* Robust dynamic Hamiltonian engineering of many-body spin systems. *Physical Review X* **10**, 031002 (2020).

[211] Zhou, H. *et al.* Quantum Metrology with Strongly Interacting Spin Systems. *Physical Review X* **10**, 031003 (2020).

[212] Hahn, E. L. Spin echoes. *Physical Review* **80**, 580 (1950).

[213] Carr, H. Y. & Purcell, E. M. Effects of diffusion on free precession in nuclear magnetic resonance experiments. *Physical Review* **94**, 630–638 (1954).

[214] Meiboom, S. & Gill, D. Modified spin-echo method for measuring nuclear relaxation times. *Review of Scientific Instruments* **29**, 688–691 (1958).

[215] Gullion, T., Baker, D. B. & Conradi, M. S. New, compensated carr-purcell sequences. *Journal of Magnetic Resonance (1969)* **89**, 479–484 (1990).

[216] Viola, L., Knill, E. & Lloyd, S. Dynamical decoupling of open quantum systems. *Physical Review Letters* **82**, 2417 (1999).

[217] Khodjasteh, K. & Lidar, D. A. Fault-tolerant quantum dynamical decoupling. *Physical Review Letters* **95**, 180501 (2005).

[218] Uhrig, G. S. Keeping a quantum bit alive by optimized π-pulse sequences. *Physical Review Letters* **98**, 100504 (2007).

[219] Waugh, J. S., Huber, L. M. & Haeberlen, U. Approach to high-resolution nmr in solids. *Physical Review Letters* **20**, 180 (1968).

[220] Moessner, R. & Sondhi, S. L. Equilibration and order in quantum Floquet matter. *Nature Physics* **13**, 424–428 (2017).

[221] Else, D. V., Bauer, B. & Nayak, C. Floquet time crystals. *Physical Review Letters* **117**, 090402 (2016).

[222] Khemani, V., Lazarides, A., Moessner, R. & Sondhi, S. L. Phase structure of driven quantum systems. *Physical Review Letters* **116**, 250401 (2016).

[223] von Keyserlingk, C. W. & Sondhi, S. L. Phase structure of one-dimensional interacting Floquet systems. II. Symmetry-broken phases. *Physical Review B* **93**, 245146 (2016).

[224] Yao, N. Y., Potter, A. C., Potirniche, I.-D. & Vishwanath, A. Discrete time crystals: Rigidity, criticality, and realizations. *Physical Review Letters* **118**, 030401 (2017).

[225] Zhang, J. *et al.* Observation of a discrete time crystal. *Nature* **543**, 217–220 (2017).

[226] Choi, S. *et al.* Observation of discrete time-crystalline order in a disordered dipolar many-body system. *Nature* **543**, 221–225 (2017).

[227] Kyprianidis, A. *et al.* Observation of a prethermal discrete time crystal. *Science* **372**, 1192–1196 (2021).

[228] Randall, J. *et al.* Many-body–localized discrete time crystal with a programmable spin-based quantum simulator. *Science* **374**, 1474–1478 (2021).

[229] Mi, X. *et al.* Time-crystalline eigenstate order on a quantum processor. *Nature* **601**, 531–536 (2022).

[230] Yao, N. Y., Nayak, C., Balents, L. & Zaletel, M. P. Classical discrete time crystals. *Nature Physics* **16**, 438–447 (2020).

[231] Pizzi, A., Nunnenkamp, A. & Knolle, J. (Classical) Prethermal phases of matter. *arXiv preprint arXiv:2104.13928* (2021).

[232] Lindner, N. H., Refael, G. & Galitski, V. Floquet topological insulator in semiconductor quantum wells. *Nature Physics* **7**, 490–495 (2011).

[233] Rechtsman, M. C. *et al.* Photonic Floquet topological insulators. *Nature* **496**, 196–200 (2013).

[234] Cayssol, J., Dóra, B., Simon, F. & Moessner, R. Floquet topological insulators. *Physica Status Solidi (RRL)–Rapid Research Letters* **7**, 101–108 (2013).

[235] Potter, A. C., Morimoto, T. & Vishwanath, A. Classification of interacting topological Floquet phases in one dimension. *Physical Review X* **6**, 041001 (2016).

[236] von Keyserlingk, C. W. & Sondhi, S. L. Phase structure of one-dimensional interacting Floquet systems. I. Abelian symmetry-protected topological phases. *Physical Review B* **93**, 245145 (2016).

[237] Roy, R. & Harper, F. Abelian floquet symmetry-protected topological phases in one dimension. *Physical Review B* **94**, 125105 (2016).

[238] Potirniche, I.-D., Potter, A. C., Schleier-Smith, M., Vishwanath, A. & Yao, N. Y. Floquet symmetry-protected topological phases in cold-atom systems. *Physical Review Letters* **119**, 123601 (2017).

[239] Schuster, T., Gazit, S., Moore, J. E. & Yao, N. Y. Floquet hopf insulators. *Physical Review Letters* **123**, 266803 (2019).

[240] Harper, F., Roy, R., Rudner, M. S. & Sondhi, S. Topology and broken symmetry in Floquet systems. *Annual Review of Condensed Matter Physics* **11**, 345–368 (2020).

[241] Rudner, M. S. & Lindner, N. H. Band structure engineering and non-equilibrium dynamics in Floquet topological insulators. *Nature Reviews Physics* **2**, 229–244 (2020).

[242] Long, D. M., Crowley, P. J. & Chandran, A. Nonadiabatic topological energy pumps with quasiperiodic driving. *Physical Review Letters* **126**, 106805 (2021).

[243] Zhang, X. *et al.* Digital quantum simulation of Floquet symmetry-protected topological phases. *Nature* **607**, 468–473 (2022).

[244] Bluvstein, D. *et al.* Controlling quantum many-body dynamics in driven rydberg atom arrays. *Science* **371**, 1355–1359 (2021).

[245] Maskara, N. *et al.* Discrete time-crystalline order enabled by quantum many-body scars: entanglement steering via periodic driving. *Physical Review Letters* **127**, 090602 (2021).

[246] Kshetrimayum, A., Eisert, J. & Kennes, D. Stark time crystals: Symmetry breaking in space and time. *Physical Review B* **102**, 195116 (2020).

[247] Liu, S., Zhang, S.-X., Hsieh, C.-Y., Zhang, S. & Yao, H. Discrete time crystal enabled by stark many-body localization. *Physical Review Letters* **130**, 120403 (2023).

[248] Rogers, W. A. Studies in metrology. first paper. *Proceedings of the American Academy of Arts and Sciences* **18**, 287–398 (1882).

[249] Helstrom, C. W. Quantum detection and estimation theory. *Journal of Statistical Physics* **1**, 231–252 (1969).

[250] Holevo, A. S. *Probabilistic and statistical aspects of quantum theory*, vol. 1 (Springer Science, New York, 2011).

[251] Braunstein, S. L. & Caves, C. M. Statistical distance and the geometry of quantum states. *Physical Review Letters* **72**, 3439–3443 (1994).

[252] Ramsey, N. *Molecular Beams*, vol. 20 (Oxford University Press, Oxford, UK, 1956).

[253] Ludwig, Z. Ein neuer interferenzrefraktor. *Zeitschrift für Instrumentenkunde* **11**, 275–285 (1891).

[254] Mach, L. Ueber einen interferenzrefraktor. *Zeitschrift für Instrumentenkunde* **12**, 89 (1892).

[255] Giovannetti, V., Lloyd, S. & Maccone, L. Quantum Metrology. *Physical Review Letters* **96**, 010401 (2006).

[256] Pezzé, L. & Smerzi, A. Entanglement, Nonlinear Dynamics, and the Heisenberg Limit. *Physical Review Letters* **102**, 100401 (2009). Publisher: American Physical Society.

[257] Yurke, B., McCall, S. L. & Klauder, J. R. SU(2) and SU(1,1) interferometers. *Physical Review A* **33**, 4033 (1986).

[258] Giovannetti, V., Lloyd, S. & Maccone, L. Quantum-enhanced measurements: beating the standard quantum limit. *Science* **306**, 1330–1336 (2004).

[259] Greenberger, D. M., Horne, M. A. & Zeilinger, A. Going beyond bell's theorem. In *Bell's theorem, quantum theory and conceptions of the universe*, 69–72 (Springer, 1989).

[260] Bollinger, J. J., Itano, W. M., Wineland, D. J. & Heinzen, D. J. Optimal frequency measurements with maximally correlated states. *Physical Review A* **54**, R4649 (1996).

[261] Lee, H., Kok, P. & Dowling, J. P. A quantum rosetta stone for interferometry. *Journal of Modern Optics* **49**, 2325–2338 (2002).

[262] Wineland, D. J., Bollinger, J. J., Itano, W. M., Moore, F. & Heinzen, D. J. Spin squeezing and reduced quantum noise in spectroscopy. *Physical Review A* **46**, R6797 (1992).

[263] Wineland, D. J. and Bollinger, J. J. and Itano, W. M. and Heinzen, D. J. Squeezed atomic states and projection noise in spectroscopy. In *Physical Review A* [669], 67–88.

[264] Kitagawa, M. & Ueda, M. Squeezed spin states. *Physical Review A* **47**, 5138–5143 (1993).

[265] Hillery, M. & Mlodinow, L. Interferometers and minimum-uncertainty states. *Physical Review A* **48**, 1548 (1993).

[266] Agarwal, G. & Puri, R. Atomic states with spectroscopic squeezing. *Physical Review A* **49**, 4968 (1994).

[267] Brif, C. & Mann, A. Nonclassical interferometry with intelligent light. *Physical Review A* **54**, 4505 (1996).

[268] Sørensen, A. S. & Mølmer, K. Entanglement and extreme spin squeezing. *Physical Review Letters* **86**, 4431 (2001).

[269] Caves, C. M. Quantum-mechanical noise in an interferometer. *Physical Review D* **23**, 1693 (1981).

[270] Bondurant, R. S. & Shapiro, J. H. Squeezed states in phase-sensing interferometers. *Physical Review D* **30**, 2548 (1984).

[271] Holland, M. J. & Burnett, K. Interferometric detection of optical phase shifts at the Heisenberg limit. *Physical Review Letters* **71**, 1355–1358 (1993).

[272] Yurke, B. Input states for enhancement of fermion interferometer sensitivity. *Physical Review Letters* **56**, 1515–1517 (1986).

[273] Sanders, B. C. & Milburn, G. J. Optimal quantum measurements for phase estimation. *Physical Review Letters* **75**, 2944–2947 (1995).

[274] Campos, R., Gerry, C. C. & Benmoussa, A. Optical interferometry at the heisenberg limit with twin fock states and parity measurements. *Physical Review A* **68**, 023810 (2003).

[275] Paris, M. G. Quantum estimation for quantum technology. *International Journal of Quantum Information* **7**, 125–137 (2009).

[276] Tóth, G. & Apellaniz, I. Quantum metrology from a quantum information science perspective. *Journal of Physics A: Mathematical and Theoretical* **47**, 424006 (2014).

[277] Pezzè, L. & Smerzi, A. Quantum theory of phase estimation. In Tino, G. & Kasevich, M. (eds.) *Atom Interferometry, Proceedings of the International School of Physics "Enrico Fermi," Course 188, Varenna* (IOS Press, Amsterdam, 2014).

[278] Tóth, G. & Petz, D. Extremal properties of the variance and the quantum fisher information. *Physical Review A* **87**, 032324 (2013).

[279] Fröwis, F., Schmied, R. & Gisin, N. Tighter quantum uncertainty relations following from a general probabilistic bound. *Physical Review A* **92**, 012102 (2015).

[280] Tóth, G. & Fröwis, F. Uncertainty relations with the variance and the quantum fisher information based on convex decompositions of density matrices. *Physical Review Research* **4**, 013075 (2022).

[281] Helstrom, C. W. Minimum mean-squared error of estimates in quantum statistics. *Physics Letters A* **25**, 101–102 (1967).

[282] Braunstein, S. L., Caves, C. M. & Milburn, G. J. Generalized uncertainty relations: theory, examples, and lorentz invariance. *Annals of Physics* **247**, 135–173 (1996).

[283] Krischek, R. *et al.* Useful multiparticle entanglement and sub-shot-noise sensitivity in experimental phase estimation. *Physical Review Letters* **107**, 080504 (2011).

[284] Tóth, G. Multipartite entanglement and high-precision metrology. *Physical Review A* **85**, 022322 (2012).

[285] Peres, A. Stability of quantum motion in chaotic and regular systems. *Physical Review A* **30**, 1610 (1984).

[286] Goldstein, G. *et al.* Environment-assisted precision measurement. *Physical Review Letters* **106**, 140502 (2011).

[287] Macrì, T., Smerzi, A. & Pezzè, L. Loschmidt echo for quantum metrology. *Physical Review A* **94**, 010102 (2016). Publisher: American Physical Society.

[288] Nolan, S. P., Szigeti, S. S. & Haine, S. A. Optimal and robust quantum metrology using interaction-based readouts. *Physical Review Letters* **119**, 193601 (2017).

[289] Toscano, F., Dalvit, D. A. R., Davidovich, L. & Zurek, W. H. Sub-planck phase-space structures and heisenberg-limited measurements. *Physical Review A* **73**, 023803 (2006).

[290] Davis, E. J., Bentsen, G. & Schleier-Smith, M. Approaching the Heisenberg limit without single-particle detection. *Physical Review Letters* **116**, 053601 (2016).

[291] Fröwis, F., Sekatski, P. & Dür, W. Detecting large quantum fisher information with finite measurement precision. *Physical Review Letters* **116**, 090801 (2016).

[292] Hosten, O., Krishnakumar, R., Engelsen, N. J. & Kasevich, M. A. Quantum phase magnification. *Science* **352**, 1552–1555 (2016).

[293] Linnemann, D. *et al.* Quantum-enhanced sensing based on time reversal of nonlinear dynamics. *Physical Review Letters* **117**, 013001 (2016).

[294] Gilmore, K. A. *et al.* Quantum-enhanced sensing of displacements and electric fields with two-dimensional trapped-ion crystals. *Science* **373**, 673–678 (2021).

[295] Colombo, S. *et al.* Time-reversal-based quantum metrology with many-body entangled states. *Nature Physics* **18**, 925–930 (2022).

[296] Mao, T.-W. *et al.* Quantum-enhanced sensing by echoing spin-nematic squeezing in atomic bose–einstein condensate. *Nature Physics* **19**, 1585–1590 (2023).

[297] Hosten, O., Engelsen, N. J., Krishnakumar, R. & Kasevich, M. A. Measurement noise 100 times lower than the quantum-projection limit using entangled atoms. *Nature* **529**, 505–508 (2016).

[298] Sørensen, A., Duan, L. M., Cirac, J. I. & Zoller, P. Many-particle entanglement with Bose-Einstein condensates. *Nature* **409**, 63–66 (2001). 0006111.

[299] Esteve, J., Gross, C., Weller, A., Giovanazzi, S. & Oberthaler, M. K. Squeezing and entanglement in a bose–einstein condensate. *Nature* **455**, 1216–1219 (2008).

[300] Gross, C., Zibold, T., Nicklas, E., Esteve, J. & Oberthaler, M. K. Nonlinear atom interferometer surpasses classical precision limit. *Nature* **464**, 1165–1169 (2010).

[301] Riedel, M. F. *et al.* Atom-chip-based generation of entanglement for quantum metrology. *Nature* **464**, 1170–1173 (2010).

[302] Mølmer, K. & Sørensen, A. Multiparticle entanglement of hot trapped ions. *Physical Review Letters* **82**, 1835 (1999).

[303] Puri, R. & Singh, R. Atomic schrödinger cat states. *Physical Review A* **56**, 2249 (1997).

[304] Law, C., Ng, H. & Leung, P. Coherent control of spin squeezing. *Physical Review A* **63**, 055601 (2001).

[305] Sørensen, A. & Mølmer, K. Entanglement and quantum computation with ions in thermal motion. *Physical Review A* **62**, 022311 (2000).

[306] Lin, H. Exact diagonalization of quantum-spin models. *Physical Review B* **42**, 6561 (1990).

[307] Brenes, M., Varma, V. K., Scardicchio, A. & Girotto, I. Massively parallel implementation and approaches to simulate quantum dynamics using krylov subspace techniques. *Computer Physics Communications* **235**, 477–488 (2019).

[308] White, S. R. Density matrix formulation for quantum renormalization groups. *Physical Review Letters* **69**, 2863–2866 (1992).

[309] White, S. R. & Huse, D. A. Numerical renormalization-group study of low-lying eigenstates of the antiferromagnetic s=1 heisenberg chain. *Physical Review B* **48**, 3844–3852 (1993).

[310] White, S. R. Density-matrix algorithms for quantum renormalization groups. *Physical Review B* **48**, 10345–10356 (1993).

[311] White, S. R. & Feiguin, A. E. Real-time evolution using the density matrix renormalization group. *Physical Review Letters* **93**, 076401 (2004).

[312] Daley, A. J., Kollath, C., Schollwöck, U. & Vidal, G. Time-dependent density-matrix renormalization-group using adaptive effective hilbert spaces. *Journal of Statistical Mechanics: Theory and Experiment* **2004**, P04005 (2004).

[313] Vidal, G. Efficient classical simulation of slightly entangled quantum computations. *Physical Review Letters* **91** (2003). ArXiv: quant-ph/0301063.

[314] Vidal, G. Efficient simulation of one-dimensional quantum many-body systems. *Physical Review Letters* **93**, 040502 (2004).

[315] Verstraete, F., García-Ripoll, J. J. & Cirac, J. I. Matrix product density operators: Simulation of finite-temperature and dissipative systems. *Physical Review Letters* **93**, 207204 (2004).

[316] Zwolak, M. & Vidal, G. Mixed-state dynamics in one-dimensional quantum lattice systems: A time-dependent superoperator renormalization algorithm. *Physical Review Letters* **93**, 207205 (2004).

[317] White, C. D., Zaletel, M., Mong, R. S. K. & Refael, G. Quantum dynamics of thermalizing systems. *Physical Review B* **97**, 035127 (2018).

[318] Ye, B., Machado, F., White, C. D., Mong, R. S. & Yao, N. Y. Emergent hydrodynamics in nonequilibrium quantum systems. *Physical Review Letters* **125**, 030601 (2020).

[319] Haegeman, J. *et al.* Time-dependent variational principle for quantum lattices. *Physical Review Letters* **107**, 070601 (2011).

[320] Zaletel, M. P., Mong, R. S. K., Karrasch, C., Moore, J. E. & Pollmann, F. Time-evolving a matrix product state with long-ranged interactions. *Physical Review B* **91** (2015). ArXiv: 1407.1832.

[321] Zaletel, M. P. & Pollmann, F. Isometric tensor network states in two dimensions. *Physical Review Letters* **124**, 037201 (2020).

[322] Carleo, G., Becca, F., Sanchez-Palencia, L., Sorella, S. & Fabrizio, M. Light-cone effect and supersonic correlations in one-and two-dimensional bosonic superfluids. *Physical Review A* **89**, 031602 (2014).

[323] Georges, A. & Kotliar, G. Hubbard model in infinite dimensions. *Physical Review B* **45**, 6479 (1992).

[324] Freericks, J., Turkowski, V. & Zlatić, V. Nonequilibrium dynamical mean-field theory. *Physical Review Letters* **97**, 266408 (2006).

[325] Schachenmayer, J., Pikovski, A. & Rey, A. M. Dynamics of correlations in two-dimensional quantum spin models with long-range interactions: A phase-space Monte-Carlo study. *New Journal of Physics* **17** (2015). 1501.06593.

[326] Schachenmayer, J., Pikovski, A. & Rey, A. M. Many-body quantum spin dynamics with monte carlo trajectories on a discrete phase space. *Physical Review X* **5**, 1–10 (2015). 1408.4441.

[327] Davidson, S. M. & Polkovnikov, A. SU(3) semiclassical representation of quantum dynamics of interacting spins. *Physical Review Letters* **114**, 045701 (2015).

[328] Davidson, S. M., Sels, D. & Polkovnikov, A. Semiclassical approach to dynamics of interacting fermions. *Annals of Physics* **384**, 128–141 (2017).

[329] Weimer, H., Kshetrimayum, A. & Orús, R. Simulation methods for open quantum many-body systems. *Reviews of Modern Physics* **93**, 015008 (2021).

[330] Schweizer, W. *Numerical quantum dynamics*, vol. 9 (Springer, New York, 2001).

[331] Weiße, A. & Fehske, H. Exact diagonalization techniques. *Computational Many-particle Physics* 529–544 (2008).

[332] Hochbruck, M. & Lubich, C. On krylov subspace approximations to the matrix exponential operator. *SIAM Journal on Numerical Analysis* **34**, 1911–1925 (1997).

[333] White, S. R. Strongly correlated electron systems and the density matrix renormalization group. *Physics Reports* **301**, 187–204 (1998).

[334] Schollwöck, U. The density-matrix renormalization group. *Reviews of Modern Physics* **77**, 259–315 (2005).

[335] Schollwöck, U. The density-matrix renormalization group in the age of matrix product states. *Annals of Physics* **326**, 96–192 (2011).

[336] Hauschild, J. & Pollmann, F. Efficient numerical simulations with tensor networks: Tensor network python (tenpy). *SciPost Phys. Lect. Notes* 5 (2018).

[337] Paeckel, S. *et al.* Time-evolution methods for matrix-product states. *Annals of Physics* **411**, 167998 (2019).

[338] Bertini, B. *et al.* Finite-temperature transport in one-dimensional quantum lattice models. *Reviews of Modern Physics* **93**, 025003 (2021).

[339] Gubernatis, J., Kawashima, N. & Werner, P. *Quantum Monte Carlo Methods* (Cambridge University Press, Cambridge, UK, 2016).

[340] Foulkes, W. & Needs, R. Quantum monte carlo simulations of solids. *Reviews of Modern Physics* **73**, 33 (2001).

[341] Georges, A., Kotliar, G., Krauth, W. & Rozenberg, M. J. Dynamical mean-field theory of strongly correlated fermion systems and the limit of infinite dimensions. *Reviews of Modern Physics* **68**, 13 (1996).

[342] Becca, F. & Sorella, S. *Quantum Monte Carlo approaches for correlated systems* (Cambridge University Press, Cambridge, UK, 2017).

[343] Aoki, H. *et al.* Nonequilibrium dynamical mean-field theory and its applications. *Reviews of Modern Physics* **86**, 779 (2014).

[344] Polkovnikov, A. Phase space representation of quantum dynamics. *Annals of Physics* **325**, 1790–1852 (2010).

[345] Wurtz, J., Polkovnikov, A. & Sels, D. Cluster Truncated Wigner Approximation in Strongly Interacting Systems. *Annals of Physics* **395**, 341–365 (2018).

[346] Python3 package: https://quspin.github.io/QuSpin.

[347] Python3 package: https://dynamite.readthedocs.io/en/latest.

[348] Python3 package: https://tenpy.readthedocs.io/en/latest
C++ package and Julia package: https://itensor.org.

[349] Python2 package based on TeNPy2: https://github.com/christopherdavidwhite/TenPy-DMT
C++ package based on ITensor: https://github.com/Jack-Kemp/dmt.

[350] Jackiw, R. & Kerman, A. Time-dependent variational principle and the effective action. *Physics Letters A* **71**, 158–162 (1979).

[351] Chib, S. & Greenberg, E. Understanding the metropolis-hastings algorithm. *The American Statistician* **49**, 327–335 (1995).

[352] Wootters, W. K. A wigner-function formulation of finite-state quantum mechanics. *Annals of Physics* **176**, 1–21 (1987).

[353] Ljubotina, M., Žnidarič, M. & Prosen, T. Spin diffusion from an inhomogeneous quench in an integrable system. *Nature Communications* **8**, 1–6 (2017).

[354] Sommer, A., Ku, M., Roati, G. & Zwierlein, M. W. Universal spin transport in a strongly interacting fermi gas. *Nature* **472**, 201–204 (2011).

[355] Moll, P. J., Kushwaha, P., Nandi, N., Schmidt, B. & Mackenzie, A. P. Evidence for hydrodynamic electron flow in $PdCoO_2$. *Science* **351**, 1061–1064 (2016).

[356] Bandurin, D. *et al.* Negative local resistance caused by viscous electron backflow in graphene. *Science* **351**, 1055–1058 (2016).

[357] Crossno, J. *et al.* Observation of the Dirac fluid and the breakdown of the Wiedemann-Franz law in graphene. *Science* **351**, 1058–1061 (2016).

[358] Cepellotti, A. *et al.* Phonon hydrodynamics in two-dimensional materials. *Nature Communications* **6**, 1–7 (2015).

[359] Spohn, H. *Large scale dynamics of interacting particles* (Springer-Verlag, New York, 1991).

[360] Birkhoff, G. *Hydrodynamics* (Princeton University Press, Princeton, NJ, 1960).

[361] Wyatt, R. E. *Quantum dynamics with trajectories: introduction to quantum hydrodynamics* (Springer-Verlag, New York, 2005).

[362] Mukerjee, S., Oganesyan, V. & Huse, D. Statistical theory of transport by strongly interacting lattice fermions. *Physical Review B* **73**, 035113 (2006).

[363] Erdős, L., Schlein, B. & Yau, H.-T. Rigorous derivation of the Gross-Pitaevskii equation. *Physical Review Letters* **98**, 040404 (2007).

[364] Zu, C. *et al.* Emergent hydrodynamics in a strongly interacting dipolar spin ensemble. *Nature* **597**, 45–50 (2021).

[365] Halliwell, J. Decoherent histories and the emergent classicality of local densities. *Physical Review Letters* **83**, 2481 (1999).

[366] Hartle, J. B. The quasiclassical realms of this quantum universe. *Foundations of Physics* **41**, 982–1006 (2011).

[367] De Nardis, J., Bernard, D. & Doyon, B. Hydrodynamic diffusion in integrable systems. *Physical Review Letters* **121**, 160603 (2018).

[368] Greenbaum, D., Kindermann, M., Ramanathan, C. & Cory, D. Hydrodynamic approach to coherent nuclear-spin transport. *Physical Review B* **71**, 054403 (2005).

[369] Andreev, A., Kivelson, S. A. & Spivak, B. Hydrodynamic description of transport in strongly correlated electron systems. *Physical Review Letters* **106**, 256804 (2011).

[370] Bulchandani, V. B., Vasseur, R., Karrasch, C. & Moore, J. E. Solvable hydrodynamics of quantum integrable systems. *Physical Review Letters* **119**, 220604 (2017).

[371] Wurtz, J. & Polkovnikov, A. Quantum diffusion in spin chains with phase space methods. *Physical Review E* **101**, 052120 (2020).

[372] Khemani, V., Vishwanath, A. & Huse, D. A. Operator spreading and the emergence of dissipative hydrodynamics under unitary evolution with conservation laws. *Physical Review X* **8**, 031057 (2018).

[373] Bertini, B. *et al.* Finite-temperature transport in one-dimensional quantum lattice models. *Reviews of Modern Physics* **93**, 025003 (2021).

[374] Ku, M. J. *et al.* Imaging viscous flow of the dirac fluid in graphene. *Nature* **583**, 537–541 (2020).

[375] Levstein, P., Pastawski, H. & Calvo, R. Spin diffusion in low-dimensional copper-amino-acid complexes. *Journal of Physics: Condensed Matter* **3**, 1877 (1991).

[376] Narozhny, B., Gornyi, I., Titov, M., Schütt, M. & Mirlin, A. Hydrodynamics in graphene: Linear-response transport. *Physical Review B* **91**, 035414 (2015).

[377] Moore, G. D. & Sohrabi, K. A. Kubo formulas for second-order hydrodynamic coefficients. *Physical Review Letters* **106**, 122302 (2011).

[378] Friedman, A. J., Gopalakrishnan, S. & Vasseur, R. Diffusive hydrodynamics from integrability breaking. *Physical Review B* **101**, 180302 (2020).

[379] Calabrese, P., Essler, F. H. & Mussardo, G. Introduction to 'quantum integrability in out of equilibrium systems'. *Journal of Statistical Mechanics: Theory and Experiment* **2016**, 064001 (2016).

[380] Luitz, D. J., Laflorencie, N. & Alet, F. Extended slow dynamical regime close to the many-body localization transition. *Physical Review B* **93**, 060201(R) (2016).

[381] Khait, I., Gazit, S., Yao, N. Y. & Auerbach, A. Spin transport of weakly disordered heisenberg chain at infinite temperature. *Physical Review B* **93**, 224205 (2016).

[382] Luitz, D. J. & Bar Lev, Y. Anomalous thermalization in ergodic systems. *Physical Review Letters* **117**, 170404 (2016).

[383] Sahu, S., Xu, S. & Swingle, B. Scrambling dynamics across a thermalization-localization quantum phase transition. *Physical Review Letters* **123**, 165902 (2019).

[384] Bohrdt, A., Mendl, C. B., Endres, M. & Knap, M. Scrambling and thermalization in a diffusive quantum many-body system. *New J. Phys.* **19**, 063001 (2017).

[385] von Keyserlingk, C. W., Khemani, V. & Sondhi, S. L. Absolute stability and spatiotemporal long-range order in Floquet systems. *Physical Review B* **94**, 085112 (2016).

[386] Kitagawa, T., Berg, E., Rudner, M. & Demler, E. Topological characterization of periodically driven quantum systems. *Physical Review B* **82**, 235114 (2010).

[387] Prosen, T. Time evolution of a quantum many-body system: Transition from integrability to ergodicity in the thermodynamic limit. *Physical Review Letters* **80**, 1808–1811 (1998).

[388] Prosen, T. Ergodic properties of a generic nonintegrable quantum many-body system in the thermodynamic limit. *Physical Review E* **60**, 3949–3968 (1999).

[389] Lazarides, A., Das, A. & Moessner, R. Equilibrium states of generic quantum systems subject to periodic driving. *Physical Review E* **90**, 012110 (2014).

[390] D'Alessio, L. & Rigol, M. Long-time behavior of isolated periodically driven interacting lattice systems. *Physical Review X* **4**, 041048 (2014).

[391] Machado, F., Kahanamoku-Meyer, G. D., Else, D. V., Nayak, C. & Yao, N. Y. Exponentially slow heating in short and long-range interacting floquet systems. *Physical Review Research* **1**, 033202 (2019).

[392] Weidinger, S. A. & Knap, M. Floquet prethermalization and regimes of heating in a periodically driven, interacting quantum system. *Sci. Rep.* **7**, 45382 (2017).

[393] Leviatan, E., Pollmann, F., Bardarson, J. H., Huse, D. A. & Altman, E. Quantum thermalization dynamics with matrix-product states. *arXiv preprint arXiv:1702.08894* (2017).

[394] Reimann, P. Typicality for generalized microcanonical ensembles. *Physical Review Letters* **99**, 160404 (2007).

[395] Parker, D. E., Cao, X., Avdoshkin, A., Scaffidi, T. & Altman, E. A universal operator growth hypothesis. *Physical Review X* **9**, 041017 (2019).

[396] Bulchandani, V. B., Vasseur, R., Karrasch, C. & Moore, J. E. Bethe-Boltzmann hydrodynamics and spin transport in the XXZ chain. *Physical Review B* **97**, 045407 (2018).

[397] Misguich, G., Mallick, K. & Krapivsky, P. L. Dynamics of the spin-$\frac{1}{2}$ heisenberg chain initialized in a domain-wall state. *Physical Review B* **96**, 195151 (2017).

[398] Gobert, D., Kollath, C., Schollwöck, U. & Schütz, G. Real-time dynamics in spin-$\frac{1}{2}$ chains with adaptive time-dependent density matrix renormalization group. *Physical Review E* **71**, 036102 (2005).

[399] Schemmer, M., Bouchoule, I., Doyon, B. & Dubail, J. Generalized hydrodynamics on an atom chip. *Physical Review Letters* **122**, 090601 (2019).

[400] Zhang, W. & Cory, D. First direct measurement of the spin diffusion rate in a homogenous solid. *Physical Review Letters* **80**, 1324 (1998).

[401] Pagliero, D. *et al.* Optically pumped spin polarization as a probe of many-body thermalization. *Science Advances* **6**, eaaz6986 (2020).

[402] Boutis, G., Greenbaum, D., Cho, H., Cory, D. & Ramanathan, C. Spin diffusion of correlated two-spin states in a dielectric crystal. *Physical Review Letters* **92**, 137201 (2004).

[403] Eberhardt, K. W., Mouaziz, S., Boero, G., Brugger, J. & Meier, B. H. Direct observation of nuclear spin diffusion in real space. *Physical Review Letters* **99**, 227603 (2007).

[404] Kardar, M., Parisi, G. & Zhang, Y.-C. Dynamic Scaling of Growing Interfaces. *Physical Review Letters* **56**, 889–892 (1986).

[405] Sinai, Y. G. The limiting behavior of a one-dimensional random walk in a random medium. *Theory of Probability & Its Applications* **27**, 256–268 (1983).

[406] Chechkin, A. V., Seno, F., Metzler, R. & Sokolov, I. M. Brownian yet non-gaussian diffusion: from superstatistics to subordination of diffusing diffusivities. *Physical Review X* **7**, 021002 (2017).

[407] Stylianidou, S., Kuwada, N. J. & Wiggins, P. A. Cytoplasmic dynamics reveals two modes of nucleoid-dependent mobility. *Biophysical Journal* **107**, 2684–2692 (2014).

[408] Kim, J., Kim, C. & Sung, B. J. Simulation study of seemingly fickian but heterogeneous dynamics of two dimensional colloids. *Physical Review Letters* **110**, 047801 (2013).

[409] Chubynsky, M. V. & Slater, G. W. Diffusing diffusivity: a model for anomalous, yet brownian, diffusion. *Physical Review Letters* **113**, 098302 (2014).

[410] Postnikov, E. B., Chechkin, A. & Sokolov, I. M. Brownian yet non-gaussian diffusion in heterogeneous media: from superstatistics to homogenization. *New Journal of Physics* (2020).

[411] Barkai, E. & Burov, S. Packets of diffusing particles exhibit universal exponential tails. *Physical Review Letters* **124**, 060603 (2020).

[412] Hall, L. *et al.* Detection of nanoscale electron spin resonance spectra demonstrated using nitrogen-vacancy centre probes in diamond. *Nature Communications* **7**, 1–9 (2016).

[413] Khutsishvili, G. Spin diffusion and magnetic relaxation of nuclei. *Soviet Physics JETP* **15** (1962).

[414] Takahashi, S., Hanson, R., Van Tol, J., Sherwin, M. S. & Awschalom, D. D. Quenching spin decoherence in diamond through spin bath polarization. *Physical Review Letters* **101**, 047601 (2008).

[415] Hunt, G. A. Some theorems concerning brownian motion. *Transactions of the American Mathematical Society* **81**, 294–319 (1956).

[416] Jarmola, A., Acosta, V., Jensen, K., Chemerisov, S. & Budker, D. Temperature-and magnetic-field-dependent longitudinal spin relaxation in nitrogen-vacancy ensembles in diamond. *Physical Review Letters* **108**, 197601 (2012).

[417] Spitzer, F. *Principles of random walk* (Springer-Verlag, New York, 1976).

[418] Einstein, A. *Investigations on the Theory of the Brownian Movement* (Dover Publications, Methuen, London, 1956).

[419] Lévy, P. *Théorie de l'addition des variables aléatoires*, vol. 1 (Gauthier-Villars, 1954).

[420] Mori, T., Ikeda, T. N., Kaminishi, E. & Ueda, M. Thermalization and prethermalization in isolated quantum systems: A theoretical overview. *Journal of Physics B: Atomic, Molecular and Optical Physics* **51**, 112001 (2018). 1712.08790.

[421] Yao, N. Y. *et al.* Many-body localization in dipolar systems. *Physical Review Letters* **113**, 243002 (2014).

[422] Nandkishore, R. M. & Sondhi, S. L. Many-body localization with long-range interactions. *Physical Review X* **7**, 041021 (2017).

[423] Rittweger, E., Han, K. Y., Irvine, S. E., Eggeling, C. & Hell, S. W. Sted microscopy reveals crystal colour centres with nanometric resolution. *Nature Photonics* **3**, 144 (2009).

[424] Arai, K. *et al.* Fourier magnetic imaging with nanoscale resolution and compressed sensing speed-up using electronic spins in diamond. *Nature Nanotechnology* **10**, 859–864 (2015).

[425] Wei, D. *et al.* Quantum gas microscopy of Kardar-Parisi-Zhang superdiffusion. *Science* **376**, 716–720 (2022).

[426] Joshi, M. K. *et al.* Observing emergent hydrodynamics in a long-range quantum magnet. *Science* **376**, 720–724 (2022).

[427] Ljubotina, M., Žnidarič, M. & Prosen, T. Kardar-Parisi-Zhang physics in the quantum Heisenberg magnet. *Physical Review Letters* **122**, 210602 (2019).

[428] Ye, B., Machado, F., Kemp, J., Hutson, R. B. & Yao, N. Y. Universal Kardar-Parisi-Zhang dynamics in integrable quantum systems. *Physical Review Letters* **129**, 230602 (2022).

[429] De Nardis, J., Gopalakrishnan, S., Vasseur, R. & Ware, B. Stability of Superdiffusion in Nearly Integrable Spin Chains. *Physical Review Letters* **127**, 057201 (2021).

[430] Altman, E. *et al.* Quantum simulators: Architectures and opportunities. *PRX Quantum* **2**, 017003 (2021).

[431] Bakr, W. S., Gillen, J. I., Peng, A., Folling, S. & Greiner, M. A quantum gas microscope for detecting single atoms in a hubbard-regime optical lattice. *Nature* **462**, 74–77 (2009).

[432] Maurer, P. *et al.* Far-field optical imaging and manipulation of individual spins with nanoscale resolution. *Nature Physics* **6**, 912–918 (2010).

[433] Chen, E. H., Gaathon, O., Trusheim, M. E. & Englund, D. Wide-field multispectral super-resolution imaging using spin-dependent fluorescence in nanodiamonds. *Nano Letters* **13**, 2073–2077 (2013).

[434] Pfender, M., Aslam, N., Waldherr, G., Neumann, P. & Wrachtrup, J. Single-spin stochastic optical reconstruction microscopy. *Proceedings of the National Academy of Sciences* **111**, 14669–14674 (2014).

[435] Comodi, P., Liu, Y., Zanazzi, P. & Montagnoli, M. Structural and vibrational behaviour of fluorapatite with pressure. part i: in situ single-crystal x-ray diffraction investigation. *Physics and Chemistry of Minerals* **28**, 219–224 (2001).

[436] Jeener, J. & Broekaert, P. Nuclear magnetic resonance in solids: thermodynamic effects of a pair of rf pulses. *Physical Review* **157**, 232 (1967).

[437] Peng, P. *et al.* Deep reinforcement learning for quantum Hamiltonian engineering. *Physical Review Applied* **18**, 024033 (2022).

[438] Grabowski, M. & Mathieu, P. Structure of the conservation laws in quantum integrable spin chains with short range interactions. *Annals of Physics* **243**, 299–371 (1995).

[439] Zotos, X., Naef, F. & Prelovsek, P. Transport and conservation laws. *Physical Review B* **55**, 11029 (1997).

[440] Klümper, A. & Johnston, D. Thermodynamics of the spin-1/2 antiferromagnetic uniform heisenberg chain. *Physical Review Letters* **84**, 4701 (2000).

[441] Sakai, K. & Klümper, A. Non-dissipative thermal transport in the massive regimes of the xxz chain. *Journal of Physics A: Mathematical and General* **36**, 11617 (2003).

[442] Prosen, T. & Žnidarič, M. Matrix product simulations of non-equilibrium steady states of quantum spin chains. *Journal of Statistical Mechanics: Theory and Experiment* **2009**, P02035 (2009).

[443] Steinigeweg, R. & Gemmer, J. Density dynamics in translationally invariant spin-1 2 chains at high temperatures: A current-autocorrelation approach to finite time and length scales. *Physical Review B* **80**, 184402 (2009).

[444] Žnidarič, M. Spin transport in a one-dimensional anisotropic Heisenberg model. *Physical Review Letters* **106**, 220601 (2011).

[445] Karrasch, C., Moore, J. & Heidrich-Meisner, F. Real-time and real-space spin and energy dynamics in one-dimensional spin-1 2 systems induced by local quantum quenches at finite temperatures. *Physical Review B* **89**, 075139 (2014).

[446] Lucioni, E. *et al.* Observation of subdiffusion in a disordered interacting system. *Physical Review Letters* **106**, 230403 (2011).

[447] Sahay, R., Machado, F., Ye, B., Laumann, C. R. & Yao, N. Y. Emergent ergodicity at the transition between many-body localized phases. *Physical Review Letters* **126**, 100604 (2021).

[448] Zaburdaev, V., Denisov, S. & Klafter, J. Lévy walks. *Reviews of Modern Physics* **87**, 483 (2015).

[449] Nahum, A., Vijay, S. & Haah, J. Operator spreading in random unitary circuits. *Physical Review X* **8**, 021014 (2018).

[450] von Keyserlingk, C. W., Rakovszky, T., Pollmann, F. & Sondhi, S. L. Operator hydrodynamics, OTOCs, and entanglement growth in systems without conservation laws. *Physical Review X* **8**, 021013 (2018).

[451] Rakovszky, T., Pollmann, F. & Von Keyserlingk, C. Diffusive hydrodynamics of out-of-time-ordered correlators with charge conservation. *Physical Review X* **8**, 031058 (2018).

[452] Xu, S. & Swingle, B. Accessing scrambling using matrix product operators. *Nature Physics* **16**, 199–204 (2020).

[453] Xu, S. & Swingle, B. Locality, quantum fluctuations, and scrambling. *Physical Review X* **9**, 031048 (2019).

[454] Schuster, T. *et al.* Many-body quantum teleportation via operator spreading in the traversable wormhole protocol. *Physical Review X* **12**, 031013 (2022).

[455] Li, J. *et al.* Measuring out-of-time-order correlators on a nuclear magnetic resonance quantum simulator. *Physical Review X* **7**, 031011 (2017).

[456] Landsman, K. A. *et al.* Verified quantum information scrambling. *Nature* **567**, 61–65 (2019).

[457] Blok, M. S. *et al.* Quantum information scrambling on a superconducting qutrit processor. *Physical Review X* **11**, 021010 (2021).

[458] Wei, K. X. *et al.* Emergent prethermalization signatures in out-of-time ordered correlations. *Physical Review Letters* **123**, 090605 (2019).

[459] Halpin-Healy, T. & Zhang, Y.-C. Kinetic roughening phenomena, stochastic growth, directed polymers and all that. Aspects of multidisciplinary statistical mechanics. *Physics Reports* **254**, 215–414 (1995).

[460] Corwin, I. The Kardar-Parisi-Zhang equation and universality class. *Random matrices: Theory and applications* **1**, 1130001 (2012).

[461] Corwin, I. Macdonald processes, quantum integrable systems and the Kardar-Parisi-Zhang universality class. *arXiv preprint arXiv:1403.6877* (2014).

[462] Baik, J., Deift, P. & Johansson, K. On the distribution of the length of the longest increasing subsequence of random permutations. *Journal of the American Mathematical Society* **12**, 1119–1178 (1999).

[463] Calabrese, P., Le Doussal, P. & Rosso, A. Free-energy distribution of the directed polymer at high temperature. *Europhysics Letters* **90**, 20002 (2010).

[464] Dotsenko, V. Bethe ansatz derivation of the tracy-widom distribution for one-dimensional directed polymers. *Europhysics Letters* **90**, 20003 (2010).

[465] Amir, G., Corwin, I. & Quastel, J. Probability distribution of the free energy of the continuum directed random polymer in 1+1 dimensions. *Communications on pure and applied mathematics* **64**, 466–537 (2011).

[466] Popkov, V., Schadschneider, A., Schmidt, J. & Schütz, G. M. Fibonacci family of dynamical universality classes. *PNAS* **112**, 12645–12650 (2015).

[467] Corwin, I., Shen, H. & Tsai, L.-C. ASEP(q, j) converges to the KPZ equation. *Annales de l'Institut Henri Poincaré, Probabilités et Statistiques* **54**, 995 – 1012 (2018).

[468] Matetski, K., Quastel, J. & Remenik, D. The kpz fixed point. *Acta Mathematica* **227**, 115–203 (2021).

[469] Corwin, I., O'Connell, N., Seppäläinen, T. & Zygouras, N. Tropical combinatorics and whittaker functions. *Duke Mathematical Journal* **163**, 513–563 (2014).

[470] de Gier, J., Schadschneider, A., Schmidt, J. & Schütz, G. M. Kardar-Parisi-Zhang universality of the Nagel-Schreckenberg model. *Physical Review E* **100**, 052111 (2019).

[471] Corwin, I., Ghosal, P., Shen, H. & Tsai, L.-C. Stochastic PDE limit of the six vertex model. *Communications in Mathematical Physics* **375**, 1945–2038 (2020).

[472] Bertini, L. & Cancrini, N. The stochastic heat equation: Feynman-kac formula and intermittence. *Journal of Statistical Physics* **78**, 1377–1401 (1995).

[473] Prähofer, M. & Spohn, H. Exact Scaling Functions for One-Dimensional Stationary KPZ Growth. *Journal of Statistical Physics* **115**, 255–279 (2004).

[474] Hairer, M. Solving the KPZ equation. *Annals of Mathematics* **178**, 559–664 (2013).

[475] Sasamoto, T. & Spohn, H. Exact height distributions for the kpz equation with narrow wedge initial condition. *Nuclear Physics B* **834**, 523–542 (2010).

[476] Corwin, I. Exactly solving the KPZ equation. *arXiv preprint arXiv:1804.05721* (2018).

[477] Ilievski, E., De Nardis, J., Medenjak, M. & Prosen, T. Superdiffusion in one-dimensional quantum lattice models. *Physical Review Letters* **121**, 230602 (2018).

[478] Rubio-Abadal, A. *et al.* Many-body delocalization in the presence of a quantum bath. *Physical Review X* **9**, 041014 (2019).

[479] Scheie, A. *et al.* Detection of Kardar-Parisi-Zhang hydrodynamics in a quantum Heisenberg spin-1/2 chain. *Nature Physics* **17**, 726–730 (2021).

[480] Krajnik, Ž., Ilievski, E. & Prosen, T. Integrable matrix models in discrete space-time. *SciPost Physics* **9**, 038 (2020).

[481] Krajnik, Ž., Ilievski, E. & Prosen, T. Absence of normal fluctuations in an integrable magnet. *Physical Review Letters* **128**, 090604 (2022).

[482] Abanov, A. G. HYDRODYNAMICS OF CORRELATED SYSTEMS. In Brézin, É., Kazakov, V., Serban, D., Wiegmann, P. & Zabrodin, A. (eds.) *Applications of Random Matrices in Physics*, NATO Science Series II: Mathematics, Physics and Chemistry, 139–161 (Springer Netherlands, Dordrecht, 2006).

[483] Bettelheim, E., Abanov, A. G. & Wiegmann, P. Nonlinear Quantum Shock Waves in Fractional Quantum Hall Edge States. *Physical Review Letters* **97**, 246401 (2006).

[484] Blake, M., Lee, H. & Liu, H. A quantum hydrodynamical description for scrambling and many-body chaos. *J. High Energ. Phys.* **2018**, 127 (2018).

[485] Vanicat, M., Zadnik, L. & Prosen, T. Integrable trotterization: local conservation laws and boundary driving. *Physical Review Letters* **121**, 030606 (2018).

[486] Gerrard, A. & Regelskis, V. Nested algebraic bethe ansatz for orthogonal and symplectic open spin chains. *Nuclear physics B* **952**, 114909 (2020).

[487] Frahm, H. & Martins, M. J. Osp(n|2m) quantum chains with free boundaries. *Nuclear Physics B* **980**, 115799 (2022).

[488] Uimin, G. One-dimensional problem for S = 1 with modified antiferromagnetic Hamiltonian. *Soviet Journal of Experimental and Theoretical Physics Letters* **12**, 225 (1970).

[489] Lai, C. Lattice gas with nearest-neighbor interaction in one dimension with arbitrary statistics. *Journal of Mathematical Physics* **15**, 1675–1676 (1974).

[490] Sutherland, B. Model for a multicomponent quantum system. *Physical Review B* **12**, 3795–3805 (1975).

[491] Dupont, M. & Moore, J. E. Universal spin dynamics in infinite-temperature one-dimensional quantum magnets. *Physical Review B* **101**, 121106 (2020).

[492] De Nardis, J., Gopalakrishnan, S., Ilievski, E. & Vasseur, R. Superdiffusion from emergent classical solitons in quantum spin chains. *Physical Review Letters* **125**, 070601 (2020).

[493] Izergin, A. G. & Korepin, V. E. The quantum inverse scattering method approach to correlation functions. *Communications in Mathematical Physics* **94**, 67–92 (1984).

[494] Vichirko, V. I. & Reshetikhin, N. Y. Excitation spectrum of the anisotropic generalization of an su(3) magnet. *Theoretical and Mathematical Physics* **56**, 805–812 (1983).

[495] Hao, K. *et al.* Exact solution of the izergin-korepin model with general non-diagonal boundary terms. *Journal of High Energy Physics* **2014**, 1–22 (2014).

[496] Izergin, A. & Korepin, V. The inverse scattering method approach to the quantum shabat-mikhailov model. *Communications in Mathematical Physics* **79**, 303–316 (1981).

[497] Jimbo, M. Quantum R matrix for the generalized Toda system. *Communications in Mathematical Physics* **102**, 537 (1985).

[498] Schultz, C. L. Solvable q-state models in lattice statistics and quantum field theory. *Physical Review Letters* **46**, 629 (1981).

[499] Korepin, V. E., Bogoliubov, N. M. & Izergin, A. G. *Quantum Inverse Scattering Method and Correlation Functions*. Cambridge Monographs on Mathematical Physics (Cambridge University Press, Cambridge, UK, 1993).

[500] Kulish, P. & Sklyanin, E. Solutions of the Yang-Baxter equation. *Journal of Soviet Mathematics* **19**, 1596–1620 (1982).

[501] Kulish, P. Integrable graded magnets. *Journal of Soviet Mathematics* **35**, 2648–2662 (1986).

[502] Kassel, C. *Quantum Groups*. Graduate Texts in Mathematics (Springer-Verlag, New York, 1995).

[503] Martins, M. & Ramos, P. The algebraic bethe ansatz for rational braid-monoid lattice models. *Nuclear Physics B* **500**, 579–620 (1997).

[504] Doyon, B. Diffusion and superdiffusion from hydrodynamic projections. *Journal of Statistical Physics* **186**, 25 (2022).

[505] Shlesinger, M. F., Zaslavsky, G. M. & Frisch, U. *Lévy flights and related topics in physics* (Springer-Verlag, Berlin, GE, 1995).

[506] Ljubotina, M., Zadnik, L. & Prosen, T. Ballistic Spin Transport in a Periodically Driven Integrable Quantum System. *Physical Review Letters* **122**, 150605 (2019).

[507] Sarkar, S. The supersymmetric t-J model in one dimension. *Journal of Physics A: Mathematical and General* **24**, 1137–1151 (1991).

[508] Essler, F. H. L., Korepin, V. E. & Schoutens, K. New exactly solvable model of strongly correlated electrons motivated by high-T_c superconductivity. *Physical Review Letters* **68**, 2960–2963 (1992).

[509] Martins, M. Exact solution of the simplest superorthosymplectic invariant magnet. *Physical Review Letters* **74**, 3316 (1995).

[510] Martins, M. The exact solution and the finite-size behaviour of the osp (1| 2)-invariant spin chain. *Nuclear Physics B* **450**, 768–788 (1995).

[511] Weitenberg, C. *et al.* Single-spin addressing in an atomic mott insulator. *Nature* **471**, 319–324 (2011).

[512] Cappellini, G. *et al.* Direct observation of coherent interorbital spin-exchange dynamics. *Physical Review Letters* **113**, 120402 (2014).

[513] Pagano, G. *et al.* A one-dimensional liquid of fermions with tunable spin. *Nature Physics* **10**, 198–201 (2014).

[514] Scazza, F. *et al.* Observation of two-orbital spin-exchange interactions with ultracold SU(N)-symmetric fermions. *Nature Physics* **10**, 779–784 (2014). 1403.4761.

[515] Zhang, X. *et al.* Spectroscopic observation of SU(N)-symmetric interactions in Sr orbital magnetism. *Science* **345**, 1467–1473 (2014). 1403.2964.

[516] Miranda, M., Inoue, R., Okuyama, Y., Nakamoto, A. & Kozuma, M. Site-resolved imaging of ytterbium atoms in a two-dimensional optical lattice. *Physical Review A* **91**, 063414 (2015).

[517] Yamamoto, R., Kobayashi, J., Kuno, T., Kato, K. & Takahashi, Y. An ytterbium quantum gas microscope with narrow-line laser cooling. *New Journal of Physics* **18**, 023016 (2016).

[518] Miranda, M., Inoue, R., Tambo, N. & Kozuma, M. Site-resolved imaging of a bosonic mott insulator using ytterbium atoms. *Physical Review A* **96**, 043626 (2017).

[519] Sonderhouse, L. *et al.* Thermodynamics of a deeply degenerate SU(N)-symmetric Fermi gas. *Nature Physics* **16**, 1216–1221 (2020). 2003.02408.

[520] Schine, N., Young, A. W., Eckner, W. J., Martin, M. J. & Kaufman, A. M. Long-lived bell states in an array of optical clock qubits. *Nature Physics* **18**, 1067–1073 (2022).

[521] Bakr, W. S. *et al.* Probing the Superfluid–to–Mott Insulator Transition at the Single-Atom Level. *Science* **329**, 547–550 (2010).

[522] Sherson, J. F. *et al.* Single-atom-resolved fluorescence imaging of an atomic Mott insulator. *Nature* **467**, 68–72 (2010).

[523] Cheuk, L. W. *et al.* Quantum-gas microscope for fermionic atoms. *Physical Review Letters* **114**, 193001 (2015).

[524] Parsons, M. F. *et al.* Site-resolved imaging of fermionic ^{6}Li in an optical lattice. *Physical Review Letters* **114**, 213002 (2015).

[525] Omran, A. *et al.* Microscopic observation of Pauli blocking in degenerate fermionic lattice gases. *Physical Review Letters* **115**, 263001 (2015).

[526] Haller, E. *et al.* Single-atom imaging of fermions in a quantum-gas microscope. *Nature Physics* **11**, 738–742 (2015).

[527] Park, A. J. *et al.* Cavity-enhanced optical lattices for scaling neutral atom quantum technologies to higher qubit numbers. *PRX Quantum* **3**, 030314 (2022).

[528] Bothwell, T. *et al.* Resolving the gravitational redshift across a millimetre-scale atomic sample. *Nature* **602**, 420–424 (2022).

[529] Ibarra-García-Padilla, E. *et al.* Universal thermodynamics of an $\mathrm{SU}(N)$ fermi-hubbard model. *Physical Review A* **104**, 043316 (2021).

[530] Bulchandani, V. B. Kardar-Parisi-Zhang universality from soft gauge modes. *Physical Review B* **101**, 041411 (2020).

[531] Gopalakrishnan, S., Morningstar, A., Vasseur, R. & Khemani, V. Distinct universality classes of diffusive transport from full counting statistics. *Physical Review B* **109**, 024417 (2024).

[532] De Nardis, J., Medenjak, M., Karrasch, C. & Ilievski, E. Anomalous spin diffusion in one-dimensional antiferromagnets. *Physical Review Letters* **123**, 186601 (2019).

[533] Krajnik, Ž. & Prosen, T. Kardar-Parisi-Zhang physics in integrable rotationally symmetric dynamics on discrete space-time lattice. *Journal of Statistical Physics* **179**, 110–130 (2020).

[534] Prosen, T. & Žunkovič, B. Macroscopic diffusive transport in a microscopically integrable Hamiltonian system. *Physical Review Letters* **111**, 040602 (2013).

[535] Das, A., Kulkarni, M., Spohn, H. & Dhar, A. Kardar-Parisi-Zhang scaling for an integrable lattice Landau-Lifshitz spin chain. *Physical Review E* **100**, 042116 (2019).

[536] Bulchandani, V. B., Gopalakrishnan, S. & Ilievski, E. Superdiffusion in spin chains. *Journal of Statistical Mechanics: Theory and Experiment* **2021**, 084001 (2021).

[537] Hild, S. *et al.* Far-from-equilibrium spin transport in Heisenberg quantum magnets. *Physical Review Letters* **113**, 1–5 (2014).

[538] Jepsen, P. N. *et al.* Spin transport in a tunable Heisenberg model realized with ultracold atoms. *Nature* **588**, 403–407 (2020).

[539] Jepsen, P. N. *et al.* Transverse spin dynamics in the anisotropic heisenberg model realized with ultracold atoms. *Physical Review X* **11**, 041054 (2021).

[540] Hartmann, A. K., Le Doussal, P., Majumdar, S. N., Rosso, A. & Schehr, G. High-precision simulation of the height distribution for the KPZ equation. *Europhysics Letters* **121**, 67004 (2018).

[541] Duan, L.-M., Demler, E. & Lukin, M. D. Controlling spin exchange interactions of ultracold atoms in optical lattices. *Physical Review Letters* **91**, 090402 (2003).

[542] Kuklov, A. B. & Svistunov, B. V. Counterflow superfluidity of two-species ultracold atoms in a commensurate optical lattice. *Physical Review Letters* **90**, 100401 (2003).

[543] Fukuhara, T. *et al.* Quantum dynamics of a mobile spin impurity. *Nature Physics* **9**, 235–241 (2013).

[544] Halimeh, J. C., Wöllert, A., McCulloch, I., Schollwöck, U. & Barthel, T. Domain-wall melting in ultracold-boson systems with hole and spin-flip defects. *Physical Review A* **89**, 063603 (2014).

[545] Gamayun, O., Miao, Y. & Ilievski, E. Domain-wall dynamics in the Landau-Lifshitz magnet and the classical-quantum correspondence for spin transport. *Physical Review B* **99**, 140301 (2019).

[546] Tang, Y. *et al.* Thermalization near integrability in a dipolar quantum Newton's cradle. *Physical Review X* **8**, 021030 (2018).

[547] Nichols, M. A. *et al.* Spin transport in a Mott insulator of ultracold fermions. *Science* **363**, 383–387 (2019).

[548] Weiner, F., Schmitteckert, P., Bera, S. & Evers, F. High-temperature spin dynamics in the Heisenberg chain: Magnon propagation and emerging Kardar-Parisi-Zhang scaling in the zero-magnetization limit. *Physical Review B* **101**, 045115 (2020).

[549] Fava, M., Ware, B., Gopalakrishnan, S., Vasseur, R. & Parameswaran, S. A. Spin crossovers and superdiffusion in the one-dimensional Hubbard model. *Physical Review B* **102**, 115121 (2020).

[550] Prähofer, M. & Spohn, H. Universal distributions for growth processes in $1 + 1$ dimensions and random matrices. *Physical Review Letters* **84**, 4882–4885 (2000).

[551] Family, F. & Vicsek, T. Scaling of the active zone in the Eden process on percolation networks and the ballistic deposition model. *Journal of Physics A: Mathematical and General* **18**, L75–L81 (1985).

[552] Spohn, H. The 1+1 dimensional Kardar-Parisi-Zhang equation: More surprises. *Journal of Statistical Mechanics: Theory and Experiment* **2020**, 044001 (2020).

[553] Basko, D., Aleiner, I. & Altshuler, B. Metal–insulator transition in a weakly interacting many-electron system with localized single-particle states. *Annals of Physics* **321**, 1126 – 1205 (2006).

[554] Basko, D., Aleiner, I. & Altshuler, B. On the problem of many-body localization. *Problems of Condensed Matter Physics* 50–70 (2006).

[555] Canovi, E., Rossini, D., Fazio, R., Santoro, G. E. & Silva, A. Quantum quenches, thermalization, and many-body localization. *Physical Review B* **83**, 094431 (2011).

[556] Bauer, B. & Nayak, C. Area laws in a many-body localized state and its implications for topological order. *Journal of Statistical Mechanics: Theory and Experiment* **2013**, P09005 (2013).

[557] Huse, D. A., Nandkishore, R., Oganesyan, V., Pal, A. & Sondhi, S. L. Localization-protected quantum order. *Physical Review B* **88**, 014206 (2013).

[558] Parameswaran, S. A. & Vasseur, R. Many-body localization, symmetry and topology. *Reports on Progress in Physics* **81**, 082501 (2018).

[559] Chandran, A., Khemani, V., Laumann, C. R. & Sondhi, S. L. Many-body localization and symmetry-protected topological order. *Physical Review B* **89**, 144201 (2014).

[560] Kjäll, J. A., Bardarson, J. H. & Pollmann, F. Many-body localization in a disordered quantum ising chain. *Physical Review Letters* **113**, 107204 (2014).

[561] Bahri, Y., Vosk, R., Altman, E. & Vishwanath, A. Localization and topology protected quantum coherence at the edge of hot matter. *Nature Communications* **6**, 7341 (2015).

[562] Yao, N. Y., Laumann, C. R. & Vishwanath, A. Many-body localization protected quantum state transfer. *arXiv preprint arXiv:1508.06995* (2015).

[563] Sachdev, S. *Quantum Phase Transitions* (Cambridge University Press, Cambridge, UK, 1999).

[564] Venderley, J., Khemani, V. & Kim, E.-A. Machine learning out-of-equilibrium phases of matter. *Physical Review Letters* **120**, 257204 (2018).

[565] Friedman, A. J., Vasseur, R., Potter, A. C. & Parameswaran, S. A. Localization-protected order in spin chains with non-abelian discrete symmetries. *Physical Review B* **98**, 064203 (2018).

[566] Vasseur, R., Friedman, A. J., Parameswaran, S. A. & Potter, A. C. Particle-hole symmetry, many-body localization, and topological edge modes. *Physical Review B* **93**, 134207 (2016).

[567] Chan, A. & Wahl, T. B. Classification of symmetry-protected topological many-body localized phases in one dimension. *Journal of Physics: Condensed Matter* **32**, 305601 (2020).

[568] Wahl, T. B. & Béri, B. Local integrals of motion for topologically ordered many-body localized systems. *Physical Review Research* **2**, 033099 (2020).

[569] Altshuler, B. L., Gefen, Y., Kamenev, A. & Levitov, L. S. Quasiparticle lifetime in a finite system: A nonperturbative approach. *Physical Review Letters* **78**, 2803 (1997).

[570] Nandkishore, R. & Potter, A. C. Marginal anderson localization and many-body delocalization. *Physical Review B* **90**, 195115 (2014).

[571] Crowley, P. J. & Chandran, A. Avalanche induced coexisting localized and thermal regions in disordered chains. *Physical Review Research* **2**, 033262 (2020).

[572] Balewski, J. B. *et al.* Rydberg dressing: understanding of collective many-body effects and implications for experiments. *New Journal of Physics* **16**, 063012 (2014).

[573] Choi, J.-Y. *et al.* Exploring the many-body localization transition in two dimensions. *Science* **352**, 1547–1552 (2016).

[574] Zeiher, J. *et al.* Coherent many-body spin dynamics in a long-range interacting ising chain. *Physical Review X* **7**, 041063 (2017).

[575] Bernien, H. *et al.* Probing many-body dynamics on a 51-atom quantum simulator. *Nature* **551**, 579–584 (2017).

[576] Cooper, A. *et al.* Alkaline-earth atoms in optical tweezers. *Physical Review X* **8**, 041055 (2018).

[577] Léséleuc, S. d. *et al.* Observation of a symmetry-protected topological phase of interacting bosons with rydberg atoms. *Science* **365**, 775–780 (2019).

[578] Wilson, J. T. *et al.* Trapping alkaline earth rydberg atoms optical tweezer arrays. *Physical Review Letters* **128**, 033201 (2022).

[579] Madjarov, I. S. *et al.* High-fidelity entanglement and detection of alkaline-earth rydberg atoms. *Nature Physics* 1–5 (2020).

[580] Abanin, D. *et al.* Distinguishing localization from chaos: Challenges in finite-size systems. *Annals of Physics* **427**, 168415 (2021).

[581] Luitz, D. J., Laflorencie, N. & Alet, F. Many-body localization edge in the random-field heisenberg chain. *Physical Review B* **91**, 081103 (2015).

[582] Luitz, D. J. Long tail distributions near the many-body localization transition. *Physical Review B* **93**, 134201 (2016).

[583] Singh, R., Bardarson, J. H. & Pollmann, F. Signatures of the many-body localization transition in the dynamics of entanglement and bipartite fluctuations. *New Journal of Physics* **18**, 023046 (2016).

[584] Khemani, V., Lim, S. P., Sheng, D. N. & Huse, D. A. Critical properties of the many-body localization transition. *Physical Review X* **7**, 021013 (2017).

[585] Dumitrescu, P. T., Vasseur, R. & Potter, A. C. Scaling theory of entanglement at the many-body localization transition. *Physical Review Letters* **119**, 110604 (2017).

[586] Alet, F. & Laflorencie, N. Many-body localization: An introduction and selected topics. *Comptes Rendus Physique* **19**, 498–525 (2018).

[587] Théveniaut, H., Lan, Z., Meyer, G. & Alet, F. Transition to a many-body localized regime in a two-dimensional disordered quantum dimer model. *Physical Review Research* **2**, 033154 (2020).

[588] Page, D. N. Average entropy of a subsystem. *Physical Review Letters* **71**, 1291–1294 (1993).

[589] Panda, R. K., Scardicchio, A., Schulz, M., Taylor, S. R. & Žnidarič, M. Can we study the many-body localisation transition? *Europhysics Letters* **128**, 67003 (2020).

[590] Papić, Z., Stoudenmire, E. M. & Abanin, D. A. Many-body localization in disorder-free systems: The importance of finite-size constraints. *Annals of Physics* **362**, 714 – 725 (2015).

[591] Chandran, A., Laumann, C. & Oganesyan, V. Finite size scaling bounds on many-body localized phase transitions arxiv e-prints. *arXiv preprint arXiv:1509.04285* (2015).

[592] Harris, A. B. Effect of random defects on the critical behaviour of ising models. *Journal of Physics C: Solid State Physics* **7**, 1671–1692 (1974).

[593] Bahri, Y. & Vishwanath, A. Detecting majorana fermions in quasi-one-dimensional topological phases using nonlocal order parameters. *Physical Review B* **89**, 155135 (2014).

[594] Ponte, P., Papić, Z., Huveneers, F. & Abanin, D. A. Many-body localization in periodically driven systems. *Physical Review Letters* **114**, 140401 (2015).

[595] Zhang, L., Khemani, V. & Huse, D. A. A Floquet model for the many-body localization transition. *Physical Review B* **94**, 224202 (2016).

[596] Evers, F. & Mirlin, A. D. Anderson transitions. *Reviews of Modern Physics* **80**, 1355–1417 (2008).

[597] Fisher, D. S. Critical behavior of random transverse-field ising spin chains. *Physical Review B* **51**, 6411–6461 (1995).

[598] Balents, L. & Fisher, M. P. A. Delocalization transition via supersymmetry in one dimension. *Physical Review B* **56**, 12970–12991 (1997).

[599] McCoy, B. M. & Wu, T. T. Theory of a two-dimensional ising model with random impurities. i. thermodynamics. *Physical Review* **176**, 631–643 (1968).

[600] Nivedita, Shackleton, H. & Sachdev, S. Spectral form factors of clean and random quantum ising chains. *Physical Review E* **101**, 042136 (2020).

[601] Kuno, Y., Orito, T. & Ichinose, I. Flat-band many-body localization and ergodicity breaking in the creutz ladder. *New Journal of Physics* **22**, 013032 (2020).

[602] Luitz, D. J., Huveneers, F. & De Roeck, W. How a small quantum bath can thermalize long localized chains. *Physical Review Letters* **119**, 150602 (2017).

[603] Thiery, T., Huveneers, F., Müller, M. & De Roeck, W. Many-body delocalization as a quantum avalanche. *Physical Review Letters* **121**, 140601 (2018).

[604] Potirniche, I.-D., Banerjee, S. & Altman, E. Exploration of the stability of many-body localization in $d > 1$. *Physical Review B* **99**, 205149 (2019).

[605] Inoue, J.-I. & Tanaka, A. Photoinduced Transition between Conventional and Topological Insulators in Two-Dimensional Electronic Systems. *Physical Review Letters* **105**, 017401 (2010). 1006.5283.

[606] Jiang, L. *et al.* Majorana Fermions in Equilibrium and in Driven Cold-Atom Quantum Wires. *Physical Review Letters* **106**, 220402 (2011). 1102.5367.

[607] Berges, J., Borsányi, S. & Wetterich, C. Prethermalization. *Physical Review Letters* **93**, 142002 (2004).

[608] Rajak, A., Dana, I. & Dalla Torre, E. G. Characterizations of prethermal states in periodically driven many-body systems with unbounded chaotic diffusion. *Physical Review B* **100**, 100302 (2019).

[609] Hodson, W. & Jarzynski, C. Energy diffusion and absorption in chaotic systems with rapid periodic driving. *Physical Review Research* **3**, 013219 (2021).

[610] Lazarides, A. & Moessner, R. Fate of a discrete time crystal in an open system. *Physical Review B* **95**, 195135 (2017).

[611] Zhu, B., Marino, J., Yao, N. Y., Lukin, M. D. & Demler, E. A. Dicke time crystals in driven-dissipative quantum many-body systems. *New Journal of Physics* **21**, 073028 (2019). 1904.01026.

[612] Dai, J., Niemi, A. J., Peng, X. & Wilczek, F. Truncated dynamics, ring molecules, and mechanical time crystals. *Physical Review A* **99**, 023425 (2019).

[613] Alekseev, A., Dai, J. & Niemi, A. J. Provenance of classical Hamiltonian time crystals. *Journal of High Energy Physics* **2020**, 1–21 (2020).

[614] Pizzi, A., Malz, D., De Tomasi, G., Knolle, J. & Nunnenkamp, A. To heat or not to heat: Time crystallinity and finite-size effects in clean Floquet systems. *Physical Review B* **102**, 214207 (2020). 2009.13527.

[615] Lazarides, A., Roy, S., Piazza, F. & Moessner, R. Time crystallinity in dissipative Floquet systems. *Physical Review Research* **2**, 022002 (2020).

[616] Pizzi, A., Knolle, J. & Nunnenkamp, A. Higher-order and fractional discrete time crystals in clean long-range interacting systems. *Nature Communications* **12**, 1–7 (2021).

[617] Pizzi, A., Nunnenkamp, A. & Knolle, J. Bistability and time crystals in long-ranged directed percolation. *Nature Communications* **12**, 1061 (2021). 2004.13034.

[618] Else, D. V. & Nayak, C. Classification of topological phases in periodically driven interacting systems. *Physical Review B* **93**, 201103 (2016).

[619] Roy, R. & Harper, F. Periodic table for Floquet topological insulators. *Physical Review B* **96**, 155118 (2017).

[620] Lerose, A., Žunkovič, B., Marino, J., Gambassi, A. & Silva, A. Impact of nonequilibrium fluctuations on prethermal dynamical phase transitions in long-range interacting spin chains. *Physical Review B* **99**, 045128 (2019).

[621] Mizuta, K., Takasan, K. & Kawakami, N. High-frequency expansion for Floquet prethermal phases with emergent symmetries: Application to time crystals and Floquet engineering. *Physical Review B* **100**, 020301 (2019).

[622] Lerose, A., Marino, J., Gambassi, A. & Silva, A. Prethermal quantum many-body kapitza phases of periodically driven spin systems. *Physical Review B* **100**, 104306 (2019).

[623] Crowley, P. J., Martin, I. & Chandran, A. Topological classification of quasiperiodically driven quantum systems. *Physical Review B* **99**, 064306 (2019).

[624] Dyson, F. J. Existence of a phase-transition in a one-dimensional Ising ferromagnet. *Communications in Mathematical Physics* **12**, 91–107 (1969).

[625] Birkhoff, G. D. *Dynamical systems* (American Mathematical Soc., Providence, 1927).

[626] Ott, E. Strange attractors and chaotic motions of dynamical systems. *Reviews of Modern Physics* **53**, 655 (1981).

[627] Strogatz, S. H. *Nonlinear dynamics and chaos with student solutions manual: With applications to physics, biology, chemistry, and engineering* (CRC press, Boca Raton, 2018).

[628] Kaneko, K. Period-doubling of kink-antikink patterns, quasiperiodicity in antiferro-like structures and spatial intermittency in coupled logistic lattice: Towards a prelude of a "field theory of chaos". *Progress of Theoretical Physics* **72**, 480–486 (1984).

[629] Kapral, R. Pattern formation in two-dimensional arrays of coupled, discrete-time oscillators. *Physical Review A* **31**, 3868 (1985).

[630] Bunimovich, L. A. & Sinai, Y. G. Spacetime chaos in coupled map lattices. *Nonlinearity* **1**, 491 (1988).

[631] Faraday, M. XVII. On a peculiar class of acoustical figures; and on certain forms assumed by groups of particles upon vibrating elastic surfaces. *Philosophical Transactions of the Royal Society of London* 299–340 (1831).

[632] Rayleigh, L. VII. On the crispations of fluid resting upon a vibrating support. *The London, Edinburgh, and Dublin Philosophical Magazine and Journal of Science* **16**, 50–58 (1883).

[633] Rayleigh, L. XXXIII. On maintained vibrations. *The London, Edinburgh, and Dublin Philosophical Magazine and Journal of Science* **15**, 229–235 (1883).

[634] Benjamin, T. B. & Ursell, F. J. The stability of the plane free surface of a liquid in vertical periodic motion. *Proceedings of the Royal Society of London. Series A. Mathematical and Physical Sciences* **225**, 505–515 (1954).

[635] McLachlan, N. Mathieu functions of fractional order. *Journal of Mathematics and Physics* **26**, 29–41 (1947).

[636] Kovacic, I., Rand, R. & Mohamed Sah, S. Mathieu's equation and its generalizations: overview of stability charts and their features. *Applied Mechanics Reviews* **70** (2018).

[637] Olver, P. J. A nonlinear Hamiltonian structure for the euler equations. *Journal of Mathematical Analysis and Applications* **89**, 233–250 (1982).

[638] Arnol'd, V. I. Proof of a theorem of A. N. Kolmogorov on the invariance of quasi-periodic motions under small perturbations of the Hamiltonian. *Russian Mathematical Surveys* **18**, 9 (1963).

[639] Möser, J. On invariant curves of area-preserving mappings of an annulus. *Nachr. Akad. Wiss. Göttingen Math. Phys. Kl.,* **II** 1–20 (1962).

[640] Kolmogorov, A. N. On conservation of conditionally periodic motions for a small change in hamilton's function. In *Dokl. Akad. Nauk SSSR*, vol. 98, 527–530 (1954).

[641] Zounes, R. S. & Rand, R. H. Subharmonic resonance in the non-linear mathieu equation. *International Journal of Non-Linear Mechanics* **37**, 43–73 (2002).

[642] Landau, L. On the theory of phase transitions. *Zh. Eksp. Teor. Fiz.* **7**, 19–32 (1937).

[643] Gong, R. *et al.* Coherent dynamics of strongly interacting electronic spin defects in hexagonal boron nitride. *Nature Communications* **14**, 3299 (2023).

[644] Hahn, W. & Dobrovitski, V. Long-lived coherence in driven many-spin systems: from two to infinite spatial dimensions. *New Journal of Physics* **23**, 073029 (2021).

[645] Qi, Z., Refael, G. & Peng, Y. Universal nonadiabatic energy pumping in a quasiperiodically driven extended system. *Physical Review B* **104**, 224301 (2021).

[646] Peng, Y. & Refael, G. Time-quasiperiodic topological superconductors with majorana multiplexing. *Physical Review B* **98**, 220509 (2018).

[647] Blekher, P., Jauslin, H. & Lebowitz, J. Floquet spectrum for two-level systems in quasiperiodic time-dependent fields. *Journal of Statistical Physics* **68**, 271–310 (1992).

[648] Zhao, H., Mintert, F., Moessner, R. & Knolle, J. Random multipolar driving: tunably slow heating through spectral engineering. *Physical Review Letters* **126**, 040601 (2021).

[649] Davis, E. J. *et al.* Probing many-body noise in a strongly interacting two-dimensional dipolar spin system. *Nature Physics* **19**, 836–844 (2023).

[650] Sambe, H. Steady states and quasienergies of a quantum-mechanical system in an oscillating field. *Physical Review A* **7**, 2203 (1973).

[651] Goldman, N. & Dalibard, J. Periodically driven quantum systems: effective Hamiltonians and engineered gauge fields. *Physical Review X* **4**, 031027 (2014).

[652] Wang, Y. H., Steinberg, H., Jarillo-Herrero, P. & Gedik, N. Observation of Floquet-Bloch states on the surface of a topological insulator. *Science* **342**, 453–457 (2013).

[653] Po, H. C., Fidkowski, L., Morimoto, T., Potter, A. C. & Vishwanath, A. Chiral Floquet phases of many-body localized bosons. *Physical Review X* **6**, 041070 (2016).

[654] Po, H. C., Fidkowski, L., Vishwanath, A. & Potter, A. C. Radical chiral Floquet phases in a periodically driven kitaev model and beyond. *Physical Review B* **96**, 245116 (2017).

[655] Dumitrescu, P. T. *et al.* Dynamical topological phase realized in a trapped-ion quantum simulator. *Nature* **607**, 463–467 (2022).

[656] Xu, P., Zheng, W. & Zhai, H. Topological micromotion of Floquet quantum systems. *Physical Review B* **105**, 045139 (2022).

[657] Schnabel, R., Mavalvala, N., McClelland, D. E. & Lam, P. K. Quantum metrology for gravitational wave astronomy. *Nature Communications* **1**, 121 (2010).

[658] Wasilewski, W. *et al.* Quantum Noise Limited and Entanglement-Assisted Magnetometry. *Physical Review Letters* **104**, 133601 (2010).

[659] Leibfried, D. *et al.* Toward Heisenberg-Limited Spectroscopy with Multiparticle Entangled States. *Science* **304**, 1476–1478 (2004).

[660] Bouwmeester, D., Pan, J.-W., Daniell, M., Weinfurter, H. & Zeilinger, A. Observation of Three-Photon Greenberger-Horne-Zeilinger Entanglement. *Physical Review Letters* **82**, 1345–1349 (1999).

[661] Pan, J.-W., Bouwmeester, D., Daniell, M., Weinfurter, H. & Zeilinger, A. Experimental test of quantum nonlocality in three-photon Greenberger–Horne–Zeilinger entanglement. *Nature* **403**, 515–519 (2000).

[662] Omran, A. *et al.* Generation and manipulation of Schrödinger cat states in Rydberg atom arrays. *Science* **365**, 570–574 (2019).

[663] Pogorelov, I. *et al.* Compact Ion-Trap Quantum Computing Demonstrator. *PRX Quantum* **2**, 020343 (2021).

[664] Jones, J. A. *et al.* Magnetic Field Sensing Beyond the Standard Quantum Limit Using 10-Spin NOON States. *Science* **324**, 1166–1168 (2009).

[665] Dicke, R. H. Coherence in Spontaneous Radiation Processes. *Physical Review* **93**, 99–110 (1954).

[666] Wieczorek, W. *et al.* Experimental Entanglement of a Six-Photon Symmetric Dicke State. *Physical Review Letters* **103**, 020504 (2009).

[667] Lücke, B. *et al.* Detecting Multiparticle Entanglement of Dicke States. *Physical Review Letters* **112**, 155304 (2014).

[668] Zou, Y.-Q. *et al.* Beating the classical precision limit with spin-1 Dicke states of more than 10,000 atoms. *Proceedings of the National Academy of Sciences* **115**, 6381–6385 (2018).

[669] Wineland, D. J. and Bollinger, J. J. and Itano, W. M. and Heinzen, D. J. Squeezed atomic states and projection noise in spectroscopy. *Physical Review A* **50**, 67–88 (1994).

[670] Estève, J., Gross, C., Weller, A., Giovanazzi, S. & Oberthaler, M. K. Squeezing and entanglement in a Bose–Einstein condensate. *Nature* **455**, 1216–1219 (2008).

[671] Appel, J. *et al.* Mesoscopic atomic entanglement for precision measurements beyond the standard quantum limit. *Proceedings of the National Academy of Sciences* **106**, 10960–10965 (2009).

[672] Muessel, W., Strobel, H., Linnemann, D., Hume, D. & Oberthaler, M. Scalable Spin Squeezing for Quantum-Enhanced Magnetometry with Bose-Einstein Condensates. *Physical Review Letters* **113**, 103004 (2014).

[673] Frérot, I., Naldesi, P. & Roscilde, T. Entanglement and fluctuations in the xxz model with power-law interactions. *Physical Review B* **95**, 245111 (2017).

[674] Hauke, P., Heyl, M., Tagliacozzo, L. & Zoller, P. Measuring multipartite entanglement through dynamic susceptibilities. *Nature Physics* **12**, 778–782 (2016).

[675] Gabbrielli, M., Smerzi, A. & Pezzè, L. Multipartite Entanglement at Finite Temperature. *Scientific Reports* **8**, 15663 (2018).

[676] Chen, C. *et al.* Continuous Symmetry Breaking in a Two-dimensional Rydberg Array. *Nature* **616**, 691–695 (2023).

[677] Comparin, T., Mezzacapo, F. & Roscilde, T. Multipartite entangled states in dipolar quantum simulators. *Physical Review Letters* **129**, 150503 (2022).

[678] Halperin, B. I. & Hohenberg, P. C. Hydrodynamic Theory of Spin Waves. *Physical Review* **188**, 898–918 (1969).

[679] Perlin, M. A., Qu, C. & Rey, A. M. Spin squeezing with short-range spin-exchange interactions. *Physical Review Letters* **125**, 223401 (2020).

[680] Comparin, T., Mezzacapo, F. & Roscilde, T. Robust spin squeezing from the tower of states of U(1)-symmetric spin Hamiltonians. *Physical Review A* **105**, 022625 (2022).

[681] Cappellaro, P. & Lukin, M. D. Quantum correlation in disordered spin systems: Applications to magnetic sensing. *Physical Review A* **80**, 032311 (2009).

[682] Davis, E. J. *et al.* Protecting Spin Coherence in a Tunable Heisenberg Model. *Physical Review Letters* **125**, 060402 (2020).

[683] Kwasigroch, M. P. & Cooper, N. R. Bose-Einstein condensation and many-body localization of rotational excitations of polar molecules following a microwave pulse. *Physical Review A* **90**, 021605 (2014).

[684] Kwasigroch, M. P. & Cooper, N. R. Synchronization transition in dipole-coupled two-level systems with positional disorder. *Physical Review A* **96**, 053610 (2017).

[685] Rey, A. M., Jiang, L., Fleischhauer, M., Demler, E. & Lukin, M. D. Many-body protected entanglement generation in interacting spin systems. *Physical Review A* **77**, 052305 (2008).

[686] Greiner, M., Mandel, O., Esslinger, T., Hänsch, T. W. & Bloch, I. Quantum phase transition from a superfluid to a Mott insulator in a gas of ultracold atoms. *Nature* **415**, 39–44 (2002).

[687] Ni, K.-K. *et al.* A high phase-space-density gas of polar molecules. *Science* **322**, 231–235 (2008).

[688] Chomaz, L. *et al.* Long-lived and transient supersolid behaviors in dipolar quantum gases. *Physical Review X* **9**, 021012 (2019).

[689] Tran, T. T., Bray, K., Ford, M. J., Toth, M. & Aharonovich, I. Quantum emission from hexagonal boron nitride monolayers. *Nature Nanotechnology* **11**, 37–41 (2016).

[690] Bruno, P. Absence of spontaneous magnetic order at nonzero temperature in one- and two-dimensional heisenberg and XY systems with long-range interactions. *Physical Review Letters* **87**, 137203 (2001).

[691] Maghrebi, M. F., Gong, Z.-X. & Gorshkov, A. V. Continuous symmetry breaking in 1d long-range interacting quantum systems. *Physical Review Letters* **119**, 023001 (2017).

[692] Roscilde, T., Mezzacapo, F. & Comparin, T. Spin squeezing from bilinear spin-spin interactions: Two simple theorems. *Physical Review A* **104**, L040601 (2021).

[693] Prokof'ev, N. V., Svistunov, B. V. & Tupitsyn, I. S. Exact, complete, and universal continuous-time worldline Monte Carlo approach to the statistics of discrete quantum systems. *Journal of Experimental and Theoretical Physics* **87**, 310–321 (1998).

[694] Tasaki, H. Long-Range Order, "Tower" of States, and Symmetry Breaking in Lattice Quantum Systems. *Journal of Statistical Physics* **174**, 735–761 (2019).

[695] Yan, B. *et al.* Observation of dipolar spin-exchange interactions with lattice-confined polar molecules. *Nature* **501**, 521–525 (2013).

[696] de Léséleuc, S., Barredo, D., Lienhard, V., Browaeys, A. & Lahaye, T. Optical Control of the Resonant Dipole-Dipole Interaction between Rydberg Atoms. *Physical Review Letters* **119**, 053202 (2017).

[697] Gottscholl, A. *et al.* Initialization and read-out of intrinsic spin defects in a van der Waals crystal at room temperature. *Nature Materials* **19**, 540–545 (2020).

[698] Chejanovsky, N. *et al.* Single-spin resonance in a van der Waals embedded paramagnetic defect. *Nature Materials* **20**, 1079–1084 (2021).

[699] Eichhorn, T. R., McLellan, C. A. & Bleszynski Jayich, A. C. Optimizing the formation of depth-confined nitrogen vacancy center spin ensembles in diamond for quantum sensing. *Physical ReviewMaterials* **3**, 113802 (2019).

[700] Smith, J. M., Meynell, S. A., Bleszynski Jayich, A. C. & Meijer, J. Colour centre generation in diamond for quantum technologies. *Nanophotonics* **8**, 1889–1906 (2019).

[701] Tse, M. *et al.* Quantum-Enhanced Advanced LIGO Detectors in the Era of Gravitational-Wave Astronomy. *Physical Review Letters* **123**, 231107 (2019).

[702] Pedrozo-Peñafiel, E. *et al.* Entanglement on an optical atomic-clock transition. *Nature* **588**, 414–418 (2020).

[703] Robinson, J. M. *et al.* Direct comparison of two spin squeezed optical clocks below the quantum projection noise limit. *arXiv preprint arXiv:2211.08621* (2022).

[704] Foss-Feig, M., Gong, Z.-X., Gorshkov, A. V. & Clark, C. W. Entanglement and spin-squeezing without infinite-range interactions. *arXiv preprint arXiv:1612.07805* (2016).

[705] Gil, L. I. R., Mukherjee, R., Bridge, E. M., Jones, M. P. A. & Pohl, T. Spin Squeezing in a Rydberg Lattice Clock. *Physical Review Letters* **112**, 103601 (2014).

[706] Comparin, T., Mezzacapo, F., Robert-de Saint-Vincent, M. & Roscilde, T. Scalable Spin Squeezing from Spontaneous Breaking of a Continuous Symmetry. *Physical Review Letters* **129**, 113201 (2022).

[707] Young, J. T., Muleady, S. R., Perlin, M. A., Kaufman, A. M. & Rey, A. M. Enhancing spin squeezing using soft-core interactions. *Physical Review Research* **5**, L012033 (2023).

[708] Block, M. *et al.* A universal theory of spin squeezing. *arXiv preprint arXiv:2301.09636* (2023).

[709] Roscilde, T., Comparin, T. & Mezzacapo, F. Entangling dynamics from effective rotor–spin-wave separation in U(1)-symmetric quantum spin models. *Physical Review Letters* **131**, 160403 (2023).

[710] Bao, Y. *et al.* Dipolar spin-exchange and entanglement between molecules in an optical tweezer array. *Science* **382**, 1138–1143 (2023).

[711] Holland, C. M., Lu, Y. & Cheuk, L. W. On-demand entanglement of molecules in a reconfigurable optical tweezer array. *Science* **382**, 1143–1147 (2023).

[712] Christakis, L. *et al.* Probing site-resolved correlations in a spin system of ultracold molecules. *Nature* **614**, 64–69 (2023).

[713] Scholl, P. *et al.* Microwave Engineering of Programmable XXZ Hamiltonians in Arrays of Rydberg Atoms. *PRX Quantum* **3**, 020303 (2022).

[714] Scholl, P. *et al.* Quantum simulation of 2D antiferromagnets with hundreds of Rydberg atoms. *Nature* **595**, 233–238 (2021).

[715] Browaeys, A. & Lahaye, T. Many-body physics with individually controlled Rydberg atoms. *Nature Physics* **16**, 132–142 (2020).

[716] Barredo, D., de Léséleuc, S., Lienhard, V., Lahaye, T. & Browaeys, A. An atom-by-atom assembler of defect-free arbitrary two-dimensional atomic arrays. *Science* **354**, 1021–1023 (2016).

[717] Sørensen, A., Duan, L.-M., Cirac, J. I. & Zoller, P. Many-particle entanglement with Bose–Einstein condensates. *Nature* **409**, 63–66 (2001).

[718] Anderson, P. W. An Approximate Quantum Theory of the Antiferromagnetic Ground State. *Physical Review* **86**, 694–701 (1952).

[719] Anderson, P. W. *Basic Notions Of Condensed Matter Physics* (Westview Press, Boulder, CO, 1997).

[720] Kahanamoku-Meyer, G. D. & Wei, J. Gregdmeyer/dynamite: v0.3.0 (2023). URL `https://doi.org/10.5281/zenodo.7622981`.

[721] Muessel, W. *et al.* Twist-and-turn spin squeezing in Bose-Einstein condensates. *Physical Review A* **92**, 023603 (2015).

[722] Sorelli, G., Gessner, M., Smerzi, A. & Pezzè, L. Fast and optimal generation of entanglement in bosonic Josephson junctions. *Physical Review A* **99**, 022329 (2019).

[723] Eckner, W. J. *et al.* Realizing spin squeezing with rydberg interactions in a programmable optical clock. *Nature* **621**, 734–739 (2023).

[724] Hines, J. A. *et al.* Spin Squeezing by Rydberg Dressing in an Array of Atomic Ensembles. *Physical Review Letters* **131**, 063401 (2023).

[725] Franke, J. *et al.* Quantum-enhanced sensing on an optical transition via emergent collective quantum correlations. *Nature* **621**, 740–745 (2023).

[726] Norcia, M. A., Young, A. W. & Kaufman, A. M. Microscopic Control and Detection of Ultracold Strontium in Optical-Tweezer Arrays. *Physical Review X* **8**, 041054 (2018).

[727] Saskin, S. and Wilson, J. T. and Grinkemeyer, B. and Thompson, J. D. Narrow-Line Cooling and Imaging of Ytterbium Atoms in an Optical Tweezer Array. *Physical Review Letters* **122**, 143002 (2019).

[728] Madjarov, I. S. *et al.* An Atomic-Array Optical Clock with Single-Atom Readout. *Physical Review X* **9**, 041052 (2019).

[729] Young, A. W. *et al.* Half-minute-scale atomic coherence and high relative stability in a tweezer clock. *Nature* **588**, 408–413 (2020).

[730] Purcell, E. M. Spontaneous emission probabilities at radio frequencies. In Burstein, E. & Weisbuch, C. (eds.) *Confined Electrons and Photons: New Physics and Applications*, 839–839 (Springer US, Boston, MA, 1995).

[731] Houck, A. *et al.* Controlling the spontaneous emission of a superconducting transmon qubit. *Physical Review Letters* **101**, 080502 (2008).

[732] de Lange, G., Wang, Z., Riste, D., Dobrovitski, V. & Hanson, R. Universal dynamical decoupling of a single solid-state spin from a spin bath. *Science* **330**, 60–63 (2010).

[733] Tyryshkin, A. M. *et al.* Electron spin coherence exceeding seconds in high-purity silicon. *Nature Materials* **11**, 143–147 (2012).

[734] Klauder, J. & Anderson, P. Spectral diffusion decay in spin resonance experiments. *Physical Review* **125**, 912 (1962).

[735] Schweiger, A. & Jeschke, G. *Principles of pulse electron paramagnetic resonance* (Oxford University Press, Oxford, UK, 2001).

[736] Kofman, A. & Kurizki, G. Acceleration of quantum decay processes by frequent observations. *Nature* **405**, 546–550 (2000).

[737] Romach, Y. *et al.* Spectroscopy of surface-induced noise using shallow spins in diamond. *Physical Review Letters* **114**, 017601 (2015).

[738] Kleppner, D. Inhibited spontaneous emission. *Physical Review Letters* **47**, 233 (1981).

[739] Kotler, S., Akerman, N., Glickman, Y., Keselman, A. & Ozeri, R. Single-ion quantum lock-in amplifier. *Nature* **473**, 61–65 (2011).

[740] Bar-Gill, N. *et al.* Suppression of spin-bath dynamics for improved coherence of multi-spin-qubit systems. *Nature Communications* **3**, 1–6 (2012).

[741] Herzog, B. & Hahn, E. L. Transient nuclear induction and double nuclear resonance in solids. *Physical Review* **103**, 148–166 (1956).

[742] Kubo, R., Toda, M. & Hashitsume, N. *Statistical physics II: nonequilibrium statistical mechanics* (Springer-Verlag, Berlin Heidelberg, 1985).

[743] Salikhov, K., Dzuba, S.-A. & Raitsimring, A. M. The theory of electron spin-echo signal decay resulting from dipole-dipole interactions between paramagnetic centers in solids. *Journal of Magnetic Resonance (1969)* **42**, 255–276 (1981).

[744] Chiba, M. & Hirai, A. Electron spin echo decay behaviours of phosphorus doped silicon. *Journal of the Physical Society of Japan* **33**, 730–738 (1972).

[745] Altman, E., Demler, E. & Lukin, M. D. Probing many-body states of ultracold atoms via noise correlations. *Physical Review A* **70**, 013603 (2004).

[746] Hofferberth, S. *et al.* Probing quantum and thermal noise in an interacting many-body system. *Nature Physics* **4**, 489–495 (2008).

[747] Fel'dman, E. B. & Lacelle, S. Configurational averaging of dipolar interactions in magnetically diluted spin networks. *The Journal of Chemical Physics* **104**, 2000–2009 (1996).

[748] Sushkov, A. *et al.* Magnetic resonance detection of individual proton spins using quantum reporters. *Physical Review Letters* **113**, 197601 (2014).

[749] Ohno, K. *et al.* Engineering shallow spins in diamond with nitrogen delta-doping. *Applied Physics Letters* **101**, 082413 (2012).

[750] McLellan, C. A. *et al.* Patterned formation of highly coherent nitrogen-vacancy centers using a focused electron irradiation technique. *Nano Letters* **16**, 2450–2454 (2016).

[751] Yao, N. Y., Zaletel, M. P., Stamper-Kurn, D. M. & Vishwanath, A. A quantum dipolar spin liquid. *Nature Physics* **14**, 405–410 (2018).

[752] Semeghini, G. *et al.* Probing topological spin liquids on a programmable quantum simulator. *Science* **374**, 1242–1247 (2021).

[753] Anderson, P. W. & Weiss, P. R. Exchange narrowing in paramagnetic resonance. *Reviews of Modern Physics* **25**, 269–276 (1953).

[754] Engelsberg, M., Lowe, I. & Carolan, J. Nuclear-magnetic-resonance line shape of a linear chain of spins. *Physical Review B* **7**, 924 (1973).

[755] Cho, G. & Yesinowski, J. P. H and 19f multiple-quantum nmr dynamics in quasi-one-dimensional spin clusters in apatites. *The Journal of Physical Chemistry* **100**, 15716–15725 (1996).

[756] Cho, H., Ladd, T. D., Baugh, J., Cory, D. G. & Ramanathan, C. Multispin dynamics of the solid-state nmr free induction decay. *Physical Review B* **72**, 054427 (2005).

[757] Mims, W. Phase memory in electron spin echoes, lattice relaxation effects in caw o 4: Er, ce, mn. *Physical Review* **168**, 370 (1968).

[758] Abe, E., Itoh, K. M., Isoya, J. & Yamasaki, S. Electron-spin phase relaxation of phosphorus donors in nuclear-spin-enriched silicon. *Physical Review B* **70**, 033204 (2004).

[759] Zhong, M. *et al.* Optically addressable nuclear spins in a solid with a six-hour coherence time. *Nature* **517**, 177–180 (2015).

[760] de Sousa, R. & Sarma, S. D. Theory of nuclear-induced spectral diffusion: Spin decoherence of phosphorus donors in si and gaas quantum dots. *Physical Review B* **68**, 115322 (2003).

[761] Wang, Z.-H. & Takahashi, S. Spin decoherence and electron spin bath noise of a nitrogen-vacancy center in diamond. *Physical Review B* **87**, 115122 (2013).

[762] Bauch, E. *et al.* Decoherence of ensembles of nitrogen-vacancy centers in diamond. *Physical Review B* **102**, 134210 (2020).

[763] Hanson, R., Dobrovitski, V., Feiguin, A., Gywat, O. & Awschalom, D. Coherent dynamics of a single spin interacting with an adjustable spin bath. *Science* **320**, 352–355 (2008).

[764] Ernst, R. R. Nuclear magnetic double resonance with an incoherent radio-frequency field. *The Journal of Chemical Physics* **45**, 3845–3861 (1966).

[765] Hu, P. & Hartmann, S. R. Theory of spectral diffusion decay using an uncorrelated-sudden-jump model. *Physical Review B* **9**, 1–13 (1974).

[766] Cucchietti, F. M., Paz, J. P. & Zurek, W. H. Decoherence from spin environments. *Physical Review A* **72**, 052113 (2005).

[767] de Sousa, R. Electron spin as a spectrometer of nuclear-spin noise and other fluctuations. In *Electron spin resonance and related phenomena in low-dimensional structures*, 183–220 (Springer, 2009).

[768] Yang, W., Ma, W.-L. & Liu, R.-B. Quantum many-body theory for electron spin decoherence in nanoscale nuclear spin baths. *Reports on Progress in Physics* **80**, 016001 (2017). 1607.03993.

[769] Kogan, S. *Electronic noise and fluctuations in solids* (Cambridge University Press, Cambridge, UK, 2008).

[770] Witzel, W. & Sarma, S. D. Quantum theory for electron spin decoherence induced by nuclear spin dynamics in semiconductor quantum computer architectures: Spectral diffusion of localized electron spins in the nuclear solid-state environment. *Physical Review B* **74**, 035322 (2006).

[771] Choi, J. *et al.* Depolarization dynamics in a strongly interacting solid-state spin ensemble. *Physical Review Letters* **118**, 093601 (2017).

[772] Zhidomirov, G. & Salikhov, K. Contribution to the theory of spectral diffusion in magnetically diluted solids. *Soviet Journal of Experimental and Theoretical Physics* **29**, 1037 (1969).

[773] Glasbeek, M. & Hond, R. Phase relaxation of photoexcited triplet spins in cao. *Physical Review B* **23**, 4220 (1981).

[774] Witzel, W. M., Carroll, M. S., Cywiński, Ł. & Sarma, S. D. Quantum decoherence of the central spin in a sparse system of dipolar coupled spins. *Physical Review B* **86**, 035452 (2012).

[775] Belthangady, C. *et al.* Dressed-State Resonant Coupling between Bright and Dark Spins in Diamond. *Physical Review Letters* **110**, 157601 (2013).

[776] Laraoui, A. & Meriles, C. A. Approach to Dark Spin Cooling in a Diamond Nanocrystal. *ACS Nano* **7**, 3403–3410 (2013).

[777] Burin, A. L. Many-body delocalization in a strongly disordered system with long-range interactions: Finite-size scaling. *Physical Review B* **91**, 094202 (2015).

[778] Hartmann, S. & Hahn, E. Nuclear double resonance in the rotating frame. *Physical Review* **128**, 2042 (1962).

[779] Cappellaro, P., Ramanathan, C. & Cory, D. G. Dynamics and control of a quasi-one-dimensional spin system. *Physical Review A* **76**, 032317 (2007).

[780] Lukin, D. M., Guidry, M. A. & Vučković, J. Integrated quantum photonics with silicon carbide: Challenges and prospects. *PRX Quantum* **1**, 020102 (2020).

[781] Rosskopf, T. *et al.* Investigation of surface magnetic noise by shallow spins in diamond. *Physical Review Letters* **112**, 147602 (2014).

[782] Aharonovich, I., Englund, D. & Toth, M. Solid-state single-photon emitters. *Nature Photonics* **10**, 631–641 (2016).

[783] Togan, E. *et al.* Quantum entanglement between an optical photon and a solid-state spin qubit. *Nature* **466**, 730–734 (2010).

[784] Pompili, M. *et al.* Realization of a multinode quantum network of remote solid-state qubits. *Science* **372**, 259–264 (2021).

[785] Zu, C. *et al.* Experimental realization of universal geometric quantum gates with solid-state spins. *Nature* **514**, 72–75 (2014).

[786] Fuchs, G., Burkard, G., Klimov, P. & Awschalom, D. A quantum memory intrinsic to single nitrogen–vacancy centres in diamond. *Nature Physics* **7**, 789–793 (2011).

[787] Sukachev, D. D. *et al.* Silicon-vacancy spin qubit in diamond: a quantum memory exceeding 10 ms with single-shot state readout. *Physical Review Letters* **119**, 223602 (2017).

[788] Koehl, W. F., Buckley, B. B., Heremans, F. J., Calusine, G. & Awschalom, D. D. Room temperature coherent control of defect spin qubits in silicon carbide. *Nature* **479**, 84–87 (2011).

[789] Nagy, R. *et al.* High-fidelity spin and optical control of single silicon-vacancy centres in silicon carbide. *Nature Communications* **10**, 1954 (2019).

[790] Hensen, B. *et al.* Loophole-free bell inequality violation using electron spins separated by 1.3 kilometres. *Nature* **526**, 682–686 (2015).

[791] Hsieh, S. *et al.* Imaging stress and magnetism at high pressures using a nanoscale quantum sensor. *Science* **366**, 1349–1354 (2019).

[792] Thiel, L. *et al.* Probing magnetism in 2d materials at the nanoscale with single-spin microscopy. *Science* **364**, 973–976 (2019).

[793] Tetienne, J.-P. Quantum sensors go flat. *Nature Physics* **17**, 1074–1075 (2021).

[794] Zhong, D. *et al.* Layer-resolved magnetic proximity effect in van der Waals heterostructures. *Nature Nanotechnology* **15**, 187–191 (2020).

[795] Healey, A. *et al.* Quantum microscopy with van der Waals heterostructures. *Nature Physics* **19**, 87–91 (2023).

[796] Broadway, D. A. *et al.* Imaging domain reversal in an ultrathin van der Waals ferromagnet. *Advanced Materials* **32**, 2003314 (2020).

[797] Gottscholl, A. *et al.* Room temperature coherent control of spin defects in hexagonal boron nitride. *Science Advances* **7**, eabf3630 (2021).

[798] Gottscholl, A. *et al.* Spin defects in hbn as promising temperature, pressure and magnetic field quantum sensors. *Nature Communications* **12**, 4480 (2021).

[799] Grosso, G. *et al.* Tunable and high-purity room temperature single-photon emission from atomic defects in hexagonal boron nitride. *Nature Communications* **8**, 705s (2017).

[800] Kianinia, M., White, S., Fröch, J. E., Bradac, C. & Aharonovich, I. Generation of spin defects in hexagonal boron nitride. *ACS photonics* **7**, 2147–2152 (2020).

[801] Stern, H. L. *et al.* Room-temperature optically detected magnetic resonance of single defects in hexagonal boron nitride. *Nature Communications* **13**, 618 (2022).

[802] Ramsay, A. J. *et al.* Coherence protection of spin qubits in hexagonal boron nitride. *Nature Communications* **14**, 461 (2023).

[803] Ivády, V. *et al.* Ab initio theory of the negatively charged boron vacancy qubit in hexagonal boron nitride. *npj Computational Materials* **6**, 41 (2020).

[804] Gao, X. *et al.* Nuclear spin polarization and control in hexagonal boron nitride. *Nature Materials* 1024–1028 (2022).

[805] Huang, M. *et al.* Wide field imaging of van der Waals ferromagnet Fe_3GeTe_2 by spin defects in hexagonal boron nitride. *Nature Communications* **13**, 5369 (2022).

[806] Fröch, J. E. *et al.* Coupling spin defects in hexagonal boron nitride to monolithic bullseye cavities. *Nano Letters* **21**, 6549–6555 (2021).

[807] Kumar, P. *et al.* Magnetic imaging with spin defects in hexagonal boron nitride. *Physical Review Applied* **18**, L061002 (2022).

[808] Geim, A. K. & Grigorieva, I. V. Van der Waals heterostructures. *Nature* **499**, 419–425 (2013).

[809] Novoselov, K., Mishchenko, o. A., Carvalho, o. A. & Castro Neto, A. 2d materials and van der Waals heterostructures. *Science* **353**, aac9439 (2016).

[810] Jin, C. *et al.* Interlayer electron–phonon coupling in wse2/hbn heterostructures. *Nature Physics* **13**, 127–131 (2017).

[811] Gurram, M., Omar, S. & van Wees, B. J. Bias induced up to 100% spin-injection and detection polarizations in ferromagnet/bilayer-hbn/graphene/hbn heterostructures. *Nature Communications* **8**, 248 (2017).

[812] Li, C. *et al.* Integration of hbn quantum emitters in monolithically fabricated waveguides. *ACS Photonics* **8**, 2966–2972 (2021).

[813] Dwyer, B. L. *et al.* Probing spin dynamics on diamond surfaces using a single quantum sensor. *PRX Quantum* **3**, 040328 (2022).

[814] Rezai, K., Choi, S., Lukin, M. D. & Sushkov, A. O. Probing dynamics of a two-dimensional dipolar spin ensemble using single qubit sensor. *arXiv preprint arXiv:2207.10688* (2022).

[815] Bordia, P. *et al.* Probing slow relaxation and many-body localization in two-dimensional quasiperiodic systems. *Physical Review X* **7**, 041047 (2017).

[816] Schwartz, T., Bartal, G., Fishman, S. & Segev, M. Transport and anderson localization in disordered two-dimensional photonic lattices. *Nature* **446**, 52–55 (2007).

[817] Haykal, A. *et al.* Decoherence of V_B^- spin defects in monoisotopic hexagonal boron nitride. *Nature Communications* **13**, 4347 (2022).

[818] Gao, X. *et al.* High-contrast plasmonic-enhanced shallow spin defects in hexagonal boron nitride for quantum sensing. *Nano Letters* **21**, 7708–7714 (2021).

[819] Liu, W. *et al.* Coherent dynamics of multi-spin V_B^- center in hexagonal boron nitride. *Nature Communications* **13**, 5713 (2022).

[820] Yang, W. & Liu, R.-B. Quantum many-body theory of qubit decoherence in a finite-size spin bath. *Physical Review B* **78**, 085315 (2008).

[821] Du, J. *et al.* Preserving electron spin coherence in solids by optimal dynamical decoupling. *Nature* **461**, 1265–1268 (2009).

[822] Pham, L. M. *et al.* Enhanced solid-state multispin metrology using dynamical decoupling. *Physical Review B* **86**, 045214 (2012).

[823] Ben'Attar, K., Farfurnik, D. & Bar-Gill, N. Hamiltonian engineering of general two-body spin-1/2 interactions. *Physical Review Research* **2**, 013061 (2020).

[824] Ziegler, J. F., Ziegler, M. D. & Biersack, J. P. Srim–the stopping and range of ions in matter (2010). *Nuclear Instruments and Methods in Physics Research Section B: Beam Interactions with Materials and Atoms* **268**, 1818–1823 (2010).

[825] Mrózek, M. *et al.* Longitudinal spin relaxation in nitrogen-vacancy ensembles in diamond. *EPJ Quantum Technology* **2**, 22 (2015).

[826] Aslam, N., Waldherr, G., Neumann, P., Jelezko, F. & Wrachtrup, J. Photo-induced ionization dynamics of the nitrogen vacancy defect in diamond investigated by single-shot charge state detection. *New Journal of Physics* **15**, 013064 (2013).

[827] Weston, L., Wickramaratne, D., Mackoit, M., Alkauskas, A. & Van de Walle, C. Native point defects and impurities in hexagonal boron nitride. *Physical Review B* **97**, 214104 (2018).

[828] Razinkovas, L., Maciaszek, M., Reinhard, F., Doherty, M. W. & Alkauskas, A. Photoionization of negatively charged nv centers in diamond: Theory and ab initio calculations. *Physical Review B* **104**, 235301 (2021).

[829] Kucsko, G. *et al.* Critical thermalization of a disordered dipolar spin system in diamond. *Physical Review Letters* **121**, 023601 (2018).

[830] Mittiga, T. *et al.* Imaging the local charge environment of nitrogen-vacancy centers in diamond. *Physical Review Letters* **121**, 246402 (2018).

[831] Block, M. *et al.* Optically enhanced electric field sensing using nitrogen-vacancy ensembles. *Physical Review Applied* **16**, 024024 (2021).

[832] Yamano, H. *et al.* Charge state stabilization of shallow nitrogen vacancy centers in diamond by oxygen surface modification. *Japanese Journal of Applied Physics* **56**, 04CK08 (2017).

[833] Grotz, B. *et al.* Charge state manipulation of qubits in diamond. *Nature Communications* **3**, 729 (2012).

[834] Doi, Y. *et al.* Deterministic electrical charge-state initialization of single nitrogen-vacancy center in diamond. *Physical Review X* **4**, 011057 (2014).

[835] White, S. J. *et al.* Electrical control of quantum emitters in a van der Waals heterostructure. *Light: Science & Applications* **11**, 186 (2022).

[836] Su, C. *et al.* Tuning colour centres at a twisted hexagonal boron nitride interface. *Nature Materials* **21**, 896–902 (2022).

[837] Dolde, F. *et al.* Electric-field sensing using single diamond spins. *Nature Physics* **7**, 459–463 (2011).

[838] Bian, K. *et al.* Nanoscale electric-field imaging based on a quantum sensor and its charge-state control under ambient condition. *Nature Communications* **12**, 2457 (2021).

[839] Barson, M. S. *et al.* Nanoscale vector electric field imaging using a single electron spin. *Nano Letters* **21**, 2962–2967 (2021).

[840] Kreuzer, H. J. Nonequilibrium thermodynamics and its statistical foundations. *Oxford and New York* (1981).

[841] Fischetti, M. V. Theory of electron transport in small semiconductor devices using the pauli master equation. *Journal of Applied Physics* **83**, 270–291 (1998).

[842] Fischetti, M. Master-equation approach to the study of electronic transport in small semiconductor devices. *Physical Review B* **59**, 4901 (1999).

[843] Robledo, L., Bernien, H., Van Der Sar, T. & Hanson, R. Spin dynamics in the optical cycle of single nitrogen-vacancy centres in diamond. *New Journal of Physics* **13**, 025013 (2011).

[844] Tetienne, J. *et al.* Magnetic-field-dependent photodynamics of single nv defects in diamond: an application to qualitative all-optical magnetic imaging. *New Journal of Physics* **14**, 103033 (2012).

[845] Martin, P. C., Siggia, E. D. & Rose, H. A. Statistical dynamics of classical systems. *Physical Review A* **8**, 423–437 (1973).

[846] Fisher, D. S. Random walks in random environments. *Physical Review A* **30**, 960–964 (1984).

[847] Yukawa, H. On the interaction of elementary particles. i. *Proceedings of the Physico-Mathematical Society of Japan. 3rd Series* **17**, 48–57 (1935).

[848] Suter, D., Liu, S., Baum, J. & Pines, A. Multiple quantum nmr excitation with a one-quantum Hamiltonian. *Chemical Physics* **114**, 103 – 109 (1987).

[849] Cho, H., Cory, D. & Ramanathan, C. Spin counting experiments in the dipolar-ordered state. *The Journal of Chemical Physics* **118**, 3686–3691 (2003).

[850] Wigner, E. *Group theory: and its application to the quantum mechanics of atomic spectra* (Academic Press, New York, 1959).

[851] van Beek, J. D., Carravetta, M., Antonioli, G. C. & Levitt, M. H. Spherical tensor analysis of nuclear magnetic resonance signals. *The Journal of Chemical Physics* **122** (2005).

[852] Doyon, B. Lecture notes on generalised hydrodynamics. *SciPost Phys. Lect. Notes 18* (2020).

[853] Hohenberg, P. C. & Halperin, B. I. Theory of dynamic critical phenomena. *Reviews of Modern Physics* **49**, 435–479 (1977).

[854] Nakano, H. & Takahashi, M. Quantum Heisenberg chain with long-range ferromagnetic interactions at low temperatures. *Journal of the Physical Society of Japan* **63**, 926–933 (1994).

[855] Nakano, H. & Takahashi, M. Quantum Heisenberg model with long-range ferromagnetic interactions. *Physical Review B* **50**, 10331–10334 (1994).

[856] Haldane, F. D. M. Exact Jastrow-Gutzwiller resonating-valence-bond ground state of the spin-$\frac{1}{2}$ antiferromagnetic Heisenberg chain with $1/r^2$ exchange. *Physical Review Letters* **60**, 635–638 (1988).

[857] Haldane, F. D. M. "spinon gas" description of the s=1/2 heisenberg chain with inverse-square exchange: Exact spectrum and thermodynamics. *Physical Review Letters* **66**, 1529–1532 (1991).

[858] Reif, F. *Fundamentals of statistical and thermal physics* (McGraw-Hill, New York, 1965).

[859] Fishman, M., White, S. & Stoudenmire, E. The itensor software library for tensor network calculations. *SciPost Physics Codebases* 4 (2022).

[860] Dobrovitski, V. V., Feiguin, A. E., Hanson, R. & Awschalom, D. D. Decay of Rabi Oscillations by Dipolar-Coupled Dynamical Spin Environments. *Physical Review Letters* **102**, 237601 (2009).

[861] Wang, Z.-H., de Lange, G., Ristè, D., Hanson, R. & Dobrovitski, V. Comparison of dynamical decoupling protocols for a nitrogen-vacancy center in diamond. *Physical Review B* **85**, 155204 (2012).

[862] Cywiński, L., Lutchyn, R. M., Nave, C. P. & Das Sarma, S. How to enhance dephasing time in superconducting qubits. *Physical Review B* **77**, 174509 (2008).

[863] Joos, M., Bluvstein, D., Lyu, Y., Weld, D. & Bleszynski Jayich, A. Protecting qubit coherence by spectrally engineered driving of the spin environment. *npj Quantum Information* **8**, 47 (2022).

[864] Meystre, P. & Sargent, M. *Elements of Quantum Optics* (Springer-Verlag, Berlin Heidelberg, 2007).